



Structure-Property Relationships of  
Selected Copper Chalcogenide  
Thermoelectric Materials

A thesis submitted for the degree of Doctor of Philosophy

**School of Chemistry, Food and Pharmacy**

Sebastian Long

June 2020



## Declaration

I confirm that this is my own work and the use of all material from other sources has been properly and fully acknowledged.

Sebastian Long



## Abstract

This thesis describes investigations of copper-chalcogenide thermoelectrics and the application of advanced structural characterization techniques to explore structure-property correlations.

An *in-situ* cell was designed and developed to study the electrical transport properties and structure of thermoelectric materials. It allows for the simultaneous collection of powder neutron diffraction data and electrical transport data as a function of temperature. An experiment on  $\text{Cu}_{2.125}\text{Ge}_{0.875}\text{ZnSe}_4$  demonstrated that the cell can reliably monitor changes in the structure and thermoelectric properties.

The *in-situ* cell was exploited to investigate n-type thermoelectric materials in the Cu-Fe-S system. A study of  $\text{CuFeS}_2$  shows the influence of different structural phases on the Seebeck coefficient. Meanwhile, the origins of anomalies in the electrical transport property data of samples with compositions  $\text{Cu}_9\text{Fe}_8\text{S}_{16}$  and  $\text{Cu}_9\text{Fe}_9\text{S}_{16}$  are revealed. The observed local maximum in the power factors are linked to structural phase transitions over temperatures of  $T = 425$  to  $500$  K.

Total neutron scattering experiments on bornite ( $\text{Cu}_5\text{FeS}_4$ ) reveal the nature of the copper and iron ordering within its three structural phases. The transition at *ca.* 475 K can be described by a partial disordering of the iron and vacancies, the transition at *ca.* 530 K leads to full disorder of the cations and vacancies. Following this, the thermoelectric performance of bornite was enhanced by introducing small deviations from the ideal stoichiometry. The thermoelectric figure of merit was improved from  $ZT=0.44$  in  $\text{Cu}_5\text{FeS}_4$  to  $ZT=0.79$  in  $\text{Cu}_{4.968}\text{Fe}_{0.972}\text{S}_4$  at 550 K.

The low-temperature structure of the high-performance thermoelectric tetrahedrite  $(\text{Cu}^{2+})_2(\text{Cu}^+)_{10}(\text{Sb}^{3+})_4(\text{S}^{2-})_{13}$  has been determined and the Cu(II) species located within the structure. This has allowed the origin of the magnetic properties of the material to be understood for the first time. This collection of studies on thermoelectric copper sulphides will contribute to bringing us closer to realising low-cost, low-toxicity thermoelectric modules.

## Acknowledgements

First of all I would like to thank my supervisors, **Prof. Anthony Powell, Dr. Paz Vaqueiro** and **Dr. Stephen Hull**. They have truly been a pleasure to work with. Their valued guidance and support during this studentship has helped me to grow and improve. This work would not have been possible without them.

I would also like to thank the University of Reading and the ISIS Neutron Facility/ STFC for financial support provided for this studentship.

I cannot understate the excellence in support that I have received from the staff at the ISIS neutron facility. There are many people to thank for their work on individual projects.

**Colin Offer** and his team for their invaluable drawings and design of the cell itself. **Jamie Nutter, Jon Bones** and the **Electronics Support Group** for fitting the electronics of the cell. **Chris Goodway, Paul McIntyre, Adam Sears** from the sample environment team for fitting and testing the cell. **Tom Williensen** and **Gareth Howells** for their support with software for running the cell and the hardware. As well as the continued support during the testing, development and experimental stages on this project.

**Dr. Ron Smith** for all his assistance and training during the many experiments on POLARIS which often seemed to land on a weekend.

**Dr. Helen Playford** for her help during the total scattering experiment and for all of the support in processing the data and running the calculations.

**Dr. Fabio Orlandi** for his assistance with the neutron diffraction experiments on WISH.

**Dr. Gavin Stenning** for the low temperature property measurements on the tetrahedrite samples at the ISIS facility materials characterisation laboratory.

The **British Council** for funding a trip to the Indo-UK thermoelectric workshop and the **UK Thermoelectric Network** for funding a visit to the thermoelectric network meeting.

The **CAF Lab** at the University of Reading for allowing me to use the SEM, XRD and DSC facilities. **Ms. Amanpreet Kuar** for her help and training using the SEM and the sputter coating instruments. **Mr. Nick Spencer** for his support with the X-ray diffraction instruments.

**Mr. Mark McClemon** for supplying many silica tubes often at a moments notice when prepping samples for neutrons experiments. As well as being available for a good chinwag if I needed a break from work.

**Mike Charij, Gary Yeo and Andy Whittam** for helping to keep the equipment in the laboratory in working condition.

The solid state chemistry group and its members over the past 4 years for their friendship and guidance. **Jethro, Jesus, John, Sarah Makin, Panos, Gabin and Jon**. A further thanks goes to Jon for submitting on my behalf.

My darling **Laura Mills** for helping me from the start to the finish of this PhD, keeping me motivated, happy and working to my fullest. You've made this journey a whole lot more enjoyable.

**Shane Bourne** for being a great housemate and writing the python script used to extract the electrical data from experiments on the cell.

**Kane McQuaid** for being a great friend for the past 8 years and taking the journey of the PhD together with me at University of Reading. I'm sure that sharing in the stress and joys of it together has helped us both.

**Gary** for proof reading.

My friends and family for their continued support and encouragement outside of the university environment which has kept me going.



# Contents

<b>Chapter 1 Introduction.....</b>	<b>1</b>
1.1. Climate Change in Recent Years .....	1
1.1.1. Importance of Cost for Low-Carbon Energy Resources .....	2
1.2. Waste Heat Energy Harvesting Using Thermoelectric Materials .....	2
1.2.1. Thermoelectric Generators (TEG) .....	3
1.2.2. Current and Possible Applications .....	5
1.2.3. Thermoelectric Efficiency and Figure of Merit .....	6
1.2.4. Seebeck Coefficient, $S$ .....	8
1.2.5. Electrical Resistivity, $\rho$ .....	8
1.2.5.1. Ionic Conductivity.....	9
1.2.6. Thermal Conductivity, $\kappa_t$ .....	9
1.3. Electronic Structure of Crystalline Solids.....	10
1.3.1. Electronic Bands and Density of States (DOS).....	11
1.3.2. Semiconductors .....	12
1.3.3. Design Strategies to Improve the Power Factor.....	13
1.3.4. Design Strategies to Reduce Thermal Conductivity .....	16
1.4. High Performance Bulk Thermoelectrics.....	17
1.5. Copper-Chalcogenide Thermoelectrics.....	18
1.5.1. Binary Copper Chalcogenides, $\text{Cu}_{2-\delta}\text{Q}$ ( $\text{Q} = \text{S}, \text{Se}$ and $\text{Te}$ ).....	19
1.5.2. Zinc-Blende Type Chalcogenides .....	20
1.5.2.1. Ternary Copper Chalcogenide, Chalcopyrite, $\text{CuFeS}_2$ .....	21
1.5.2.2. Other Ternary Copper Chalcogenides.....	22
1.5.2.3. Quaternary Copper Chalcogenide Thermoelectrics .....	24
1.5.3. Cation-Rich Copper Zinc-Blende Phases.....	25
1.5.3.1. Colusite .....	25
1.5.3.2. Talnakhite and Mooihoekite .....	27
1.5.3.3. Bornite.....	30
1.5.4. Other Complex Copper Chalcogenide Mineral Phases.....	31
1.5.4.1. Tetrahedrite .....	31
1.5.4.2. Argyrodites.....	32
1.6. Structural Transitions in Cu-based Chalcogenides .....	34
1.7. Aims of This Work.....	34
<b>Chapter 2 - Experimental and Synthetic Methods.....</b>	<b>37</b>
2.1. Synthetic Methods.....	37

2.1.1.	Considerations in Synthesis.....	37
2.1.2.	High-Temperature Techniques .....	37
2.1.3.	Mechanochemical Techniques.....	38
2.1.4.	Sample Consolidation.....	39
2.2.	Structural Analysis and Characterisation.....	40
2.2.1.	Powder X-ray Diffraction.....	41
2.2.1.1.	The Bruker D8 Advance Diffractometer .....	42
2.2.2.	Powder Neutron Diffraction .....	43
2.2.2.1.	The ISIS Neutron Facility.....	46
2.2.2.2.	The POLARIS Neutron Diffractometer.....	46
2.2.2.3.	The WISH Neutron Diffractometer .....	47
2.2.3.	X-Ray and Neutron Interaction with Matter.....	48
2.2.4.	The Rietveld Method.....	49
2.2.5.	Polyhedral Distortion Parameters .....	50
2.2.6.	The Le Bail Method.....	51
2.2.7.	Total Scattering.....	52
2.2.7.1.	PDF Analysis.....	52
2.3.	Characterisation of Thermoelectric Properties .....	54
2.3.1.	Electrical Resistivity.....	54
2.3.1.1.	4-Probe Resistance Measurement.....	54
2.3.1.2.	The Van der Pauw Method.....	56
2.3.2.	Seebeck Coefficient Measurement .....	57
2.3.3.	Linseis LSR-3.....	58
2.4.	Thermal Characterisation of Thermoelectric Materials.....	59
2.4.1.	Differential Scanning Calorimetry (DSC).....	59
2.4.2.	Thermal Diffusivity .....	60
2.4.2.1.	Dulong-Petit Heat Law .....	61
2.5.	Energy Dispersive X-ray (EDX) Spectroscopy .....	62
2.6.	Superconducting Quantum Interface Device (SQUID) Magnetometry .....	62
<b>Chapter 3 Seebeck-Resistance-Diffraction <i>in-situ</i> Cell: Development and Structure-Property Studies.....</b>		<b>65</b>
3.1.	Introduction .....	65
3.2.	Final Design of the Cell.....	66
3.3.	Testing and Development of the In-Situ Cell.....	67
3.3.1.	Minimising Contact Resistances .....	72
3.3.2.	Preliminary Diffraction Experiments on Tetrahedrite, $\text{Cu}_{12}\text{Sb}_4\text{S}_{13}$ .....	73

3.4.	In-Situ Investigations into Copper-Chalcogenide Thermoelectrics .....	76
3.5.	Kesterite Thermoelectrics, $\text{Cu}_2\text{ZnGeSe}_4$ .....	76
3.5.1.	Experimental Procedures for the In-Situ Investigations of $\text{Cu}_{2.125}\text{Ge}_{0.875}\text{ZnSe}_4$ .....	77
3.5.2.	Diffraction Results from the Experiment on $\text{Cu}_{2.125}\text{Ge}_{0.875}\text{ZnSe}_4$ .....	78
3.5.3.	Electrical Behaviour of $\text{Cu}_{2.125}\text{ZnGe}_{0.875}\text{Se}_4$ .....	83
3.6.	In-Situ Experiments Investigating some Cu-Fe-S Based Thermoelectrics .....	84
3.6.1.	Experimental Procedure for ‘ $\text{CuFeS}_2$ ’.....	85
3.6.2.	Results from In-Situ Neutron Diffraction Experiments on ‘ $\text{CuFeS}_2$ ’ .....	86
3.6.3.	Evolution of Structural Phases as a Function of Temperature in ‘ $\text{CuFeS}_2$ ’ .....	86
3.6.4.	Influence on the Thermoelectric Properties of Chalcopyrite .....	91
3.7.	Mooihoekite and Talnakhite Experiments .....	94
3.7.1.	Experimental Procedure .....	94
3.7.2.	Room Temperature Structure of Cu-Fe-S Samples.....	96
3.7.3.	Magnetic Diffraction of the Different Structural Phases.....	97
3.8.	Variable Temperature Neutron Diffraction of Chalcopyrite, $\text{Cu}_9\text{Fe}_8\text{S}_{16}$ .....	101
3.8.1.	Temperature Dependent Electrical Transport Properties of Chalcopyrite, $\text{Cu}_9\text{Fe}_8\text{S}_{16}$	104
3.9.	Observations from the Variable Temperature Diffraction Experiment on Talnakhite, $\text{Cu}_9\text{Fe}_9\text{S}_{16}$ .....	105
3.9.1.	Temperature Dependence of the Electrical Properties of Talnakhite, $\text{Cu}_9\text{Fe}_9\text{S}_{16}$ .....	108
3.10.	Conclusions .....	109
<b>Chapter 4 – The Long-Range and Short-Range Structure of Stoichiometric Bornite, <math>\text{Cu}_5\text{FeS}_4</math></b>		
.....		<b>115</b>
4.1	Crystal Structure of Bornite .....	115
4.1.1	Synthesis and Experimental .....	116
4.2	Diffraction Results and Discussion.....	117
4.2.1	Room Temperature X-ray Diffraction.....	117
4.2.2	Advantages of Neutron Diffraction for a Mixed Cu-Fe Material .....	117
4.2.3	Ambient-Temperature Orthorhombic Phase of Bornite, 4a .....	118
4.2.4	High-Temperature Cubic Phase of Bornite, a .....	125
4.2.5	Intermediate Cubic Phase of Bornite, 2a.....	130
4.2.5.1	Structural Models Used in Refinements.....	130
4.2.5.2	Cation Ordering in Intermediate Bornite, 2a.....	134
4.3	Pair Distribution Function Analysis of Bornite.....	137
4.3.1	Experimental Procedure and Data Preparation .....	137
4.3.2	Insights into the Copper/Iron Ordering from Total Scattering Experiments.....	138
4.3.2.1	Diagrammatic Representation of Structural Models Considered for PDF Analysis..	138

4.3.3	Results from PDF Analysis of Ambient Temperature Bornite, 4a .....	139
4.3.3.1	Iron Ordering in Ambient-Temperature Bornite 4a.....	141
4.3.4	Results from PDF Analysis of Intermediate Bornite, 2a .....	145
4.3.4.1	Iron Ordering in Intermediate Bornite, 2a .....	147
4.3.5	Results from PDF Analysis of High-Temperature Bornite, a.....	150
4.3.6	Change of Local Structure with Temperature .....	152
4.4	Conclusions .....	154
<b>Chapter 5 Structure and Thermoelectric Properties of Non-Stoichiometric Bornite.....</b>		<b>157</b>
5.1.	Introduction .....	157
5.2.	Experimental Procedure .....	157
5.3.	Sample Composition and Phase Analysis .....	160
5.3.1.	Phase Analysis of Powder X-ray Diffraction Data.....	160
5.3.2.	Composition and its Influence on Phase Transition Temperatures .....	162
5.4.	Variable Temperature Neutron Diffraction of Non-Stoichiometric Bornite .....	164
5.4.1.	Structural Refinement Constraints and Parameters .....	165
5.4.2.	Ambient Temperature Phase .....	165
5.4.2.1.	Cation Disorder in ZB Sub-Cells at Ambient Temperature .....	165
5.4.2.2.	Refinement Constraints Used .....	169
5.4.2.3.	Behaviour of Cations within ZB and AF Sub-Cells .....	169
5.4.3.	Cation Disorder in the Intermediate Temperature Phase.....	171
5.4.3.1.	Constraints used During Refinement.....	171
5.4.3.2.	Results from Rietveld Analysis of Intermediate Bornites .....	172
5.4.4.	Structure of the High-Temperature Phase .....	176
5.4.4.1.	Constraints Used in Refinements.....	176
5.4.4.2.	Results from Rietveld Analysis of the High-Temperature Phase of Bornite, a.....	179
5.4.5.	Variable Temperature Observations from Neutron Diffraction .....	179
5.4.5.1.	Evolution of Structural Phases .....	179
5.4.5.2.	Changes in Lattice Parameters .....	181
5.5.	Thermoelectric Properties of Chemically Substituted Bornite .....	183
5.5.1.	Performance Over the Temperature Range $T = 300$ to $600$ K.....	183
5.5.1.1.	Thermoelectric Properties of Series 1, $\text{Cu}_{5-x}\text{FeS}_4$ , ( $x > 0$ ) .....	183
5.5.2.	Thermoelectric Properties of Series 2, $\text{Cu}_{5+y}\text{Fe}_{1-y}\text{S}_4$ , ( $y > 0$ ) .....	185
5.5.3.	Thermoelectric Properties of Series 3, $\text{Cu}_{4.94+z}\text{Fe}_{1-z}\text{S}_4$ , ( $z > 0$ ).....	186
5.5.4.	High-Temperature Performance of Substituted Bornite.....	188
5.5.5.	Stability and Application of Non-Stoichiometric Bornite .....	190
5.5.6.	Influence of Cu(II) on the Thermoelectric Properties .....	190

5.5.7.	Linking the Changes in Structural and Physical Behaviour.....	192
5.6.	Conclusions.....	195
<b>Chapter 6</b>	<b>Structural characterisation of tetrahedrite at low temperatures .....</b>	<b>197</b>
6.1.	Introduction.....	197
6.2.	Experimental Procedure.....	198
6.3.	Diffraction Results and Analysis .....	199
6.3.1.	Phase Analysis at Room Temperature .....	199
6.3.2.	Variable Temperature Neutron Diffraction.....	200
6.3.2.1.	Structure of the Low-Temperature Phase of Tetrahedrite.....	205
6.3.2.2.	Temperature Dependence of Cu-S Bonding Parameters.....	206
6.3.2.3.	Changes in the Behaviour of the Cu(2)-S Bond Distances .....	206
6.4.	Investigating Charge Ordering within Tetrahedrite .....	210
6.4.1.	Copper-Copper Interactions in the Low-Temperature Structure.....	210
6.4.2.	Temperature Dependence of the Atomic Displacement Parameters.....	213
6.5.	Physical Properties.....	213
6.6.	Conclusions.....	216
<b>Chapter 7</b>	<b>Conclusions and Further Work.....</b>	<b>218</b>
7.1.	Diffraction Resistance Seebeck Cell.....	218
7.2.	Chalcopyrite Related Samples of the Cu-Fe-S System.....	219
7.3.	Structural and Thermoelectric Behaviour of Bornite.....	220
7.4.	Structural Observations in Tetrahedrite .....	222
7.5.	Further Work.....	222



# Chapter 1 Introduction

## 1.1. Climate Change in Recent Years

One of the biggest challenges that all the inhabitants of Earth are currently faced with is the threat posed by anthropogenic global warming. The reports by USDOE provide data on the global CO<sub>2</sub> emissions from human activity over the last *ca.* 260 years.<sup>1</sup> These data have been used to produce Figure 1-1(a,b) which reveals an almost exponential growth in the emissions and atmospheric concentration of carbon dioxide (Figure 1-1(a,b)).<sup>2</sup> Global average temperature records over the past 167 years are presented in Figure 1-1(b) and they show that the average global temperature is increasing.<sup>3</sup> It is widely accepted within the scientific community that the rising temperature is due to the increasing level of greenhouse gases. If average global temperatures continue to increase at their current rate, then the Earth may face catastrophic consequences in the next 50-100 years. The effects of this are already being seen in the sea ice volume.<sup>4,5</sup>

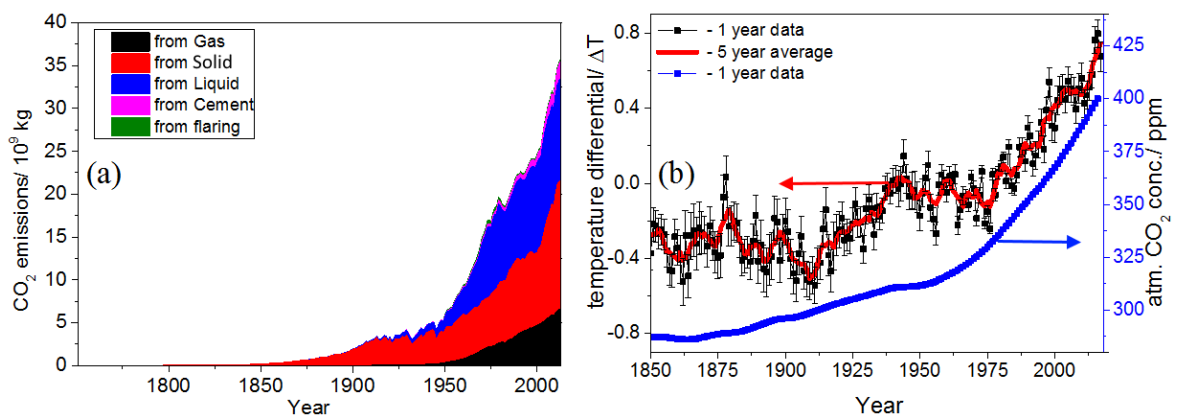


**Figure 1-1** – Yearly data for: (a) CO<sub>2</sub> emissions from sources of human activity. (b) Global average temperature ( $\Delta T$ / K) and CO<sub>2</sub> concentration in the atmosphere. Zero in the global temperature differential is the global average temperature in the pre-industrial era.

The burning of fossil fuels produces nearly all of the CO<sub>2</sub> emissions responsible for the increasing global temperatures.<sup>1</sup> Climate models predict that global average temperatures will increase by up to 4 K higher than pre-industrial revolution values if action is not taken to combat increasing emissions.<sup>6</sup> This is because there is an ever increasing human population and reliance on energy.<sup>7</sup> Therefore, it is critical that we make our methods of producing energy more efficient or that we find alternative methods of producing energy. Technologies which do so should be competitively priced compared to fossil fuels and should aim to reduce the CO<sub>2</sub> emissions per unit energy during their operating life-cycle.

### ***1.1.1. Importance of Cost for Low-Carbon Energy Resources***

Current energy technologies that are classified as either renewable or low emission sources include traditional biofuels, hydropower, wave and tidal, nuclear, wind, solar, and geothermal. There has been a huge growth in the amount of energy produced from renewable sources over the past 50 years.<sup>3</sup> However, comparing the amount of energy produced from these renewable sources, to the energy produced by the combustion of fossil fuels shows the clear and huge dominance that fossil fuels still have on the global market. Renewable sources, in 2017, produced *ca.* 9,000 TWh whereas fossil fuels produced *ca.* 134,000 TWh of energy.<sup>8</sup> Clearly fossil fuels will continue to dominate the energy market for many years to follow, so increasing the efficiency of the combustion processes would be critical for reducing their impact on the climate.

The amount of energy generated from solar harvesting technologies has seen an exponential increase over the past 30 years owing to the research efforts into photovoltaics (PV) which has driven down the price per unit of energy produced (Figure 1-2(b)), and prices are now as low as 69 \$ MWh<sup>-1</sup>. Notably, the drop in PV module price that occurred over 2007- 2010 led to a dramatic increase in the electricity consumption from PV. By contrast, fossil fuels have remained at *ca.* 50 – 100 \$ MWh<sup>-1</sup> for many decades.<sup>9,11</sup> Figure 1-2(a,b) clearly demonstrates that, for energy technologies to have an application in the global energy market, they must be competitively priced. This outlook is similar for energy technologies utilising hydropower, geothermal and wind.<sup>9</sup> Whilst PV and wind etc. technologies will certainly flourish in the following years, it is clear that new energy technologies will also need to be developed. The following section will look into an emerging energy technology that allows for recovery of the wasted thermal energy that is lost in the combustion of fossil fuels.

### ***1.1. Waste Heat Energy Harvesting Using Thermoelectric Materials***

Thermoelectric generator (TEG) modules provide the opportunity to improve the CO<sub>2</sub> emission profile of the fossil fuel combustion process by increasing the efficiency. TEGs can take advantage of a thermal gradient to generate electricity from a multitude of heat sources. Global energy consumption as of 2014 was of the order of 150,000 TWh. A review by Forman *et al.* provides an estimate of the amount of energy lost as waste heat per year, and in 2012 this was estimated to be of the order of 68,000 TWh (determined from an estimated total energy consumption of 130,000 TWh).<sup>12</sup>

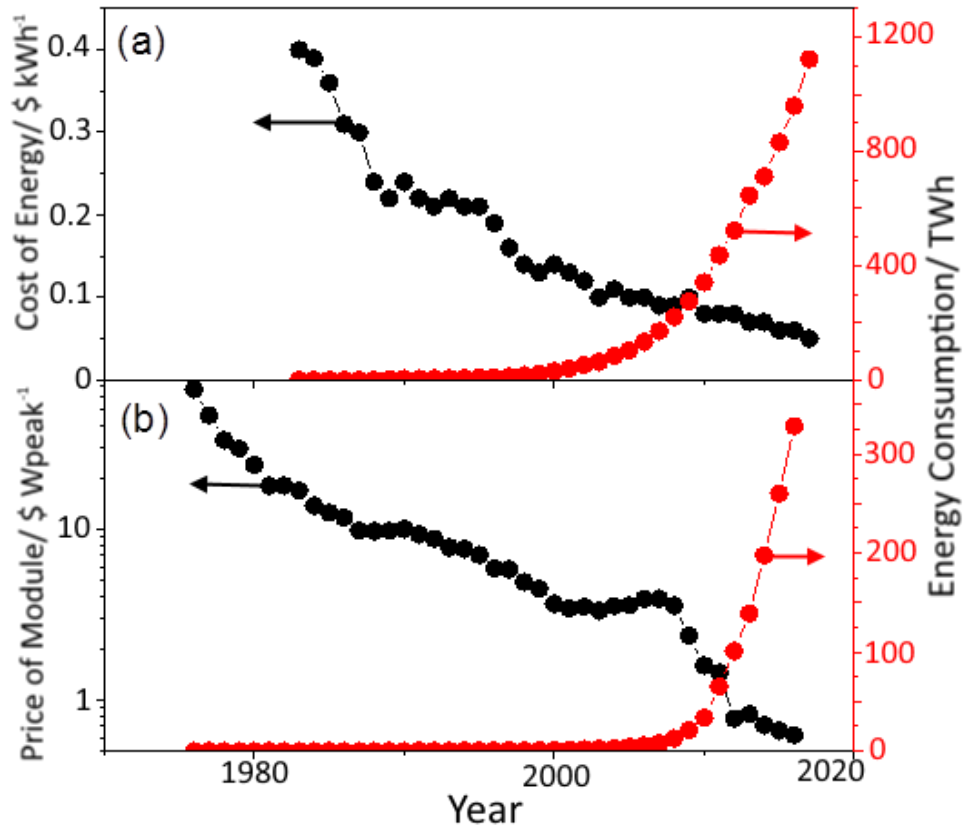


**Figure 1-2** –Cost and energy consumption per year for selected renewable energy resources. (a) – Wind,<sup>9</sup> (b) – Solar.<sup>10</sup>

The majority of this waste energy is produced over the temperature range  $T=295 - 595$  K as gaseous waste heat.<sup>13</sup> This would provide a Carnot potential of 13,000 TWh that would be available to TEG technologies. The Carnot efficiency,  $\eta_{carnot}$ , is described by the equation:

$$\eta_{carnot} = 1 - \frac{T_{cold}}{T_{hot}} \quad (1-1)$$

Where,  $T_{cold}$  and  $T_{hot}$  are the temperatures of the heat sink and heat source, respectively. However, the high cost of the thermoelectric materials, which are used to construct modules, currently prevents their use on an industrial/commercial scale. The work encompassed within this thesis is driven by the motivation to find and understand novel low-cost thermoelectric materials. The later sections of this chapter will investigate some of the materials that show potential as low-cost alternatives but first it is important to understand the function of these materials.

### **1.1.1. Thermoelectric Generators (TEG)**

Thermoelectric materials allow for the direct conversion of thermal energy into electrical energy. TEGs are solid-state devices that exploit this phenomenon and are constructed

from a combination of different materials; semiconducting, electrically insulating and metallic (Figure 1-3).<sup>14-16</sup> The electrically insulating parts are used as a substrate at either end of the device, allowing for heat transfer between the semiconducting thermoelectric legs and the hot or cold junctions. Meanwhile, the metallic parts are used to provide an electrical connection between each of the thermoelectric legs. Two types of semiconductor are used in the device, n-type and p-type, and they should show comparable performance over a given temperature range. In p-type semiconductors, electrical conduction is dominated by the movement of electron holes (positive charge carriers), for n-type semiconductors, this is dominated by the movement of electrons (negative charge carriers).

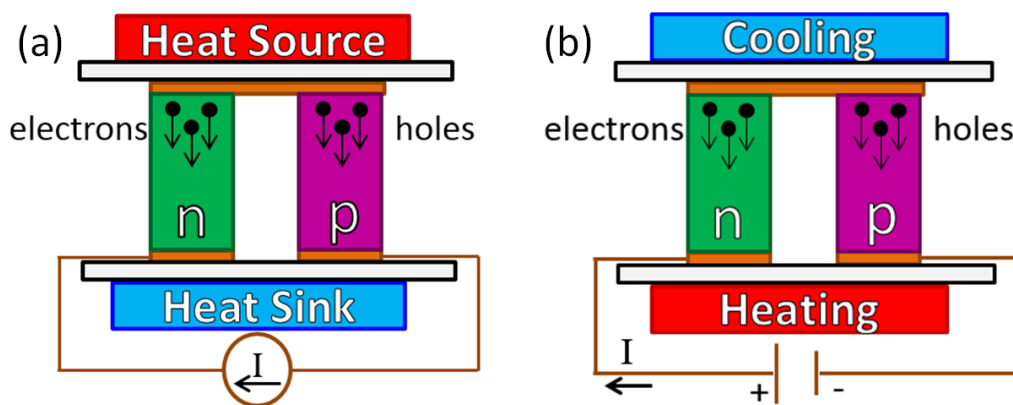


**Figure 1-3** – Schematic diagram of the geometry of a thermoelectric module. (a) – Power generation mode; (b) – refrigeration mode. Light Grey – electrically insulating substrate, Orange – electrical contacts, green – n-type leg, pink – p-type leg.

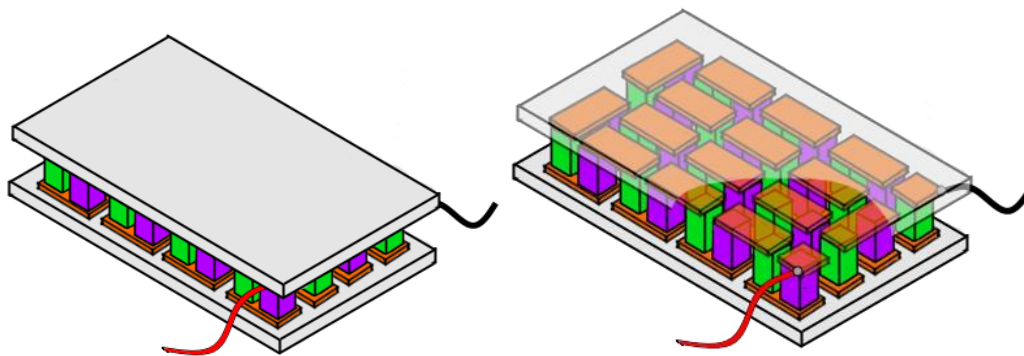


**Figure 1-4** – Schematic diagram of the arrangement of electrodes and thermoelectric elements in a thermoelectric module. Light Grey – electrically insulating substrate, Orange – electrical contacts, green – n-type leg, pink – p-type leg.

When a temperature difference is applied to a TEG module, the dominant charge carriers will diffuse towards the cold junction. Thus, the direction of the electrical current will either travel towards the hot junction in p-type semiconductors and towards the cold

junction in n-type semiconductors (Figure 1-3). This phenomenon was discovered by John Seebeck.<sup>17</sup> In a thermoelectric module, many thermoelectric elements are used.<sup>18</sup> The arrangement of these thermoelectric legs within a conventional TEG has a specific geometry in order to exploit the Seebeck or Peltier effects. The p- and n-type legs are connected electrically in series and thermally in parallel. Figure 1-4 shows a schematic diagram of the construction of a conventional thermoelectric module. Alternative TEG module geometries can also allow for power generation or Peltier cooling.<sup>18</sup>

### ***1.1.2. Current and Possible Applications***

Thermoelectric (TE) modules do not require maintenance because they are solid-state devices with no moving parts. If a thermoelectric module is supplied with a constant heat flux (assuming the materials constituting the module are stable), it will provide a continuous power output. This is a clear advantage for this technology compared to wind or solar technologies, for which, power generation is intermittent. However, it is essential that the TE materials within the device have good thermal stability and longevity.

State-of-the art/commercial TE modules, usually consisting of: PbTe, Te/Sb/Ge/Ag or Bi<sub>2</sub>Te<sub>3</sub>,<sup>16,19,20</sup> have extraordinarily long life-times over which they can maintain a high thermoelectric performance and power output. This set of attractive properties makes them ideal for providing electrical energy in niche applications. They have seen considerable use in long term experiments in remote locations where maintenance is not possible. NASA have used radioisotope thermoelectric generators to power several of their space probes.<sup>21,22</sup> The Voyager 1 and 2 space probes have been travelling for *ca.* 40 years to explore the outer reaches of our solar system. There has been a significant research effort into recovering the waste heat from exhaust gasses of automotive vehicles.<sup>23,24</sup> In other areas, considerable work is underway to design TEGs that can harvest the energy from the human body, sometimes through the use of thin film devices.<sup>25</sup> They may also be utilised for harvesting energy from the sun, TEG devices may be used in specially designed solar-TEG devices or in conjunction with conventional solar harvesting techniques (Photovoltaics).<sup>26,27</sup>

The Peltier effect is related to the Seebeck effect and allows the function of a thermoelectric module to be inverted. If an electrical current is introduced across the TEG, a thermal gradient will be created. One face of the module will cool whilst the other will heat up, this can be utilised as a cooling device (Figure 1-3(b)). Thermoelectric devices have seen considerable use for refrigeration applications and are used regularly in scientific

equipment.<sup>18,28,29</sup> They generally find use as cooling devices in niche applications where cost is not a great issue and long-term reliability is desired.

### 1.1.3. Thermoelectric Efficiency and Figure of Merit

Of course, the effectiveness of these devices is dependent on their ability to convert thermal energy into electrical energy. The performance of individual materials is determined by their thermoelectric figure of merit,  $ZT$ .<sup>30</sup> The dimensionless figure of merit can be determined from the electrical and thermal transport properties of a material:

$$ZT = \frac{S^2 T}{\rho(\kappa_L + \kappa_e)} = \frac{S^2 \sigma T}{(\kappa_L + \kappa_e)} \quad (1-2)$$

Here,  $S$ , is the Seebeck coefficient,  $\rho$ , is the electrical resistivity (the inverse of electrical conductivity,  $\sigma$ ),  $\kappa_L$  and  $\kappa_e$  are the lattice thermal conductivity and the electrical contribution to the thermal conductivity, respectively. The term  $S^2 \sigma = S^2 / \rho$  is used to denote the power factor of a material. The difficulty in finding high-performance materials becomes apparent when the interplay between these transport properties is considered (Figure 1-5).

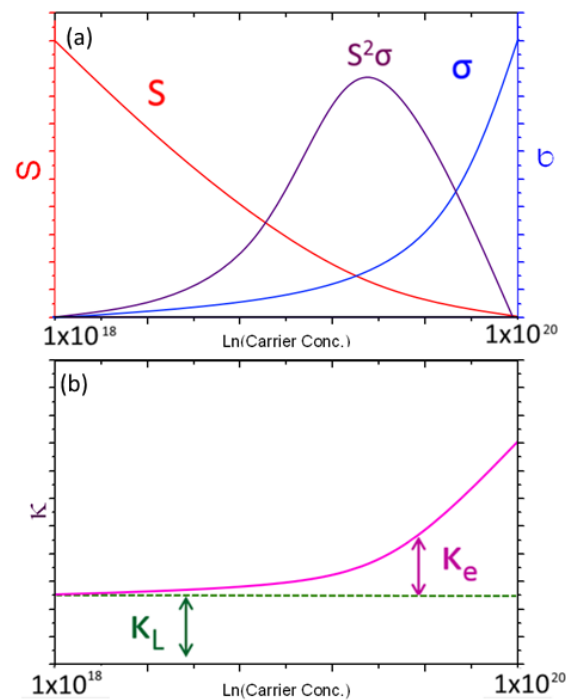


**Figure 1-5** – Schematic representation of carrier concentration dependence of the: (a) – electrical transport properties, (b) – thermal transport properties.<sup>31</sup>

The charge carrier concentration of the material has an influence on each of the physical properties  $S$ ,  $\rho$  and  $\kappa_e$ . Figure 1-5 shows a schematic representation of the effect of the

charge carrier concentration on each of these properties, including the power factor. Fundamentally,  $\sigma$  and  $\kappa_e$  both have a direct relationship to the carrier concentration whilst  $S$  has an inverse relationship. Ideally materials with a high power factor and low thermal conductivity are key to achieving high thermoelectric performance. Optimum TE performance is usually expected between a charge carrier concentration of  $n= 10^{19} - 10^{20} \text{ cm}^{-3}$  as the power factor peaks in this range whilst thermal conductivity is relatively low.<sup>32</sup> The efficiency of a thermoelectric device,  $\eta$ , is dependent upon the temperature at the hot side,  $T_h$ , and the temperature at the cold side of the thermoelectric module,  $T_c$ . More importantly, the thermal and electronic transport properties of the two semiconducting materials used in the device (given by their average figures of merit,  $ZT_{average}$ ) critically influence the device's performance.<sup>33</sup> The efficiency of the device can be estimated by the equation:

$$\eta = \frac{T_h - T_c}{T_h} \left[ \frac{\sqrt{1 + ZT_{average}} - 1}{\sqrt{1 + ZT_{average}} + \frac{T_c}{T_h}} \right] \quad (1-3)$$

Here an increase in the  $ZT_{average}$  leads to improvements in conversion efficiency,  $\eta$ , of the module (Figure 1-6).<sup>34</sup> A  $ZT_{average} = 1$  would allow for a device efficiency of  $\eta = 10\%$  at a  $\Delta T = 300 \text{ K}$  and the cold side at room temperature provided there are no contact resistances. Efficiencies of  $\eta = 6.5\%$  and  $16.5\%$  would be observed for a system with  $ZT_{average} = 0.5$  and  $2$  respectively.<sup>16</sup> Therefore, it is imperative that high performance thermoelectric materials are developed, if thermoelectric device's are to be realised as a useful technology for harvesting waste-heat.

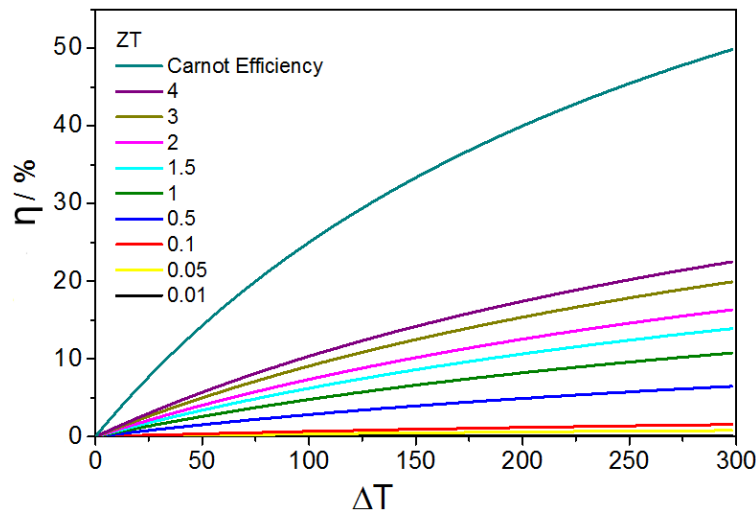


**Figure 1-6** – Efficiency of a thermoelectric module as a function of temperature difference and for different  $ZT$  values, calculated for a cold side temperature of  $300 \text{ K}$ .

### 1.1.4. Seebeck Coefficient, $S$

The Seebeck coefficient is the physical property that quantifies the electrical voltage,  $V$ , that is produced when the material is under a thermal gradient,  $\Delta T$ . This electromotive force is largely influenced by the charge carriers as well as the magnetic structure and the interactions between phonons and carriers.<sup>35</sup> This property is defined by the equation:

$$S = \frac{\Delta V}{\Delta T} \quad (1-4)$$

Thus the units are usually given in  $\mu\text{V K}^{-1}$ . The sign of the Seebeck coefficient may be positive or negative and is determined by the dominant charge carrier of the material. This quantity can be used experimentally to determine whether a material is n-type, where  $S$  is negative, or p-type, where  $S$  is positive. An approximation of the Seebeck coefficient in metallic solids or degenerate semiconductors can be given by the equation<sup>36</sup>:

$$S = \frac{8\pi^2 k_b^2}{3eh^2} m^* T \left(\frac{\pi}{3n}\right)^{2/3} \quad (1-5)$$

Here,  $k_b$ , is the Boltzmann constant,  $h$ , is Planck's constant and,  $e$ , is the electrical charge. This reveals that the value of the Seebeck coefficient is influenced by the number of charge carriers,  $n$ , as well as the effective mass of the charge carriers,  $m^*$ , of the material. The effective mass of the electron or electron hole is largely influenced by the electronic structure of the material. Efforts to increase the Seebeck coefficient must therefore aim to increase the effective mass of the charge carriers or decrease the total number of charge carriers in the material.<sup>37</sup> Generally medium-band gap semiconductors are desired because they tend to have a large carrier effective mass,  $m^*$ , which is conducive to a large Seebeck coefficient.

### 1.1.5. Electrical Resistivity, $\rho$

The electrical resistivity quantifies a materials ability to transport an electrical current and this is determined by equation 1-6. This equation shows that  $\rho$  is influenced by both the charge carrier concentration,  $n$ , and the carrier mobility,  $\mu$ :

$$\frac{1}{\rho} = \sigma = ne\mu \quad (1-6)$$

The charge of an electron,  $e$ , is constant ( $e = 1.602 \times 10^{-19}$  C). Approaches to decreasing the electrical resistivity should aim to increase the total charge carrier concentration and decrease the carrier mobility. The electronic structure of the material has a significant influence on the mobility of the carriers, for electrons and holes, as well as the number of charge carriers.

Clearly, having an understanding of the electronic structure of thermoelectric materials is a key to elucidating their inherent electronic transport properties. Thus, a rudimentary outline of the electronic structure of materials will be provided in section 1.2.

### ***1.1.5.1. Ionic Conductivity***

In some materials, such as mixed ion-electron conductors or superionic conductors, the conductivity of ions in the structure can contribute to the total measured electrical resistivity.<sup>38</sup> In these instances the charge of the carrier,  $e$ , can also be present as a variable,  $Ze$ , when there is a significant degree of ionic conduction within a material.<sup>39</sup> In these classes of material the activation energy of transporting ions should be comparable to or lower than the activation energy of promoting electrons across the band gap. The presence of vacant or interstitial sites in the structure facilitates a low activation energy as they can provide ionic conduction pathways.<sup>40</sup>

### ***1.1.6. Thermal Conductivity, $\kappa_t$***

The thermal conductivity of a material describes its ability to transport heat and is determined experimentally as the total thermal conductivity. There are different modes of thermal transport that contribute to the total thermal conductivity. Thus, it can be represented as a sum of the electronic contribution,  $\kappa_e$ , and the lattice contribution,  $\kappa_L$ :

$$\kappa_t = \kappa_L + \kappa_e \quad (1-7)$$

It is useful to decouple these two parts of the thermal conductivity to understand the approaches that might be useful in improving the thermal behaviour of a material. The electronic contribution originates from the ability of the charge carriers to transport heat and is quantified by the Wiedemann-Franz law.<sup>41</sup> This law states that, for metals, the electrical conductivity and the electrical component of the thermal conductivity,  $\kappa_e$ , are directly linked and related to one another by:

$$\sigma = \frac{\kappa_e}{LT} \quad (1-8)$$

$$\kappa_e = ne\mu LT \quad (1-9)$$

Here,  $L$ , is the Lorenz number ( $L = 2.44 \times 10^{-8} \text{ W } \Omega \text{ K}^{-1}$ ). Therefore, the approaches towards maintaining a low electrical contribution to the thermal conductivity are in direct conflict to those for decreasing the electrical resistivity.

The lattice contribution to the thermal conductivity,  $\kappa_L$ , is primarily influenced instead by the lattice vibrations (phonons) and phonon-phonon interactions. This can be written in

terms of the phonon mean free path,  $\Lambda$ , specific heat capacity,  $C_p$  and the velocity of sound in the solid,  $v$ :

$$\kappa_L = \frac{1}{3} C_p v \Lambda \quad (1-10)$$

The mean free path of the phonons is influenced by the crystal structure and grain structure of the material,<sup>42</sup> and the velocity of sound is influenced by the phonon band structure of the material.<sup>43</sup> Approaches to decreasing the lattice thermal conductivity aim to minimise the phonon mean free path through the scattering of phonons. This can be highly effective in increasing the figure of merit and will be discussed further in section 1.2.4.

The phonon band structure of a material is directly linked to its crystal structure. Phonons are modes of vibrational waves within condensed matter that transmit thermal energy across the crystal, independent of electrons. The ability of a material to transport heat through these phonon modes is determined by the phonon-phonon interactions within the material. The Keyes expression (Equation 1-11) can be used to estimate the lattice thermal conductivity for materials when  $T$  is higher than the Debye temperature and links the thermal conductivity to the atomic mass, density and thermal vibration of atoms.<sup>44</sup> Phonon-phonon scattering is more likely to occur when the atomic mass of atoms,  $A$ , is large or when the density,  $\rho$ , is low. The amplitude of interatomic thermal vibration,  $\varepsilon$ , also has a marked influence on the lattice thermal conductivity and has an indirect relationship:

$$\kappa_L T = \frac{R^{3/2}}{3\gamma^2 \varepsilon^3 N_0^{1/3}} \frac{T_m^{3/2} \rho^{2/3}}{A^{7/6}} \quad (1-11)$$

Here,  $T_m$ , is the melting point,  $R$ , is the gas constant,  $\gamma$ , is the Grüneisen parameter, which is material dependent and considers the lattice parameters, and  $N_0$  is Avogadro's number. However other complex structural features can indeed contribute to the scattering of phonons within the lattice. For example, defects within the structure, in the form of vacancies or guest atoms, may provide local disorder in the effective mass, structure and interatomic forces.<sup>45</sup> Classical approaches in thermoelectric material research have used solid solutions to scatter acoustic phonons which are the primary transporters of thermal energy.<sup>46</sup>

## ***1.2. Electronic Structure of Crystalline Solids***

The electronic and atomic structure of materials are inextricably linked and the crystal structure of a material must be known in order to determine its electronic structure. The models examining the band theory of solids and density of states are simplified

representations of the electronic structure of a material that are reliable enough to outline the physical properties of materials. As this thesis is concerned with the physical properties of materials it is important to investigate these models in order to understand the approaches that are implemented in improving electrical behaviour of TE materials.

### 1.2.1. *Electronic Bands and Density of States (DOS)*

The theory of the linear combinations of atomic orbitals, LCAO, provides a model for interpreting the bonding and anti-bonding orbitals within discrete molecules and this theory can be expanded to account for the energy bands in extended solids (Figure 1-7).<sup>47</sup> An infinite three dimensional lattice will have an infinite number of molecular orbitals, for a specific set of interacting orbitals and their energies will fall within a defined energy range, giving rise to an electronic band (Figure 1-7(d)).<sup>48</sup>

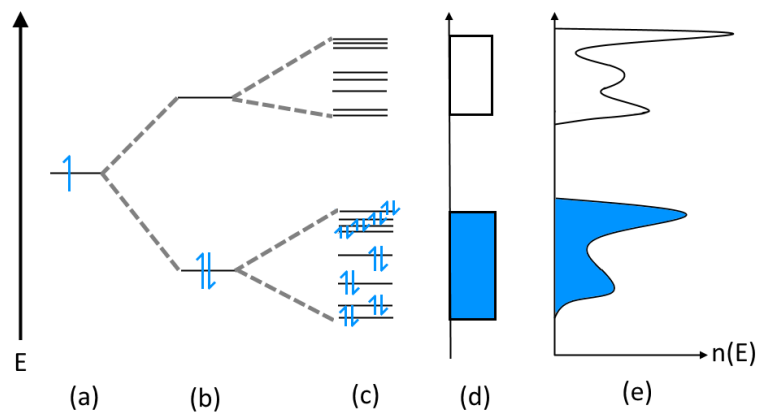


**Figure 1-7** – Schematic diagram showing hypothetical energy levels/bands for undefined electron orbitals for: (a) an atom (b) a diatomic molecule (c) a large molecule (d) energy bands for a solid (e) density of states for a solid.

The density-of-states reveals the relative number of energy states or molecular orbitals that are available over a small energy range ( $E+\delta E$ ) (Figure 1-7(e)) and the Fermi energy,  $E_F$ , of the system is the highest occupied energy level at 0 K. The eventual electron filling and energy separation between the bands in the DOS provides some insight to the electrical characteristics of the material.<sup>49</sup>

For metallic solids, the Fermi-level occupies the centre of an electronic band, thus the valence band is partially filled (Figure 1-8 (a)). The valence electrons are described as fully delocalised over the entire crystal and no activation energy is required to promote the electrons into the conduction band. In metals, the electrical conductivity decreases as temperature increases due to the increased rate of phonon-electron interactions that

decrease the electron mobility in the material. In semiconductors and insulators, the band gap,  $E_g$ , is an energy separation between the valence and conduction bands (Figure 1-8 (b,c)). For electrical conduction to occur in these solids the electrons must be promoted into the conduction band by thermal or optical excitation. Increasing the temperature of a semiconductor increases the number of electrons that can contribute to electrical conduction, thus the electrical conductivity increases with increasing temperature. The same temperature dependence is observed for insulators which tend to have a bandgap that is very large and usually several orders of magnitude larger than  $2k_bT$ , where  $2k_bT_{298 K} = 0.05 \text{ eV}$ . An approximation of the energy bands and in turn the band gap can be estimated for solid-state materials using the extended Hückel method or DFT calculations.<sup>49,50</sup>

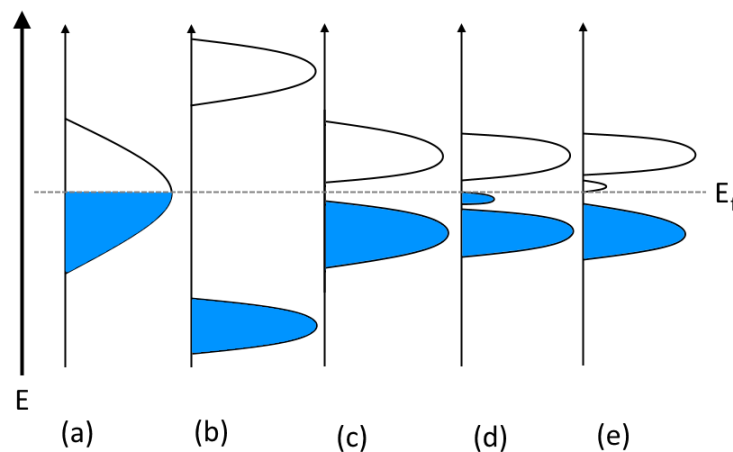


**Figure 1-8** – Schematic diagram of the valence and conduction bands for: (a) a metal; (b) an insulator; (c) an intrinsic semiconductor; (d) and (e) doped n and p-type semiconductors.

### 1.2.2. Semiconductors

Semiconductors can be n-type or p-type, as discussed briefly in section 1.1.3. For intrinsic semiconductors, the Fermi energy occupies the centre of the band-gap and an equal number of electrons and holes are present at  $T \gg 0 \text{ K}$ . Extrinsic semiconductors are doped with a low concentration of impurity atoms that may introduce donor or acceptor levels into the band gap encouraging p-type or n-type conduction, respectively ( Figure 1-9(e)), or provide a reliable method of tuning the Fermi level which can also encourage n- or p-type conduction (Figure 1-9(b)). This can have a profound influence on the rate of recombination of electrons and holes.<sup>51</sup> Solid-state materials in their natural intrinsic state will exhibit either n- or p-type conduction. The characteristics of the DOS of the valence

and conduction bands has a significant influence on the conduction type a material exhibits. A larger density of states in the valence band will result in the formation of more electrons than electron holes and lead to n-type conduction.

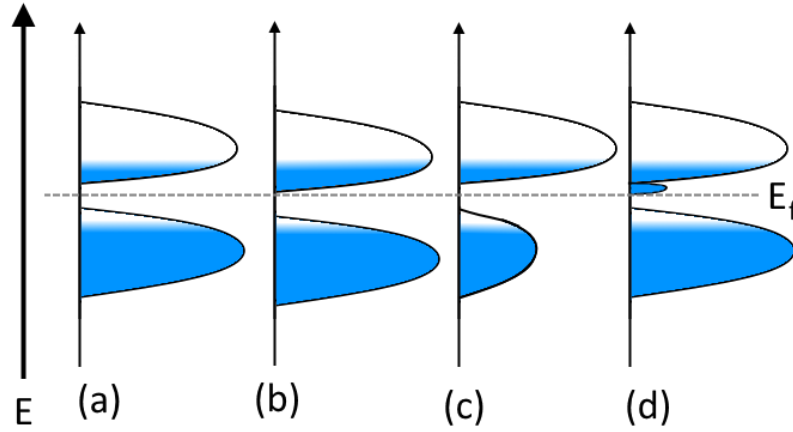


**Figure 1-9** – Schematic diagram showing electron distribution (blue) in the valence and conduction bands for: (a) - an intrinsic semiconductor; (b) – a semiconductor doped to tune the Fermi energy and encourage n-type conduction; (c) – an n-type semiconductor that has not been doped and (d) n-type semiconductor with acceptor levels in the band gap.

### 1.2.3. Design Strategies to Improve the Power Factor

With these principles outlined, the available strategies for designing thermoelectric materials with excellent electrical and thermal properties can be considered. The following section investigates the design strategies and gives examples where they have been implemented.

Optimisation of the charge carrier concentration is often approached by deviating from the ideal stoichiometry.<sup>52</sup> When modifying the charge carrier concentrations of the material, an increase in only the dominant charge carriers should be sought. Introduction of the carriers of opposite charge is detrimental to the Seebeck coefficient as the rate of electron-hole recombination increases greatly.<sup>53</sup> This is because the Seebeck coefficient depends upon the individual Seebeck coefficients of both the electrons,  $S_n$ , and holes,  $S_p$ , through the relationship:

$$S = \frac{\sigma_p S_p - |\sigma_n S_n|}{\sigma_p + \sigma_n} \quad (1-12)$$

Tin-for-antimony substitution in half-Heusler compounds,  $\text{Ti}_{0.3}\text{Zr}_{0.35}\text{Hf}_{0.35}\text{CoSb}_{1-x}\text{Sn}_x$ , provides a reliable method to increase the charge carrier (hole) concentration. This p-type thermoelectric is doped with a lower-valent anion which allows for incremental increases in the electrical conductivity with increasing  $x$ .<sup>54</sup> Conversely, doping the cation site of n-

type half-Heusler,  $\text{Ti}_{1-x}\text{Mn}_x\text{NiSn}$ , with a higher-valent cation does not demonstrate such a direct correlation.<sup>55</sup> Thus doping the material to impact the carrier concentration may not always be a straightforward process. In many instances however, cation doping has certainly proved to be an effective method for tuning the charge carrier concentration and in effect the Fermi-energy.<sup>56</sup>

Techniques are available to manipulate the electronic structure of materials to allow for tuning of the electrical properties. Doping can also provide effective pathways for influencing the band structure of the material. Established techniques in thermoelectric research include band-flattening (as seen in lanthanum for lead doping in  $\text{La}_x\text{Pb}_{1-x}\text{Te}$ ),<sup>57</sup> and introducing resonant levels. Indium-for-tin substitution in  $\text{In}_x\text{Sn}_{1-x}\text{Te}$  should increase the number of dominant charge carriers in this p-type thermoelectric. The resulting increase in the Seebeck coefficient observed here is attributed to the introduction of these resonant states through indium doping.<sup>58</sup>

It is also possible to tune the size of the band gap. It has been shown in clathrates with composition  $\text{Ba}_8\text{Ni}_x\text{Zn}_y\text{Ge}_{46-x-y-z}\text{Sn}_z$  that an increased nickel content is linked to a smaller band gap.<sup>59</sup> However, techniques for optimising the size of the band gap are not utilised frequently in thermoelectric research as they are not always reliable.

Band-convergence techniques can be more effectively implemented to influence the DOS effective mass and in turn the Seebeck coefficient.<sup>60,61</sup> Furthermore, implementing band convergence techniques in solid solutions may in some cases influence the size of the band gap.<sup>62</sup>

Band-structure engineering has proved to be a very effective method to enhancing the electrical transport properties. The Seebeck coefficient can be expressed as a function of the density of states by the Mott-relationship<sup>63</sup>:

$$S = \frac{\pi^2}{3} \left( \frac{k_b^2 T}{e} \right) \left( \frac{d \ln \sigma(E)}{d(E)} \right)_{E=E_f} \quad (1-13)$$

Here,  $k_b$ , is the Boltzmann constant,  $e$  is the charge of an electron and,  $\sigma(E)$ , is the electrical conductivity as a function of energy. The expression  $d \ln \sigma(E)/d(E)$  defines the slope in the density of states and large absolute Seebeck coefficients are expected when the  $d \ln \sigma(E)/d(E)$  is large at the Fermi level,  $E=E_f$ . Figure 1-10 provides a schematic diagram of the valence and conduction bands for two materials which might have a high and lower Seebeck coefficient.

Importantly, the dimensionality of a material has a remarkable influence on the electronic transport properties of a material. The influence of lower dimensionality on the DOS has

been understood for many years.<sup>65</sup> Much sharper features in the DOS are expected with each decreasing degree of dimensionality as displayed in Figure 1-11. Thus, larger Seebeck coefficients should occur in low-dimensional solids.

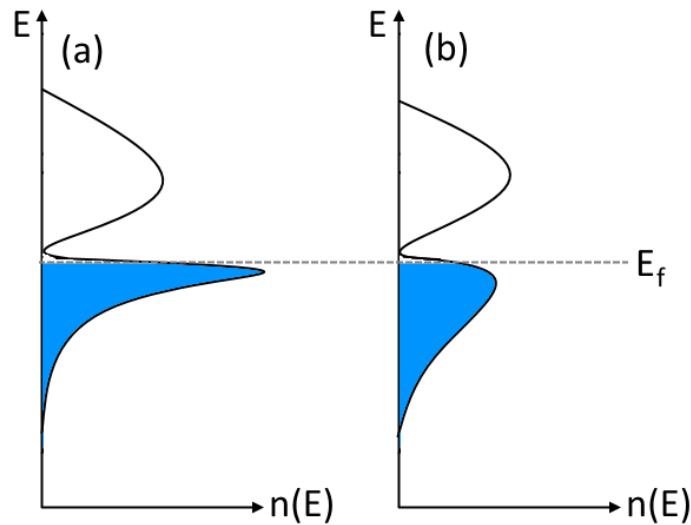


**Figure 1-10** – Schematic diagram of hypothetical density of states with: (a) a large value of  $d \ln \sigma(E)/d(E)$ ; (b) a smaller value of  $d \ln \sigma(E)/d(E)$ .

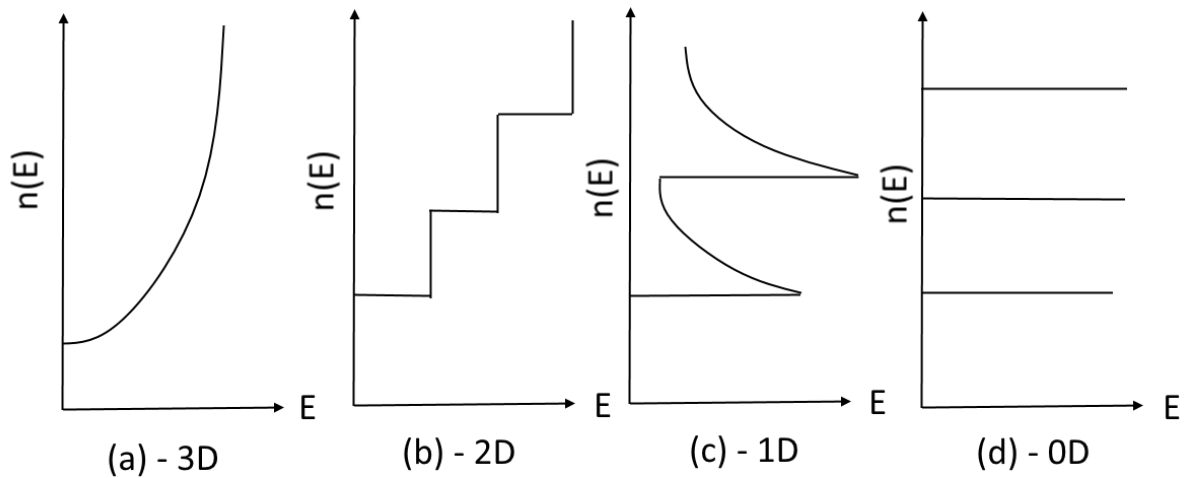


**Figure 1-11** – The density of states for materials with different degrees of dimensionality. (a) 3-dimensional bulk semiconductor (b) 2-dimensional quantum well structure; (c) 1-dimensional nanowire or nanotube; (d) 0-dimensional quantum dot.<sup>64</sup>

In practice, implementing these design strategies into thermoelectric materials has proven an extremely effective method for enhancing thermoelectric performance of some materials.<sup>64</sup> The early experimental work by Dresselhaus *et al.* indicated that these theorised density of states may indeed be observed for low dimensional structures as the thermoelectric performance is seen to improve.<sup>66,67</sup> These discoveries have driven a huge amount of research into nanostructured thermoelectrics.<sup>68–70</sup> However, the effects of these

multi-quantum well structures may drive marked improvements in  $ZT$  owing to better thermal behaviour rather than the expected influence on the DOS.<sup>67</sup>

#### 1.2.4. Design Strategies to Reduce Thermal Conductivity

In the design of novel thermoelectrics or the enhancement of known ones, a consideration of the structural behaviour is critical. Recent advancements in this field reveal the importance not only of the atomic-scale structure but also the nano- and macro-scale structure of thermoelectric materials. There are a number of approaches towards finding materials with more desirable thermal conductivities. Whilst the principal aim of each technique is similar -to increase the phonon scattering within a material- the length scales at which these are effective differs enormously (Figure 1-12).

The phonon-liquid electron crystal and phonon-glass electron crystal (PGEC) approaches are quite different, but both utilise interesting crystal chemistry to effectively scatter phonons. PLEC materials are described as having a liquid-like sub-lattice. The high ionic conductivity of cationic species within the structure allows for effective scattering of transverse phonons, such that their contribution to the lattice thermal conductivity is almost completely suppressed.<sup>71</sup> The result is the observation of lattice thermal conductivities that are comparable to liquids.<sup>71</sup> PGEC materials are rather different and contain atoms that have large or anisotropic vibrations for some weakly bound atoms within the structure. The rattling vibrational modes of these atoms are effective in scattering phonons and allow for lattice thermal conductivities that are comparable to amorphous materials/glasses.<sup>72</sup>

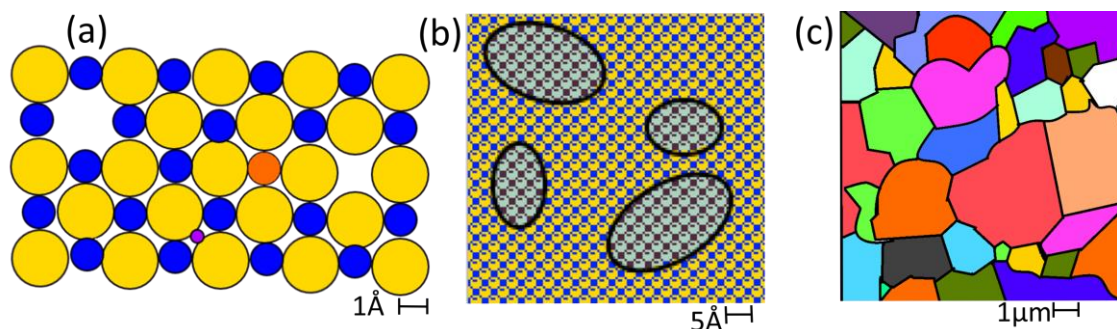


**Figure 1-12** – schematic diagrams of the features that can scatter phonons at different length scales: (a) atomic scale- vacancies and defects (orange/purple atoms); (b) nanoscale – nano-inclusions, shown by circles and (c) microscale – grain-structure.

Nano-structuring within bulk thermoelectrics can be implemented through the exploitation of phase segregation phenomena creating nano-scale inclusions of chemically and structurally related phases (Figure 1-12(b)).<sup>70</sup> These can provide increased phonon

scattering without negatively impacting the electrical properties. Other methods of nano-structuring include nano-scale compositing. Additional and structurally unrelated phases of nano-scale materials are processed into the bulk material providing a solid-state mixture of phases, these processes have proved to be an effective method of reducing lattice thermal conductivities.<sup>73,74</sup> Micro-scale structuring can be implemented through the engineering of grain-boundary effects and increasing the scattering of phonons at grain interface boundaries through encouraging the formation of nanoprecipitates or dislocation arrays (Figure 1-12(c)).<sup>75,76</sup> Many techniques are available to implement the improvements in thermoelectric materials and an overview of some of these classes of material will be reviewed in the following section.

### 1.3. High Performance Bulk Thermoelectrics

There are many comprehensive reviews on the progress and performance of thermoelectric materials which investigate many of the key topics relating to TE materials.<sup>33,37,68,77–79</sup> Some of these resources provide an overview and comparison of the many classes of thermoelectric materials, often in graphical representations similar to the one presented in Figure 1-13.<sup>33,37,68,77–79</sup> These provide an insight into the performance of select materials and the temperature range over which they might be applicable. In the following sections, the maximum in the thermoelectric figure of merit ( $ZT_{max}$ ) is given rather than the  $ZT$  over the entire temperature range.

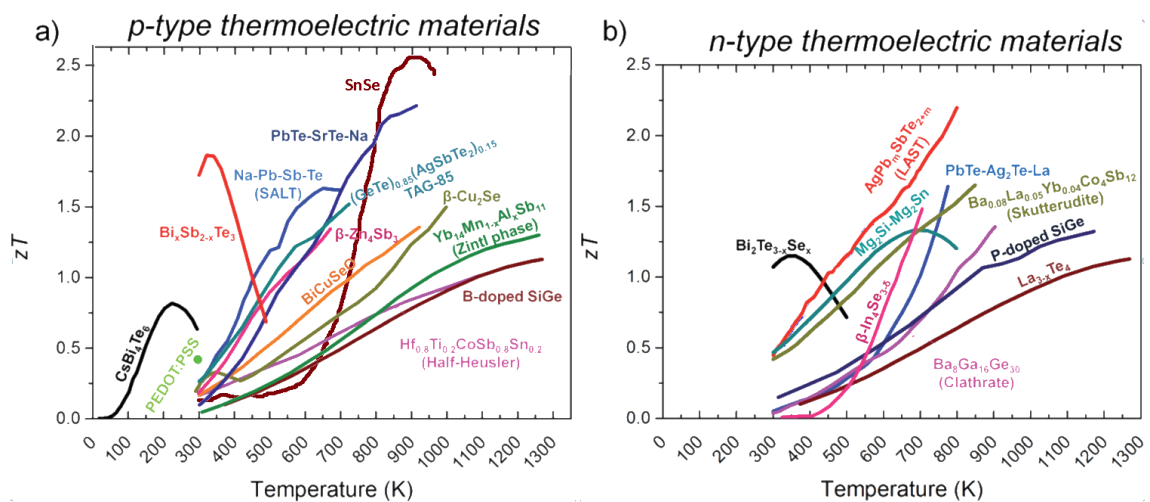


**Figure 1-13** – A summary of high performance TE materials. Thermoelectric figure of merit as a function of temperature for (a) p and (b) n-type bulk thermoelectric materials which are known to have excellent performance. Reproduced from 77. Reprinted with permission from RSC Publishing.

The most prominent of these materials are certainly the lead tellurides for medium-temperature applications, bismuth telluride for low-temperature applications and silicon-germanium alloys for high-temperature applications.<sup>77</sup> All of these have been known to the thermoelectric community for many years. Over the past 15-20 years, many materials have been categorised as high-performance thermoelectrics including: half-Heuslers (ABX), Zintl phases, clathrates, skutterudites, BiCuOSe, SnSe and Cu<sub>2</sub>Se (Figure 1-13).<sup>33</sup> However, for a thermoelectric material to be truly viable in commercial and industrial applications the material must be mechanically, thermally and chemically stable, have a high availability of the constituent elements and have a scalable synthesis process all whilst showing a high  $ZT$  over a desired temperature range. This set of criteria is not collectively satisfied by any single thermoelectric material.

#### ***1.4. Copper-Chalcogenide Thermoelectrics***

The motivation behind the research in this thesis is largely influenced by the limitations resulting from the low-availability of raw materials for many state-of-the-art or commercially available bulk-thermoelectric materials, such as PbTe and Bi<sub>2</sub>Te<sub>3</sub>. They have not seen widespread application due to the scarcity and cost of tellurium. It is difficult to manufacture tellurium in large quantities as it is a by-product of ore refinement and its resources are finite, putting it at risk of depletion.<sup>80</sup> The prices of raw tellurium and selenium, 100 and 45 \$ kg<sup>-1</sup>, respectively, are considerably higher than the cost of sulphur, 0.1 \$ kg<sup>-1</sup>, whilst the cost of many different metallic compounds used in TEs are comparable to one another.<sup>81</sup>

The ideal thermoelectric should not only show excellent performance and long term-stability, but also have an elemental composition that allows it to be commercially viable. Figure 1-14 shows the abundance of each of the naturally occurring elements, clearly the scarcity of tellurium is comparable to gold and platinum. This situation has encouraged a search for thermoelectric materials that comprise of materials with a high abundance in the earth's crust.<sup>83</sup> Currently there are no established thermoelectric materials that meet all of the aforementioned criteria but more pressingly, few perform maximally over the desired temperature range for waste heat recovery,  $T = 295 - 595$  K.<sup>13,77</sup> This temperature range accounts for *ca.* 90% of the gaseous waste heat energy that could viably be recovered from sources such as gaseous exhaust streams or water pipes.<sup>13</sup>

### 1.4.1. Binary Copper Chalcogenides, $\text{Cu}_{2-\delta}\text{Q}$ ( $\text{Q} = \text{S}, \text{Se}$ and $\text{Te}$ )

In recent years, research into binary copper-chalcogenide thermoelectrics,  $\text{Cu}_2\text{S}$  and  $\text{Cu}_2\text{Se}$ , has gained traction owing to their excellent thermoelectric figure of merit. This has occurred notwithstanding the drawbacks of these materials, which have been known for many years.<sup>84</sup> The exceptional thermoelectric performance of  $\text{Cu}_{2-\delta}\text{Se}$  in the  $\beta$ -phase and at high temperatures was reported by Liu *et al.* and Yu *et al.*,<sup>85,86</sup> who reported  $ZT = 1.5$  and  $1.6$  at  $1000\text{ K}$  and  $700\text{ K}$ , respectively. The performance of copper-deficient sulphide analogues,  $\text{Cu}_{2-\delta}\text{S}$ , showed comparable figures of merit,  $ZT = 1.6$  at  $1000\text{ K}$ . This new-found interest evolved as they posed the possibility of achieving low-cost low-toxicity thermoelectric materials.<sup>71</sup>

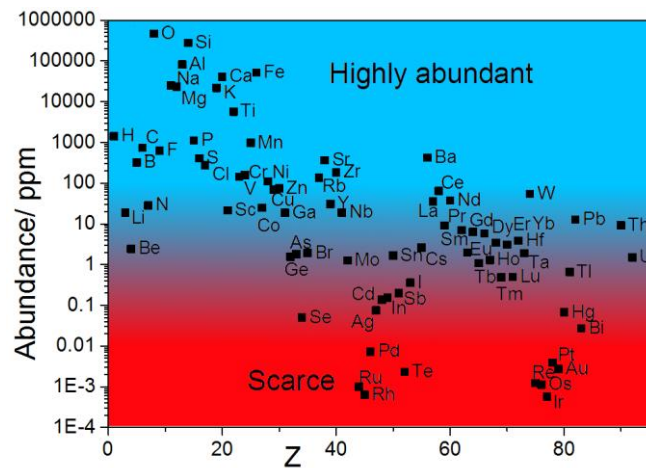


**Figure 1-14** – Graphic representation for the value of the abundance in the earths crust for all naturally occurring elements, denoted by a point and labelled by their elemental symbol. This is plotted as a function of the atomic number,  $Z$ .<sup>82</sup>

Both materials show several structural phases. The  $\alpha$  and  $\beta$ -phases are found over the  $300 - 1000\text{ K}$  temperature range with a phase transition at *ca.*  $700\text{ K}$  in  $\text{Cu}_2\text{S}$  and  $400\text{ K}$  in  $\text{Cu}_2\text{Se}$ .<sup>87,88</sup> The high-temperature phase of each material can be described by the anti-fluorite type structure and space group  $Fm\bar{3}m$  with two crystallographic sites within each of the tetrahedral holes in the rigid FCC sulphur/selenium sub-lattice (Figure 1-15(b)). The first site is centred on the  $\text{S}_4$  tetrahedral hole and the second is displaced from the centre along the body diagonal of the unit cell.<sup>85,89</sup> The copper cations within this structure are highly mobile and display a liquid-like behaviour allowing for excellent thermal and electrical behaviour.<sup>71,85</sup> The behaviour of the copper cations in the high-temperature phase has led to the copper atoms being modelled, in some instances, as a highly disordered state across the interstitial sites. In the low-temperature  $\beta$ -phase of  $\text{Cu}_{2-\delta}\text{Se}$ , the structure can be

described in hexagonal space group,  $R\bar{3}m$ . It maintains the FCC sulphur sub lattice and the cations are ordered into copper-rich and copper-poor layers in the  $z$ -direction of the hexagonal unit cell (Figure 1-15(a)).<sup>89</sup>

These materials have been termed PLECs. The characteristic structural properties of the material that allows for the exceptional thermoelectric properties are also responsible for its short life-times. Copper migration across thermoelectric elements leads to sample degradation.<sup>84,90</sup> This and the low thermal conductivity are linked to the liquid-like sub-lattice behaviour. The nature of this sub-lattice allows for effective scattering of transverse phonons, essentially suppressing these phonon-modes, resulting in exceptionally low thermal conductivities that are below the glass limit.<sup>71,85,91</sup> More recently the anharmonicity in bonding and the local-site disorder in the crystal structure has also been linked to this low thermal conductivity.<sup>92</sup>

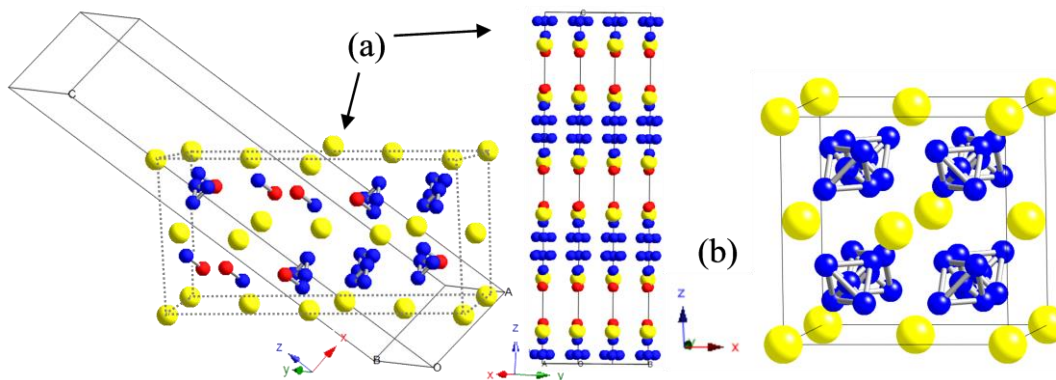


**Figure 1-15** – Perspective view of the crystal structure of: (a) the low temperature  $\beta$ -phase of chalcocite -grey dotted lines highlighting relation to the anti-fluorite structure; (b) high temperature  $\alpha$ -phase of chalcocite. Blue – copper sites (Red – Copper in Cu-poor layers) and Yellow – Selenium sites.

#### 1.4.2. Zinc-Blende Type Chalcogenides

The binary chalcogenides above have copper cations occupying each of the tetrahedral holes within the structure and require a composition of close to  $M_2Q$  ( $Q = S, Se$ ). However, there are also high-performance copper containing chalcogenide thermoelectrics with a composition of  $MQ$ , where  $M$  is a combination of metallic cations that give an average oxidation state of  $M(II)$  to counter balance the  $Q^{2-}$  anion. These are the chalcogenides with the zinc-blende structure which do not suffer from the detrimental damage caused by copper-ion migration. The structure is described by an FCC sulphur sublattice with half of the tetrahedral holes filled by cations.

For this structure type to form, valences of the M and Q atoms must be balanced to give average oxidation states of  $M^{2+}$  and  $S/Se^{2-}$ . In copper containing minerals, copper is primarily found in the Cu(I) state, thus, structure types for ternary compounds containing copper should have compositions of Cu(I)-M(III)-S/Se<sub>2</sub>, Cu(I)<sub>2</sub>-M(IV)- S/Se<sub>3</sub>, Cu(I)<sub>3</sub>-M(V)- S/Se<sub>4</sub>.<sup>60</sup> Quaternary Cu-based thermoelectric materials generally have composition Cu(I)<sub>2</sub>-M'(II)- M''(IV)- S/Se<sub>4</sub>, as discussed in section 1.4.2.3, although different compositions may certainly be feasible.

The existence of compositionally similar thermoelectric materials allows for solid-solution mixtures to be investigated. In addition, the existence of similar unit-cell parameters may allow for complex nano-structuring of ternary and quaternary compounds to further enhance thermoelectric properties.

#### ***1.4.2.1. Ternary Copper Chalcogenide, Chalcopyrite, CuFeS<sub>2</sub>***

Chalcopyrite has garnered attention among the thermoelectric community owing to its excellent electrical transport properties and its inherent n-type conduction which is uncommon.<sup>93</sup> However, the  $ZT$  for chalcopyrite samples after optimisation is generally close to a maximum  $ZT \approx 0.2$  at  $T = 600 - 700$  K.<sup>94-102</sup> Notably, substitution of cobalt for copper, Cu<sub>1-x</sub>Co<sub>x</sub>FeS<sub>2</sub>, has been shown to have an influence on the electrical and thermal transport properties of chalcopyrite.  $ZT$  values of the order of 0.22 have been demonstrated at temperatures of 675 K in Cu<sub>0.96</sub>Co<sub>0.04</sub>FeS<sub>4</sub>.<sup>102</sup> Solid-solution behaviour in samples with anion-site substitution with selenium, CuFeS<sub>2-x</sub>Se<sub>x</sub>, can lead to improvements in the power factor and in turn the  $ZT$ .<sup>97</sup> Similarly, substituting iron for copper can lead to significant improvements in thermoelectric performance and results in the highest performing chalcopyrite samples with  $ZT = 0.33$  at  $T = 700$  K in Cu<sub>0.97</sub>Fe<sub>1.03</sub>S<sub>2</sub> and Cu<sub>0.95</sub>Fe<sub>1.05</sub>S<sub>2</sub>.<sup>99</sup> For all samples presented within the literature,  $ZT_{max}$  values fall within the range  $ZT = 0.02 - 0.35$ .<sup>94-102</sup> Despite numerous attempts to maximise the thermoelectric performance of this material, its performance is rather modest owing to a relatively high thermal conductivity. A recent first-principles study suggests a  $ZT = 0.6$  at medium temperatures of *ca.* 500 K, and  $ZT = 0.8$  at high temperatures of  $T = 700$  K, could be attained if the lattice thermal conductivity is reduced.<sup>103</sup>

TG-DTA data presented by Tsujii *et al.* reveal a structural phase transition at  $T_t = 823$  K followed by decomposition with increasing temperature and evidence of sulphur loss at  $T > 700$  K for SPS samples.<sup>104</sup> The structural phase transition is an order-disorder transition from the tetragonal space group  $I\bar{4}2d$  at low-temperatures into the cubic space group

$Fm\bar{3}m$  at 823 K.<sup>105,106</sup> In the low-temperature phase the structure can be described as an  $a \times a \times 2a$  super-cell of zinc-blende type sub cells, here the copper and iron cations are ordered over  $4a$  and  $4b$  sites, respectively (Figure 1-16). Meanwhile the high-temperature structure can be described by a zinc-blende cubic  $a \times a \times a$  unit cell with space group  $F\bar{4}3m$ . Here, the copper and iron cations are disordered over the  $4c$  site. This transition has a large hysteresis and cubic structure type will remain upon cooling chalcopyrite to ambient temperatures.<sup>106</sup>

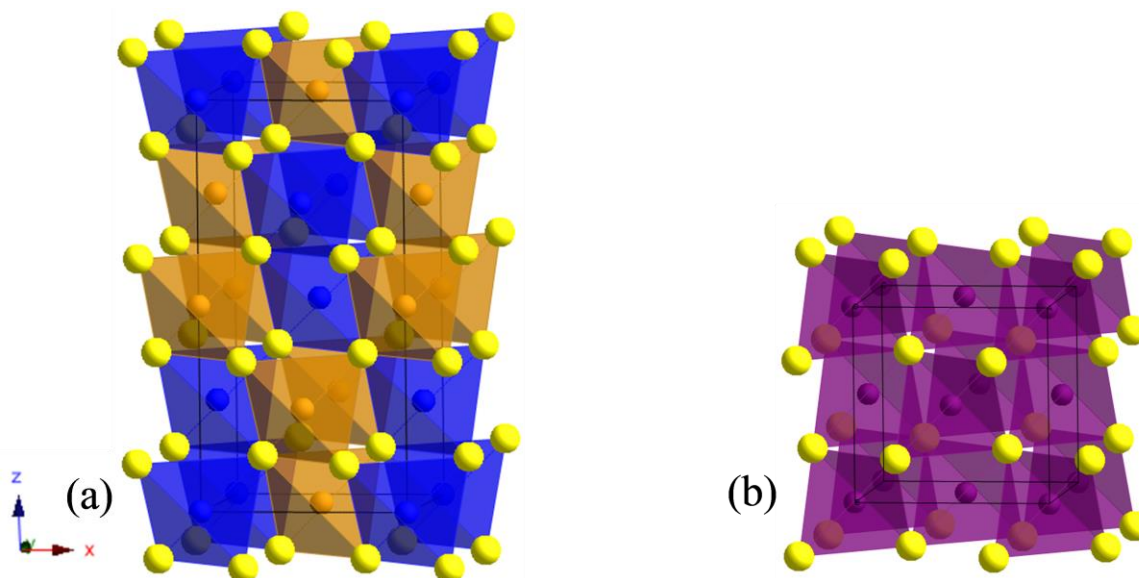


**Figure 1-16** – Perspective view of vertex-sharing tetrahedra,  $MS_4$ , in (a) Low-temperature tetragonal structure of chalcopyrite,  $CuFeS_2$ , with space group  $I\bar{4}2d$ . (b) High-temperature cubic structure  $F\bar{4}3m$ . Yellow spheres- sulphur; Orange- iron tetrahedra; Blue- copper tetrahedra and Purple- Mixed Cu/Fe tetrahedra.

#### 1.4.2.2. Other Ternary Copper Chalcogenides

Many of the materials categorised as ternary copper chalcogenides are structurally similar to the chalcopyrite phase and have the  $a \times a \times 2a$  superstructure, or another pseudo-cubic superstructure of the zinc-blende structure type. There is a myriad of chemical compositions allowed in this family of materials, such as  $CuInQ_2$ ;  $CuGaQ_2$ ;  $Cu_2SnS_3$ ;  $Cu_3SbS_4$ ;  $Cu_3VS_4$  and  $Cu_3AsS_4$ ; and thus, a range of cation ordering modes across the zinc-blende structure type.<sup>107</sup> The thermoelectric performance of these ternary chalcogenides shows a huge variation, a selected few are presented below.

The variations in structure type and cation ordering can be observed by comparing the crystal structure of the mohite,  $Cu_2SnS_3$ , and kuramite,  $Cu_3SbS_4$ , phases (Figure 1-17). The

structure of mohite,  $\text{Cu}_2\text{SnS}_3$ , is characterised by a monoclinic unit cell, space group  $Cc$ , which allows for a description of the cation ordering within the zinc-blende type structure.<sup>108</sup> In this structure, the tin-sulphur tetrahedra,  $\text{SnS}_4$ , are connected at their vertices creating an interconnected tetrahedral  $\text{SnS}_4$  framework. Copper cations occupy 40% of the remaining tetrahedral sites. This structure type allows for high thermoelectric performance at high temperatures. Cobalt-for-tin substituted samples exhibit a  $ZT = 0.85$  at 725 K in  $\text{Cu}_2\text{Sn}_{0.8}\text{Co}_{0.2}\text{S}_3$ . Indium doped samples of the sulphide,  $\text{Cu}_2\text{Sn}_{0.9}\text{In}_{0.1}\text{S}_3$ , and selenide,  $\text{Cu}_2\text{Sn}_{0.9}\text{In}_{0.1}\text{Se}_3$ , exhibit  $ZT_{max} = 0.56$  and 1.14, respectively.<sup>108–110</sup>

The thermoelectric mineral-type phase kuramite,  $\text{Cu}_3\text{SbS}_4$  in space group  $I\bar{4}2m$ , has antimony cations ordered over the layers at  $z = 0.375$  and  $z = 0.875$ . This mode of cation ordering also allows for good thermoelectric performance within germanium-doped  $\text{Cu}_3\text{SbS}_4$ - $\text{Cu}_3\text{SbSe}_4$  solid solutions, for example  $ZT = 0.9$  at 650 K in  $\text{Cu}_3\text{Sb}_{0.97}\text{Ge}_{0.03}\text{Se}_{2.8}\text{S}_{1.2}$ .<sup>111</sup> By contrast, the germanium doped selenium-free analogues of kuramite show relatively poorer thermoelectric performance,  $ZT_{max} = 0.095$  in  $\text{Cu}_3\text{Sb}_{0.98}\text{Ge}_{0.02}\text{S}_4$ .<sup>112</sup> High thermoelectric performance can be attained in selenium-free kuramite by utilising tin-for-antimony doping to introduce acceptor levels into the electronic structure,  $ZT_{max} = 0.72$  in  $\text{Cu}_3\text{Sb}_{0.95}\text{Sn}_{0.05}\text{S}_4$ .<sup>113</sup>

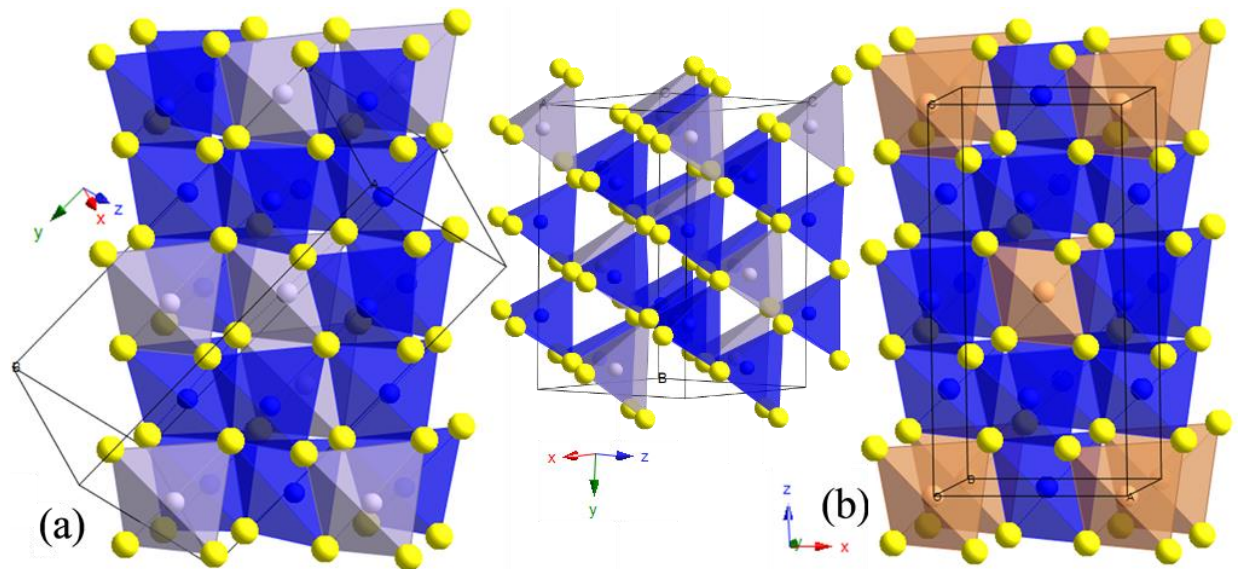


**Figure 1-17** – Perspective views of vertex-sharing tetrahedra,  $MS_4$ , in (a)  $\text{Cu}_2\text{SnS}_3$  and (b)  $\text{Cu}_3\text{SbS}_4$  phases showing the cation ordering in each of the structures within a typical tetragonal unit cell. Yellow spheres – sulphur; Blue – copper tetrahedra ; Grey – tin tetrahedra and Orange – antimony tetrahedra.

### 1.4.2.3. *Quaternary Copper Chalcogenide Thermoelectrics*

The kesterite/stannite class of materials belong to the family of natural mineral phases with the structural formula,  $A_2BCQ_4$ , where  $A = \text{Cu,Ag}$ ;  $B = \text{Zn,Cd,Fe}$ ;  $C = \text{Sn,Ge}$  and  $Q = \text{S,Se}$ .<sup>114</sup> These materials have been of interest to the energy materials community for their potential use both in thermoelectric and photovoltaic applications.<sup>115</sup> Bag *et al.*<sup>115</sup> demonstrated, in 2010, that  $\text{Cu}_2\text{ZnSnSe}_4$ -based solar cells are capable of achieving a conversion efficiency of 10%.<sup>116</sup> Meanwhile Wang *et al.* achieved efficiency of 12.6% in 2014,<sup>117</sup> with comparable efficiencies being achieved by Yang *et al.* more recently.<sup>118</sup> Interest in these materials for medium-high temperature thermoelectric applications arose around the same time, also owing to their band gap of  $E_g = 0.9 - 1 \text{ eV}$ .<sup>119</sup> For the kesterites, this band gap is responsible for their large Seebeck coefficients, as well as the electron excitation from visible light. The high thermoelectric performance at high temperatures for  $\text{Cu}_2\text{ZnSnS}_4$  (CZTS) and related phases has been known for some time. Shi *et al.* reported an outstanding thermoelectric figure of merit  $ZT = 0.95$  at 850 K in 2009 for indium-doped  $\text{Cu}_2\text{ZnSnSe}_4$  (CZTSe),<sup>120</sup> however later studies on the same solid solution suggest a more modest  $ZT = 0.45$  at 773 K, as the material begins to decompose at higher temperatures.<sup>121</sup> Many  $A_2BCQ_4$  related phases show good thermoelectric performance at close to 750 K with  $ZT$  in the range of  $ZT_{max} = 0.1 - 0.5$ .<sup>122-125</sup> Most notably, the copper-doped Cu-Cd-Sn-Se system shows a  $ZT = 0.65$  at 700 K in  $\text{Cu}_{2.10}\text{Cd}_{0.90}\text{SnSe}_4$ ,<sup>123</sup> and cold-pressed nano-structured solid solutions of the same system show a  $ZT_{max} = 0.71$  in  $\text{Cu}_{2.15}\text{Cd}_{0.85}\text{SnSe}_{3.9}$ .<sup>126</sup>

The structure of the kesterite and stannite phases can be described in the space groups  $I\bar{4}$  and  $I\bar{4}2m$  respectively with both being described by an  $a \times a \times 2a$  super-cell of zinc-blende type sub-cells. These two structure types differ in their cation ordering across tetrahedral cation sites with both types showing order across the cation layers in the  $z$ -axis. Figure 1-18(a) shows cation ordering in the stannite type structure, here the  $A$  cations order over the planes of  $z = 0.125$  and  $z = 0.625$  meanwhile  $B$  and  $C$  cations are ordered over the  $z = 0.375$  and  $z = 0.875$  planes.<sup>127</sup> The  $A$  cations are ordered over all layers in the kesterite structure (Figure 1-18(b)), whilst the  $B$  cations are ordered over planes  $z = 0.125$  and  $z = 0.625$  and  $C$  cations over planes  $z = 0.375$  and  $z = 0.875$ .<sup>128,129</sup> Characterising these materials by X-ray diffraction poses difficulty due to the presence of elements with similar atomic numbers, thus there is some dispute in the literature as to whether certain compositions of  $A_2BCQ_4$  should be described by the kesterite or stannite structure types.

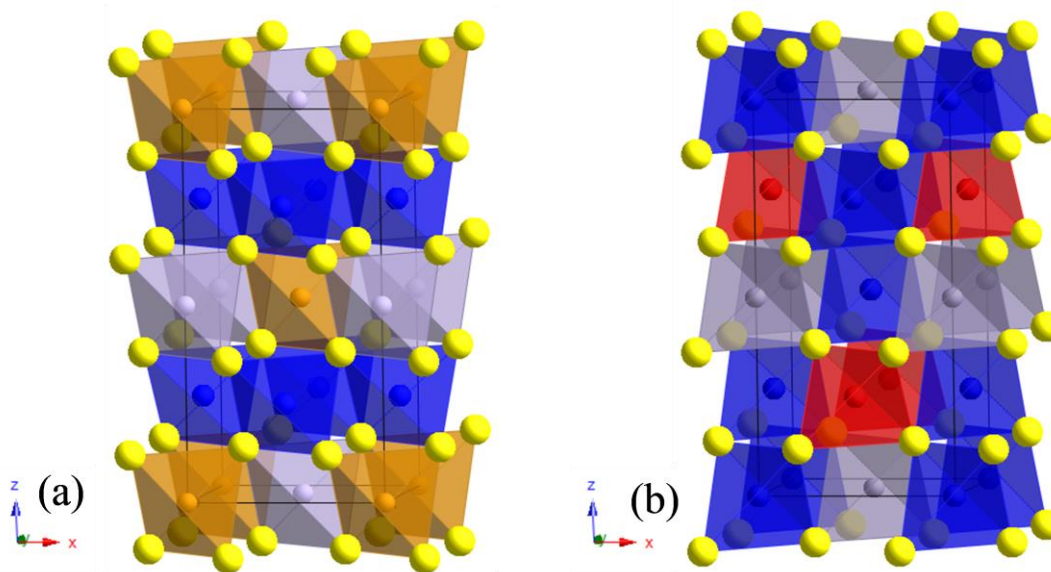


**Figure 1-18**– Perspective view of vertex sharing tetrahedra,  $MS_4$ , for (a) The stannite structure type of  $Cu_2FeSnSe_4$ , Inorganic crystal structure database (ICSD) collection code: 93409. Space group:  $\bar{I}4_2m$ . (b) - The kesterite structure type of  $Cu_2ZnSnS_4$ , ICSD collection code: 171983. Space group:  $\bar{I}4$ . Blue tetrahedra – copper; Grey tetrahedra – tin; Orange tetrahedra – iron and Red tetrahedra - zinc; Yellow spheres- Sulphur.

### 1.4.3. Cation-Rich Copper Zinc-Blende Phases

There are a few known copper chalcogenides with an elemental composition that lies between  $M_2Q$  and  $MQ$  and that have structures related to the anti-fluorite and zinc-blende structure types. That is, they maintain a regular FCC sulphur sub-lattice and the cations order within the tetrahedral holes of the structure. Some of these materials have already proved to be good thermoelectric materials and others could show potential as low cost thermoelectrics. The following section will describe a few of these compounds.

#### 1.4.3.1. Colusite

Colusite is a rarely occurring Cu-S containing mineral with a metal to sulphur ratio of 1.0625:1 and a structure type similar to that of zinc blende, but with additional vanadium cations ordered over the remaining tetrahedral sites (labelled  $V^i$ ). Colusite is described by the general formula,  $Cu_{26-y}V^i_2M_6S_{32}$ , where  $M = As, Ge, Sn, Sb, V$ .<sup>130</sup> Its structure can be characterised on the basis of the cubic  $P\bar{4}3m$  unit cell that is a  $2a \times 2a \times 2a$  supercell of  $a \times a \times a$  sub-cells. Here the additional vanadium cations order within the interstices of the zinc-blende framework. The vanadium cations are positioned at  $(0,0,0)$  and  $(\frac{1}{2}, \frac{1}{2}, \frac{1}{2})$  forming discrete  $VCu_6$  metallic clusters, that are not interconnected by edge-sharing

tetrahedra (Figure 1-19). In each direction,  $a$ ,  $b$  and  $c$ , the cation layers are arranged into alternating vanadium containing,  $VM_2Cu_6$ , and vanadium-free layers,  $M_2Cu_7$ .

Recently colusites have attracted much interest from the thermoelectric community.<sup>131</sup> In 2014 Suekuni *et al.* demonstrated that the material could show promising thermoelectric properties with a lattice thermal conductivity of *ca.*  $\kappa_L = 1 \text{ W m}^{-1} \text{ K}^{-1}$  at 300 K in  $Cu_{26}V_2Sn_6S_{32}$ .<sup>132</sup> This was shortly followed by high-temperature studies on  $M = \text{Ge}$ ,  $Cu_{26}V_2Ge_6S_{32}$ , and  $M = \text{Sn}$ ,  $Cu_{26}V_2Sn_6S_{32}$ , analogues of colusite. Both analogues showed good thermoelectric performance,  $ZT_{max} = 0.8$  and  $0.6$  at 700 K respectively, and excellent thermal conductivities of *ca.*  $\kappa_L = 0.6 \text{ W m}^{-1} \text{ K}^{-1}$ .<sup>133</sup> Excellent thermoelectric performance was eventually realised in the tantalum-tin analogues,  $Cu_{26}Ta_2Sn_{5.5}S_{32}$ , with  $ZT_{max} = 1$  at 700 K.<sup>134,135</sup> The low thermal conductivity has been linked to the inherent cation site disorder over the additional ‘unoccupied’ tetrahedral sites. These disordered states, in the form of atom-scale defects, are effective at scattering phonons and this behaviour is more pronounced in sulphur-deficient samples.<sup>136</sup> The excellent thermoelectric performance that is observed in colusites, compared to other Cu-S TEs, may be attributed to their particularly high power factors.<sup>137</sup> Good thermoelectric performance has been observed for the colusites over a range of elemental compositions, with maximum figure of merit generally having a value of  $ZT_{max} = 0.2 - 0.9$  at 700 K.<sup>137-141</sup> In comparison, the structurally related germanite type phase,  $Cu_{22}Fe_8Ge_4S_{32}$ ;  $ZT_{max}=0.17$ , shows relatively poor thermoelectric performance.<sup>142</sup>

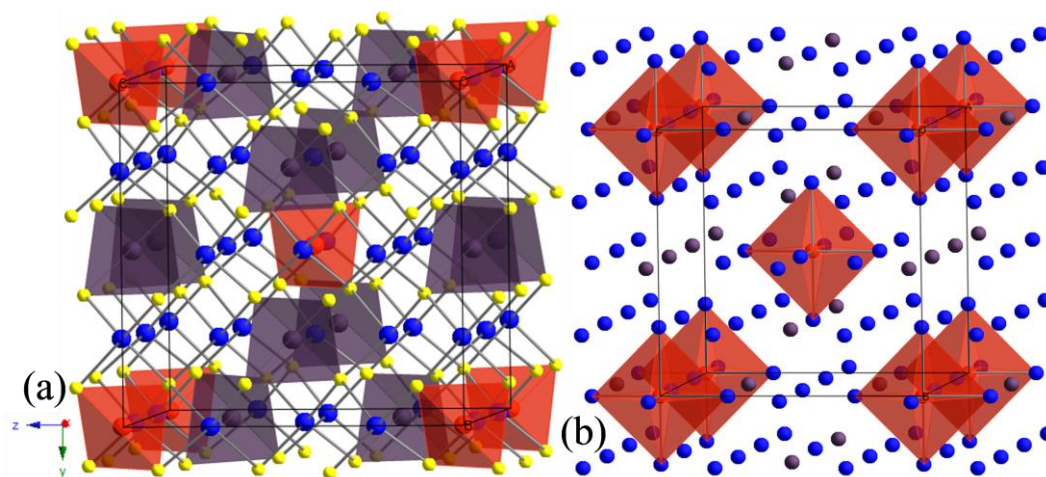


**Figure 1-19** – (a) - Perspective view of the crystal structure of colusite,  $Cu_{26}V_2M_6S_{32}$ , with  $MS_4$  and  $VS_4$  represented as filled tetrahedra. (b) – View of the interstitial atoms as central atoms in metal centred  $VCu_6$  octahedra. Red Tetrahedra/octahedra – vanadium; Blue spheres – copper; Purple tetrahedra –  $M$  cation and Yellow spheres- sulphur.

### 1.4.3.2. Talnakhite and Mooihoekite

Within the scope of known thermoelectrics there are many fewer n-type TEs than p-type, this is also true for the tellurium-free copper chalcogenides. Chalcopyrite is one of few n-type Cu-S TE materials but its performance is rather lacklustre in comparison to its p-type counterparts, many of which have shown high thermoelectric performance.<sup>133,143,144</sup> However, there is an opportunity to uncover alternative n-type thermoelectrics within the Cu-Fe-S system (Figure 1-20).<sup>145,146</sup>

Talnakhite,  $\text{Cu}_9\text{Fe}_9\text{S}_{16}$  ( $\text{M}_{1.125}\text{S}$ ), and mooihoekite,  $\text{Cu}_9\text{Fe}_8\text{S}_{16}$  ( $\text{M}_{1.0625}\text{S}$ ), show similar structural characteristics and elemental composition to the chalcopyrite phase (Figure 1-20). The additional cations within the zinc-blende structure type are ordered within the interstitial tetrahedral sites leading to more complex crystal structures than the chalcopyrite type.<sup>147–149</sup> Hall *et al.* characterised the crystal structures of talnakhite and mooihoekite through single-crystal X-ray diffraction techniques. Despite insufficient contrast between these transition metals, the copper and iron ordering over cation sites was proposed.<sup>147,148</sup> Compositional analysis of the samples was determined by electron probe analysis as performed by Cabri *et al.*<sup>150</sup>

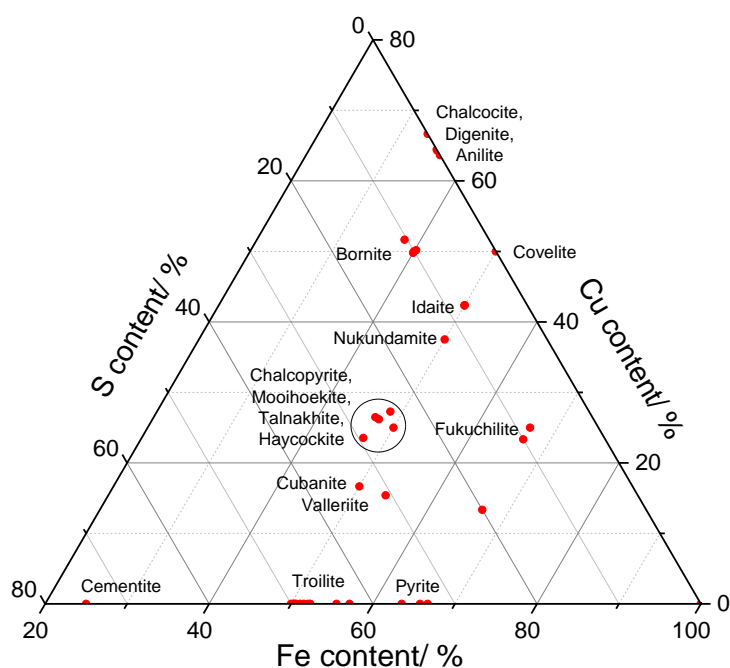


**Figure 1-20.** – Ternary phase diagram for each of the phases of mineral types in the Cu-Fe-S system which can be found within the ICSD.<sup>145,146</sup>

The talnakhite sample with composition,  $\text{Cu}_{18}\text{Fe}_{16}\text{S}_{32}$ , adopts a cubic  $2a \times 2a \times 2a$  supercell, space group  $I\bar{4}3m$ , composed of  $a \times a \times a$  sub-cells.<sup>147</sup> There are 8 occupied crystallographic

interstices within the structure that otherwise shows a zinc-blende structure. Iron cations are positioned over 2 of the interstices at  $(0,0,0)$  and  $(\frac{1}{2}, \frac{1}{2}, \frac{1}{2})$  forming an  $\text{FeM}_6$  metallic cluster, these sites are fully occupied. The remaining 6 occupied interstices, which are disordered with vacancies and copper cations (Vacancy:Cu of 0.95:0.05), form  $\text{CuM}_6$  clusters. The interstitial cation sites edge share with six surrounding octahedra and form a 3D framework of edge-sharing tetrahedral sites (Figure 1-21).<sup>107</sup> The interconnectivity of the  $\text{FeM}_6$  and  $\text{CuM}_6$  metallic clusters can be described by the perovskite structure type where the voids are occupied by copper cations.

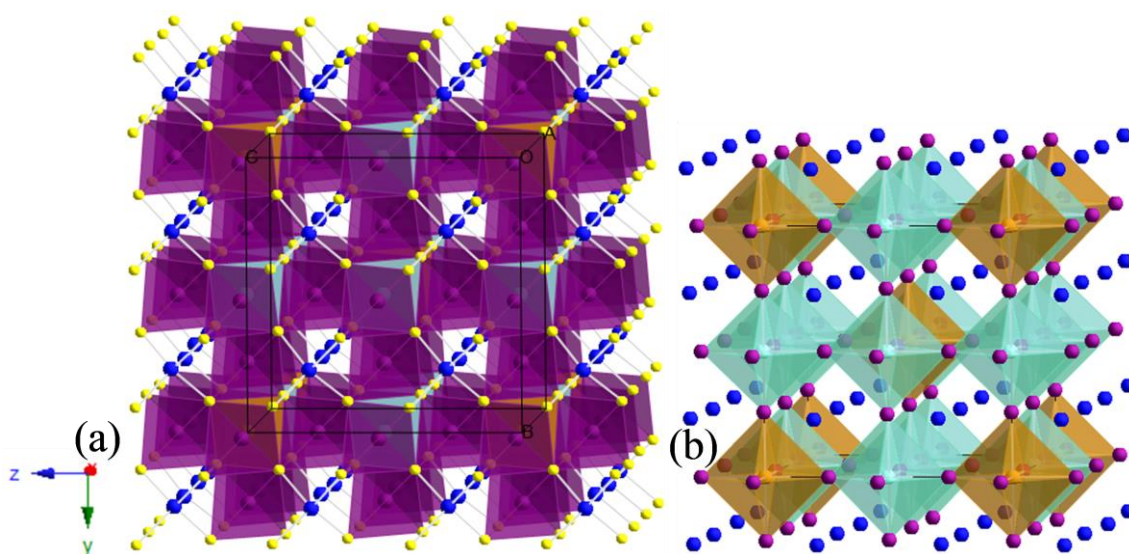


**Figure 1-21** – (a) - Perspective view of the structural model of the talnakhite,  $\text{Cu}_9\text{Fe}_8\text{S}_{16}$ ,<sup>147</sup> showing the interconnected edge-sharing  $\text{MS}_4$  Tetrahedra. (b) – View of the vertex-sharing  $\text{CuM}_6$  and  $\text{FeM}_6$  octahedra in  $\text{Cu}_9\text{Fe}_8\text{S}_{16}$ . Blue spheres– copper only sites; Pastel blue tetrahedra/ octahedra – mixed copper/vacancy sites; Orange tetrahedra/ octahedra – iron only sites and Purple tetrahedra – mixed Cu/Fe Sites.

Mooihoekite,  $\text{Cu}_9\text{Fe}_9\text{S}_{16}$ , has a structure related to talnakhite. As above the copper and iron ordering has been resolved from X-ray diffraction analysis. The tetragonal  $2a \times 2a \times 1a$  supercell has pseudo-cubic  $a_p \times a_p \times a_p$  zinc-blende sub-cells (cell parameter  $a/2 \neq c$ , they differ in length slightly so  $a_p$  is used in their place) and is described by the space group  $P\bar{4}2m$ . Here a further increase in the number of cations leads to more regular ordering of cations within the structure.<sup>148</sup> Iron cations occupy each of the interstitial sites at  $(0,0,0)$  and  $(\frac{1}{2}, \frac{1}{2}, 0)$  forming metal centred octahedra of  $\text{FeFe}_2\text{Cu}_4$  and  $\text{FeCu}_2\text{Fe}_4$ , respectively, thus creating an infinite chain of interconnected metal cations in the  $z$ -direction. This is in contrast to the talnakhite structure, here each of the  $\text{FeM}_6$  clusters are not interconnected

through edge-sharing  $MS_4$  tetrahedra and corner sharing of the  $FeM_6$  octahedra occurs only along the  $z$ -direction.<sup>107</sup>

Tsujii *et al.* reported the low-temperature thermoelectric performance of a sample with composition  $Cu_9Fe_9S_{16}$  and suggested a poor thermoelectric performance at room temperature,  $ZT = 0.06$ .<sup>151</sup> Recent research within the group at the University of Reading has revealed interesting physical property behaviour in materials with the talnakhite structure type. Most notably, Athar *et al.*<sup>152</sup> demonstrated that materials with the talnakhite type structure can exhibit a minimum in the lattice thermal conductivity of *ca.*  $\kappa = 0.85 \text{ W m}^{-1} \text{ K}^{-1}$  at 500 K that coincides with a maximum in the power factor of *ca.*  $S^2\sigma = 0.40 \mu\text{W K}^{-2}$  at 475 K. This observation reveals a lattice thermal conductivity that is substantially lower than that of the  $CuFeS_2$  mineral, chalcopyrite. Here thermoelectric performance was shown to peak at 475 K and  $ZT = 0.17$ , a much lower temperature than the  $ZT_{max}$  temperature observed in chalcopyrite. Even lower thermal conductivities,  $\kappa = 0.6 \text{ W m}^{-1} \text{ K}^{-1}$  at 675 K for  $Cu_{17.6}Fe_{17.6}S_{32}$ , have more recently been reported by Tsujii *et al.* for samples with the talnakhite structure.<sup>153</sup> These recent revelations make talnakhite an attractive candidate for medium-temperature applications if the thermoelectric properties can be optimised.

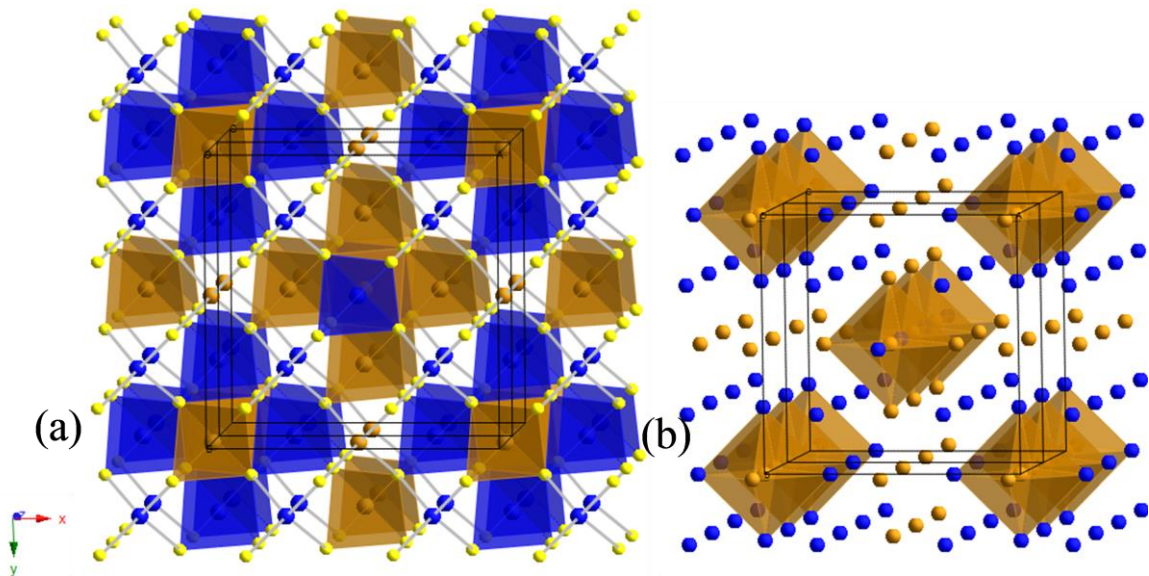


**Figure 1-22** – (a) Perspective view of the structural model of mooihoekite,  $Cu_9Fe_9S_{16}$ ,<sup>148</sup> the filled  $MS_4$  tetrahedra are edge-sharing. (b) – View of the vertex-sharing  $FeM_6$  octahedra in  $Cu_9Fe_9S_{16}$ . Blue tetrahedra/ spheres – copper only sites; Orange tetrahedra/ octahedra/ spheres – iron only sites and Yellow spheres - sulphur.

Additionally, DSC experiments performed on the samples presented above reveal the presence of a structural phase transition at *ca.* 510 K, and some weak evidence of an earlier transition across the temperature range  $T = 300 - 400$  K. Meanwhile, early diffraction studies by Cabri *et al.* suggest numerous structural transitions across the  $T = 300 - 600$  K temperature range.<sup>146</sup> There is some interesting crystal chemistry in this class of materials and they are discussed further in chapter 3.

### 1.4.3.3. *Bornite*

Bornite,  $\text{Cu}_5\text{FeS}_4$ , is an Earth-abundant mineral that is found in mineral deposits across the world and usually appears alongside other Cu-S based minerals, such as chalcopyrite and chalcocite. These sources are mined extensively for production of copper metal.<sup>154</sup> Bornite is another example of a cation-rich zinc-blende type phase. It has a metal to sulphur ratio half-way between the zinc-blende (ZB) and anti-fluorite (AF) structures,  $\text{M}_{1.5}\text{S}$ . The crystal structure of the room-temperature structure can be described by an ordered array of ZB and AF types sub-cells ( $a \times a \times a$ ). These are ordered throughout the structure, with the AF and ZB sub-cells alternating in each of the  $a$ ,  $b$  and  $c$  directions.<sup>155</sup> Bornite shows a number of structural phase transitions and these are outlined in chapter 4.

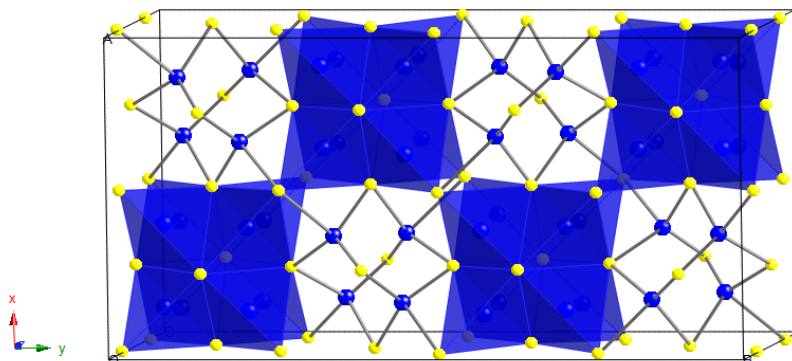


**Figure 1-23** – *Perspective view of the structure of bornite,  $\text{Cu}_5\text{FeS}_4$ , at ambient temperature with edge sharing tetrahedra highlighted as filled polyhedra to outline the AF and ZB ordering within the structure. Blue – cation sites, Cu and Fe; Yellow – Sulphur.*

This material has gained interest from the thermoelectric community because of its exceptionally low lattice thermal conductivity,  $\kappa_L = 0.3 \text{ W m}^{-1} \text{ K}^{-1}$  at 300 K.<sup>156</sup> This value is well below the glass limit and comparable to that of the cation-poor  $\alpha$ -chalcocite phase,  $\text{Cu}_{2-\delta}\text{S}$ . Bornite poses an advantage with respect to its chemical stability under electrical stress. The presence of  $\text{Fe}^{3+}$  has been suggested as a means to suppress the ion migration in bornite. This is supported by the demonstration that constant current stress tests at peak

performance temperature result in minimal degradation of electrical performance.<sup>156</sup> Furthermore, the material shows a peak in performance at *ca.* 575 K, which is ideal for recovery of industrial waste-heat.<sup>13</sup> The stoichiometric phase has shown in many instances to have a reasonable thermoelectric performance,  $ZT_{max} \approx 0.4$ .<sup>143,156–159</sup> It is possible to increase the Seebeck coefficient by doping with small quantities of manganese.<sup>157</sup> Co-substitution of transition metals for copper and iron has proven to increase the power factor and the figure of merit,  $ZT_{max} = 0.6$  at  $T = 590$  K in  $\text{Cu}_{4.96}\text{Co}_{0.04}\text{Fe}_{0.96}\text{Zn}_{0.04}\text{S}_4$ .<sup>158</sup> Interestingly,  $\text{Cu}_5\text{FeS}_{4-x}\text{Se}_x$  solid solutions allow for vast improvements in the electrical resistivity and allow for a  $ZT_{max} = 0.66$  at  $T = 675$  K in  $\text{Cu}_5\text{FeS}_{3.6}\text{Se}_{0.4}$ .<sup>159</sup> There are clearly some strategies to improving the performance of this material and its stability makes it a potentially viable low-cost thermoelectric.<sup>143</sup> Chapter 5 investigates the effects of the structural phase transitions on the thermoelectric properties of bornite in more detail.

#### ***1.4.4. Other Complex Copper Chalcogenide Mineral Phases***

Ternary and quaternary Cu-S based chalcogenides are not limited to these types of structures. In the examples above, the cations only occupy tetrahedrally coordinated sites. In practice and under different chemical environments, copper can adopt other coordinations. There are a few copper rich Te-free chalcogenides that are of interest to the thermoelectric community. In these structures, unique behaviour of the copper atoms results in desirable thermoelectric properties. A few of these complex ternary structures are described in this following section.

##### ***1.4.4.1. Tetrahedrite***

The structure of tetrahedrite may be described by a framework of edge-sharing  $\text{CuS}_4$  tetrahedra that form a collapsed sodalite-type structure. A sulphur-centred spinner unit composed of six  $\text{CuS}_3$  trigonal-planar units occupies the sodalite cage and antimony cations, with trigonal-pyramidal geometry, cap the octahedral windows of the sodalite cages (Figure 1-24).

The temperature dependence of the thermoelectric properties of tetrahedrite have been well documented over  $T = 2 - 800$  K.<sup>160,161</sup> At  $T > 800$  K, tetrahedrite is thermally unstable.<sup>162,163</sup> A low thermal conductivity is observed across the entire temperature range recorded for tetrahedrite and the attractive thermoelectric performance originates from a glass-like thermal behaviour.<sup>162,164–167</sup> An out-of-plane rattling mode of vibration for trigonally coordinated copper cations is attributed to this thermal behaviour. This is modelled in the crystal structure by a large and anisotropic displacement parameter

(ADP).<sup>164,168,169</sup> This peculiar behaviour of the copper cation is a consequence of interactions with lone pairs located on two antimony cations perpendicular to the plane of the  $\text{CuS}_3$  polyhedra (Figure 1-24(c)).<sup>170</sup> This rattling mode is effective at scattering transverse phonons.

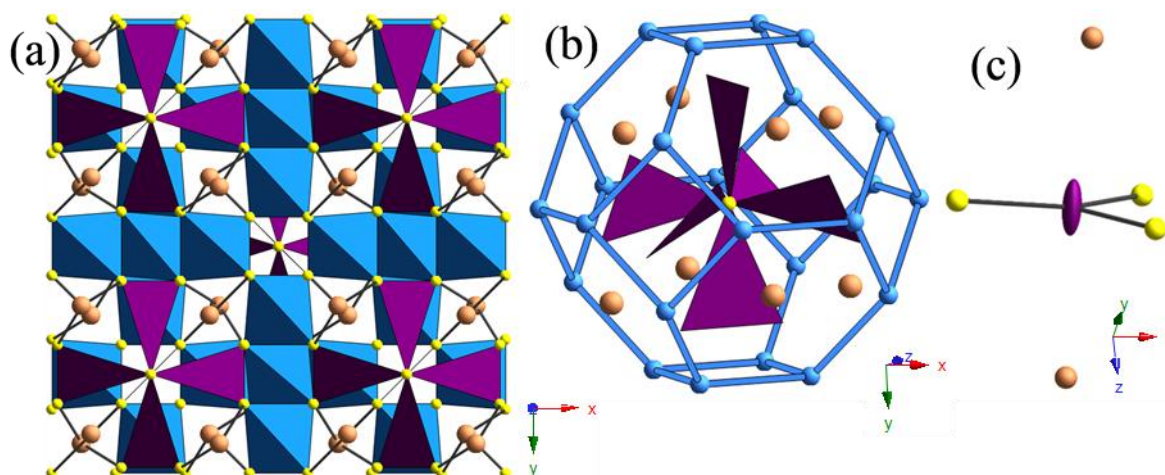


**Figure 1-24** - a) Projection view parallel along the  $[001]$  direction of the tetrahedrite crystal structure. Blue –  $\text{CuS}_4$  tetrahedra; purple –  $\text{CuS}_3$  trigonal-planar polyhedra; orange – antimony atoms; yellow – sulphur atoms. b) Perspective view displaying the sodalite cage, with each  $\text{CuS}_4$  shown as a node. c) Coordination of the trigonal-planar copper cation.

Tetrahedrite,  $\text{Cu}_{12}\text{Sb}_4\text{S}_{13}$ , is a recently investigated thermoelectric material that has shown excellent performance at higher temperatures, *ca.*  $ZT_{max} = 1$  at 700 K.<sup>171–174</sup> This high thermoelectric performance has been observed in many chemically-substituted or co-substituted samples.<sup>171–174</sup> The high performance of this class of materials can be attributed to a combination of excellent thermal characteristics and good electrical properties. At ambient temperatures, the lattice thermal conductivity of tetrahedrite is *ca.*  $\kappa_L = 0.45 \text{ W m}^{-1} \text{ K}^{-1}$  in stoichiometric tetrahedrite.<sup>174</sup> This material is investigated further in chapter 6.

#### 1.4.4.2. Argyrodites

Argyrodite is a naturally occurring mineral with the chemical formula,  $\text{Ag}_8\text{GeSe}_6$ . The family of argyrodites encompasses a range of materials that are structurally alike but chemically different. They can be described by the general formula,  $\text{A}^{m+}_{(12-n)/m}\text{B}^{n+}\text{Q}_6$ , A = Cu, Ag, Cd and Hg; B = Si, Ge, P, As, Ga and Sn; Q = S, Se, Te, and crystallise in the space group  $F\bar{4}3m$  in the high-temperature phase.<sup>175</sup> The structure consists of an anionic cage, which is constructed from the sulphides on the triangular faces of the  $\text{MS}_4$  tetrahedra

along with the independent sulphide anions positioned at  $(\frac{1}{4}, \frac{1}{4}, \frac{1}{4})$ . The sulphide anions positioned at the corner and faces of the cubic unit cell centre this anionic cage that has 24 faces (Figure 1-25(a)).<sup>107</sup> There are 3 distinct cations within the anionic cage. Six cations in the  $16e$  sites form  $\text{CuS}_3$  units each share a common central vertex, giving a spinner unit within the anion cage. The  $24f$  copper cations form a Laves polyhedra with copper atoms occupying each corner of the polyhedra, and each cation having  $\text{CuS}_4$  tetrahedral coordination. The  $48h$  copper cations cap half of the triangular faces of the anion cage (Figure 1-25(b) and appendix A). These cations show a distinct cation conduction pathway. In the low-temperature phase, the anionic sub-lattice is persistent but the cation ordering within the cage varies depending on the elemental composition. In the low-temperature phase different space groups are used to describe the structure of different analogues.<sup>175</sup>

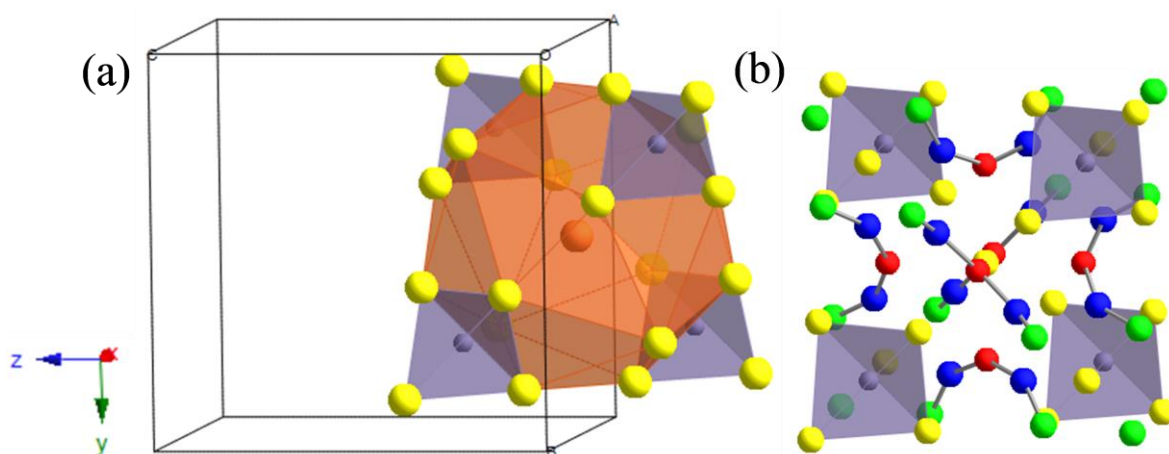


**Figure 1-25** – Perspective view of argyrodite,  $\text{Cu}_8\text{GeS}_6$ , showing the  $\text{GeS}_4$  tetrahedra and (a) the argyrodite anion sublattice to highlight the anion cage structure; (b) –the three types of cation site. Grey – germanium; Yellow – sulphur; Orange – anion cage; red –  $16e$  cations that forms the spinner; green –  $24f$  cations that forms the Laves polyhedra and blue –  $48h$  cation which cap the triangular faces of the anion cage. Cu-Cu bonds show the ion conduction pathways.

Lithium analogues of argyrodite have been of interest to the battery-material community owing to an unusually high Li ion mobility in  $\text{Li}_6\text{PS}_5\text{X}$ .<sup>176</sup> This behaviour has made them potential candidates as solid electrolytes in all-solid-state battery technologies.<sup>176–178</sup> Other compositions of argyrodites are known for their high mobility of the A cations, thus providing ideal conditions for PLEC behaviour.<sup>179</sup> This leads to a low velocity of sound and exceptionally low thermal conductivities,  $\kappa_L = 0.2 - 0.6 \text{ mW K}^{-1}$  at 300 K, in a range of group 11 chalcogenide based argyrodites.<sup>180–182</sup> There have been relatively few

investigations of the thermoelectric properties of the materials in the argyrodite family. However, the few studies that have been carried out have clearly demonstrated their potential as thermoelectrics.  $ZT_{max} = 1.1$  has been observed in  $\text{Ag}_8\text{SnSe}_6$  at 700 K,<sup>183</sup>  $ZT_{max} = 1$  has been observed in silver for copper and tellurium for selenium doped samples  $\text{Cu}_{7.6}\text{Ag}_{0.4}\text{GeSe}_{5.1}\text{Te}_{0.9}$  at 800 K,<sup>182</sup> and  $ZT_{max} = 1.1$  in selenium deficient  $\text{Ag}_9\text{GaSe}_6$ .<sup>184</sup> Thus far, there does not appear to be any literature on the thermoelectric performance of sulphide based analogues. Investigation into the copper-sulphide argyrodite analogues has formed part of this research project. However, the data from those investigations will not form part of this thesis and instead will be released as research papers at a later date.

### ***1.5. Structural Transitions in Cu-based Chalcogenides***

In sections 1.3 and 1.4, the types of structures that allow for high thermoelectric performance have been presented. A critical feature that is prevalent in the chemistry of copper-chalcogenide materials is that they are often subject to structural phase transitions as a function of temperature. This behaviour has been discussed for a few of the materials above, but the influence on the physical properties has not been outlined. This thesis describes these phenomena in more depth for some specific materials. Figure 1-26 shows the temperature dependence of the Seebeck coefficient for selected copper-chalcogenide materials. The star represents the phase transition temperature of each material. For each of the materials presented, there is a discontinuity or change in the behaviour consistent with this phase-transition temperature. It is important to understand the structural behaviour of the material in all structural phases if further improvements in thermoelectric performance are to be realised.

### ***1.6. Aims of This Work***

The aims of this thesis are to provide a better understanding of the relationship between the temperature dependence of the crystal structure, electrical transport properties and thermal transport properties of some selected copper-chalcogenide thermoelectric materials. This goal could be encompassed by the study of the structure and properties simultaneously. As such, this work hopes to create a novel *in-situ* cell that will allow for the collection of electrical transport data as well as neutron diffraction data in a single experiment. The changes in the properties occur with increasing temperature and chalcogenides are sensitive to oxidation or decomposition, so the cell should be able to accommodate the conditions necessary to prevent sample degradation.

For each of the structural phases of bornite the structure is not completely understood and the ordering of iron within the structure remains uncertain. This work seeks to exploit neutron diffraction techniques in order to resolve the ordering of iron within the structure. In addition, the thermoelectric properties of this material have not been optimised so this work endeavours to further improve the thermoelectric performance of bornite.

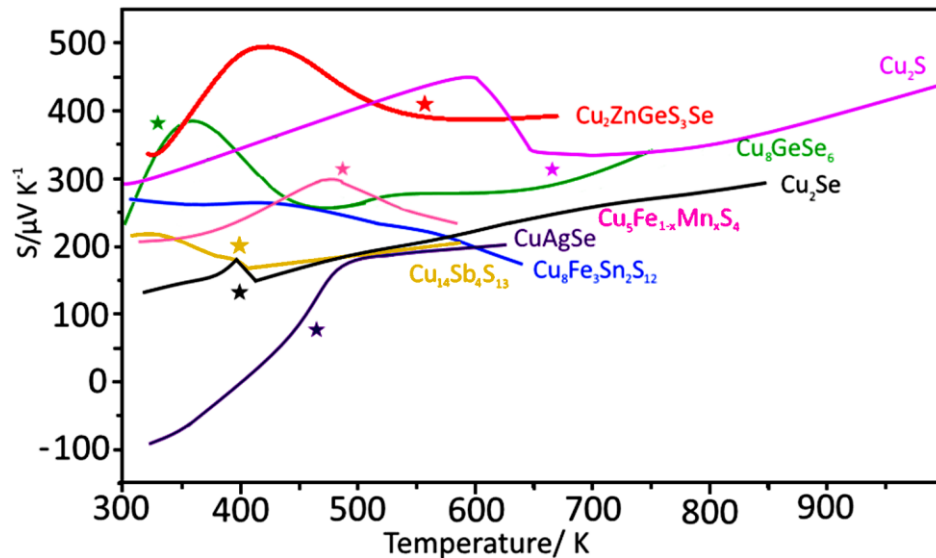


**Figure 1-26** – Temperature dependence of the Seebeck coefficient for selected copper chalcogenide materials. \* - Indicates the phase transition temperature for each material.

71,157,164,182,185–189

The high temperature structure and performance of tetrahedrite is well resolved, but more recent studies have revealed a magnetic transition in the material at low temperatures. Neutrons offer an opportunity to investigate the magnetic structure of materials so these will be used in order to try and understand the origins of the magnetic transition of the material.

The mooihoekite and talnakhite family of thermoelectrics offer an opportunity to provide viable low-cost low-toxicity n-type thermoelectrics. The high-temperature crystal structure and electrical transport properties of this family of materials has not been studied to any considerable extent. The work within this thesis will try to establish critical insights into the behaviour of these materials.

The compounds and experiments presented in this thesis include:

- Testing and development of an *in-situ* cell for powder neutron diffraction (PND) experiments

- High temperature *in-situ* PND experiments on  $\text{Cu}_{2.125}\text{Ge}_{0.875}\text{ZnSe}_4$
- High temperature *in-situ* PND experiments on  $\text{CuFeS}_2$
- High temperature *in-situ* PND experiments on  $\text{Cu}_9\text{Fe}_9\text{S}_{16}$  and  $\text{Cu}_9\text{Fe}_8\text{S}_{16}$
- High temperature PND experiments on  $\text{Cu}_5\text{FeS}_4$ ,  $\text{Cu}_{5.08}\text{Fe}_{0.92}\text{S}_4$  and  $\text{Cu}_{4.97}\text{Fe}_{0.97}\text{S}_4$
- Chemical substitution and thermoelectric studies on  $\text{Cu}_{5-x+y}\text{Fe}_{1-y}\text{S}_4$
- Low temperature PND experiments on  $\text{Cu}_{12}\text{Sb}_4\text{S}_{13}$

## Chapter 2 - Experimental and Synthetic Methods

### *2.1. Synthetic Methods*

In solid-state chemistry it is important to synthesise materials that are pure, and which exhibit a single crystallographic phase. If this is achieved, the structural and physical properties of the specific phase may be determined by further experimental analysis. This section will investigate the synthetic and analytical methods that have been used to synthesise and analyse samples.

For any combination of elements, many different phases can exist, for example  $\text{SiO}_2$ , can adopt a number of different polymorphs at room temperature, crystalline and amorphous.<sup>190</sup> Further to this, the elemental composition is usually flexible in a multiple element system. The Cu-Fe-S system presented in Figure 1-20 provides an excellent example of this.<sup>145,146</sup> The experimental composition of samples and the reaction conditions need to be controlled precisely to create the desired product. For all samples presented, the powdered samples were carefully weighed to match the stoichiometric amount of each element in the desired material.

#### *2.1.1. Considerations in Synthesis*

Dry chemistry techniques were used throughout this work to create the polycrystalline samples. A mixture of elemental powders were ground together under ambient conditions using an agate pestle and mortar. Transition metals are sensitive to oxidation by atmospheric oxygen if heated to high temperatures under air. Meanwhile, sulphur volatilises at relatively low temperatures. Therefore, reaction vessels that allow for an inert atmosphere and a closed system were used in the high-temperature and mechanochemical techniques described here.

#### *2.1.2. High-Temperature Techniques*

The combination of a very low boiling point for sulphur, high melting point for the metals and relatively low melting points of reaction intermediates, results in a solid-liquid-gas state reactions.<sup>83</sup> Under these conditions, atomic diffusion occurs more readily and a homogenous starting mixture of elements is crucial to ensure a uniform reaction. These methods of synthesis will typically lead to the thermodynamically favoured structure for the combination of elements, so meta-stable products are generally not achieved through high-temperature techniques.<sup>191</sup>

The homogenous reaction mixture of elemental solids were sealed into evacuated silica ampoules and placed into Lenton furnaces for either one or two consecutive firings. Silica ampoules were used because they offer a high melting point ( $T_m > 1900$  K) and an inherently low reactivity. A slow heating rate was used in these high-temperature reactions to prevent the rapid evaporation of sulphur that would lead to a build-up of pressure and risks explosion of the glass ampoule. Meanwhile, different approaches to cooling have been employed, such as quenching in water, cooling naturally or controlled cooling.

The reactions were generally performed over a few days or up to a week per firing and temperatures of the order of  $T = 600 - 1000$  K were used for these chalcogenide-based materials. These methods have been used in the synthesis of the talnakhite, mooihoekite and copper-rich chalcopyrite samples presented in section 3.7 as well as for the kesterite sample presented in section 3.5. Details of the reaction conditions are provided within those experimental sections.

### ***2.1.3. Mechanochemical Techniques***

Ball milling techniques were classically used to micronize or mechanically alloy materials. More recently, mechanochemical techniques have been applied to materials synthesis. It is a useful tool for creating materials, such as intermetallics, ceramics, composites, polymers and meta-stable phases, such as metal-organic frameworks.<sup>192,193</sup> Further to this, it has shown success in the synthesis of a range of metal oxides, halides and sulphides.<sup>194,195</sup> The use of these techniques in materials research has grown in recent years as it offers an easily scalable process and the opportunity to create nanoparticles and nanocrystalline samples.<sup>196</sup>

Ball mills are available as attritor, shaker or planetary mills, they differ in their efficiency, capacity and heat or energy transfer to the material. The collision of balls with the walls of the vessel or other balls at high velocities creates localised instantaneous temperatures which allows for chemical reactions to take place.<sup>197</sup> In a planetary mill (Figure 2-1) there are two rotational axes: ( $r_1$ ) rotation around a central fixed point that leads to a centrifugal force ( $F_1$ ) and ( $r_2$ ) rotation around a secondary axis, centred on the milling vessel, forces the balls to migrate through the system, grinding the materials against the vessel and facilitating the high energy collision of the milling balls leading to chemical reaction.

A planetary mill was used to synthesise all the bornite samples, the tetrahedrite sample and the chalcopyrite sample with composition  $\text{CuFeS}_2$ . Specific details of each experiment can be found in the respective experimental sections. The elemental powders were ground

together in air then loaded into the milling vessel (25 mL steel vessel or 50 mL tungsten vessels) along with milling balls (5 mm, 0.5 g steel balls or 5 mm, 1 g tungsten carbide balls) and using a specific weight ratio of powder to balls. The vessel was taken into an argon glove box and sealed under the inert atmosphere. The filled milling vessel was then clamped into a planetary mill RETSCH PM100 pulverisette, and milled for consecutive millings of between  $t = 8 - 24$  hr at  $RPM(revolutions\ per\ minute) = 400 - 600$ , the resulting powder was agitated between consecutive millings to prevent sample agglomeration.

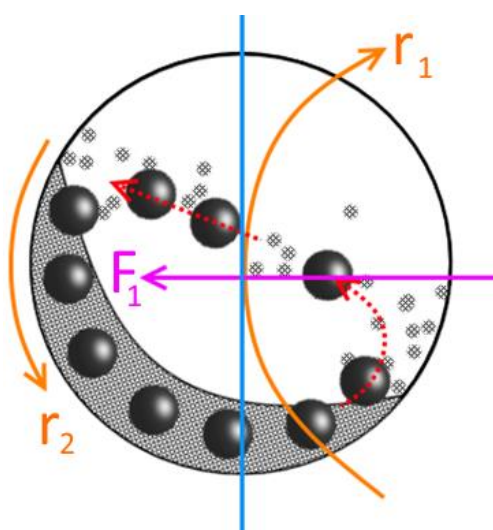


**Figure 2-1.** – Schematic diagram of the rotational forces acting on a ball mill jar. Orange arrows – rotational motions; Pink arrow - Centrifugal force; Red arrow - Path of milling balls.

#### 2.1.4. Sample Consolidation

After high-temperature syntheses, the products were either in the form of a polycrystalline powder or an ingot with a density significantly lower than the crystal density. The resulting products from the mechanochemical synthesis were non-crystalline powders. Low-temperature consolidation of samples is possible but leads to poor mechanical properties, thus high-pressure high-temperature techniques, such as hot-pressing (Figure 2-2) or spark plasma sintering are conventional. Furthermore, high-temperature consolidation acts as a final sintering step for mechanochemically alloyed samples leading to the formation of a polycrystalline ingot. This consolidation process can heavily influence the microstructure of the polycrystalline material.<sup>198</sup> For example, in 2D-layered materials the layers may preferentially stack perpendicular to the direction of the applied force.<sup>199</sup>

In the hot pressing system (Figure 2-2), the internal face of the tungsten-carbide moulds, with an internal diameter of 12.7 mm, were coated with graphite spray to allow for easy removal of the sample after synthesis. The powdered sample was then loaded into the mould, sandwiched between two graphite foils and two tungsten carbide dies. An external resistive heating jacket was fastened around the perimeter of the tungsten carbide mould, then placed into the Macor® ceramic and mineral wool insulation. The set-up was then tightened and sealed into the in-house hot-pressing enclosure that allows for inert atmospheres. The sample environment was purged with N<sub>2</sub> gas before heating and pressing. Temperature,  $T = 675 - 875$  K, and pressure,  $P = 60 - 140$  MPa, were tuned depending on the sample. Details for each sample can be found in their respective experimental sections. Pressure was controlled by a hydraulic press and the temperature was controlled using a thermocouple inserted into the mould and connected to a temperature controller.

The resulting samples were coin-shaped pellets with densities of *ca.* 99% of the theoretical crystal density. The densities of all samples were measured using an AE Adam PW 184 Archimedes balance and the buoyancy method by weighing the samples in air and water.

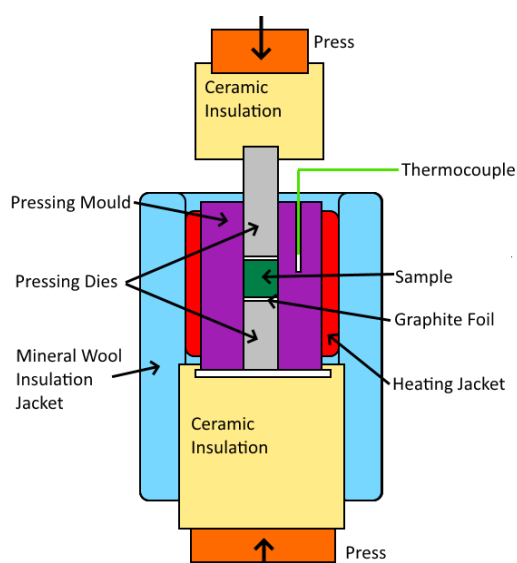


*Figure 2-2.* – Schematic diagram of the hot-pressing system used in the in-house equipment.

## **2.2. Structural Analysis and Characterisation**

Powder X-ray and neutron diffraction techniques have been used throughout this work for structure and phase analysis of the powdered samples. An outline of the theory, facilities and instruments used is given in the following section.

### 2.2.1. Powder X-ray Diffraction

X-radiation was discovered in 1895 by Willhelm Roentgen. This EM radiation was discovered inadvertently during his experimental work on vacuum tubes. A high voltage was used to pass a current between two electrodes separated by a vacuum. High energy electrons are emitted from the high-temperature cathode and are accelerated by a high voltage and collide with the metallic anode.<sup>200</sup> This interaction ionises the core-shell electrons of the metallic anode. Electrons occupying higher energy levels drop to fill the lower energy level, in the process releasing a photon with energy equivalent to the change in energy of the demoted electron. The energy of the emitted photon is dependent on the element used in the cathode, each individual element will give off characteristic wavelengths of light.<sup>201</sup> The wavelength of X-ray radiation is similar to interatomic distances and allows for the investigation of the details of a crystal at the atomic-scale. The radiation interacts with the electron cloud of the crystalline matter, scattering and re-radiating the X-rays. Interference effects between the reflected radiation leads to constructive and destructive wave interferences. Constructive interferences of the incident radiation leads to Bragg diffraction, this diffracted radiation holds information of the crystal structure of a material.

The crystal structure of a material will be constructed from a series of planes of atoms along many different directions,  $(h, k, l)$ . These planes of atoms repeat regularly in space and have an interplanar spacing,  $d_{hkl}$ . Each of these planes will reflect a small percentage of the X-radiation that it interacts with.<sup>202</sup> Wave interference effects lead to constructive and destructive interference between photons in the reflected beam, constructive interference is observed as spikes in radiation intensity – giving Bragg peaks in a diffraction pattern. This will occur for the radiation reflected from lattice planes with the same values of  $h, k$  and  $l$ , but only when the geometric restriction  $\overline{AB} + \overline{BC} = n\lambda$ , is satisfied (Figure 2-3). Interacting waves from adjacent and parallel atomic planes will have travelled different distances after they have interacted with the crystal. The additional distance travelled between points A and B,  $\overline{AB}$ , in Figure 2-3 will be related to  $d_{hkl}$  through the relationship:

$$\overline{AB} = d_{hkl} \sin\theta \quad (2-1)$$

Here,  $\theta$ , is the angle between the incident radiation and the atomic plane. The reflected beam also travels an additional distance between B to C that is equal to the distance of  $\overline{AB}$ , giving  $2\overline{AB}$ .

Providing that the distance travelled by interacting photons is related through some integer of the wavelength,  $n\lambda$ , they will remain in-phase,  $2\overline{AB} = n\lambda$ . It is usually assumed that  $n = 1$  and this relationship between the incident beam and atomic planes provides the Bragg equation:

$$\lambda = 2d \sin\theta \quad (2-2)$$

Where,  $\lambda$ , is the wavelength of the radiation,  $\theta$ , is the angle of incidence and,  $d$ , is the  $d$ -spacing. From the  $d$ -spacing values, the unit cell information can be determined, and the reflection intensities and systematic absences hold the structural information of the crystal system being studied. Diffraction from polycrystalline materials gives a 1-dimensional diffraction pattern, this is a compression of the 3D diffraction pattern given by a single crystal. There is a loss of information in this compression due to peak overlap, among other things. A powdered sample consists of thousands of minute crystals, essentially satisfying each possible orientation. The radiation diffracted from the powder appears as cones of intensity in real space, known as Debye-Scherrer cones, that can be analysed in a diffractogram.

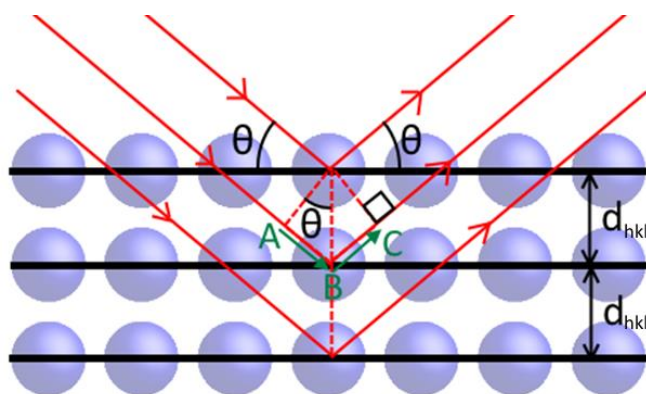


**Figure 2-3.** – Schematic diagram of Bragg diffraction of radiation by parallel and adjacent lattice planes. Thick black lines are used to show the planes of the atoms, red lines represent the incident and reflected beams.

### 2.2.1.1. The Bruker D8 Advance Diffractometer

The laboratory X-ray diffractometer used here, a Bruker D8 Advance, was installed with an X-ray tube containing a copper anode target, and a LynxEye linear detector that rotates through an angle of  $2\theta/^\circ$ . The characteristic X-ray wavelengths for Cu are  $K_{\alpha 1}$ ,  $\lambda = 1.5405 \text{ \AA}$ ;  $K_{\alpha 2}$ ,  $\lambda = 1.5443 \text{ \AA}$  and  $K_{\beta}$ ,  $\lambda = 1.3922 \text{ \AA}$ , a single-crystal Ge monochromator selects the desired  $K_{\alpha 1}$  wavelength. Prior to measurement the samples were ground into a fine powder using an agate pestle and mortar, then loaded into the diffractometer. For the flat plate

instrument with reflection geometry, powders were loaded into a recessed PMMA polymer holder and pressed flush to the holder surface or a few milligrams was adhered to the surface of a Si-low background holder using Vaseline. For the capillary instrument with transmission geometry, the fine powders were loaded into a sodium borosilicate capillary with diameter 0.5 mm and sealed with wax before loading onto a goniometer. For preliminary phase analysis of samples the collection times and angular ranges used were,  $t_{total} = 1$  hr,  $5 < 2\theta / ^\circ < 85$ ,  $t_{step} = 0.74$  s and  $2\theta_{step} = 0.0145^\circ$ , for higher quality diffraction data with better statistics,  $t_{total} = 6$  hr,  $10 < 2\theta / ^\circ < 120$ ,  $t_{step} = 1.36$  s and  $2\theta_{step} = 0.0066^\circ$ . The Inorganic Crystal Structure Database, ICSD, contains the published structures of all known crystalline inorganic phases and was used to provide starting models of crystal structures. The software package DIFFRAC.EVA together with the ICDD PDF2 materials database allows for phase identification through a peak search and match function allowing for a very basic phase analysis of the material.<sup>203</sup>

### ***2.2.2. Powder Neutron Diffraction***

Large-scale national and international facilities are required to exploit neutrons for scientific analysis of materials.<sup>203</sup> There are two prominent methods for generating neutrons and both involve breaking the nuclei of atoms. In both instances, the generated neutrons have energies of MeV but the neutrons need to be slowed to the order of meV to be useful for materials research. So they are passed through a low-temperature moderator before reaching samples.

Nuclear reactor sources generate neutrons through a controlled fission process which provides a continuous flux of neutron radiation with a polychromatic spectrum. For diffraction purposes, a single wavelength is usually selected. Moderation of the neutron beam provides a range of lower energy neutron wavelengths, the single neutron wavelength can then be selected using choppers or a monochromator. Similar to an X-ray diffractometer, the detectors will collect diffracted neutron intensity as a function of  $2\theta$ .

By contrast, spallation sources produce a ‘white’ beam of neutrons with a specific structure of pulses that are tailored to provide an energy separation and resolution that is desired.<sup>204</sup> The white beam of neutrons is a spectrum of neutron energies that have a varying wavelength,  $\lambda$ , and because the wavelength is variable, the angle,  $2\theta$ , must be fixed.<sup>205</sup> The structure of the pulse,  $\lambda(t)$ , is known and this allows for the diffracted radiation to be measured as a function of the time-of-flight (TOF) through the modified Bragg equation<sup>206</sup>:

$$\frac{h}{\lambda} = \frac{m_n L}{t} \quad (2-3)$$

$$t = 505.56 L d \sin\theta \quad (2-4)$$

Here,  $h$ , is Planck's constant,  $m_n$ , is the mass of a neutron,  $L$ , is the length of the flight paths and,  $t$ , is time.

Neutrons provide advantages over X-rays for certain chemical systems because they interact with the nucleus of the atoms rather than the electron cloud. In the case of diffraction, the form factor of X-rays is dependent on the atomic number,  $Z$ , where higher  $Z$  correlates with a higher form factor (Table 2-1). As a result the differentiation between elements with a similar  $Z$  can be difficult when using X-ray diffraction. In addition to this, diffraction from light elements is weak so detecting them in the presence of heavy elements can be very difficult.

**Table 2-1** – X-ray form factor,  $f_1$ , at 8.04 keV and neutron coherent scattering length (SL) for selected elements.  $^1\text{H}$  and  $^2\text{H}$  neutron scattering cross sections shown.

Z	Element	$f_1/ \text{e atom}^{-1}$	Neutron SL/ fm
1	$^1\text{H}, ^2\text{H}$	0.99998	-3.7406, 6.671
2	He	2.00014	3.26
5	B	5.00961	5.3
16	S	16.3351	2.847
26	Fe	24.8575	9.45
27	Co	24.6213	2.49
29	Cu	27.0246	7.718
34	Se	33.2061	7.97
52	Te	51.9423	5.8
82	Pb	78.2721	9.405

By contrast, neutron scattering does not show a direct dependence on the atomic number. For example, iron and cobalt would be indistinguishable using X-ray diffraction techniques, due to very similar form factors, but easily distinguishable using neutron diffraction due to hugely different scattering lengths. Meanwhile, the neutron SL of the deuterium isotope is higher than that of the heavy element tellurium, so it would be trivial to detect using neutrons. This characteristic of neutrons also allows for isotopic enrichment of samples which can allow for further distinction between elements. Neutrons also have a magnetic moment that interacts with the magnetic moments of ions in a material enabling the investigation of long-range magnetic order.

The TOF neutron diffraction data presented in this thesis have been collected at the ISIS neutron facility (Figure 2-4) using two separate instrument, POLARIS and WISH.

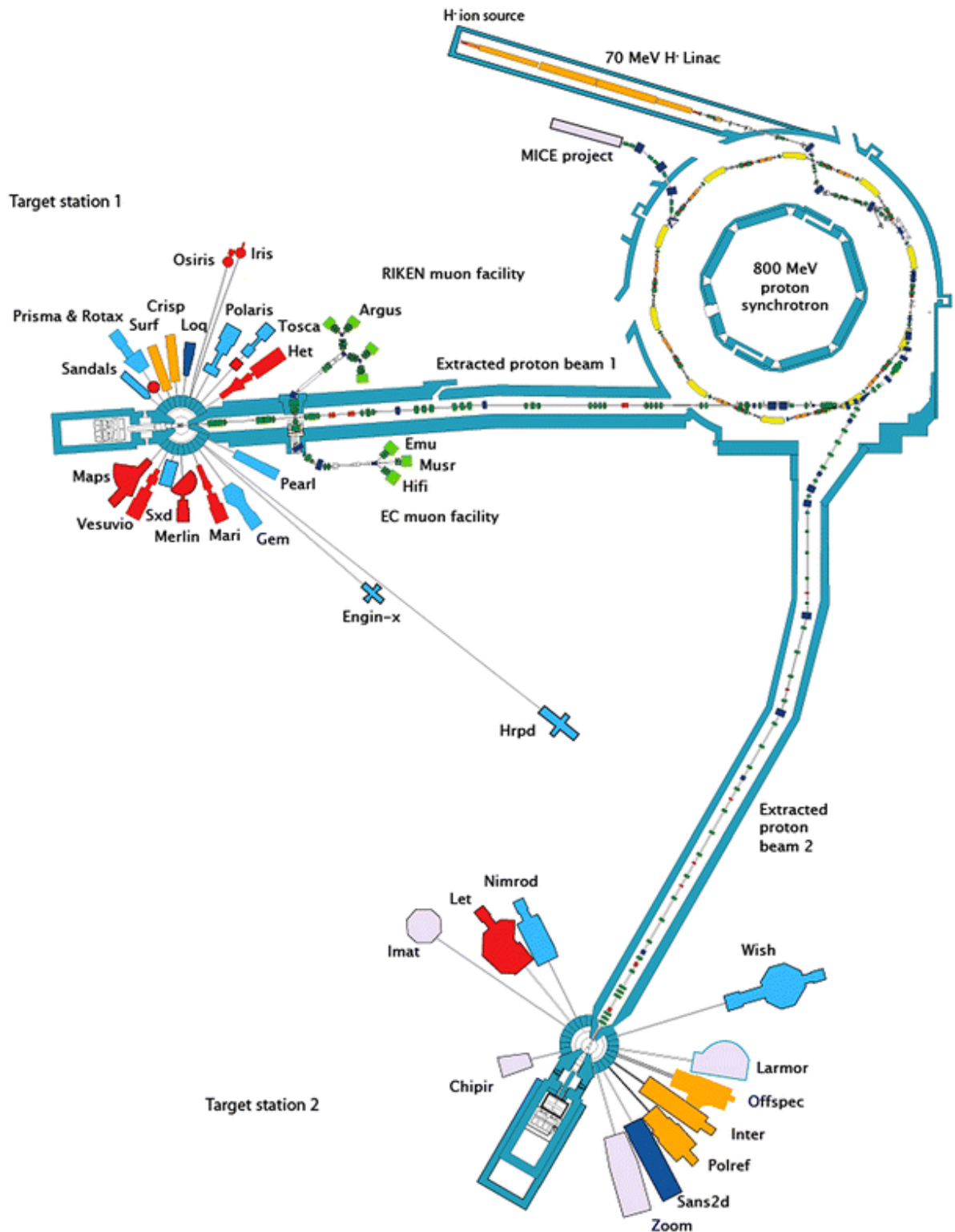


*Figure 2-4 – Schematic Diagram of the layout of the ISIS neutron facility; synchrotron and instruments. Reproduced from 207 which is distributed under a creative commons licence.*

### 2.2.2.1. *The ISIS Neutron Facility*

The production of neutrons at the ISIS neutron facility begins at the ion source. Here,  $H^+$  ions are created from a hydrogen stream and acquire an energy of  $E = 35$  eV. They are passed through a linear accelerator and acquire an energy of  $E = 70$  MeV. Prior to entry to the synchrotron the  $H^+$  ions are stripped of electrons by being passed through  $0.3 \mu\text{m}$  aluminum oxide foil. Dipole magnets are used to give the beam of protons a circular orbit around a synchrotron with a 26 m radius, around which they are accelerated to  $E = 800$  MeV. The protons are ejected from the synchrotron in pulses of 100 ns and a frequency of 50 Hz to two target stations providing  $160 \mu\text{A}$  and  $40 \mu\text{A}$  of beam current to target stations (TS) 1 and 2 respectively. The high energy protons collide with a tantalum-clad tungsten target where the neutrons are created by nuclear fission.<sup>208</sup> These neutrons are directed towards the neutron scattering instruments at each target station after passing through cooling water and one of four moderators, two water at room temperature, one methane at 100 K and one hydrogen at 20 K.

### 2.2.2.2. *The POLARIS Neutron Diffractometer*

The majority of the neutron diffraction experiments in this research project have been carried out on the POLARIS diffractometer on TS1 (Figure 2-4 and Figure 2-5), the *in-situ* diffraction cell described and presented in chapter 3 of this thesis has been designed for use on the POLARIS and GEM diffractometers. POLARIS is a medium-resolution diffractometer, with 6 detector banks that are positioned over different angles of  $2\theta$  (Table 2-2). It receives a high flux of thermal neutrons from a 298 K water cooled moderator. The instrument allows for characterisation of materials under different external variables. The in-house low-temperature and high-temperature furnaces, with operating temperatures  $T = 300 - 600$  K and  $T = 300 - 1000$  K, respectively, that were used here were built and developed by the Rutherford Appleton laboratory. The samples (*ca.* 3 g) were loaded into thin walled vanadium cans (internal diameter  $l = 6$  mm) for ambient-temperature measurements. For variable-temperature experiments ( $\text{Cu}_5\text{FeS}_4$ ,  $\text{Cu}_{5.08}\text{Fe}_{0.92}\text{S}_4$ ,  $\text{Cu}_{4.96}\text{Fe}_{0.98}\text{S}_4$ ), the samples (*ca.* 3 g) were loaded into evacuated (at  $10^{-3}$  bar) high purity silica ampoules (of internal diameter  $l = 8$  mm) within V cans (of internal diameter  $l = 10$  mm), or used the *in-situ* Seebeck diffraction resistance cell ( $\text{Cu}_{2.125}\text{Ge}_{0.875}\text{ZnSe}_4$ ,  $\text{CuFeS}_2$ ,  $\text{Cu}_9\text{Fe}_9\text{S}_{16}$ ,  $\text{Cu}_9\text{Fe}_8\text{S}_{16}$ ) where specified. The sample tank was evacuated of air and the *in-situ* cell had a static He atmosphere. The diffraction data from detector banks 3, 4 and 5/6 (Figure 2-5) were used for structural analysis using the GSAS software package.<sup>209</sup> For

Rietveld analysis (see section 2.2.4), the background contribution from the furnaces and silica ampoules were subtracted using the Mantid analysis software package,<sup>210</sup> and using the Gudrun analysis software package for PDF experiments.

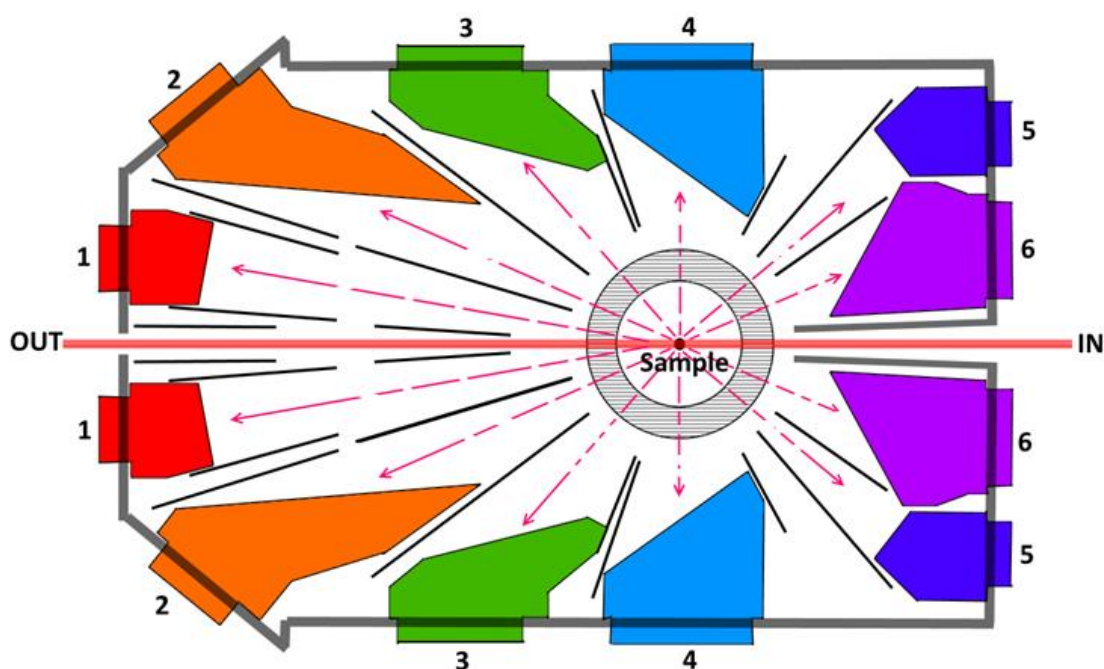


**Figure 2-5-** A 2-D schematic diagram of the detector bank array in the POLARIS diffractometer. Banks: 1 – Very low angle; 2 and 3 – Low angle; 4 – 90 degree bank; 5 and 6 – back scattering.

**Table 2-2 –** Parameters of the detector banks of the POLARIS diffractometer.<sup>211</sup>

detector bank	1	2	3	4	5, 6
scattering angle, $2\theta/^\circ$	6 - 14	19 - 34	40 - 67	75 - 113	135 - 143, 146 - 168
Resolution, $\Delta d/d / \%$	2.7	1.2 - 1.9	0.85	0.51	0.3, 0.3
$d_{max}/\text{\AA}$	>40	13.5	7	4.1	2.7, 2.7

### 2.2.2.3. The WISH Neutron Diffractometer

The WISH diffractometer is a high-brilliance medium-resolution diffractometer located on TS2 that views a 40 K solid-methane moderator and allows for rapid collection of single-crystal and powder diffraction data.<sup>212</sup> Ten <sup>3</sup>He detectors panels over 5 detector banks are situated 2.2 m from the sample position and each covers an angular range of  $\theta = 32^\circ$  (Figure 2-6, Table 2-3).<sup>213</sup> These are positioned cylindrically over the angular range  $10 < 2\theta < 170$ . This along with a low frequency pulse of 10 Hz, allows for the collection of diffraction data over a wide  $d$ -spacing range,  $d = 0.7 - 50 \text{ \AA}$ . The instrument is primarily used for the investigation of magnetic materials and allows for the study of materials in

different sample environments. The experiment on this instrument was performed at low temperature,  $T = 1.5 - 300$  K, using an in-house cryogen free cryostat for a sample of  $\text{Cu}_{12}\text{Sb}_4\text{S}_{13}$  to investigate the origin of the magnetic behaviour in the material at low temperature. The sample (*ca.* 3 g) was loaded into a thin walled vanadium can with an internal diameter of 6 mm.

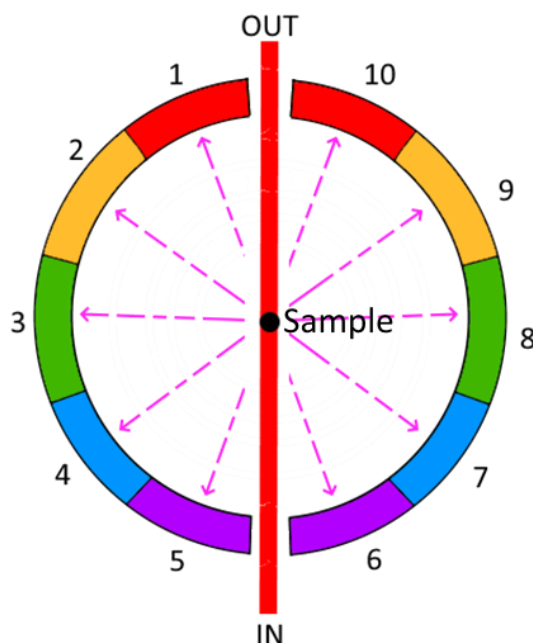


**Figure 2-6** – A 2-D schematic diagram of the detector bank array for the WISH diffractometer. Numbers indicate the detector bank number and colours indicate the coupled detectors.

**Table 2-3** – Parameters of the detector banks of the WISH diffractometer.

detector bank	1,10	2,9	3,8	4,7	5, 6
scattering angle, $2\theta / ^\circ$	27.08	58.33	90	121.66	152.83
Resolution, $\Delta d/d / \%$	1.6	0.8	0.55	0.4	0.3, 0.3
$d_{max} / \text{\AA}$	48	12.9	6.8	5.8	5.0

### 2.2.3. X-Ray and Neutron Interaction with Matter

The difference in contrast between dissimilar elements, ions or isotopes that is provided by neutrons and X-rays was highlighted in section 2.2.2. Here, the interaction of these radiation sources with matter will be discussed briefly.

X-rays interact with the electron cloud of atoms, this is relatively large in respect to the wavelength of the X-radiation. Therefore, the incident radiation will reflect from different parts of the electron cloud, causing destructive interferences. This results in a fall-off in

Bragg intensity with increasing  $\sin\theta/\lambda$ . By contrast, neutrons interact with the nuclei of atoms which are much smaller than the wavelength of the incident neutrons. Hence a constant diffraction intensity over all values of  $\sin\theta/\lambda$  can be expected when using a constant wavelength neutron source. Meanwhile the diffraction intensity as a function of  $\sin\theta/\lambda$  at a pulsed source is dependent on the structure of the incident beam. Furthermore, magnetic reflections in neutron diffraction data will show behaviour with  $\sin\theta/\lambda$  that is more similar to X-ray diffraction as the neutron will interact with the electron cloud under these circumstances.

It is also important to note that, as shown in Table 2-1, different elements have different form factors,  $f_l$ , or scattering lengths which contribute to the scattering factor of a given plane of atoms,  $f_{hkl}$ . This has a significant influence on the intensity of each of the observed Bragg reflections,  $I_{hkl}$ , which is proportional to the square of the structure factor:

$$F_{hkl} = \sum_j f_j g_j e^{2\pi i(hx_j + ky_j + lz_j)} e^{-B_j \sin^2 \theta / \lambda^2} \quad (2-5)$$

Here,  $f_j$ , is the structure factor of the  $j$ -th atom in the and,  $x_j, y_j, z_j$ , are its coordinates,  $g_j$ , is the site occupancy factor and,  $B_j$ , is the root-mean-square of the atomic thermal vibrations. In powder diffraction techniques the diffraction intensity,  $I_{hkl}$ , can be calculated (this is termed  $y_i^{calc}$  in the following section) using the structure factor along with instrument and experiment parameters in the equation:

$$I_{hkl} = s \sum_{hkl} L m_{hkl} |F_{hkl}|^2 \varphi(2\theta_i - 2\theta_{hkl}) P_{hkl} A + I_{bi} \quad (2-6)$$

Here,  $s$ , is the scale factor,  $m_{hkl}$ , is the site multiplicity,  $L$ , is the Lorentz-polarisation factors,  $P_{hkl}$ , is the preferred orientation function,  $\varphi(2\theta_i - 2\theta_{hkl})$ , is the profile function corrected for the zero error,  $A$ , is the absorption correction and,  $I_{bi}$ , is the background scattering at the  $i$ -th point.

#### 2.2.4. The Rietveld Method

The Rietveld method enables the refinement of the average structure of crystalline materials using the powder diffraction data.<sup>214</sup> The starting inputs for refinement are: a reliable structural model (including: the space group, lattice parameters, atom positions, thermal parameters and site occupancies), the instrument parameters, high quality diffraction data, a background function and a starting peak shape. Conventionally the peak shape is modelled using a pseudo-Voigt function with Gaussian and Lorentzian contributions to the function.

The Rietveld method seeks to minimise the value of the residual,  $S_y$  (Equation 2-7), by

refinement of a structural model. In this least-squares approach, a simulated diffraction pattern calculated from the structural models (Equation 2-6) is fitted to the experimental diffraction pattern.

$$S_y = \sum_i w_i (y_i^{calc} - y_i^{obs})^2 \quad (2-7)$$

$$w_i = \frac{1}{y_i^{obs}} \quad (2-8)$$

Here,  $y_i^{obs}$ , is the observed data at the  $i$ -th point,  $y_i^{calc}$ , is the calculated intensity at the  $i$ -th point and  $w_i$ , is a weighting factor. During the refinement process, the user systematically introduces parameters for refinement until the refinement reaches convergence and there is a good fit to the data.<sup>215</sup> The residual of the weighted pattern,  $R_{wp}$ , and ‘goodness-of-fit’,  $\chi^2$ , are used as an indication of the quality of the fit of  $y_i^{calc}$  to  $y_i^{obs}$ . Thus, a low value for each of these values is sought:

$$R_{wp} = \left( \frac{\sum_i w_i (y_i^{calc} - y_i^{obs})^2}{\sum_i w_i (y_i^{obs})^2} \right)^{\frac{1}{2}} \quad (2-9)$$

The  $R_{wp}$  will tend towards zero as the structural model improves but should not decrease to below a minimum value that is determined from the experimental R value,  $R_{exp}$ :

$$R_{exp} = \left( \frac{N - P + C}{\sum_i^N w_i (y_i^{obs})^2} \right)^{\frac{1}{2}} \quad (2-10)$$

The  $R_{exp}$  is essentially a measure of the data quality and is dependent on the number of observations,  $N$ , the number of parameters refined,  $P$ , and the number of constraints used,  $C$ .

$$\chi^2 = \left( \frac{R_{wp}}{R_{exp}} \right)^2 \quad (2-11)$$

The  $\chi^2$  describes the goodness-of-fit between the two  $R$  values and should approach unity as the structural model improves during refinement. Typically the parameters for the structural model, peak shape and background may be refined to improve the fit to the diffraction data. In this thesis all Rietveld refinements shown in the results sections have been performed using the GSAS software package with the EXPGUI extension.<sup>209</sup>

### 2.2.5. Polyhedral Distortion Parameters

Bond distances and bond angles can be extracted from the structural models resulting from Rietveld analysis. These parameters can be used to investigate the structural geometries of

the atoms. In mineral type phases, these polyhedra often deviate from perfect geometry. The internal angular distortions within structural polyhedra may be quantified through the equation:

$$\sigma_{poly}^2 = \frac{1}{m-1} \sum_{i=1}^m (\phi_i - \phi_{poly})^2 \quad (2-12)$$

Here,  $\sigma_{poly}^2$ , is the bond angle variance,  $\phi_i$ , is the observed bond angle,  $\phi_{poly}$ , is the nominal bond angle for a given polyhedron (*i.e.* 90° for octahedra, 109.47° for tetrahedra and 120° for trigonal units) and,  $m$ , is the number of bond angles.<sup>216</sup> The distortions for internal bond distances may be calculated from:

$$\Delta_{poly} = \frac{1000}{n} \sum_{i=1}^n [(l_i - \bar{l})/\bar{l}]^2 \quad (2-13)$$

Here,  $\Delta_{poly}$ , is the bond length deviation,  $l_i$ , is the observed bond distance,  $\bar{l}$ , is the mean bond distance and,  $n$ , is the number of bond distances.<sup>217</sup> Expected values for mineral type phases have been described in the literature:  $\sigma_{oct}^2 < 250$ ;  $\Delta_{oct} \times 10^3 < 3$ ;  $\sigma_{tet}^2 < 100$ ;  $\Delta_{tet} \times 10^3 < 3$ , and provide a benchmark for quantifying the distortion of the structural polyhedra.<sup>218</sup> A high value for these parameters would indicate large polyhedral distortions and this behaviour is often associated with ions that show Jahn-Teller distortions.<sup>218</sup> Values of  $\sigma^2$  and  $\Delta$  have been calculated for the metal-centred polyhedra and some sulphur-centred polyhedra for the bornite samples and tetrahedrite samples in the later chapters.

### ***2.2.6. The Le Bail Method***

The Le Bail method is a less computationally intensive process than the Rietveld method and is useful in instances where full structure refinement is not required. It provides a means of calculating the expected diffraction intensity without a structural model and may give more reliable values of the lattice parameters, compared to values from the Rietveld method.<sup>219</sup> The least-squares whole-pattern refinement requires starting parameters for the instrument, background and peak shape. The only crystal information needed however is the space group and the lattice parameters. The intensity of the reflections are calculated using this information. The process is useful for monitoring the evolution of lattice parameters as a function of temperature, pressure and composition among other things. All Le Bail refinements performed in the following sections have been carried out using the GSAS software package with the EXPGUI extension.<sup>209</sup>

### 2.2.7. Total Scattering

In amorphous solids, such as glasses, there is no long-range order and Bragg's law cannot be satisfied. For these materials, the X-ray or neutron scattering data will exhibit broad features with relatively low intensity in the absence of Bragg peaks. This is the result of diffuse scattering and contains structural information for the short-range order within a solid or liquid phase. The data can be interpreted more readily when visualised as a radial distribution function, a simplified schematic is given below. Here the curve of  $G(r)$  is a density map of the next-nearest neighbors (Figure 2-7). Similarly, diffuse scattering will occur in crystalline materials when the Bragg equation is not satisfied. Signatures of nanoscale disorder will be observed in the data at small scattering vectors, low- $Q$ , and typically high-quality scattering data over a wide  $Q$  range are needed for analysis of the total scattering data. This approach allows the study of local structure within ordered materials.<sup>220,221</sup>

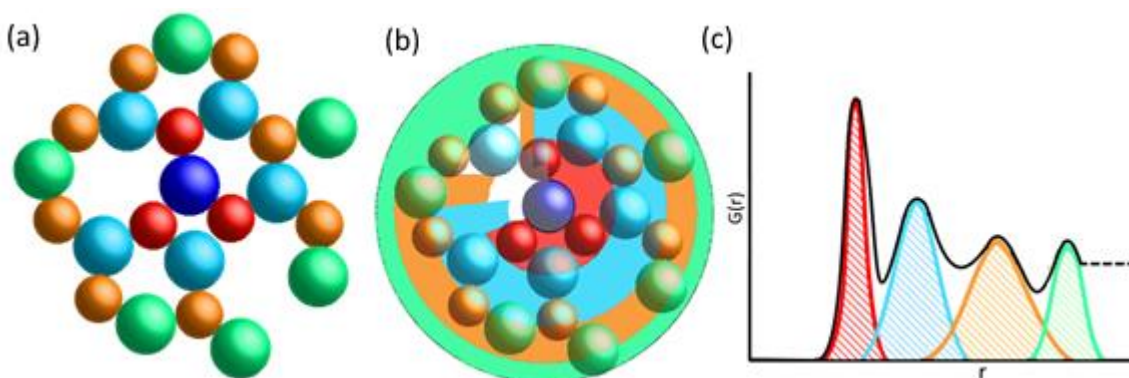


**Figure 2-7** – (a)- 2-D representation of a disordered material; (b) – Rings showing the radial distribution of the atoms with distance  $n=1$  to  $n=4$  from a central atom; (c) - Graphical representation of the radial distribution.

#### 2.2.7.1. PDF Analysis

The model-based Reverse Monte Carlo (RMC) technique was developed as a tool to extract structural information about disordered materials from the total-scattering data.<sup>222,223</sup> This technique has been extended to understand structural disorder within crystalline materials. This technique is a least-squares approach that refines a structural model to fit the Bragg contribution and total scattering contribution to the data. It uses the Bragg diffraction data as well as the pair distribution function (PDF),  $G(r)$ , and the isotropic average of the scattering vector,  $S(Q)$ . The curve,  $G(r)$ , is a histogram defining the probability of finding a pair of atoms with a distance,  $r$ , expressed by:

$$G(r) = 4\pi r[\rho(r) - \rho_0] \quad (2-14)$$

Here,  $\rho(r)$ , is the local atom no. density and,  $\rho_0$ , is the average atom no. density. This density map is constructed from the total-scattering data by applying a Fourier transform. This approach is ideal for modelling local structure that cannot be probed with reciprocal space diffraction techniques and applies a real-space approach.<sup>224</sup>

This computational technique uses a large atom box, generally with upward of  $10^4$  atoms and supercell dimensions that are some integer of the unit-cell parameter. The starting point for this model is the refined unit-cell from a preceding Rietveld analysis, which is subsequently refined during the RMC profile analysis. The RMC process works on the basis of the minimisation of a  $\chi^2$  value that is a product of the difference between the experimental data,  $y_i^{obs}$ , and the calculated pattern,  $y_i^{calc}$ :

$$\chi^2 = \sum_i \frac{1}{\sigma_i^2} (y_i^{calc} - y_i^{obs}) \quad (2-15)$$

here,  $\sigma_i^2$ , is a weighting factor and each data set included in the fitting process is used to determine a total  $\chi_{RMC}^2$ . Each of the separate histograms, can be given a weighting towards the total  $\chi_{RMC}^2$  where:

$$\chi_{RMC}^2 = \sum_m S_m \chi_m^2 \quad (2-16)$$

here,  $S_m = 0, +1$ , and,  $m$ , is the histogram,  $G(r)$ ,  $S(Q)$  or Bragg. During the Monte Carlo approach, changes are made to the large box structural model. If  $\chi^2$  decreases as a result of the change, the program accepts the change in the structure. The least-squares process also includes a function to prevent the refinement process from becoming trapped in a local minimum. Some of the unfavourable moves that yield a higher  $\chi^2$  are accepted with a probability,  $P$ .<sup>225</sup>

$$P = e^{\left(\frac{-\Delta\chi^2}{2}\right)} \quad (2-17)$$

The total-scattering data were collected at the POLARIS diffractometer at the ISIS neutron facility for the sample with composition  $\text{Cu}_5\text{FeS}_4$  at three temperatures. Long data collection times of 8 hours were used to ensure high-quality data was achieved with good statistics across the background signal. The background diffraction data from the sample environment equipment were collected at each temperature for all material in the path of the beam this includes furnaces, silica ampoules and a vanadium rod. The Gudrun software package was used to remove background contributions to the total scattering data.<sup>226</sup> Bragg diffraction data were processed through the Mantid analysis software.<sup>210</sup> The RMCprofile

software package was used to perform RMC calculations and four histograms, each a transformation of the same data set, were included: Bragg diffraction data from the 90° detector bank,  $G(r)$  data calculated from the contribution for each of the detector banks and over to length scales  $0 < r / \text{Å} < 10$  and  $0 < r / \text{Å} < 50$ , and the  $S(Q)$  summed from the contribution from each detector bank. Structural models were constructed using the data2config program included with the RMCprofile software package.<sup>227</sup>

### ***2.3. Characterisation of Thermoelectric Properties***

The importance of investigating the thermal and electrical transport properties of thermoelectric materials was outlined in Chapter 1. Effective measurement of these properties is crucial for their development. The following section will look into some of the methods used for the measurement of these physical properties.

#### ***2.3.1. Electrical Resistivity***

The electrical resistance,  $R$ , of a system can be determined by either passing an electrical current,  $I$ , and measuring a voltage,  $V$ , or using a fixed voltage and measuring the electrical current. In practice it can be interpreted through the relationship:

$$R = V/I \quad (2-18)$$

The physical dimensions of the system being studied directly influences the measured electrical resistance of the system. For a sample with length,  $l$ , and a uniform cross-sectional area,  $A$ , the length is proportional to  $R$ , and the area is inversely proportional.

Both are related through the resistivity,  $\rho$ :

$$R = \rho \frac{l}{A} \quad (2-19)$$

Therefore the resistivity of a material can be determined by measuring the resistance of a sample with known dimensions.

##### ***2.3.1.1. 4-Probe Resistance Measurement***

A 2-probe resistance measurement uses a pair of wires to pass a current and to measure a voltage (Figure 2-8). This method can be useful for testing electrical equipment and has proven to be useful in determining the electrical efficiency of thermoelectric elements by measuring thermoelectric voltage and current.<sup>228,229</sup> However, the 2-probe method is not entirely accurate for determining the electrical resistivity of materials owing to a contribution to the total resistance from the contact resistance between the electrode and

sample. The resistances may originate from surface roughness, poor contacts or Schottky barriers across semiconductor-metal interfaces.

The 4-probe DC measurement can provide a value for the electrical resistance that does not include the contribution from any contact resistances. The resistance is determined by passing a current through two electrodes and measuring the voltage between two additional electrodes (Figure 2-9). The voltage electrodes will have an effectively negligible current, and therefore the resistance is effectively zero.<sup>230</sup> Given that the voltage leads have a known separation,  $l$ , and the sample has a uniform cross-sectional area, then the resistivity of the material can be determined using Equation 2-19.

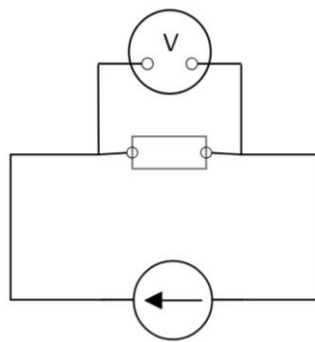


**Figure 2-8** – Circuit diagram of a 2-probe measurement set-up where the box represents the sample/ a resistor,  $V$  is a voltage probe,  $\leftarrow$  is the current source and circles connected to the sample represent the electrode-sample contact interfaces.

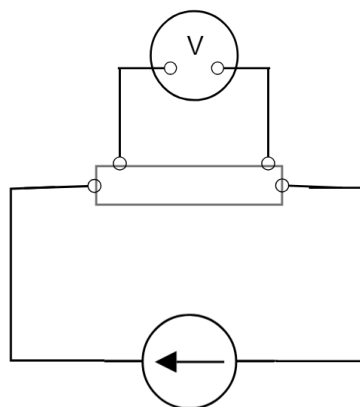


**Figure 2-9** – Circuit diagram of the standard set-up required for a 4-probe measurement the box represents the sample/ a resistor,  $V$  is a voltage probe,  $\leftarrow$  is the current source and circles connected to the sample represent the electrode-sample contact interfaces.

The four-probe DC measurement has been used in this work to determine electrical resistivities for samples in each of the bornite series,  $\text{Cu}_{5-x+y}\text{Fe}_{1-y}\text{S}_4$ , as well as the samples

with compositions,  $\text{Cu}_9\text{Fe}_9\text{S}_{16}$  and  $\text{Cu}_9\text{Fe}_8\text{S}_{16}$ . Measurements were performed using a Linseis LSR-3 instrument with disc-shaped pellets with dimensions  $diameter=12.7$  mm  $\pm 0.2$  and  $thickness=1-4$  mm with a separation between the voltage probes of  $length=8$  mm. A current of between  $I=10-100$   $\mu\text{A}$  was used during measurements on samples mounted between spring loaded platinum electrode contacts.

The electrical resistivity measurements described throughout have been performed under a dynamic thermal gradient. Under these conditions, an inherent Seebeck voltage,  $V_{seebeck}$ , will also persist throughout measurement. For any single measurement the resistance will be equal to:

$$R_{\rightarrow} = \frac{V_{\rightarrow} + V_{seebeck}}{I_{\rightarrow}}, \quad R_{\leftarrow} = \frac{V_{\leftarrow} - V_{seebeck}}{I_{\leftarrow}} \quad (2-20)$$

Here  $\rightarrow$  denotes a direction of current. Therefore, bidirectional resistance measurements were performed in all instances to remove any contribution from the induced Seebeck voltage.<sup>231</sup>

### 2.3.1.2. The Van der Pauw Method

In the Van der Pauw method, four electrodes contact one face of a sample with an arbitrary shape of uniform thickness.<sup>232</sup> The thickness,  $t$ , of the sample is considerably less than both the length and the width of the sample and the measurement effectively provides a sheet resistance. In the measurement, 8 voltage readings are taken around the periphery of the sample as shown in Figure 2-10. Assuming that the sample has perfect symmetry, the resistivity of the sample can be determined from an average of two resistivities:

$$\rho_A = \frac{\pi}{\ln 2} t \frac{(V_1 - V_2 + V_3 - V_4)}{4I} \quad (2-21)$$

$$\rho_B = \frac{\pi}{\ln 2} t \frac{(V_5 - V_6 + V_7 - V_8)}{4I} \quad (2-22)$$

In addition to electrical resistivity measurements, this electrode arrangement can also allow for Hall resistivity measurements.<sup>233</sup>

Van der Pauw resistivity measurements have been performed on the sample with composition  $\text{Cu}_{12}\text{Sb}_4\text{S}_{13}$ . A Quantum Design PPMS-9 instrument was used in the resistivity mode configuration. The sample was a square pellet with dimensions  $length=5$  mm,  $width=5$  mm and  $thickness=1$  mm. Silver soldered contacts were made to each corner of the face of the square and data were recorded over the temperature range  $T=1.5 - 300$  K.

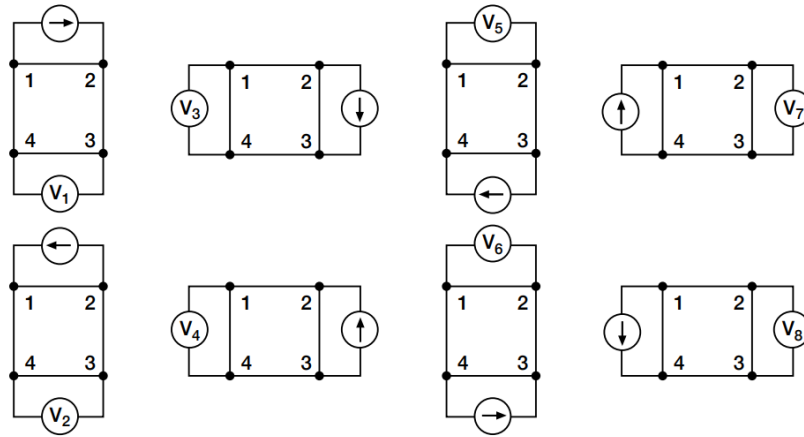


**Figure 2-10** – Eight electrode arrangements used to determine the resistivity using the Van der Pauw method.<sup>233</sup> The square shape connecting each black dot simply represents the electrical connections across a sample with an arbitrary shape. Reproduced from 233 Copyright© Tektronix. Reprinted with permission. All Rights Reserved.

### 2.3.2. Seebeck Coefficient Measurement

The Seebeck coefficient,  $S$ , is the fundamental physical property that describes the material's ability to turn a thermal gradient into an electrical voltage. Therefore, it can be determined experimentally from the measurement of a thermal gradient and the induced voltage,<sup>234–236</sup> and defined by the equation:

$$S = \frac{\Delta V}{\Delta T} \quad (2-23)$$

Here,  $\Delta T$ , is the temperature difference and,  $\Delta V$ , the voltage difference. A thermal gradient is applied to the sample and the measurement of the voltage and the temperature should be performed at the same point of contact and at the same time. In practice this is not possible as the two measurements interfere with one another. Often the compromise allows for the thermal gradient and voltage to be measured from a shared point of contact, and hence there is a short time delay between the  $\Delta T$  and  $\Delta V$  measurements.

There are two conventional methods to extract the Seebeck coefficient from the data. The first uses a linear interpolation over multiple points in the curve of  $\Delta T$  vs.  $\Delta V$  and the value of the gradient is the Seebeck coefficient, this allows for the removal of any offset in the measurement.<sup>235</sup> This is typically used for small values of  $\Delta T$  and has been used throughout this work. It is also possible to calculate the Seebeck coefficient over large temperature differentials using an integral method.<sup>235</sup>

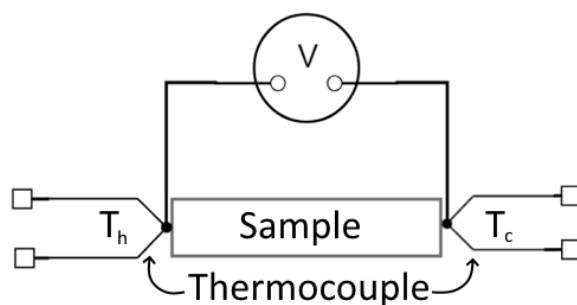


**Figure 2-11** – Circuit diagram of the thermocouple and voltmeter layout used for measurement of the Seebeck coefficient:  $V$  is a voltage probe,  $T_h$  and  $T_c$  are the hot side and the cold side.

Seebeck coefficient measurements were performed using a Linseis LSR-3 with a temperature difference between the heating elements of  $\Delta T = 50$  K leading to a temperature difference of *ca.*  $\Delta T = 3-11$  K between the Seebeck measurement electrodes. The contribution to the Seebeck coefficient from the platinum electrodes was subtracted using the Linseis evaluation software and the Seebeck coefficients were calculated using the differential method over 3 increments of  $\Delta T$ . The experiments were performed under a He atmosphere and over the temperature range  $T = 300 - 925$  K with temperature increments of 10 K for each of the bornite samples,  $\text{Cu}_{5-x+y}\text{Fe}_{1-y}\text{S}_4$ , as well as the samples with composition  $\text{Cu}_9\text{Fe}_9\text{S}_{16}$ ,  $\text{Cu}_9\text{Fe}_8\text{S}_{16}$  and  $\text{CuFeS}_2$ .

### 2.3.3. Linseis LSR-3

This instrument was used for variable temperature Seebeck coefficient and electrical resistivity measurements during a single experiment and is equipped with a water cooled infra-red furnace. Two alumina arms provide a large thermal pathway to reduce thermal transport between either end of the sample. The samples were loaded between the two arms which house a pair of platinum electrodes that were used to pass a current during the resistivity measurement. The bottom arm houses a heating element that produced the temperature gradient. Two additional thermocouples extend from a third arm, these thermocouples were used to monitor the voltage and temperature difference for the electrical resistivity and Seebeck coefficient measurements (Figure 2-12).<sup>236</sup>

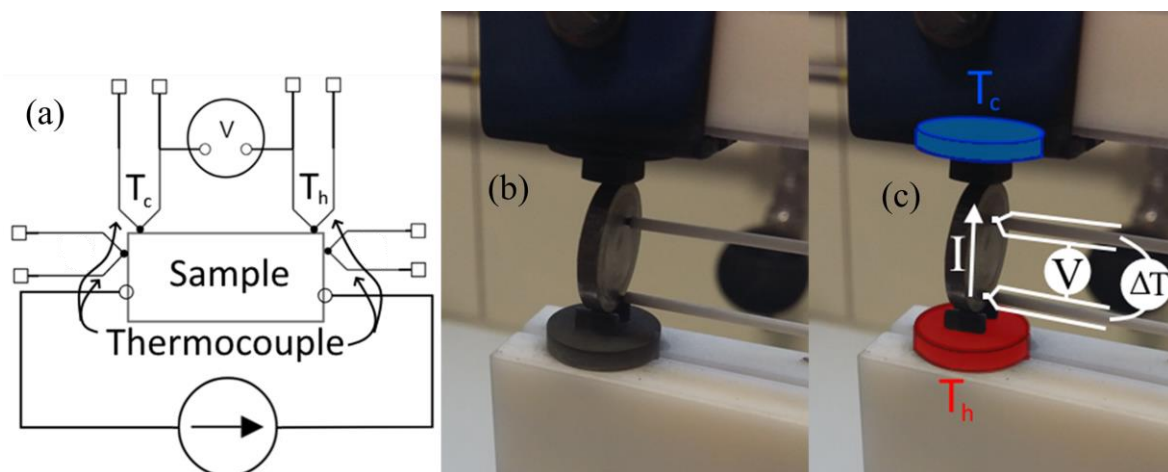


**Figure 2-12** – (a) – Circuit diagram of the measurement set-up used on the LSR-3 instrument:  $V$  is a voltage probe,  $\leftarrow$  is the current source and circles connected to the sample represent the electrode-sample contact interfaces,  $T_h$  and  $T_c$  are the hot side and the cold side. (b) – image of the sample enclosure in the Linseis. ((c) annotated image)

## 2.4. Thermal Characterisation of Thermoelectric Materials

The importance of the thermal conductivity was outlined in chapter 1, this can be determined experimentally by measuring the thermal diffusivity. In addition to the thermal conductivity, the specific heat capacity provides critical information on the phase behaviour of materials. Modelling the curve of  $C_p$  at low temperatures can provide important information on the thermal transport constants of a material. The experimental methods to determining these properties will be investigated here.

### 2.4.1. Differential Scanning Calorimetry (DSC)

The specific heat capacity,  $C_p$  with units  $\text{J K}^{-1} \text{g}^{-1}$ , represents the amount of energy required to heat a material by a unit of temperature, K. The temperature dependence of this quantity reveals the phase-transformation behaviour of matter because the transformations are thermodynamic events. DSC provides a fast and reliable technique for determining the specific heat capacity of samples as a function of temperature.

Prior to collection of the DSC data, samples are typically loaded into a pan of known material (aluminium) and weight. Data were collected for the sample-loaded pan and a reference pan so that any contribution from the pan could be subtracted. In the TA DSC Q2000 calorimeter, the pans sit on a constantan heat-flow assembly within the furnace of the heat-flux DSC. The constantan assembly transfers heat to the two pans, its thermal resistivity and temperature is monitored, and the temperature of each pan is monitored to give values for  $\Delta T$ . The heat flow,  $q$  with units W, is calculated from:

$$q = \frac{\Delta T}{R} \quad (2-24)$$

Here,  $R$  with units  $\text{K W}^{-1}$ , is the thermal resistance. The heat capacity of material can be determined by a comparison method of the reference, with a known heat capacity, to the sample:

$$C_{p_{sample}} = \frac{(m \cdot C_p \cdot \Delta T)_{reference}}{(m \cdot \Delta T)_{sample}} \quad (2-25)$$

Here,  $m$ , is the mass. The phase-transition temperatures can be determined from the maximum in intensity for the signatures in the heat-capacity data.

Finely ground powdered samples of bornite,  $\text{Cu}_{5-x+y}\text{Fe}_{1-y}\text{S}_4$ , *ca.* 5-15 mg were loaded, sealed and clamped into capped aluminium pans. DSC measurements were carried out across the temperature range  $T = 163 - 673$  K with a heating rate of  $20 \text{ K min}^{-1}$  using a TA DSC Q2000 calorimeter. For the tetrahedrite,  $\text{Cu}_{12}\text{Sb}_4\text{S}_{13}$ , measurements were performed between  $T = 1.5 - 300$  K on a small fragment of the pelletised sample (*ca.* 3 mg) and using a Quantum Design PPMS-9 in the Heat Capacity configuration.

#### 2.4.2. Thermal Diffusivity

The thermal conductivity of solids can be determined through a number of methods. Early techniques involved measurement of the growth of a temperature gradient,  $\Delta T$ , across two points of a sample using thermocouples. However, thermal losses through surface radiation and to thermocouple wires may lead to significant measurement errors. As a result, these techniques are not reliable at high temperatures. The light-flash analysis (LFA) technique is conventionally used for ambient-temperature and high-temperature measurements.<sup>237</sup>

The lamp produces a pulse of light that strikes the rear face of the sample and a detector monitors the change in temperature on the opposing face (Figure 2-13). This method allows for the thermal diffusivity,  $\alpha$  with units  $\text{mm}^2 \text{ s}^{-1}$ , of the material to be quantified by the equation:

$$\alpha = 0.1388 \cdot \frac{l^2}{t_{1/2}} \quad (2-26)$$

Here,  $l$ , is the length of the sample and,  $t_{1/2}$ , is the temperature decay time. The temperature of the sample increases for a short time after the pulse of light to  $\Delta T_{max}$  and  $t_{1/2}$  is the temperature decay time for the system to reach  $\Delta T_{1/2max}$ . This equation assumes a 1-dimensional system with no thermal losses. There are numerous pulse corrections that can

be applied to appropriately model the 3D system on which measurements are made. The thermal conductivity,  $\kappa$ , can be calculated using the thermal diffusivity in the equation:

$$\kappa = \rho \cdot C_p \cdot \alpha \quad (2-27)$$

Here,  $\rho$ , is the sample density. This technique gives the total thermal conductivity,  $\kappa_t$ , and the electrical contribution to the thermal conductivity,  $\kappa_e$ , can be estimated from the resistivity measurements mentioned in section 2.1.3 and using equation 1-9. The specific heat capacity can be determined using equation 2-25 and a reference sample. In this work, the Dulong-Petit heat capacity (see below) has been used, in place of the experimental specific heat capacity, to determine the thermal conductivity of samples.

For all variable temperature thermal diffusivity measurements, the circular faces of samples, with dimensions *diameter* = 12.7 mm  $\pm$  0.2 and *thickness* = 0.7-1.4 mm, were coated with graphite spray. This allows for better absorptivity and emissivity of the light radiation. The coated samples were loaded into the sample holder of the instrument and measurements were performed between  $T = 300 - 600$  K using a NETZSCH LFA-447 fitted with a liquid N<sub>2</sub> cooled indium-antimonide detector (Figure 2-13). Measurements to higher temperatures ( $T = 300 - 900$  K) were performed using an Anter FlashLine3000 fitted with a liquid-nitrogen-cooled indium-antimonide detector. The Cowan pulse correction<sup>238</sup> was applied to samples with composition, Cu<sub>5-x+y</sub>Fe<sub>1-y</sub>S<sub>4</sub>, for measurements performed in the NETZSCH LFA-447, meanwhile the Clarke and Taylor pulse correction<sup>239</sup> was applied to the measurements performed on the Anter FlashLine3000 and for sample Cu<sub>4.97</sub>Fe<sub>0.97</sub>S<sub>4</sub>.

#### 2.4.2.1. *Dulong-Petit Heat Law*

This law states that the molar heat capacity of compounds is close to a constant value,  $3R$ , where  $R = 8.314 \text{ J mol}^{-1} \text{ K}^{-1}$  is the gas constant. This holds true for many elementary solids as it derives from the three rotational degrees of freedom of an atom. This approximation to  $C_p$  can be calculated from:<sup>240</sup>

$$C_p = \frac{3R}{M} \quad (2-28)$$

Here,  $M$ , is the average mass of an atom in the sample. This value is an estimate, but it allows for consistency between laboratories. Also, using this estimation allows for the removal of local maximum or minimum in  $C_p$  that occur with structural phase transitions.

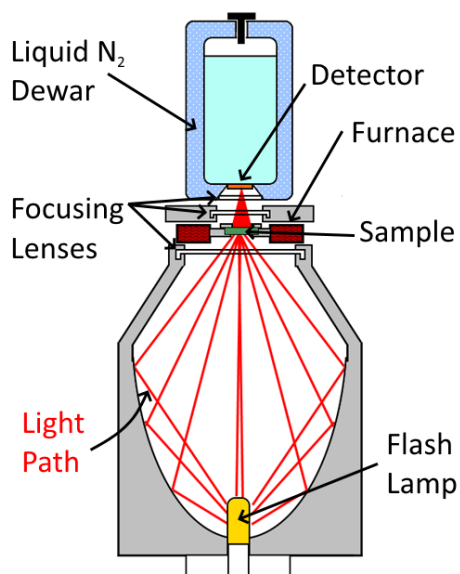


**Figure 2-13** – Schematic diagram of the Netzsch LFA-447 equipment used for the thermal diffusivity measurements.

### 2.5. Energy Dispersive X-ray (EDX) Spectroscopy

The generation of X-rays was described in section 2.2.1 and the characteristic  $K_{\alpha 1}$ ,  $K_{\alpha 2}$  and  $K_{\beta}$  wavelengths were stated for copper. The set of characteristic wavelengths that are generated is unique for each of the elements. Therefore, the elemental components in a sample and their quantity can be determined using EDX spectroscopy. In the measurement the sample is bombarded by a high-energy electron beam and a detector measures the emitted X-radiation over a wide energy range. The position and relative intensities of the characteristic peaks are analysed against a database to quantify the data.

EDX measurements were performed using a scanning electron microscope instrument, ThermoFisher Scientific Quanta 600F, under an atmospheric pressure of *ca.*  $10^{-3}$  bar and using an accelerating voltage of 20 kV. Pelleted samples with a composition,  $\text{Cu}_{5-x+y}\text{Fe}_{1-y}\text{S}_4$ , and dimensions *diameter* = 12.7 mm  $\pm$  0.2 and *thickness* = 0.7-1.4 mm were mounted onto aluminium stubs with carbon tabs prior to loading them into the instrument. The sample composition was calculated from an average value over 6 individual EDX area spectra.

### 2.6. Superconducting Quantum Interface Device (SQUID) Magnetometry

The magnetic susceptibility of materials can be determined by applying a magnetic field to the sample and measuring the magnetisation. SQUID magnetometers allow for the detection of very weak magnetic phenomena by exploiting quantum effects across

Josephson junctions. Two thin layers of non-superconducting material are parallel to one another within a superconducting ring. An external magnetic field is applied, and a sample is systematically passed through the internal diameter of the SQUID leading to quantum electrodynamic interactions across the Josephson junction. This causes oscillations in the measured voltage across the ring which can be related to the magnetisation of the material.

Magnetic susceptibility measurements were performed by the staff at the materials characterisation lab at the ISIS neutron facility using a SQUID Magnetometer, Quantum Design MPMS XL-7. Prior to loading the sample into the instrument, a small amount (*ca.* 10 mg) of the sample with composition,  $\text{Cu}_{12}\text{Sb}_4\text{S}_{13}$ , was loaded into a gelatine capsule with PTFE tape and sealed into a plastic drink straw. This was used as a sample vessel during the experiment and the data was corrected by subtracting the contribution from the gelatine capsule of known weight.



## Chapter 3 Seebeck-Resistance-Diffraction *in-situ* Cell: Development and Structure-Property Studies

### 3.1. Introduction

Instruments such as the Linseis LSR-3 allow for variable temperature and simultaneous measurement of the electrical properties of bulk or thin-film thermoelectric materials and provide the Seebeck coefficient,  $S$ , and electrical resistivity,  $\rho$  (Figure 2-12(b)).<sup>241,242</sup> This type of equipment is crucial for the study of thermoelectric materials.<sup>234–236,243,244</sup>

Meanwhile, the high-intensity neutron diffraction instruments, such as POLARIS, can provide conclusive structural information of solid-state materials. Modern techniques allow for the collection of these structural data with external experimental parameters, such as variable temperature or pressure.

In practice the observed changes within the electrical transport properties and structural behaviour are decoupled because the electrical and structural data are measured in different instances. This may introduce inconsistencies between the individual experiments.

Measurement of the electrical transport properties simultaneously with the collection of diffraction data would greatly enhance the merit of these experiments, especially when the materials are known to show structural phase transitions. An *in-situ* measurement of these data would allow for the structure and properties of materials to be directly linked by removing the discrepancies introduced by experimental procedures, temperature monitoring and sample preparations. In order for these types of experiments to be realised, bespoke sample environment cells must be designed, built and tested.

As part of the user program at the ISIS neutron facility, an *in-situ* cell is available for variable temperature and simultaneous measurement of neutron diffraction data with either electrical resistivity data,  $\rho$ , or electrical impedance spectroscopy data.<sup>245–247</sup> Meanwhile Yuan *et al.* have developed a high-temperature high-pressure Seebeck-resistance XRD cell that measures resistance using the Van der Pauw method and utilises the natural gradient across the sample, thus using a single  $\Delta T$  vs.  $\Delta V$  point to determine the Seebeck coefficient.<sup>248</sup> This work seeks to create a first of its kind *in-situ* cell that can simultaneously measure the Seebeck coefficient,  $S$ , electrical resistivity,  $\rho$ , and neutron diffraction data. The diffraction-resistance cell provided a starting drawing for this novel cell, further additions to the design included the installation of a heater to allow for the

creation of a thermal gradient across a sample and additional temperature probes to allow for the temperature gradients to be monitored and quantified.<sup>235,236,249</sup>

### ***3.2. Final Design of the Cell***

The new cell (Figure 3-1, Figure 3-2(a)) was designed for use within the RAL-4 furnace and on the beamlines POLARIS and GEM at the ISIS neutron diffraction facility.<sup>250,251</sup> On the exterior face of the mounting flange, two 16KF Jaeger adapters are fitted at 180° to one another, allowing for the electrical connections to pass through a gas-tight seal (Figure 3-2(b)). The first of these has 3 thermocouple connections and 4 connections to electrodes (Figure 3-2(c)), the second fitting allows for a power supply to be connected to an internal heating element (Figure 3-2(d)). At 60° from the Jaeger fittings there is a pair of gas inlet/outlet tubes passing through the flange to allow for the sample chamber to be evacuated of air or filled with gas as per the experimental requirement (Figure 3-2(b)). Two additional gas-tight fittings, at 30° from the Jaeger fittings, allow K-type thermocouples to pass through the mounting flange (Figure 3-2(b)). At the centre of the mounting flange is an adjustable screw that can increase pressure across a spring loaded system in the cell that extends to the sample enclosure assembly (Figure 3-2(b)).

On the internal face of the mounting flange there is a seat for a rubber O-ring (Figure 3-2(c)), allowing for a gas tight metal-to-glass junction between the glass sheath and the mounting flange. The external heat shielding baffle array over-lays the glass sheath and is tightened onto the faceplate providing pressure between the glass sheath and the O-ring (Figure 3-3(c)).

The glass sheath is thinned, from an internal:external diameter of 40:42 mm to 40:41 mm, around the circumference of the sample area as to minimise the intensity of background contribution from the glass sheath (Figure 3-3(b)). The glass sheath has an internal diameter of 40 mm, all of the electrical connectors are contained within the glass sheath.

On the internal face of the mounting flange, a pair of threaded holes at -30° from the Jaeger fitting allow for alumina arms to be inserted (Figure 3-2(c)). These extend to the sample enclosure. A metal guide tube extends from the centre of the mounting flange to the sample enclosure, to which the secondary heat shielding baffle array is fitted. The spring-loaded mechanism extends through the guide tube and into a copper block, onto which the load is applied.

The load-contacting copper block is threaded onto a smaller copper block which allows for the fastening of the boron-nitride enclosure (flange-end). Similarly at the opposing end of the sample enclosure, a copper block is attached to the boron-nitride housing (heater-end). This end of the sample enclosure is secured to the body of the cell by means of the alumina arms and a set of ceramic screws (Figure 3-2(d)). Two platinum electrodes sit at either end of the copper block/ boron-nitride assembly, a ceramic disc is fitted between the flange-end copper block and the platinum electrode.

The two K-type thermocouples that pass through individual thermocouple fittings measure the gaseous temperature in the sample environment area and allow for furnace temperature control. Three K-type thermocouples are fitted into the Jaeger fitting; one is inserted into the heating block to allow for temperature control of the heating element, the other two are in contact with the two Pt electrodes in the sample enclosure and monitor the temperature gradient of the sample. Two platinum wires are connected to each platinum electrode. Each wire is fitted with ceramic beads and the wires that cross the pathway of the diffracted radiation are enclosed in a boron-nitride wire feed. The copper block at the heater end of the sample enclosure is wrapped with resistive heating wire and allows for the thermal gradient to be induced across the sample.

The final cell design was reached after testing rounds on the cell. An overview of this testing phase is presented in the following section.

### ***3.3. Testing and Development of the In-Situ Cell***

When measuring the Seebeck coefficient, it is essential to measure the voltage and temperature at the same points on the sample.<sup>235</sup> The first prototype of the cell included two platinum thermocouple wires attached to the Pt electrode discs, this led to an electrical interference with the thermocouples and unreliable temperature data.<sup>252</sup> Further to this, it was clear that an electrical short across the cell was impeding electrical measurements. Modifications were made to the design of the cell: the platinum thermocouples were replaced with electrically insulated K-type thermocouples and a ceramic spacer was installed to provide electrical insulation.

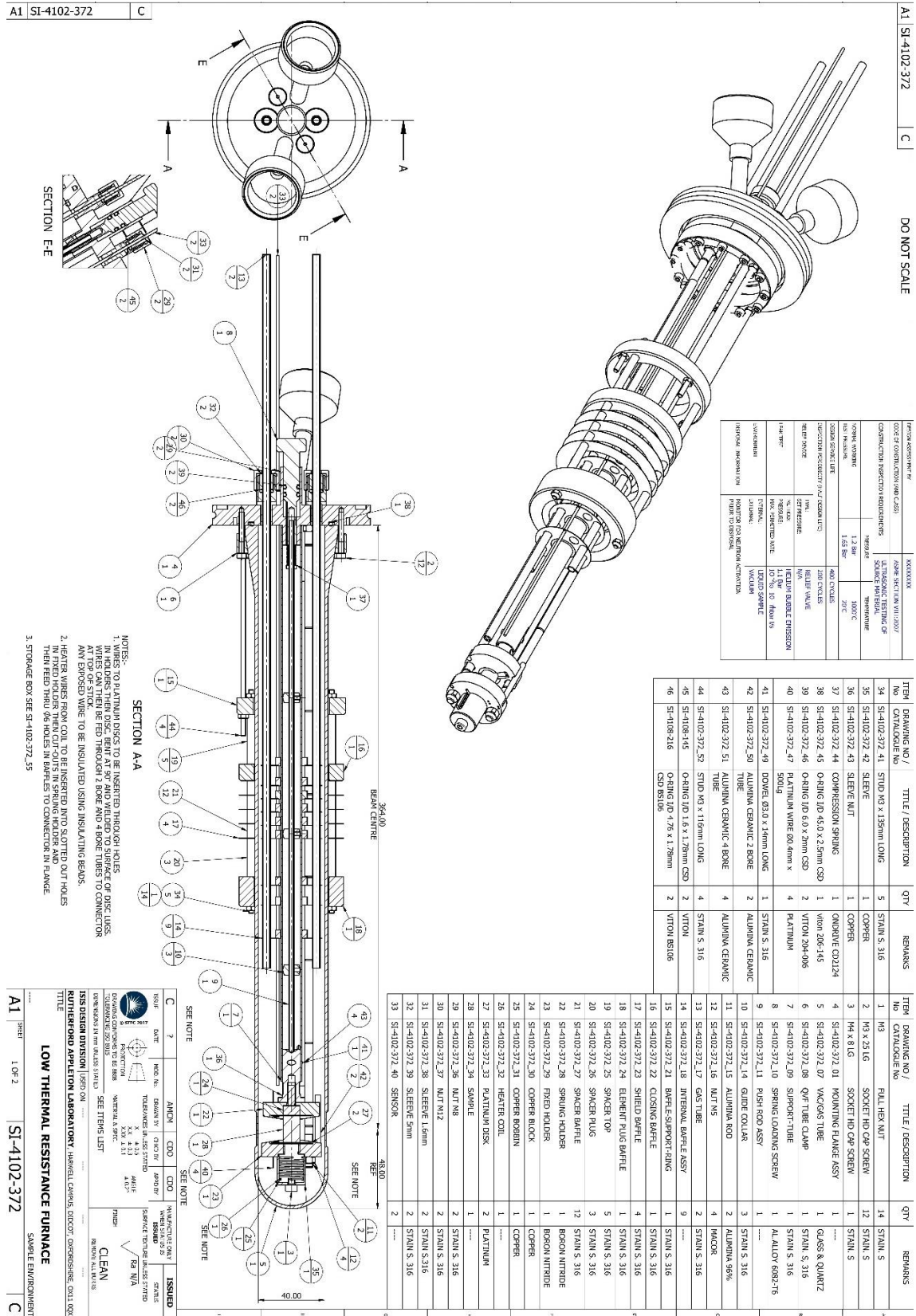
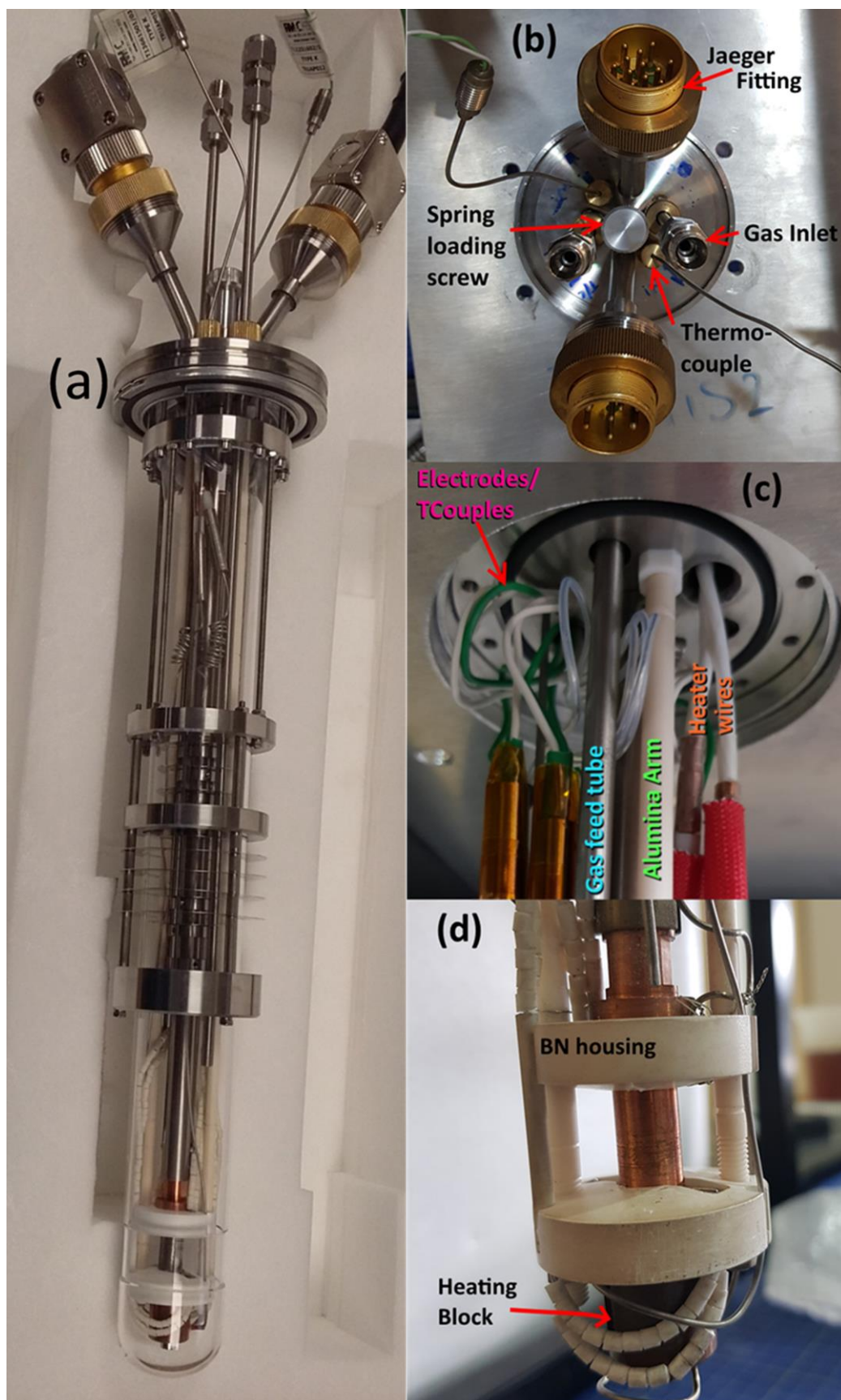
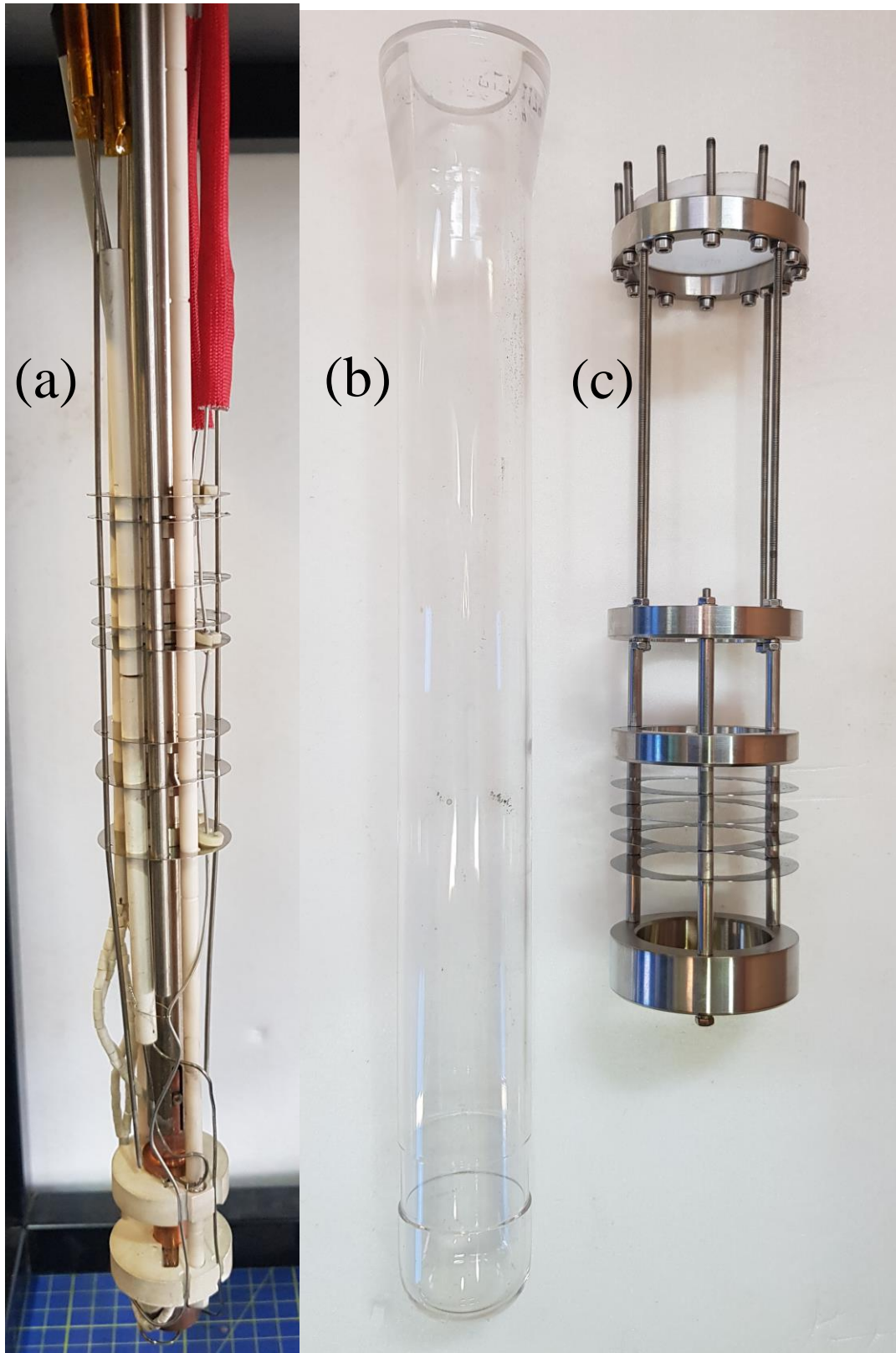


Figure 3-1 – Schematic drawing of the thermopower-diffraction cell for use at high temperatures. Acknowledgement is made to the ISIS drawing office.



*Figure 3-2 – (a) Image of the in-situ cell with the glass sheath and heat-shield baffle-array. Images provide a visual guide to the (b,c) flange fittings; and (d) sample enclosure.*



*Figure 3-3 – Image of the in-situ cell with the glass sheath and exterior heat-shield baffle-array pictured separately.*

Electrical tests on the modified device showed that reliable electrical and thermal data were being recorded. A preliminary temperature-dependence experiment utilised LabView<sup>253</sup> to control the hardware and the electrical current was measured bi-directionally to subtract the contribution of the Seebeck voltage.<sup>249</sup> The electrical and temperature data were recorded for a sample of bornite, composition  $\text{Cu}_{4.99}\text{Fe}_{0.98}\text{S}_4$ ; dimensions *ca.*  $r = 5$  mm,  $l = 10$  mm, prepared using the mechanochemical and hot-pressing technique described in Chapter 4. During the experiment, a single temperature point,  $\Delta T = 50$  K, was used to determine the Seebeck coefficient. The method employed here to extract the Seebeck coefficient is not conventional;<sup>249,254</sup> even so, the experiment clearly demonstrated that the cell is capable of monitoring anomalies in the electrical behaviour (Figure 3-4).<sup>143</sup>

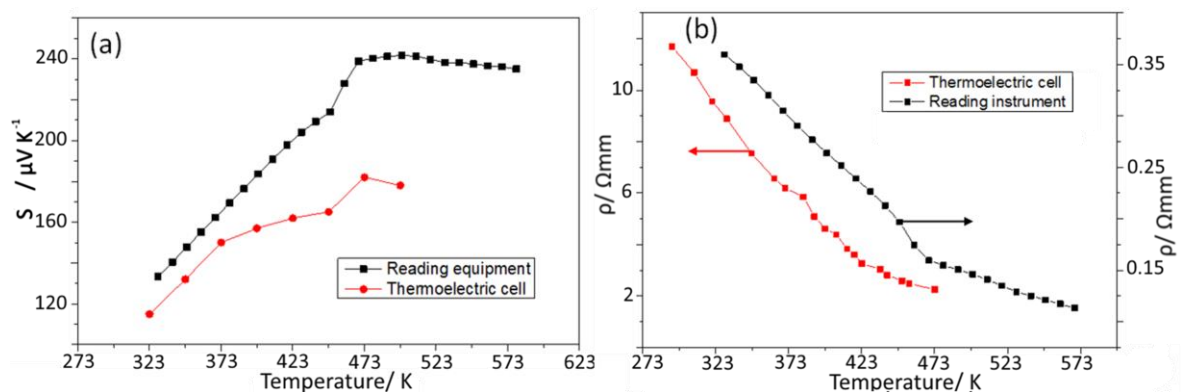


**Figure 3-4** – Temperature dependence of (a) the Seebeck coefficient and (b) the electrical resistivity for the sample with composition  $\text{Cu}_{4.99}\text{Fe}_{0.98}\text{S}_4$ . Black – Linseis LSR-3 data; Red – *in-situ* cell data.

These experiments demonstrated limitations in the hardware<sup>255</sup> and the Seebeck measurement technique. In following experiments, the electrical measurement hardware<sup>256</sup> was changed and software procedures were adapted to work with the IBEX beamline control software.<sup>257</sup> In a repeated experiment, the  $\Delta T$  vs.  $\Delta V$  data recorded at each temperature showed a linear relationship which extends close to the origin,  $\Delta T = 0$  K,  $\Delta V = 0$  V (Figure 3-5). The observation of a linear relationship in  $\Delta T$  vs.  $\Delta V$ , as seen here, is crucial and shows that there is good thermal and electrical contact at the metal-semiconductor interface.<sup>236</sup>

After the first round of modifications, there was a small separation in distance between the thermocouple and the electrodes. Following rounds of off-line and on-line experiments, a final modification sought to ensure that the electrically insulated thermocouples were in

direct contact with the electrodes to improve determination of the Seebeck coefficient. This modification allows for more accurate monitoring of the temperature gradient as the thermocouples are in direct contact with the electrodes that monitor the Seebeck voltage.

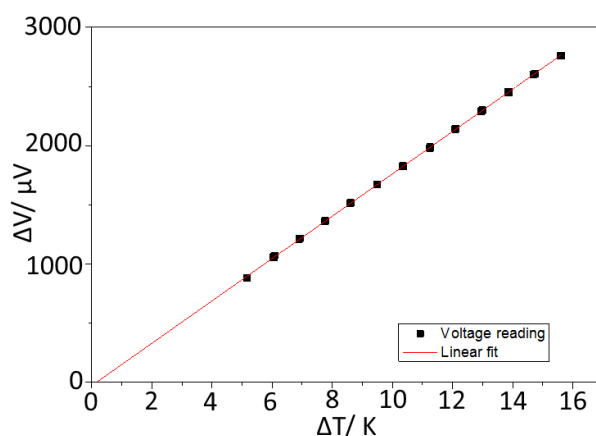


**Figure 3-5** -  $\Delta T$  vs.  $\Delta V$  data recorded on the bornite sample with composition  $Cu_{4.99}Fe_{0.98}S_4$  at 510 K and determined using the *in-situ* cell.

### 3.3.1. Minimising Contact Resistances

The electrode layout used in this *in-situ* cell leads to an inherent contact resistance between the electrodes and the sample because it is not a true 4-probe resistance geometry.<sup>258,259</sup> In an attempt to remove or reduce the contact resistance between the sample and electrodes, intermediate electrodes and alternative electrode geometries were investigated.

In other studies of thermoelectric materials, the use of eutectic metals as intermediary electrodes has proved to be effective for removing contact resistances.<sup>260</sup> Using these eutectic metals in the cell would ultimately lead to the corrosion of the platinum electrodes. Improvements in the contact resistance could reasonably be made by following better preparation methods for the electrode-contacting surfaces of the pelletised sample, using intermediate graphite electrodes or by sputter coating the electrode-contacting surfaces of the sample with gold or platinum.<sup>261,262</sup> However, the contact resistance could not be removed completely. Therefore it is expected that the use of other intermediary electrodes, such as hot-pressed contacts or colloidal solutions, would show similar results.<sup>263–265</sup>

The investigation into an alternative electrode geometry sought to split the electrodes at either end of the sample into two discrete electrodes to provide four electrical points of contact to the sample. An explanation of the two-probe<sup>266</sup> and four-probe<sup>249</sup> electrode geometries is provided in chapter 2. An explanation of the proposed electrode geometry is not found in the literature however. The experiments carried out here proved that splitting

the electrode would not allow for the removal of contact resistances. No modifications to the cell resulted from these experiments, however the sample preparation techniques and employment of sputter coated surfaces were implemented in the following on-line experiments.

### 3.3.2. Preliminary Diffraction Experiments on Tetrahedrite, $\text{Cu}_{12}\text{Sb}_4\text{S}_{13}$

The neutron diffraction data collected on this *in-situ* cell should be of sufficiently high quality as to allow for full Rietveld refinements of structural models. Here a synthetic sample of the high-performance thermoelectric mineral tetrahedrite,  $\text{Cu}_{12}\text{Sb}_4\text{S}_{13}$ , prepared using mechanochemical and hot pressing techniques (described in chapter 6) was taken for diffraction experiments on the POLARIS beam line.<sup>160</sup> Neutron data were collected for *ca.* 1 hr or 170  $\mu\text{A}$  at room temperature. Background diffraction data for the glass sheath and boron-nitride housing were recorded on an empty cell *ca.* 0.5 hr or 85  $\mu\text{A}$  at room temperature.

Figure 3-6 shows the diffraction patterns for the empty cell. Bragg reflections corresponding to the boron-nitride holder and platinum electrodes are present. There is also a diffuse scattering contribution to the background from the glass sheath. Upon comparing the diffraction pattern of the empty cell to the diffraction pattern of the cell with a sample inserted, it is clear that the relative intensity from the sample environment is minimal (Figure 3-6). The Mantid analysis software may be used to subtract the background contribution, the resulting diffraction pattern is also shown in Figure 3-6.<sup>210</sup>

Individual Rietveld analyses were performed using the powder neutron diffraction data including and excluding the background contribution. The multi-bank refinements, 150°, 90° and 50° (banks 5, 4 and 3, respectively), of the sample revealed a majority tetrahedrite phase,  $\text{Cu}_{12}\text{Sb}_4\text{S}_{13}$  (indexed using the cubic unit cell with space group  $I\bar{4}3m$ ) and an impurity kuramite-type phase ( $\text{Cu}_3\text{SbS}_4$  which could be indexed to a tetragonal unit cell, in space group  $I\bar{4}2m$ ).<sup>164</sup> For the data including the background contribution, the Bragg reflections from the boron-nitride holder were not modelled and the reflections corresponding to this phase are visible in the difference curve. For the data from each bank, the background interference from the glass sheath was modelled with many background parameters, *ca.* 30, and the shifted Chebyshev function.

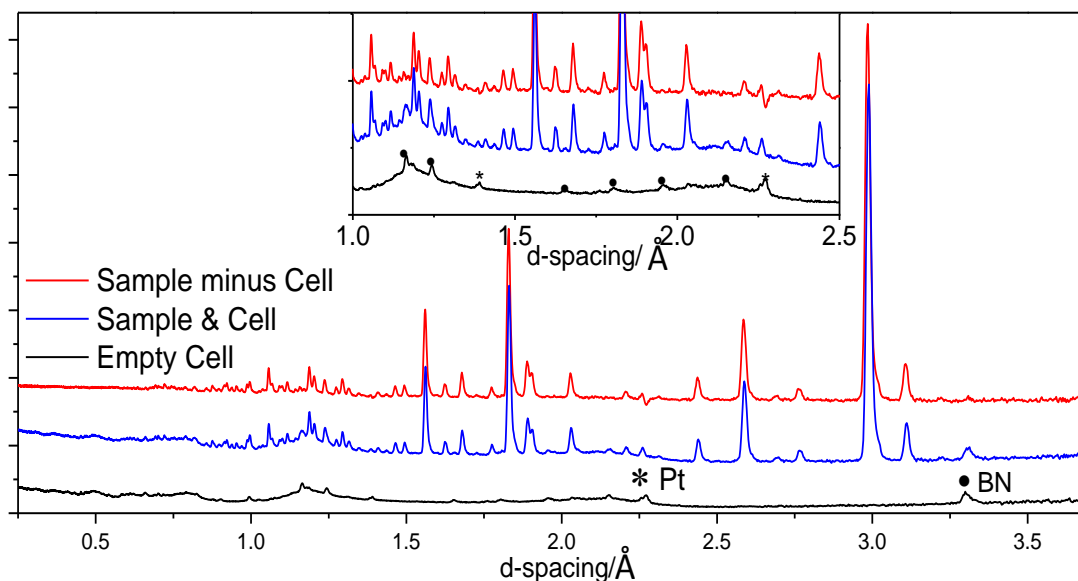


**Figure 3-6** – Room temperature neutron diffraction patterns for  $\text{Cu}_{12}\text{Sb}_4\text{S}_{13}$  collected using the in-situ cell. Black - the contribution to the background from the glass sheath, boron-nitride holder and platinum disc and; red - the resulting pattern after subtracting the background pattern from; blue – the collected diffraction pattern of the sample in the cell.

The goodness-of fit parameters from each of the Rietveld analyses were reliable. The data including the background contribution gave  $\chi^2 = 6.066$ ,  $R_{wp} = 3.90$ , 3.73 and 3.55 % for the 150°, 90° and 50° banks, respectively (Figure 3-7). In comparison, the goodness of fit parameters for the data with the background subtracted gave  $\chi^2 = 2.409$ ,  $R_{wp} = 5.59$ , 4.81 and 3.82 % for the 150°, 90° and 50° banks, respectively (appendix B). Therefore, it is not necessary to implement a background subtraction in order to achieve a reliable structural analysis of thermoelectric materials when using the Seebeck-Resistance-Diffraction cell. However, it should be noted that higher values of  $\chi^2$  can be expected when the background diffraction data is not subtracted. Furthermore, the resulting structural model from Rietveld refinement shows that the expected ‘rattler’ site has a large and anisotropic thermal displacement parameter, indicating that the finer details of crystal structures can be determined after Rietveld analysis using data collected using this cell (see e-appendix).

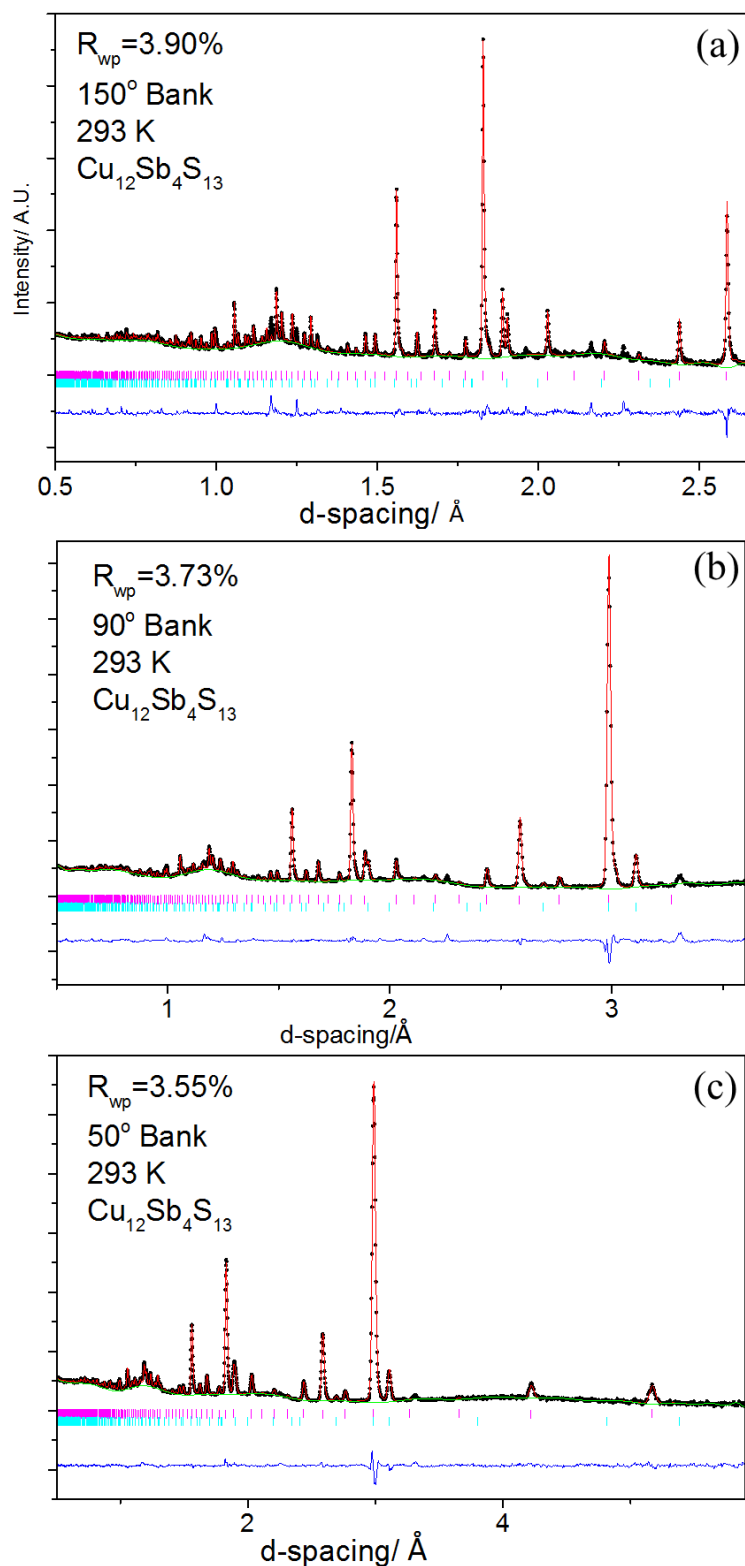


**Figure 3-7** – Full Rietveld refinement profiles from multi-bank refinements; (a),(b) and (c) correspond to the diffraction data collected at 293 K on  $\text{Cu}_{12}\text{Sb}_4\text{S}_{13}$  for the 150°, 90° and 50° degree banks (banks 5, 4 and 3), respectively. Black points – observed, Red line – calculated, Blue line – difference profile. Pink markers -  $I\bar{4}3m$  phase of tetrahedrite and blue markers -  $I\bar{4}2m$  phase of kuramite-type phase.

### 3.4. In-Situ Investigations into Copper-Chalcogenide Thermoelectrics

#### 3.5. Kesterite Thermoelectrics, $\text{Cu}_2\text{ZnGeSe}_4$

Validation of this cell was pursued through a variable-temperature experiment on a known thermoelectric material with subtle structural anomalies to demonstrate that the advantages afforded by neutrons can be utilised with this cell. Previous neutron diffraction experiments on  $\text{Cu}_2\text{ZnGeSe}_4$  (CZGSe) at room temperature by P. Mangelis *et al.* and S. Schorr *et al.* reveal an inherent partial cation disorder over a number of the cation sites.<sup>267,268</sup> Here copper occupies three sites,  $2a$ ,  $2b$  and  $2c$ .

In a fully ordered kesterite structure, the  $2a$  and  $2b$  sites would be occupied by Cu and Zn, respectively. The CZGSe kesterite is not fully ordered at room temperature and instead has site occupancy factors at the crystallographic sites of *ca.*  $\text{SOF}_{\text{Cu}}=0.85$  and  $\text{SOF}_{\text{Zn}}=0.15$  for the  $2a$  site, and *vice versa* for the  $2b$  site,<sup>267,268</sup> or *ca.*  $\text{SOF}_{\text{Cu}}=0.7$  and  $\text{SOF}_{\text{Zn}}=0.3$  at the  $2a$  site.<sup>269</sup> In each of these studies, the  $2c$  site has  $\text{SOF}_{\text{Cu}}=1$  at room temperature. For the stoichiometric phase, variable temperature  $^{63}\text{Cu}$  NMR spectroscopy data collected by Zeier *et al.* revealed that, at room temperature, there are at least two unique copper sites within the structure.<sup>270</sup>

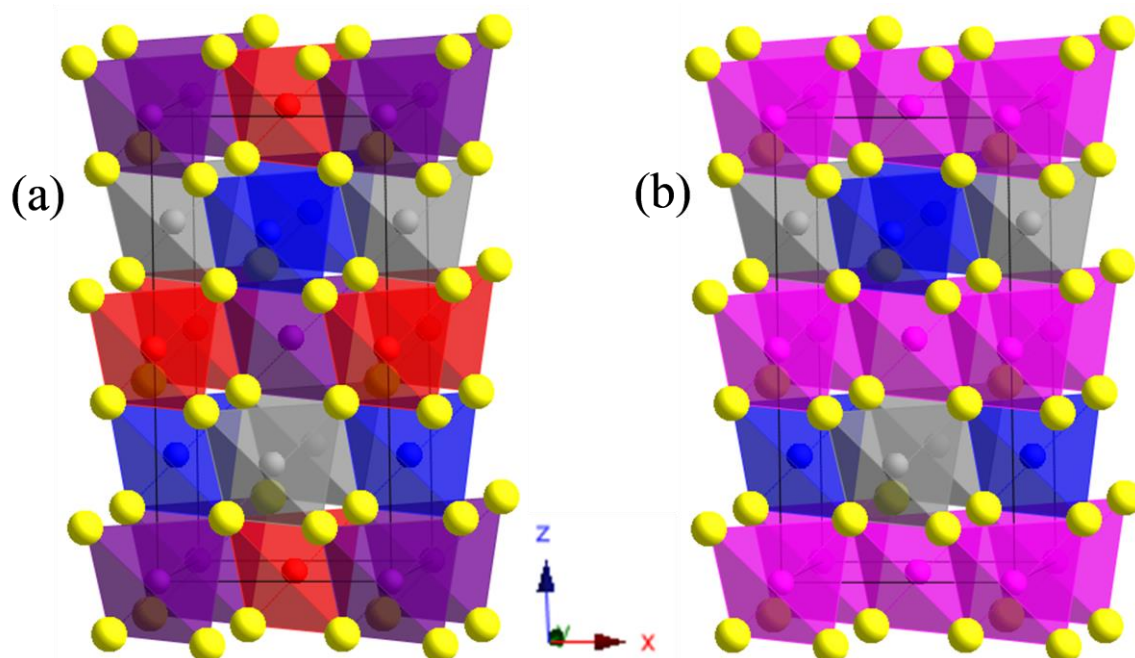


**Figure 3-8** – Perspective view of the structure of  $\text{Cu}_2\text{GeZnSe}_4$  as suggested by Mangelis *et al.*<sup>269</sup> at (a) – 300 K; (b) -525 K; Space group:  $\bar{1}\bar{4}$ , Yellow: Sulphur; Grey – Germanium; blue – copper  $2c$  site; Red – Zinc rich  $2b$  site; Purple - Copper rich  $2a$  site and; Pink – disordered copper and zinc  $2a/2b$  sites.

Upon heating, two of the Cu environments ( $2a$  and  $2b$  in Figure 3-8) transform into a single Cu environment, this behaviour has been proposed as an order-disorder transition. Variable-temperature neutron diffraction and DSC data collected by Mangelis *et al.* confirm that this is a second-order structural phase transition. This observation is supported by the DSC data collected by Zeier *et al.*<sup>271</sup> High-temperature neutron diffraction data analysis revealed that the  $2a$  and  $2b$  sites, which are partially disordered at room temperature, become fully disordered with an equal occupancy of copper and zinc cations at each site, and the  $2c$  site maintains a  $SOF_{Cu}=1$ .

The sample with composition  $Cu_{2.125}ZnGe_{0.875}Se_4$  showed improved thermoelectric performance compared to the stoichiometric phase. This was a result of substantial improvements in the electrical behaviour of the material. As such, the sample was taken for *in-situ* neutron diffraction experiments to provide an understanding of the electrical behaviour as a function of temperature.

### ***3.5.1. Experimental Procedures for the In-Situ Investigations of $Cu_{2.125}Ge_{0.875}ZnSe_4$***

A sample with composition  $Cu_{2.125}Ge_{0.875}ZnSe_4$  was synthesised using the same techniques as described by Mangelis *et al.*<sup>269</sup> Elemental components, copper (Sigma Aldrich, powder, 99.95%), zinc (Sigma Aldrich, powder, <150  $\mu$ m, 99.99%), germanium (Sigma Aldrich, powder, 99.99%) and selenium (Sigma Aldrich, shot, 99.99%), were ground together in an agate pestle and mortar then sealed into a fused silica tube under a pressure of  $10^{-4}$  mBar. The mixture was heated at  $2\text{ K min}^{-1}$  to 923 K and held there for 48 hours then cooled naturally. After grinding, the sample was heated to 1073 K for 96 hours. The resulting crystalline powder was hot pressed at 873 K and 65 bar under a  $N_2$  atmosphere for 45 minutes. The resulting pellet had dimensions of *ca.*  $l = 14$  mm and *diameter* = 12.7 mm, the pellet was sanded to a diameter of 10 mm and the circular faces were polished with up to 7000 grit sandpaper and coated by platinum sputter coating.

The neutron diffraction experiments were performed over the temperature range  $T = 300 - 500$  K using the POLARIS diffractometer in the RAL-4 furnace. Diffraction and electrical data were collected using the *in-situ* cell and recorded every 25 K on heating and every 50 K on cooling down to 380 K. Multibank refinements were carried out using data from the  $150^\circ$ ,  $90^\circ$  and  $50^\circ$  banks and the GSAS software package.<sup>209</sup>

The initial structural model was constructed using the description of the room-temperature structure of CZGSe provided by Mangelis *et al.*<sup>269</sup> During Rietveld analysis using the neutron diffraction data, the thermal parameters of cations at each site were allowed to refine individually. The site occupancy factors were constrained during Rietveld refinement to maintain the nominal composition of  $\text{Cu}_{2.125}\text{ZnGe}_{0.875}\text{Se}_4$  for  $T < 400$  K. At temperatures,  $T > 400$  K, least-squares refinements of the structural model become unstable if partial ordering of the Cu and Zn was modelled across the  $2a$  and  $2b$  sites. Therefore, these sites were constrained to a common value, this provided a stable least-squares refinement and allowed for convergence to be achieved.

### 3.5.2. Diffraction Results from the Experiment on $\text{Cu}_{2.125}\text{Ge}_{0.875}\text{ZnSe}_4$

X-Ray diffraction analysis revealed the presence of impurity phases; zinc selenide in small quantities and copper selenide in trace quantities. This is consistent with the observations made by Mangelis *et al.* when synthesising copper-substituted CZGSe kesterites.<sup>269</sup> The zinc-selenide impurity phase was included during Rietveld analysis of the neutron diffraction data and was present in 8.615(8) wt% at 300 K. The electronic phase transition at low-temperature is described as a second-order metal-semiconductor phase transition.<sup>188,271</sup> This transition is known to be second order in nature and no new Bragg reflections are observed in the diffraction pattern at temperatures above the metal-semiconductor phase transition (Figure 3-9).

The lattice-parameters,  $a$  and  $c$ , increase with increasing temperature across the entire temperature range. There is an anomaly in the lattice parameter behaviour observed at  $T = 350 - 375$  K, *ca.* 100 K below the expected metal-semiconductor transition temperature (Figure 3-10). Temperature dependence of the lattice parameters for the stoichiometric phase, as investigated by Mangelis *et al.*, showed a linear increase over the entire temperature range investigated. Here, the temperature increments across  $T = 300 - 400$  K were smaller,  $T_n = T_{n-1} + 25$  K compared to  $T_n = T_{n-1} + 50$  K, allowing for the observation of this anomaly in the lattice parameters at 350 K (Figure 3-10).

At 300 K, the fractional site occupancies of copper at the  $2a$  and  $2b$  sites in the  $c = 0$  plane are  $\text{SOF}_{\text{Cu}} = 0.778(59)$  and  $0.222(59)$  (Figure 3-11), with the remaining fraction at each site being occupied by zinc. This observation is in excellent agreement with the  $\text{SOF}_{\text{Cu}}$  values proposed by both Schorr *et al.*<sup>268</sup> and Mangelis *et al.*<sup>269</sup>

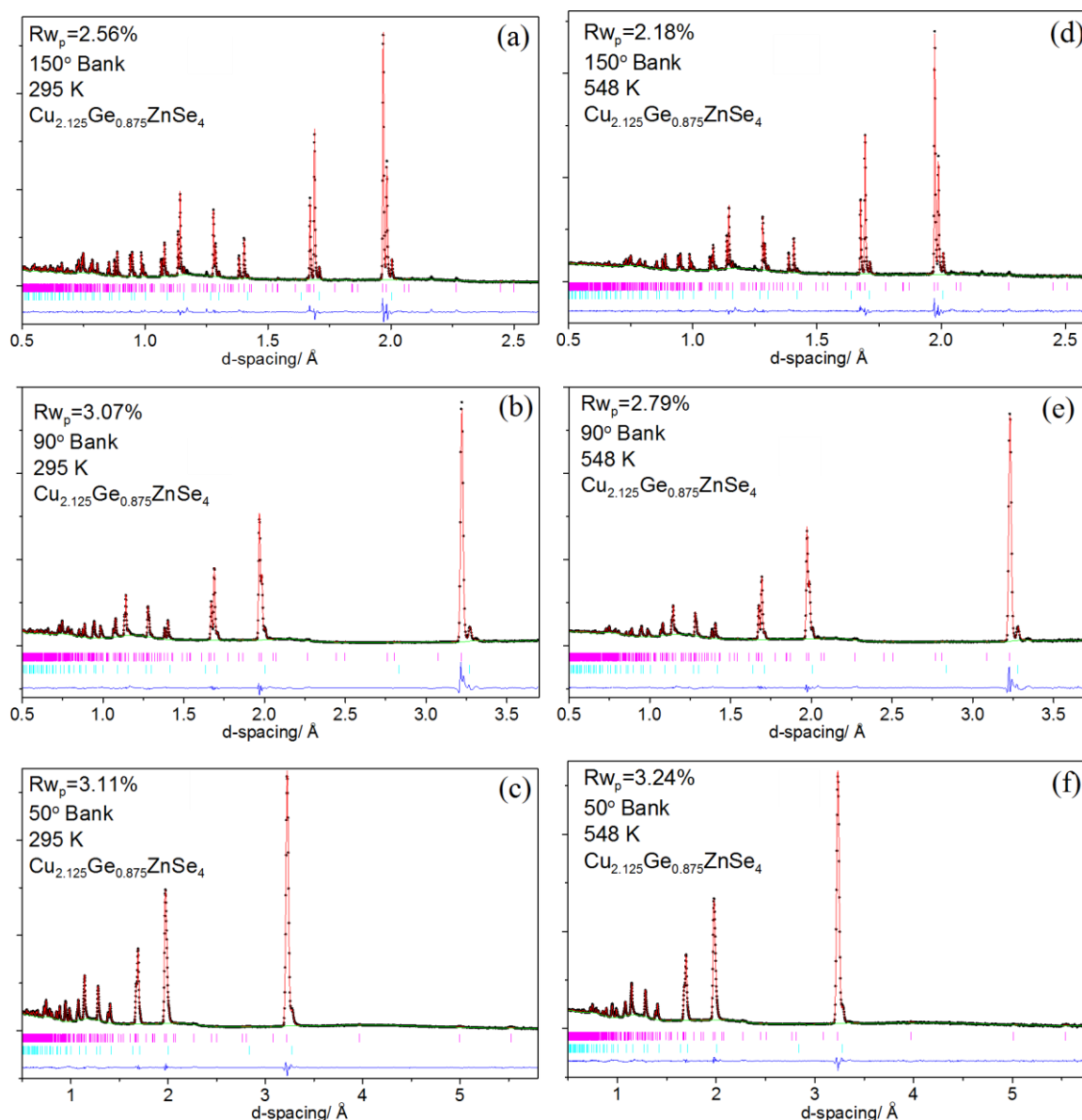


**Figure 3-9** – Full Rietveld refinement profiles from multi-bank refinements of  $\text{Cu}_{2.125}\text{Ge}_{0.875}\text{ZnSe}_4$ ; (a),(b) and (c) correspond to the diffraction data collected at 295 K on for the 150°, 90° and 50° degree banks (banks 5, 4 and 3), respectively; (d), (e) and (f) correspond to the diffraction data collected at 548 K. Black points – observed, Red line – calculated, Blue line – difference profile, green line – background, pink lines -  $\bar{1}4$  phase of  $\text{Cu}_{2.125}\text{Ge}_{0.875}\text{ZnSe}_4$  and blue lines -  $F\bar{4}3m$  phase of  $\text{ZnSe}$ .

Here, the site occupancy factors of the copper and zinc at the  $2a$  and  $2b$  sites appear to have some temperature dependence, i.e. they become more disordered with increasing temperature up to *ca.* 425 K, at which point they become fully disordered. This is consistent with the observations made by Mangelis *et al.*<sup>269</sup> This order-disorder transition is observed over the temperature range  $T = 450 - 475$  K for the stoichiometric sample. For

the substituted sample  $\text{Cu}_{2.125}\text{ZnGe}_{0.875}\text{Se}_4$  investigated here the transition is observed over  $T = 400 - 425$  K, suggesting the transition temperature decreases as a result of substituting copper for germanium. The summed site occupancy factor at the  $2a$  and  $2b$  sites are  $\text{SOF}_{\text{Cu+Zn}} = 0.90(12)$  at 525 K. The presence of a  $\text{SOF}_{\text{Cu+Zn}} < 1$  indicates that some of the copper and zinc may become delocalised, and occupy the remaining tetrahedral holes, in the high-temperature phase.

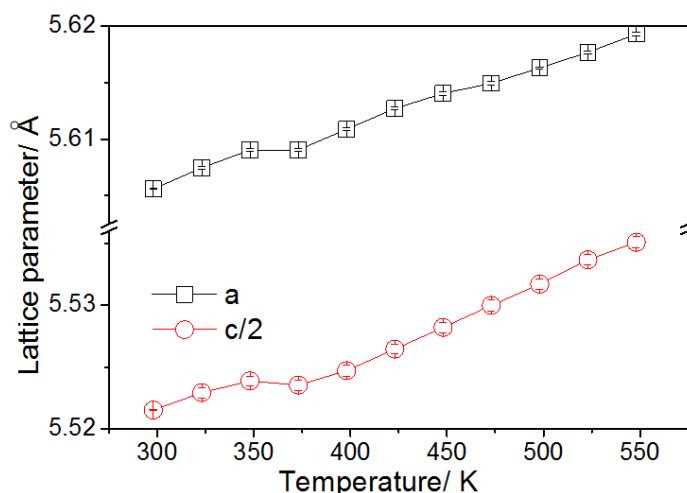


**Figure 3-10** – Temperature dependence of the lattice parameters of the sample with nominal composition  $\text{Cu}_{2.125}\text{Ge}_{0.875}\text{ZnSe}_4$ , determined from multibank Rietveld refinements.

Error bars are shown and appear within points.

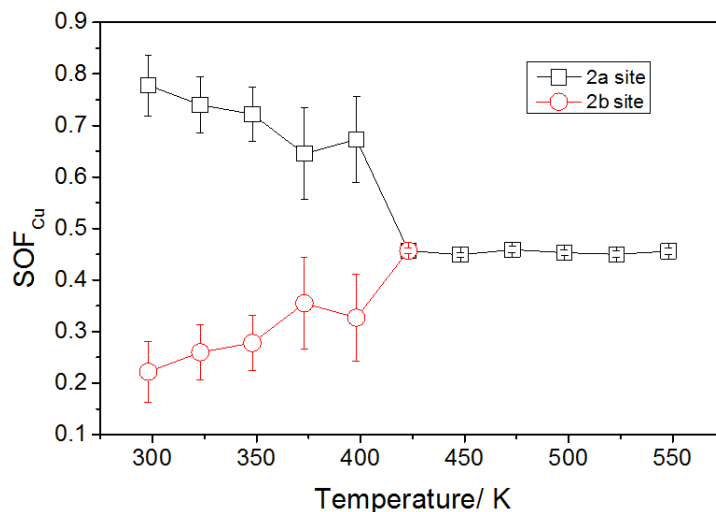


**Figure 3-11** – Temperature dependence of the site occupancy factor of copper at the  $2a$  and  $2b$  sites for the sample with nominal composition  $\text{Cu}_{2.125}\text{Ge}_{0.875}\text{ZnSe}_4$ , determined from multibank Rietveld refinements. Error bars are shown and appear within points above 400 K.

**Table 3-1** – Crystallographic parameters determined from the neutron diffraction data collected at 295 K for the sample with composition  $\text{Cu}_{2.125}\text{Ge}_{0.875}\text{ZnSe}_4$ .

Temperature		295 K				
<b>Kesterite Phase</b>						
Space group		$I\bar{4}$				
Phase fraction	wt%	91.39(9)				
$a/\text{\AA}$		5.60559(3)				
$c/\text{\AA}$		11.04303(9)				
Name	Wy. Sym.	$x$	$y$	$z$	$U_{iso}/\text{\AA}^2$	$SOF$
Cu(1)	$2c$	0	0.5	0.25	0.010(1)	1
Cu(2)	$2a$	0	0	0	0.0074(27)	0.22(6)
Zn(2)	$2a$	0	0	0	0.0074(27)	0.78(6)
Cu(3)	$2b$	0	0	0.5	0.0082(29)	0.78(6)
Zn(3)	$2b$	0	0	0.5	0.0082(29)	0.22(6)
Cu(4)	$2d$	0	0.5	0.75	0.029(1)	0.125
Ge(4)	$2d$	0	0.5	0.75	0.029(1)	0.875
Se	$8g$	0.2484(26)	0.2581(6)	0.1251(5)	0.0108(3)	1
<b>ZnSe phase</b>						
Space group		$F\bar{4}3m$				
Phase fraction	wt%	8.61(9)				
$a/\text{\AA}$		5.66439(14)				
Name	Wy. Sym.	$x$	$y$	$z$	$U_{iso}/\text{\AA}^2$	$SOF$
Zn	$4a$	0	0	0	0.0088(3)	1
Se	$4c$	0.25	0.25	0.25	0.0088(3)	1
Bank 3	$R_{wp}/\%$	3.11	$R_p/\%$	2.76		
Bank 4	$R_{wp}/\%$	3.07	$R_p/\%$	4.24		
Bank 5	$R_{wp}/\%$	2.56	$R_p/\%$	3.30		
Overall	$R_{wp}/\%$	2.92	$R_p/\%$	3.45		
	$\chi^2$	15.01				

**Table 3-2** – Crystallographic parameters determined from the neutron diffraction data collected at 548 K for the sample with composition  $\text{Cu}_{2.125}\text{Ge}_{0.875}\text{ZnSe}_4$ .

Temperature		548 K				
<b>Kesterite Phase</b>						
Space group		$I\bar{4}$				
fraction	wt%	92.177(11)				
$a/\text{\AA}$		5.619281(1)				
$c/\text{\AA}$		11.0702(9)				
Name	Wy. Sym.	$x$	$y$	$z$	$U_{iso}/\text{\AA}^2$	SOF
Cu(1)	$2c$	0	0.5	0.25	0.0140(10)	1
Cu(2)	$2a$	0	0	0	0.0095(8)	0.456(6)
Zn(2)	$2a$	0	0	0	0.0095(8)	0.456(6)
Cu(3)	$2b$	0	0	0.5	0.0095(8)	0.456(6)
Zn(3)	$2b$	0	0	0.5	0.0095(8)	0.456(6)
Cu(4)	$2d$	0	0.5	0.75	0.0388(15)	0.125
Ge(4)	$2d$	0	0.5	0.75	0.0388(15)	0.875
Se	$8g$	0.2418	0.2587	0.12514	0.0296(4)	1
<b>ZnSe phase</b>						
Space group		$F\bar{4}3m$				
fraction	wt%	7.823(11)				
$a/\text{\AA}$		5.67710(17)				
Name	Wy. Sym.	$x$	$y$	$z$	$U_{iso}/\text{\AA}^2$	SOF
Zn	$4a$	0	0	0	0.0137(5)	1
Se	$4c$	0.25	0.25	0.25	0.0137(5)	1
Bank 3	$R_{wp}/\%$	3.24	$R_p/\%$	3.56		
Bank 4	$R_{wp}/\%$	2.79	$R_p/\%$	3.99		
Bank 5	$R_{wp}/\%$	2.18	$R_p/\%$	3.15		
Overall	$R_{wp}/\%$	2.73	$R_p/\%$	3.57		
$\chi^2$		4.578				

### 3.5.3. Electrical Behaviour of $\text{Cu}_{2.125}\text{ZnGe}_{0.875}\text{Se}_4$

Figure 3-12(a) and Figure 3-12(b) show the absolute and relative Seebeck coefficients determined from variable temperature experiments. These data were collected on the *in-situ* cell and the sample with nominal composition  $\text{Cu}_{2.125}\text{ZnGe}_{0.875}\text{Se}_4$  synthesised as described above; and the equivalent data from the Linseis LSR-3 collected on sample from a different synthesis batch by P. Mangelis. Figure 3-12(c) and Figure 3-12(d) show the relative and absolute resistivity for these two samples. The relative resistivity was calculated from:  $\rho_i^{(T)} = \rho(T)/\rho_{375K}$  and relative Seebeck coefficient from:  $S_i^{(T)} = S(T)/S_{300K}$ . This was done to provide a more direct comparison between the two sets of data.

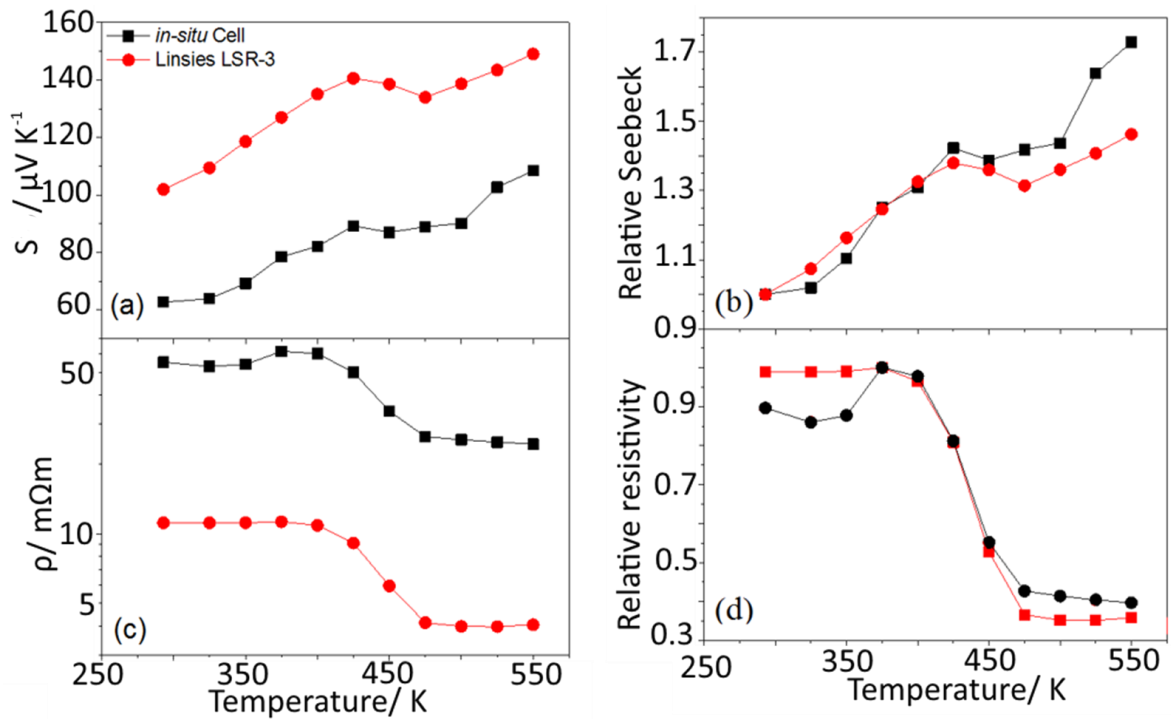


**Figure 3-12** – Temperature dependence of the electrical transport properties of samples with nominal composition  $\text{Cu}_{2.125}\text{Ge}_{0.875}\text{ZnSe}_4$ , data recorded on the Linsies LSR-3 were collected on a sample synthesised by P. Mangelis. (a) Measured Seebeck coefficient; (b) relative Seebeck coefficient; (c) measured electrical resistivity; (d) relative resistivity.

Though there is some discrepancy between the absolute values determined from the *in-situ* device and the LSR-3, the relative Seebeck coefficient and resistivity clearly demonstrate that there is excellent agreement for the temperature dependence of the electrical transport properties. The anomalies in the Seebeck coefficient are reliably mapped and the marked drop in the electrical resistivity across the temperature range  $T = 400 - 475$  K is observed.

This anomaly coincides with the temperature of the order-disorder transition as observed in the diffraction data, where the cation ordering over the  $2a$  and  $2b$  sites becomes fully disordered. Notably the temperature at which this anomaly is observed is also in excellent agreement between the two instruments.

Interestingly, the behaviour in the low-temperature part of the curve of  $\rho(T)$ , determined using the *in-situ* cell, exhibits an additional anomaly that is not seen in the data recorded on the LSR-3. There is however an anomaly in the lattice parameter values with increasing temperature that coincides with this anomaly in the electrical properties (Figure 3-10).

This experiment clearly demonstrated the reliability of the cell in monitoring structure property relationships in thermoelectric materials. With this strong confirmation of the reliability of the cell the following investigations sought to investigate the n-type copper chalcogenides which show interesting structural behaviour with temperature.

### ***3.6. In-Situ Experiments Investigating some Cu-Fe-S Based Thermoelectrics***

Chalcopyrite,  $\text{CuFeS}_2$ , is the most abundant of copper-containing sulphide minerals. The Cu-Fe-S system that it belongs to has been studied by mineralogists for many years due to the rich structural chemistry that this system offers. The central area of the Cu-Fe-S phase diagram at high temperature is characterised by a multitude of structural phases, such as chalcopyrite, talnakhite and mooihoekite, along with an intermediate solid state (*iss*) cubic phase.<sup>146</sup> These structural phases are closely related and show remarkably similar diffraction patterns.

Chalcopyrite has been studied for its potential as a thermoelectric material for many years, however characterisation of the thermoelectric properties of chalcopyrite are not always in agreement. The Seebeck coefficient for stoichiometric synthetic samples of chalcopyrite may vary between  $S = -320$  to  $-580 \mu\text{V K}^{-1}$ .<sup>95,96</sup> The variation in the Seebeck coefficient with temperature is not consistent between studies.  $S(T)$  has been shown to not change significantly with increasing temperature or increase with increasing temperature. In other instances,  $S(T)$  reduces drastically with increasing temperature.<sup>96,97,101</sup> Neutron diffraction studies here seek to gain a deeper understanding of this behaviour.

More recently the mooihoekite and talnakhite type-phases have come to light as potential thermoelectric materials.<sup>151,153</sup> They are all attractive candidates for use in thermoelectric applications because they show n-type behaviour which is a rare phenomenon in low-cost

copper-sulphide based thermoelectrics. This following section seeks to provide further insight into the structure-property relationship in the Cu-Fe-S system.

### ***3.6.1. Experimental Procedure for 'CuFeS<sub>2</sub>'***

Samples with a nominal composition of CuFeS<sub>2</sub> were prepared by mechanochemical alloying. A stoichiometric mixture of copper (99.5%, Sigma Aldrich), iron (99.9+%, Sigma Aldrich) and sulphur (flakes, 99.99%, Sigma Aldrich) was ground together in an agate pestle and mortar. Two consecutive millings of the powder were performed (20 hr, 550 rpm with a reverse in rotational direction every 15 minutes) in a steel milling jar (25 mL) with steel milling balls (8 : 24 g, powder:balls). This was sealed under an argon atmosphere and the powder was agitated between each milling. The powder was consolidated by hot pressing under a N<sub>2</sub> atmosphere (80 bar, 850 K). The sample with dimensions of *ca.*  $l = 12$  mm and *diameter* = 13 mm was sanded by hand down to *diameter* = 10 mm. The circular faces of each pellet were polished with SiC wet and dry paper up to 7000 grit. The pellet was coated using a Edwards S150B platinum sputter coater for 15 minutes on each side and under a vacuum of  $1 \times 10^{-3}$  mbar, the residual platinum on the sides of the sample was removed by sanding.

The sample was placed into the boron-nitride clamp assembly of the *in-situ* cell with the set up described in section 3.2. Neutron diffraction data were collected at the POLARIS diffractometer, with collection times of 2 hours at each temperature and at temperature increments of 50 K over the temperature range 300 – 500 K, increments of *ca.* 35 K over 500 – 675 K and increments of 25 K over 675 – 825 K.

X-Ray diffraction data were collected on the Bruker D8 Advanced using powdered sample of chalcopyrite and a zero-background holder for 1 hour and over the angular range,  $5 < 2\theta / ^\circ < 85$ . Phase analysis was performed using the PDF2-ICDD database in the EVA software package.<sup>203</sup> Neutron diffraction data at each temperature were collected for 1 hour with no induced thermal gradient and 1 hour during the thermal cycling for Seebeck measurements. The temperature at the gradient heater was increased by 1 K every 15 minutes, for each temperature increment the sample was allowed to equilibrate under these conditions for 10 minutes and electrical transport data were collected over the following 5 minutes. Diffraction data from the detector banks at 150°, 90° and 50° (bank 5, 4 and 3) and the GSAS software package were used to perform Rietveld refinement of the neutron

diffraction data.<sup>272</sup> Bragg reflections from the boron-nitride holder were modelled using the Le Bail method and a rhombohedral unit cell with space group,  $P\bar{6}m2$ .<sup>273</sup>

### 3.6.2. Results from In-Situ Neutron Diffraction Experiments on ‘CuFeS<sub>2</sub>’

A preliminary phase analysis of the laboratory X-ray diffraction data collected at room temperature on the sample with nominal composition CuFeS<sub>2</sub> suggested that the sample showed single-phase behaviour (appendix C). However, the neutron diffraction data collected at room temperature revealed that a secondary phase was present in the sample (Figure 3-13). The primary chalcopyrite phase was indexed on the basis of the tetragonal space group  $I\bar{4}2d$  for an  $a \times a \times 2a$  super-cell of ZB type structure. The additional reflections were indexed using the talnakhite, Cu<sub>18</sub>Fe<sub>16</sub>S<sub>32</sub>, crystal structure with space group  $I\bar{4}3m$  and a cubic  $2a \times 2a \times 2a$  super-cell. Each of the  $U_{iso}$  values for the cations in this phase were constrained to a common value. The additional Bragg reflections observed in the neutron diffraction data at room temperature, corresponding to the secondary phase, had significant overlap with the Bragg reflections corresponding to the chalcopyrite phase. This is due to a remarkably similar pseudo cubic sub-cell parameter for the tetragonal chalcopyrite phase  $a_p = 5.3162(2) \text{ \AA}$  and  $c_p = 5.24888(7) \text{ \AA}$  and the cubic impurity phase  $a_p = 5.3297(5) \text{ \AA}$ .

The presence of two phases with many overlapping Bragg reflections makes full structural refinement more challenging. The ordering of Fe<sup>3+</sup> cations in chalcopyrite which leads to magnetic scattering adds further complexity to this analysis. The magnetic reflections in the neutron diffraction data have been modelled using the Le Bail method and the tetragonal space group  $I\bar{4}2d$  for an  $a \times a \times 2a$  super-cell with the same lattice parameters as the nuclear tetragonal phase,  $I\bar{4}2d$ . Engin *et al.* showed that the iron in chalcopyrite has antiferromagnetic interactions along the  $c$ -axis between ferromagnetically ordered layers along the  $a$ - $b$  plane.<sup>246</sup> The reflections at  $ca. d = 3.7$  and  $4.7 \text{ \AA}$  - along with others at lower  $d$ -spacings- can be attributed to the magnetic ordering within the structure (Figure 3-14).

### 3.6.3. Evolution of Structural Phases as a Function of Temperature in ‘CuFeS<sub>2</sub>’

Rietveld analysis of the diffraction data collected on the sample with nominal composition CuFeS<sub>2</sub> reveals the nature of structural phase transitions in this mixed-phase chalcopyrite (Figure 3-15). A phase transition in the impurity phase is observed between 450 and 500 K. Supercell peaks corresponding to the  $2a$  super structure of the talnakhite-type phase,  $d$ -spacing  $\approx 4.8$  and  $5.8 \text{ \AA}$ , are present across the temperature range  $T = 300 - 450 \text{ K}$ . Above

this temperature there is no diffraction intensity at  $d$ -spacing  $\approx 4.8$  and  $5.8 \text{ \AA}$  (Figure 3-13). This would be consistent with the observations in the literature that describe structural phase transitions of talnakhite phases in this temperature range.<sup>146</sup>

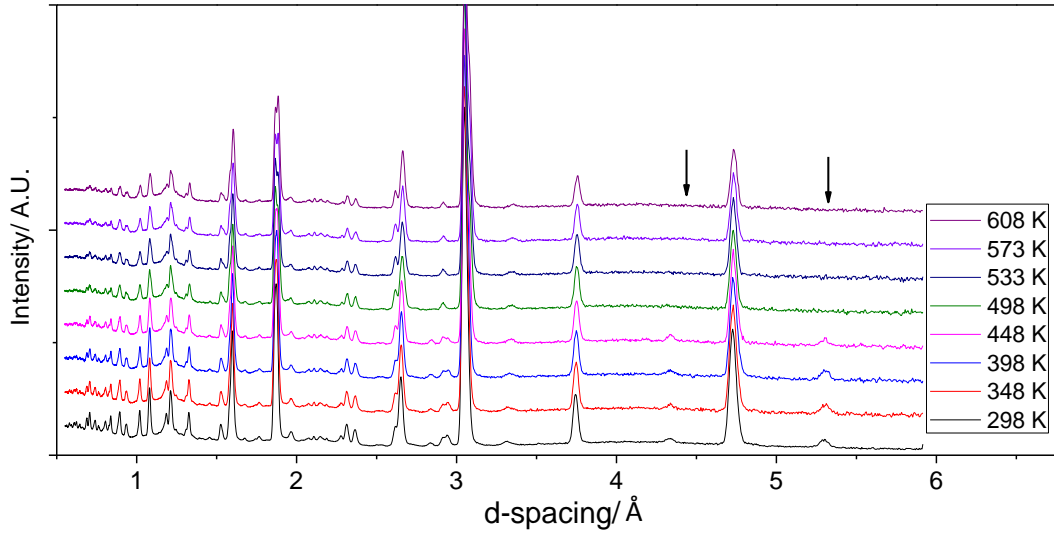


**Figure 3-13** – Diffraction patterns collected on POLARIS using the  $50^\circ$  bank for the sample with nominal composition  $\text{CuFeS}_2$  and across the temperature range  $T = 295 - 610 \text{ K}$ . Arrows indicate the expected position of the supercell peaks for a  $2a$  structure.

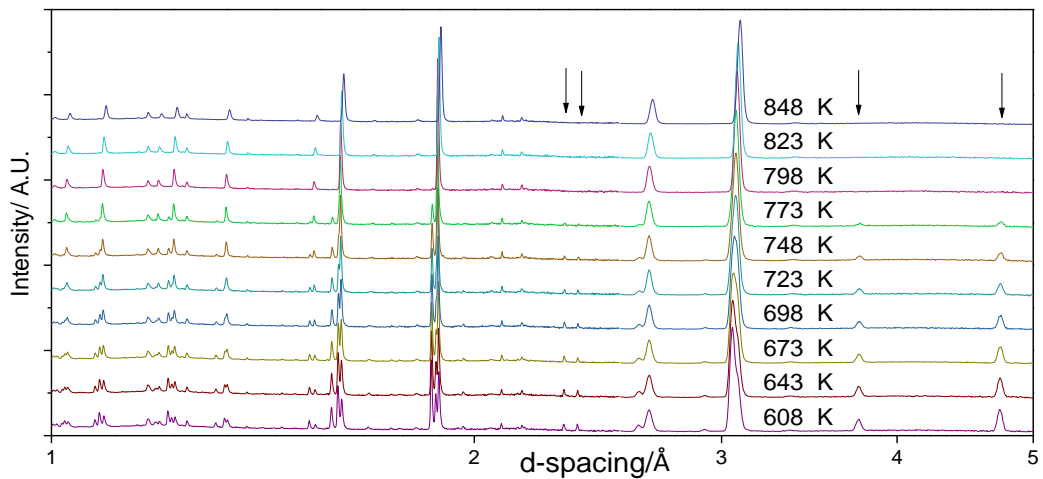


**Figure 3-14** – Diffraction patterns collected on POLARIS using the  $150^\circ$  ( $1.5 < d/\text{\AA} < 2.5$ ) and  $50^\circ$  ( $2.5 < d/\text{\AA} < 5$ ) bank for the sample with nominal composition  $\text{CuFeS}_2$  and over the temperature range  $T = 605 - 850 \text{ K}$ . Arrows indicate the magnetic reflections corresponding to the tetragonal magnetic structure.

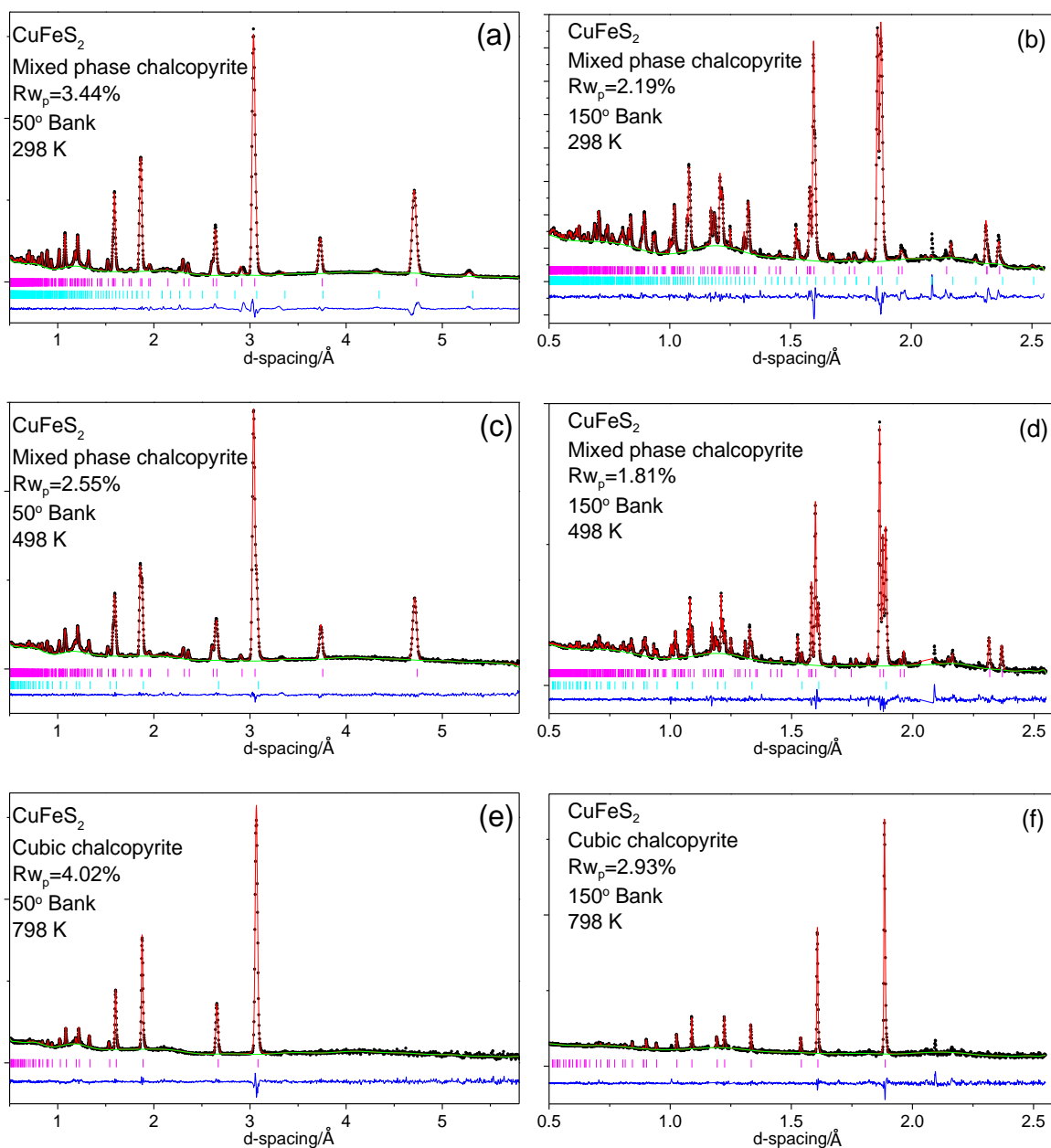


**Figure 3-15** – Rietveld refinement profiles for the neutron diffraction data collected on  $\text{CuFeS}_2$  at representative temperatures for each phases of the sample. (a,b) – mixed chalcopyrite-talnakhite phase at 298 K; (c,d) – mixed chalcopyrite-intermediate solid state phase at 498 K; (e,f) – high-temperature cubic chalcopyrite at 798 K. Black points – observed, Red line – calculated, Blue line – difference profile, pink markers - chalcopyrite phase,  $\bar{1}\bar{4}2d$  and blue markers – talnakhite phase  $\bar{1}\bar{4}3m$ . Magnetic reflections have been excluded from the data set.

At  $T = 450$  K, the chalcopyrite and talnakhite phases are present in  $wt\% = 63.01(38)$  and  $36.99(38)$ . Over the temperature range  $T = 500 - 775$  K the sample shows mixed-phase behaviour of the tetragonal chalcopyrite phase and the secondary *iss* (intermediate solid

solution) phase with an  $a \times a \times a$  cubic unit cell and space group  $F\bar{4}3m$ . There is a dynamic relationship between the two structural phases over the temperature range  $T = 500 - 775$  K. With increasing temperature, the weight fraction of the  $a \times a \times a$  cubic phase increases meanwhile, the weight fraction of the  $a \times a \times 2a$  tetragonal type phase decreases (Figure 3-16, Table 3-3).

At  $T > 775$  K the sample shows single-phase behaviour and the diffraction pattern can be indexed on the basis of a single  $a \times a \times a$  cubic unit cell,  $F\bar{4}3m$ . This is consistent with the expected phase-transition temperature of tetragonal chalcopyrite (Figure 3-14). This transition is known to be irreversible upon cooling the sample to room temperature.<sup>274</sup> The diffraction data collected here after cooling the sample back to  $T = 525$  K showed that the sample remained in the cubic  $a \times a \times a$  phase and space group  $F\bar{4}3m$ . There was no evidence of a secondary-phase or any magnetic scattering after cooling. The magnetic reflections decrease in diffraction intensity with increasing temperature and are completely absent once the sample has transformed into the single-phase cubic chalcopyrite-type phase, consistent with previous observations across the high-temperature transition.<sup>245</sup>

**Table 3-3** – Table of the weight percentages of each structural phase at each recorded temperature for the sample with composition  $CuFeS_2$ . † - denotes the iss phase; \* - denotes the high temperature cubic phase.

$T/$ K	$a \times a \times 2a$	$2a \times 2a \times 2a$	$a \times a \times a$
298	0.614(2)	0.386(2)	0
348	0.627(2)	0.373(2)	0
398	0.623(2)	0.377(2)	0
448	0.609(2)	0.391(2)	0
498	0.651(2)	0	0.348(2)†
533	0.622(2)	0	0.378(2)†
573	0.601(2)	0	0.399(2)†
608	0.567(2)	0	0.433(2)†
643	0.536(2)	0	0.464(2)†

$T/$ K	$a \times a \times 2a$	$2a \times 2a \times 2a$	$a \times a \times a$
673	0.483(2)	0	0.517(2)†
698	0.428(2)	0	0.572(2)†
723	0.358(2)	0	0.642(2)†
748	0.282(2)	0	0.718(2)†
773	0.123(2)	0	0.877(2)†
798	0	0	1*
823	0	0	1*
848	0	0	1*

The lattice parameters show a peculiar temperature dependence. With increasing temperature the pseudo-cubic sub-cell parameters of the chalcopyrite phase increase with increasing temperature (Figure 3-16(b)). However, for the secondary phase and across the temperature range  $T = 500 - 775$  K, the lattice parameters decrease with increasing temperature. At the phase-transition temperature of the secondary phase, there is a marked anomaly in the lattice parameters; the sub-cell parameter  $a_c$  increases significantly between

450 K and 500 K (Figure 3-16(b)). Upon transformation from the two-phase mixture to a single cubic phase at *ca.* 780 K and over the temperature range  $T = 800 - 850$  K the cubic lattice parameter increases with increasing temperature.

The  $a \times a \times a$  cubic phase of chalcopyrite is usually described by the zinc-blende structure type. The secondary *iss*  $a \times a \times a$  cubic phase observed at  $T = 500 - 775$  K shows the zinc-blende structure type but the iron cations exhibit a considerable degree of anti-site disorder. This is shown in the structure by the  $SOF_{M(2)} = 0.096(1)$ . The degree of anti-site disorder decreases with increasing temperature and continues into the high-temperature phase with the high temperature phase showing  $SOF_{M(2)} = 0.040(1)$  at 800 K.

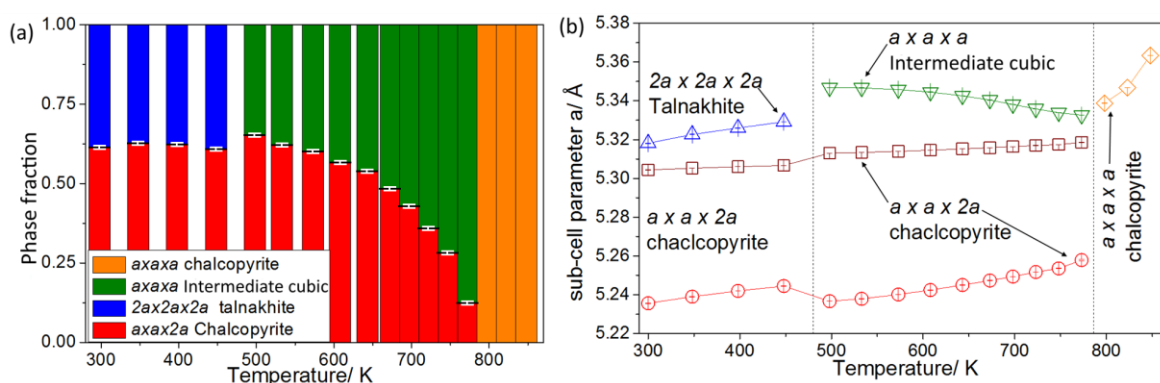


**Figure 3-16** – Data extracted from Rietveld refinement for the sample with nominal composition  $CuFeS_2$  and over the temperature range  $T = 343 - 850$  K. (a) Calculated weight percentages, Error bars are within phase fraction lines and shown by the white bars. (b) Lattice parameters of each of the structural phases, error bars within points.

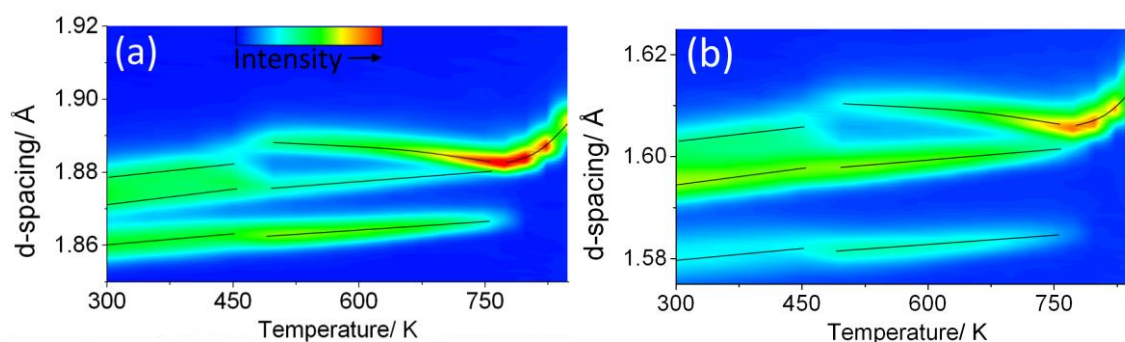


**Figure 3-17** – Neutron diffraction data collected on the  $150^\circ$  bank on POLARIS over the selected ranges (a)  $1.85 < d/\text{Å} < 1.92$  and (b)  $1.57 < d/\text{Å} < 1.63$  showing the change in reflections as a function of temperature over the temperature range  $T = 298 - 850$  K for the sample with nominal composition  $CuFeS_2$ . Black overlaid lines are given as a guide to the eye.

### 3.6.4. Influence on the Thermoelectric Properties of Chalcopyrite

The Seebeck data were determined using the *in-situ* cell for the sample with nominal composition CuFeS<sub>2</sub>. The Seebeck coefficient data were also recorded on a second sample with nominal composition CuFeS<sub>2</sub> from another synthesis batch using the Linseis LSR-3 (Figure 3-18). The data from the two experiments show excellent agreement at high temperature. The  $S(T)$  data from each experiment show a considerable temperature dependence.

**Table 3-4** – Crystallographic parameters determined from the neutron diffraction data collected at 298 K for the sample with composition CuFeS<sub>2</sub>.

Temperature	298 K					
Chalcopyrite phase						
Space Group		$I\bar{4}2d$				
Fraction	wt%	61.4(2)				
$a/\text{\AA}$		5.30437(3)				
$c/\text{\AA}$		10.4712(2)				
Atom Label	Wy. Sym	$x$	$y$	$z$	$U_{iso}/\text{\AA}^2$	$SOF$
Fe	$4a$	0	0	0	0.0118(1)	1
Cu	$4b$	0	0	$\frac{1}{2}$	0.0118(1)	1
S	$8d$	0.2504(20)	$\frac{1}{4}$	$\frac{1}{8}$	0.0044(3)	1
Talnakhite phase						
Space Group		$I\bar{4}3m$				
Fraction	wt%	38.6(2)				
$a/\text{\AA}$		10.6363(2)				
Atom Label	Wy. Sym	$x$	$y$	$z$	$U_{iso}/\text{\AA}^2$	$SOF$
Fe(1)	$2a$	0	0	0	0.0147(2)	1
Cu(1)	$12e$	0.2545(6)	0	0	0.0147(2)	0.42
Fe(2)	$12e$	0.2545(6)	0	0	0.0147(2)	0.58
Cu(2)	$12d$	$\frac{1}{2}$	$\frac{1}{4}$	0	0.0147(2)	0.42
Fe(3)	$12d$	$\frac{1}{2}$	$\frac{1}{4}$	0	0.0147(2)	0.58
Cu(3)	$8c$	0.2481(7)	0.2481(7)	0.2481(7)	0.0147(2)	1
Cu(4)	$6b$	$\frac{1}{2}$	0	0	0.0166(2)	0.04
S(1)	$8c$	0.1176(15)	0.1176(15)	0.1176(15)	0.0095(8)	1
S(2)	$24g$	0.1213(15)	0.3782(11)	0.3782(11)	0.0095(8)	1
goodness of fit						
Bank 3	$R_{wp}/\%$	3.64	$R_p/\%$	4.40		
Bank 4	$R_{wp}/\%$	3.63	$R_p/\%$	4.93		
Bank 5	$R_{wp}/\%$	2.25	$R_p/\%$	3.29		
Overall	$R_{wp}/\%$	3.18	$R_p/\%$	4.20		
	$\chi^2$	16.99				

**Table 3-5** – Crystallographic parameters determined from the neutron diffraction data collected at 498 K for the sample with composition  $\text{CuFeS}_2$

Temperature	498 K					
Chalcopyrite phase						
Space Group			$I\bar{4}2d$			
Fraction	wt%	65.97(12)				
$a/\text{\AA}$			5.31304(2)			
$c/\text{\AA}$			10.4732(1)			
Atom Label	Wyckoff.	$x$	$y$	$z$	$U_{iso}/\text{\AA}^2$	SOF
Fe	$4a$	0	0	0	0.0209(1)	1
Cu	$4b$	0	0	$\frac{1}{2}$	0.0209(1)	1
S	$8d$	0.2442(14)	$\frac{1}{4}$	$\frac{1}{8}$	0.0126(3)	1
Secondary phase						
Space Group			$F\bar{4}3m$			
Fraction	wt%	34.03(12)				
$a/\text{\AA}$			5.34681(8)			
Atom Label	Wyckoff.	$x$	$y$	$z$	$U_{iso}/\text{\AA}^2$	SOF
Fe(1)	$4a$	0	0	0	0.0206(3)	0.085(1)
Cu(1)	$4a$	0	0	0	0.0206(3)	0.009(1)
Cu(2)	$4b$	$\frac{1}{2}$	0	0	0.0206(3)	0.491(1)
Fe(2)	$4b$	$\frac{1}{2}$	0	0	0.0206(3)	0.415(1)
S(1)	$4c$	$\frac{1}{4}$	$\frac{1}{4}$	$\frac{1}{4}$	0.0317(9)	1
goodness of fit						
Bank 3	$R_{wp}/\%$	2.60	$R_p/\%$	3.90		
Bank 4	$R_{wp}/\%$	3.05	$R_p/\%$	3.56		
Bank 5	$R_{wp}/\%$	1.82	$R_p/\%$	2.80		
Total	$R_{wp}/\%$	2.53	$R_p/\%$	3.41		
	$\chi^2$	3.206				

**Table 3-6** – Crystallographic parameters determined from the neutron diffraction data collected at 798 K for the sample with composition  $\text{CuFeS}_2$ .

Temperature	798 K					
Chalcopyrite phase						
Space Group	$F-43m$					
$a/\text{\AA}$	5.33881(4)					
Atom Label	Wy. Sym	$x$	$y$	$z$	$U_{iso}/\text{\AA}^2$	$SOF$
Cu(1)	$4a$	0	0	0	0.0411(2)	0.473
Cu(2)	$4b$	0	0	$\frac{1}{2}$	0.0411(2)	0.027
Fe(1)	$4a$	0	0	0	0.0411(2)	0.485
Fe(2)	$4b$	0	0	$\frac{1}{2}$	0.0411(2)	0.015
S	$4c$	$\frac{1}{4}$	$\frac{1}{4}$	$\frac{1}{4}$	0.0338(2)	1
goodness of fit						
Bank 3	$R_{wp}/\%$	4.03	$R_p/\%$	5.55		
Bank 4	$R_{wp}/\%$	2.87	$R_p/\%$	5.18		
Bank 5	$R_{wp}/\%$	2.93	$R_p/\%$	4.39		
Total	$R_{wp}/\%$	3.17	$R_p/\%$	5.02		
	$\chi^2$	1.404				

The data recorded in the *in-situ* cell show that the Seebeck coefficient increases slightly with increasing temperature across the temperature range  $T = 400 - 600$  K. This is followed by a significant decrease in the magnitude of the Seebeck coefficient over the temperature range  $T = 600 - 850$  K, from  $S = -160$  to  $-80 \mu\text{V K}^{-1}$ , with the lowest values for  $S$  being observed in the high-temperature phase. In addition, this experiment reveals the behaviour of the dynamic interchange between the structural phases in this solid-state mixture. The decrease in the Seebeck coefficient can be attributed to the increasing presence of the secondary *iss* cubic phase. Meanwhile, the decrease in the Seebeck coefficient between  $T = 300 - 400$  K observed for the *in-situ* cell data and the anomaly at 350 K in the LSR-3 data can be attributed to the low-temperature phase transition of the talnakhite phase.

The behaviour of the Seebeck coefficient at temperature up to 850 K for chalcopyrite is not well documented.<sup>94,97,99,100</sup> Generally the property data measurements on chalcopyrite are limited to 700 K because it begins to show evidence of sulphur loss at temperatures higher than 600 K.<sup>96</sup> The behaviour of  $S(T)$  reported here demonstrates the detrimental effect of the high-temperature metal-semiconductor phase transition on the Seebeck coefficient of

chalcopyrite. Furthermore, the magnitude of  $S(T)$  decreases as a result of an increasing concentration of the secondary *iss* phase that develops at higher temperatures. Early observations by Cabri *et al.* revealed the presence of the *iss* phase which may occur at high temperatures in samples with a range of compositions close to  $\text{CuFeS}_2$ .<sup>146</sup> The observation of decreasing Seebeck coefficient of chalcopyrite phases in the literature may also be linked to the evolution of the *iss* type phase. This experiment outlines the importance of performing full profile diffraction analysis on chalcopyrite-type samples that are used for electrical transport studies. This has not been performed regularly throughout the investigation of chalcopyrite thermoelectrics shown in the literature.

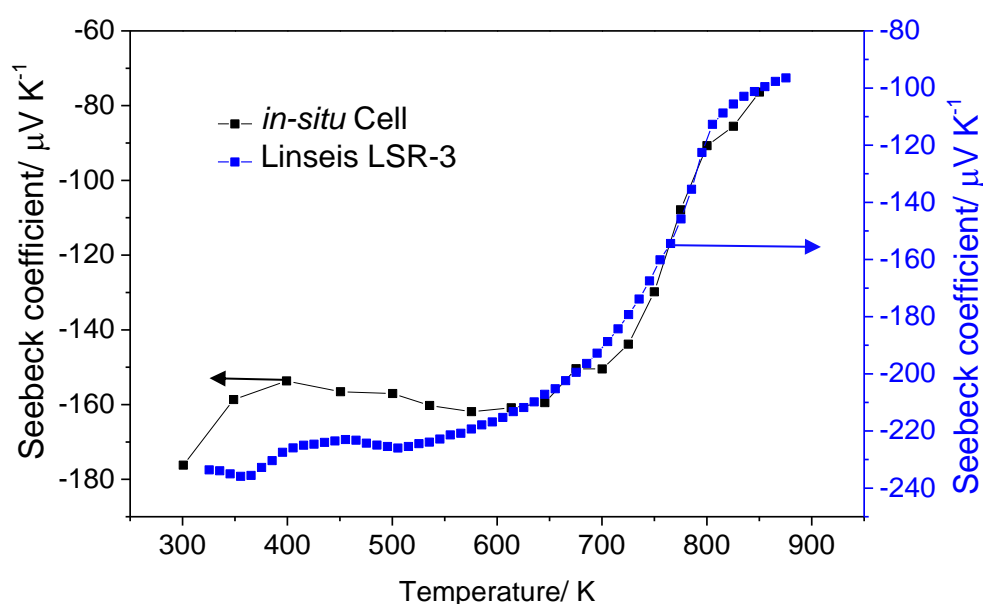


**Figure 3-18** – Seebeck coefficients for two samples with nominal composition  $\text{CuFeS}_2$  synthesised using the same method. Black points – data collected on the *in-situ* cell during diffraction experiments; Blue points – data collected using the LSR-3.

### 3.7. Mooihoekite and Talnakhite Experiments

#### 3.7.1. Experimental Procedure

Two synthetic processes were followed during the attempted syntheses of single-phase talnakhite and mooihoekite. These phases are suggested as having nominal elemental compositions of  $\text{Cu}_9\text{Fe}_9\text{S}_{16}$  and  $\text{Cu}_{18}\text{Fe}_{16}\text{S}_{32}$ , respectively.<sup>147,148</sup> In the preparation of each, stoichiometric amounts of elemental powders of copper (99.5%, Sigma Aldrich), iron (99.9+%, Sigma Aldrich) and sulphur (flakes, 99.99%, Sigma Aldrich) were mixed together in an agate pestle and mortar then sealed into fused silica ampoules at *ca.*  $10^{-4}$

mBar. The powdered samples were subject to two consecutive firings with a grinding and re-sealing step between each firing. Each of the sintering steps followed the same temperature conditions.

The temperature programs followed were: Method A; heating to 825 K at 2 K min<sup>-1</sup> holding at temperature for 144 hours, then cooling at a natural cooling rate. Method B; heating to 768 K at 3 K min<sup>-1</sup> and holding at temperature for 48 hours, then decreasing the temperature to 463 K at 0.3 K min<sup>-1</sup> and holding at temperature for 4 hours before cooling to room temperature at a natural cooling rate. The samples were then consolidated by hot pressing at 723 K and 60 MPa for 30 minutes.

Room-temperature X-ray diffraction data were recorded on powdered samples for each of the four samples synthesised before and after hot pressing and phase analysis was performed using the EVA software package. Room-temperature neutron diffraction data were collected on all hot-pressed samples and on the sample with composition Cu<sub>9</sub>Fe<sub>9</sub>S<sub>16</sub> synthesised with method A before hot-pressing. The room-temperature neutron diffraction data were collected on powdered samples loaded into vanadium cans and using the POLARIS diffractometer.

**Table 3-7** – Primary phases present in each of the samples as determined from phase analysis using EVA software, † indicates samples taken for room-temperature neutron diffraction experiments, ‡ indicates samples taken for variable temperature neutron diffraction experiments in the *in-situ* cell.

Phases achieved		Experimental composition	
		Cu <sub>9</sub> Fe <sub>8</sub> S <sub>16</sub>	Cu <sub>9</sub> Fe <sub>9</sub> S <sub>16</sub>
before hot - pressing	Method A	Chalcopyrite	Mooihoekite†
	Method B	Chalcopyrite	Talnakhite
Phases achieved after hot- pressing	Method A	Chalcopyrite†	Talnakhite‡
	Method B	Chalcopyrite‡	Talnakhite†

The variable-temperature neutron diffraction and electrical data were collected for pellets using the *in-situ* cell for the chalcopyrite phase with composition Cu<sub>9</sub>Fe<sub>8</sub>S<sub>16</sub> (Method B) and talnakhite sample with composition Cu<sub>9</sub>Fe<sub>9</sub>S<sub>16</sub> (Method A). Data were recorded over the temperature range  $T = 300 - 700$  K with temperature increments of between 15 – 50 K. The smallest steps were used over the temperature range of the expected phase transition

temperature. Rietveld analysis of all diffraction data was performed using the GSAS software package.

### 3.7.2. Room Temperature Structure of Cu-Fe-S Samples

Samples with three different structure-types have resulted from the synthesis methods followed here. Namely: tetragonal chalcopyrite ( $a \times a \times a$ ); tetragonal mooihoekite ( $2a \times 2a \times a$ ) and cubic talnakhite ( $2a \times 2a \times 2a$ ). Powder X-ray diffraction data collected on samples with each of these structure types (excluding cubic chalcopyrite) are presented in Figure 3-19. Positions of the reflections are similar for each structure type, the effects of tetragonal splitting and peak intensity distribution leads to slightly different diffraction patterns for each structure type. The peaks at *ca.*  $2\theta = 49^\circ$  and  $2\theta = 58^\circ$  (see arrows in Figure 3-19) demonstrate the difference in diffraction patterns of different samples.

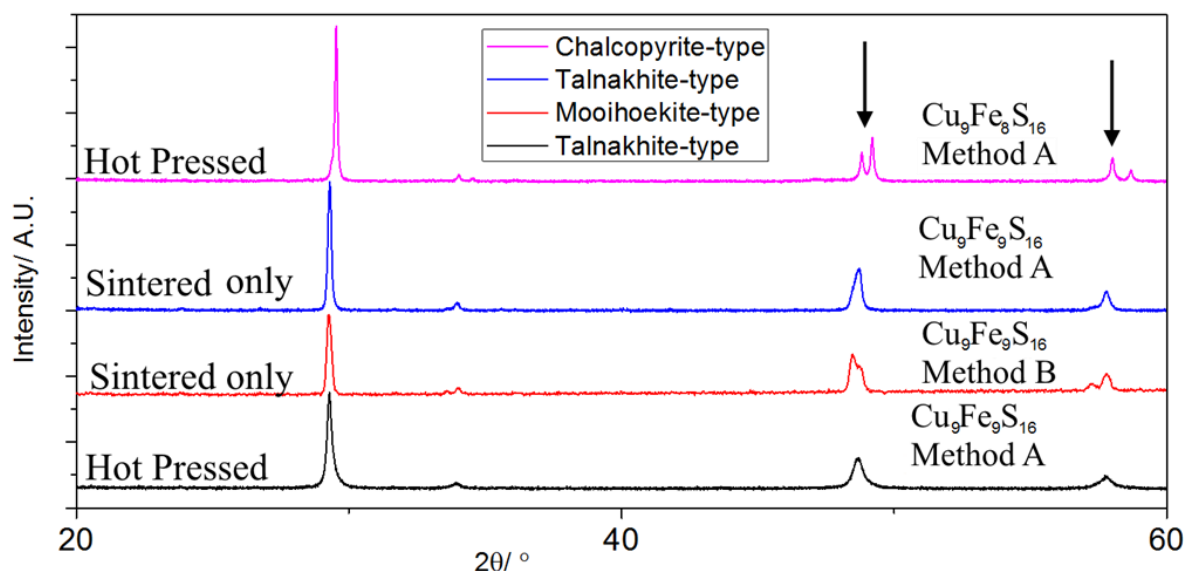


**Figure 3-19** - X-Ray diffraction patterns of samples synthesised to demonstrate the different diffraction patterns of: pink line - chalcopyrite type phases; black and blue line - talnakhite-type phases; and red line - mooihoekite-type phases. Arrows show the peaks with tetragonal splitting.

The synthesis method A and a nominal composition  $\text{Cu}_9\text{Fe}_9\text{S}_{16}$  allows for a talnakhite type-phase to be achieved after sintering (Figure 3-19). Rietveld analysis of the neutron diffraction data collected on this sample revealed that it was mixed phase with a majority phase of mooihoekite in the presence of a minority phase of talnakhite. The weight fractions for these phases were  $\text{wt}\% = 71.41(23)$  and  $28.59(23)$ , respectively. Interestingly, the X-ray diffraction pattern of this sample after hot-pressing revealed a change in

structure. The observed reflections after hot-pressing correspond to the talnakhite type structure with the space group  $I\bar{4}3m$  (Figure 3-20).

The room-temperature powder neutron diffraction pattern recorded for the hot-pressed samples with nominal compositions  $\text{Cu}_9\text{Fe}_9\text{S}_{16}$ , method A and B, showed reflections corresponding to the talnakhite type structure only. Rietveld analysis of the diffraction data for the sample synthesised with method A showed that using a single phase of talnakhite was sufficient to model each of the reflections corresponding to the nuclear structural phase (Figure 3-21). Magnetic reflections were excluded from the structural refinement. Consolidation of these samples through high-temperature high-pressure techniques appears to induce an irreversible structural phase transition to the  $2a \times 2a \times 2a$  superstructure, consistent with observations by Athar *et al.*<sup>152</sup>

The room-temperature powder neutron diffraction data for the samples with nominal composition  $\text{Cu}_9\text{Fe}_8\text{S}_{16}$  could be indexed on the basis of the  $I\bar{4}2d$  space group that is used to describe chalcopyrite structure (Figure 3-19). Additional reflections corresponding to the magnetic structure are observed in the neutron diffraction pattern, consistent with the magnetic reflections expected for chalcopyrite.<sup>106</sup> This phase was formed after the first sintering step and persisted after hot pressing (Figure 3-22).

### ***3.7.3. Magnetic Diffraction of the Different Structural Phases***

A significant observation made from this structural study of chalcopyrite and its related phases is the presence of magnetic diffraction reflections for each of the samples. There is a difference in the magnetic behaviour of samples with different structure types. The samples with nominal composition  $\text{Cu}_9\text{Fe}_8\text{S}_{16}$  exhibit the chalcopyrite structure type and show the magnetic reflections corresponding to the antiferromagnetic structure of chalcopyrite (appendix D).<sup>106</sup> The samples with nominal composition  $\text{Cu}_9\text{Fe}_9\text{S}_{16}$  with the talnakhite and mooihoekite structure types express markedly different magnetic diffraction patterns compared to that of the chalcopyrite phase (appendix D). The magnetic diffraction patterns of the mooihoekite and talnakhite structure types are more similar to one another than to the chalcopyrite type sample. The two nuclear structure types are closely related and they may exhibit a similar magnetic structure. The finer details of the structural and magnetic behaviour of these materials will not form part of the discussion in this thesis.

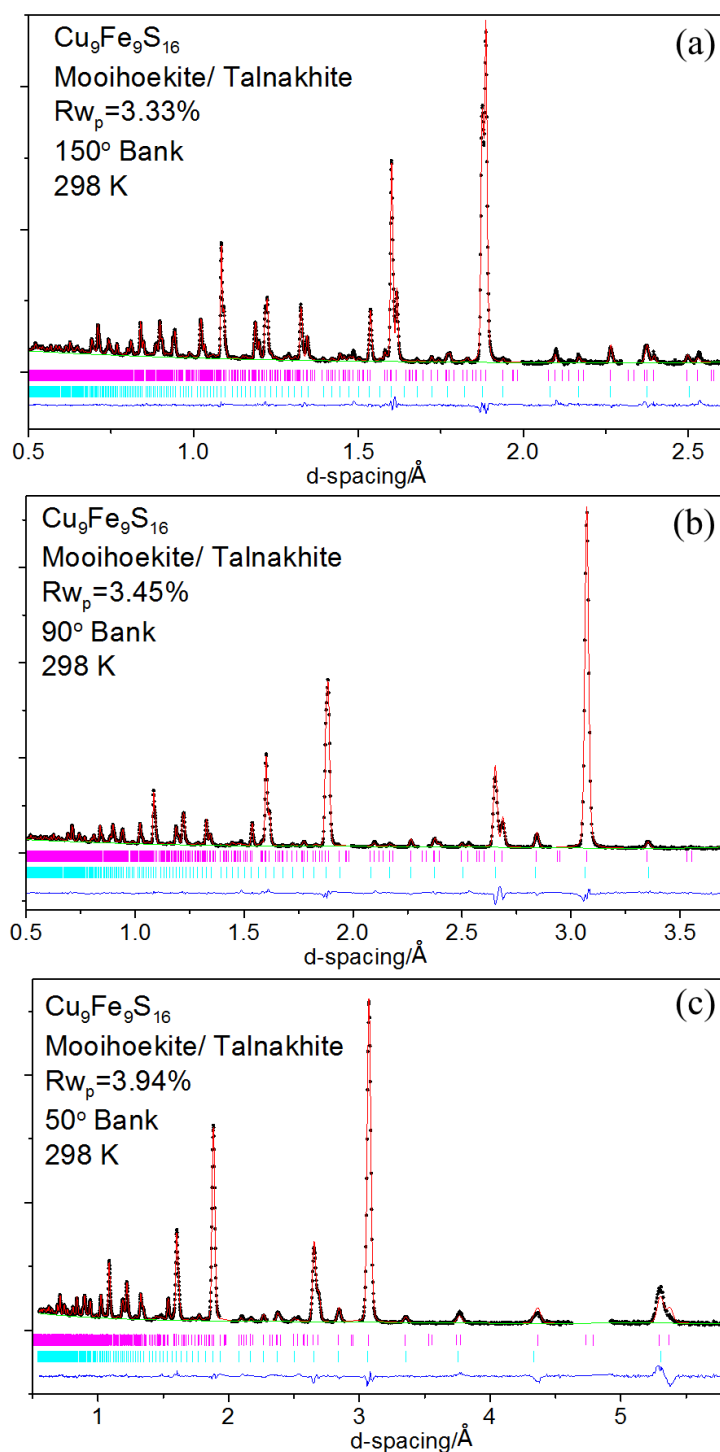


**Figure 3-20** – Rietveld refinement profiles for neutron diffraction data collected at room temperature for a sample with a nominal composition  $\text{Cu}_9\text{Fe}_9\text{S}_{16}$  which was sintered only and synthesised using method A. (a), (b) and (c) are the data from 150°, 90° and 50° degree banks (5, 4 and 3), respectively. Black points – observed; Red line – calculated; Blue line – difference profile; pink markers - Mooihoekite phase and blue markers – talnakhite phase  $\bar{I}43m$ . Magnetic reflections have been omitted (Appendix E – tabulated parameters).

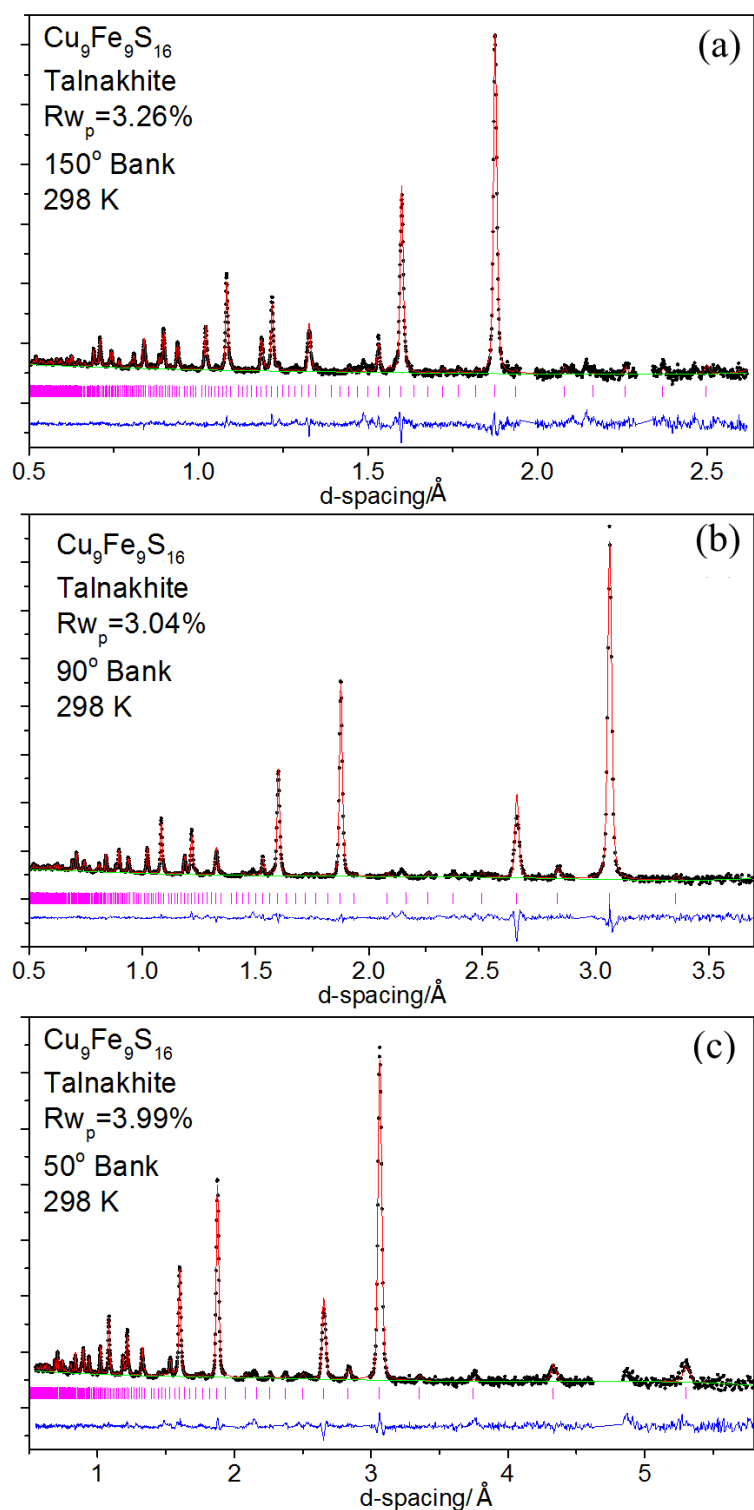


**Figure 3-21** – Full Rietveld profiles for the neutron diffraction data and the nuclear structure of a sample with nominal composition  $\text{Cu}_9\text{Fe}_9\text{S}_{16}$ , synthesised with method A and hot-pressed. (a), (b) and (c) are the data from 150°, 90° and 50° degree banks (5, 4 and 3), respectively. Black points – observed; Red line – calculated; Blue line – difference profile; pink lines -  $I\bar{4}3m$  phase of talnakhite. Magnetic reflections have been excluded from the data set (Appendix F – tabulated parameters).

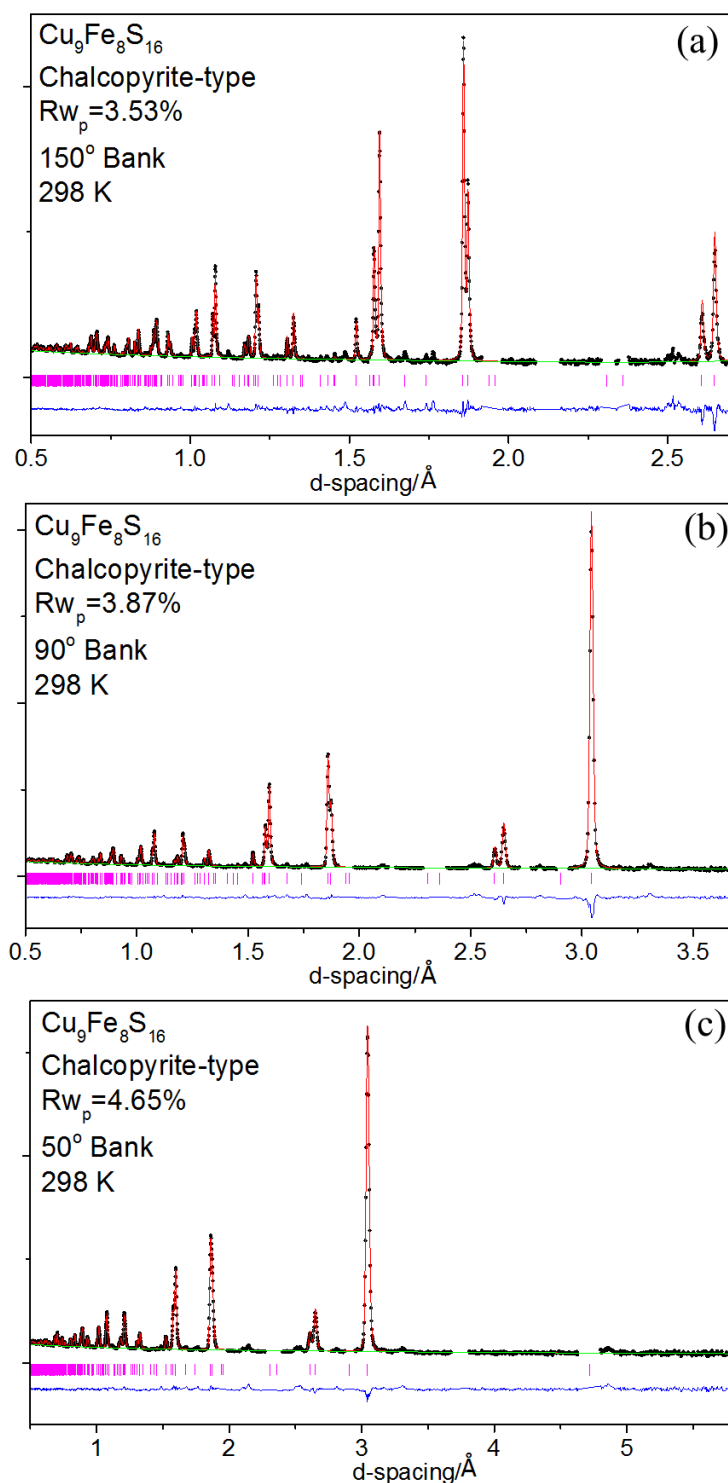


**Figure 3-22** – Rietveld profiles for the neutron diffraction data and nuclear structure of a sample with nominal composition  $\text{Cu}_9\text{Fe}_8\text{S}_{16}$  as synthesised with method B and hot-pressed; (a), (b) and (c) correspond to the diffraction data collected on the 150°, 90° and 50° degree banks (5, 4 and 3), respectively. Black points – observed; red line – calculated; blue line – difference profile; pink lines -  $\bar{1}\bar{4}2d$  phase of Chalcopyrite. Magnetic reflections have been omitted (tabulated data found in e-appendix, chapter 3 folder).

### 3.8. Variable Temperature Neutron Diffraction of Chalcopyrite, $\text{Cu}_9\text{Fe}_8\text{S}_{16}$

The Le Bail method was used to model the nuclear and magnetic diffraction intensity for powder neutron diffraction data collected at each temperature. For samples with composition  $\text{Cu}_9\text{Fe}_8\text{S}_{16}$ , the nuclear reflections observed at each temperature were indexed using the  $\bar{I}42d$  space group, consistent with the nuclear structure of chalcopyrite. The reflections corresponding to the boron-nitride enclosure have been omitted from each diffraction pattern.

Across the temperature range  $T = 300 - 450$  K, a refinement of the lattice parameters and peak profiles for the nuclear and magnetic phase provided a good fit to the reflections corresponding to the nuclear and magnetic structures. However, at temperatures  $T > 450$  K the space group  $\bar{I}42d$  with lattice parameters  $a \times a \times 2a$  does not provide a good fit to the magnetic reflections at low  $d$ -spacings. Thus, some of the magnetic reflections in the  $150^\circ$  bank have been omitted, e.g.  $d = 1.95$  and  $1.67$  Å, to allow for the lattice parameters of the nuclear structure to be determined from this Le Bail analysis (Figure 3-24). The lattice parameters of the copper-rich chalcopyrite phase increase almost linearly with increasing temperature across the entire temperature range  $T = 298 - 575$  K (Figure 3-23). This is consistent with the expected behaviour of chalcopyrite with increasing temperature.<sup>106</sup> The presence of the  $\bar{I}42d$  phase across the entire temperature range would indicate that there is not a structural phase transition in the nuclear phase of the sample, which is surprising when we consider that there is a marked exotherm at  $T \approx 450$  K in the DSC data collected on samples from a different synthesis batch (Figure 3-23).

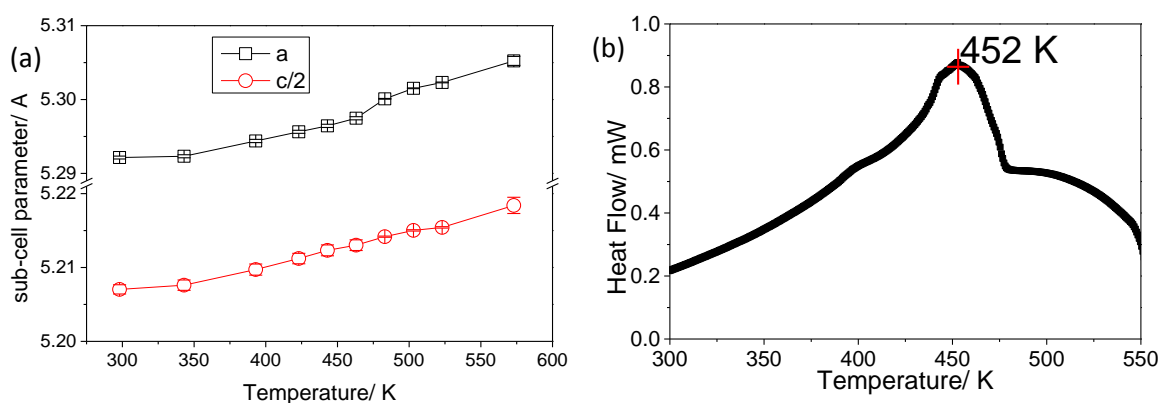


**Figure 3-23** –(a) Temperature dependence of the lattice parameters for the sample with nominal composition,  $\text{Cu}_9\text{Fe}_8\text{S}_{16}$ , ESD's are within points. (b) Temperature-dependent DSC data for the sample with nominal composition  $\text{Cu}_9\text{Fe}_8\text{S}_{16}$  and the chalcopyrite type structure at room temperature.

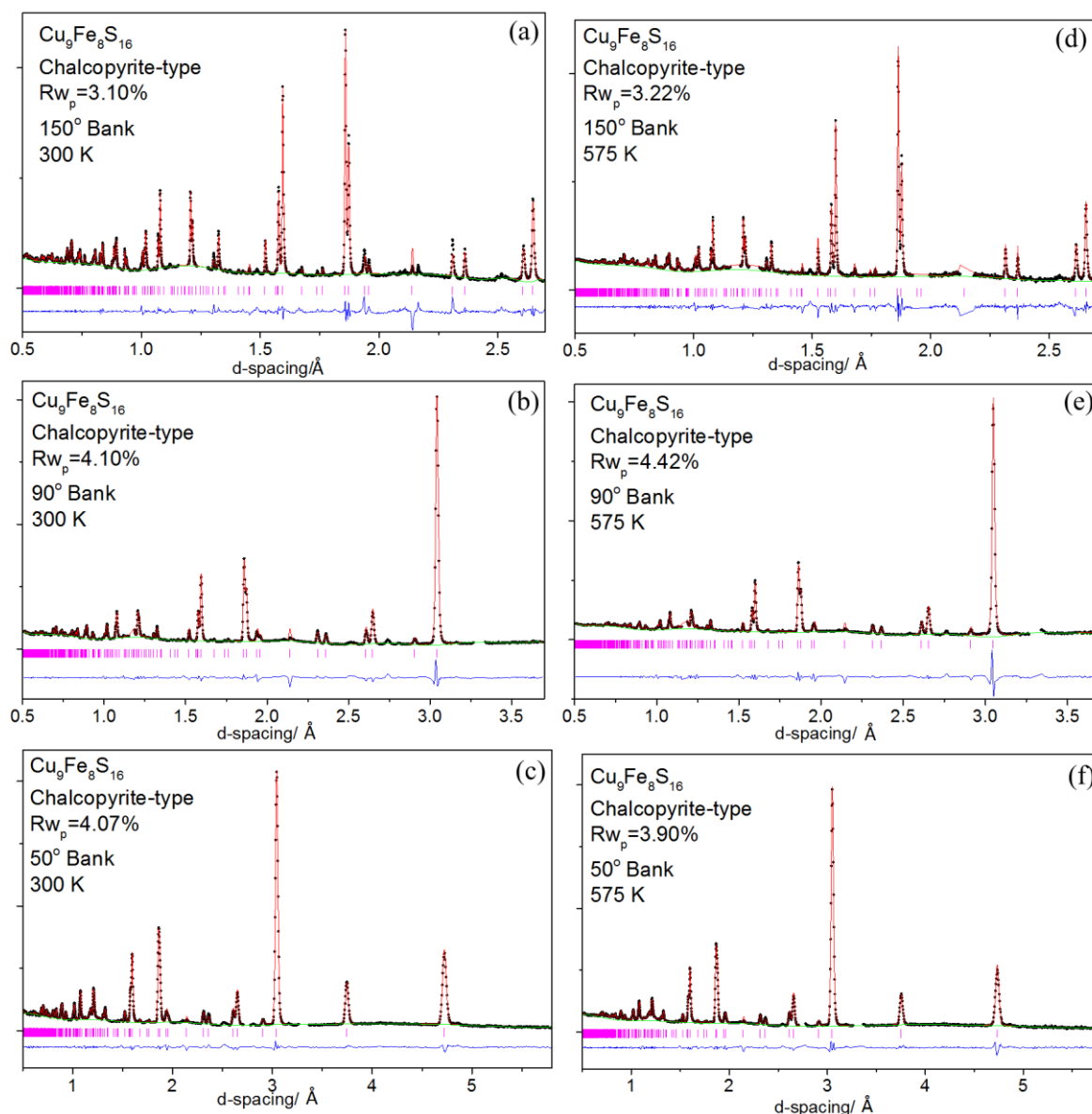


**Figure 3-24** – Le Bail refinement profiles for neutron diffraction data and the sample with composition  $\text{Cu}_9\text{Fe}_8\text{S}_{16}$  using the magnetic and nuclear structure of the chalcopyrite phase  $\bar{I}4_2d$ . (a), (b) and (c) correspond to the diffraction data collected at ca. 300 K for the 150°, 90° and 50° degree banks (5, 4 and 3), respectively. (d), (e) and (f) correspond to the diffraction data collected at ca. 575 K. Black points – observed, Red line – calculated, Blue line – difference profile, green line – background, pink lines – reflection of the  $\bar{I}4_2d$  phase of chalcopyrite.

However, there is evidence of a phase transition within the diffraction data. Figure 3-25 shows a selected  $d$ -spacing range from the Rietveld analysis of the copper-rich chalcopyrite phase. The absence of calculated intensity for the peaks at  $d = 1.94$  and  $1.96$  Å reveals that these reflections are likely to be magnetic in nature (Figure 3-25(a)). The

change in the diffraction intensity with increasing temperature is shown in Figure 3-25(b) for this set of reflections. The nuclear reflections do not show any significant changes with increasing temperature. Meanwhile, the reflections that are suspected to arise as a result of magnetic scattering appear to show a marked temperature dependence by means of an anomaly at  $T \approx 450$  K. This is consistent with the expected transition temperature determined from the DSC data. Therefore, these data reveal evidence of a magnetic transition between  $T = 445 - 485$  K. The magnetic reflections show a 2:1 ratio at lower temperature, similar to the nuclear phase, at the transition temperature they coalesce into a single reflection. This behaviour may indicate that the transition is a tetragonal-to-cubic transition as this would eliminate the tetragonal splitting seen in the low-temperature phase. The origins of this magnetic transition have not been identified here, however it is important to acknowledge this change in the behaviour of the material. Furthermore, the diffraction data collected here provide the first structural observation for a magnetic phase transition at this temperature in a chalcopyrite-like phase.

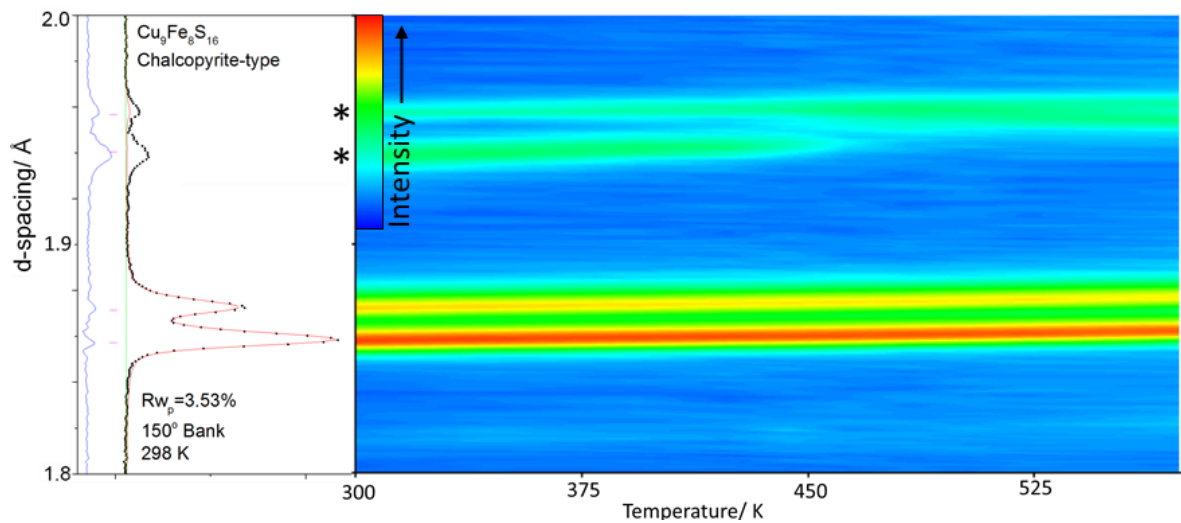


**Figure 3-25** – Neutron diffraction data for the sample with nominal composition  $\text{Cu}_9\text{Fe}_9\text{S}_{16}$  collected on the  $150^\circ$  bank of POLARIS and over the selected range  $1.8 < d/\text{\AA} < 2.0$ . Showing the Rietveld profile for the refinement of the nuclear structure at 298 K: Black points – observed, Red line – calculated, pink markers -  $I\bar{4}2d$  phase of Chalcopyrite; and the variable temperature diffraction highlighting the change in reflections over the temperature range  $T = 300 - 575$  K. The asterisk indicates magnetic reflections.

### 3.8.1. Temperature-Dependent Electrical Transport Properties of Chalcopyrite, $\text{Cu}_9\text{Fe}_8\text{S}_{16}$

The electrical resistivity (Figure 3-26(b)) and Seebeck coefficient (Figure 3-26(a)) data were recorded for the copper-rich chalcopyrite sample with nominal composition  $\text{Cu}_9\text{Fe}_8\text{S}_{16}$  using the *in-situ* cell and simultaneously with the collection of the powder neutron diffraction data that is presented above. The electrical resistivity decreases with increasing temperature across the temperature range  $T = 293 - 400$  K, consistent with semi-conducting behaviour. As the transition temperature is approached, the resistivity begins to increase with increasing temperature reaching a maximum at 483 K, after which it begins to decrease. The anomaly in the resistivity across the temperature range  $T = 400 - 500$  K can be linked to the proposed magnetic transition observed for this copper rich chalcopyrite phase (Figure 3-26).

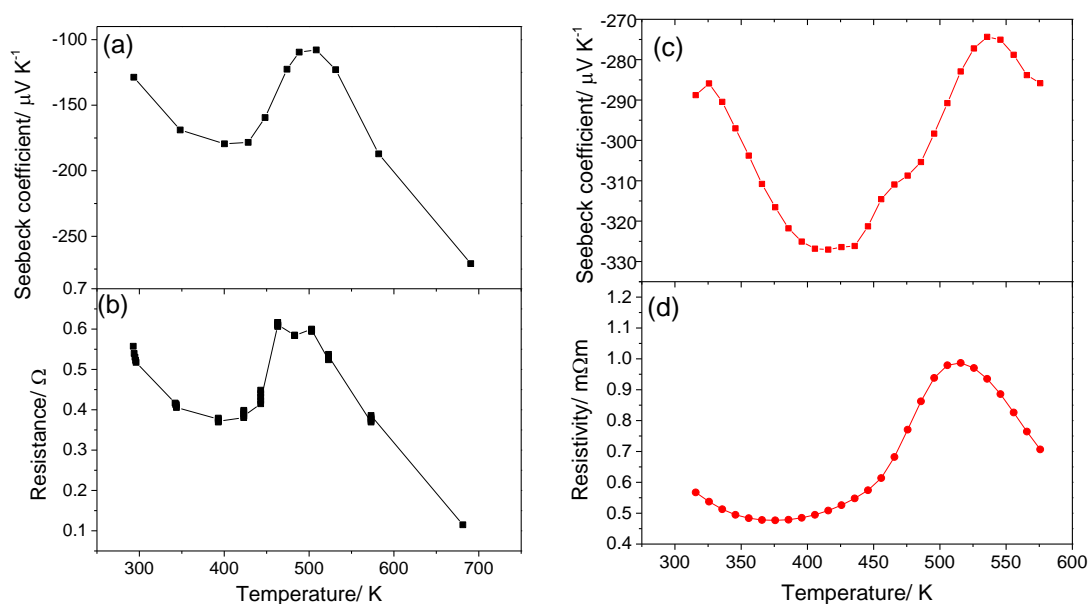


**Figure 3-26** – Temperature dependence of electrical transport properties of the sample with composition  $\text{Cu}_9\text{Fe}_8\text{S}_{16}$  recorded over the temperature range  $T = 300 - 700$  K, (a, b) using the *in-situ* cell, (c, d) using the LSR-3.

The Seebeck coefficient data show a similar behaviour as a function of temperature, where the  $S$  increases with increasing temperature with a marked anomaly across the temperature range  $T = 400 - 500$  K, consistent with the observed anomaly in the electrical resistivity data and the changes in the structural behaviour of the material (Figure 3-26). The electrical data were also collected using a Linseis LSR-3 (Figure 3-26(c, d)) and a sample

from a different synthesis batch. These data show that the electrical transport properties exhibit the same temperature dependence between the two instruments, again demonstrating the reliability of the electrical data collected from the *in-situ* cell and also revealing a local maximum in the power-factor (appendix G).

### ***3.9. Observations from the Variable Temperature Diffraction Experiment on Talnakhite, Cu<sub>9</sub>Fe<sub>9</sub>S<sub>16</sub>***

The Rietveld analysis of the room temperature powder neutron diffraction data showed that the samples with nominal composition, Cu<sub>9</sub>Fe<sub>9</sub>S<sub>16</sub>, can be indexed on the basis of a single phase of talnakhite, with space group  $I\bar{4}3m$ . For the neutron diffraction data collected at 693 K on the same sample using the *in-situ* cell, mixed-phase behaviour is observed. The high-temperature diffraction data collected here can be indexed on the basis of a cubic  $a \times a \times a$  phase with the space group  $F\bar{4}3m$  and a tetragonal phase with chalcopyrite-like structure,  $I\bar{4}2d$ . This suggests that the talnakhite phase transforms into the *iss* phase and a chalcopyrite-like phase, present in *wt%* = 7.87(5) and 22.13(4), respectively, thus showing a significant change in structural behaviour compared to the room-temperature structure. The cubic/pseudo cubic sub-cell parameters of these two phases are  $a=5.3406(5)$  Å for the cubic phase and  $a_p=5.3155(3)$  and  $5.2307(7)$  Å for the tetragonal phase at 693 K. The cubic phase has larger lattice parameters, similar to the behaviour observed in the mixed phase chalcopyrite with nominal composition CuFeS<sub>2</sub> presented earlier.

The variable temperature diffraction data recorded for this sample with nominal composition, Cu<sub>9</sub>Fe<sub>9</sub>S<sub>16</sub>, reveals a dynamic phase transformation behaviour and the formation of this intermediate solid-state phase outlined by Cabri *et al.*<sup>146</sup> The DSC data revealed an exotherm at  $T = 473$  K suggesting a first-order phase-transition (Figure 3-29(d)). At the expected phase transition temperature,  $T = 495$  K, there is a marked change in the neutron diffraction pattern. Most notably, the supercell reflections corresponding to the  $2a \times 2a \times 2a$  unit cell, observed at *ca.*  $d = 4.4$  and  $5.45$  Å, are absent above  $T = 496$  K. This suggests that the talnakhite type phase is subject to a structural phase transition into what appears to be a tetragonal chalcopyrite-type and the cubic *iss* phase. The details of the phase fractions are not investigated here in depth as a Le Bail analysis would not provide this information. However, at temperatures above the phase, transition the intensity of Bragg reflections corresponding to the tetragonal and cubic phases show a significant temperature dependence. The intensities of the reflections

corresponding to the tetragonal phase decrease with increasing temperature, meanwhile the intensities of reflections corresponding to the *iss* cubic phase increase. From this observation along with the observation for the mixed-phase chalcopyrite in section 3.6.3, it is expected that the weight fraction of the cubic phase increases with increasing temperature.

The powder neutron diffraction data collected over  $T = 300 - 495$  K show the emergence of new reflections with increasing temperature. Whilst the room temperature diffraction pattern can be characterised on the basis of the  $I\bar{4}3m$   $2a \times 2a \times 2a$  supercell only, Le Bail refinements with the same unit cell and using a single phase provide a poor fit to the diffraction data at 393 K owing to the appearance of the additional reflections. Le Bail analysis using possible tetragonal phases has ruled out the possibility of a tetragonal distortion of the unit cell. The emerging secondary phase across the temperature range,  $T = 300 - 495$  K, is suspected to be a tetragonal chalcopyrite-type phase. This is supported by the observations of a tetragonal chalcopyrite-type phase at high temperature, and that the phase transition at  $T = 495$  K occurs in the talnakhite  $2a \times 2a \times 2a$  phase, which is clearly shown by the disappearance of the supercell reflections (Figure 3-27).

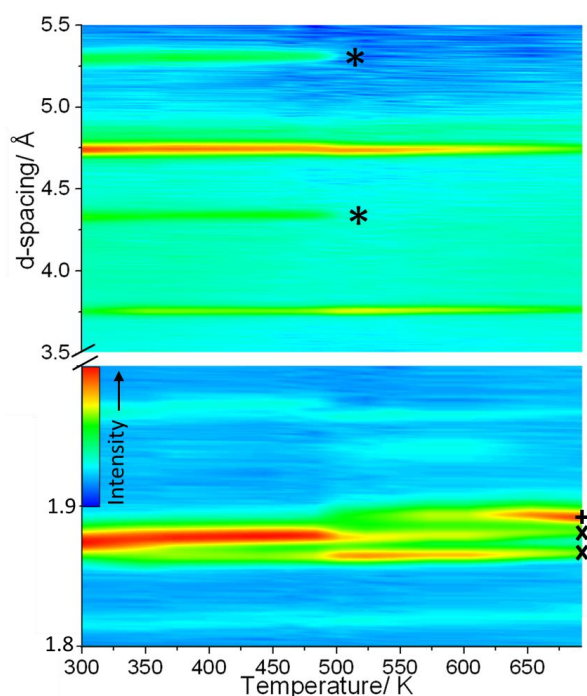


**Figure 3-27** - Neutron diffraction data collected on the  $150^\circ$  bank 5 on POLARIS over the selected range  $1.8 < d/\text{\AA} < 2.0$  showing the change in reflections as a function of temperature over the temperature range  $T = 300 - 575$  K. \*, + and  $\times$  correspond to the  $2a$  supercell, *iss* cubic and chalcopyrite reflections, respectively.

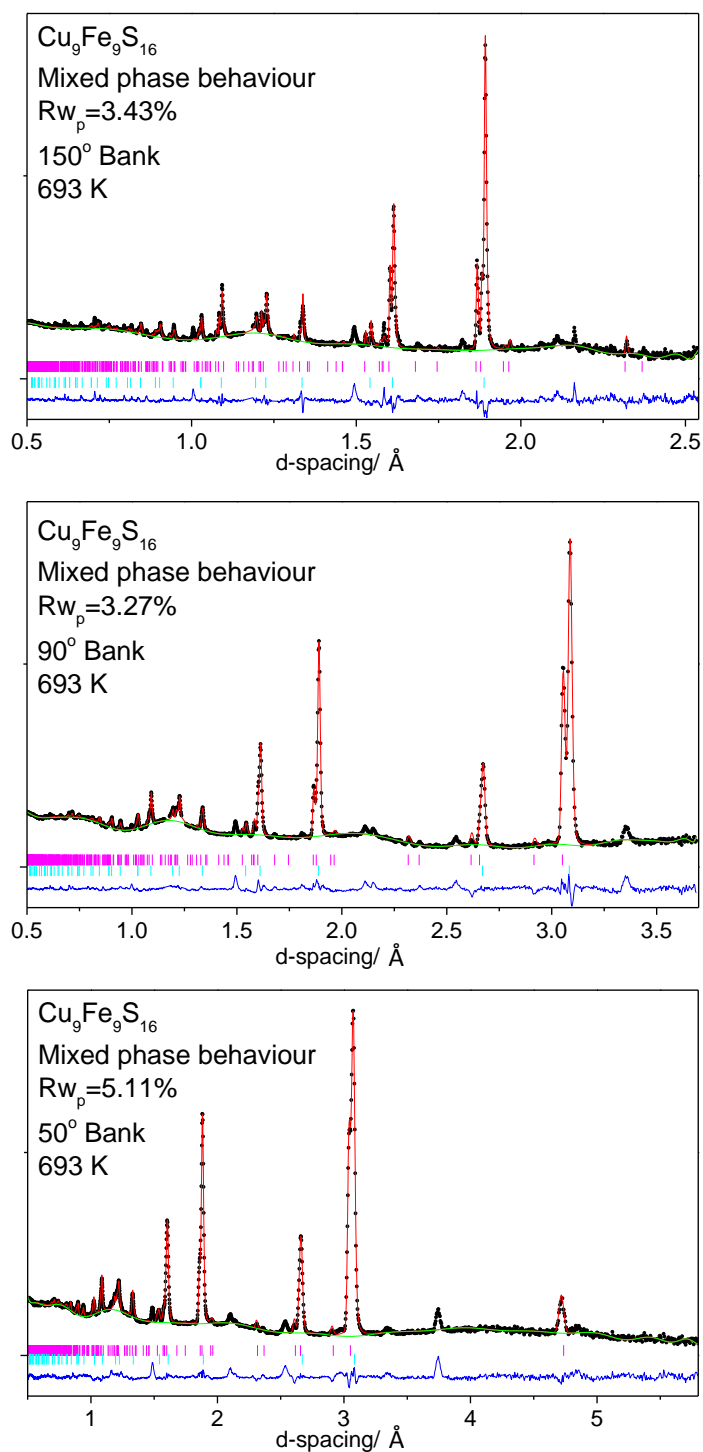


**Figure 3-28** –Rietveld refinement profiles for the sample with composition  $\text{Cu}_9\text{Fe}_9\text{S}_{16}$ . (a),(b) and (c) correspond to the diffraction data collected at ca. 693 K for the 150°, 90° and 50° degree banks (5, 4 and 3), respectively. Black points – observed; Red line – calculated; Blue line – difference profile; green line – background; pink markers – reflections of the  $\bar{I}4_2d$  tetragonal chalcopyrite-like phase; blue markers - reflections for the  $F\bar{4}3m$  cubic chalcopyrite-like phase (Appendix F – tabulated parameters).

### 3.9.1. Temperature Dependence of the Electrical Properties of Talnakhite, $\text{Cu}_9\text{Fe}_9\text{S}_{16}$

The electrical resistivity and Seebeck coefficient data were recorded on the sample with nominal composition  $\text{Cu}_9\text{Fe}_9\text{S}_{16}$  simultaneously with the neutron diffraction data using the *in-situ* cell. The recorded electrical resistance decreases exponentially with increasing temperature. Plotting the electrical resistivity on a log scale shows two linear regions. At low temperature, Arrhenius behaviour is observed between  $T = 290 - 440$  K with an activation energy of  $E_a = 0.138(4)$  eV and at high temperatures, Arrhenius behaviour is observed at  $T = 580 - 700$  K with  $E_a = 0.180(7)$  eV (appendix H). In a 4-probe system the affect of the phase transition on the electrical band-gap could be postulated from this observed change in  $E_a$ . However, in this instance there is a significant contribution to the resistivity arising from the surface-electrode interface. The inset in Figure 3-29(b) shows a speculative representation of the resistivity with this contribution subtracted. Importantly, the curve of  $\rho(T)$  reveals the anomalies in the electrical resistivity that occur as a result of the structural phase transition.

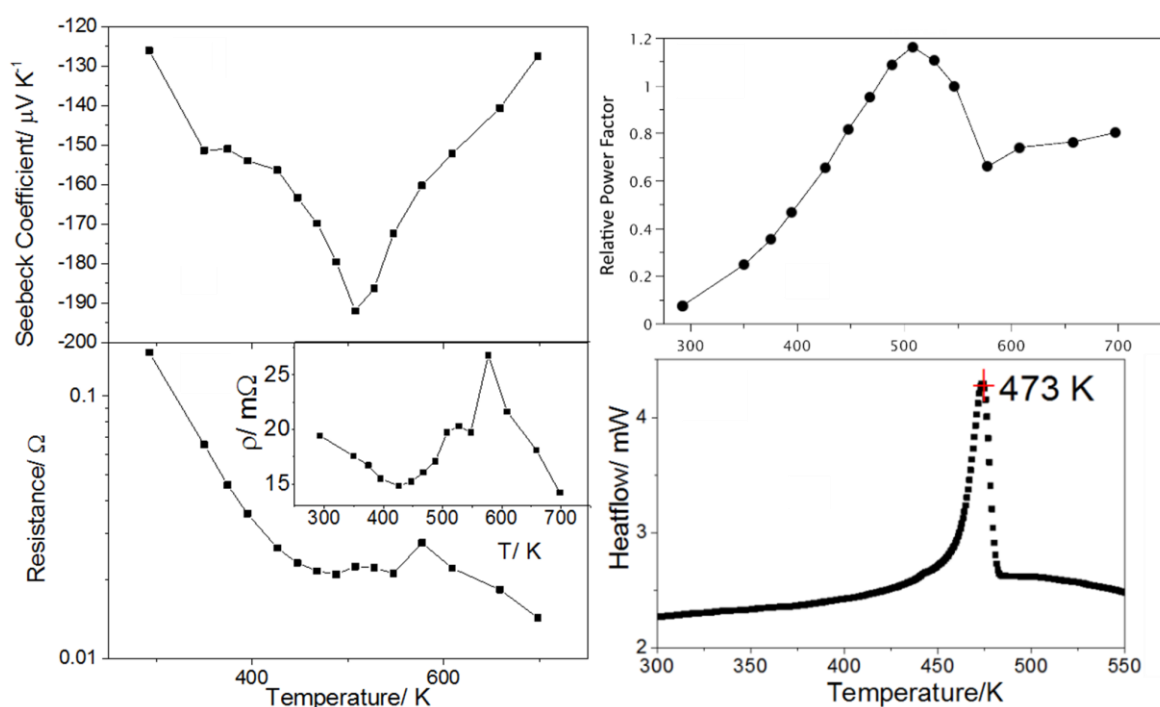


**Figure 3-29** –Electrical data recorded using the *in-situ* cell for the sample with nominal composition  $\text{Cu}_9\text{Fe}_9\text{S}_{16}$ . (a) the Seebeck coefficient and (b) electrical resistance, inset show the electrical data with an exponential subtracted to highlight the effect of the structural phase transition (c) relative power factor. (d) DSC data.

The behaviour across this temperature region is consistent with the structural phase transition observed in the neutron diffraction data. Notably there is a significant jump in the electrical resistivity at 578 K (Figure 3-29(a,b)). Electrical transport data recorded using the Linseis LSR-3 on a sample from the same synthesis batch also exhibits this marked increase in the electrical resistivity (appendix H.). This electrical transition is observed at slightly different temperatures in the two experiments. The heating profile followed during each of the experiments are remarkably different, therefore the difference in electrical behaviour with temperature may be influenced by the kinetics of the structural transition.

The Seebeck coefficient data recorded using the *in-situ* cell reveals a maximum of *ca.*  $S = -190 \mu\text{V K}^{-1}$  at 510 K, just above the transition temperature of the talnakhite phase. The anomalies in the electrical behaviour around the phase-transition temperature leads to a peak in the relative power factor at  $T = 510$  K. A maximum in the Seebeck coefficient and the power factor is also observed in the variable temperature data recorded on the Linseis LSR-3 (appendix H.), the peak in these properties are observed at *ca.*  $T = 480$  K so there is some discrepancy between the observed peak performance temperature. This is driven by a marked increase in  $\rho(T)$  at  $T = 510$  K and  $T = 480$  K for the data from the *in-situ* cell and LSR-3, respectively. The sample measured using the LSR-3 shows a single anomaly in  $\rho(T)$  whereas the corresponding data from the *in-situ* cell shows a comparatively small increase in  $\rho(T)$  at  $T > 420$  K then a large increase at  $T = 510$  K. The lower temperature anomaly is attributed to the transition of the talnakhite-type phase to the mixed *iss*-chalcopyrite phase. Meanwhile, the second anomaly at  $T > 575$  K occurs as the reflections corresponding to the *iss* phase show a marked increase in diffraction intensity. The difference in electrical behaviour between the two experiments is likely to arise from a difference in the interplay between the two structural phases. The experimental conditions are substantially different, it is suspected that this results in a difference in the kinetics of the phase transitions and the mixed-phase behaviour. This observation highlights the importance of measuring the structure and properties simultaneously.

### **3.10. Conclusions**

A cell for the simultaneous measurement of the Seebeck coefficient, electrical resistance and neutron diffraction data has been successfully developed. The instrument allows for the collection of high-quality neutron diffraction data that is suitable for Rietveld analysis of solid-state samples. Furthermore, the collection time required for excellent quality

diffraction data is of the order of 1-3 hours of beam exposure per temperature point using the POLARIS diffractometer. The collection time for samples in variable temperature diffraction-only experiments on POLARIS is usually of the same time scale. The electrical data are collected over *ca.* 30 minutes and this can be included as part of the collection time for the diffraction data at a single temperature point. This, along with the data presented above, highlights the benefit of combining the two techniques into a single experiment. The *in-situ* cell provides an excellent opportunity for the structural study of any thermoelectric material which exhibits structural phase transformations as a function of temperature. Any variable temperature diffraction experiment on such materials at the POLARIS diffractometer would benefit from the novel insight that this cell can offer.

The *in-situ* device was designed so that it could be re-used multiple times. Electrical and diffraction data collected using this cell and the POLARIS diffractometer have been presented above for many samples which demonstrates that this goal has been achieved. The samples can be retrieved from the device intact, but this has come at the cost of providing relative values for the electrical properties rather than the absolute values for the electrical resistivity and Seebeck coefficient in some instances. However, the purpose of this device was to monitor the electrical transitions along with the structural transitions. The data presented within this chapter have certainly outlined that the cell is capable of doing so.

The experiment on the CZGSe sample showed that the diffraction data collected over 1 hour are sufficient to determine the site occupancy factors of elements with similar atomic numbers within mixed transition-metal semiconductors. An electrical transition is observed over the temperature range  $T = 400 - 475$  K and although there is not a marked change in the diffraction data, the Rietveld analysis reveals a structural transition between  $T = 400 - 425$  K (Figure 3-30). Half of the copper atoms and all of the zinc cations are partially ordered over the  $2a$  and  $2b$  sites at lower temperatures. An order-disorder transition results in the copper and zinc becoming fully disordered over these sites at high temperatures.

The diffraction-Seebeck experiment on the sample with nominal composition  $\text{CuFeS}_2$  allowed for the study of a mixed crystalline system (Figure 3-31). The Rietveld analysis revealed evidence of a structural phase transition in the talnakhite-type phase from a  $2a \times 2a \times 2a$  structure to an intermediate solid-state cubic phase at  $T = 450 - 500$  K. This is followed by a dynamic change in the concentration of chalcopyrite and intermediate solid-state cubic phases for the solid-state mixture.

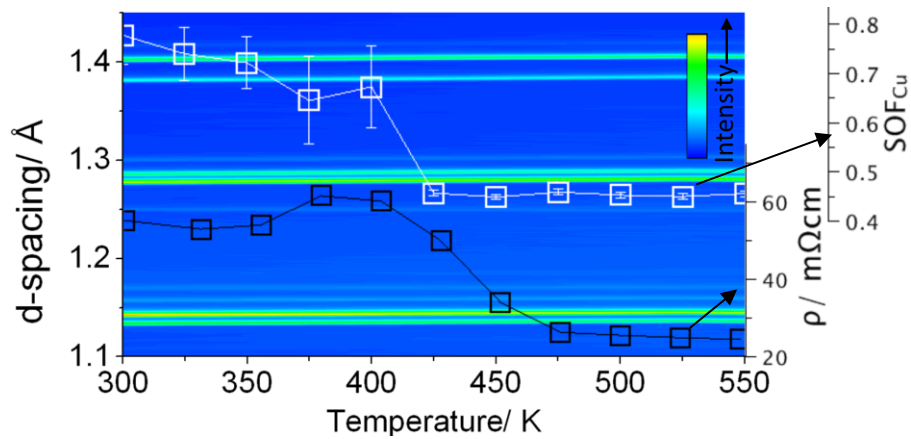


**Figure 3-30** – Overlaid data and extracted parameters for  $\text{Cu}_{2.125}\text{Ge}_{0.875}\text{ZnSe}_4$  showing the temperature dependence of: white – Site occupancy factor of Cu at the 2a site; Black – electrical resistivity; and coloured background – diffraction intensity.

The tetragonal chalcopyrite type phase completes transformation to the cubic chalcopyrite phase between  $T = 775 - 800$  K. The decreasing Seebeck coefficient with increasing temperature can be attributed to the evolution of this intermediate solid-state cubic phase. Advanced techniques for developing and improving thermoelectric materials includes nano-structuring with different phases of material. The highly-penetrating neutron radiation offers an advantage to study the bulk of materials. This experiment demonstrates that samples with a complex mixture of phases (*e.g.* nano-structured thermoelectrics) may be studied using this cell as neutrons allow for the bulk of the high-density solid-state materials to be investigated.

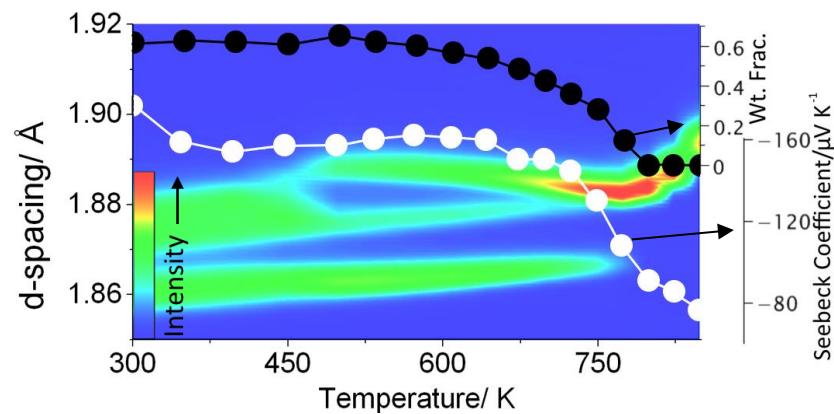


**Figure 3-31** – Overlaid data and extracted parameters for sample with nominal composition  $\text{CuFeS}_2$  showing the temperature dependence of: white – the Seebeck coefficient; Black – weight fraction of the chalcopyrite phase; and coloured background – diffraction intensity.

Experiments on two chalcopyrite related minerals have provided new insights into the structural and electrical behaviour of copper-rich chalcopyrite and talnakhite. A possible magnetic transition at *ca.*  $T = 425$  K has been observed for the first time in a sample with the chalcopyrite structure type and nominal composition  $\text{Cu}_9\text{Fe}_8\text{S}_{16}$  (Figure 3-32). This magnetic transition leads to an electrical transition and a local maximum in the power factor is observed close to the transition temperature (appendix G.). The talnakhite sample shows a complex structural behaviour and a secondary chalcopyrite-type phase exsolves with a small increase in temperature. A structural phase transition from the talnakhite structure to an intermediate solid-state phase occurs at the expected phase transition temperature. This structural transition is also accompanied by an electrical transition which leads to a local maximum in the power factor of the material close to the phase transition temperature. The peak in the power factor of these two materials are observed at *ca.*  $T = 425$  K and  $T = 500$  K. These studies provide a first insight into the structural behaviour of two potential and novel low-cost thermoelectric materials that might be used for low-grade waste heat recovery and provide new options of n-type thermoelectric materials to be coupled with other copper-sulphide based thermoelectrics.

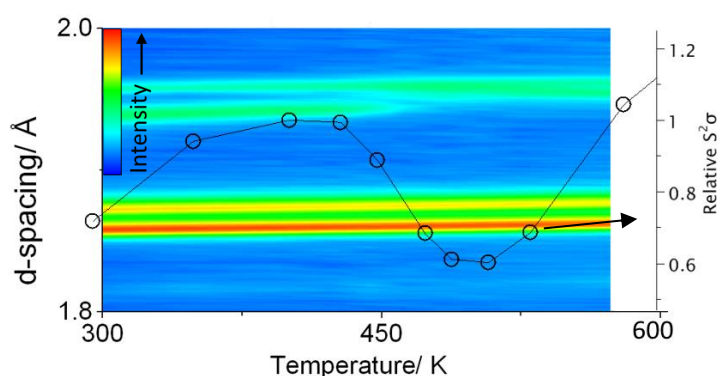


**Figure 3-32** – Overlaid data for sample with nominal composition  $\text{Cu}_9\text{Fe}_8\text{S}_{16}$  showing the temperature dependence of: Black – the relative power factor; and coloured background – diffraction intensity. Relative  $S^2\sigma$  is calculated from  $S^2\sigma_i^{(T)} = S^2\sigma(T)/S^2\sigma_{398K}$ .

This set of experiments also demonstrate that the cell can be utilised in the study of magnetic semiconductors, again exploiting the advantages of neutron diffraction techniques. Here it has helped to uncover magnetic structural anomalies that would otherwise have been unnoticed. The experiment on the sample with composition  $\text{Cu}_9\text{Fe}_9\text{S}_{16}$  outlines the importance of studying the structure and electrical properties simultaneously. The heating profiles followed in electrical transport measurements and diffraction experiments are significantly different and the behaviour of the material across structural

phase transition may therefore be influenced by changes in the measurement procedure. The simultaneous study of these can allow the structure and properties to be directly linked to one another.

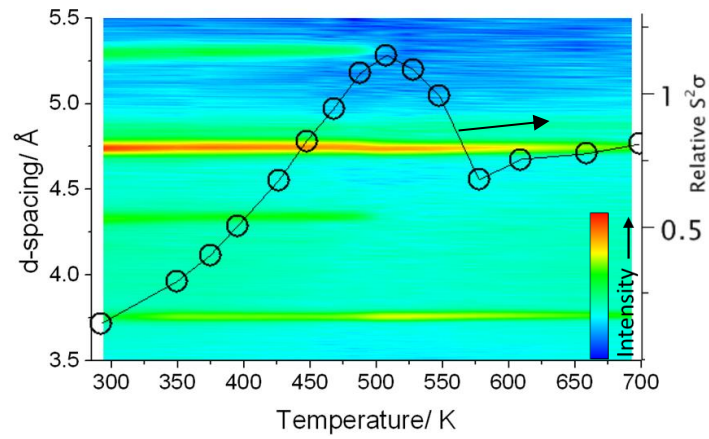


**Figure 3-33** – Overlaid data for talnakhite sample with composition  $\text{Cu}_9\text{Fe}_9\text{S}_{16}$  showing the temperature dependence of: Black – the relative power factor; and coloured background – diffraction intensity. Relative  $S^2\sigma$  is calculated from  $S^2\sigma_i^{(T)} = S^2\sigma(T)/S^2\sigma_{438K}$



## Chapter 4 – The Long-Range and Short-Range Structure of Stoichiometric Bornite, $\text{Cu}_5\text{FeS}_4$

### 4.1 Crystal Structure of Bornite

The literature reports four distinct phases of bornite. The high, intermediate and ambient temperature phases exist at  $T > 530$  K, between  $T = 460$  to  $530$  and  $T < 460$  K, respectively, and the average structure for each was described in the 1980's.<sup>155,275,276</sup> The structure of the sub-ambient temperature phase which exists at  $T < 65$  K was identified more recently.<sup>277</sup> Each of the structures may be described on the basis of cubic sub-cells that display either zinc-blende (ZB) or anti-fluorite (AF) structure types.

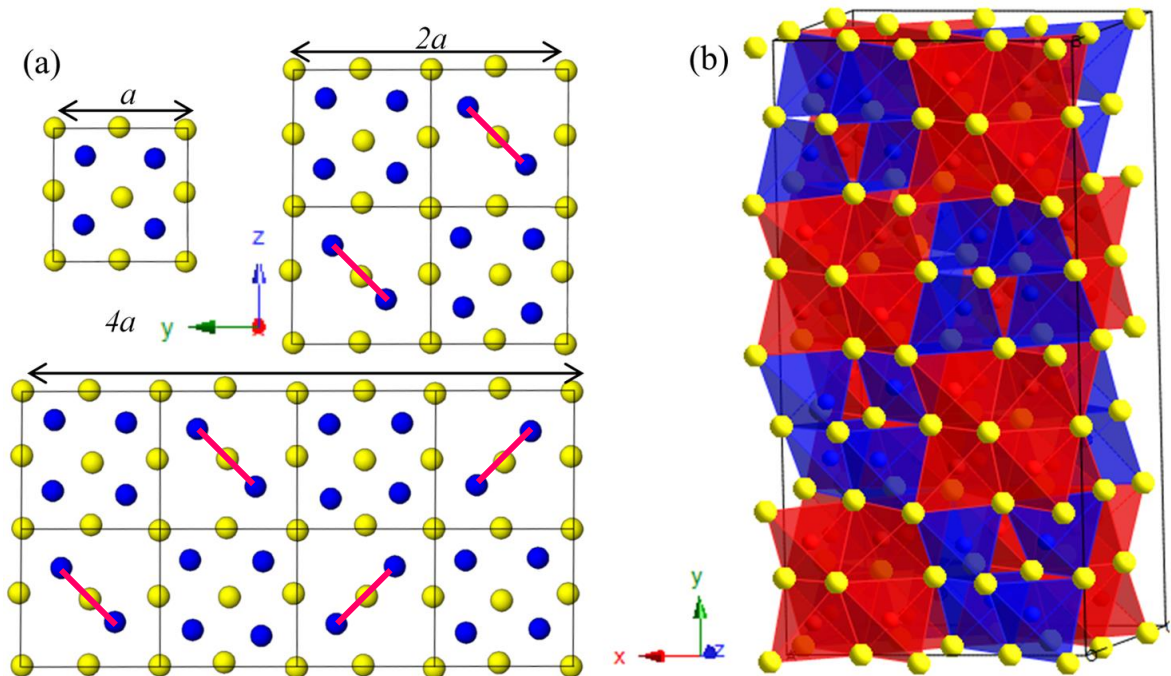


**Figure 4-1** –(a) Projection view along the  $[100]$  direction and showing the cation ordering in the structure of bornite at:  $a$  – high-temperature;  $2a$  – intermediate-temperature;  $4a$  – ambient-temperature structures, respectively. Blue spheres – cation sites of Cu and Fe; Yellow spheres – sulphur; Pink lines are used to outline the cation ordering in neighbouring ZB sub-cells. (b) – Perspective view of the cation sub-cell ordering in the ambient temperature,  $4a$ , structure. Blue - AF sub-cells, Red – ZB sub-cells.

The high-temperature  $a$  phase (space group  $Fm\bar{3}m$ ) has lattice parameters  $a_p \times a_p \times a_p$  where  $a_p \approx 5.5$  Å and a cation deficient AF structure type (Figure 4-1(a)). Here the 2 cation vacancies,  $\square$  in  $\text{Cu}_5\text{Fe}\square_2\text{S}_4$ , are disordered over each of the tetrahedral sites. Upon decreasing the temperature to below *ca.*  $T = 535$  K, bornite undergoes a structural phase

transition to the intermediate  $2a$  phase (space group  $Fm\bar{3}m$ ). In this phase the cation vacancies order within one of two distinct sub-cell types in the structure that can be described by a supercell with lattice parameters  $2a_p \times 2a_p \times 2a_p$  (Figure 4-1(a)). ZB and AF type sub-cells alternate in each direction within the crystal structure.

A second structural transformation occurs at *ca.*  $T = 460$  K where the orthorhombic ambient-temperature  $4a$  phase (space group  $Pbca$ ) doubles the size of the supercell to  $2a_p \times 4a_p \times 2a_p$  (Figure 4-1(a)). The AF and ZB sub-cells alternate along each crystallographic direction in the  $4a$  phase (Figure 4-1(b)). The ordering of the vacancies at interstices within ZB sub-cells alternates along the  $b$ -axis, as highlighted by the pink lines in  $4a$  that are either perpendicular or parallel to one another (Figure 4-1).

The final transformation to the low-temperature phase (space group  $Pca2_1$ ) can also be described on the basis of a  $2a_p \times 4a_p \times 2a_p$  supercell with further deviation from the cubic geometry for each sub-cell ( $a_p \times a_p \times a_p$ ). This structural transition is accompanied by a magnetic transition.<sup>277</sup>

Ding *et al.* have speculated on the Cu and Fe ordering in the  $4a$  and  $2a$  structures but, to date there has been no unambiguous assignment of the Cu-Fe ordering across the tetrahedral sites.<sup>278</sup> Here neutron diffraction and total scattering techniques have been exploited to provide further insight into the copper and iron order within the  $4a$ ,  $2a$  and  $a$  structures.

#### **4.1.1 Synthesis and Experimental**

Bornite was prepared using the mechanochemical techniques described by Guélou *et al.*<sup>157</sup> The elemental powders of copper (99.5%, Sigma Aldrich), iron (99.9+%, Sigma Aldrich) and sulphur (flakes, 99.99%, Sigma Aldrich) were combined using an agate pestle and mortar and transferred into a steel milling jar (25 mL). Steel milling balls were added (2 : 5 g, powder: balls, total mass 28 g) and the mixture was sealed under an Ar atmosphere. The powdered reaction mixture was agitated between the two consecutive millings (40 hrs total; 20 hrs, 500 rpm, 15 mins intervals between reverse in rotation). The powdered sample was then consolidated by hot pressing under a  $N_2$  atmosphere (823 K, 90 MPa, 30 minutes). The sample was finally ground before the diffraction experiments.

All neutron data were collected on the POLARIS diffractometer with the sample sealed in an evacuated quartz silica ampoule, with 1 mm walls, to minimise sulphur loss. Data for total scattering were collected at 300 K, 500 K and 575 K to allow for an analysis of each

of the polymorphs that appear above room temperature. Neutron scattering data were collected for 8 hrs, equating to 1300  $\mu\text{A}$ , at each temperature for the stoichiometric bornite,  $\text{Cu}_5\text{FeS}_4$ . Diffraction data from the 50 °, 90 ° and 150 ° banks (3, 4 and 5) were used in Rietveld analysis. Data from each of the detector banks were combined and used for analysis of the total scattering data. Background scattering data for the furnace, ampoule and vanadium were also recorded. These data were reduced and the background was subtracted from the total scattering data using the Gudrun analysis software.<sup>226</sup> The Mantid analysis software was used to process the Bragg diffraction data.<sup>210</sup>

Thermal parameters, atom positions, site occupancies and lattice parameters were allowed to refine whilst the composition was constrained to  $\text{Cu}_5\text{FeS}_4$  during Rietveld analysis at each temperature. The GSAS software package and the EXPGUI was used to perform Rietveld analysis of the Bragg diffraction data.<sup>209</sup>

## ***4.2 Diffraction Results and Discussion***

### ***4.2.1 Room Temperature X-ray Diffraction***

The room temperature X-ray diffraction data collected on a sample of bornite, synthesised through mechanochemical techniques followed by hot pressing, can be indexed on the basis of the orthorhombic  $4a$  supercell ( $a = 10.953(1) \text{ \AA}$ ,  $b = 21.8694(16) \text{ \AA}$ ,  $c = 10.9464(10) \text{ \AA}$ ), consistent with a single phase of the stoichiometric parent phase (Figure 4-2). This is in contrast to the suggestion, from HRTEM studies on stoichiometric bornite, that a mixture  $6a$ ,  $4a$ ,  $2a$  and  $a$  phases should coexist at room temperature.<sup>279</sup> Refinements including two phases, with  $4a$  and either  $2a$  or  $a$  phases, did not lead to an improvement in the fit to the diffraction data.

### ***4.2.2 Advantages of Neutron Diffraction for a Mixed Cu-Fe Material***

Total scattering experiments should allow for the Cu-Fe ordering within bornite to be established. The bound coherent scattering lengths and the total scattering cross sections of Cu and Fe provide significant contrast, *coherent*  $b = 7.72$  and  $9.45 \text{ fm}$  and;  $x_s = 8.03$  and  $11.62 \text{ barns}$ , respectively. Meanwhile, the X-ray form factors of copper and iron are very similar (Table 2-1). Therefore the proposed cation ordering models from X-ray diffraction studies and computational studies are speculative. The data presented in the following chapter, and subsequent analysis of these data, seek to provide further insights into the cation ordering in the structure.

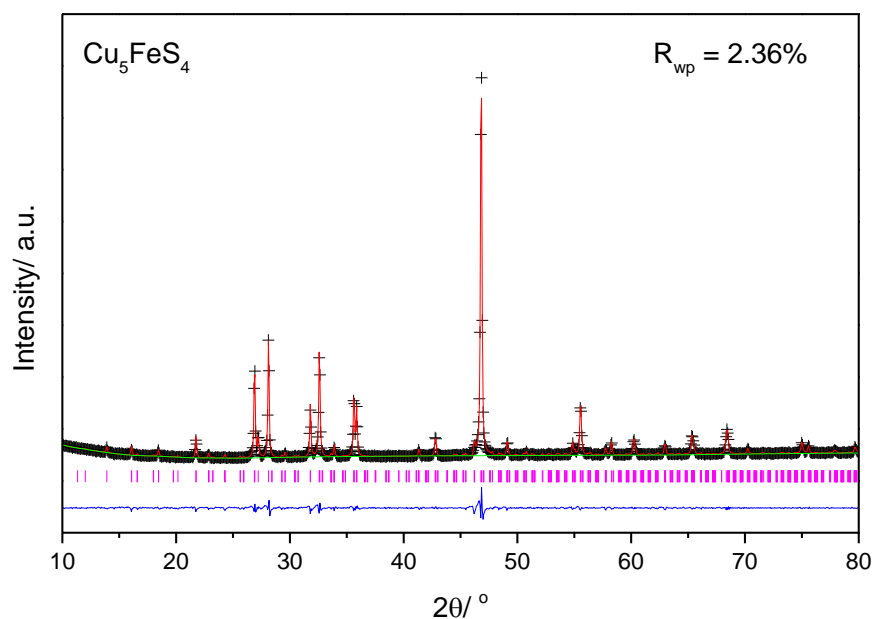


**Figure 4-2** – Le Bail refinement using powder X-ray diffraction data for  $\text{Cu}_5\text{FeS}_4$ . The observed, calculated and difference profiles are denoted by crosses, the red solid line and the lower full line respectively. Markers represent the reflection positions for the 4a phase of  $\text{Cu}_5\text{FeS}_4$  (space group  $Pbca$ ).

### 4.2.3 Ambient-Temperature Orthorhombic Phase of Bornite, 4a

Powder neutron diffraction data were collected to investigate the Cu and Fe ordering in stoichiometric bornite. The asymmetric unit cell of ambient-temperature bornite has 12 crystallographically unique cation sites: 8 within the AF sub-cell and 4 within the ZB sub-cell. The asymmetric unit contains 2 formula units,  $Z = 2$ ,  $\text{Cu}_{10}\text{Fe}_2\text{S}_8$ . In a fully ordered structure, 10 Cu atoms and 2 Fe atoms would occupy the 12 crystallographically unique cation sites. Alternatively, the iron may be partially ordered. This structural complexity results in many possible configurations of cation ordering across the asymmetric unit. Here, order and disorder of iron cations within the discrete AF and ZB sub-cells was considered in the diffraction analysis. The different modes of cation ordering can be considered in terms of the asymmetric unit cell and the AF and ZB sub-cells. These are displayed in Figure 4-3.

The fully disordered model has a site occupancy of  $\text{SOF}_{\text{Fe}} = 1/6$  at each cation site and gives an even distribution of iron cations (Figure 4-3<sup>(A1)</sup>). Partially ordered models have the iron cations evenly distributed over either the AF sites only,  $\text{SOF}_{\text{Fe}} = 1/4$  (Figure 4-3<sup>(A3)</sup>), or the ZB sites only,  $\text{SOF}_{\text{Fe}} = 1/2$  (Figure 4-3<sup>(A2)</sup>). For the iron to be fully ordered within the ZB sub-cell, two sites must have  $\text{SOF}_{\text{Fe}} = 1$ . These two sites will always appear

as vertex-sharing FeS<sub>4</sub> tetrahedra, hence there is one mode of iron ordering in these sub-cells (Figure 4-3<sup>(A4)</sup>). Meanwhile, full ordering of iron cations within the AF type sub-cell, where two cation sites have a  $SO_{Fe} = 1$ , leads the three distinct modes of iron ordering. The iron tetrahedra, FeS<sub>4</sub>, may be edge sharing and have edge-pair correlations within the AF sub-cell (Figure 4-3<sup>(A7)</sup>). FeS<sub>4</sub> tetrahedra may also be vertex-sharing within the AF sub-cells with face-diagonal correlations (Figure 4-3<sup>(A5)</sup>), or they can occupy body-diagonal positions within the AF sub-cell and show no inter-connection between FeS<sub>4</sub> tetrahedra (Figure 4-3<sup>(A6)</sup>).

This gives 7 distinct cation ordering modes, and these may be satisfied by different combinations of occupied crystallographic sites. Many of these are equivalent or very similar through symmetry. This can therefore be simplified into the specific set of ordering configurations (<sup>A</sup>n, where the A subscript denotes ‘Ambient’-temperature):

- (<sup>A</sup>1) Fe is fully disordered over all cation sites
- (<sup>A</sup>2) Fe is disordered over ZB cation sites
- (<sup>A</sup>3) Fe is disordered over AF cation sites
- (<sup>A</sup>4) Fe occupies face diagonal positions in ZB sub-cells
- (<sup>A</sup>5) Fe occupies face diagonal positions in AF sub-cells
- (<sup>A</sup>6) Fe occupies body diagonal positions in AF sub-cells
- (<sup>A</sup>7) Fe occupies edge pair positions in AF sub-cells

Full Rietveld analysis was performed for each of the Cu-Fe ordering schemes described above. The values for the  $R_{wp}$  and  $\chi^2$  resulting from this analysis provide some evidence toward a preferred Cu-Fe ordering scheme in bornite. Lower values of  $R_{wp}$  and  $\chi^2$  are observed in models where iron is ordered in AF sub-cells, i.e. in models <sup>A</sup>5 to <sup>A</sup>7 (Table 4-1).

Each of the models provide a good fit to the diffraction data. A visual analysis of the difference profiles also led to the same conclusion – a better fit is achieved when iron is located in the AF sub-cells.

A comparison of the difference curves from each refinement is provided in Figure 4-4. This diagram shows that ordering schemes <sup>A</sup>2 and <sup>A</sup>4 have marked mis-match in intensity at  $d = 2.5, 3.25, 4.1$  and  $6.5 \text{ \AA}$  (full Rietveld profiles in the e-appendix). This provides further evidence that Fe is unlikely to be ordered over the ZB sites and supports the ordering schemes proposed by Koto & Morimoto, model <sup>A</sup>6.<sup>155</sup>

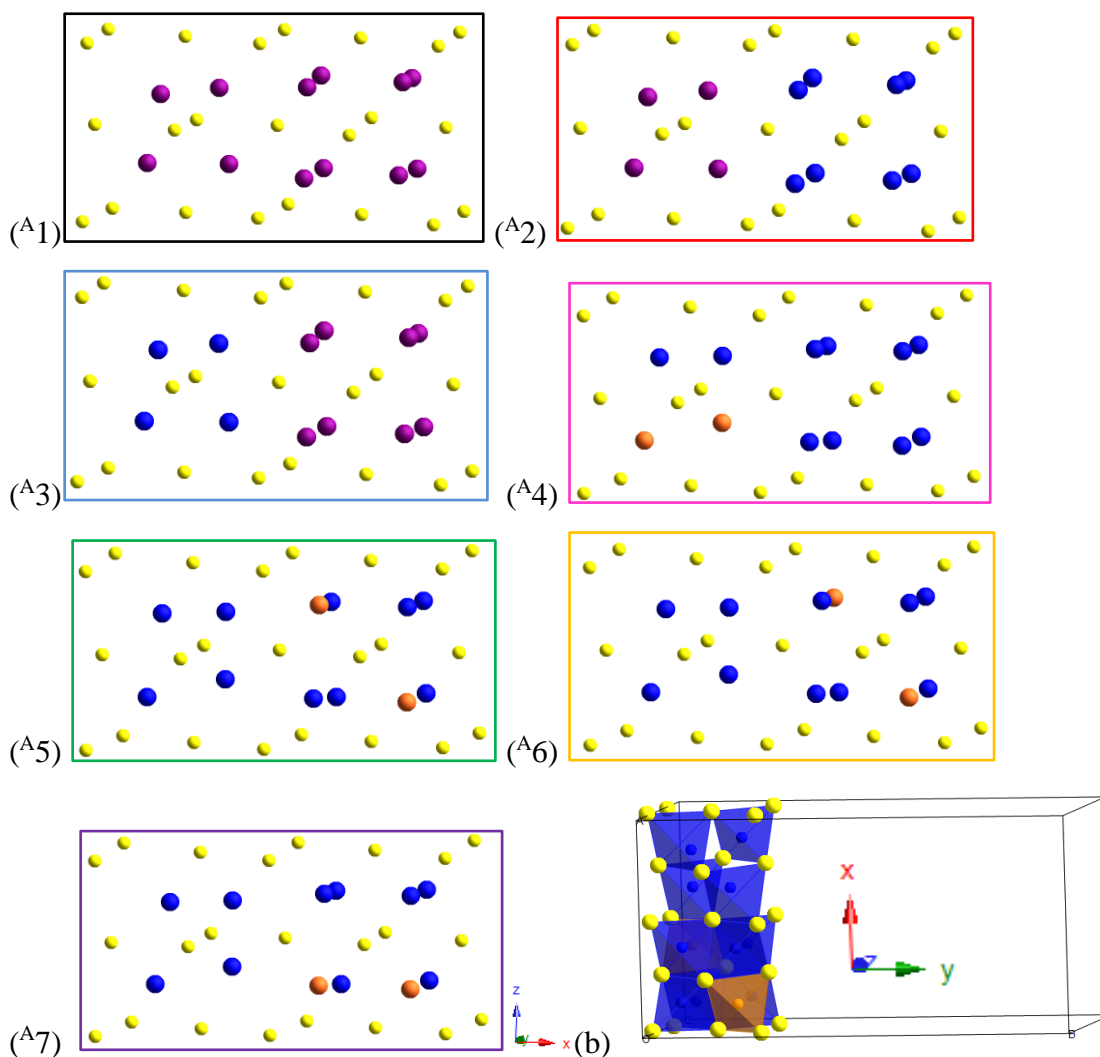


**Figure 4-3** -Perspective view of the possible iron ordering configurations across the two sub-cells/ asymmetric unit cell and which are used in Rietveld refinements. Numbered items correspond to the model number and are described above and in Table 4.1, (b) – perspective view of the section of the unit cell (model <sup>A6</sup>) used in the diagrams <sup>A1</sup>-<sup>A7</sup>. Blue – copper; orange – iron; purple – mixed copper-iron sites and yellow – sulphur. The coloured boxes correspond to line colours in Figure 4-4.

The ordering scheme determined by Koto *et al.* was suggested from X-ray diffraction data on the basis that tetrahedral distortion is more likely to occur for  $\text{Cu}^{1+}\text{S}_4$  tetrahedra than  $\text{Fe}^{3+}\text{S}_4$  tetrahedra. Due to the differentiation in scattering cross sections of copper and iron afforded by neutrons, this analysis has confirmed that iron is located within the AF sub-cells in the *4a* phase of stoichiometric bornite.

Whilst these data certainly indicate that Fe is in the AF sub-cell, they do not provide an unambiguous answer to how the iron orders within the AF sub-cell. Here models <sup>A3</sup>, <sup>A5</sup>, <sup>A6</sup>

and <sup>A</sup>7 provide a similar fit to the diffraction data. Models <sup>A</sup>5 to <sup>A</sup>7 showing a slightly better fit to the data compared to the disordered model, <sup>A</sup>3, suggesting that the iron is likely to be ordered within the AF sub-cells. The Fe<sup>3+</sup>S<sub>4</sub> tetrahedra in the structure should be less inclined to form corner and edge sharing tetrahedra due to electrostatic interactions. Thus, the body-diagonal model <sup>A</sup>6 is used here to describe the ambient-temperature 4a structure of bornite (Table 4-2).

**Table 4-1** – Goodness-of-fit parameters for each of the iron ordering configurations used in Rietveld analysis of bornite at room temperature

Iron order config.	Bank 3	Bank 4	Bank 5	$\chi^2$
	$R_{wp}/\%$	$R_{wp}/\%$	$R_{wp}/\%$	
( <sup>A</sup> 1) Fully disordered	3.12	2.51	2.95	2.030
( <sup>A</sup> 2) Disordered in ZB	3.7	2.96	3.22	2.679
( <sup>A</sup> 3) Disordered in AF	2.98	2.41	2.89	1.881
( <sup>A</sup> 4) Ordered in ZB	3.78	2.98	3.21	2.713
( <sup>A</sup> 5) Face diagonal AF	2.98	2.41	2.87	1.873
( <sup>A</sup> 6) Body diagonal AF	2.96	2.39	2.82	1.835
( <sup>A</sup> 7) Edge pairs AF	2.93	2.39	2.83	1.826

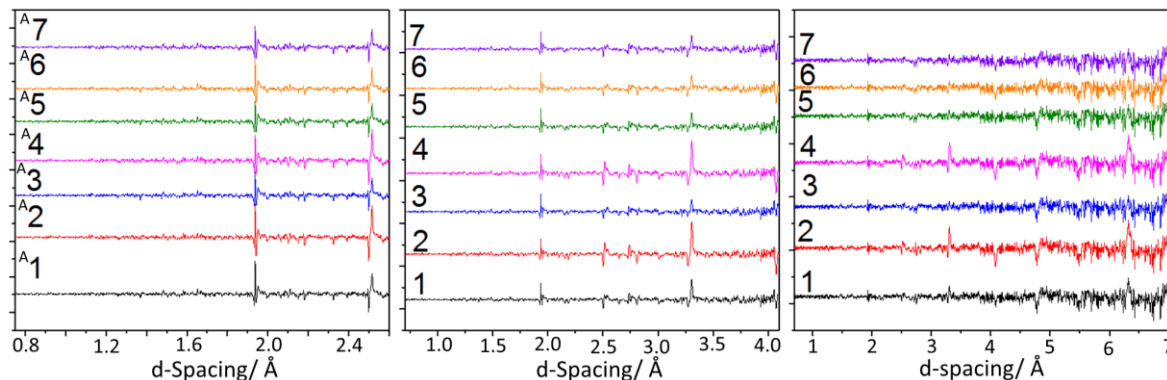


**Figure 4-4** – Difference profiles resulting from each of the iron ordering configurations used in Rietveld analysis of bornite at room temperature. Numbered items correspond to the numbered items in Figure 4-3 and Table 4-1.

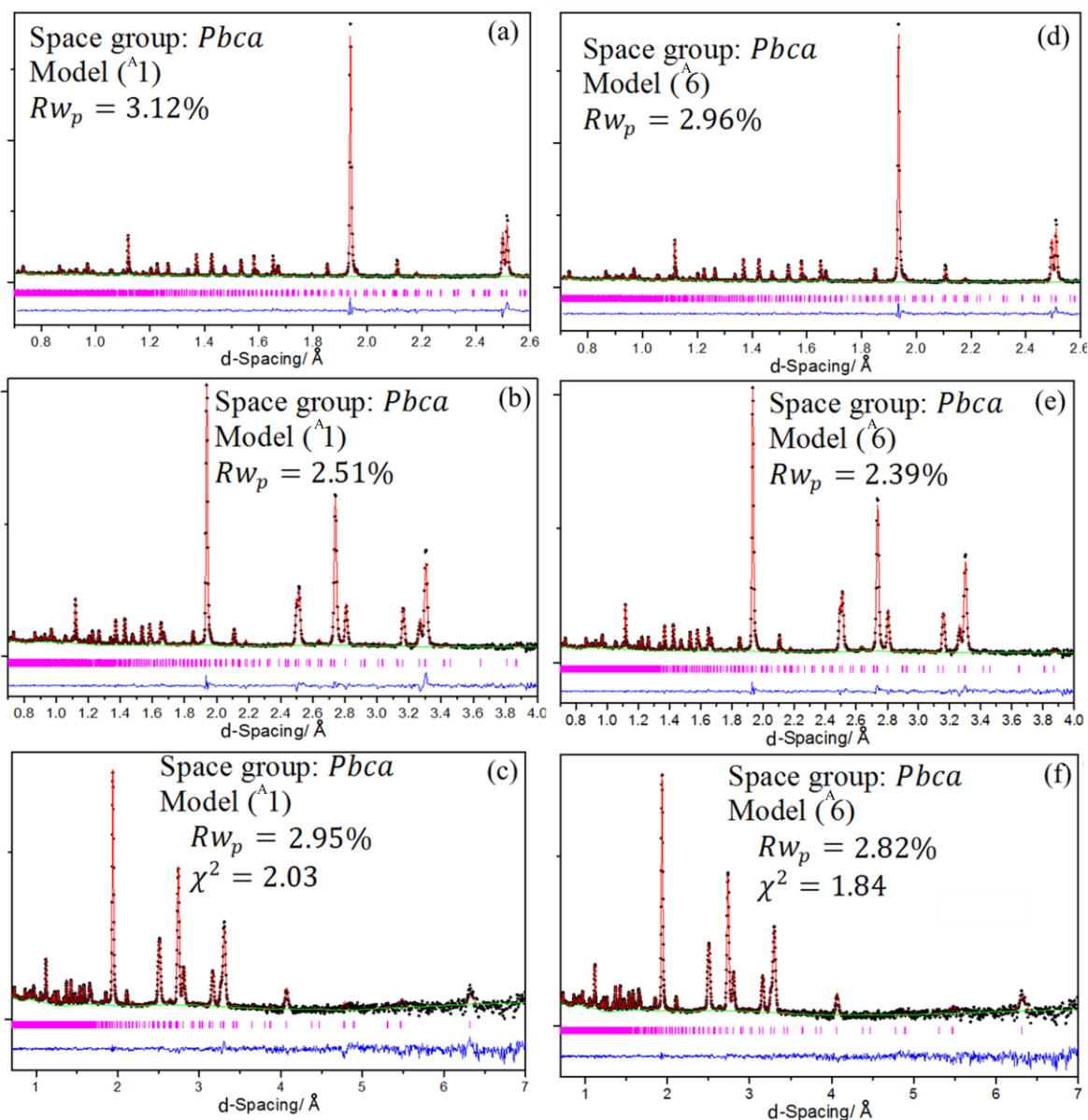


**Figure 4-5** – Full Rietveld refinement profiles from multi-bank refinements of the data collected at room temperature for the sample with composition  $\text{Cu}_5\text{FeS}_4$ . (a), (b) and (c)/ (d), (e) and (f) correspond to the 150°, 90° and 50° banks (5, 4 and 3), respectively. (a, b, c) – are the resulting profiles for model  $A1$ ; (d, e, f) – are the resulting profiles from model  $A6$ . Black points – Observed; red line – calculated, blue line – difference profile; Pink markers – Bragg reflections for the  $Pbca$  phase.

**Table 4-2** – Crystallographic parameters for the body-diagonal-ordered model, <sup>A</sup>6, of bornite at room-temperature determined from Rietveld analysis of neutron diffraction data.

Temperature/ K	300		
Space group	<i>Pbca</i>		
Lattice Parameters/ Å	<i>a</i> / Å	10.945(1)	
	<i>b</i> / Å	21.858(1)	
	<i>c</i> / Å	10.945(1)	
S(all)	$U_{iso}$ / Å <sup>2</sup>	0.0060(6)	
Cu/Fe(all)	$U_{iso}$ / Å <sup>2</sup>	0.0257(2)	
Cu/Fe/S	<i>SOF</i> <sub>all</sub>	1	
Wyckoff symbol – $\delta c$ all	<i>x</i>	<i>y</i>	<i>z</i>
S(1)	0.010(2)	0.001(2)	0.248(3)
S(2)	0.006(3)	0.257(1)	0.260(3)
S(3)	0.242(3)	0.125(2)	0.258(31)
S(4)	0.249(3)	0.000(1)	0.498(4)
S(5)	0.003(3)	0.128(2)	0.502(3)
S(6)	0.002(3)	0.125(2)	0.004(3)
S(7)	0.260(3)	0.128(2)	0.739(3)
S(8)	0.263(3)	0.251(1)	0.498(3)
Cu(1)	0.129(2)	0.058(1)	0.368(2)
Cu(2)	0.113(1)	0.063(1)	0.631(2)
Cu(3)	0.383(2)	0.062(1)	0.370(2)
Fe(4)	0.373(1)	0.059(1)	0.632(1)
Fe(5)	0.124(1)	0.190(1)	0.377(1)
Cu(6)	0.133(1)	0.195(1)	0.645(1)
Cu(7)	0.380(1)	0.188(1)	0.358(1)
Cu(8)	0.377(1)	0.189(1)	0.623(2)
Cu(9)	0.146(1)	0.071(1)	0.897(1)
Cu(10)	0.325(1)	0.085(1)	0.078(1)
Cu(11)	0.1476(1)	0.1786(1)	0.010(1)
Cu(12)	0.365(1)	0.186(1)	0.889(1)
Goodness of fit	$R_{wp}/\%$	$R_{exp}/\%$	
Bank 3, 50°	2.96	9.05	
Bank 4, 90°	2.39	4.53	
Bank 5, 140°	2.82	4.54	
Average	2.64	6.15	
	$\chi^2$	1.835	

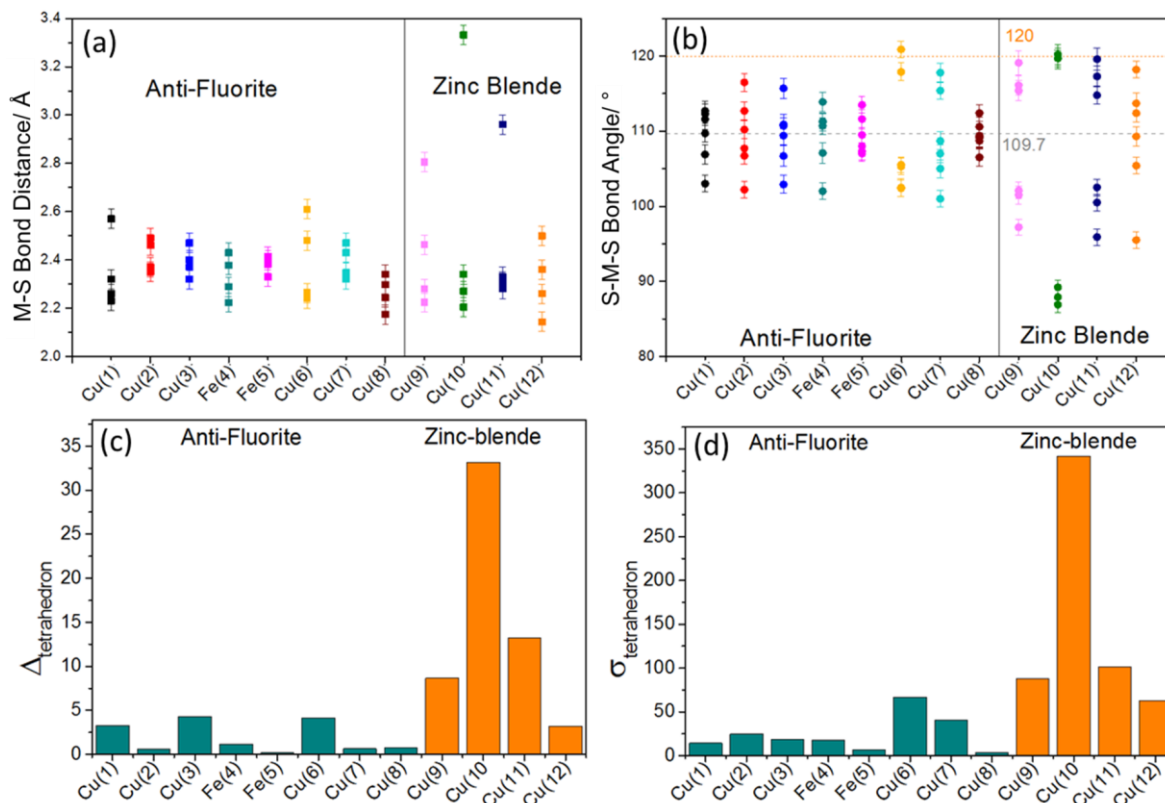


**Figure 4-6** - Extracted or calculated structural parameters for each cation site in model  $A_6$ , as determined from the structural data after Rietveld analysis of room temperature neutron diffraction data for sample with composition  $Cu_5FeS_4$ . (a) – Bond distances; (b) – bond angles; (c) – bond length deviation and (d) – bond angle variance.

Relatively small polyhedral distortion parameters are observed for most of the cations within the AF sub cells, M(1) through to M(8), where mean bond angles are very close to the ideal tetrahedral angle (Appendix I). Cu(6) is an exception and shows Cu-S bond angles that are more similar to trigonal-planar geometry as well as a relatively large value of bond angle variance (Appendix I and  $\sigma_{tetrahedron} = 66$ ). Large polyhedral distortion parameters are observed for each of the copper sites in the ZB sub-cell, Cu(9) through to Cu(12) have  $\sigma_{tetrahedron} = 88, 342, 101$  and  $62$ ;  $\Delta_{tetrahedron} = 8.6, 33.1, 13.2$  and  $3.19$ , respectively, and cation sites Cu(9,10,11) show bond angles that are more similar to trigonal-planar geometry cations,  $mean \theta_{S-Cu-S} = 116.9, 119.9$  and  $117.2^\circ$ , respectively. Cu(12) on the other hand, does not exhibit as significant trigonal-like bond angle geometry,  $mean \theta_{S-Cu-S} = 114.8^\circ$ , despite large polyhedral distortions. Figure 4-7 shows a cation layer,  $b = 0$  to  $1/4$ , of the unit cell for the structure and the distribution of the trigonally distorted and tetrahedral cation sites within  $4a$  bornite. These observations are in

strong agreement with observations made by Martinelli *et al.* Their data also show that at ambient temperatures, the ZB cation sites show marked bond-TO angle distortions.<sup>277</sup>

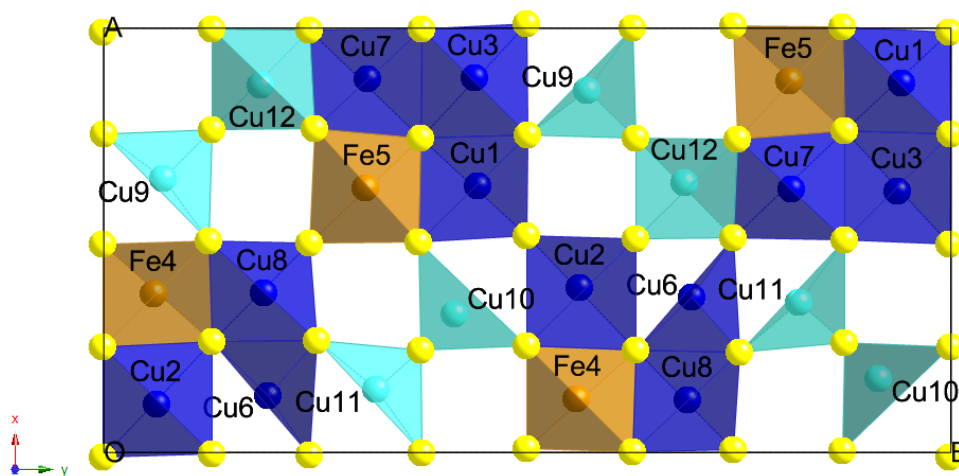


**Figure 4-7** – Projection view of the along the [001] direction for a ‘slice’ of the unit cell,  $b = 0$  to  $1/4$ , showing the arrangement of polyhedra in the unit cell of 4a bornite, model <sup>A</sup>6. A maximum Cu-S bond distance of  $2.6 \text{ \AA}$  is used to show the trigonally distorted sites. Dark Blue – AF copper; Light Blue, ZB copper; orange – iron and yellow sulphur.

#### 4.2.4 High-Temperature Cubic Phase of Bornite, a

The high-temperature structure of bornite has been described in the space group  $Fm\bar{3}m$ . This cation-deficient anti-fluorite structure consists of an equal distribution of the copper, iron and vacancies over each of the cation sites.<sup>159,280</sup> For the following models denoted <sup>H</sup>n, the H subscript denotes ‘High’-temperature. In the model proposed by Morimoto *et al.*, the iron and copper occupy the same 192 fold site, with a total site occupancy  $SOFCu,Fe = 0.031$  (model <sup>H</sup>1, Table 4-3).<sup>275</sup> Effectively this models the tetrahedral site as a smear of electron intensity over the tetrahedral centre. This behaviour is often observed for PLEC-type thermoelectrics.<sup>281</sup> Alternatively, the iron may be modelled at the centre of the tetrahedral site using the same space group with cations located at  $(1/4, 1/4, 1/4)$  and have a multiplicity of  $8c$ . Here the fractional occupancy at each site is  $SOFCu = 5/8$  and  $SOFFe = 1/8$ , consistent with the chemical formula  $Cu_5Fe\Box_2S_4$  (model <sup>H</sup>2, Table 4-3).

Another description of the unit cell is available in the ICSD and presented in an earlier paper by Tunell *et al.*<sup>282</sup> In this study they described the ambient-temperature structure on the basis of an  $a \times a \times a$  unit cell with space group  $F23$ . This model provides a reasonable description of the average sub-cell of the high-temperature structure.<sup>282</sup> Here cations occupy two crystallographic sites, located at  $(1/4, 1/4, 1/4)$  and  $(3/4, 3/4, 3/4)$ , each has a

multiplicity of  $4c$  or  $4d$  (model <sup>H3</sup>, Table 4-4). Thus, three models are available for the analysis of the high-temperature structure and a representation of each is provided in Figure 4-8.

**Table 4-3** – Crystal structure data for the high-temperature cubic phase of bornite for: model <sup>H1</sup>, as available from the ICSD, Collection Code 43271;<sup>275</sup> and model <sup>H2</sup>, an equivalent model (using the same space group) with low multiplicity at the cation sites.

space group	$Fm\bar{3}m$
$a/\text{Å}$	5.5

Model <sup>H1</sup>	Wyck. Symb.	$x$	$y$	$z$	SOF
S	$4a$	0	0	0	1
Cu	$192l$	0.31	0.29	0.27	0.026
Fe	$192l$	0.31	0.29	0.27	0.005

Model <sup>H2</sup>	Wyck. Symb.	$x$	$y$	$z$	SOF
S	$4a$	0	0	0	1
Cu	$8c$	$\frac{1}{4}$	$\frac{1}{4}$	$\frac{1}{4}$	0.625
Fe	$8c$	$\frac{1}{4}$	$\frac{1}{4}$	$\frac{1}{4}$	0.125

**Table 4-4** – Crystal structure data for the high-temperature cubic phase of bornite, model <sup>H3</sup> as available from the ICSD, Collection Code 24174.<sup>282</sup>

space group	$F23$
$a/\text{Å}$	5.47

Model <sup>H3</sup>	Wyck. Symb.	$x$	$y$	$z$	SOF
S	$4a$	0	0	0	1
Cu	$4c$	$\frac{1}{4}$	$\frac{1}{4}$	$\frac{1}{4}$	0.833
Fe	$4c$	$\frac{1}{4}$	$\frac{1}{4}$	$\frac{1}{4}$	0.167
Cu	$4d$	$\frac{3}{4}$	$\frac{3}{4}$	$\frac{3}{4}$	0.417
Fe	$4d$	$\frac{3}{4}$	$\frac{3}{4}$	$\frac{3}{4}$	0.083

Phase analysis of the neutron diffraction data, collected at 575 K, revealed that a secondary chalcopyrite-type phase is present. This behaviour was also observed by Kumar *et al.* for stoichiometric and selenium-doped samples.<sup>159</sup> This phase may form as a result of heating the sample in an evacuated chamber leading to a loss of sulphur.

Rietveld analysis was performed using each of the structural models described above, along with an additional model, <sup>H4</sup> (space group  $Fm\bar{3}m$ ), where cations are positioned over  $32f$ ,  $(x, x, x)$ , sites. Each of these 4 models, <sup>H1</sup> to <sup>H4</sup>, provided a reasonable and comparable fit to the neutron diffraction data collected at 575 K. There was, however a considerable

mis-match in diffraction intensity for several of the Bragg reflections, notably those corresponding to  $d \approx 1.25, 1.4, 1.65$  and  $3.18 \text{ \AA}$  (Figure 4-9(c-d)). This suggests that some structural information is missing from these models.

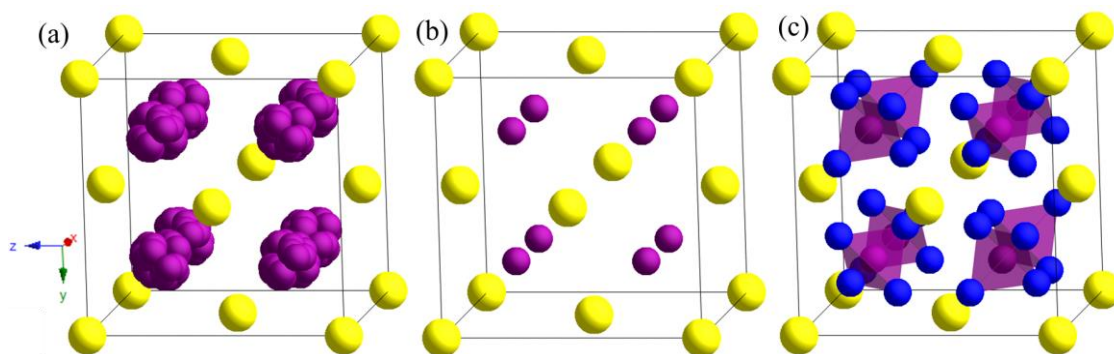


**Figure 4-8** – Perspective view of the structure of high-temperature models used in the Rietveld analysis (a); (b); and (c) are models <sup>H1</sup> and <sup>H4</sup>; <sup>H2</sup> and <sup>H3</sup>; and <sup>H5</sup> respectively. Yellow spheres – sulphur; Purple spheres/tetrahedra – mixed Cu/Fe sites; and blue spheres – copper sites.

A structural model with two crystallographically distinct cation sites around the tetrahedral centre, <sup>H5</sup>, allowed for an improved fit to the neutron diffraction data (Figure 4-9(a-c)). In this model, <sup>H5</sup> with space group  $F23$ , additional  $16e$  cation site were added and positioned at  $(x, x, x)$  coordinates of  $(0.3, 0.3, 0.3)$  and  $(0.6, 0.6, 0.6)$  along with the cations positioned at  $(\frac{1}{4}, \frac{1}{4}, \frac{1}{4})$  and  $(\frac{3}{4}, \frac{3}{4}, \frac{3}{4})$ ,  $4c$  and  $4d$ , sites (model <sup>H5</sup>, Figure 4-9). The occurrence of both tetrahedrally coordinated sites and trigonally coordinates sites is consistent with the observations made for the low-temperature phase. Additionally, this type of split-site behaviour is also observed in the  $\beta$ -phase of the fast-ion conductor thermoelectric material CuAgSe.<sup>187</sup> This analysis has therefore provided a new structural model for the high-temperature phase of stoichiometric bornite.

In order to determine the cation ordering in the structure, using model <sup>H5</sup>, several cation ordering configurations were used during the Rietveld analysis of the diffraction data. The two trigonally-distorted  $16e$  Wyckoff sites are referred to as the  $16e'$  and  $16e''$  sites here onward and these occupy the same tetrahedral hole as the  $4d$  and  $4c$  site, respectively. A tabulated analysis of these configurations is presented in Table 4-5:

- (<sup>H5</sup><sub>i</sub>) Fe is fully disordered over all cation sites
- (<sup>H5</sup><sub>ii</sub>) Fe occupies all cation sites and  $SOF_{Fe}$  was refined
- (<sup>H5</sup><sub>iii</sub>) Fe only occupies the tetrahedrally centred positions,  $4c$  and  $4d$
- (<sup>H5</sup><sub>iv</sub>) Fe only occupies the trigonally distorted positions,  $16e'$  and  $16e''$

(<sup>H5<sub>v</sub></sup>) Fe has zinc-blende type arrangement,  $4c$  and  $16e''$

(<sup>H5<sub>vi</sub></sup>) Fe has zinc-blende type arrangement in tetrahedral centres,  $4c$

(<sup>H5<sub>vii</sub></sup>) Fe has zinc-blende type arrangement in distorted sites,  $16e''$

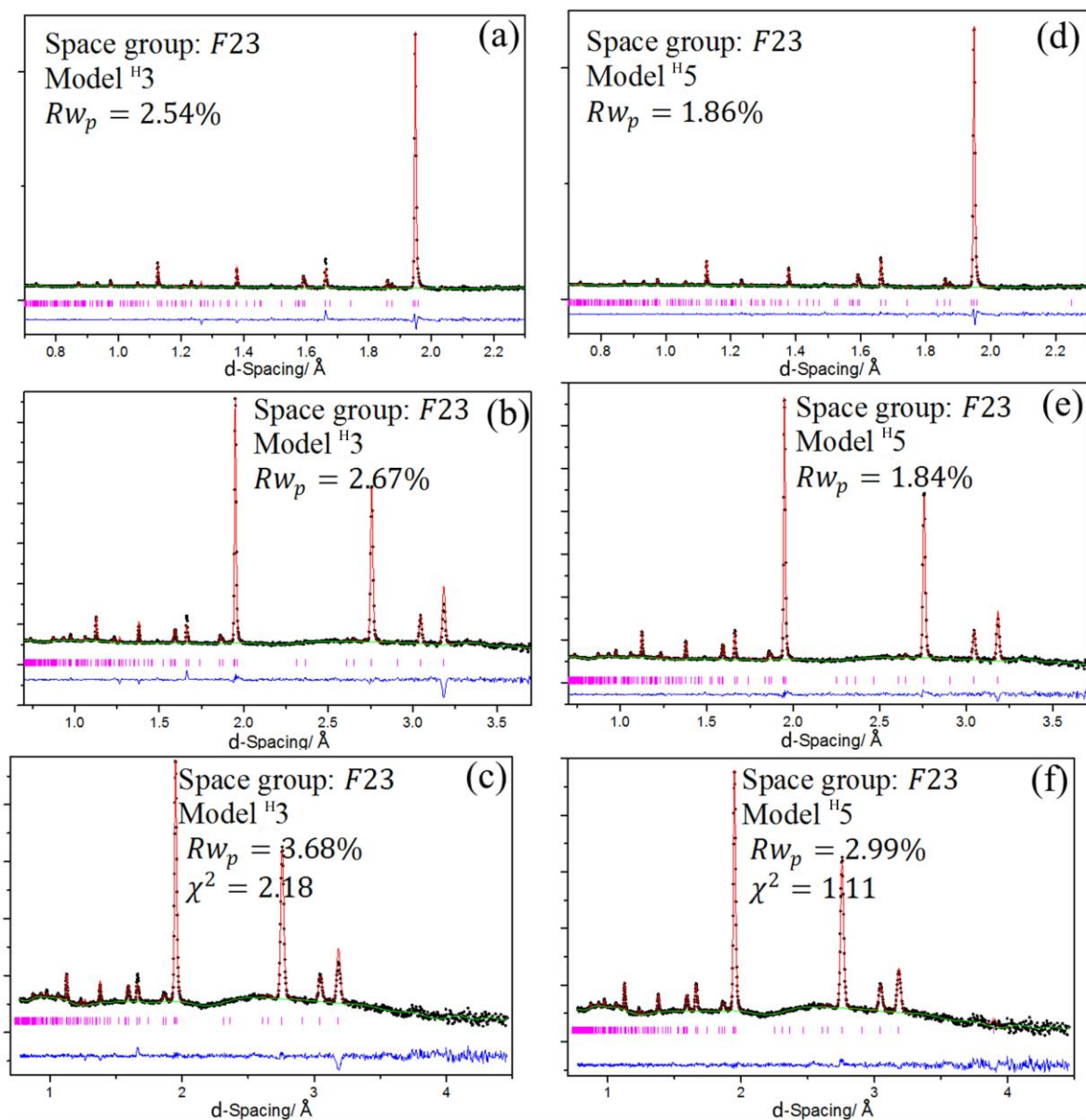


**Figure 4-9** – Full Rietveld refinement profiles from multi-bank refinements of the data collected at 575 K for the sample with composition  $Cu_5FeS_4$ . (a), (b) and (c)/(d), (e) and (f) correspond to 150 °, 90 ° and 50 ° banks (5, 4 and 3), respectively. (a, b, c) - are the resulting profiles for model <sup>H3</sup>; (d, e, f) – are the resulting profiles from model <sup>H5</sup>. Black points – Observed; red line – calculated, blue line – difference profile; Pink markers – Bragg reflections for the F23 phase.

Each of the cation ordering models (<sup>H5<sub>i</sub></sup> – <sup>H5<sub>vii</sub></sup>) investigated shows an excellent fit to the neutron diffraction data (Table 4-5). The observed  $Rw_p$  and  $\chi^2$  values do not provide a

definitive basis to determine an iron ordering configuration for the structure. However, there does appear to be a preference toward Fe ordering at the tetrahedrally-centred sites,  $4c$  and  $4d$ .  $\text{Fe}^{3+}$  is less likely to form distorted tetrahedra in mineral type phases than  $\text{Cu}^+$ . Therefore, the cation ordering configuration in model  ${}^{\text{H}}5_{\text{iii}}$  is used here to describe the structure of high-temperature bornite (Table 4-6). As a side note,  $\chi^2$  below unity have occurred in this analysis. This is because many background terms were needed to get a flat difference curve.

**Table 4-5** – (a) Iron ordering configurations investigated, a tick or cross denotes whether or not iron occupies that site. (b) Goodness of fit for each of the structural models.

(a) Fe Ordering type	Wyckoff Sym				(b) Bank 3	Bank 4	Bank 5	$\chi^2$
	$4c$	$4d$	$16e'$	$16e''$				
$({}^{\text{H}}5_{\text{i}})$	✓	✓	✓	✓	$R_{wp}$	$R_{wp}$	$R_{wp}$	
$({}^{\text{H}}5_{\text{ii}})$	✓	✓	✓	✓	2.99	1.84	1.86	1.11
$({}^{\text{H}}5_{\text{iii}})$	✓	✓	x	x	2.94	1.76	1.81	1.04
$({}^{\text{H}}5_{\text{iv}})$	x	x	✓	✓	2.89	1.76	1.79	0.986
$({}^{\text{H}}5_{\text{v}})$	✓	x	✓	x	2.92	1.73	1.79	1.02
$({}^{\text{H}}5_{\text{vi}})$	✓	x	x	x	2.89	1.67	1.79	0.987
$({}^{\text{H}}5_{\text{vii}})$	x	x	✓	x	2.89	1.67	1.78	0.981
					2.91	1.72	1.78	1.01

**Table 4-6** - Crystallographic parameters for the high-temperature phase of bornite determined using Rietveld refinement and model  ${}^{\text{H}}5_{\text{iii}}$ , with iron occupying  $4c$  and  $4d$  sites, for neutron diffraction data collected at 575 K. \* - fixed values before reaching convergence.

space group	$F23$				
$a/\text{Å}$	5.50891(2)				
$M - U_{iso}/\text{Å}^2$	0.0588(4)				
$S - U_{iso}/\text{Å}^2$	0.0310(4)				
	Wyck. Symb.	$x$	$y$	$z$	$SOF$
S	$4a$	0	0	0	1
Cu(1)	$4c$	$\frac{1}{4}$	$\frac{1}{4}$	$\frac{1}{4}$	0.36(1)
Fe(1)	$4c$	$\frac{1}{4}$	$\frac{1}{4}$	$\frac{1}{4}$	0.11(1)
Cu(3)	$16e'$	0.33*	0.33*	0.33*	0.068(3)
Cu(2)	$4d$	$\frac{1}{4}$	$\frac{1}{4}$	$\frac{3}{4}$	0.48(1)
Fe(2)	$4d$	$\frac{1}{4}$	$\frac{1}{4}$	$\frac{3}{4}$	0.13(1)
Cu(4)	$16e''$	0.65*	0.65*	0.65*	0.033(3)
50° Bank	$R_{wp}/\%$	2.89	$R_p/\%$	7.47	
90° Bank	$R_{wp}/\%$	1.76	$R_p/\%$	2.63	
150° Bank	$R_{wp}/\%$	1.79	$R_p/\%$	2.73	
Overall	$R_{wp}/\%$	1.91	$R_p/\%$	4.18	
	$\chi^2$	0.986			

## 4.2.5 Intermediate Cubic Phase of Bornite, 2a

### 4.2.5.1 Structural Models Used in Refinements

The structural model available through the ICSD for the intermediate phase, space group  $Fm\bar{3}m$ , includes cation sites with a high multiplicity. This is a super-group of the orthorhombic space group  $Pbca$  (For the following models the superscript I denotes ‘Intermediate’-temperature). The structure is described by the  $2a_p \times 2a_p \times 2a_p$  cubic unit cell with 3 crystallographically distinct cation sites and 2 anion sites (model <sup>I</sup>1, Figure 4-10(a), Table 4-7).<sup>276</sup> Two of the cation sites have multiplicity  $96k$ , position  $(x, x, z)$  and the third cation site has a multiplicity of  $32f$  and position  $(x, x, x)$ . These three cation sites model the tetrahedral centre sites and the distorted site with trigonal geometry. A structural model with lower multiplicities can be built using the same space group and cations sitting at general positions along with the additional site,  $32f$  (model <sup>I</sup>2, Figure 4-10(b)). Both of these models represent a superstructure devoid of any vacancy ordering in ZB sub-cells, the structure consists of alternating fully-occupied AF sub cells and cation deficient AF-type sub-cells, where  $SOF = 0.5$ , these deficient sub-cells are referred to here onwards as ZB\* sub-cells.

Ding *et al.* has described the structure of 2a bornite with structural models that are fully ordered variations of the structures described above. Each is described in the space group  $F\bar{4}3m$ , with cations positioned at the general positions,  $16e$ ,  $(x, x, x) \approx (\frac{1}{8}, \frac{1}{8}, \frac{1}{8}), (\frac{3}{8}, \frac{1}{8}, \frac{1}{8}), (\frac{5}{8}, \frac{1}{8}, \frac{1}{8})$  and  $(\frac{7}{8}, \frac{1}{8}, \frac{1}{8})$ .<sup>278</sup> These models were constructed for a computational study of the Cu-Fe ordering and their results suggested that Fe may be ordered within the AF sub-cells. The site occupancy factors were modified here in order to match the chemical formula of bornite,  $Cu_5FeS_4$ . Removal of any single cation site introduces the vacancy ordering described in section 4.1 (model <sup>I</sup>3, Figure 4-10(c), Table 4-8). Models used in Rietveld analysis include a vacancy ordered model,  $SOF_{16e} = 1, 0, 1$  and  $1$  (model <sup>I</sup>3); and an additional structural model with atomic density over each of the tetrahedral sites. Here the SOF’s correspond to a chemical formula of  $Cu_5FeS_4$ , e.g.  $SOF_{16e} = 1, 1, 0.5$  and  $0.5$  (model <sup>I</sup>4, Figure 4-10(d)).

Each of the structural models, <sup>I</sup>1 to <sup>I</sup>4, described above has been used to provide a fit to the neutron diffraction data. A new structural model has also been constructed to take into account the structural information available in the  $F\bar{4}3m$  and  $Fm\bar{3}m$  models. This new model, <sup>I</sup>5, uses space group  $F23$  to describe the structure of intermediate bornite. This

model provides 4 crystallographically unique tetrahedral sites, similar to  $F\bar{4}3m$  – models <sup>13</sup> and <sup>14</sup>, and allows for split-sites around the tetrahedral centres (Figure 4-10(e)) to account for the trigonally distorted behaviour of cations, as observed in  $Fm\bar{3}m$  – models <sup>11</sup> and <sup>12</sup>.

**Table 4-7** – Crystal structure data for the intermediate-temperature cubic phase of bornite for model <sup>11</sup> with space group  $Fm\bar{3}m$  as available from the ICSD, Collection Code 200424.<sup>276</sup>

Space group		$Fm\bar{3}m$			
$a/\text{Å}$		10.981			
	Wy. Symb.	$x$	$y$	$z$	$SOF$
Cu	32 $f$	0.091(1)	0.091(1)	0.091(1)	0.258
Fe	32 $f$	0.091(1)	0.091(1)	0.091(1)	0.052
Cu	96 $k$	0.130(2)	0.130(2)	0.130(2)	0.058
Fe	96 $k$	0.130(2)	0.130(2)	0.130(2)	0.012
Cu	96 $k$	0.361(1)	0.139(1)	0.113(1)	0.275
Fe	96 $k$	0.361(1)	0.139(1)	0.113(1)	0.055
S	24 $e$	0.254(1)	0	0	1
S	8 $c$	¼	¼	¼	1

**Table 4-8** – Crystal structure data for the intermediate-temperature structure of bornite for model <sup>13</sup> with space group  $F\bar{4}3m$ , as proposed by Ding et al.<sup>278</sup>

Space group		$F\bar{4}3m$			
$a/\text{Å}$		10.981			
	Wyck. Symb.	$x$	$y$	$z$	$SOF$
Cu	16 $e$	1/8	1/8	1/8	1
Cu	16 $e$	3/8	1/8	1/8	0
Cu	16 $e$	5/8	1/8	1/8	1
Fe	16 $e$	7/8	1/8	1/8	1
S	4 $a$	0	0	0	1
S	4 $b$	½	0	0	1
S	24 $g$	¼	¼	0	1

The results from Rietveld analysis on these structural models show that it is not necessary to include high multiplicity sites. Models <sup>11</sup> and <sup>12</sup> show a similar fit to the neutron diffraction data. Full vacancy ordering is only present in model <sup>13</sup> and the Bragg reflections at  $d \approx 2.75, 3.17$  and  $3.32 \text{ Å}$  do not fit correctly for any cation ordering configuration used in the Rietveld analysis. Introducing atomic intensity into the vacant sites, as in model <sup>14</sup>, markedly improves the fit to the diffraction data. This indicates that the vacant sites in the ZB sub-cells are not fully ordered and the structure of intermediate bornite should indeed be described by alternating AF and ZB\* sub-cells. Furthermore, the  $R_{wp}$  and  $\chi^2$  values

clearly demonstrate that models <sup>1</sup>1, <sup>1</sup>2 and <sup>1</sup>5 are more appropriate. This indicates that it is necessary to include the trigonally distorted cation sites into the structural models of the intermediate phase of bornite.

**Table 4-9** – Goodness of fit parameters as determined for each of the structural models. (Detailed structural data in e-appendix)

	bank 5	bank 4	bank 3	
Space group	$R_{wp}/\%$	$R_{wp}/\%$	$R_{wp}/\%$	$\chi^2$
Model <sup>1</sup> 1 – $Fm\bar{3}m$	3.03	2.34	4.39	1.116
Model <sup>1</sup> 2 – $Fm\bar{3}m$	3.03	2.39	4.38	1.152
Model <sup>1</sup> 3 – $F\bar{4}3m$	3.75	4.27	8.08	3.012
Model <sup>1</sup> 4 – $F\bar{4}3m$	3.75	3.09	5.59	1.835
Model <sup>1</sup> 5 – $F23$	2.96	2.34	4.31	1.106

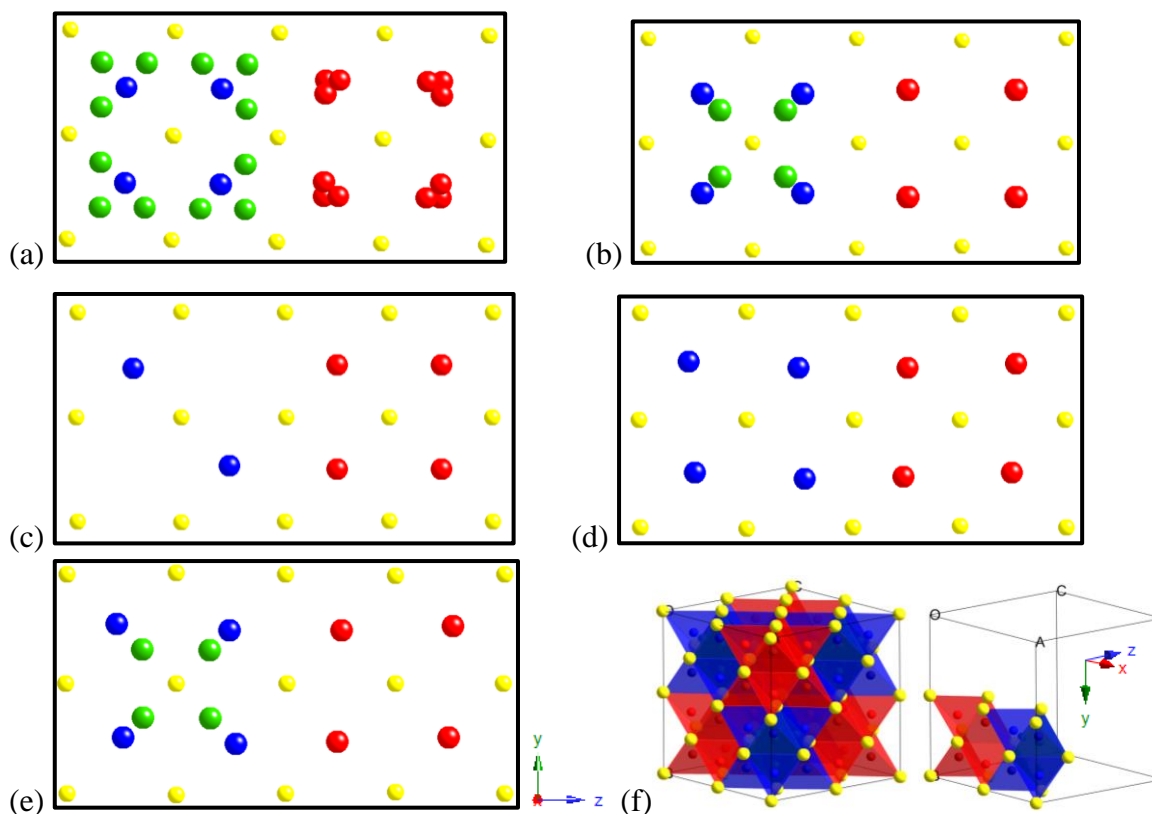


**Figure 4-10** – Projection views along the  $[100]$  direction of half ( $y = b/2$ ) of the unit cell (as shown in *f*) for the intermediate-temperature phase of bornite,  $Cu_5FeS_4$ , to show the cation ordering and site-splitting in the sub-cells. (a, b, c, d and e/f) – Model <sup>1</sup>1, <sup>1</sup>2, <sup>1</sup>3, <sup>1</sup>4 and <sup>1</sup>5. Yellow spheres -sulphur; Red spheres – cations in AF sub-cells; Blue spheres – tetrahedrally centred cations in ZB\* sub-cells and; green spheres - trigonally distorted cations in ZB\* sub-cells.

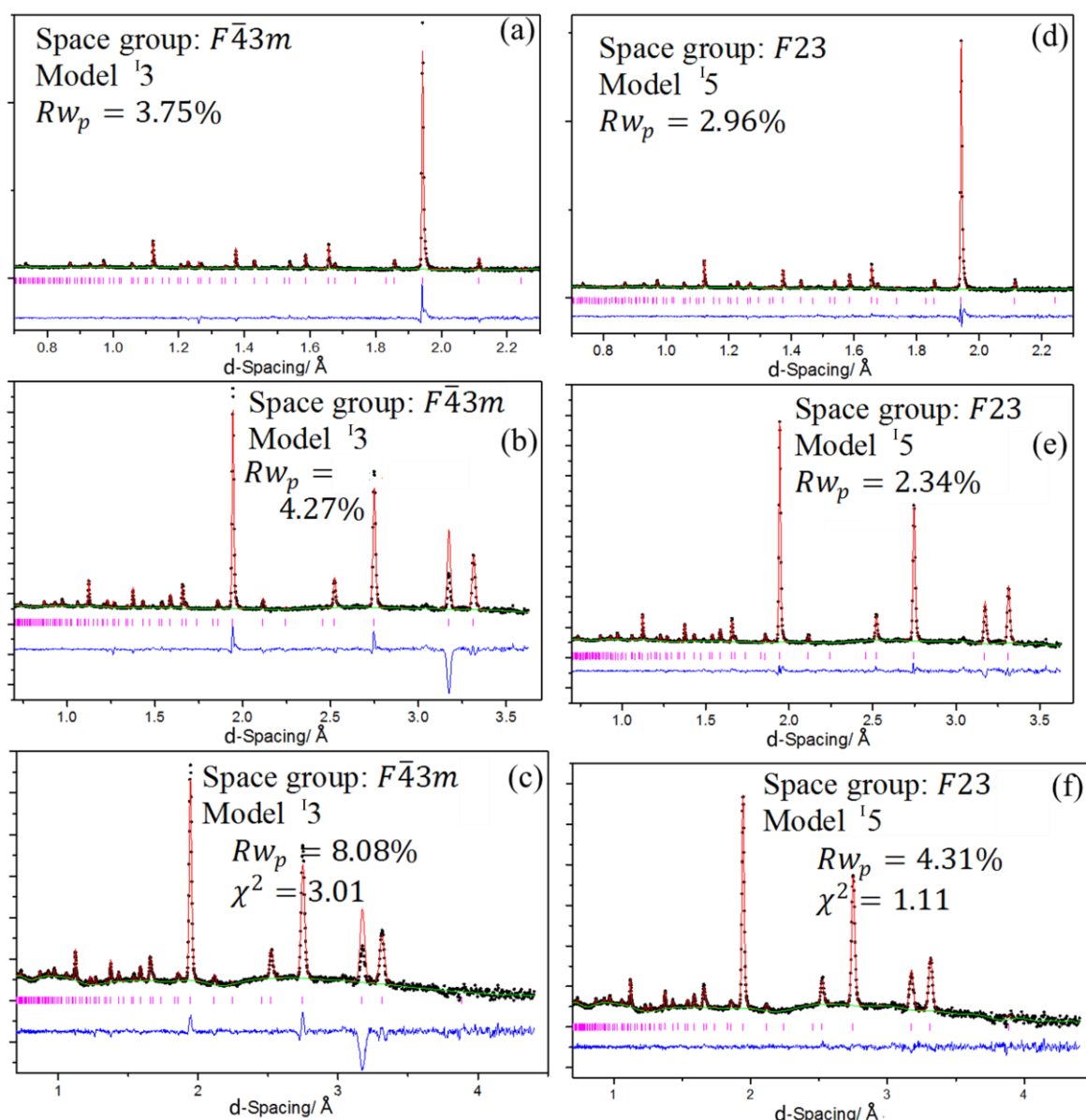


**Figure 4-11** – Full Rietveld refinement profiles from multi-bank refinements of the neutron diffraction data collected at 500 K for the sample with composition  $\text{Cu}_5\text{FeS}_4$ . (a), (b) and (c)/(d), (e) and (f) correspond to banks 5, 4 and 3 (150, 90 and 50 °), respectively. (a, b, c) are the resulting profiles from model <sup>1</sup>3.(d, e, f) are the resulting profiles for model <sup>1</sup>5. Black points – Observed; red line – calculated, blue line – difference profile; Pink markers – Bragg reflections for the  $F\bar{4}3m$  or  $F23$  phase, respectively.

#### 4.2.5.2 Cation Ordering in Intermediate Bornite, 2a

The structural models, model  $^12$  and model  $^15$  with space group  $Fm\bar{3}m$  and  $F23$ , respectively, were used to explore copper/iron ordering in the intermediate phase of bornite. Four cation ordering configurations were used for the investigation of each structure type. These models differ in respect to the number of crystallographically unique tetrahedral centres there are, 2 in model  $^12$  and 4 in model  $^15$ . This allowed the same ordering configurations to be investigated. In these structural models, iron was only modelled over the tetrahedral sites. The models were:

- ( $^12_i$ ,  $^15_i$ ) Fe is fully disordered over all tetrahedral sites (Site occupancy factor of iron is fixed during refinements)
- ( $^12_{ii}$ ,  $^15_{ii}$ ) Fe only occupies AF sites
- ( $^12_{iii}$ ,  $^15_{iii}$ ) Fe only occupies ZB sites
- ( $^12_{iv}$ ,  $^15_{iv}$ ) Fe is partially ordered over all tetrahedral sites (Site occupancy factor of iron is also refined)

There are 2 distinct sub-cells within the structure. The first is a ‘fully’ occupied AF-type sub-cell ( $a \times a \times a$ ), in models  $^12_i$  and  $^15_i$  this is represented by their respective site occupancy factors of close to 1:  $SOF_{M(1)}=0.912$  in  $^12_i$  and  $SOF_{M(1),M(2)}=0.970, 0.928$  in  $^15_i$ . The second is an AF-type sub-cell, ( $a \times a \times a$ ), where each of the tetrahedral sites is occupied by close to a half by metal atoms and a half by vacancies:  $SOF_{M(2)}=0.575$  in  $^12_i$  and  $SOF_{M(3),M(4)}=0.433, 0.6742$  in  $^15_i$ . This represents a disorder of cations and vacancies across those sites. This observation is in excellent agreement with the description of intermediate bornite by Kanazawa *et al.*<sup>276</sup> This vacancy-disordered AF-type sub-cell would represent the ZB\* type sub-cell, this nomenclature is used to maintain some consistency with the  $4a$  phase and to provide clear distinction between the two sub-cell types.

Similar to the  $4a$  phase the structure can still be described by alternating AF and ZB\* sub-cells in each direction,  $x$ ,  $y$  and  $z$ . However, ZB\* sub-cells now show a significant degree of disorder. The type of disorder within or between the sub-cells is not revealed by this analysis of the average structure. Furthermore, the mode of copper - iron ordering within the structure is not revealed by this order/disorder analysis. Each of the cation ordering models gives a comparable fit to the neutron diffraction data. This is true for both the  $^12_n$  and  $^15_n$  ( $Fm\bar{3}m$  and  $F23$ ) structure types. These models provide an excellent fit to the data and the resulting  $R_{wp}$  and  $\chi^2$  values provide no evidence that any single cation ordering

configuration best represents the intermediate structure of bornite but the models with space group  $F23$  tend to provide a better fit to the data (Table 4-10). As such, model ( $15_i$ ) with the space group  $F23$  is used here to describe the intermediate structure of bornite.

**Table 4-10** – Site occupancy factor at each tetrahedral centre and goodness of fit parameters for the structural models used in cation ordering analysis, † signifies that the distorted  $M(nt')$  and tetrahedral  $M(nt'')$  centres have been summed. ESDs 0.01 for all SOF.

Model no.	AF-SOF	ZB*-SOF	Bank 5	Bank 4	Bank 3	
	M(1)	M(2 <sup>†</sup> )	$R_{wp}/\%$	$R_{wp}/\%$	$R_{wp}/\%$	$\chi^2$
<b>12<sub>i</sub></b>	0.91	0.58	3.04	2.39	4.39	1.16
<b>12<sub>ii</sub></b>	0.9	0.61	3.03	2.39	4.37	1.15
<b>12<sub>iii</sub></b>	0.91	0.57	3.02	2.39	4.37	1.15
<b>12<sub>iv</sub></b>	0.95	0.55	3.03	2.39	4.38	1.15
<b>Site av.</b>	0.92	0.58				

Model no.	AF-SOF		ZB*-SOF		Bank 5	Bank 4	Bank 3	
	M(1)	M(2 <sup>†</sup> )	M(3 <sup>†</sup> )	M(4 <sup>†</sup> )	$R_{wp}/\%$	$R_{wp}/\%$	$R_{wp}/\%$	$\chi^2$
<b>15<sub>i</sub></b>	0.97	0.93	0.43	0.67	2.96	2.34	4.31	1.11
<b>15<sub>ii</sub></b>	0.98	0.77	0.52	0.74	2.99	2.34	4.29	1.11
<b>15<sub>iii</sub></b>	0.97	0.93	0.47	0.63	3.16	2.38	4.27	1.18
<b>15<sub>iv</sub></b>	0.98	0.9	0.45	0.63	2.97	2.31	4.28	1.09
<b>Site av.</b>	0.98	0.88	0.47	0.67				
<b>Subcell av.</b>	0.93		0.55					

The average occupancy data from each model provides some further insight to the structure. Notably, the AF sub-cells are slightly cation deficient and the ZB\* sub-cells are slightly cation rich, as compared to the ideal  $SOF = 1$  and  $0.5$ . AF sites are *ca.* 90% occupied whereas the ZB\* sites are *ca.* 60% occupied. However, from this study alone there is no strong evidence to support either of the suggested iron ordering schemes proposed by Ding *et al.*<sup>278</sup> Location of Fe in this complex structure is not possible through Bragg diffraction techniques alone, despite the advantages afforded by using neutrons. Here, the total scattering data were collected (this includes the Bragg diffraction data

analysed above) which provide further insight toward the Cu-Fe ordering within each of these structural phases of stoichiometric bornite. These data will be examined in the following section.

**Table 4-11** – Crystallographic parameters for the intermediate-temperature phase of bornite determined using Rietveld refinement and model <sup>15</sup><sub>i</sub> for the neutron diffraction data collected at 500 K.

Temperature/ K	500					
Space group	<i>F</i> 23					
	<i>a</i> / Å		10.98381(6)			
S(all)	<i>U</i> <sub>iso</sub> / Å <sup>2</sup>		0.0202(4)			
Cu/Fe(all)	<i>U</i> <sub>iso</sub> / Å <sup>2</sup>		0.0530(4)			
Atom Label	Wy. Sym	<i>x</i>	<i>y</i>	<i>z</i>	<i>SOF</i>	
S(1)	<i>4a</i>	0	0	0	1	
S(2)	<i>4b</i>	0	0	0.5	1	
S(3)	<i>24g</i>	¼	¼	-0.0038(5)	1	
M(1)	Cu(1)	<i>16e</i>	0.8736(4)	0.8736(4)	0.8736(4)	0.845(6)
	Fe(1)	<i>16e</i>	0.8736(4)	0.8736(4)	0.8736(4)	0.125
M(2)	Cu(2)	<i>16e</i>	0.8816(4)	0.8816(4)	0.6184(4)	0.549(8)
	Fe(2)	<i>16e</i>	0.8816(4)	0.8816(4)	0.6184(4)	0.125
M(3t')	Cu(3t')	<i>16e</i>	0.1182(13)	0.1182(13)	0.3818(13)	0.025(4)
	Fe(3t')	<i>16e</i>	0.1182(13)	0.1182(13)	0.3818(13)	0.125
M(3t'')	Cu(3t'')	<i>16e</i>	0.1721(6)	0.1721(6)	0.3279(6)	0.283(4)
M(4t')	Cu(4t')	<i>16e</i>	1.1269(4)	1.1269(4)	1.1269(4)	0.526(3)
	Fe(4t')	<i>16e</i>	1.1269(4)	1.1269(4)	1.1269(4)	0.125
M(4t'')	Cu(4t'')	<i>16e</i>	1.1656(8)	1.1656(8)	1.1656(8)	0.277(3)
Bank 3, 50°	<i>R</i> <sub>wp</sub> / %		2.96	<i>R</i> <sub>p</sub> / %		4.98
Bank 4, 90°	<i>R</i> <sub>wp</sub> / %		2.34	<i>R</i> <sub>p</sub> / %		3.70
Bank 5, 140°	<i>R</i> <sub>wp</sub> / %		4.31	<i>R</i> <sub>p</sub> / %		6.03
Total	<i>R</i> <sub>wp</sub> / %		2.81	<i>R</i> <sub>p</sub> / %		4.73
	$\chi^2$		1.106			

### 4.3 Pair Distribution Function Analysis of Bornite

#### 4.3.1 Experimental Procedure and Data Preparation

The results from section 4.2 demonstrate the difficulty in pinpointing the location of the iron within these complex crystal structures. The following analysis seeks to further understand the ordering of copper and iron within the structure. The data collected during the diffraction experiment above also contains the total scattering data to a high  $Q$ . These data can be used for analysis of the pair distribution function of bornite at each temperature.

The Gudrun analysis software was used to subtract the background contributions to the data and to prepare the total scattering data.<sup>226</sup> The  $G(r)$  and  $S(Q)$  functions were produced using the *stog\_new* extension in the RMCprofile software package which carries out the Fourier transform of the total scattering data.<sup>227,283</sup> The *data2config* extension in RMCprofile was used to create the supercells for each structure providing supercells of  $8 \times 4 \times 8$ ,  $6 \times 6 \times 6$  and  $12 \times 12 \times 12$  for the orthorhombic structure at 300 K (Table 4-2), the cubic structure at 500 K (Table 4-11), and the cubic structure at 575 K (Table 4-6), respectively. These large box models were refined during the Reverse Monte-Carlo calculations. The RMC model was refined against 4 input data sets: Bragg diffraction data from POLARIS bank 4,  $90^\circ$  and over the  $d$ -spacing range  $1 < d/\text{\AA} < 3.6$ , reciprocal space data,  $S(Q)$ , to  $Q = 30 \text{\AA}^{-1}$  and real-space data,  $G(r)$ , over the range (i)  $1 < r/\text{\AA} < 10$  and (ii)  $1 < r/\text{\AA} < 50$ . Two ranges for the real-space data were used to ensure that the ordering in the low  $r$ -region could be modelled more accurately and to ensure the ordering to high  $r$  was not inaccurate.

The weighting of each data set was 0.002, 0.01, 0.002 and 2.0 for the Bragg, reciprocal space, real space (i) and real space (ii) data respectively. A lower value signifies a larger influence on the calculated goodness-of-fit functions.

Minimum distance windows were set for each of the atom-atom pairs at  $2.09 \text{\AA}$ . During the RMCprofile analysis, an atom swap parameter was included to allow copper and iron cations to swap positions with one another. Vacancies in the tetrahedral holes were modelled as dummy atoms into the supercell arrangements at each temperature and a second swap parameter allowed for the cations and vacancies to swap. The inclusion of both of these swapping parameters allows the system to swap between all available tetrahedral centres allowing for a large degree of randomisation in the calculation. A total

of 50 individual runs were performed for each of the starting configurations with each swapping parameter. From this, 50 structural configurations are generated for each set of calculations, the PDF partial plots presented in the following sections are generated from an average of the 50 structural configurations that resulted from calculations which used the same set of starting parameters.

### ***4.3.2 Insights into the Copper/Iron Ordering from Total Scattering Experiments***

#### ***4.3.2.1 Diagrammatic Representation of Structural Models Considered for PDF Analysis***

The resulting large-box structural models from the RMCprofile analysis were compressed onto their respective unit cells in space group  $P1$ . These unit cells containing *ca.* 30,000 atoms were used here to investigate the short-range copper/iron ordering correlations in the ambient, intermediate and high-temperature phases of bornite.

In the following section, diagrams are used to present the structural information gathered from these models. These diagrams depict the fractional occupancy of atoms present at each tetrahedral site. The unconventional approach used here is in favour of tables or graphs because there is a large number of sites for the ambient- and intermediate-temperature phases: 128 and 64 tetrahedral centres, respectively for the unit cells in  $P1$ . These diagrams provide a more meaningful insight into the cation ordering across the tetrahedral sites.

For the ambient and intermediate temperature phases, the structure is divided into four ‘slices’. Each of these four ‘slices’ encompasses the cell-parameter range  $a = 0$  to  $1$ ,  $b = 0$  to  $1$  and  $c = n$  to  $n + \frac{1}{4}$  where  $n = 0, \frac{1}{4}, \frac{1}{2}$  and  $\frac{3}{4}$ . The supercells of bornite are constructed from AF and ZB type sub cells and different colours are used here to distinguish between the tetrahedral sites in the AF and ZB sub cells, coloured as red and blue in the table, respectively (Figure 4-12).

An equivalent to the site occupancy factor has been determined from the resulting structural models in the space group  $P1$ . This has been calculated from:

$$SOF_M = \frac{n_M^{site}}{n_{max}} \quad (4-1)$$

Here  $M = \text{copper} + \text{iron}$ , *copper* or *iron* and these are given by  $SOF_{cation}$ ,  $SOF_{Cu}$  and  $SOF_{Fe}$  respectively,  $n_M^{site}$ , is the number of cations at a given site in the compressed supercell and  $n_{max}$  is the maximum number of cations that could be found at any given site.  $n_{max}$  is

determined by the total number of unit cells in the original large-box supercell. For example, in the  $8 \times 4 \times 8$  supercell of  $Pbca$  unit cells, there are 256 unit cells with dimensions  $2a \times 4a \times 2a$  and  $n_{max}=256$ .

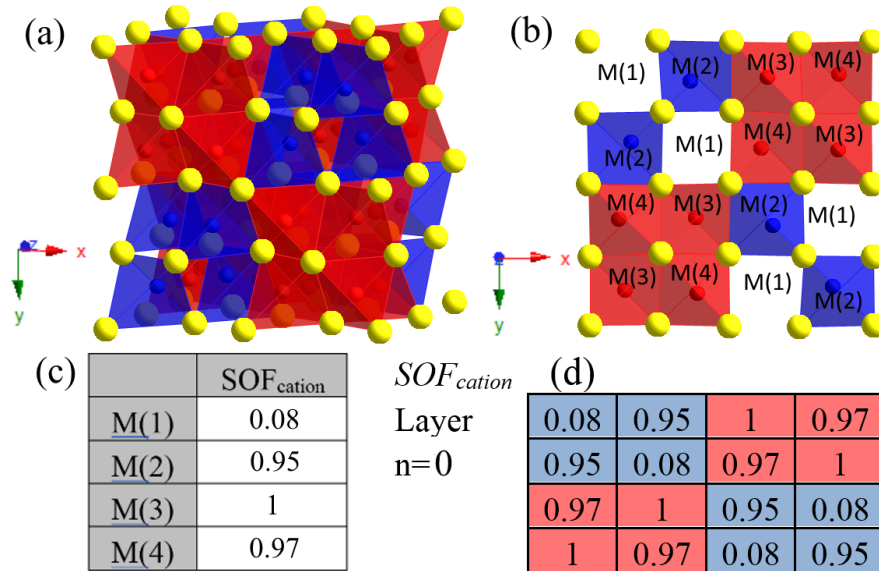


**Figure 4-12** – Diagram depicting the relationship between the structural model, site occupancy data and the site occupancy tables as presented in the following sections. (a) – Perspective view of intermediate bornite with space group  $F23$ , red and blue depict AF or ZB tetrahedra, respectively, yellow spheres - sulphur; (b) – projection view along the  $[001]$  direction for a ‘slice’ of the unit cell between  $c = 0$  to  $1/4$ ; (c) - shows the hypothetical  $SOF_{cation}$  values; and (d) – is the resulting diagram for one ‘slice’,  $c = 0$  to  $1/4$ , in the structure, red and blue depict AF or ZB tetrahedral sites.

### 4.3.3 Results from PDF Analysis of Ambient Temperature Bornite, 4a

Two different starting structural configurations were used during the RMCprofile calculations. Each of these  $8 \times 4 \times 8$  supercells were constructed from different cation ordering models of the  $2a \times 4a \times 2a$  unit cell for 4a bornite, space group  $Pbca$ . The starting models had:

(<sup>A</sup>i) iron ordered in AF sites (Bragg model <sup>A</sup>6) or

(<sup>A</sup>ii) iron ordered in ZB sites (Bragg model <sup>A</sup>4)

For each, calculations were performed with 2 different sets of calculation parameters:

(a) Atom swapping function: Cu and vacancies swap or

(b) Multiple atom swapping functions: Cu and vacancy; Fe and vacancy; Cu and Fe swap

This totals 4 sets of RMCprofile calculations for the ambient temperature phase,  $^A i-a$ ,  $^A i-b$ ,  $^A ii-a$  and  $^A ii-b$ . The two starting models were chosen because: ( $^A i$ ) the Bragg-diffraction model provided the ‘best’ fit after Rietveld analysis; ( $^A ii$ ) the Bragg-diffraction model gave a less-good fit to the data but provided a substantially different starting point for the calculation.

For the final models where swapping function ( $b$ ) was used, the difference curves are near identical, the fit of  $^A i-b$  to each data set is shown in Figure 4-13. In contrast, the final model from calculations  $^A ii-a$  showed a poorer fit to the experimental data. A plot of the difference curves is provided in Figure 4-14 as a visual guide for the difference in fit for each of the resulting structural models. Calculations using parameters,  $^A i-b$  and  $^A ii-b$ , provided a strikingly similar final model and fit to the experimental data. The attainment of this common final model suggests that a reliable representation of the short-range ordering within the structure is achieved. Thus, the resulting structural models,  $^A i-b$  and  $^A ii-b$  are discussed in the following section.

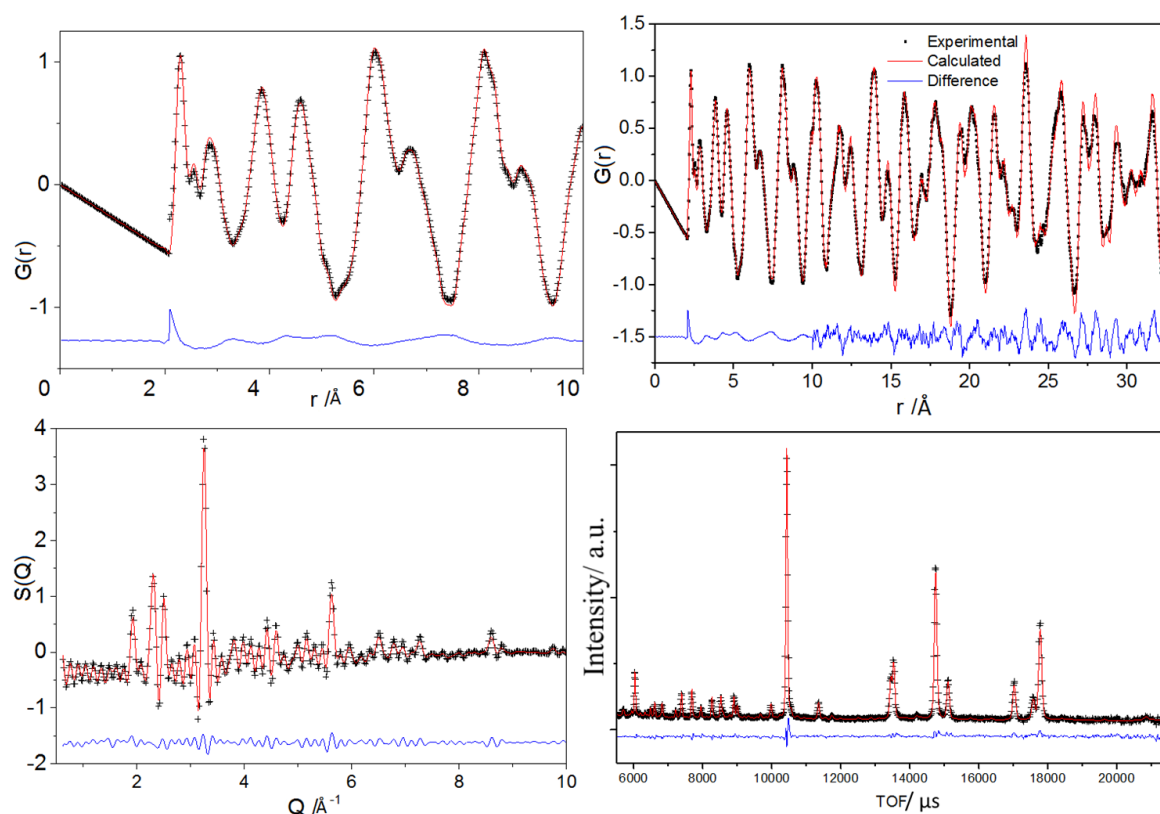


**Figure 4-13** - Difference profiles for  $G(r)$ ,  $S(Q)$  & Bragg diffraction for the room temperature data and the calculations run using starting parameters,  $^A i-b$ , constructed from the  $Pbca$  starting model  $^A 6$ . Here the observed, calculated and difference profiles are denoted by crosses, the red solid line and the lower full line, respectively.

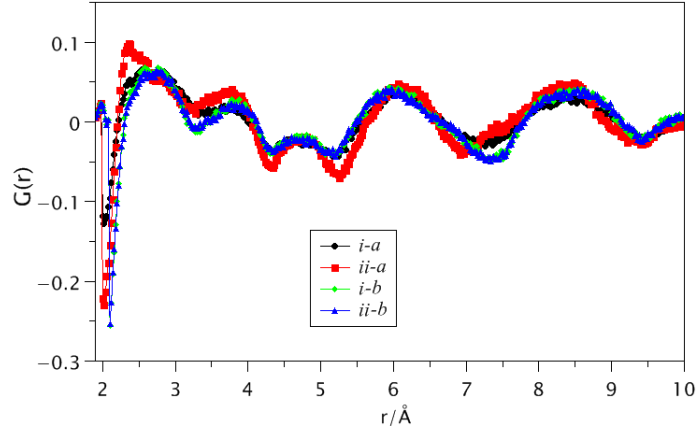


**Figure 4-14** – The difference curves after running RMCprofile for the fit of the respective structural models to the real-space data  $G(r)$ .

### 4.3.3.1 Iron Ordering in Ambient-Temperature Bornite 4a

The observations made in section 4.2.3 led to a conclusion that the iron cations were ordered in the AF sub-cells in 4a phase of bornite. This was consistent with the suggestion that iron orders over AF sub-cells in the low-temperature phase,  $T < 65$  K.<sup>277</sup> The observations made here as a result of RMCprofile analysis using the total scattering data are consistent with the expected iron ordering. The average site occupancy factor for iron over the ZB and AF sites are  $SOF_{Fe} = 0$  and  $SOF_{Fe} = 0.25$ , respectively in the  $8 \times 4 \times 8$  supercell, corresponding to 2 of the 8 cation sites in the AF sub-cells.

More significantly this structural analysis provides new insight to the ordering of iron cations within these sub-cells. In the compressed super-cell – a  $2a \times 4a \times 2a$  unit cell represented by the space group,  $P1$ - there are 128 unique tetrahedral holes. For the structural model to show full iron ordering, all of the iron cations should be contained within 16 cations positions. Each of these tetrahedral sites would have an  $SOF_{Fe} = 1$ . In the resulting models there is strong evidence that iron ordering occurs. In two randomly selected final configurations from the (<sup>A</sup>*i*) and (<sup>A</sup>*ii*) starting models there are: (<sup>A</sup>*i-b*) 11 cation sites with  $SOF_{Fe} > 0.7$  and (<sup>A</sup>*ii-b*) 14 cation positions  $SOF_{Fe} > 0.7$ . The values of the  $SOF_{Fe}$  at each site reveals the iron ordering within the structure. Both final configurations (<sup>A</sup>*i-b* and <sup>A</sup>*ii-b*) show evidence of iron-iron pairs most commonly occupying a face-diagonal geometry within the AF unit cells and thus appear as vertex sharing  $FeS_4$  tetrahedra. In both of these configurations, 4 of the 8 AF sub-cells have very prominent face-diagonal ordering  $SOF_{Fe} > 0.7$ . The remaining iron cations occupy tetrahedral sites in the compressed super cell that would correspond to face-edge pairs of edge-sharing  $FeS_4$  and body-diagonal pairs where  $FeS_4$  are not interconnected in the AF subcell. However,

quantifying the number of these correlations in the compressed supercell is more challenging.

These iron ordering correlations are supported by the peaks observed in the PDF partials of the metal-metal distances. In the lower  $r$  region of the  $G(r)$ , there are 3 distinct peaks for iron-iron geometries that corresponds to vertex-sharing, edge-sharing and body-diagonal pairs. The distance window for each of these are: *ca.*  $2.5 < r/\text{\AA} < 3.25$ ; *ca.*  $3.25 < r/\text{\AA} < 4.25$ ; and *ca.*  $4.25 < r/\text{\AA} < 5.25$ , respectively. In addition, the ZB face-diagonal/vertex-sharing distance window is *ca.*  $2.7 < r/\text{\AA} < 3.5$  (Figure 4-15). The  $G(r)$  for the resulting models from experiments  $^{Ai-b}$  and  $^{Aii-b}$  exhibit a higher intensity for the peaks corresponding to the face-diagonal/vertex-sharing pairs. It is worth noting that, the intensity observed at *ca.*  $3.8 < r/\text{\AA} < 4.3$  and  $4.5 < r/\text{\AA} < 5.0$  would arise from correlations between vertex sharing sub-cells as well as from the correlations within defined sub-cells (PDF partial plots for all sets of calculations are provided in the appendix J, K, L for each temperature, respectively).

The RMC analysis of the data presented here clearly demonstrate that iron cations preferentially order within face-diagonal positions within at least half of the AF sub-cell. This is in contrast to observations made by Martinelli *et al.*<sup>277</sup> Furthermore, these results reveal why there is a difficulty in pinpointing the location of iron within the average structure. In section 4.2.3, the body-diagonal geometry within AF sub-cells was suggested based on the theory that the iron cations may be unlikely to vertex or edge share and this mode of ordering was in line with previous suggestions.<sup>277,278</sup>

Most strikingly, this analysis reveals the possible crystallographic positions that iron should occupy within the average structure and using the space group  $Pbca$ . A comparison of the final structural model from RMC profile analysis can be made with the structural model for the average structure of the  $4a$  phase. The local ordering of iron cations in the RMC structures, to a large extent, obey the symmetry imposed by the unit cell of the average structure with space group  $Pbca$ . A graphical representation of an iron framework constructed from edge-sharing and vertex-sharing iron cations positioned at sites M(1), M(4), M(5) and M(8) only (Table 4-2) is shown in Figure 4-16(a). Here, these Fe sites are given as nodes and are interconnected with lines to show the spatial arrangement of this  $FeS_4$  framework. Each of the iron cations in the compressed  $P1$  unit cell are shown in Figure 4-16(b), they clearly show the same arrangement in space as shown with the overlaid tetrahedral framework. Therefore, the RMC analysis of the structure reveals that the occupied iron sites would correspond to Fe(1,4,5 and 8) in the  $Pbca$  unit cell.

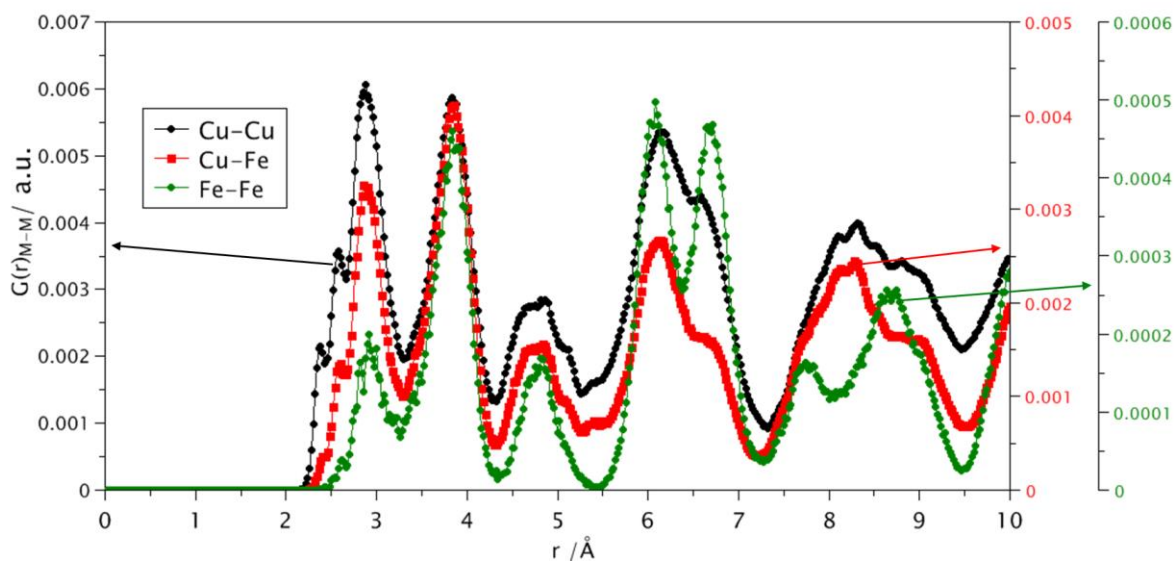


**Figure 4-15** – PDF partials of the Metal-Metal distances in the 4a phase of bornite determined using model  $A_i$  and experiment parameter  $b$  using the average data from 50 final models.

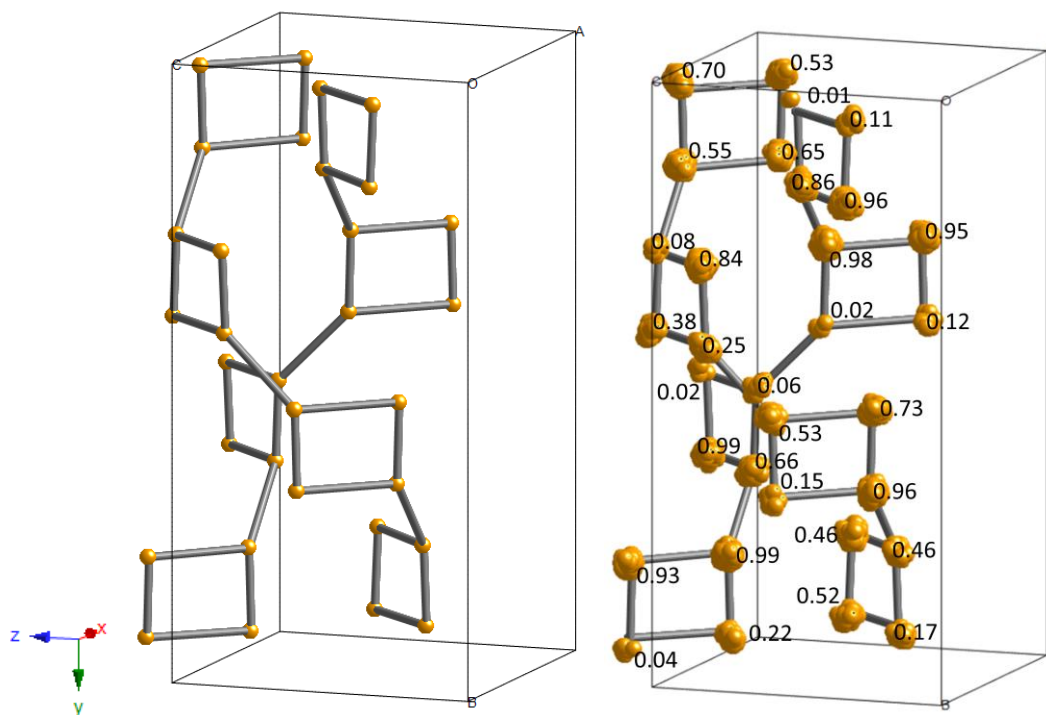


**Figure 4-16** – (a) – Framework of interconnected  $FeS_4$  tetrahedral sites with the central Fe cations given as nodes. Nodes correspond the  $M(1, 4, 5$  and  $8)$  sites in the 4a structure of bornite (sulphur and copper sites are excluded from the diagram) space group  $Pbca$ , Table 4-2.

(b) – All observed iron cations in the compressed  $8 \times 4 \times 8$  supercell from calculation using parameters  $A_i-b$ , with the  $FeS_4$  framework overlaid and SOF values given for each site.

$SOF_{cation}$	(a)				$SOF_{Fe}$	(b)					
Layer		0.99	1	0.88	0.14	Layer		0.11	0	0	0
n=0		1	0.98	0.11	0.95	n=0		0.96	0	0	0
		0.07	0.91	1	0.99			0	0	0.84	0
		0.95	0.13	1	0.99			0	0	0.25	0
		0.99	1	0.12	0.93			0	0.53	0	0
		0.97	1	0.88	0.08			0	0.15	0	0
		0.88	0.11	0.97	1			0	0	0	0.93
		0.11	0.94	0.99	0.98			0	0	0	0.04
$SOF_{cation}$	(a)					$SOF_{Fe}$	(b)				
Layer		1	0.98	0.12	0.96	Layer		0	0.01	0	0
n=1/4		0.99	1	0.84	0.09	n=1/4		0	0.86	0	0
		0.85	0.12	0.98	0.98			0	0	0	0.08
		0.08	0.93	1	0.99			0	0	0	0.38
		1	0.98	0.88	0.17			0.73	0	0	0
		1	0.99	0.07	0.93			0.96	0	0	0
		0.05	0.95	1	0.99			0	0	0.99	0
		0.88	0.16	1	0.99			0	0	0.22	0
$SOF_{cation}$	(a)					$SOF_{Fe}$	(b)				
Layer		0.14	0.91	0.98	1	Layer		0	0	0	0.7
n=1/2		0.95	0.07	0.99	1	n=1/2		0	0	0	0.55
		0.97	1	0.95	0.14			0	0.98	0	0
		1	1	0.14	0.9			0.01	0.02	0	0
		0.93	0.1	1	0.98			0	0	0.06	0
		0.11	0.89	1	0.99			0	0	0.66	0
		1	0.98	0.07	0.84			0.46	0	0	0
		1	0.99	0.97	0.11			0.17	0	0	0
$SOF_{cation}$	(a)					$SOF_{Fe}$	(b)				
Layer		0.94	0.13	0.99	0.98	Layer		0	0	0.53	0
n=3/4		0.05	0.86	0.99	0.96	n=3/4		0	0	0.65	0
		1	0.98	0.07	0.87			0.95	0	0	0
		1	0.98	0.9	0.13			0.12	0	0	0
		0.14	0.95	0.99	0.99			0	0	0	0.02
		0.86	0.12	0.98	1			0	0	0	0.99
		0.99	1	0.9	0.08			0	0.46	0	0
		0.99	1	0.13	0.87			0	0.52	0	0

**Figure 4-17** – Ordering of iron and cations in the  $n \leq a \leq n+1/4$  layers for the collapsed supercell of the ambient temperature phase of bornite. Red – tetrahedral sites in AF sub-cells; Blue – tetrahedral sites in ZB sub-cells; numbers – the SOF at each tetrahedral site.

However, on viewing the structure of the supercell down the z-axis, there are distinct channels with dimensions  $a \times a$  ( $a \approx 5.5 \text{ \AA}$ ) that have low or close to zero occupancy of iron atoms (Figure 4-18). These iron deficient channels could not be modelled using the space group  $Pbca$  and the cation sites M(1), M(4), M(5) and M(8). The  $SOF_{Fe}$  for the M(1, 4, 5, 8) equivalent sites in the compressed supercell  $P1$  were determined and are shown in appendix J. For each  $Pbca$  equivalent site, there are 8 sites in the  $P1$  unit cell. 7 out of the 16 M(1,4) equivalent sites have a  $SOF_{Fe}$  of effectively zero ( $SOF_{Fe} \leq 0.12$ ) for the resulting models from the RMC calculations with parameters  $^A i-b$  and  $^A ii-b$ . These sites correspond to the iron deficient channels seen in the Figure 4-18. This observation suggests that the current model for the  $4a$  average structure of bornite,  $Pbca$ , can effectively model a partially ordered representation of the iron ordering and should use the site occupancy factors:  $SOF_{Fe(1)} = 0.25$ ,  $SOF_{Fe(4)} = 0.25$ ,  $SOF_{Fe(5)} = 0.6$ ,  $SOF_{Fe(8)} = 0.9$ . A new average structural model would be needed to fully describe the iron ordering within the structure of  $4a$  bornite.

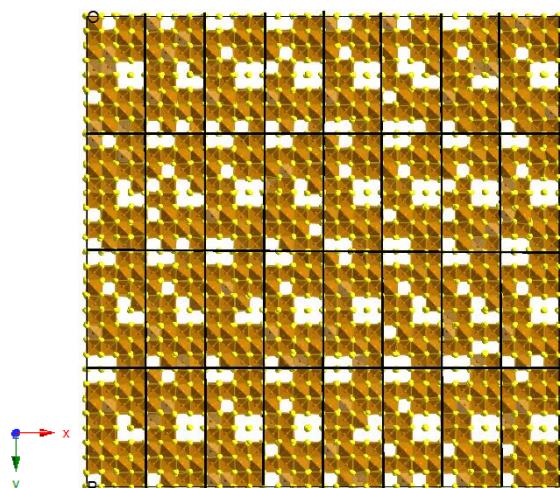


**Figure 4-18** – Projection view along the  $[001]$  direction of the  $FeS_4/FeS_3$  polyhedra in the room-temperature structure of bornite,  $4a$ , as determined from RMC profile analysis using calculation parameters  $^A i-b$  and showing the entire  $8 \times 4 \times 8$  supercell. Orange polyhedra – iron; yellow spheres – sulphur; Black outline –  $2a \times 4a \times 2a$  unit cell sections.

#### 4.3.4 Results from PDF Analysis of Intermediate Bornite, $2a$

Three different starting models were used for the RMCprofile calculations. Each of the  $6 \times 6 \times 6$  supercells were constructed from different cation ordering models of the  $2a \times 2a \times 2a$  unit cell for the intermediate phase of bornite, space group  $F23$ . The starting models had the:

- (<sup>i</sup>) iron ordered in AF sites (Bragg model <sup>1</sup>5<sub>ii</sub>) or
- (<sup>ii</sup>) iron ordered in ZB sites (Bragg model <sup>1</sup>5<sub>iii</sub>) or
- (<sup>iii</sup>) iron disordered over all cation sites (Bragg model <sup>1</sup>5<sub>i</sub>)

For each, calculations were performed with 2 different sets of calculation parameters:

- (a) Atom swapping function: Cu and Vacancies or
- (b) Multiple atom swapping functions: Cu and Vacancy; Fe and Vacancy; Cu and Fe

In total, RMC calculations were performed using 6 sets of calculation parameters, <sup>1</sup>*i-a*, <sup>1</sup>*ii-a*, <sup>1</sup>*iii-a*, <sup>1</sup>*i-b*, <sup>1</sup>*ii-b* and <sup>1</sup>*iii-b*. A comparison of the difference curves for these final configurations does not provide any basis to differentiate between the structural models. The goodness of fit,  $\chi^2$ , from each set of calculations does however provide some insight Figure 4-19. There appears to be some difference in the  $\chi^2$  for each of calculations run with swapping parameter (a). Crucially, the results from runs using swapping parameter (b) generally exhibit a lower  $\chi^2$ . The minimum  $\chi^2$  values are all achieved for experiments with swapping parameter (b).

The resulting configurations for calculations carried out using swapping parameter *b* are used to describe the short-range order of intermediate bornite, an example of the fit to the experimental data is given in Figure 4-20. They each provide a comparable goodness of fit to the experimental data and the resulting structural models from the calculations run with parameters <sup>1</sup>*i-b*, <sup>1</sup>*ii-b* and <sup>1</sup>*iii-b* all provide data that lead to the same conclusions for the structural behaviour (appendix L).

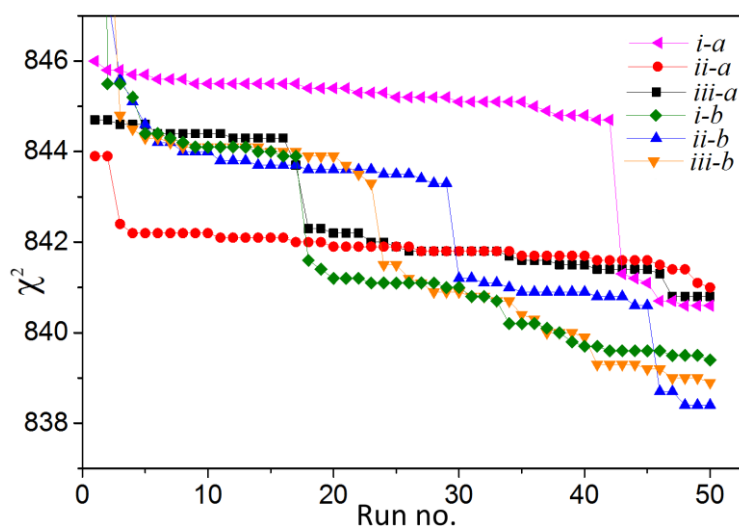


**Figure 4-19** – Final goodness-of-fit parameter for each the RMC calculations run with the six different sets of starting parameters, as differentiated by the 6 different colours, for the intermediate phase of bornite, 2a. Results are sorted in descending order for clarity.

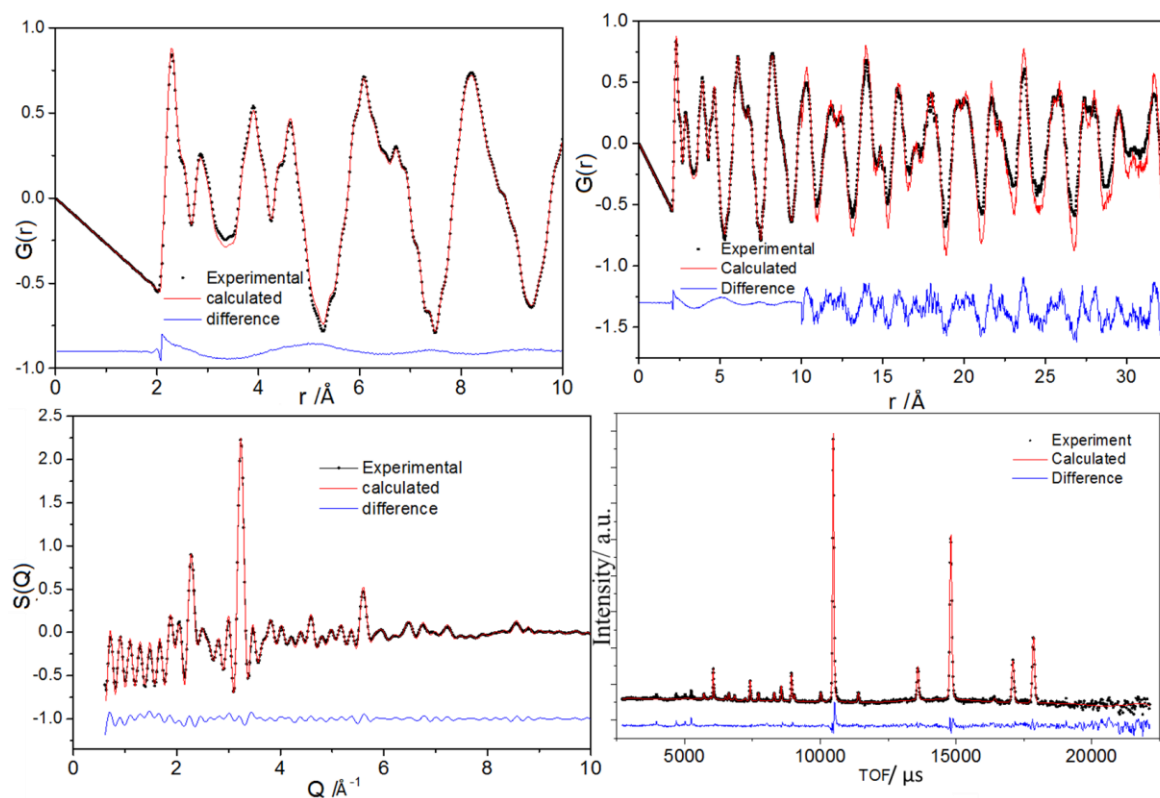


**Figure 4-20-** Difference profiles for  $G(r)$ ,  $S(Q)$  & Bragg diffraction for the neutron total scattering data collected at 500 K for the intermediate form of bornite and with experiment parameters  $^1i$ - $b$ . Here the observed, calculated and difference profiles are denoted by crosses, the red solid line and the lower full line, respectively.

#### 4.3.4.1 Iron Ordering in Intermediate Bornite, $2a$

So far, the structural analyses of intermediate bornite, both in the literature and presented above in section 4.2.5, have not been able to determine whether iron is ordered within the AF or ZB sub-cells.<sup>276</sup> Computational studies have suggested that iron is more likely to order within the AF sub-cell, similar to the  $4a$  phase.<sup>278</sup> The Bragg diffraction experiments above had intended to exploit the advantages offered by neutrons to model the iron within the structure. However, the analysis did not provide a clear preference for any iron ordering configuration, therefore the three models,  $^1i$ - $b$ ,  $^1ii$ - $b$  and  $^1iii$ - $b$ , were employed in total scattering analysis.

The total scattering data collected here along with the RMCprofile analysis allow for further insight to the copper and iron ordering within the  $2a$  structure. The summed site occupancy factors of the copper and iron in each of the tetrahedral holes are consistent with those observed for the average structure and show AF – ZB\* sub-cell ordering (Figure 4-21). Here there are 4 AF type sub-cells where each of the tetrahedral sites have a

$SOF_{cation} = 0.87$  to 1, corresponding to the ‘fully’ occupied AF sub-cells seen in the average structure. In the remaining 4 ZB\*-type sub-cells, each of the tetrahedral sites has a  $SOF_{cation} = 0.44$  to 0.7, which would correspond to the sub-cells that are disordered with cations and vacancies. These AF and ZB\* sub-cells alternate in each direction as previously described (Figure 4-21). So clearly this analysis has reliably modelled the sub-cell ordering in the structure.

Most significantly however, these experiments demonstrate that it is more likely to find iron occupying cation sites within the AF type sub-cells. In the resulting structural models, iron is shown to occupy both ZB\* and AF sub-cells, however, it appears more frequently within the AF sub-cells. This can be expressed in terms of the percentage of all iron found within each sub cell type:

$$\%_{Fe}^{sub-cell} = \frac{\frac{1}{32} \sum_{i=32}^{sub-cell} SOF_{Fe}}{\frac{1}{32} \sum_{i=32}^{sub-cell} SOF_{cation}} \quad (4-2)$$

Here, ‘sub-cell’ corresponds to AF and ZB\* respectively. For each of the resulting models from experiments  ${}^1i-b$ ,  ${}^1ii-b$  and  ${}^1iii-b$ , similar values for  $\%_{Fe}^{AF}$  and  $\%_{Fe}^{ZB^*}$  were observed and an average between the 3 models gave a  $\%_{Fe}^{AF} = 22$  and  $\%_{Fe}^{ZB^*} = 7.5$ , respectively. This corresponds to *ca.* 82 % of all iron cations occupying the AF sub-cells in the intermediate structure of bornite. This is consistent with the suggestion from Ding *et al.* that iron is more likely to occupy the AF sub-cells.<sup>278</sup> Despite this new insight offered by the compressed supercell of the 2a phase, P1, it provides no clear distinction between edge-sharing, vertex-sharing or body-diagonal pairs of iron within this phase (Figure 4-21).

The PDF partials from the set of calculations with starting parameters  ${}^1i-b$  are shown in Figure 4-22. The intensity over the regions of  $r$  that correspond to edge-sharing, vertex-sharing and body-diagonal pairs shows a strikingly different behaviour to the 4a phase (Figure 4-22). The intensity of the peaks is similar over the regions in the  $G(r)$  plot corresponding to the edge-sharing and vertex-sharing pairs in the 2a phase, suggesting a similar number of these correlations. By contrast, the 4a phase showed a significantly higher number of vertex-sharing iron correlations. There is clearly a change in the ordering between adjacent and next-nearest sub-cells. There are two clearly defined peaks across  $5.5 < r/\text{\AA} < 7.3$  for the 4a phase (Figure 4-15), whilst the same region of the  $G(r)$  plot for the 2a phase shows a single peak (Figure 4-22). This suggests that the iron-iron correlations in the intermediate phase are significantly more disordered. Furthermore, there is a

substantial change in the Cu-Cu correlations at  $r < 2.75 \text{ \AA}$ , this will be investigated in section 4.3.6.

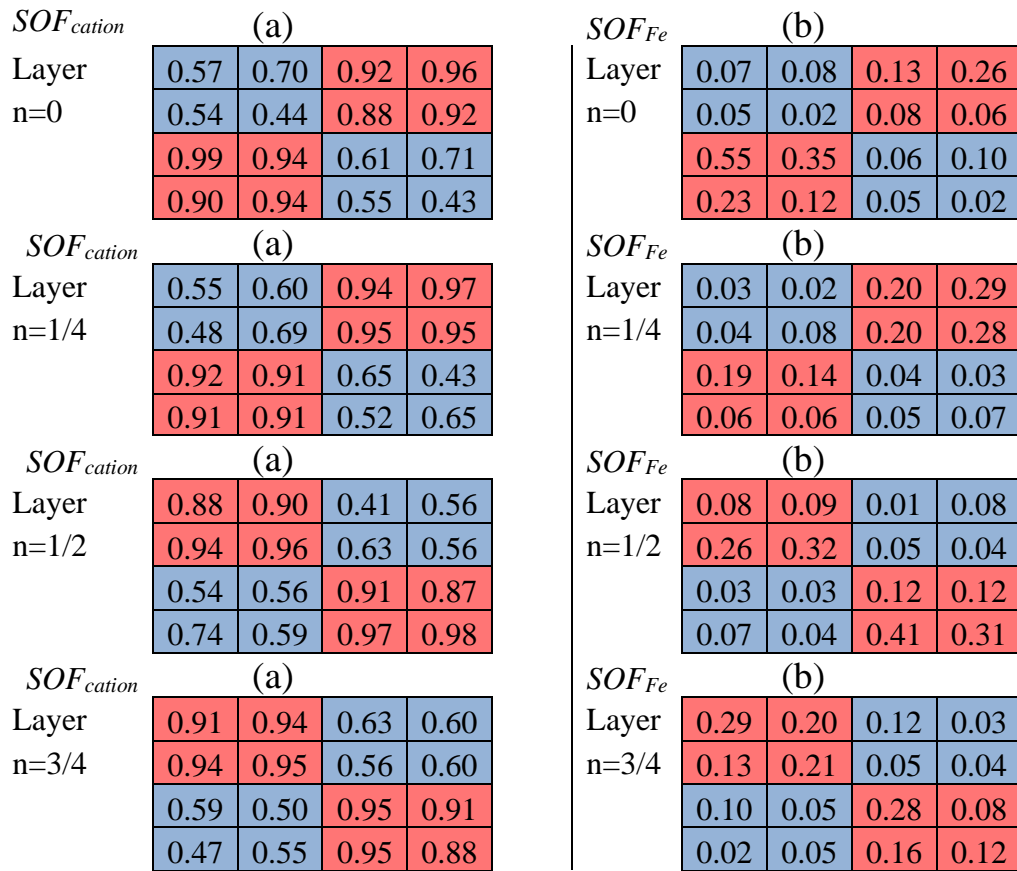


**Figure 4-21** - Cation ordering in the  $n \leq z \leq n + 1/4$  layers for the collapsed RMC large box supercell of the intermediate phase of bornite. Red – tetrahedral sites in AF sub-cells; Blue – tetrahedral sites in ZB sub-cells; numbers – the SOF at each tetrahedral site.

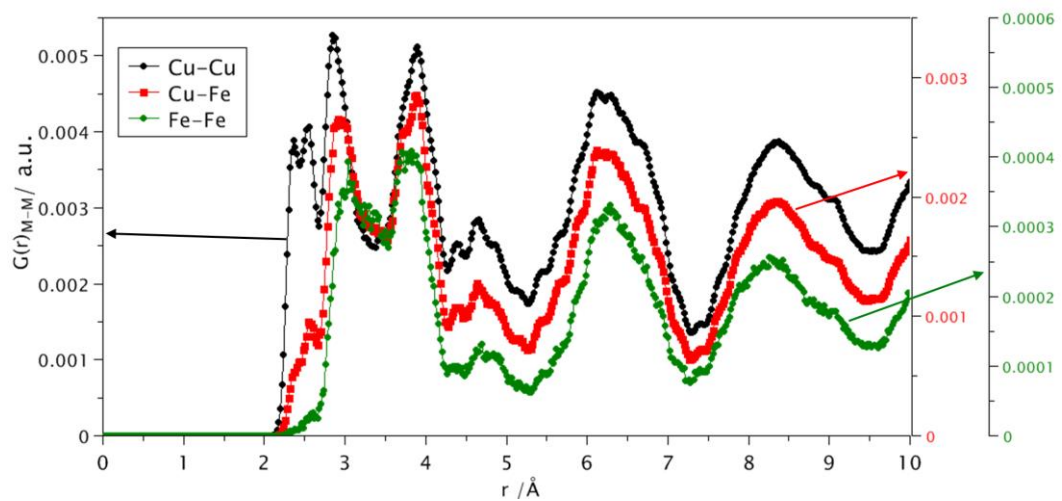


**Figure 4-22** – PDF partials of the Metal-Metal distances in the intermediate temperature phase of bornite determined from experiment <sup>1</sup>i-b.

### 4.3.5 Results from PDF Analysis of High-Temperature Bornite, *a*

The results from neutron diffraction analysis of the high-temperature phase revealed that, as suspected, iron should occupy the tetrahedrally centred cation positions which show little polyhedral distortion. The structural models did not provide any substantial insight towards the Fe-Fe correlations within the high-temperature structure. The disordered and ordered iron models provided a comparable fit to the neutron diffraction data. RMCprofile analysis of the total scattering data collected at 575 K was performed here to understand the local structure in *a* phase of bornite. The starting configurations for the RMC calculations had:

(<sup>H</sup>*i*) iron ordered over the tetrahedral sites (Bragg model <sup>H</sup>5<sub>iii</sub>) or

(<sup>H</sup>*ii*) iron disordered over the tetrahedral sites (Bragg model <sup>H</sup>5<sub>i</sub>)

For each, calculations were performed with 2 different sets of calculation parameters:

(*a*) Atom swapping function: Cu and Vacancies or

(*b*) Multiple atom swapping functions: Cu and Vacancy; Fe and Vacancy; Cu and Fe

As each of the models showed a high degree of disorder, they each provided a good fit to the total scattering data, the fit from one run using calculation parameter <sup>H</sup>*ii*-*b* is shown in Figure 4-23. The resulting structural models from RMC calculations with parameters <sup>H</sup>*i*-*b* and <sup>H</sup>*ii*-*b* showed remarkably similar structural behaviour. Therefore, the resulting data from these calculations are used to describe the *a* phase of bornite. Compression of the 12×12×12 super-cell into the *a*×*a*×*a* unit cell in *P*1 again provides a means to analyse cation ordering within the structure.

The two resulting models from the RMC calculations which used swapping parameter *b* showed some evidence of cation ordering. 4 of the 8 tetrahedral sites had  $SOF_{cation} = 0.78$  to 0.82 and were arranged over the *a*×*a*×*a* cell such that each of the tetrahedra are vertex-sharing. The remaining 4 tetrahedral holes had  $SOF_{cation} = 0.69$  to 0.72. This is not a huge deviation from the full disorder which would have  $SOF_{cation} = 0.75$  at each site. Meanwhile the results from the Rietveld analysis using the *F*23 model showed full disorder *ca.*

$SOF_{cation} = 0.75$ .

The PDF partials (Figure 4-24) provide some insight toward the iron-iron geometries in the high temperature structure. Similar behaviour to the intermediate *2a* phase is observed for the iron correlations in the *a* phase. There are peaks in intensity in the  $G(r)$  corresponding to vertex-sharing and edge-sharing pairs meanwhile there is not a peak in intensity at *r*

corresponding to distance for body-diagonal geometries. Here, the peak corresponding to the vertex-sharing iron-iron geometry has a slightly higher intensity than that of the edge-sharing peak. This suggests that there are more vertex sharing  $\text{FeS}_4$  tetrahedra than edge sharing  $\text{FeS}_4$  tetrahedra in the high-temperature  $a$  phase of bornite. There do not appear to be any significant iron-iron correlations at length scales larger than  $r > 5 \text{ \AA}$  suggesting that the iron is disordered over the average structure.

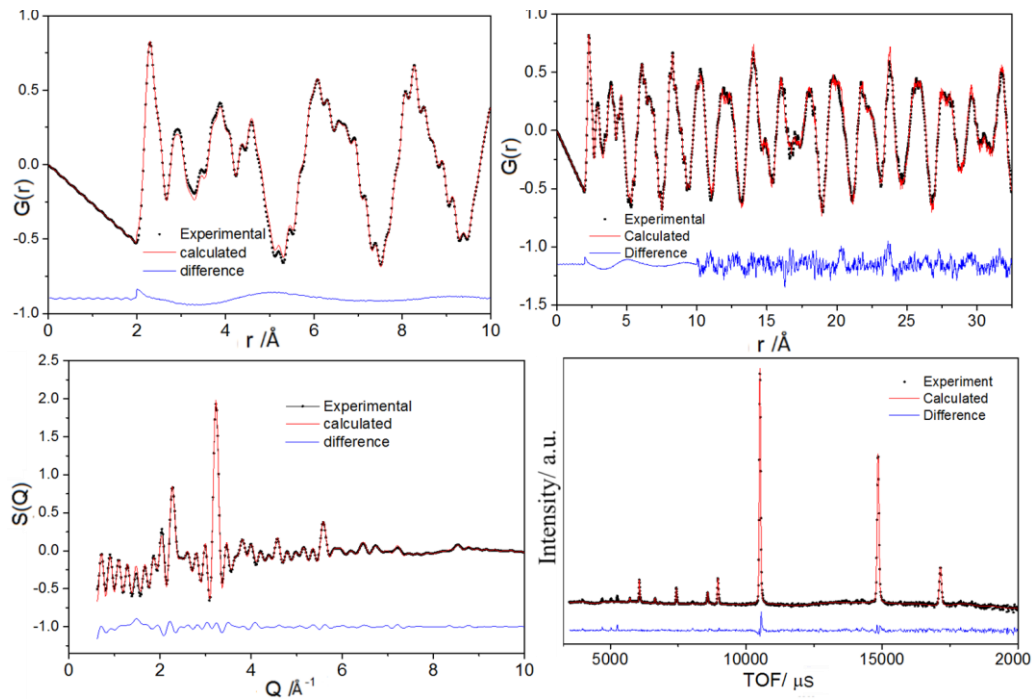


**Figure 4-23** - Difference profiles for  $G(r)$ ,  $S(Q)$  & Bragg diffraction of the total scattering data collected at 575 K for high-temperature bornite and from the starting configuration  $H_{ii-b}$ . Here the observed, calculated and difference profiles are denoted by crosses, the red solid line and the lower full line, respectively.

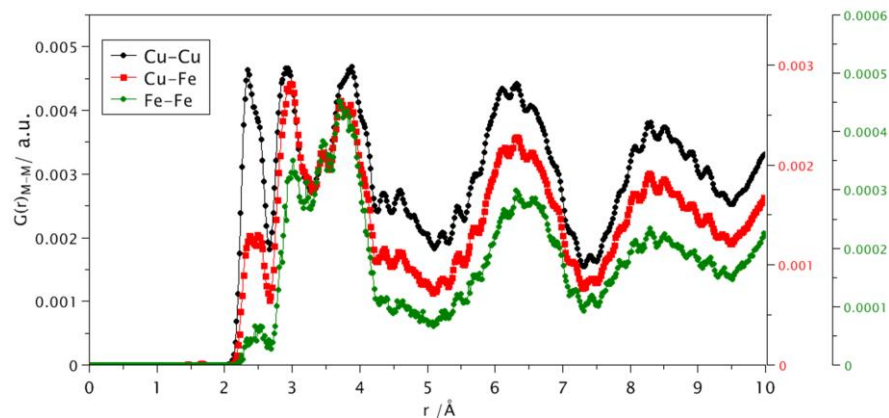


**Figure 4-24** – PDF partials of the Metal-Metal distances in the high-temperature phase of bornite determined from experiment  $H_{ii-b}$ .

### 4.3.6 Change of Local Structure with Temperature

A comparison of the  $G(r)$  at each temperature demonstrates that there is a change in the local structure of bornite with each phase transition. The maxima in peak intensities occur at roughly the same values of  $r$  for the  $4a$ ,  $2a$  and  $a$  phases, i.e.  $r = 3.9$  and  $4.6$  Å (Figure 4-25(b)). The peaks are well defined for the  $4a$  phase and some of the peaks begin to merge with increasing temperature, i.e. between  $5.2 < r/\text{Å} < 7.4$  and  $7.5 < r/\text{Å} < 9.0$ , as the disorder in the structure increases. The results from the RMC analysis reveal changes in the Cu-Cu and Cu-Fe distances observed in each of the phase as well as changes in the M-S distances.

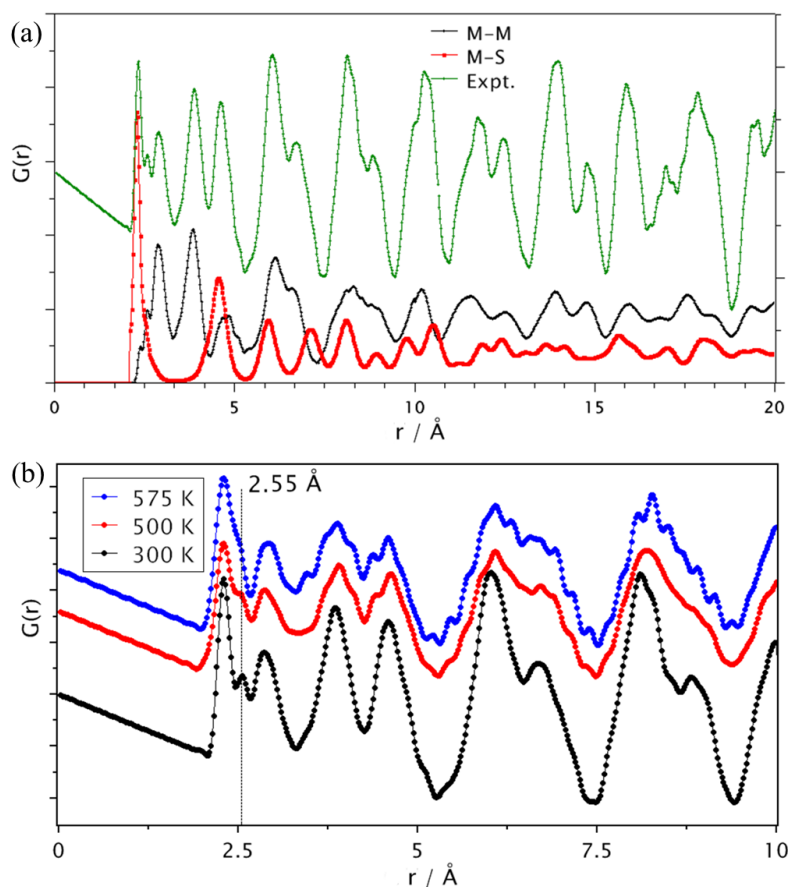


**Figure 4-25** – (a) The contribution of the partial PDFs for (Red) metal-sulphur distances and (Black) metal-metal distances to (Green) the total PDF function of bornite at 300 K. (b) A comparison of the total PDF function of bornite at each temperature recorded, after subtraction of the background contribution.

In the experimental  $G(r)$  data collected at room temperature there is a small peak in intensity at  $r = 2.55$  Å shown by the line in Figure 4-25(b). The PDF partial of the Metal-Metal distances for the room temperature structure exhibits two distinct peaks at  $r = 2.55$  Å

and 2.36 Å (Figure 4-25(b)). In the average structural model, as determined from Rietveld analysis, at room temperature (Table 4-2) the shortest metal-metal distance is observed for cations occupying edge sharing MS<sub>4</sub> tetrahedra. These bond distances are shortest when one of the tetrahedra shows considerable distortion (e.g. Cu(8)-Cu(6) = 2.68 Å and Cu(6) is a distorted tetrahedron, Figure 4-6). The observation of intensity at  $r < 2.6$  Å would therefore correspond to cations in edge-sharing tetrahedra where both sites show considerable trigonal distortion.

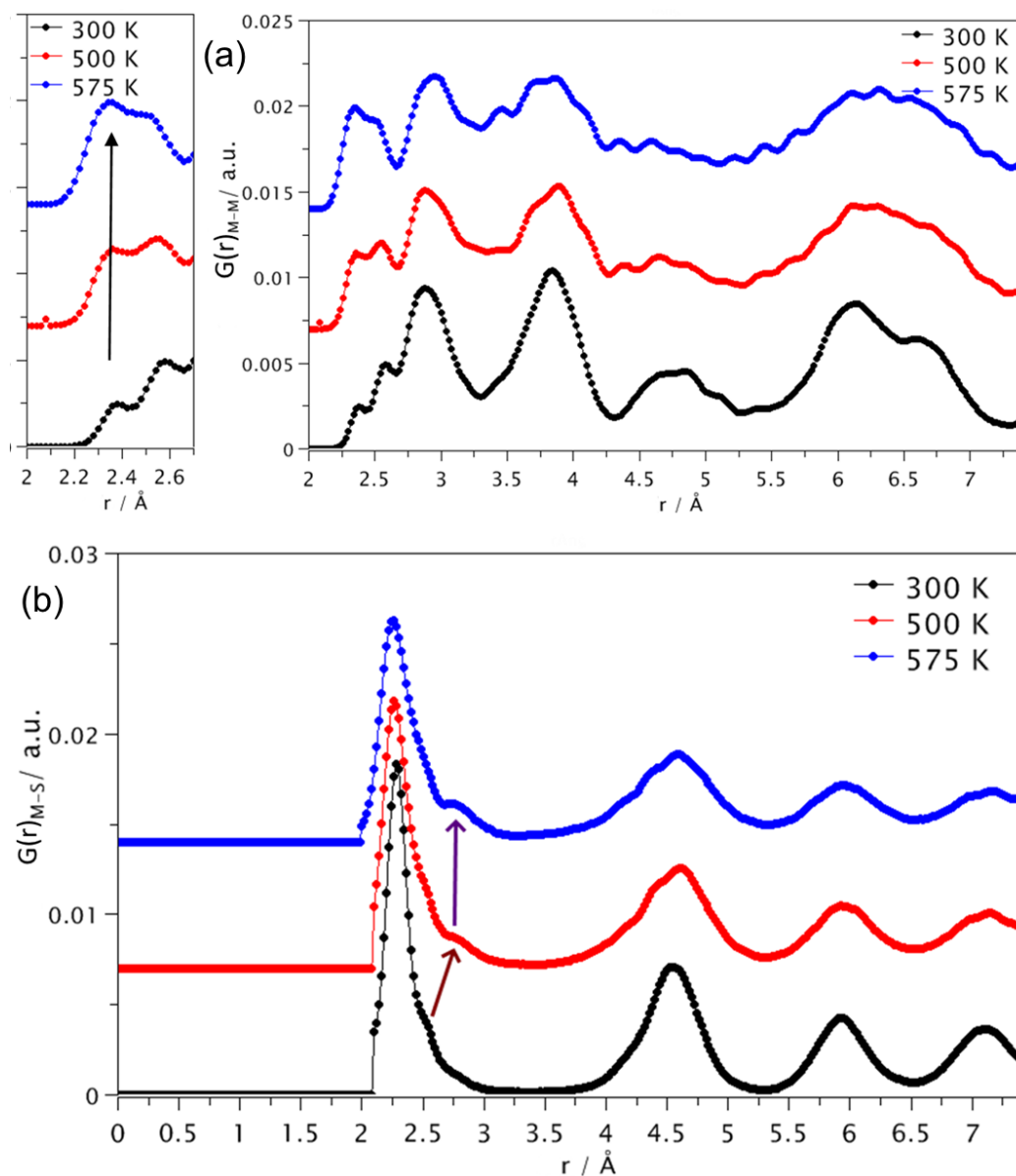


**Figure 4-26** – PDF partials for (a) the Cu-Cu distances and (b) the Cu-S distances to show the changes with increasing temperature.

Interestingly, in the PDF partials of the M-M distances, there is an intense peak observed at  $r=2.36$  Å for the *a* phase (Figure 4-26). Metal-metal bond distances of d<sup>10</sup>-d<sup>10</sup> copper

cations are known to exist between  $2.35 < r_{\text{Cu-Cu}}/\text{Å} < 2.9$ ,<sup>284</sup> and the van der Waals distance of Cu-Cu in copper metal is  $r_{\text{Cu-Cu}} = 2.56 \text{ Å}$ . The individual PDF partials show that these metal-metal interactions are observed frequently between two copper atoms and very rarely between two iron atoms for each of the structural phases (Figure 4-15, Figure 4-22, Figure 4-24). These very short copper-copper distances indicate that there are relatively strong metal-metal interactions within in the  $2a$  and  $a$  phases. Furthermore, the intensity of this peak at  $G(r) = 2.36 \text{ Å}$  increases with increasing temperature suggesting that these interactions occur more frequently with increasing temperature. This is accompanied by an increase in intensity at *ca.*  $G(r) = 2.8 \text{ Å}$  in the M-S partials, which corresponds to the longer bond distance that is usually observed in distorted  $\text{MS}_4$  tetrahedra. It is expected that these metal-metal interactions would have a significant influence on the physical properties of Bornite.

#### 4.4 Conclusions

In summary, the structural analysis of the three structural phases of bornite carried out here reveal new structural information on bornite. This information will contribute toward the development of bornite as a thermoelectric material. More reliable models of the structure will allow for more representative electronic band-structures to be calculated for the material. The Rietveld analysis of the Bragg diffraction data confirmed that the iron cations occupy the AF sub-cells only for the ambient-temperature phase of bornite,  $4a$ . This analysis also showed that each of the cation sites within the ZB sub-cells shows rather substantial structural distortion. RMC profile analysis of the total scattering data allowed for the location of iron within the  $4a$  phase of bornite to be determined for the first time. The relative crystallographic positions of iron cations, within the space group  $Pbca$ , have been determined and defined as M(1, 4, 5 and 8). However, the analysis has revealed that the iron cations are partially ordered over these sites. A complete crystallographic representation of the fully iron-ordered model of bornite would require the use of another space group with lower symmetry.

The Rietveld analysis of the intermediate  $2a$  phase of bornite has led to a new structural model that may be used to describe the ambient-temperature structure of bornite and uses the space group  $F23$ . The analysis outlines the importance of modelling the ZB\* sub-cells as cation-deficient AF types and the necessity of using trigonally-distorted cation sites in the structure. Furthermore, the RMC analysis of the total scattering data presented here indicate that iron cations will occupy both the AF and ZB sites. However, the majority of

the iron cations, *ca.* 80 %, appear within the AF sub-cells. Specific site ordering within AF and ZB sub-cells is not revealed. Thus, the observations here suggest that the iron is not ordered across neighbouring sub-cells (Appendix M). However, local ordering of iron-iron cations is seen within the structure and there are a similar number of face-edge and face-diagonal iron-iron correlations but rather few body-diagonal correlations.

New structural models for the high-temperature phase have also been described using space group  $F23$ . The structural model includes trigonally-distorted cation sites along with a tetrahedrally centred site. Investigation of the iron ordering across these crystallographic sites within the same tetrahedral hole has provided evidence that iron should occupy the less-distorted sites. The RMC analysis of this phase showed that the iron has a local order and exhibits more face-edge and face-diagonal iron-iron correlations than body-diagonal correlations.

The necessity to model the trigonally distorted cation sites in the  $2a$  and  $a$  phases is outlined. The implications of this behaviour on the local structure are revealed by the RMCprofile analysis. With increasing temperature there is an increase in the number of short metal-metal interactions, these appear primarily as Cu-Cu interactions that are expected to occur between edge-sharing tetrahedra. This behaviour will have a significant influence on the electrical and thermal transport properties of bornite.



# Chapter 5 Structure and Thermoelectric Properties of Non-Stoichiometric Bornite

## 5.1. Introduction

In the following sections of this chapter, the composition of bornite was altered systematically in an attempt to improve the thermoelectric performance. The data presented in sections 5.2 and 5.4 have been published in “High Thermoelectric Performance of Bornite through Control of the Cu(II) Content and Vacancy Concentration”, S. Long *et al.*, *Chem. Mater.*, **2018**, 30, 456. This chapter follows directly from the work in chapter 4 on the structural characterisation of the stoichiometric bornite.

Here the influence of sample composition on the transition temperatures, lattice parameters, thermoelectric properties and other structural features is investigated for bornite. X-ray diffraction data of all chemically substituted bornite samples is presented along with variable-temperature neutron diffraction data collected on two selected samples, nominal compositions:  $\text{Cu}_{5.08}\text{Fe}_{0.92}\text{S}_4$  and  $\text{Cu}_{4.96}\text{Fe}_{0.98}\text{S}_4$ . The work encompassed by this chapter aims to enhance the thermoelectric performance of bornite and to identify structural changes that influence the thermoelectric properties.

## 5.2. Experimental Procedure

The elemental powders of copper (99.5%, Sigma-Aldrich), iron (99.9+%, Sigma-Aldrich) and sulphur (flakes, 99.99%, Sigma Aldrich) were combined using an agate pestle and mortar and transferred into a steel milling jar (25 mL). Steel milling balls were added (2 : 5 g, powder : balls, total mass 28 g) and the mixture was sealed under an Ar atmosphere. Consecutive millings (40 hr total;  $2 \times 20$  hr, 500 rpm, 15 min intervals between a reverse in rotation) were interspersed with an agitation of the coagulated powder. The powdered sample was then consolidated using a uniaxial high-temperature high-pressure press under a  $\text{N}_2$  atmosphere (823 K, 90 MPa, 30 min). Sample densities were on the order of > 98% of the theoretical crystallographic density. A list of all samples investigated is provided in Table 5-1.

Powder X-ray diffraction data were collected on pelleted samples of bornite, over the angular range  $10 < 2\theta / ^\circ < 80$ , with a step size of  $0.0079^\circ$ , a scan rate of 1.62 seconds per step and a collection time of 4 hours. Phase analysis was performed using the search and

match function in the DIFFRAC.EVA software.<sup>203</sup> Lattice parameters and impurity phases were confirmed by Le Bail refinement using the GSAS software package.<sup>209</sup>

**Table 5-1** – All bornite samples synthesised and investigated in chapter 5 where  $x$  and  $y$  apply to the formula  $\text{Cu}_{5-x+y}\text{Fe}_{1-y}\text{S}_4$ . The labels refer to the sample in: Red – series 1; Green – series 2; Yellow – series 3; and Blue - series 4.

Series no.	Label	$x$	$y$ (or $z$ )	Nominal Cu(II) content	Nominal Composition
Parent	*	0	0	0	$\text{Cu}_5\text{FeS}_4$
Series 1	●	0.02	0	0.02	$\text{Cu}_{4.98}\text{FeS}_4$
	●	0.04	0	0.04	$\text{Cu}_{4.96}\text{FeS}_4$
	●	0.06	0	0.06	$\text{Cu}_{4.94}\text{FeS}_4$
	●	0.1	0	0.1	$\text{Cu}_{4.9}\text{FeS}_4$
	●	0.12	0	0.12	$\text{Cu}_{4.88}\text{FeS}_4$
	●	0.16	0	0.16	$\text{Cu}_{4.84}\text{FeS}_4$
Series 2	●	0	0.02	0.04	$\text{Cu}_{5.02}\text{Fe}_{0.98}\text{S}_4$
	●	0	0.04	0.08	$\text{Cu}_{5.04}\text{Fe}_{0.96}\text{S}_4$
	●	0	0.06	0.12	$\text{Cu}_{5.06}\text{Fe}_{0.94}\text{S}_4$
	●	0	0.08	0.16	$\text{Cu}_{5.08}\text{Fe}_{0.92}\text{S}_4$
	●	0	0.1	0.2	$\text{Cu}_{5.1}\text{Fe}_{0.9}\text{S}_4$
Series 3	●	0.06	0.02	0.1	$\text{Cu}_{4.96}\text{Fe}_{0.98}\text{S}_4$
	●	0.06	0.032	0.124	$\text{Cu}_{4.972}\text{Fe}_{0.968}\text{S}_4$
	●	0.06	0.04	0.14	$\text{Cu}_{4.98}\text{Fe}_{0.96}\text{S}_4$
	●	0.06	0.06	0.18	$\text{Cu}_5\text{Fe}_{0.94}\text{S}_4$
	●	0.06	0.1	0.26	$\text{Cu}_{5.04}\text{Fe}_{0.9}\text{S}_4$
Series 4	■	-0.02	0	0	$\text{Cu}_{5.02}\text{FeS}_4$
	■	-0.04	0	0	$\text{Cu}_{5.04}\text{FeS}_4$
	■	-0.06	0	0	$\text{Cu}_{5.06}\text{FeS}_4$
	■	-0.08	0	0	$\text{Cu}_{5.08}\text{FeS}_4$

Variable-temperature neutron powder diffraction data were collected using the low-temperature furnace on the POLARIS diffractometer at the ISIS neutron facility. The powdered samples (*ca.* 3.5 g) were loaded into 10 mm fused silica ampoules with 1 mm thick walls then sealed at a pressure of  $10^{-3}$  mbar. Data were collected first at a temperature close to room-temperature and then at higher temperatures in increments of *ca.* 15-30 K. Each temperature increment had a collection time of *ca.* 240  $\mu\text{A}$ . Data were collected on an empty silica ampoule (from the same batch of glass tubing) at temperatures of 40 and 185 K. These were contained in vanadium cans during the diffraction experiment. The data from three detector banks,  $150^\circ$ ,  $90^\circ$  and  $50^\circ$  (5, 4 and 3), were used to provide a fit to the neutron diffraction data. The MANTID analysis software package was used to focus the

diffraction data and remove the contribution from the glass ampoule.<sup>210,285</sup> The GSAS software package was used to perform Rietveld analysis on the processed data. The results from these refinements are discussed in section 5.4.<sup>272</sup>

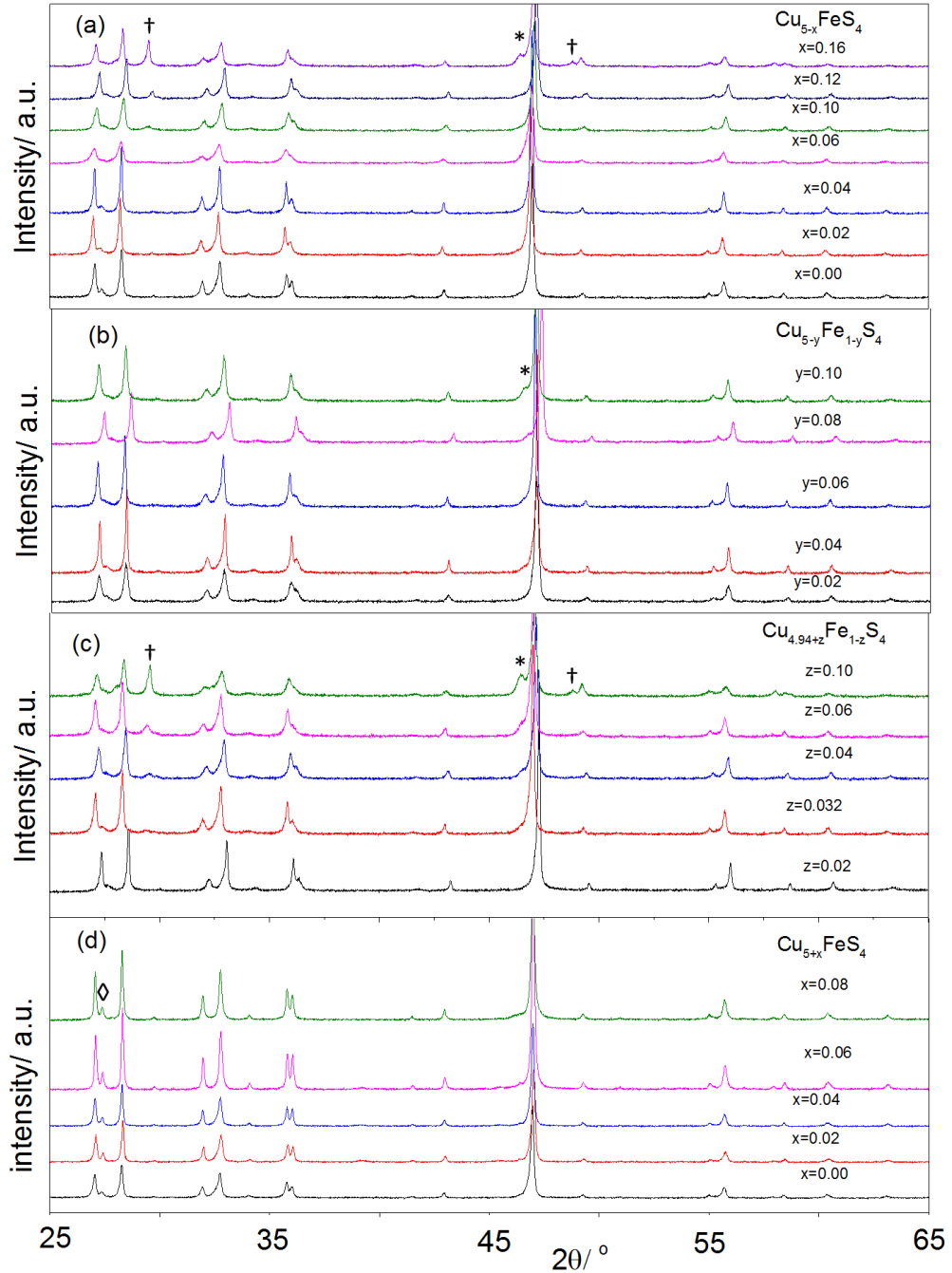


**Figure 5-1** - Powder X-ray diffraction patterns for all bornite samples shown in table 1 and in (a) Series 1:  $\text{Cu}_{5-x}\text{FeS}_4$ , (b) Series 2:  $\text{Cu}_{5+y}\text{Fe}_{1-y}\text{S}_4$ , (c) Series 3:  $\text{Cu}_{4.94+z}\text{Fe}_{1-z}\text{S}_4$  and (d) Series 4:  $\text{Cu}_{5+x}\text{FeS}_4$  over the angular range  $25 \leq \theta/^\circ \leq 65$ . † corresponds to reflections for the  $\text{CuFeS}_2$  impurity; \* corresponds to reflections from the  $\text{Cu}_{1.8}\text{S}$  impurity; and ◇ highlights a reflection, indexable in space group  $Pbca$  of the majority bornite phase, that is observed in series 4 only,  $\text{Cu}_{5+x}\text{FeS}_4$ .

### 5.3. Sample Composition and Phase Analysis

#### 5.3.1. Phase Analysis of Powder X-ray Diffraction Data

Each of the samples in the four series show either a single phase or majority phase of bornite, indexed using the *Pbca* space group and with comparable unit-cell parameters. The presence of impurity phases is apparent in a number of samples. In each series, a greater degree of deviation from  $\text{Cu}_5\text{FeS}_4$  is accompanied by higher concentrations of impurity phases, suggesting limits to the solid solution. Diffraction peaks from these impurity phases can be assigned to a chalcopyrite-type phase and a digenite-type phase. Nominally these should have compositions  $\text{CuFeS}_2$  and  $\text{Cu}_{1.8}\text{S}$ , respectively.<sup>146</sup>

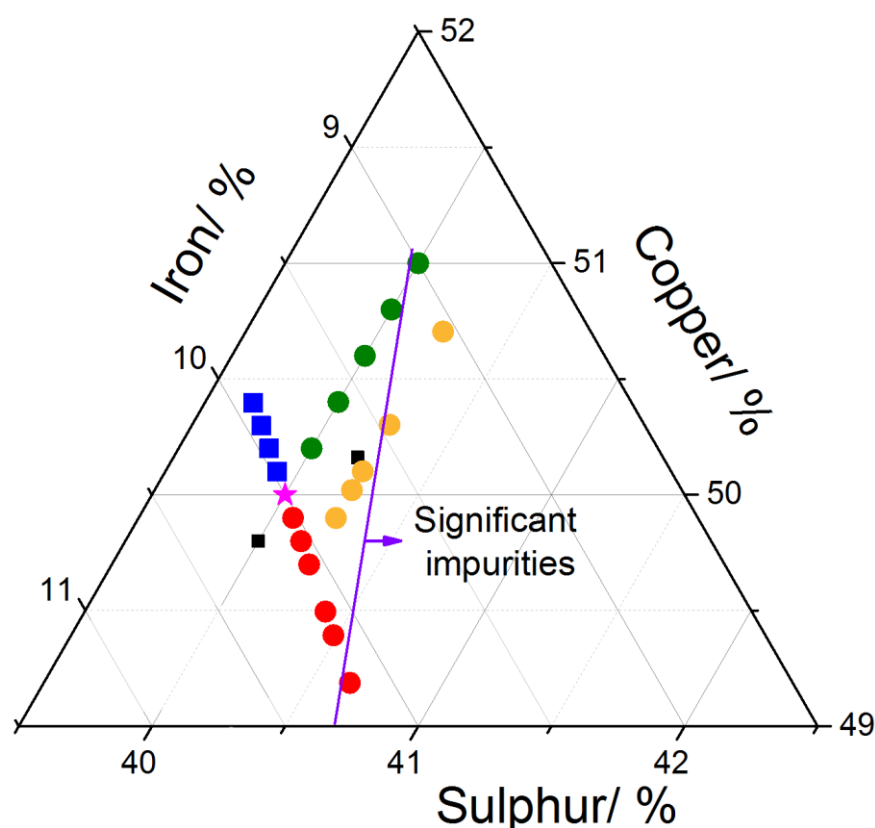


**Figure 5-2** – Ternary diagram showing all nominal sample compositions synthesised. Pink star- Parent phaser; Red – Series 1; Green – Series 2; Yellow – series 3; Blue – Series 4 and black – compositions of samples in the ICSD.

For samples in series 1,  $\text{Cu}_{5-x}\text{FeS}_4$ , the chalcopyrite- and digenite-related reflections are evident in samples with composition,  $x > 0.1$ . Increasing values of  $x$  is concurrent with increasing concentration of the impurity phases (Figure 5-1(a)). Samples with increasing values of  $x$ , thus an increase of the total copper content, in series 4  $\text{Cu}_{5+x}\text{FeS}_4$ , show no evidence for the formation of these impurity phases up to  $x = 0.08$  (Figure 5-1(d)). For all samples with composition  $\text{Cu}_{5+x}\text{FeS}_4$ , an additional peak is observed at *ca.*  $2\theta = 27.4^\circ$ , this

can be indexed on the *Pbca* unit cell and is represented by a diamond on the diffraction pattern. This reflection is absent for samples in the series 1 and 2,  $\text{Cu}_{5-x}\text{FeS}_4$  and  $\text{Cu}_{5+y}\text{Fe}_{1-y}\text{S}_4$ . This suggests there may be some structural differences between the cation-rich samples and all other samples. This does not appear to impact on the unit-cell size however as all samples with composition  $\text{Cu}_{5-x}\text{FeS}_4$  ( $-0.08 \leq x \leq 0.16$ ) show a variation of  $\Delta a_p < 1\%$  in the lattice parameters across these two related series (see e-appendix for each series).

For samples in series 2,  $\text{Cu}_{5+y}\text{Fe}_{1-y}\text{S}_4$ , no chalcopyrite peaks are present across the series. Trace amounts of digenite become evident in samples at  $y > 0.08$  (Figure 5-1(b)). This is supported by a signature in the DSC data where there is an endotherm peak at *ca.* 50 K, representative of the phase transition in digenite. This series also shows that the lattice parameters are insensitive to the sample composition.

The samples in series 3, with composition  $\text{Cu}_{4.94+z}\text{Fe}_{1-z}\text{S}_4$ , exhibit single-phase behaviour at low levels of additional iron for copper substitution. Reflections for two impurity phases, digenite and chalcopyrite, becoming evident at  $z > 0.4$ . Additionally, the DSC curve shows evidence of the digenite impurity when  $z = 0.1$ . Consistent with series 1,  $\text{Cu}_{5-x}\text{FeS}_4$ , and the chalcopyrite peaks in the diffraction pattern become more intense with increasing levels of chemical substitution. Meanwhile, the orthorhombic unit-cell parameters are insensitive to changes in the cation concentration.

From this analysis, solid-solution limits can be suggested for samples of bornite with altered stoichiometry. Here a complex dependence between the S:Cu:Fe content appears to exist, where increasing the total copper content and/or decreasing the total cation content will lead to the formation of impurities. The purple line on the ternary diagram represents the solid-solution limit (Figure 5-2). The observations made here indicate that increasing the total atom percentages beyond this limit coincides with a significant increase in the formation of impurities.

Grguric *et al.* performed an extensive study into the phase behaviour of generally cation-rich species of synthetic and natural bornite samples with different compositions. In many of the samples investigated there, the presence of impurity Cu-S containing mineral phases such as chalcocite, djulerite and digenite, were identified. Significant levels of impurity phases are found in synthetic samples with a sulphur content of less than 39% and/or an iron content of more than 10% for sulphur-deficient specimens, thus outlining the solid-solution limits for cation-rich samples of bornite.<sup>286</sup>

### 5.3.2. Composition and its Influence on Phase Transition Temperatures

Elemental analysis of the samples was performed on selected pelletized samples (Table 5-2). Energy Dispersive X-ray (EDX) spectroscopy was used to determine the constituent elements within the sample. The EDX spectrum shows the presence of only the expected elements within the sample (example in Figure 5-3). This allows comparison between nominal and actual Cu:Fe ratios in the samples. The stoichiometric sample shows an excellent correlation to the EDX data. The substituted samples show a small deviation from the nominal values whilst still displaying reasonable agreement to the expected values.

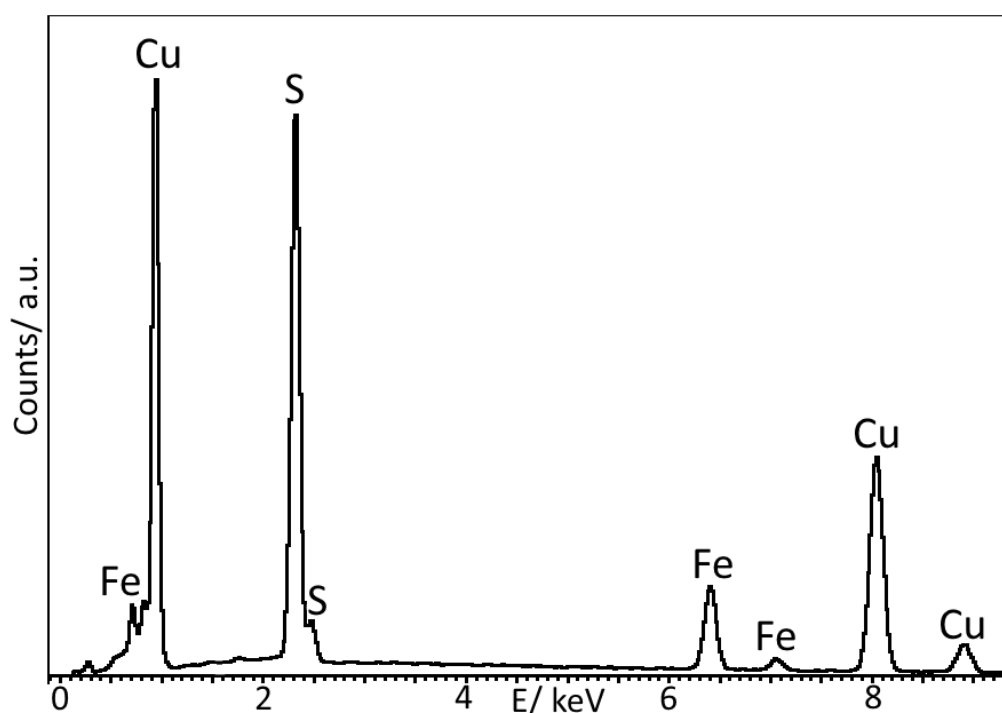


**Figure 5-3** – Example EDX spectrum, collected on a sample of  $\text{Cu}_5\text{FeS}_4$ .

**Table 5-2** – Select sample compositions determined from EDX analysis compared to their nominal composition.

Nominal	Experimental
$\text{Cu}_5\text{FeS}_4$	$\text{Cu}_{5.00(2)}\text{Fe}_{0.99(1)}\text{S}_4$
$\text{Cu}_{4.94}\text{FeS}_4$	$\text{Cu}_{4.91(2)}\text{Fe}_{1.00(1)}\text{S}_4$
$\text{Cu}_{4.9}\text{FeS}_4$	$\text{Cu}_{4.85(2)}\text{Fe}_{1.05(1)}\text{S}_4$
$\text{Cu}_{5.06}\text{FeS}_4$	$\text{Cu}_{5.14(1)}\text{Fe}_{0.91(1)}\text{S}_4$
$\text{Cu}_{5.08}\text{Fe}_{0.92}\text{S}_4$	$\text{Cu}_{5.06(2)}\text{Fe}_{0.94(1)}\text{S}_4$
$\text{Cu}_{4.972}\text{Fe}_{0.968}\text{S}_4$	$\text{Cu}_{4.89(2)}\text{Fe}_{1.02(1)}\text{S}_4$

Heat capacity data for some naturally occurring and synthetic samples of bornite have been published previously by Grguric *et al.*<sup>280,286</sup> The  $4a \rightarrow 2a$  phase-transition temperature,  $T_1$ , of non-stoichiometric bornite, on heating, is reported between  $T_1 = 425 - 480$  K, with hysteresis of,  $\Delta T_1 \approx 40$  K. The  $2a \rightarrow a$  phase-transition temperature,  $T_2$ , on heating, is reported between,  $T_2 = 512 - 546$  K, with hysteresis  $\Delta T_1 \approx 3.5$  K. In this work, DSC data have been collected on samples in the series 1 to 4,  $\text{Cu}_{5\pm x}\text{FeS}_4$ ,  $\text{Cu}_{5+y}\text{Fe}_{1-y}\text{S}_4$  and  $\text{Cu}_{4.94+z}\text{Fe}_{1-z}\text{S}_4$ . The results are largely consistent with the observations made on other natural and synthetic samples.<sup>280,286</sup>

The transition temperatures have been calculated from the temperature vs. heat flow curves that were recorded on both heating and cooling across the temperature range  $T = 273 - 573$  K (e-appendix for each series). The  $T_1$  transition has been calculated from the maximum of the peak corresponding to the transition, the  $T_2$  transition has been determined by the change in slope (Figure 5-4(a)).

A deviation in both the vacancy content and total cation content is observed for the samples with formula  $\text{Cu}_{5-x}\text{FeS}_4$ ,  $x = -0.08$  to  $0.16$ . The  $T_2$  transition temperature shows little dependence on the total cation vacancy concentration up to  $x \leq 0.1$ , above which significant impurity phases develop and  $T_2$  drops significantly. The  $T_1$  shows a slight decrease with increasing  $x$  when  $x \geq -0.04$  (Figure 5-4(b)).

Samples with formula  $\text{Cu}_{5+y}\text{Fe}_{1-y}\text{S}_4$ ,  $x = 0$  to  $0.1$ , show an increased Cu:Fe ratio and a fixed vacancy concentration. Both  $T_1$  and  $T_2$  show a similar dependence on the Cu:Fe content in these bornite samples. With the phase-transition temperatures generally decreasing with increasing  $y$ , this relationship is more pronounced in the  $T_2$  transition with variation of 20 K across the series (Figure 5-4(c)).

The thermal behaviour of samples in the series  $\text{Cu}_{4.94+z}\text{Fe}_{1-z}\text{S}_4$  show little variation of  $T_2$  when  $z \leq 0.4$ . A substantial drop in  $T_2$  occurs at values of  $z > 0.4$ , coincident with the formation of the chalcopyrite-type phase. This trend is observed in the series  $\text{Cu}_{4.94+z}\text{Fe}_{1-z}\text{S}_4$  and  $\text{Cu}_{5-x}\text{FeS}_4$  and indicates that the coexistence of phases has a more marked effect on the transition temperature  $T_2$  than the Cu:Fe ratio or vacancy concentration within bornite itself (Figure 5-4(d)). These observations are consistent with data presented by Grguric *et al.* who report values of  $T_2 < 520$  K only in the presence of impurity phases.<sup>286</sup>

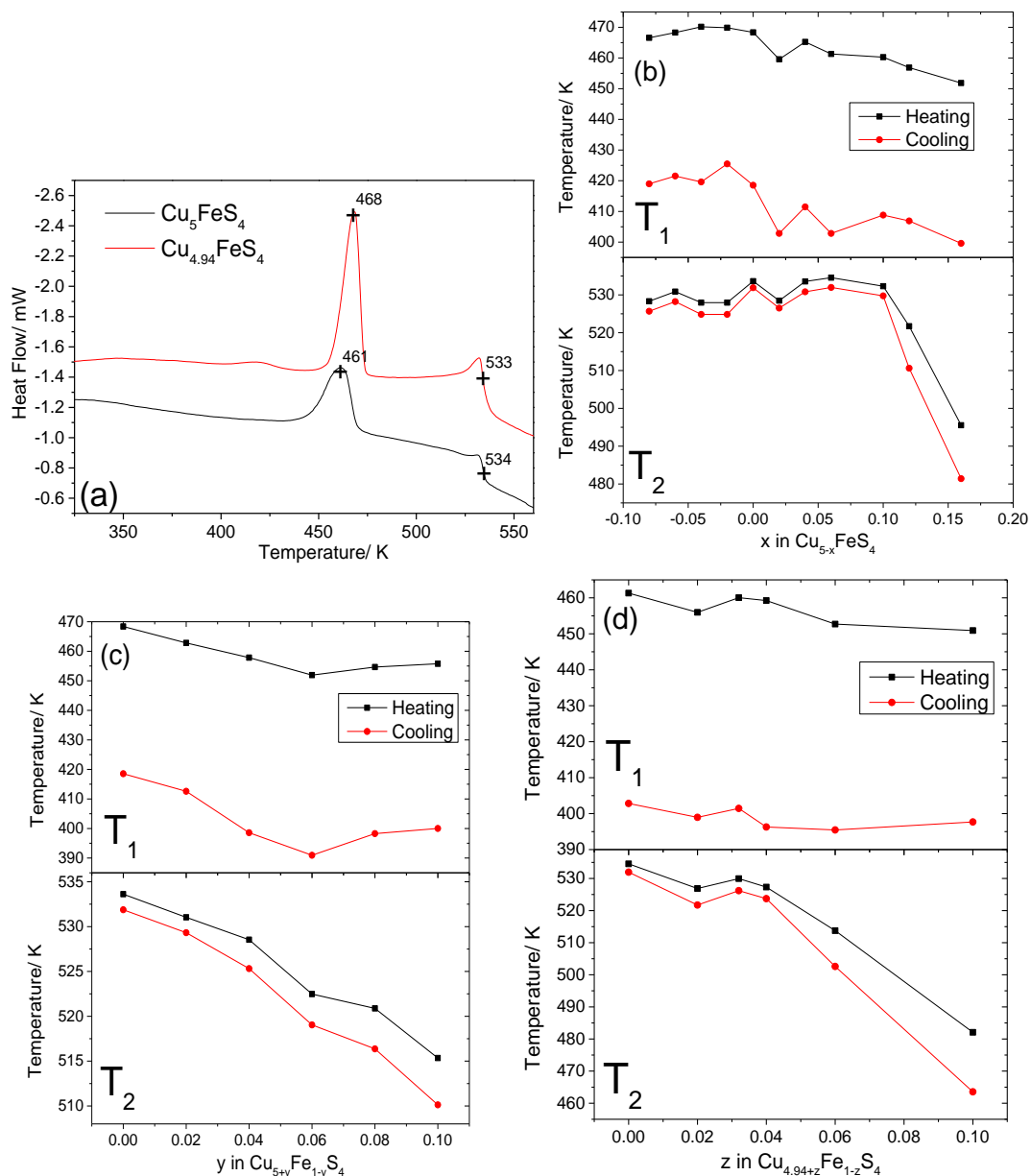


**Figure 5-4** – (a) – heat flow curves from two select samples, showing the two transitions and how the transition temperatures were extracted,  $T_1$  and  $T_2$  given by a cross on the curve. (b, c, d) Phase transition temperatures on heating and cooling for the  $T_1$  and  $T_2$  transitions for samples in the series: (b) Series 1 and 4:  $\text{Cu}_{5-x}\text{FeS}_4$ ; (c) Series 2:  $\text{Cu}_{5+y}\text{Fe}_{1-y}\text{S}_4$  and (d) Series 3:  $\text{Cu}_{4.94+z}\text{Fe}_{1-z}\text{S}_4$ .

#### 5.4. Variable Temperature Neutron Diffraction of Non-Stoichiometric Bornite

Neutron diffraction data collected on the stoichiometric sample  $\text{Cu}_5\text{FeS}_4$ , were presented in the previous chapter and this includes data from measurements performed at three different temperatures. The results from that experiment provide a benchmark to compare

observations made here on the samples with nominal composition  $\text{Cu}_{4.96}\text{Fe}_{0.98}\text{S}_4$  (from Series 3) and  $\text{Cu}_{5.08}\text{Fe}_{0.92}\text{S}_4$  (from Series 2).

#### **5.4.1. Structural Refinement Constraints and Parameters**

The analysis of the cation ordering in each of the structural phases of bornite was determined in chapter 4. Here, the resulting structural models from those Rietveld analyses are used. Namely, the models labelled  $^A5$ ,  $^I5_i$  and  $^H5_{iii}$  provided starting models for refinement using the ambient-, intermediate- and high-temperature neutron diffraction data, respectively.

Initial structural refinements were carried out at a single temperature representative of each phase. The resulting model was used for subsequent refinements of the diffraction data at each of the temperatures depending on the structural phases,  $4a$ ,  $2a$  or  $a$ , present.

The sample with composition  $\text{Cu}_{4.96}\text{Fe}_{0.98}\text{S}_4$  shows single-phase behaviour in the ambient- and intermediate-temperature phase region, whilst there is the evolution of a chalcopyrite-type phase at high temperature. This behaviour at high temperature has been observed in previous temperature-dependent diffraction experiments by Kumar *et al.*<sup>159</sup> The sample with composition  $\text{Cu}_{5.08}\text{Fe}_{0.92}\text{S}_4$ , shows a chalcocite/digenite-type secondary phase in the ambient- and intermediate-temperature diffraction patterns. However, this is only observed as a shoulder on a number of the peaks and the DSC data of a sample with the same composition does not include the signature of this secondary phase.

The secondary phases are present in small quantities of  $wt\% < 10\%$ , and the exact chemical compositions of these impurity phases is not known. Therefore, it has been assumed that there is no influence from the impurity on the total cation content in the bornite phases. In addition, the nominal cation content of the doped samples shows a rather small deviation from the composition of the stoichiometric phase. Here the elemental composition of the structural models used during the Rietveld refinements with the neutron diffraction data were fixed at 5:1:4 for Cu:Fe:S, representative of the parent composition  $\text{Cu}_5\text{FeS}_4$ .

#### **5.4.2. Ambient Temperature Phase**

##### **5.4.2.1. Cation Disorder in ZB Sub-Cells at Ambient Temperature**

The model for the ambient-temperature phase of stoichiometric bornite,  $\text{Cu}_5\text{FeS}_4$ , was determined by Rietveld refinements of neutron diffraction data in chapter 4, model  $^A5$ . This structural model will be referred to as Model 1, the model has 12 crystallographically unique cation sites with the iron ordered over the edge-pair positions (Figure 5-5(a)).

Model 1 was initially used to fit the neutron diffraction data collected on the chemically substituted samples at 300 K. This model provided a reasonable fit to the diffraction data after refinement of lattice parameters, atom positions, thermal parameters and peak profiles.

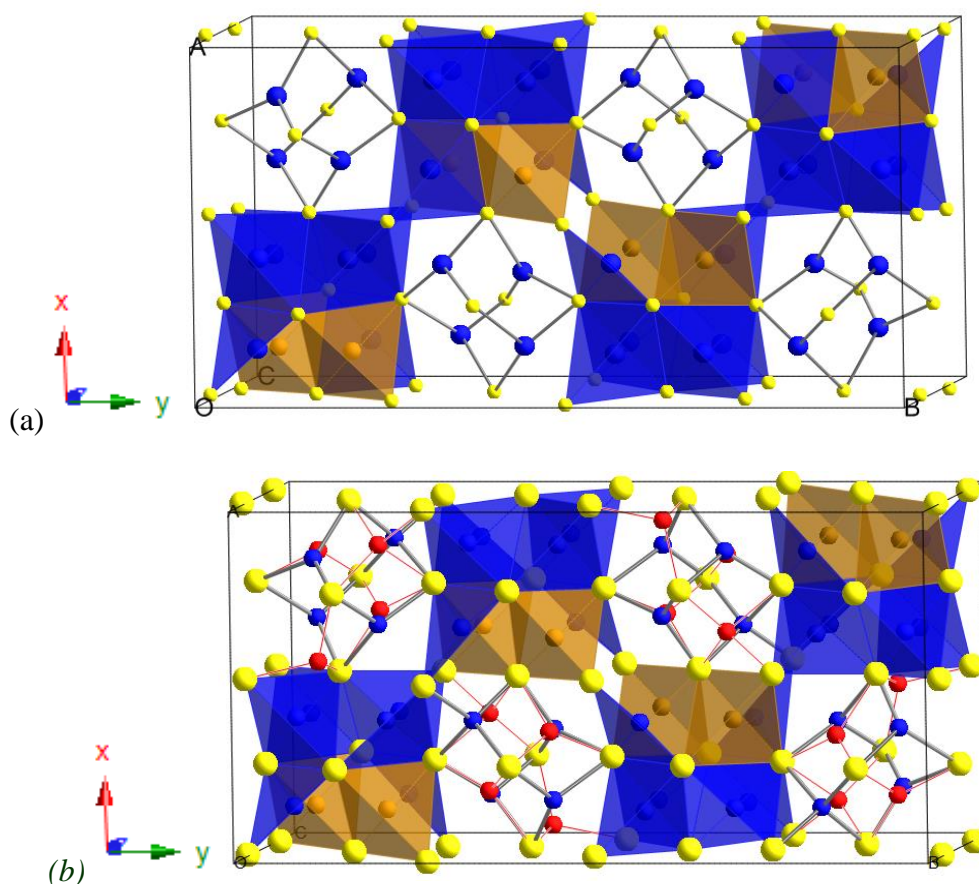


**Figure 5-5** – Perspective view of two structural models, with space group *Pbca*. (a) Model 1- with 12 cation sites ( $\text{Cu}_5\text{FeS}_4$  at 298 K) (b) Model 2 – with 16 cation sites ( $\text{Cu}_{4.96}\text{Fe}_{0.98}\text{S}_4$  at 298 K) as determined from Rietveld refinements using neutron diffraction data. Yellow atoms – Sulphur; Blue atoms – Cu; Orange atoms – Fe and Red atoms – additional Cu sites- *t*”.

However there was a clear discrepancy in the intensity of the calculated and observed diffraction patterns (Figure 5-6(a-c)). Ding *et al.* proposed that *6a*, *4a*, *2a* and *a* phases may coexist at low temperatures.<sup>279</sup> The following attempts in the refinement of the structural model looked to map the disorder of a mixture of supercells onto a single unit cell. Model 2 was therefore constructed by introducing atomic density into the supposedly vacant sites of the ZB sub-cells, giving 16 crystallographically unique sites. By manually introducing additional atomic density to the vacant sites, the disorder in ZB sub-cells can be modelled effectively (Figure 5-5(b)).

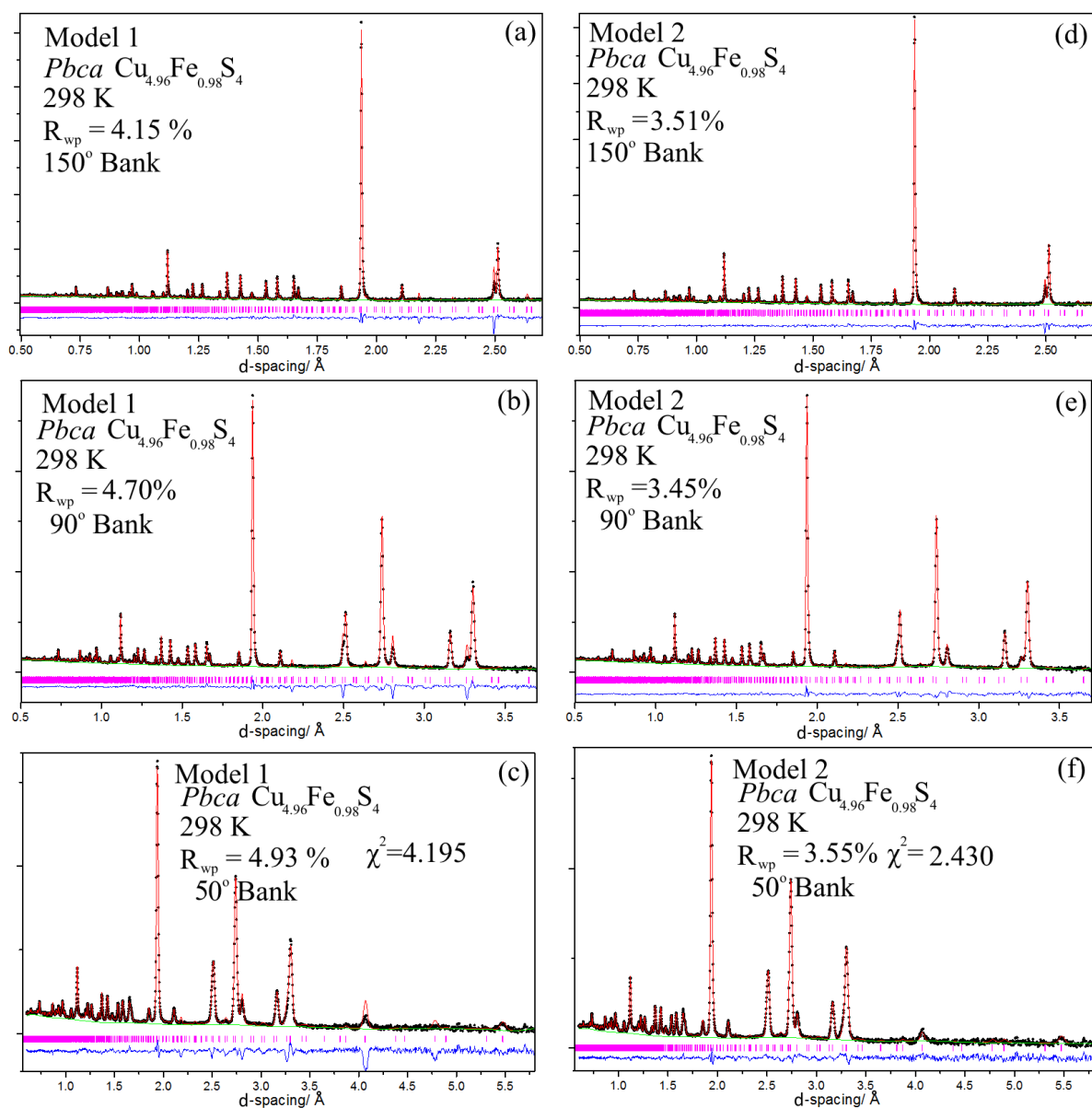


**Figure 5-6** - Powder neutron diffraction data for  $Cu_{4.96}Fe_{0.98}S_4$ , collected at 298 K, together with analysis by the Rietveld method. Observed, calculated and difference profiles are noted by points, red solid line and blue lower line. Markers represent the reflections for the low temperature phase of bornite (space group  $Pbca$ ) for (a,b,c) Model 1 (<sup>A</sup>5 in chapter 4) and (d,e,f) Model 2. (a,d) bank 5 – 150 °; (b,e) bank 4 – 120 °; (c,f) bank 3 – 90 ° (see Appendix N for tabulated parameters).

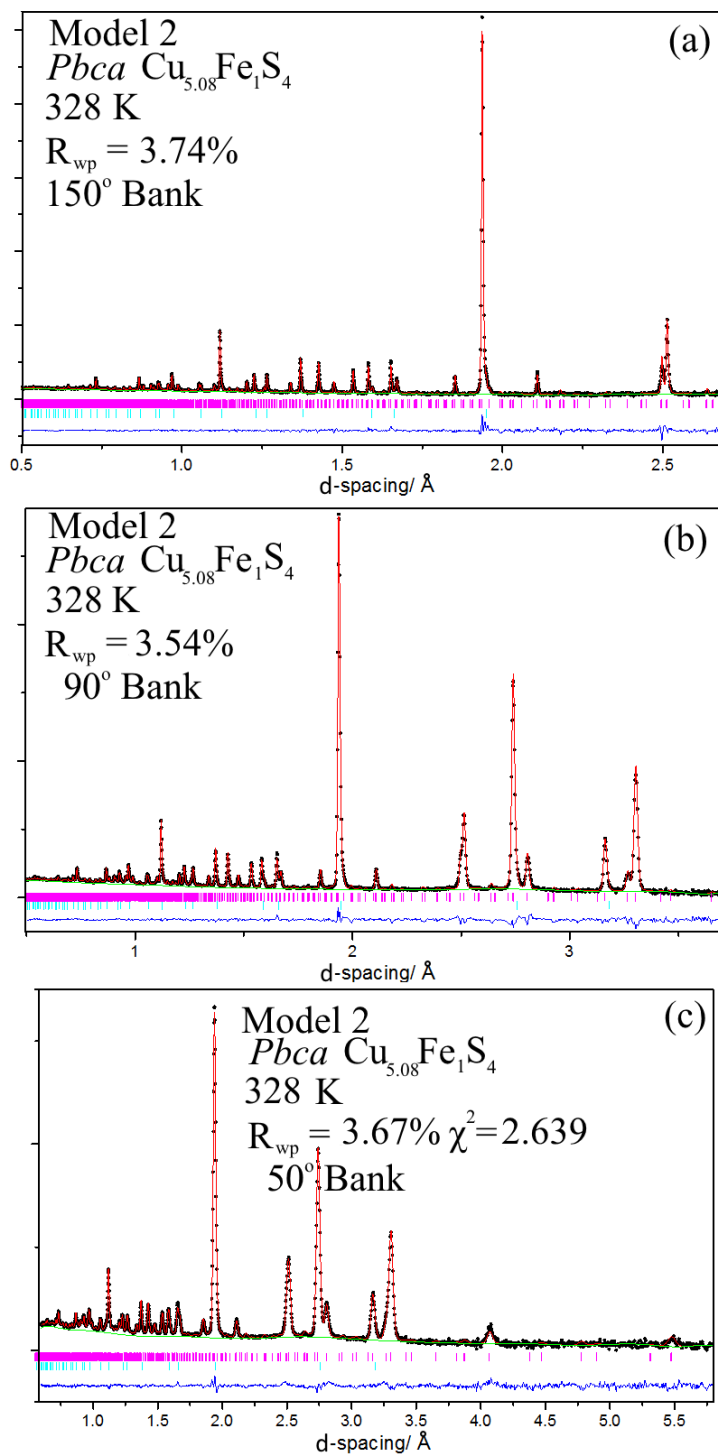


**Figure 5-7** - Powder neutron diffraction data for  $\text{Cu}_{5.08}\text{Fe}_{0.92}\text{S}_4$ , collected at 328 K, together with analysis by the Rietveld method. Observed, calculated and difference profiles are noted by points, red solid line and blue lower line. Pink Markers represent the reflections for the low temperature phase of bornite (space group  $Pbca$ ); blue markers represent the reflections for the a-type phase (fitted with the space group  $Fm\bar{3}m$ ). (a) bank 5 - 150°; (b) bank 4 – 120 °; (c) bank 3 – 90 ° (see Appendix O for tabulated parameters).

### 5.4.2.2. Refinement Constraints Used

During the Rietveld refinement using Model 2, space group *Pbca*, the fractional coordinates of all atoms and site occupancy factors of cation sites, Cu(9)-Cu(16) only, were refined. Sites Cu(9)-Cu(12) are tetrahedrally coordinated and make up a ZB type structure within their sub-cell, these will be referred to as t'-cations. Sites Cu(13)-Cu(16) occupy what should be the vacancies of the ZB sub-cells and are referred to here onward as the t''-cations. The t'-cation sites started at  $SOF = 1$  and t''-cation sites started at  $SOF = 0$ , whilst sites M(1)-M(8) were set to  $SOF = 1$  and were not refined. The elemental composition was constrained to maintain  $Cu_5FeS_4$ .

When the  $\chi^2$  and  $R_{wp}$  values stopped decreasing it was apparent that, possibly due to the large number of refining parameters, convergence could not be achieved with all atom positions and the  $SOF$ 's of cations Cu(9)-Cu(16) refining. Therefore, the cation positions were not refined once an excellent fit was achieved. Thus, *esds* for atom positions and bond distances of the t' and t'' cations are not provided for the tabulated values in the e-appendix. This is the case for the samples with composition,  $Cu_{5.08}Fe_{0.92}S_4$  and  $Cu_{4.96}Fe_{0.98}S_4$ .

### 5.4.2.3. Behaviour of Cations within ZB and AF Sub-Cells

The resulting  $SOF$ s show that there is a deviation from the perfectly ordered *4a* structure, space group *Pbca*, that has alternating ZB and AF sub-cells. The ideal structure as shown in Figure 4-1, displays a change in the vacancy-ordering within neighbouring ZB sub-cells along the *b*-axis in the *4a* supercell. The data for both the  $Cu_{4.96}Fe_{0.98}S_4$  and  $Cu_{5.08}Fe_{0.92}S_4$  samples suggest that we see a deviation from this perfectly-ordered behaviour of *ca.* 20%, or 1 in 5, for the ZB sub-cells. The absence of any significant atomic density in the vacant sites for the stoichiometric phase,  $SOF = 0$  for Cu(13)-Cu(16), suggests that ZB anti-site disorder is more likely to occur in chemically substituted samples. The  $SOF$  data in Figure 5-8 highlights that the atomic density moves away from the ideal ZB sites with *ca.*  $SOF = 0.80$  for Cu(9)-Cu(12) and into the vacant sites *ca.*  $SOF = 0.20$  for Cu(13)-Cu(16). A deviation from perfect vacancy ordering is inherent to the intermediate phase, as shown in section 4.2.5 for the stoichiometric phase of bornite.

There appears to be some temperature dependence to this structural disorder across the vacancy sites in the ZB sub-cells. The  $SOF$  of the regular ZB is lower at 298 K than at all other temperatures, whilst values of  $SOF$  is highest at 298 K for the sites Cu(13)-(16) for

$\text{Cu}_{4.96}\text{Fe}_{0.98}\text{S}_4$ . This is indicated by the arrow on Figure 5-8(a). This temperature dependence is not observed for  $\text{Cu}_{5.08}\text{Fe}_{0.92}\text{S}_4$ .

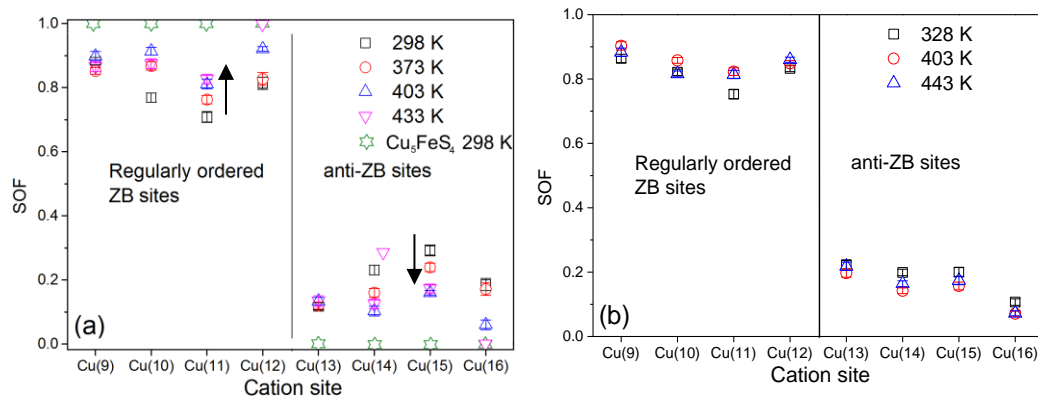


**Figure 5-8** – Site occupancy factors of regular ZB sites and anti-ZB sites for: (a)  $\text{Cu}_{4.96}\text{Fe}_{0.98}\text{S}_4$ , with  $\text{Cu}_5\text{FeS}_4$  data added for comparison and (b)  $\text{Cu}_{5.08}\text{Fe}_{0.92}\text{S}_4$ . Error bars are present within the points. The arrow is used to show the change in SOF with increasing temperature.

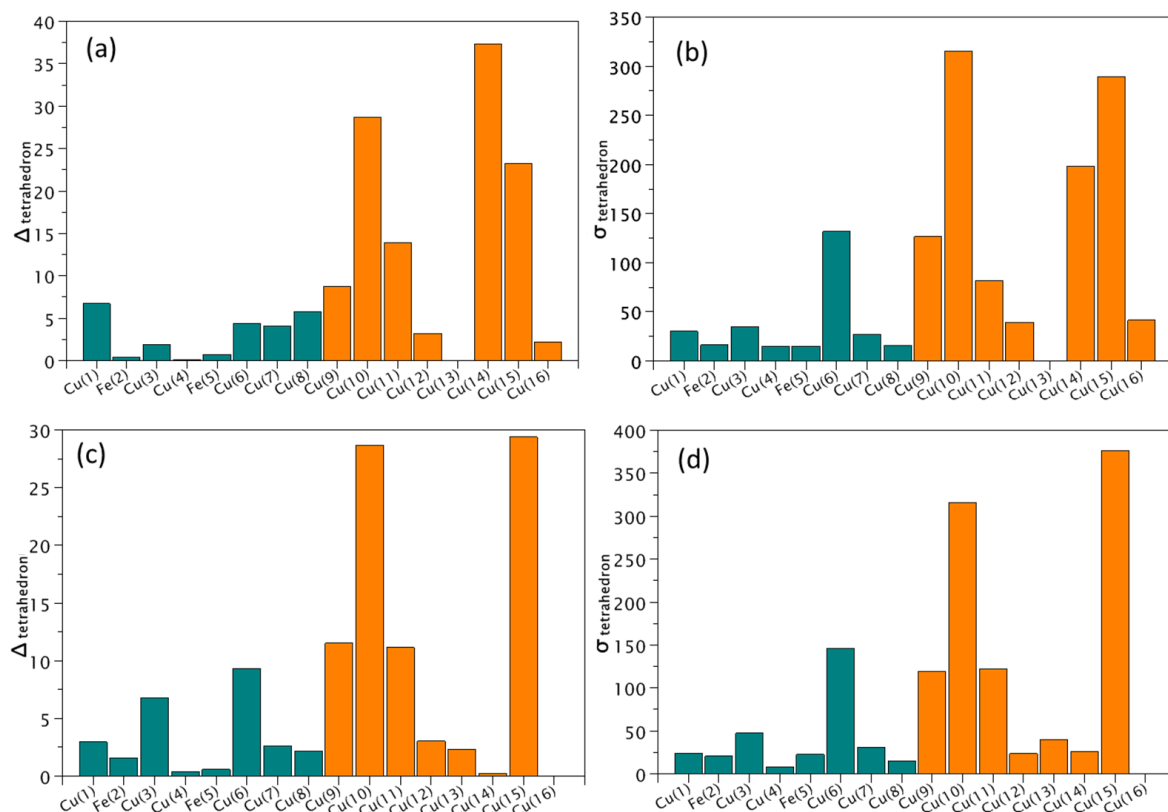


**Figure 5-9** – Polyhedral distortion parameters: (a,b) tetrahedral bond distance and bond angle distortion parameters for  $\text{Cu}_{4.96}\text{Fe}_{0.98}\text{S}_4$  and (c,d) tetrahedral bond distance and bond angle distortion parameters for  $\text{Cu}_{5.08}\text{Fe}_{0.92}\text{S}_4$ .

The tetrahedral distortion parameters suggest that, similar to the stoichiometric phase, there is a tendency for cations in the ZB sub-cell to have trigonal distortion within the tetrahedral holes (Figure 5-9 and mean values in Appendix I). This is observed in the large polyhedral distortion parameters of the ZB cations. For all bornite samples investigated here using neutron diffraction techniques, the t' cations Cu(9), (10) and (11) show considerable polyhedral distortion, whilst Cu(12) does not. In these chemically substituted samples, the data also suggest that there is some significant trigonal distortion within the AF sub-cells for the Cu(6) site in  $\text{Cu}_{5.08}\text{Fe}_{0.92}\text{S}_4$ , adjacent to the Cu(12) tetragonal ZB site, as shown by the larger values of  $\sigma_{tetrahedon}$  and  $\Delta_{tetrahedron}$ , this is consistent with the observation for the stoichiometric sample and the behaviour described by Martinelli *et al.*<sup>277</sup>

### 5.4.3. Cation Disorder in the Intermediate Temperature Phase

Model 1, with space group  $F23$ , describes the intermediate phase as outlined in the start of chapter 4 and suggests a  $2a \times 2a \times 2a$  superstructure with alternating ZB and AF sub cells. Here all ZB sub-cells have the same vacancy ordering. The metal site occupancies of M(1), M(2), M(3) are all equal to 1 and M(4) equal to zero (Figure 5-10(a)). However, using Model 1 does not provide a good fit to the diffraction data, as demonstrated in chapter 4. Thus, Model 2, space group  $F23$  with six  $16e$  metal sites over 4 crystallographically unique tetrahedral holes, is used to describe the structure for both samples,  $\text{Cu}_{4.96}\text{Fe}_{0.98}\text{S}_4$  and  $\text{Cu}_{5.08}\text{Fe}_{0.92}\text{S}_4$ . This is referred to as model <sup>15</sup><sub>i</sub> in chapter 4 and the parameters in Table 4-11 were used as the starting point for refinements. Nuclear density is modelled within each of the tetrahedral holes of the FCC sulphur sub-lattice. The ambient-temperature orthorhombic phase showed two modes of bonding behaviour for the metal cations: a regular tetrahedral coordination (t' cation) and a trigonally distorted tetrahedral coordination (t'' cation). It is necessary to model distorted tetrahedral sites into the structure of the intermediate phase to get a good fit to the observed diffraction pattern. Four unique crystallographic sites are required to provide nuclear density into each tetrahedral hole. To model the trigonally distorted sites, a second set of two atom positions are modelled into two of the four tetrahedral sites.

#### 5.4.3.1. Constraints used During Refinement

Model 2 was used in the refinements of the diffraction data collected at intermediate temperatures (Figure 5-10(b)). The site occupancy factor of iron at each of the metal sites M(1), M(2), M(3t') and M(4t') was fixed to  $SOF=0.125$  and not refined. Iron content was not modelled in trigonally distorted cation sites M(3t'') and M(4t''). The copper occupancy

at each of the cation sites was allowed to refine. Constraints were made to keep a composition of  $\text{Cu}_5\text{FeS}_4$  and to prevent individual sites from showing unrealistic values,  $\text{SOF} > 1$  or  $\text{SOF} < 0$ . During Rietveld analysis for both the samples, the atom positions, site occupancy factors, thermal parameters and lattice parameters were refined. Convergence was achieved for each of the samples with these parameters refining. The cation sites denoted  $\text{M}(4\text{t}')$  and  $\text{M}(4\text{t}'')$  exist within the same crystallographically distinct tetrahedral hole and are constrained so that the summed  $\text{SOF}$  of these sites does not exceed unity. This is also the case for the  $\text{M}(3\text{t}')$  and  $\text{M}(3\text{t}'')$  sites. These will be referred to collectively as  $\text{M}(3)$  or  $\text{M}(4)$  in the following section.

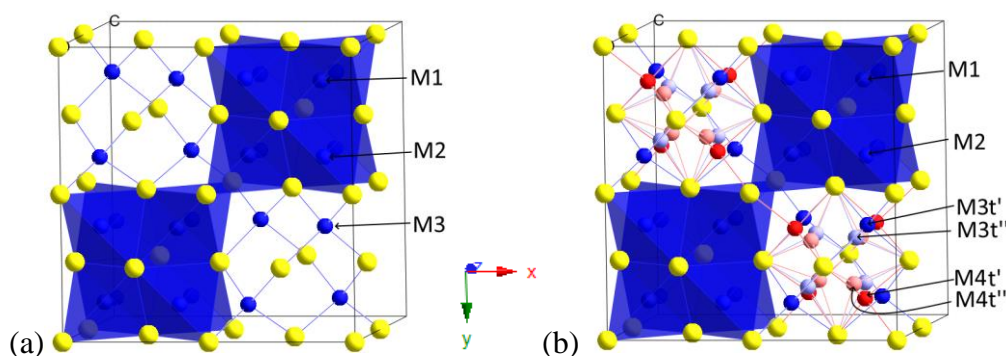


**Figure 5-10** – Two models, with space group  $F23$ , showing cation site denomination for the (a) fully ordered (Model 1); (b) and the disordered (Model 2) models. The cation sites in AF – sub-cells are shown as filled polyhedra and the cation sites in the ZB-type sub cells are shown as spheres. Yellow spheres – Sulphur; Blue spheres – ‘ordered’ cation sites; Red spheres – additional ‘ZB’ sites; light blue and light red spheres – trigonally distorted sites.

#### 5.4.3.2. Results from Rietveld Analysis of Intermediate Bornites

The data suggest that the vacancy ordering of the ZB and AF type sub-cells begins to diminish further upon transformation from the ambient-temperature phase to the intermediate phase. Each of the samples with different composition appears to show slight differences in the long-range ordering over the  $\text{ZB}^*$  type cation sites.

The stoichiometric sample has the cation sites  $\text{M}(1)$  and  $\text{M}(2)$  near full occupancy, these would therefore make up the AF type sub-cells, whilst  $\text{M}(3)$  and  $\text{M}(4)$  make up the  $\text{ZB}^*$  sub-cells and have occupancies of  $\text{SOF} = 0.67$  and  $0.43$ , respectively. This observation suggests that the AF –  $\text{ZB}^*$  ordering is still persistent in the intermediate phase, but the vacancy ordering within neighbouring  $\text{ZB}^*$  sub-cells is not fully correlated.

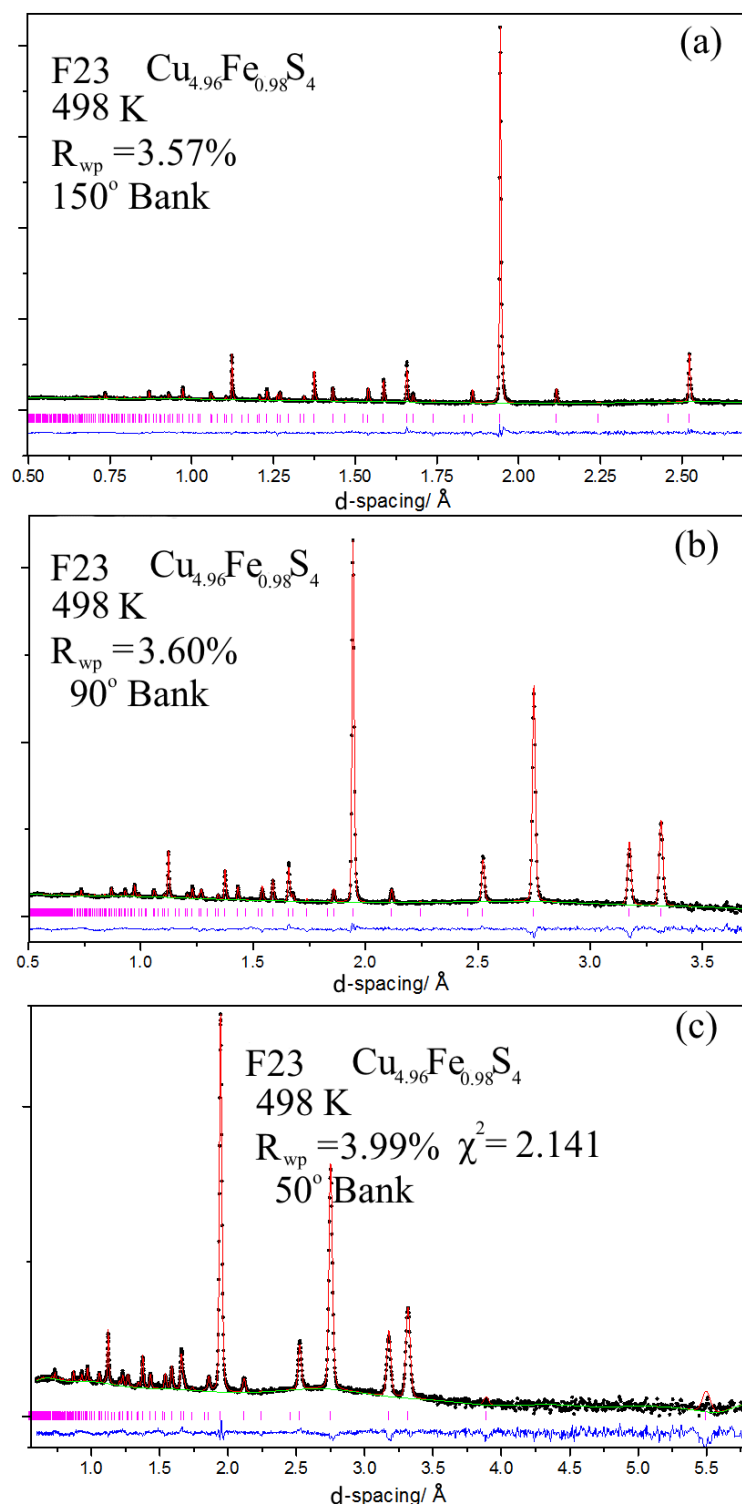


**Figure 5-11** - Powder neutron diffraction data for  $\text{Cu}_{4.96}\text{Fe}_{0.98}\text{S}_4$ , collected at 498 K, together with analysis by the structure dependent Rietveld method. Observed, calculated and difference profiles are noted by points, red solid line and blue lower line. Markers represent the reflections for the intermediate temperature phase of bornite (space group F23, model  $^15_i$  from chapter 4). (a) bank 5 – 150°; (b) bank 4 – 120°; (c) bank 3 – 90°.(see Appendix N for tabulated parameters).

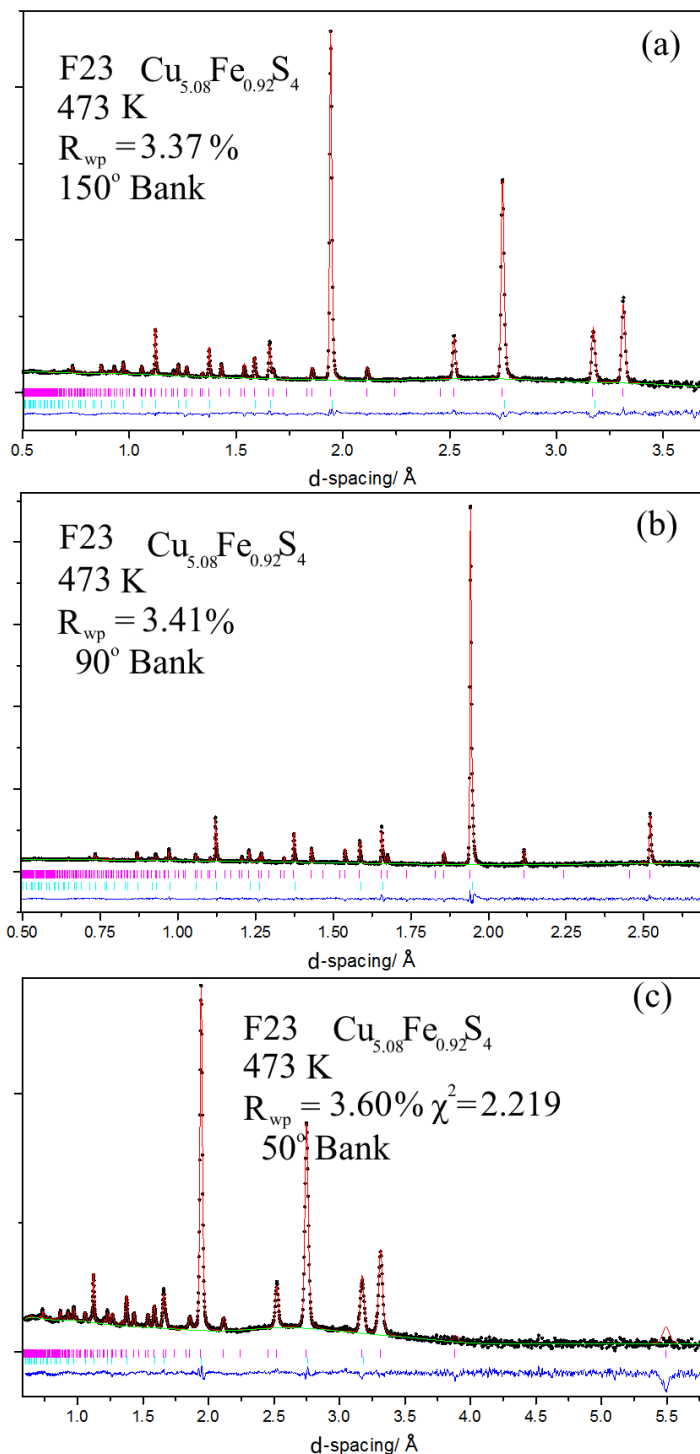


**Figure 5-12** - Powder neutron diffraction data for  $\text{Cu}_{5.08}\text{Fe}_{0.92}\text{S}_4$ , collected at 498 K, together with analysis by the structure dependent Rietveld method. Observed, calculated and difference profiles are noted by points, red solid line and blue lower line. Pink markers represent the reflections for the intermediate temperature phase of bornite (space group F23, model  $^15_i$  from chapter 4); blue markers represent the reflections for the a-type phase (fitted with the space group  $Fm\bar{3}m$ ). (a) bank 5 – 150°; (b) bank 4 – 120°; (c) bank 3 – 90°.(see Appendix O for tabulated parameters).

The M(3) and M(4) sites in  $\text{Cu}_{5.08}\text{Fe}_{0.92}\text{S}_4$  have similar site occupancy factors of *ca.*  $\text{SOF} = 0.55$  at each site, suggesting that they describe the ZB\* type sub-cell. Here the M(1) and M(2) sites show site occupancy factors close to 1. Similarly to the stoichiometric sample, AF-ZB\* ordering is still observed in this sample. The vacancy ordering within neighbouring ZB sub-cells appears to be random.

The data for the sample with composition  $\text{Cu}_{4.96}\text{Fe}_{0.98}\text{S}_4$  shows that the sub-cell ordering of AF and ZB\* type sub-cells begins to diminish, possibly as a result of introducing cation vacancies. The M(1) site has a site occupancy close to 1, whilst both M(2) and M(4) have site occupancies close to 0.8, suggesting that the ZB\*-AF ordering is not strictly followed over the long-range structure.

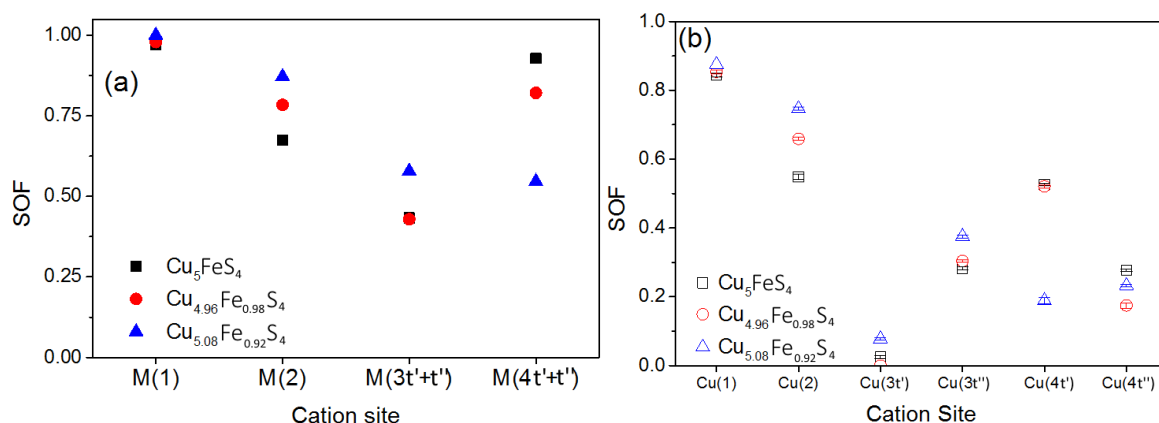


**Figure 5-13** – Site occupancy factor plots showing the difference in: (a) total cation content within each tetrahedral hole and (b) copper content at of the cation sites, for samples  $\text{Cu}_5\text{FeS}_4$ ,  $\text{Cu}_{4.96}\text{Fe}_{0.98}\text{S}_4$  and  $\text{Cu}_{5.08}\text{Fe}_{0.92}\text{S}_4$ . Error bars are provided for the copper site plot (b) and appear within the points.

These results show that there is significant disorder within the unit cell compared to ideal ordering models, as proposed by Ding *et al.*<sup>278</sup> Interestingly this paper indicates that the iron cations may indeed occupy either the AF type sites or ZB type sites as seen in this study. However, their HRTEM measurements were not performed at high temperature. The structure at higher temperatures may be substantially different whilst still conforming to the  $2a$  supercell. The literature shows copper mobility increasing drastically at critical temperatures for a number of Cu-S based minerals,<sup>281</sup> this may influence the rise of the ZB site disorder seen here.

There is a significant correlation between the copper site occupancies for each of the samples investigated. Each of the sites Cu(1), Cu(3t'') and Cu(4t'') have a similar copper content,  $\text{SOF}$  differs by +/- 0.03, 0.09 and 0.1 respectively. The trigonally distorted sites,

Cu(3t'') and Cu(4t''), account for *ca.* 20 - 25% of the total copper. This trigonally distorted geometry is typically observed in the ZB type sites in the ambient-temperature phase, where 3 out of the 10 copper sites show substantial trigonal distortion (Cu-S bond distances available in the e-appendix), so there does not appear to be any substantial change in the number of distorted sites. Meanwhile, the *a* phase may show a higher occurrence of this distorted geometry and this will be investigated in the following section.

#### 5.4.4. Structure of the High-Temperature Phase

##### 5.4.4.1. Constraints Used in Refinements

The models used here are derived from the Rietveld refinements performed using the neutron diffraction data of the stoichiometric phase at high temperature as presented in the chapter 4 and referred to as  $H5_{iii}$ , space group *F23* with one *4c*, one *4d* and two *16e* metal sites over 2 crystallographically unique tetrahedral sites (Table 4-6). Similar to the intermediate phase, two types of cation site are present within a single tetrahedral hole. A tetrahedrally coordinated site, t'-cation site, and a trigonally distorted site, t''-cation site, are used to describe this structure type (Figure 5-14). Meanwhile there are two crystallographically unique tetrahedral holes, M(1) and M(2), and thus 4 cation sites. The presence of the chalcopyrite-type phase is observed in the diffraction patterns for both samples, Cu<sub>4.96</sub>Fe<sub>0.98</sub>S<sub>4</sub> and Cu<sub>5.08</sub>Fe<sub>0.92</sub>S<sub>4</sub>, with the most intense peak appearing at  $d = 3.07$  Å (Figure 5-15, Figure 5-16). The constraints used in these refinements allowed for the *SOFs* of both the t'- and t''-cation sites to refine, whilst keeping the sum of t' and t'' within a single site below  $SOF_{M(n)} = 1$  for any given tetrahedral hole and maintaining a stoichiometry of Cu<sub>5</sub>FeS<sub>4</sub>.

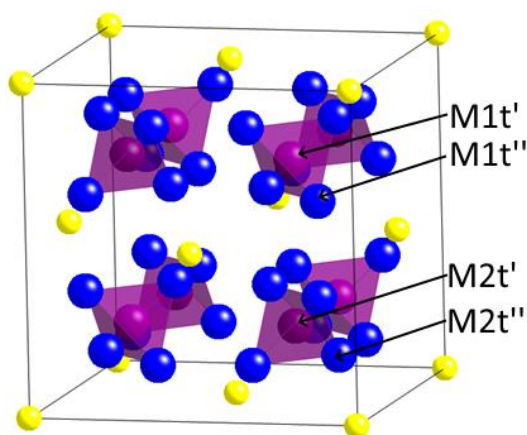


**Figure 5-14** – High-temperature model with space group *F23* showing the: Purple spheres - tetrahedrally coordinated t' sites that contain Cu and Fe; Blue spheres – trigonally distorted t'' sites that contain Cu only; and Yellow spheres - sulphur.

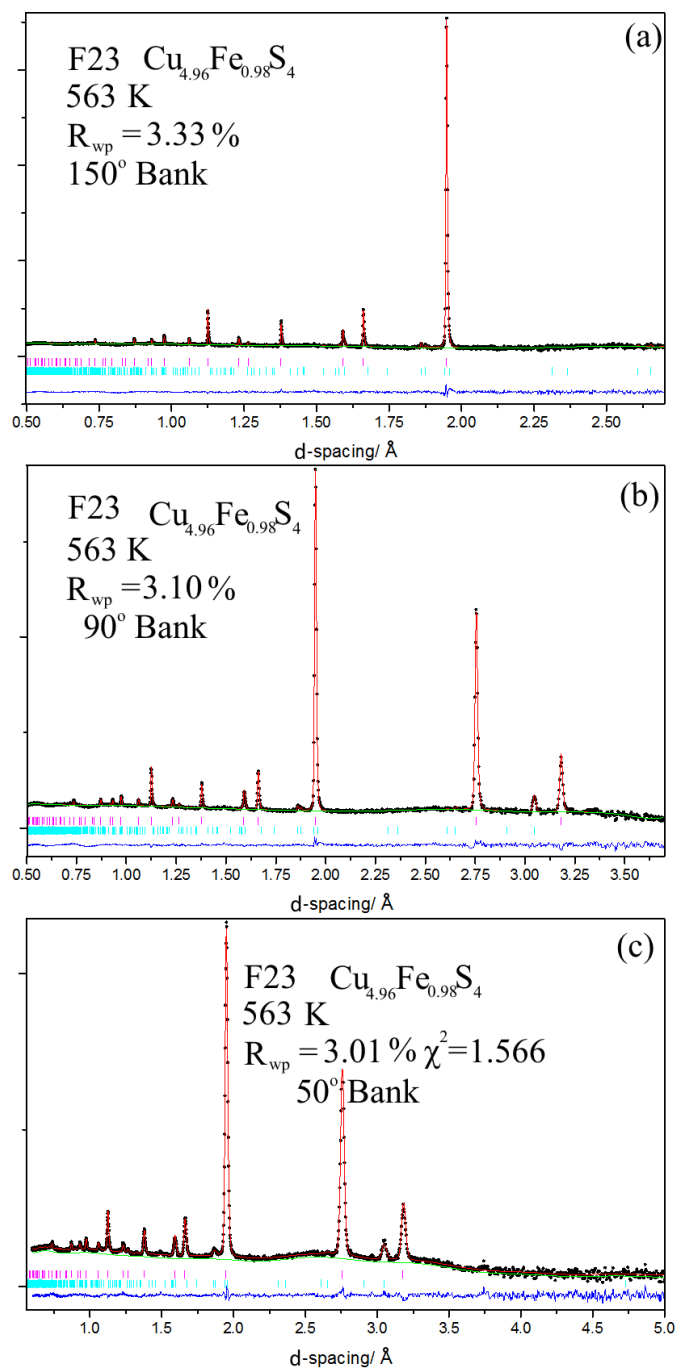


**Figure 5-15** - Powder neutron diffraction data for  $\text{Cu}_{4.96}\text{Fe}_{0.98}\text{S}_4$ , collected at 563 K, together with analysis by the structure dependent Rietveld method. Observed, calculated and difference profiles are noted by points, red solid line and blue lower line. Pink markers represent the reflections for the high-temperature phase of bornite (space group F23, model  $^H5_{\text{iii}}$  from chapter 4); Blue markers – secondary chalcopyrite-type phase. (a) bank 5 – 150 °; (b) bank 4 – 120 °; (c) bank 3 – 90 °.(see Appendix N for tabulated parameters).

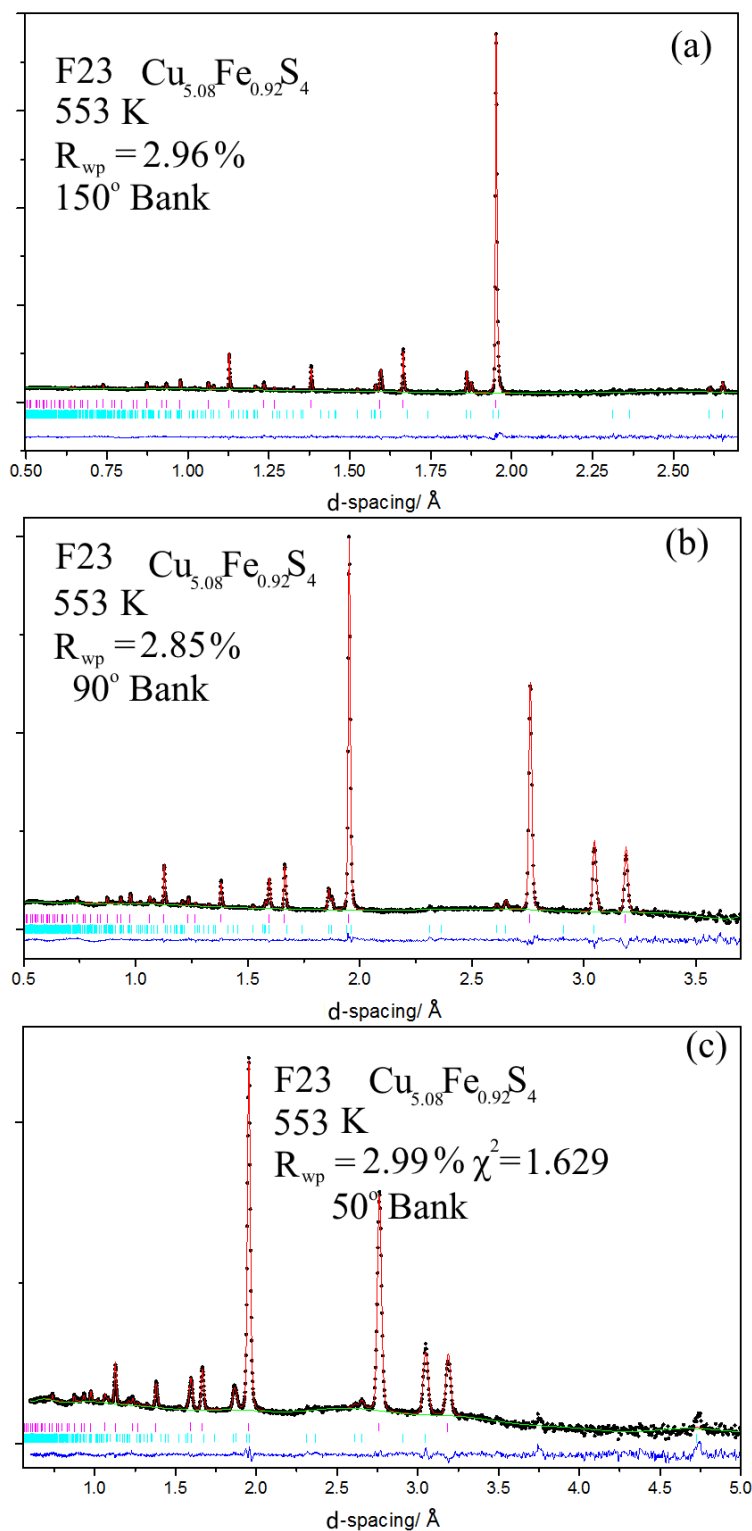


**Figure 5-16-** Powder neutron diffraction data for  $\text{Cu}_{5.08}\text{Fe}_{0.92}\text{S}_4$ , collected at 498 K, together with analysis by the structure dependent Rietveld method. Observed, calculated and difference profiles are noted by points, red solid line and blue lower line. Pink markers - reflections for the high-temperature phase of bornite (space group F23, model  $H5_{\text{iii}}$  from chapter 4); blue markers - reflections for the chalcopyrite-type phase. (a) 150°; (b) 90°; (c) 50° banks. (see Appendix O for tabulated parameters)

### 5.4.4.2. Results from Rietveld Analysis of the High-Temperature Phase of Bornite, a

For these compositionally different bornite samples, there appears to be some difference in the ordering of cations in the long-range structure. For each sample, one of the two  $t''$ -cation sites,  $\text{Cu}(1t'')$ , has more nuclear density. The total cation content at each tetrahedral hole,  $M(1)$  and  $M(2)$  is determined by summing  $\text{SOF}_{M(1)} = \text{SOF}_{\text{Cu}(1t')} + \text{SOF}_{\text{Fe}(1t')} + \text{SOF}_{\text{Cu}(1t'')}$  and provides an interesting insight. The stoichiometric phase appears to have an equal distribution of cations at each site, whereas the non-stoichiometric samples appear to show some preferential filling at the  $M(1)$  site. This is by a rather small margin, *ca.* 80% and 60% for  $M(1)$  and  $M(2)$  respectively in both  $\text{Cu}_{5.08}\text{Fe}_{0.92}\text{S}_4$  and  $\text{Cu}_{4.96}\text{Fe}_{0.98}\text{S}_4$ . The Fe:Cu cation content at each of these sites appears to vary considerably between samples. The *SOFs* are presented as total % of Fe present, at  $\text{Fe}(1t')$  and  $\text{Fe}(2t')$ , respectively. The stoichiometric sample shows a ratio of 47 : 53 % at these two sites whereas the samples with composition  $\text{Cu}_{5.08}\text{Fe}_{0.92}\text{S}_4$  and  $\text{Cu}_{4.96}\text{Fe}_{0.98}\text{S}_4$  have site compositions of 24 : 76% and 5 : 95 %, respectively. This indicates that moving away from nominal stoichiometry of  $\text{Cu}_5\text{FeS}_4$  toward Cu(II) rich compositions allows for a more ordered structure in the high-temperature phase and is shown in Figure 5-17.

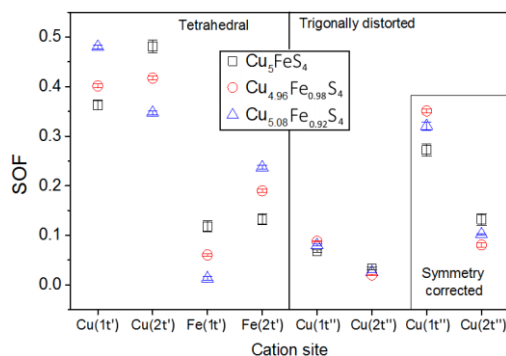


**Figure 5-17** – Site occupancy factor plots showing the difference in cation content at each of the cation sites, for samples  $\text{Cu}_5\text{FeS}_4$ ,  $\text{Cu}_{4.96}\text{Fe}_{0.98}\text{S}_4$  and  $\text{Cu}_{5.08}\text{Fe}_{0.92}\text{S}_4$ . Error bars are provided for each of the sites and appear within the points. Inset shows a symmetry adjusted plot is to display the relative contribution to the total site occupancy for  $\text{Cu}(1t'')$  and  $\text{Cu}(2t'')$ .

### 5.4.5. Variable Temperature Observations from Neutron Diffraction

#### 5.4.5.1. Evolution of Structural Phases

The sample with composition  $\text{Cu}_{4.96}\text{Fe}_{0.98}\text{S}_4$  shows the inclusion of a small concentration of chalcopyrite-type phase at high temperatures  $T > 525$  K. The refinement of the data

collected at 460 K required the inclusion of a  $4a$  and  $2a$  phases, which are present in 43 and 57 wt%, respectively. The copper-rich sample,  $\text{Cu}_{5.08}\text{Fe}_{0.92}\text{S}_4$ , required the inclusion of a secondary phase to fit a shoulder on a number of the peaks in the low-temperature phase. A chalcocite-type unit-cell, with sub-cell parameters  $a \times a \times a$  and space group  $Fm\bar{3}m$  was used to fit this diffraction intensity. The concentration of this phase varies from 3.5 to 12% across the temperature range and increases with increasing temperature. The inclusion of this secondary phase is not required to provide a good fit during the Rietveld analysis of the data collected at high temperatures,  $T \geq 500$  K. Upon transformation to the  $a$  phase the bornite type phase percentage increases to 99.6 wt% with 0.4 wt% contribution from chalcopyrite. This suggests that the secondary phase fitted in the ambient-temperature region is likely to be an  $a \times a \times a$  bornite-type phase in  $\text{Cu}_{5.08}\text{Fe}_{0.92}\text{S}_4$ . At 460 K the respective sub-cell parameters are  $a_p = 5.4872(2)$  and  $a_p = 5.5148(1)$  for the majority and minority bornite phases, respectively (Figure 5-18(b)).

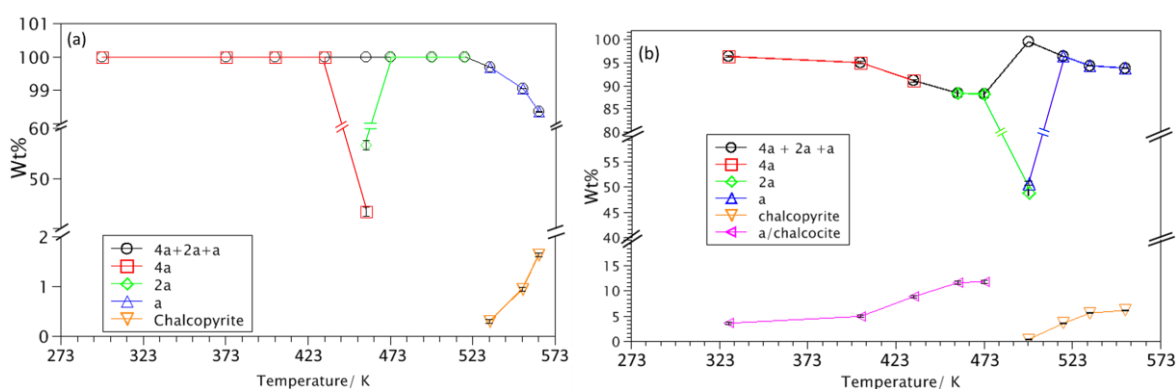


**Figure 5-18** - Percentage of phases present at each temperature determined from Rietveld refinements for samples with nominal compositions: (a)  $\text{Cu}_{4.96}\text{Fe}_{0.98}\text{S}_4$  and (b)  $\text{Cu}_{5.08}\text{Fe}_{0.92}\text{S}_4$ .

For both the copper rich and cation deficient samples,  $\text{Cu}_{5.08}\text{Fe}_{0.92}\text{S}_4$  and  $\text{Cu}_{4.96}\text{Fe}_{0.98}\text{S}_4$ , full transformation from the  $2a \rightarrow a$  phase occurs between  $T = 500 - 525$  K, comparable to the recorded  $T_2$  transition described by the DSC data. Appreciable levels of the  $a$  phase are present at 500 K, *ca.* 50%, for  $\text{Cu}_{5.08}\text{Fe}_{0.92}\text{S}_4$ . In contrast, the  $T_1$  transitions for the samples are observed at slightly different temperatures. Full transformation from  $4a \rightarrow 2a$  for  $\text{Cu}_{4.96}\text{Fe}_{0.98}\text{S}_4$  occurs between,  $T = 458 - 473$  K, with evidence of significant levels of  $2a$ , *ca.* 60%, at 458 K (Figure 5-18(a)), whereas  $\text{Cu}_{5.08}\text{Fe}_{0.92}\text{S}_4$  undergoes complete transformation to the  $2a$  phase between,  $T = 438 - 458$  K. These observations are consistent with  $T_1$  and  $T_2$  transitions observed in the DSC data, both of which are *ca.* 10 K lower for  $\text{Cu}_{5.08}\text{Fe}_{0.92}\text{S}_4$  compared to  $\text{Cu}_{4.96}\text{Fe}_{0.98}\text{S}_4$ .

### 5.4.5.2. Changes in Lattice Parameters

The pseudo-cubic sub-cell parameter,  $a_p$ , shows an increase with increasing temperature for  $\text{Cu}_{4.96}\text{Fe}_{0.98}\square_{2.06}\text{S}_4$  (Figure 5-19). The average value for  $a_p$  in the orthorhombic phase is included in Figure 5-19(c) and shows that the lattice parameters increase, almost linearly, over the entire temperature range and across each of the phase transitions.

The temperature dependence of the lattice parameters of  $\text{Cu}_{5.08}\text{Fe}_{0.92}\text{S}_4$  show a similar temperature dependence to the cation deficient phase. The lattice parameters increase with increasing temperature and the average  $a_p$  of the orthorhombic phase shows regular behaviour across the  $T_1$  phase transition. Interestingly, the  $T_2$  transition is coincident with an anomaly in  $a_p$ . There is a marked increase in the unit-cell parameter as the material transforms from the  $2a \rightarrow a$  phase, this disparity is observed directly at 500 K where two phase behaviour is observed. This leads to a more substantial increase in  $a_p$  at  $T_2$  compared to  $\text{Cu}_{4.96}\text{Fe}_{0.98}\text{S}_4$ . This structural anomaly may have an influence on the physical properties for the high-temperature phase.

To quantify and compare the anomaly across the  $T_2$  transition, the gradient in the curve of  $a_p(T)$ ,  $\Delta a_p/\Delta T$ , was extracted using the data points at  $2a_{498\text{K}}$  and  $a_{563\text{T}}$  or  $a_{553\text{T}}$ . This provides a thermal expansion coefficient of the lattice parameters. Here,  $\frac{1000 \cdot \Delta a_p}{\Delta T} = 0.227$ , 0.191 and 0.303  $\text{m}\text{\AA} \text{K}^{-1}$  for  $\text{Cu}_5\text{FeS}_4$ ,  $\text{Cu}_{4.96}\text{Fe}_{0.98}\text{S}_4$  and  $\text{Cu}_{5.08}\text{Fe}_{0.92}\text{S}_4$ , respectively. The thermal expansion coefficient for stoichiometric bornite across the  $T_2$  transition is larger than that of the cation-deficient sample,  $\text{Cu}_{4.96}\text{Fe}_{0.98}\text{S}_4$ , and smaller than that of the copper-rich sample,  $\text{Cu}_{5.08}\text{Fe}_{0.92}\text{S}_4$ . The observation of an anomaly at the  $T_2$  transition for  $\text{Cu}_{5.08}\text{Fe}_{0.92}\text{S}_4$  is consistent with data collected on natural specimens of bornite and presented by Grguric *et al.*<sup>280</sup> The sample composition and method of formation may have a marked influence on the structural features of bornite. In the  $4a$  phase,  $a_p$  of  $a$ ,  $b$  and  $c$  can deviate by as much as 0.02  $\text{\AA}$  for natural samples and 0.012  $\text{\AA}$  in synthetic samples,<sup>277</sup> with deviation in  $a_p$  as low as 0.004  $\text{\AA}$  observed in the chemically substituted samples reported here. The geometry of the sub-cells for the orthorhombic phase are very close to cubic.

The thermal parameters extracted from each of the three samples show comparable values for the  $4a$ ,  $2a$  and  $a$  phases. The  $U_{iso}$  value in the  $4a$  temperature phase is slightly higher for the stoichiometric parent phase (e-appendix). Further insights from the extracted  $U_{iso}$  are provided in section 5.5.7.

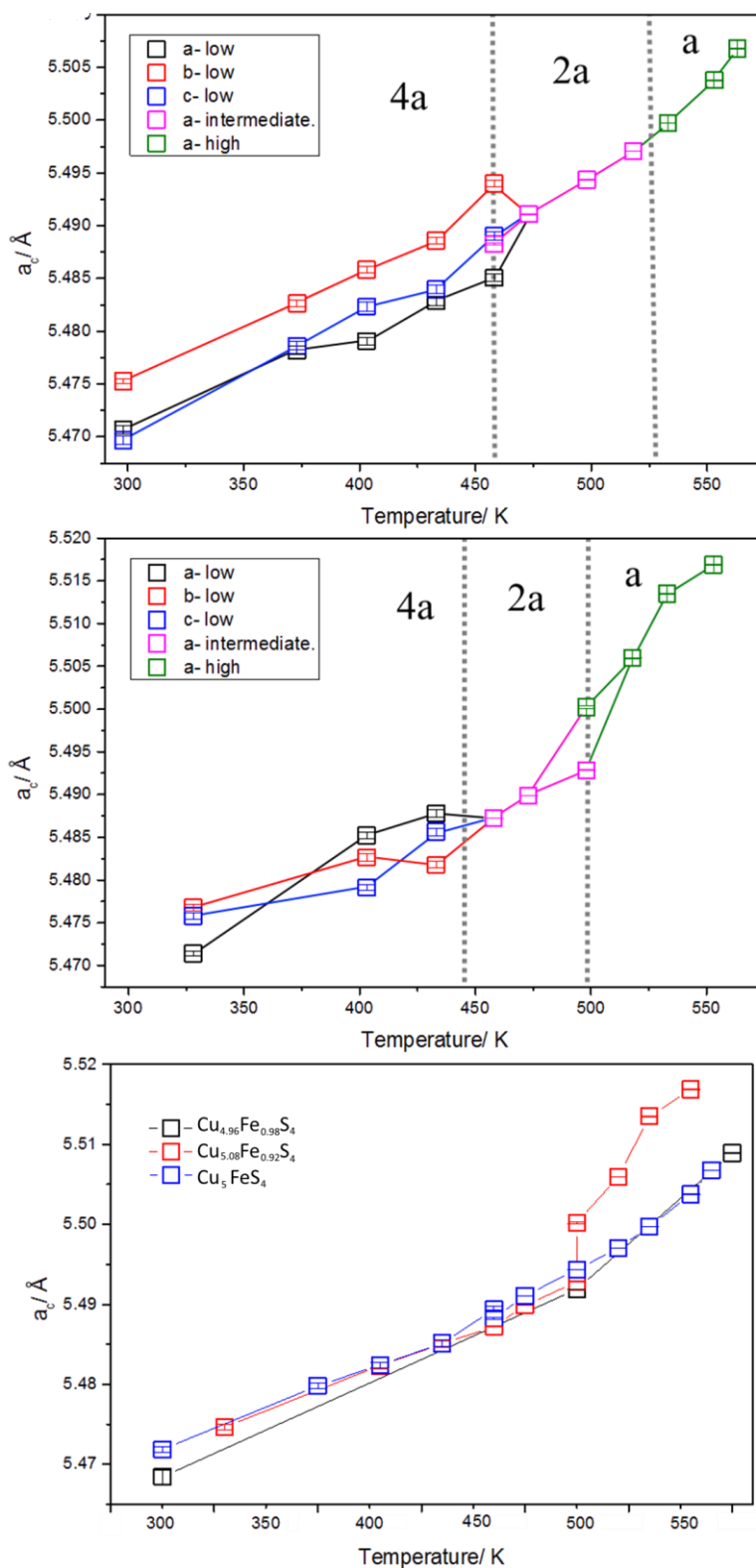


**Figure 5-19** –Temperature dependence of the pseudo-cubic lattice parameters as determined from Rietveld analysis of neutron diffraction data for: (a)  $\text{Cu}_{4.96}\text{Fe}_{0.98}\text{S}_4$ ; (b)  $\text{Cu}_{5.08}\text{Fe}_{0.92}\text{S}_4$  and (c)  $\text{Cu}_5\text{FeS}_4$ ,  $\text{Cu}_{4.96}\text{Fe}_{0.98}\text{S}_4$  and  $\text{Cu}_{5.08}\text{Fe}_{0.92}\text{S}_4$ . The latter provides direct comparison of the three samples taken for neutron diffraction experiments. Error bars are within the points.

## 5.5. Thermoelectric Properties of Chemically Substituted Bornite

The stoichiometric phase of bornite,  $\text{Cu}_5\text{FeS}_4$ , is included in each of the following figures that compares the thermoelectric properties of chemically substituted bornites. This is to provide a benchmark for comparison to other samples and is given by the black line. The data recorded for the stoichiometric sample are in good agreement with data presented in the literature;  $ZT$  values for the stoichiometric phase vary from  $ZT_{550\text{K}} = 0.3$  to  $0.55$ ,<sup>156-159,287</sup> with the sample presented here showing  $ZT_{550\text{K}} = 0.43$ .<sup>143</sup> The Seebeck coefficient of  $\text{Cu}_5\text{FeS}_4$  exhibits a maximum of  $S = 350 \mu\text{V K}^{-1}$  at 460 K, coincident with the  $T_1$  phase transition.  $S(T)$  is positive across the entire temperature range suggesting p-type behaviour. Semiconducting behaviour across the entire temperature range is indicated by the temperature dependence of the electrical resistivity with a marked anomaly observed in the region of the  $T_1$  transition. No signature of the  $T_2$  phase transition is observed in the electrical data. In contrast, the minimum observed in the thermal conductivity,  $\kappa = 0.26 \text{ W m}^{-1} \text{ K}^{-1}$ , data occurs close to the  $T_2$  phase transition.

### 5.5.1. Performance Over the Temperature Range $T = 300$ to $600 \text{ K}$

#### 5.5.1.1. Thermoelectric Properties of Series 1, $\text{Cu}_{5-x}\text{FeS}_4$ , ( $x > 0$ )

Samples with both positive and negative values of  $x$  were synthesised, for which the XRD and DSC data are presented in Figure 5-4(b) and section 5.3.2. Samples with a higher total cation content showed an increased resistivity (e.g.  $x = -0.06$ ,  $\rho = 86 \text{ m}\Omega \text{ m}$ , 300 K). The intent of these experiments was to reduce the electrical resistivity of bornite. As such, samples with composition,  $\text{Cu}_{5-x}\text{FeS}_4$ , ( $x < 0$ ) were not used in subsequent transport property measurements. Copper deficient samples, in general, exhibit a lower resistivity as a result of increasing  $x$ , and in turn increasing the number of vacant tetrahedral sites (Figure 5-20(a)). Decreasing copper content is expected to increase the concentration of holes, which leads to a reduced resistivity upon increasing  $x$ . This observation is consistent with Townsend's *et al.* formulation of  $\text{Cu}^{\text{I}}_5\text{Fe}^{\text{III}}\text{S}_4$ , quantified through Mössbauer spectroscopy.<sup>288</sup> A relatively low resistivity is achieved in the  $a$  phase for numerous samples. Despite this, all samples display semiconducting, p-type, behaviour across the entire temperature range. The  $T_1$  and  $T_2$  transitions are both semiconductor-semiconductor transitions. Anomalies are observed in  $\rho(T)$  and  $S(T)$  at the  $T_1$  transition for many of the samples in the series, consistent with the stoichiometric phase. This behaviour is less pronounced for samples where,  $x = 0.06$  to  $0.12$  (Figure 5-20(b)).

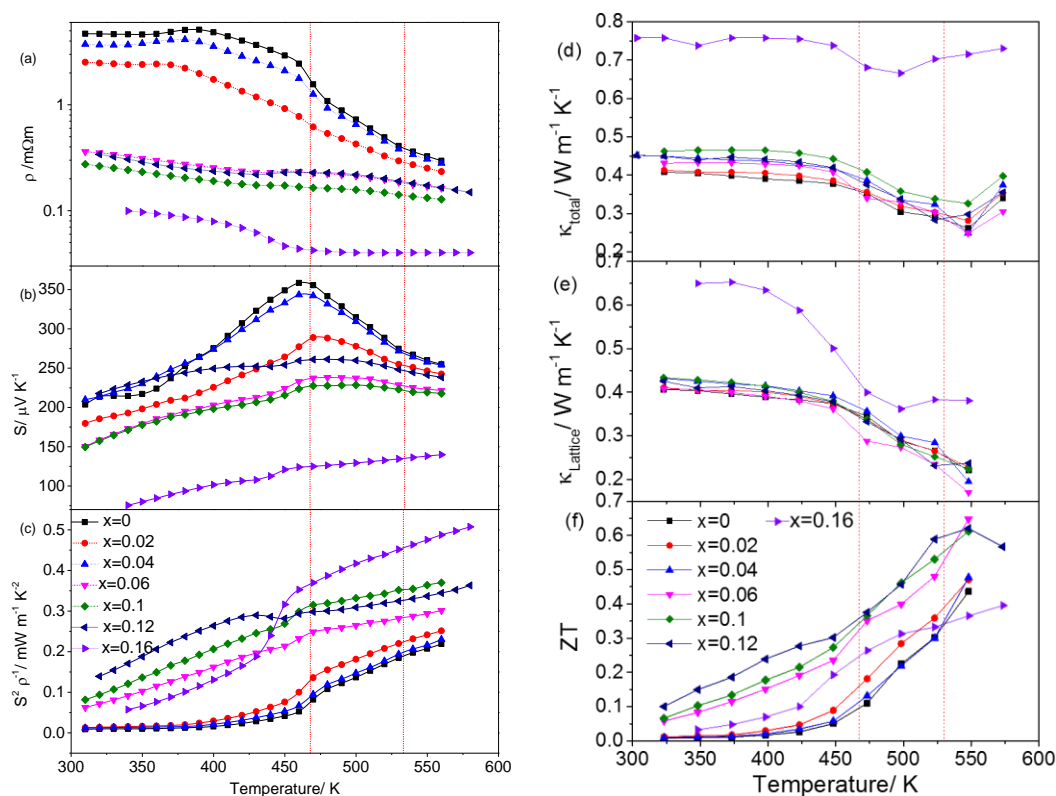


**Figure 5-20** – Temperature dependence of electrical and thermal transport properties of  $\text{Cu}_{5-x}\text{FeS}_4$  ( $0 \leq x \leq 0.16$ ): (a) electrical resistivity; (b) Seebeck coefficient and (c) power factor; (d) thermal conductivity; (e) lattice thermal conductivity and (f) thermoelectric figure of merit. Red dotted lines indicate the  $T_1$  and  $T_2$  transition temperatures for  $\text{Cu}_5\text{FeS}_4$ .

The ultra-low thermal conductivity which makes these materials desirable is observed through,  $x = 0$  to  $0.12$ , where  $\kappa_{325\text{K}} = 0.40$  to  $0.47 \text{ W m}^{-1} \text{ K}^{-1}$  and  $\kappa_{550\text{K}} = 0.24$  to  $0.33 \text{ W m}^{-1} \text{ K}^{-1}$  (Figure 5-20(d)). The variation across the series shows increasing  $\kappa_{total}$  with increasing  $x$  and can be attributed to the higher  $\kappa_{electronic}$  contribution that results from increasing the charge carrier concentration. The  $\kappa_{total}(T)$  data exhibit an anomaly close to the  $T_2$  transition similar to the stoichiometric phase. This minimum shifts to lower  $T$  when  $x > 0.1$ , consistent with the observation in the DSC data where the  $T_2$  phase transition moves to lower  $T$ . Approximation of  $\kappa_{Lattice}$  data can be made by applying the Wiedemann-Franz law ( $L = 2.44 \times 10^{-8} \text{ W } \Omega \text{ K}^{-2}$ ) to extract  $\kappa_e$  from  $\rho(T)$ . From this analysis, the minimum in  $\kappa_L = 0.22 \text{ W m}^{-1} \text{ K}^{-1}$  for the parent phase sample. Samples with  $x = 0.02, 0.1$  and  $0.12$  show comparable values of  $\kappa_L$ , whereas samples with,  $x = 0.04$  and  $0.06$ , exhibit  $\kappa_L < 0.20 \text{ W m}^{-1} \text{ K}^{-1}$  suggesting a decrease in the lattice thermal conductivity (Figure 5-20(e)). This should contribute to improvements in the thermoelectric figure of merit.

Samples with composition  $x = 0$  to  $0.12$  all show improved thermoelectric behaviour compared to the stoichiometric parent phase. Figures of merit in excess of  $ZT_{max} > 0.6$  are achieved for samples with composition  $\text{Cu}_{4.94}\text{FeS}_4$ ,  $\text{Cu}_{4.9}\text{FeS}_4$  and  $\text{Cu}_{4.88}\text{FeS}_4$  owing to improved electrical behaviour in all cases, with improved thermal behaviour in the sample  $x = 0.06$  (Figure 5-20(d)). The sample with composition  $x = 0.16$  is the only material in this series with  $ZT_{max}$  lower than that of the parent phase. The presence of substantial chalcopyrite impurity leads to anomalous transport properties,  $\rho(T)$ ,  $S(T)$  and  $\kappa_{total}(T)$ . This sample displays a significantly larger thermal conductivity, *ca.*  $\kappa = 0.7 \text{ W m}^{-1} \text{ K}^{-1}$ , which can be attributed to the high thermal conductivity of chalcopyrite (*ca.*  $\kappa = 7 \text{ W m}^{-1} \text{ K}^{-1}$ ,  $300 \text{ K}$ ).<sup>97</sup>

### 5.5.2. Thermoelectric Properties of Series 2, $\text{Cu}_{5+y}\text{Fe}_{1-y}\text{S}_4$ , ( $y > 0$ )

On the basis of Townsend's studies of cation oxidation states in bornite, the copper to iron ratio was increased in an attempt to increase the hole concentration. The electrical transport properties show strong dependence on the  $\text{Cu}^{\text{II}}$  content,  $\rho(T)$  decreases with increasing  $y$  (Figure 5-21(a)).  $S(T)$  shows the same relationship, supporting the suggestion of an increased charge carrier concentration (Figure 5-21(b)). Copper for iron substitution in bornite allows for the realisation of significantly enhanced power factors. The power factors for the stoichiometric parent phase  $S^2\sigma_{550\text{K}} = 0.22 \text{ mW m}^{-1} \text{ K}^{-1}$  and for samples in the series  $\text{Cu}_{5-x}\text{FeS}_4$ , *ca.*  $S^2\sigma_{550\text{K}} = 0.3 \text{ mW m}^{-1} \text{ K}^{-1}$ , are significantly lower than those for samples with copper for iron substitution, where *ca.*  $S^2\sigma_{550\text{K}} = 0.45 \text{ mW m}^{-1} \text{ K}^{-1}$  when  $y = 0.08$  (Figure 5-21(c)). Specifically, these improvements in the power factor are observed above the  $T_I$  transition.

Ultra-low thermal conductivity is observed for all samples in the series  $\text{Cu}_{5+y}\text{Fe}_{1-y}\text{S}_4$ . However, a higher charge carrier concentration can be inferred from the lower resistivity of these samples. As a result,  $\kappa_{total}$  increases with increasing  $y$  up to  $\kappa_{300\text{K}} = 0.55 \text{ W m}^{-1} \text{ K}^{-1}$ . A minimum close to the  $T_2$  transition is observed for each of these samples. This minimum moves to lower  $T$  with increasing  $y$  and is linked to the decreasing  $T_2$  transition (Figure 5-4(c)), which is consistent with the DSC data (Figure 5-21(d,e)).

A corresponding plateau in the temperature of the  $ZT_{max}$  is observed for samples  $y = 0.06$  to  $0.1$  where  $ZT_{525\text{K}} = ZT_{550\text{K}}$ . For each of the samples in the series, an improvement in the  $ZT_{max}$  is achieved compared to the parent phase,  $\text{Cu}_5\text{FeS}_4$ . The materials with composition  $y = 0.04$  and  $0.08$  exhibit the best performance with *ca.*  $ZT_{max} = 0.61$  and  $0.59$ , respectively. Whilst there are improvements in the power factor for each increment of  $y$ ,

this does not translate to an increasing  $ZT_{max}$  for each increasing increment of  $y$  (Figure 5-21(f)). The higher thermal conductivity values mitigate these improvements. These observations are consistent with data published by Qui *et al.* who also report improved  $ZT$  as a result of copper for iron substitution.<sup>156</sup>

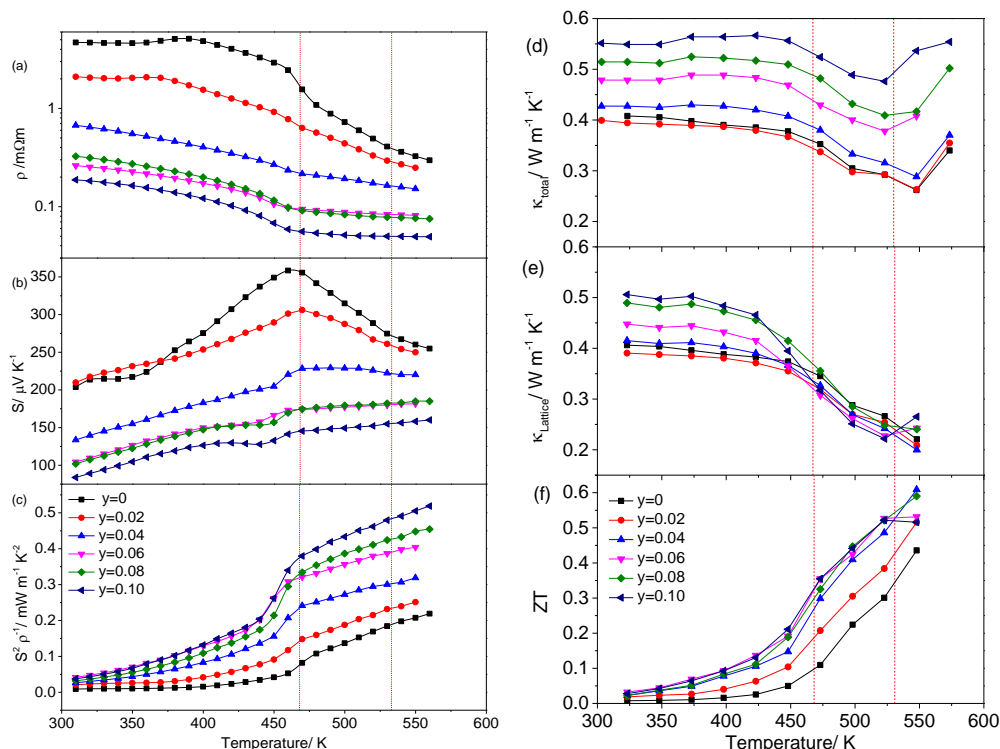


**Figure 5-21** – Temperature dependence of electrical and thermal transport properties of  $\text{Cu}_{5+y}\text{Fe}_{1-y}\text{S}_4$  ( $0 \leq x \leq 0.1$ ): (a) electrical resistivity; (b) Seebeck coefficient and (c) power factor; (d) thermal conductivity; (e) lattice thermal conductivity and (f) thermoelectric figure of merit. Red dotted lines indicate the  $T_1$  and  $T_2$  transition temperatures for  $\text{Cu}_5\text{FeS}_4$ .

### 5.5.3. Thermoelectric Properties of Series 3, $\text{Cu}_{4.94+z}\text{Fe}_{1-z}\text{S}_4$ ( $z > 0$ )

The primary findings from these first two series described in sections 5.5.1 and 5.5.2 show that decreasing the M:S ratio may lead to improvements in the  $\kappa_L$ , while increasing the Cu:Fe ratio can lead to significant improvements in the power factor of the material. To find further improvements in the  $ZT_{max}$  of non-stoichiometric bornite, the copper-to-iron ratio was increased and a fixed cation deficiency was used, effectively combining the two previous methods of increasing the hole concentration. Similar to the series  $\text{Cu}_{5+y}\text{Fe}_{1-y}\text{S}_4$ , increasing the level of copper for iron substitution,  $z$  in  $\text{Cu}_{4.94+z}\text{Fe}_{1-z}\square_{2.06}\text{S}_4$ , is consistent with decreasing  $S(T)$  and  $\rho(T)$  across the series and again all samples show p-type behaviour (Figure 5-22(a,b)). In all cases for samples with  $z > 0$ , and in comparison to the

end member sample  $z = 0$ , significant improvements in the power factor are observed above the  $T_I$  transition. The three samples with  $z = 0.02$  to  $0.04$  show comparable performance across  $S(T)$ ,  $\rho(T)$  and  $S^2\sigma$  with *ca.*  $S^2\sigma_{560K} = 0.43 \text{ mW m}^{-1} \text{ K}^{-2}$  increased from  $S^2\sigma_{560K} = 0.30 \text{ mW m}^{-1} \text{ K}^{-2}$  when  $z = 0$  (Figure 5-22(c)).

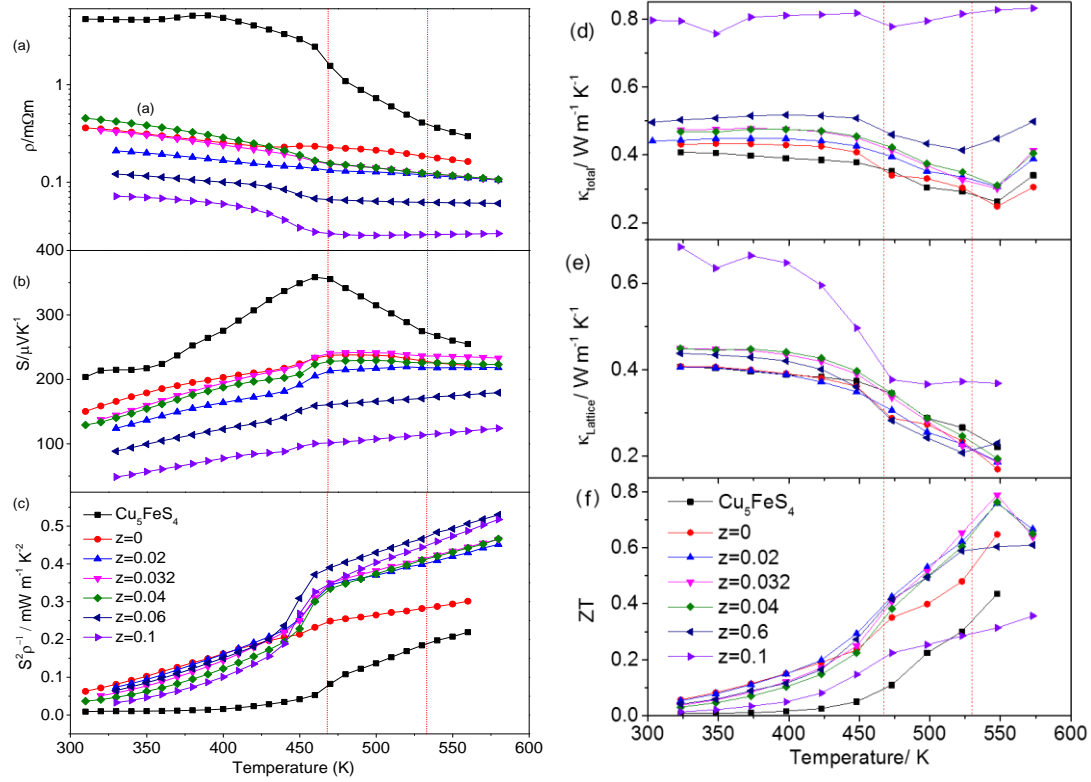


**Figure 5-22** – Temperature dependence of electrical and thermal transport properties of  $\text{Cu}_{4.94+z}\text{Fe}_{1-z}\text{S}_4$  ( $0 \leq z \leq 0.1$ ): (a) electrical resistivity; (b) Seebeck coefficient and (c) power factor; (d) thermal conductivity; (e) lattice thermal conductivity and (f) thermoelectric figure of merit. Red dotted lines indicate the  $T_1$  and  $T_2$  transition temperatures for  $\text{Cu}_5\text{FeS}_4$ .

In the temperature range of the  $4a$  phase, materials with composition  $\text{Cu}_{4.94+z}\text{Fe}_{1-z}\text{S}_4$  show an increasing  $\kappa_i(T)$  with increasing  $z$ . The minimum in  $\kappa_i(T)$  is close to the  $T_2$  transition and is consistent with observations for other samples of bornite discussed above (Figure 5-22(d)). Samples with  $z = 0.02$  to  $0.04$  show convergence of  $\kappa_{min}$  to a common value, whereas samples  $z = 0.06$  and  $0.1$  the temperature of  $\kappa_{min}$ , and thus  $T_2$ , shifts to lower temperatures consistent with the DSC data. Relatively high thermal conductivity is observed in the sample with  $z = 0.1$ . Powder X-ray diffraction data revealed the presence of appreciable levels of a chalcopyrite impurity, the presence of which is believed to increase the  $\kappa_{total}$  of the bornite sample due to chalcopyrites large  $\kappa_{total}$ . Estimation of  $\kappa_L(T)$

from the Wiedemann-Franz law suggests that a M:S ratio lower than 6:4 in bornite can result in a reduced lattice thermal conductivity. The smallest values of lattice thermal conductivity  $\kappa_{L-min} < 0.20 \text{ W m}^{-1} \text{ K}^{-1}$  are observed for samples with,  $z = 0$  to 0.04 (Figure 5-22(e)).

Improved electrical transport properties concomitant with consistently low thermal conductivity results in significant improvements in the thermoelectric performance. This study demonstrated three samples with the highest thermoelectric figure of merit for any bornite samples measured when the  $ZT_{max} > 0.76$  specifically for samples where  $z = 0.02$  to 0.04. With  $ZT_{max} = 0.79$  being achieved for sample with nominal composition  $\text{Cu}_{4.972}\text{Fe}_{0.968}\text{S}_4$ . This represents an improvement of 88% compared to the end-member phase  $\text{Cu}_5\text{FeS}_4$  (Figure 5-22(f)). Notably, peak performance is observed at 550 K, ideal for recovery of waste heat from low-grade sources.

#### **5.5.4. High-Temperature Performance of Substituted Bornite**

Thermoelectric performance of other synthetic bornite samples has been reported in the literature up to temperatures of 700 K.<sup>156,159,287</sup> These sources describe continual improvements in the  $ZT$  with increasing temperature, with  $ZT_{max}$  being achieved close to 700 K (Table 5-3). On the basis of TGA/DSC measurements of bornite performed by Guélou *et al.* (Figure 5-23), transport measurements were capped at 575 K. At temperatures above 600 K the data show that, under nitrogen flow, gradual weight loss occurs, suggesting slow degradation of the sample.<sup>157</sup> In addition to this, the neutron diffraction data have demonstrated that chalcopyrite formation can occur at higher temperatures, consistent with observations by Kumar *et al.*<sup>159</sup>

Higher-temperature thermoelectric measurements have been performed on a sample with nominal composition  $\text{Cu}_{4.97}\text{Fe}_{0.93}\text{S}_4$ . The thermoelectric data of bornite that has been reported in the literature and is measured up to 700 K, thus we can provide a reliable comparison. The power factor of the sample continues to increase with increasing temperature (Figure 5-24(a)). Meanwhile, the thermal conductivity increases significantly after the minimum at 550 K, then plateaus after 600 K (Figure 5-24(b)). Two peaks in performance are observed at 550 K and 675 K with  $ZT = 0.74$  and 0.84, respectively, demonstrating an increase of *ca.* 13% in the  $ZT$  between the two temperatures (Figure 5-24(c)). This demonstrates that these samples out-perform other bornite samples by a significant margin over the entire temperature range.

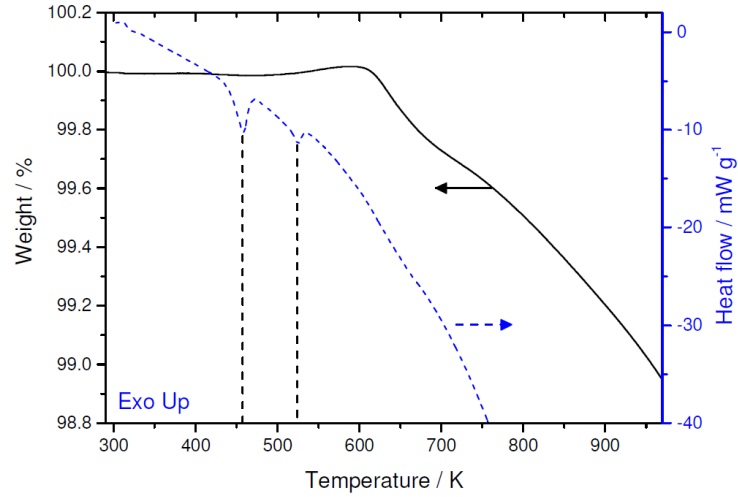


**Figure 5-23** – Temperature dependence data from TGA/DSC analysis of  $\text{Cu}_5\text{FeS}_4$  as performed by Guélou. Black solid line – Weight percentage; Blue dashed line – Heat flow and Black dashed lines –  $T_1$  and  $T_2$ . Reproduced from reference 157, reprinted with permission of RSC publishing.

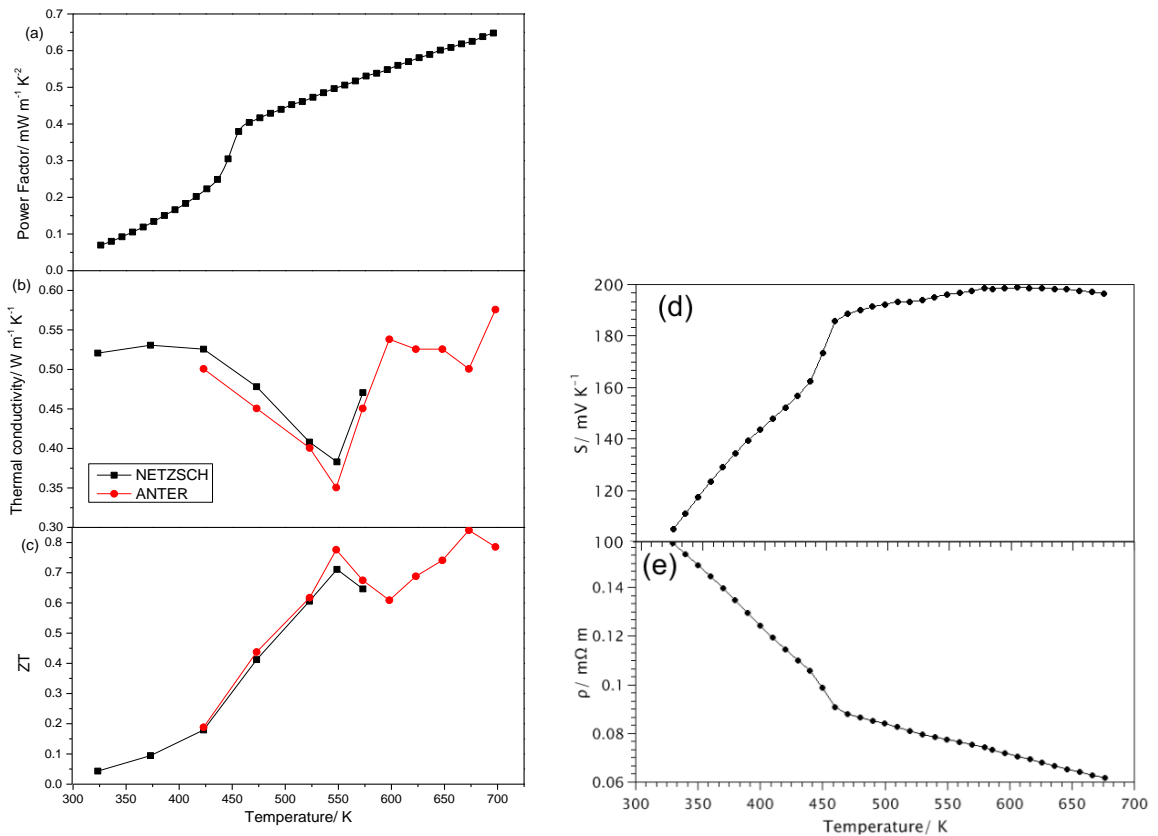


**Figure 5-24** – The temperature dependence of thermoelectric data for  $\text{Cu}_{4.97}\text{Fe}_{0.97}\text{S}_4$  recorded to higher temperatures: (a) power factor; (b) thermal conductivity; (c) thermoelectric figure of merit; (d) Seebeck coefficient and (e) electrical resistivity.

**Table 5-3** – Thermoelectric figures of merit for synthetic samples of bornite.

Composition	ZT max	ZT max Temperature/ K	ZT <sub>550K</sub>	Reference
Cu <sub>4.972</sub> Fe <sub>0.968</sub> S <sub>4</sub> /Cu <sub>4.97</sub> Fe <sub>0.97</sub> S <sub>4</sub>	0.84	675	0.79	This work
Cu <sub>5</sub> Fe <sub>1-x</sub> Mn <sub>x</sub> S <sub>4</sub> , x=0,0.05,0.1	0.55	540	0.55	157
Cu <sub>5</sub> FeS <sub>4-x</sub> Se <sub>x</sub> , x=0.4	0.66	675	0.51	159
Cu <sub>5+x</sub> Fe <sub>1-x</sub> S <sub>4</sub> , x=0.04	0.53	700	0.49	156
Cu <sub>5.23</sub> Fe <sub>0.9</sub> S <sub>4</sub>	0.56	680	0.50	287
Cu <sub>4.96</sub> Co <sub>0.04</sub> Fe <sub>0.96</sub> Zn <sub>0.04</sub> S <sub>4</sub>	0.60	590	0.60	158

### 5.5.5. Stability and Application of Non-Stoichiometric Bornite

For bornites to be applicable for use in thermoelectric modules, the materials must display long term stability. The instability of the PLEC Cu<sub>2-δ</sub>S type thermoelectrics has been brought to light through constant current-stress tests; the high Cu ion mobility is suspected to cause copper migration which leads to degradation. The origins of this are discussed in section 4.1. Bornite shows significant structural, compositional and behavioural similarities to this iron-free counterpart. Thus it is important to establish that bornite does not experience such degradation pathways through copper-ion migration. Further research into Cu<sub>2-δ</sub>S showed that partial substitution of immobile ions is an effective technique to minimise the degradation in PLECs with mobile Cu cations as they can effectively block the ionic pathway channels.<sup>185</sup>

A cycle of repeated electrical transport measurements was carried out on a high-performance sample of substituted bornite. After 8 measurements, with data collected every 10 K, the sample showed no significant change in electrical performance, suggesting that the presence of immobile Fe cation may suppress the Cu migration (Appendix P).

### 5.5.6. Influence of Cu(II) on the Thermoelectric Properties

The presence of Cu(I) and Fe(III) in the stoichiometric phase, established by near-edge absorption spectroscopy and magnetic measurements, implies that substitution methods followed here should increase Cu(II) content and hence the hole concentration.<sup>288</sup>

Regardless, oxidation must occur at one of the transition-metal species. There is sufficient evidence in the literature that confirms the existence of Cu(II) in sulphide minerals, although it is certainly less abundant than Cu(I),<sup>107</sup> whereas the existence of Fe(IV) in an S<sup>2-</sup> matrix is far less likely.

Through charge balancing, each of the synthetic bornite samples presented here can be

compared in regard to their nominal Cu(II) content. A formulation of  $\text{Cu}_{5-x+y}\text{Fe}_{1-y}\text{S}_4$  can be used to describe each of the 3 cation substituted series described in this chapter. The nominal Cu(I) and Cu(II) contents can be formulated by,  $\text{Cu(I)} = 5 - 2x + y$  and  $\text{Cu(II)} = x + 2y$ , where  $x$  is the nominal amount of copper removed from the chemical system and  $y$  is the nominal amount of copper substituted for iron. Thus an increase in the Cu:Fe ratio can be attributed to a larger increase in the nominal Cu(II) content, compared to decreasing the M:S ratio. Meanwhile, the interplay between these two chemical substitution mechanisms and their physical properties appears to show a dependence on the Cu(II) content (Figure 5-25). There is a strong, almost linear correlation of increasing power factor with increasing Cu(II) content for the three series (Figure 5-25(a)).

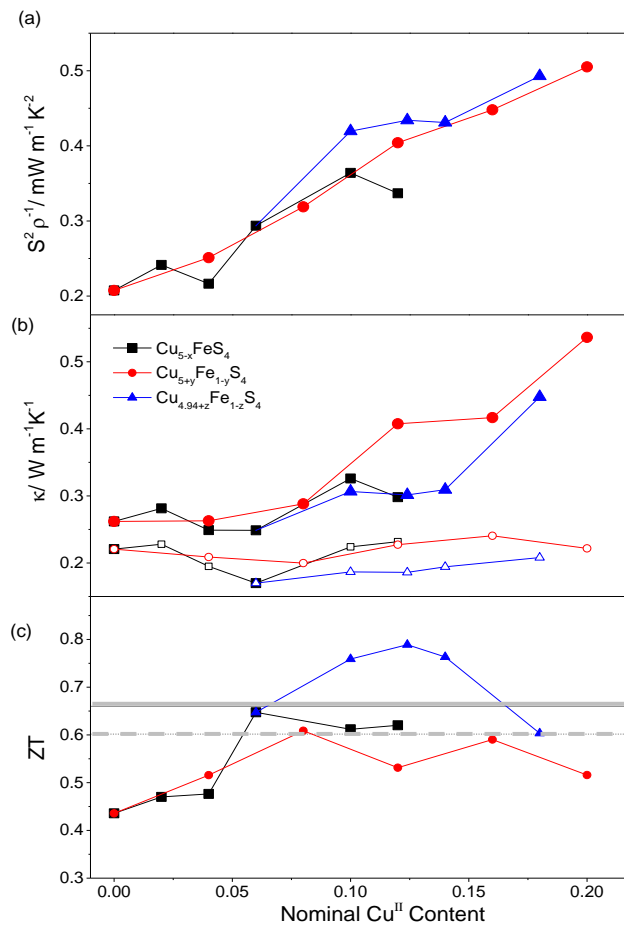


**Figure 5-25** – Thermoelectric properties recorded at 550 K for  $\text{Cu}_{5-x+y}\text{Fe}_{1-y}\text{S}_4$  samples that showed single phase behaviour. (a) power factor; (b) closed circles – total thermal conductivity, open circles – lattice thermal conductivity and (c) thermoelectric figure of merit. Grey solid line – highest ZT max of synthetic bornite and grey dashed line – highest  $ZT_{550\text{K}}$  of a synthetic bornite (Table 5-3)

A more complex relationship between the Cu(II) content and the thermal conductivity appears to exist. There is a general increase in  $\kappa_t$  with increasing Cu(II) content that can be attributed to the increasing hole concentration and in turn the  $\kappa_e$ . Conversely, the  $\kappa_L$  shows no dependence on the Cu(II) content and instead appears to be dependent on the total cation content. These data clearly demonstrate that samples with an increased vacancy concentration are more inclined to exhibit lower lattice thermal conductivity (Figure 5-25(b)). As such, a balance between a lower  $\kappa_t$  and higher power factors can be found in cation deficient species. The negligible influence of Cu(II) on  $\kappa_L$  in combination with increased power factor allows higher performance to be realised between Cu(II) = 0.06 to 0.16 and peak performance observed Cu(II) = 0.06 to 0.16. This study reveals that the introduction of cation vacancies is critical for the realisation of improvements in the thermoelectric figure of merit. However, this alone is not sufficient to achieve maximum performance, as increasing the Cu(II) content is required to maximise the power factor.

In summary, small deviations from the ideal stoichiometry of bornite,  $\text{Cu}_5\text{FeS}_4$ , can lead to significant improvements in the thermoelectric figure of merit. The majority of samples investigated here show  $ZT > 0.59$  at temperatures as low as 550 K with a peak in performance of  $ZT = 0.79$  for  $\text{Cu}_{4.972}\text{Fe}_{0.968}\text{S}_4$  at 550 K (and a maximum of  $ZT = 0.84$  at 675 K). This represents a marked improvement in  $ZT_{550\text{K}}$  of *ca.* 44% and an improvement in  $ZT_{675\text{K}}$  of 27% compared to the literature. In addition, it has been demonstrated that these results are repeatable for cation deficient samples, here 4 samples achieved  $ZT_{550\text{K}} > 0.74$ . The effects of altering the stoichiometry or introducing dopants on the thermoelectric properties has been investigated in a few studies thus far. Substitution with transition metal dopants that should drive the Cu(II) content to higher values has provided an increase in the  $ZT$  of 100% for nanostructured bornites.<sup>158</sup> Meanwhile, selenium for sulphur substitution provides enhancements in the power factor and hints that the  $\kappa_L$  may be further suppressed.<sup>159</sup> This indicates that further improvements to the thermoelectric performance may be realised through a combination of transition-metal and anion doping concomitant with an increased vacancy concentration.

### ***5.5.7. Linking the Changes in Structural and Physical Behaviour***

The Debye temperatures,  $\Theta_D$ , of the each of the  $4a$ ,  $2a$  and  $a$  phases, have been extracted from the variable temperature neutron diffraction data for the samples  $\text{Cu}_{4.96}\text{Fe}_{0.98}\text{S}_4$  and  $\text{Cu}_{5.08}\text{Fe}_{0.92}\text{S}_4$ . The total  $U_{iso}$  of the sample was calculated from the  $U_{iso}$  of both the cations and anions. A linear least-square fit to the  $U_{iso}(T)$  data was used across the temperature

range for a given structural phase and the Debye temperature is determined from the equation:<sup>293</sup>

$$U_{iso} = \frac{3h^2T}{mk_b\theta_D^2 4\pi^2} \quad (5-1)$$

For the sample with composition  $\text{Cu}_{4.96}\text{Fe}_{0.98}\text{S}_4$ , the Debye temperature for the  $4a$ ,  $2a$  and  $a$  phases are calculated as  $\theta_D = 212(6)$ ,  $154(3)$  and  $185(1)$  K, respectively. For  $\text{Cu}_{5.08}\text{Fe}_{0.92}\text{S}_4$  values of  $\theta_D = 185(1)$ ,  $162(4)$  and  $180(8)$  K are obtained. Qiu *et al.* determined the Debye temperature for the sub-ambient phase of stoichiometric bornite to be  $\theta_D = 250$  K by fitting the specific heat capacity data at low temperature.<sup>156</sup> The value of  $\theta_D = 212(6)$  K for  $\text{Cu}_{4.96}\text{Fe}_{0.98}\text{S}_4$  is in good agreement with this. The difference in values observed here may indeed be influenced by the different structural behaviour of the samples with different composition, as well as the values presented here being determined for the higher temperature phases. Low-temperature specific heat capacity measurements would be needed to confirm this. The extracted values for the  $2a$  and  $a$  phase appear to be consistent between the two samples investigated. The behaviour across the phase transitions is strikingly similar for both samples. There is a decrease in  $\theta_D$  across the  $4a \rightarrow 2a$  transition, this is followed by an increase in  $\theta_D$  across the  $2a \rightarrow a$  transition.

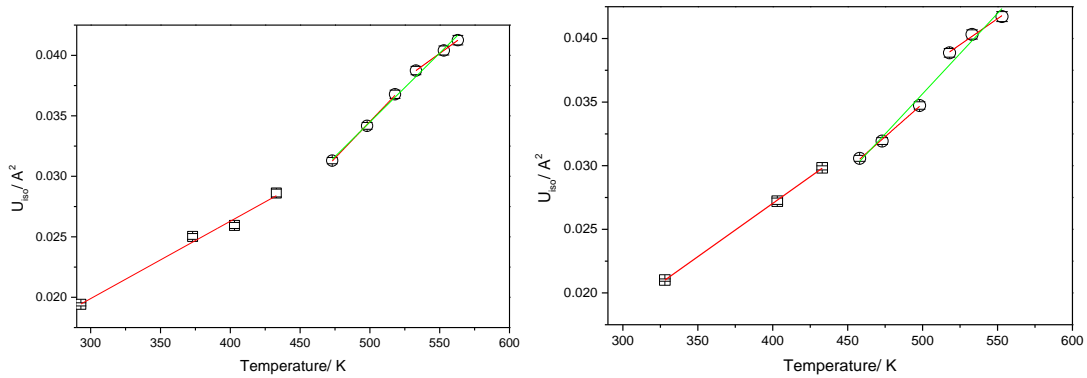


**Figure 5-26** – Temperature dependence of the total  $U_{iso}$  with a least squares linear interpolation fit to the data and used to extract the  $U_{iso}/T$  values for the high, intermediate and ambient temperature phases for: (a)  $\text{Cu}_{4.96}\text{Fe}_{0.98}\text{S}_4$ ; and (b)  $\text{Cu}_{5.08}\text{Fe}_{0.92}\text{S}_4$ .

The behaviour of the thermal parameters with temperature reveal the origin of the anomalies observed in the thermal conductivity data. An estimate of the lattice thermal conductivity can be determined from the equation:<sup>293</sup>

$$\kappa_{lattice} = 8 \times 10^{-8} \left(\frac{k_b}{h}\right)^3 MV^{\frac{1}{3}} \theta_D^3 / (\gamma^2 T) \quad (5-2)$$

Here  $M$  is the average mass of an atom and  $V$  is the average volume of an atom. This relationship shows there is a direct relationship between the Debye temperature and the expected lattice thermal conductivity.

The Debye temperatures extracted from the  $U_{iso}$  data appear to be at their lowest for the intermediate phase. This coincides with the minimum in the measured lattice thermal conductivity which is observed within the region of the intermediate phase (Figure 5-27). With  $\kappa_L$  increasing once the material enters the high temperature phase. Therefore, the minimum of the lattice thermal conductivity can be associated to the minimum in the Debye temperature.

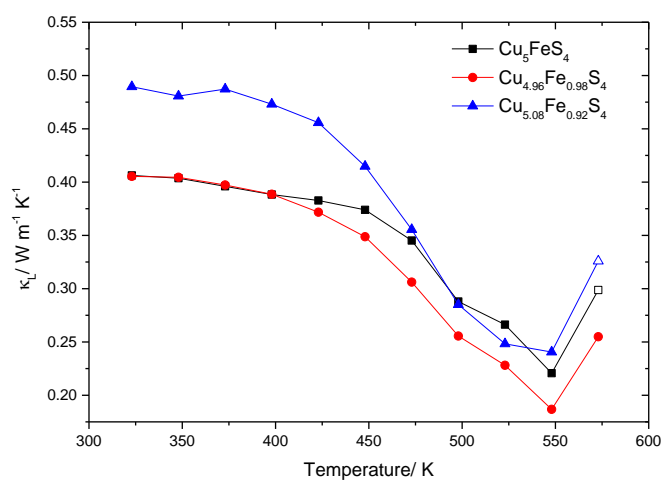


**Figure 5-27** – Temperature dependence of the lattice thermal conductivities of each of the samples taken for neutron diffraction experiments. Open symbols are predicted values determined by extrapolating the electrical resistivity data for the sample.

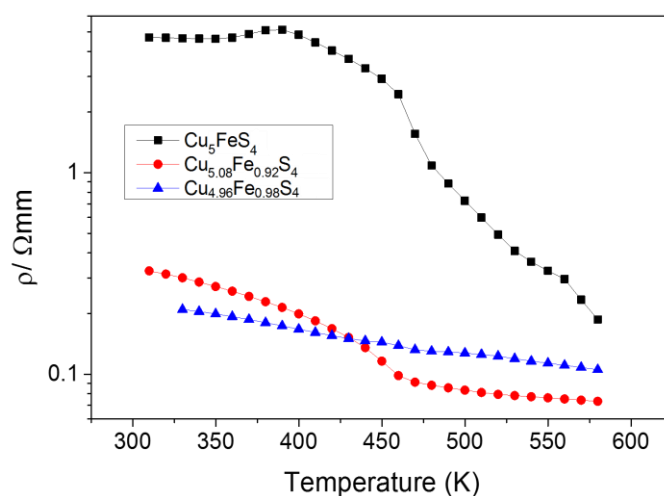


**Figure 5-28** - Temperature dependence of the electrical resistivities of each of the samples taken for neutron diffraction experiments.

## 5.6. Conclusions

In the *4a* phase, the most remarkable difference in the structural models of the stoichiometric and chemically-substituted samples was the observed nuclear density within the expected vacancy sites. This vacant site disorder is also observed in the *2a* phase but to a higher extent. For the stoichiometric phase, there is a marked anomaly in both the Seebeck coefficient and electrical resistivity data associated with the *4a* to *2a* structural phase transition. In many of the chemically-substituted samples, the signature of this  $T_1$  structural transition on the electrical transition appears to be suppressed. The existence of more *2a*-like structural characteristics may be responsible for the suppression of these electric anomalies observed in bornite (Figure 5-28).

The investigations into chemical substitution of the bornite samples intended to improve the thermoelectric performance of the material by increasing the charge carrier concentration and in turn reduce the electrical resistivity. This was achieved by decreasing the total copper content of the sample which led to increases in the power factor of the samples along with decreases in the lattice thermal conductivity. Meanwhile increasing the Cu:Fe ratio by substitution of Fe with Cu was also successful in increasing the power factor. Samples with a  $ZT_{max} < 0.6$  were achieved as a result of these chemical substitution methods, increasing the performance from  $ZT_{max} = 0.45$  in the stoichiometric sample (Table 5-4).

**Table 5-4 – Thermoelectric figures of merit for the highest performing synthetic Cu-S containing thermoelectrical materials as observed in the literature**

Mineral Type	Nominal Composition	$ZT_{max}$	$ZT_{max}$ Temperature/ K	$ZT_{550K}$	Ref
Bornite	$Cu_{4.972}Fe_{0.968}S_4$	0.84	673	0.79	This Work
Chalcopyrite	$Cu_{0.97}Fe_{1.03}S_2$	0.33	700	0.19	39
Digenite/Chalcocite	$Cu_{1.8}S/ Cu_{1.96}S$	0.5	673	0.28	35
Chalcocite	$Cu_{1.97}S$	1.7	1000	0.25	14
Tetrahedrite	$Cu_{10.5}Ni_1Zn_{0.5}Sb_4S_{13}$	1.03	575	0.77	13
Colusite	$Cu_{26}Nb_2Ge_6S_{32}$	1.0	663	0.71	36
Mohite	$Cu_2Sn_{0.9}In_{0.1}S_3$	0.56	773	0.34	37

The power factors were clearly higher in the series  $Cu_{5+y}Fe_{1-y}S_4$  and the series  $Cu_{5-x}FeS_4$  clearly showed better thermal performance. As such, the two chemical substitution methods were combined in an attempt to exploit the advantages offered by each method.

This allowed for the achievement of higher power factors without negatively impacting the thermal conductivity of the samples. As a result the highest performing known bornite samples were achieved with  $ZT = 0.79$  at 550 K and  $ZT_{max} = 0.84$  (Table 5-4). With further enhancements bornite could provide a low-cost choice for thermoelectric materials for use in the recovery of low-grade industrial waste heat.

## Chapter 6 Structural characterisation of tetrahedrite at low temperatures

### 6.1. Introduction

In recent years, the natural mineral tetrahedrite,  $\text{Cu}_{12}\text{Sb}_4\text{S}_{14}$ , has shown potential as an alternative p-type thermoelectric owing to its low cost and high thermoelectric performance.<sup>294</sup> It has attracted considerable interest because of these valuable characteristics.<sup>295</sup> Tetrahedrite crystallises in the space group  $I\bar{4}3m$  at room temperature (Figure 1-24(a)),<sup>296</sup> and is known to be a mixed-valence semiconductor, thus the ionic composition may be formulated as  $(\text{Cu}^{2+})_2(\text{Cu}^+)_{10}(\text{Sb}^{3+})_4(\text{S}^{2-})_{13}$ .

Although the physical behaviour of tetrahedrite is known across the temperature range  $T = 2 - 800$  K, there was only a complete description of the structure over the temperature range,  $T = 100 - 800$  K prior to the work in this chapter being presented in the publication “Jahn–Teller Driven Electronic Instability in Thermoelectric Tetrahedrite” S. Long *et al.*, *Adv. Func. Mater.*, 1909409.<sup>297</sup> The low-temperature behaviour of tetrahedrite has not attracted significant interest until recently. Heat capacity data presented by Lara-Curzio *et al.* revealed evidence of a low-temperature structural phase transition in stoichiometric tetrahedrite, however the peak in the  $C_p$  data at  $T \approx 85$  K corresponding to the transition was not observed for zinc-substituted samples.<sup>298</sup> Powder X-ray diffraction experiments at  $T < 90$  K reveal the presence of additional Bragg reflections in stoichiometric tetrahedrite samples. These reflections have been indexed on the basis of tetragonal supercells of tetrahedrite, May *et al.* and Tanaka *et al.* propose a primitive tetragonal  $\sqrt{2}a \times \sqrt{2}a \times a$  supercell and a body-centered tetragonal  $2a \times 2a \times 2c$  supercell, respectively.<sup>299–301</sup> By contrast, Nasanova *et al.* do not report on any observations in the diffraction data that are indicative of a structural phase transition and the data at  $T < 90$  K is indexed using the cubic space group  $I\bar{4}3m$ .<sup>161</sup>

Each of these structure-property investigations reports an anomaly in the lattice parameter at *ca.* 90 K coexisting with anomalies in the thermal and electrical transport properties. This is accepted as a metal-to-semiconductor transition (MST).<sup>302</sup> Moreover, a marked dip in the magnetic susceptibility occurs at this transition temperature and may be attributed to antiferromagnetic ordering of the magnetic moments of the  $\text{Cu}^{2+}$  ions. Insights from EPR spectroscopy, heat capacity and magnetic measurements led Di Benedetto *et al.* to conclude that, in the cubic phase, two Cu(II) cations per formula unit should be disordered

over the tetrahedral sites.<sup>303</sup> Results from XPS analysis of tetrahedrite give a conflicting observation that copper is present in tetrahedrite only as monovalent cations, Cu(I), thus eliminating the possibility of antiferromagnetic order and the Jahn-Teller instability inherent to a Cu(II) system.<sup>300</sup> Furthermore, <sup>63</sup>Cu-NMR data collected on stoichiometric tetrahedrite are indicative of a nonmagnetic insulating ground state.<sup>304</sup> Clearly there is some uncertainty regarding the structural behaviour of tetrahedrite at low temperatures and the origin of the magnetic and electronic phase transition. We have sought to address this problem through the collection of neutron diffraction, electrical transport and magnetic susceptibility data on a stoichiometric sample of tetrahedrite.

### ***6.2. Experimental Procedure***

A sample with composition  $\text{Cu}_{12}\text{Sb}_4\text{S}_{13}$  has been synthesised from a stoichiometric mixture of the elements copper (99.5%, Sigma Aldrich), antimony (99.5%, Alfa Aesar) and dried sulphur (flakes, 99.99%, Sigma Aldrich). After the elements were ground together in an agate mortar, the powdered mixture was added to a 25 mL stainless steel milling jar under an argon atmosphere with 6 mm milling balls (2 : 7 g ratio of powder to balls). The sample was milled for 8 h in a Retsch Planetary Ball Mill PM100 operating at 600 rpm with a change in rotational direction every 30 min. The resulting powder was loaded into a tungsten carbide mould and sandwiched between graphite foil and tungsten carbide dies. The mould was heated to 693 K under a nitrogen atmosphere and a pressure of 125 MPa was applied for 30 mins to complete synthesis and consolidate the sample. The pelleted sample was then ground into a powder using an agate mortar, this was used in the diffraction and magnetism experiments. A second pressing was performed on a fraction of this powdered sample, using the same conditions as the first pressing, for electrical transport and thermal property measurements.

Powder X-Ray diffraction data were collected on a Bruker D8 Advance (Cu  $K\alpha_1$ :  $\lambda = 1.5405 \text{ \AA}$ ) diffractometer, using a LynxEye detector and a Ge monochromator, prior to and after neutron diffraction experiments. Neutron powder diffraction data were collected using the WISH diffractometer at the ISIS neutron facility. The sample was loaded into a cryostat and neutron diffraction data were collected on cooling, between 120 K to 1.5 K, and on heating, between 1.5 K and 300 K in steps of roughly 10 – 20 K. All Rietveld refinements performed on all powder diffraction data were carried out using the GSAS software package.<sup>272</sup>

Magnetic susceptibility measurements were performed on a SQUID Magnetometer, Quantum Design MPMS XL-7. Data were collected over the temperature range  $T = 1.5 - 300$  K for both Field Cooled and Zero Field Cooled measurements, using a field of  $H = 10$  kOe. Field sweep experiments were performed at a temperature of 1.5 K between  $H = -10$  to 10 kOe.

Resistivity and heat capacity data were collected on a Physical Property Measurement System, Quantum Design PPMS-9. The electrical resistivity was recorded over the temperature range  $T = 1.5 - 300$  K and using the Van der Pauw geometry. Specific heat capacity was measured on a fragment of the same pellet, and data were collected over the temperature range  $T = 1.5 - 300$  K using the Quantum Design PPMS-9.

### ***6.3. Diffraction Results and Analysis***

#### ***6.3.1. Phase Analysis at Room Temperature***

Powder X-ray diffraction data were collected at room temperature for the product from mechanochemical and hot-pressing methods. Phase analysis was performed using the EVA software and revealed the presence of a majority tetrahedrite phase and the presence of a secondary stannite-like phase,  $\text{Cu}_3\text{SbS}_4$ , in small quantities. This is consistent with observations in the literature which show that, regardless of the synthesis method, this impurity phase will be present in the sample if the reaction mixture is stoichiometric.<sup>144,305-308</sup> However, single-phase behaviour is commonly observed for chemically substituted samples of tetrahedrite. For example, sulphur deficiency, substitution of copper for divalent transition metals, substitution at the antimony cation site or substitution at the anion sites will provide single-phase tetrahedrite.<sup>144,161,305-308</sup>

Phase analysis of the neutron diffraction data for the same sample of tetrahedrite revealed an additional phase. These weak reflections were present as shoulders on each of the reflections corresponding to the majority tetrahedrite phase (Figure 6-1), and could be indexed on the basis of a slightly larger cubic unit cell of tetrahedrite, ( $a = 10.4501(25)$  Å at 300 K, compared to  $a = 10.32889(2)$  Å at 300 K in the majority phase) indicating that this was an additional tetrahedrite phase, present in small quantities. Comparably larger unit cells are observed in copper-rich variants of tetrahedrite,<sup>164</sup> suggesting that a copper-rich phase may be present in the sample. The presence of this secondary tetrahedrite phase was not evident on initial characterisation using laboratory X-ray diffraction. A phase analysis of the sample using X-ray diffraction data collected some months later reveal the persistence of this Cu-rich tetrahedrite phase. Relative weight percentages of each of these

phases were determined from Rietveld analysis of the powder neutron diffraction data collected at 300 K and indicates a sample composition of:  $wt\% = 84.39(3)$  of a tetrahedrite phase with  $a = 10.3289(2)$  Å,  $wt\% = 7.70(7)$  of the second tetrahedrite phase with an enlarged unit cell and  $wt\% = 7.92(4)$  of  $Cu_3SbS_4$ .

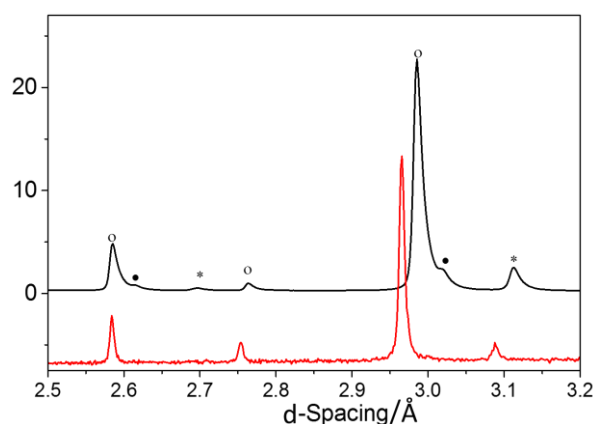


**Figure 6-1** – Room-temperature diffraction patterns as recorded on the same sample of tetrahedrite, collected at room temperature on: red – Bruker D8 Advanced X-ray diffractometer (before neutron experiments); black – WISH diffractometer at the ISIS neutron facility. Open circles – Majority tetrahedrite phase; Closed circles – minority tetrahedrite phase; Stars –  $Cu_3SbS_4$ .

### 6.3.2. Variable Temperature Neutron Diffraction

Although the neutron-diffraction patterns recorded at high- and low-temperatures are broadly similar (Figure 6-3(a,d)), there are additional Bragg reflections with relatively low intensity apparent in diffraction patterns when  $T < 90$  K (Figure 6-2). These reflections cannot be assigned to any reflections using the cubic structural model of the high-temperature phase (space group  $I\bar{4}3m$ ). These observations are consistent with the proposed lattice parameters of the low-temperature phase suggested by May *et al.*<sup>299</sup> They state that a tetragonal supercell with lattice parameters,  $a_t = \sqrt{2}a_c$ ,  $c_t = a_c$ , can be used to describe the low-temperature phase, allowing for all reflections to be indexed. Meanwhile, the secondary tetrahedrite phase can be indexed on the basis of the cubic unit cell at low-temperatures.

The presence of residual magnetic scattering at long  $d$ -spacings was investigated by subtracting the diffraction data recorded at 80 K from data recorded at base temperature, 1.5 K. The peaks that appear at 1.5 K and not at 80 K,  $d \approx 5.5$  and  $14.6$  Å, correspond to nuclear reflections of the tetragonal  $a_t = \sqrt{2}a_c$  super cell (Table 6-2). The absence of any

other additional intensity suggests that there is no magnetic scattering at low-temperatures (Figure 6-2(b)).

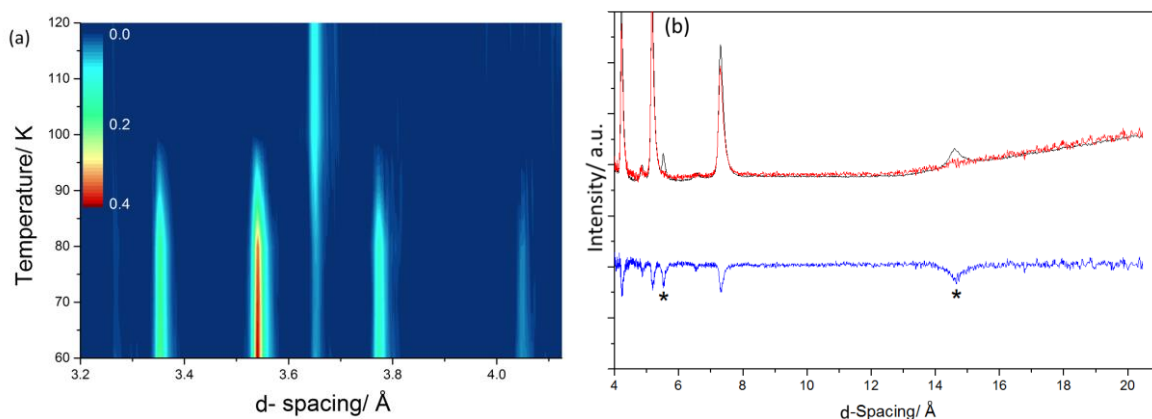


**Figure 6-2** - (a) – Powder neutron diffraction data as a function of temperature over a selected temperature and d-spacing range, clearly showing the appearance of additional Bragg reflections; (b) – Plot to show additional high d-spacing reflections, \* correspond to nuclear supercell reflections. Red – 80 K diffraction data; Black – 1.5 K diffraction data; and Blue – difference profile for  $y_{80K} - y_{1.5K}$ .

The structure transformations using the ISODISTORT<sup>309</sup> software package were performed by Dr P. Vaqueiro and were used to investigate possible tetragonal subgroups of the high-temperature parent phase. The cubic lattice parameters, determined by Rietveld refinement of the higher temperature phase, were transformed to their equivalent tetragonal lattice parameters using the matrix:

$$\begin{pmatrix} 1 & -1 & 0 \\ 1 & 1 & 0 \\ 0 & 0 & 1 \end{pmatrix}$$

$P\bar{4}$ ,  $P\bar{4}m2$ ,  $P\bar{4}c2$ ,  $P\bar{4}b2$  and  $P\bar{4}n2$ , were the five alternative tetragonal space groups, output by the ISODISTORT software as full structural models, that could describe a distorted structure of the space group  $I\bar{4}3m$ . The GSAS software package and the neutron diffraction data collected at 1.5 K from 3 banks ( $2\theta = 90, 120$  and  $150^\circ$ , banks 3, 4 and 5) were used in subsequent Rietveld refinements for each of these structural models. The resulting observations from these refinements indicated that the space group  $P\bar{4}c2$  provides the best description of the structure of tetrahedrite below 1.5 K. The alternative structural models resulted in larger  $R_{wp}$  and  $\chi^2$  values or negative thermal parameters. This new structural model now allowed for a reliable description of the structure of tetrahedrite at each temperature recorded in this experiment. All diffraction data recorded above  $T = 90$  K can

be described using the cubic structure in  $I\bar{4}3m$  (Table 6-1 and e-appendix). Below  $T = 80$  K the structure can be described using the new structural model with space group  $P\bar{4}c2$  (Table 6-2 and e-appendix).

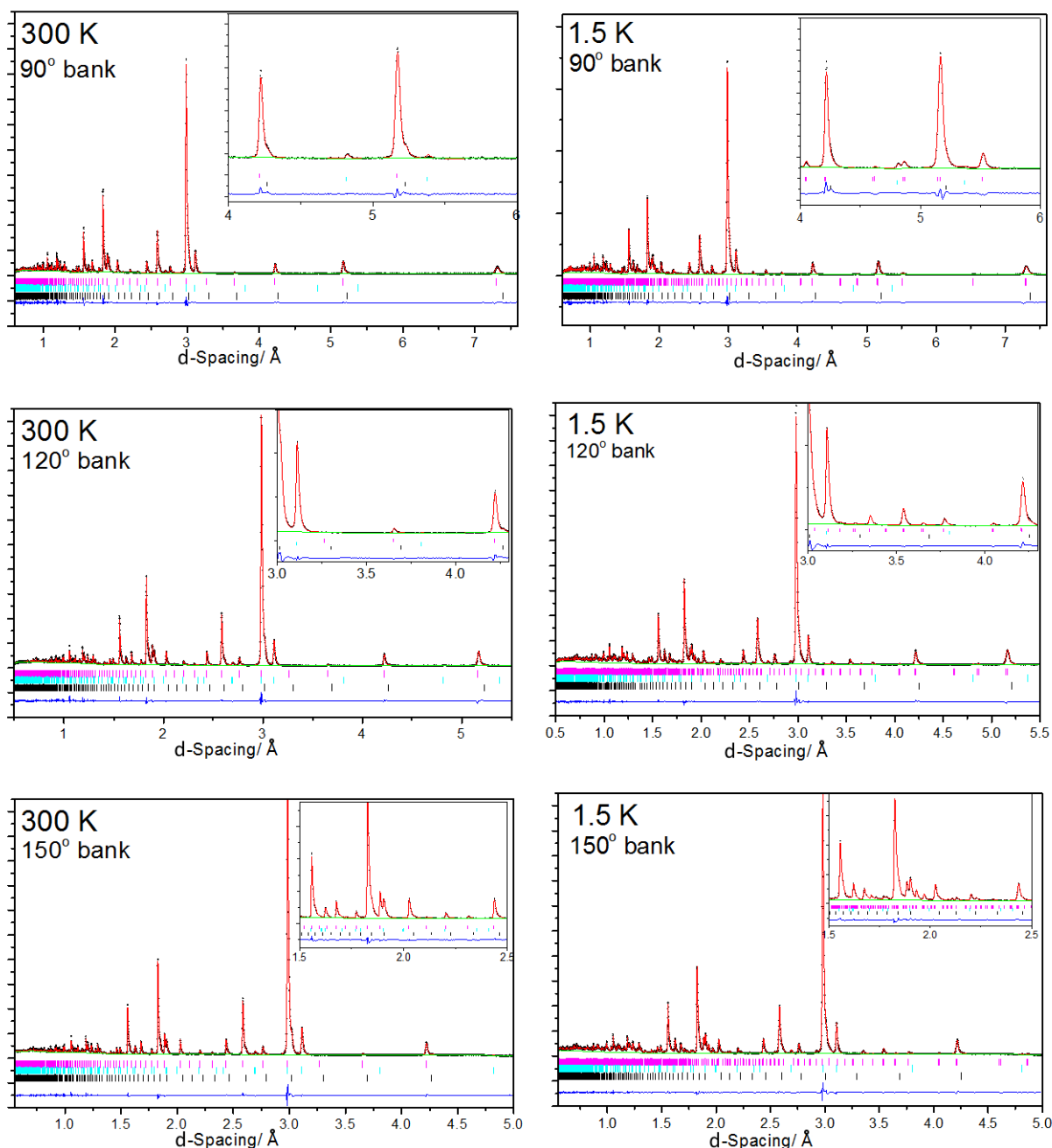


**Figure 6-3** – Rietveld refinement profiles of the neutron diffraction data collected from three detector banks,  $2\theta = 90, 120$  and  $150^\circ$ , banks 3, 4 and 5, for tetrahedrite at 300 K and 1.5 K. The observed, calculated and difference profiles are denoted by crosses, the red solid line and the lower full line respectively. Markers correspond to the Bragg reflection for: Pink – Majority tetrahedrite phase; Blue –  $\text{Cu}_3\text{SbS}_4$ ; Black – minority tetrahedrite phase.

**Table 6-1** - Crystallographic parameters, determined from Rietveld refinements, for the majority tetrahedrite phase at 300 K with space group  $I\bar{4}3m$ . The atomic positions of the occupied crystallographic sites are:  $12d$  ( $1/2, 1/4, 0$ );  $12e$  ( $0, 0, z$ );  $8c$  ( $x, x, x$ );  $24g$  ( $x, x, z$ ) and  $2e$  ( $0, 0, 0$ ).

Temperature/ K	300 K			
Majority Tetrahedrite Phase				
Space Group	$I-43m$			
Phase Fraction/ %	84.39(3)			
Lattice Parameters	$a/ \text{Å}$	10.32889(2)		
S(all)	$U_{iso} / \text{Å}^2$	0.0205(4)		
Cu(1), Sb	$U_{iso} / \text{Å}^2$	0.0213(2)		
Cu(2)	$U_{iso}^* / \text{Å}^2$	0.0629(7)*		
all Cu, S, Sb	SOF	1		
Atom Label	Wykoff Symbol	$x$	$y$	$z$
Cu(1)	$12d$	$1/2$	0	$1/4$
Cu(2)	$12e$	0	0	0.2176(1)
Sb	$8c$	0.2683(1)	0.2683(1)	0.2683(1)
S(1)	$24g$	0.8852(1)	0.8852(1)	0.3632(2)
S(2)	$2e$	0	0	0
Goodness of fit parameters	$\chi^2$	15.66		
total	$R_{wp}/\%$	3.63	$R_p/\%$	3.02
150° bank	$R_{wp}/\%$	3.35	$R_p/\%$	2.61
120° bank	$R_{wp}/\%$	3.68	$R_p/\%$	3.03
90° bank	$R_{wp}/\%$	3.91	$R_p/\%$	3.55

\* $U_{ij}$  vales have been converted to a single value for  $U_{iso}$ , which are presented above

**Table 6-2** - Crystallographic parameters, determined from Rietveld refinements using neutron diffraction data, for the majority tetrahedrite phase at 1.5 K, in space group  $P\bar{4}c2$ .

The atomic positions of the occupied crystallographic sites are:  $8j(x, y, z)$ ;  $4e(x, x, 1/4)$ ;

$2d(1/2, 1/2, 0)$ ;  $4i(0, 1/2, z)$ ;  $2c(0, 0, 0)$ ;  $4f(x, x, 3/4)$ .

Temperature/ K	1.5 K			
Majority Tetrahedrite Phase				
Space Group	$P-4c2$			
Phase Fraction/ %	80.62(3)			
Lattice Parameters	$a/\text{Å}$	14.60192(6)		
	$c/\text{Å}$	10.29187(8)		
S(all)	$U_{iso}/\text{Å}^2$	0.0032(4)		
Cu(1all), Sb(all)	$U_{iso}/\text{Å}^2$	0.00918(23)		
Cu(2all)	$U_{iso}/\text{Å}^2$	0.01257(38)		
all Cu, S, Sb	SOF	1		
Atom Label	Wykoff Symbol	$x$	$y$	$z$
Cu(1 <sup>i</sup> )	$8j$	0.8801(3)	0.3753(3)	0.7570(3)
Cu(1 <sup>ii</sup> )	$4e$	0.8645(3)	0.8645(3)	1/4
Cu(1 <sup>iii</sup> )	$4e$	0.3799(3)	0.3799(3)	1/4
Cu(1 <sup>iv</sup> )	$2d$	1/2	1/2	0
Cu(1 <sup>v</sup> )	$4i$	0	1/2	0.5224(4)
Cu(1 <sup>vi</sup> )	$2c$	0	0	0
Cu(2 <sup>i</sup> )	$4f$	0.6491(3)	0.6491(3)	3/4
Cu(2 <sup>ii</sup> )	$8j$	0.6383(2)	0.1410(2)	0.2180(3)
Cu(2 <sup>iii</sup> )	$4f$	0.1290(2)	0.1290(2)	0.75
Cu(2 <sup>iv</sup> )	$8j$	0.7507(2)	0.7276(2)	0.0404(3)
Sb( <sup>i</sup> )	$8j$	0.7444(4)	0.4775(3)	0.0218(5)
Sb( <sup>ii</sup> )	$8j$	0.7451(4)	0.0071(3)	0.5085(5)
S(1 <sup>i</sup> )	$8j$	0.7426(6)	0.8484(5)	0.0898(7)
S(1 <sup>ii</sup> )	$8j$	0.7545(6)	0.3670(6)	0.6212(7)
S(1 <sup>iii</sup> )	$8j$	0.0142(6)	0.6296(6)	0.652(1)
S(1 <sup>iv</sup> )	$8j$	0.0031(6)	0.1196(6)	0.140(1)
S(1 <sup>v</sup> )	$8j$	0.4862(6)	0.6222(6)	0.135(1)
S(1 <sup>vi</sup> )	$8j$	0.4954(5)	0.1332(6)	0.616(1)
S(2)	$4f$	0.7676(3)	0.7676(3)	3/4
Goodness of fit parameters	$\chi^2$	83.8		
total	$R_{wp}/\%$	3.52	$R_p/\%$	3.09
150° bank	$R_{wp}/\%$	3.21	$R_p/\%$	2.76
120° bank	$R_{wp}/\%$	3.57	$R_p/\%$	3.13
90° bank	$R_{wp}/\%$	3.82	$R_p/\%$	3.48

### 6.3.2.1. Structure of the Low-Temperature Phase of Tetrahedrite

The structure of tetrahedrite at low temperature is an ordered tetragonal supercell,  $Z = 4$ , of the high temperature phase,  $Z = 2$ . Therefore, the structural features are largely similar but distorted in the low-temperature phase. The collapsed sodalite framework of  $\text{CuS}_4$  tetrahedra is distorted, with both the ‘square’ windows and the ‘hexagonal’ windows showing imperfect geometry. Similarly the  $\text{SbS}_3$  trigonal pyramids and the  $(\text{Cu}(2)\text{S}(1)_2)_6\text{S}(2)$  spinner units become distorted. The sulphur atom that centres the spinner unit and the sodalite cage shifts from the very centre of the sodalite cage, displacing towards one of the ‘square’ windows (Figure 6-4).

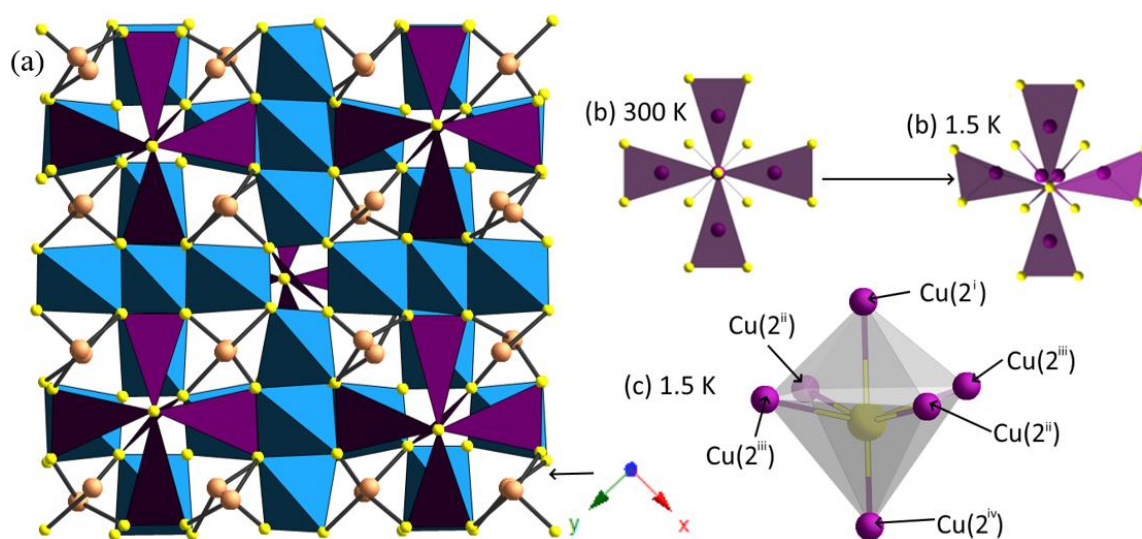


**Figure 6-4** – (a) Rotated projection view along the [001] direction of the low-temperature crystal structure of tetrahedrite as determined from Rietveld refinement against neutron diffraction data. (b) Distortion of the spinner unit that occurs with the structural transformation. (c) The four individual cation sites of the  $\text{Cu}(2)_6\text{S}(2)$  octahedron. Blue – tetrahedral copper; Purple – trigonal copper; yellow spheres – sulphur and orange spheres – Antimony.

Most notably, the distortion of the S(2) environment and that of the surrounding Cu(2) atoms may be responsible for the changes in the physical properties. This  $\text{Cu}(2)_6\text{S}(2)$  octahedron is regular at high temperature, with six identical Cu-S bond lengths and Cu-S-Cu bond angles of  $90^\circ$ . Upon transformation to the  $P\bar{4}c2$  space group, the sulphur centred octahedron shows significant structural distortion, with the S(2) atom shifting off-centre. Furthermore, the change of space group allows for this distortion because the change in symmetry leads to an increase in the number of crystallographically distinct sites, coupled with a doubling of the unit cell size. The two distinct cation sites, at high temperature, are

the tetrahedral and trigonal sites. The tetrahedral, Cu(1), type cations are described by 6 individual sites in the low-temperature phase while the trigonal Cu(2) sites are described by 4 individual sites. The distortions across these crystallographic sites will be investigated in the following sections.

### 6.3.2.2. Temperature Dependence of Cu-S Bonding Parameters

The neutron diffraction data were collected on cooling and heating. The structural refinements using data collected at each temperature reveal a hysteresis in the phase transition temperature of *ca.* 10 K, between heating and cooling. The tetragonal unit cell describes the diffraction data below 80 K on cooling and 90 K on heating, meanwhile the cubic unit cell describes the diffraction data above these temperatures. The lattice parameter and unit-cell volume data, as determined by Rietveld refinements, highlight this hysteresis (Figure 6-5(a,b)). These data are presented in Figure 6-5 as the pseudo cubic lattice parameters,  $a_c = b_c = a_t/\sqrt{2}$ ,  $c_c = c_t$  (and volume) to enable comparison.

With decreasing temperature, the cubic lattice parameter decreases from  $a = 10.32889(2)$  Å at 300 K to  $a = 10.30653(2)$  Å at 100 K. At the phase-transition temperature the pseudo-cubic lattice parameters of the unit cell diverge,  $a_c$  markedly increases and  $c_c$  parameter decreases. This observation is consistent with observations made by May *et al.*<sup>299</sup> Below 80 K the lattice parameters do not show any notable variation with decreasing temperature. The divergence of lattice parameters at the phase transition also leads to an anomaly in the lattice volume. The tetragonal phase exhibits a comparatively larger lattice volume.

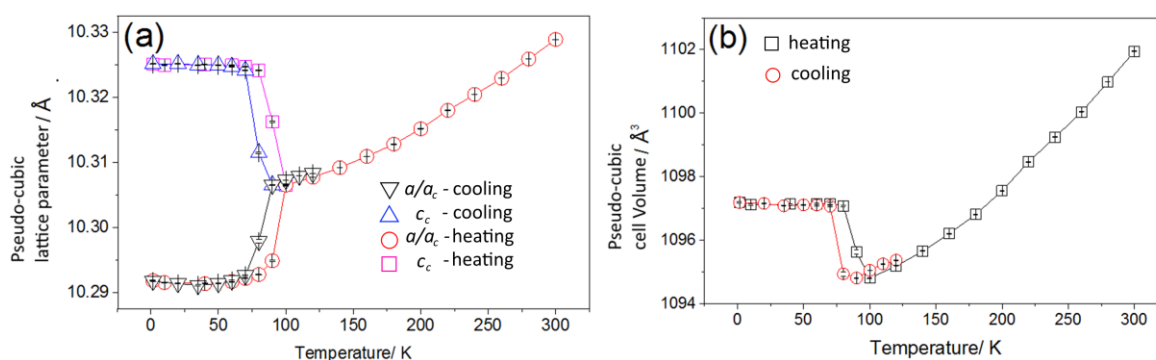


**Figure 6-5** – Temperature dependence of the pseudo-cubic lattice parameters for tetrahedrite: (a) cell-parameters; (b) cell volume.

### 6.3.2.3. Changes in the Behaviour of the Cu(2)-S Bond Distances

In the following section some of the bond distances, angles and distortion parameters are presented in variable temperature plots (tabulated data in e-appendix). The change in the

Cu(2)-S bond distances and bond angles as a function of temperature provide further insight to the structural distortion within the  $(\text{Cu}(2)\text{S}(1)_2)_6\text{S}(2)$  spinner moiety.

The Cu(2)-S(2) bond distance shows little variation with temperature in the cubic phase, which exhibits a length of *ca.* 2.25 Å between  $T = 100 - 300$  K. In the tetragonal phase the Cu(2) site splits into 4 crystallographically distinct sites, giving 4 unique Cu(2)-S(2) bond distances in the octahedral unit (Figure 6-4(c)). The Cu-S bond distances of the  $8j$  Cu(2) cations, Cu(2<sup>ii</sup>)-S(2) and Cu(2<sup>iv</sup>)-S(2) which are adjacent to one another, show little change as a result of the structural phase transition with values of *ca.* 2.26 and 2.25 Å, respectively (Figure 6-6(a)). By contrast, the Cu-S distances for the  $4f$  Cu(2) cations - which sit trans to one another- show marked changes as a result of the phase transition (Figure 6-6(a)). The Cu(2<sup>i</sup>)-S(2) distance increases significantly to 2.45 Å a change of *ca.* 9 % and the Cu(2<sup>iii</sup>)-S(2) distance decreases by *ca.* 6% to 2.12 Å. The S(2) cation moves out of the plane of the Cu(2<sup>ii</sup>) and Cu(2<sup>iv</sup>) cations towards the Cu(2<sup>iii</sup>) position. Anomalies in the bond angles accompany the changing bond distances.

In the cubic phase, each pair of trans Cu(2) cations has a Cu(2)-S(2)-Cu(2) bond angle of 180°. This behaviour is preserved in the tetragonal phase for the Cu(2<sup>i</sup>) and Cu(2<sup>iii</sup>) trans pair, Cu(2<sup>i</sup>)-S(2)-Cu(2<sup>iii</sup>) = 180°. The Cu(2)-S(2)-Cu(2) bond angles for the Cu(2<sup>ii</sup>)-Cu(2<sup>ii</sup>) and Cu(2<sup>iv</sup>)-Cu(2<sup>iv</sup>) trans pairs do not display linear behaviour in the tetragonal phase. Each Cu(2<sup>ii/iv</sup>)-S(2)-Cu(2<sup>ii/iv</sup>) show a striking deviation on the order of 25 – 30° around the phase transition (Figure 6-6(b)).

Each of the Cu(2) cations is coordinated to two S(1) and one S(2) anions. The structural distortion centred around the S(2) has an impact on the next nearest neighbours and thus the Cu(2)-S(1) bond distances, the most notable of which is the behaviour around the Cu(2<sup>i</sup>) and Cu(2<sup>iii</sup>) centres. The Cu(2)-S(1) bond distances in the cubic phase are comparable to the Cu(2)-S(2) distances at *ca.* 2.25 Å. Interestingly all of the Cu-S bond distances for the Cu(2<sup>iii</sup>) cation contract as a result of the cubic to tetragonal phase transformation with a Cu(2<sup>iii</sup>)-S(1<sup>iv</sup>) distance of *ca.* 2.17 Å. Similarly each of the Cu-S bond distances for the Cu(2<sup>i</sup>) cation expand during this transformation with a Cu(2<sup>i</sup>)-S(1<sup>v</sup>) distance of *ca.* 2.32 Å.

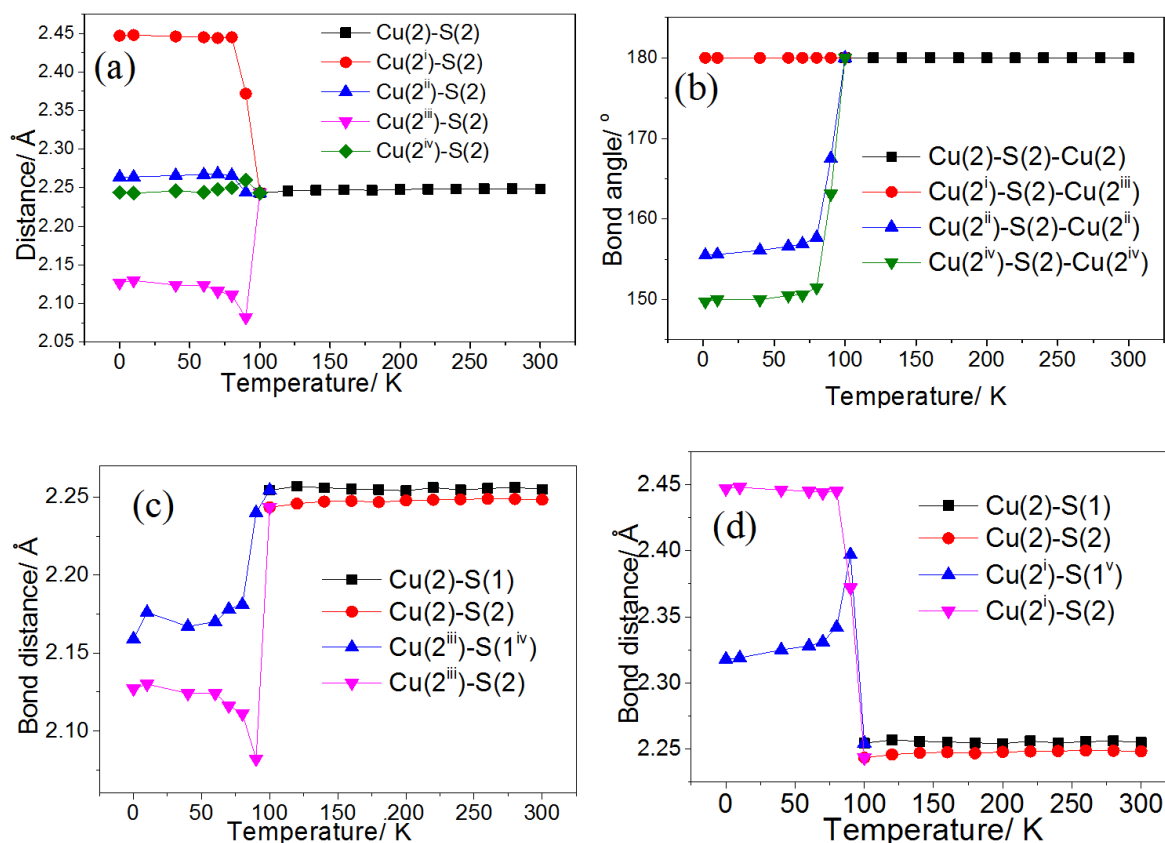


**Figure 6-6** – Temperature dependence of the Cu-S bond distances and angles for the Cu(2) cations in the spinner unit in Cu<sub>12</sub>Sb<sub>4</sub>S<sub>13</sub>. (a) – Cu(2)-S(2) bond distances and (b) angles for the sulphur centred octahedra; (c) – Bond distances for the Cu(2<sup>iii</sup>)-S<sub>3</sub> unit; (d) – Bond distances for the Cu(2<sup>i</sup>)-S<sub>3</sub> unit.

The calculated polyhedral distortion parameters reveal a huge overall distortion for the S(2)Cu(2)<sub>6</sub> octahedron in the tetragonal phase. The S(2) displacement results in huge bond angle distortions,  $\sigma_{oct}^2 > 200$  at 1.5 K, and is linked to the aforementioned Cu(2<sup>ii</sup>) and Cu(2<sup>iv</sup>) cations. Meanwhile the large bond length distortion parameter,  $\Delta_{oct} \times 10^3 = 1.6$  at 1.5 K, is linked to the Cu(2<sup>i</sup>) and Cu(2<sup>iii</sup>) cations (Figure 6-7). Individual bond lengths for the Cu(1)S(1)<sub>4</sub> tetrahedra are available in the e-appendix. These data reveal the distortion of the tetrahedra within the sodalite cage. In the cubic phase the degree of tetrahedral bond distortion is trivial,  $\sigma_{tet}^2 < 10$ , and all Cu(1)-S(1) bond distances are equal. At base temperature, 1.5 K, each of the tetrahedra exhibit,  $\sigma_{tet}^2$ ,  $\Delta_{tet}$ , values that are not substantial, but show the distortion across the S(2)Cu(2)<sub>6</sub> octahedron further influences the structure of the sodalite cage.

In the high-temperature phase the trigonal CuS<sub>3</sub> unit is distorted. S-Cu-S bond angles show a significant variation, 132 ° to 96 °, and have a bond angle variance of,  $\sigma_{trig}^2 \approx 400$ . The

Cu(2<sup>ii,iv</sup>) metal centres display an increase in polyhedral distortion upon transformation to the tetragonal phase. The Cu(2<sup>iv</sup>) cation is subject to relatively large angular distortions owing to the S(1<sup>ii</sup>)-Cu(2<sup>iv</sup>)-S(2) coordination which approaches linearity,  $\theta \approx 155^\circ$ , as a result of the Cu(2) cations displacement from the centre of the polyhedra. The Cu(2<sup>iv</sup>) cation displays a similar behaviour,  $\theta \approx 145^\circ$ .

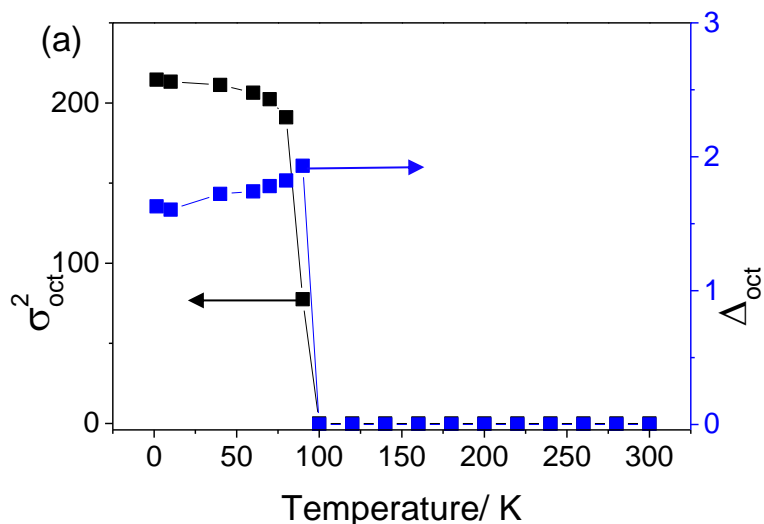


**Figure 6-7** – Temperature dependence of the distortion parameters for the S(2)Cu(2)<sub>6</sub> octahedron. Black – bond angle distortion parameter; Blue – Bond length deviation parameter.

The Cu(2<sup>iii</sup>)S<sub>3</sub> and Cu(1<sup>iv</sup>)S<sub>4</sub> polyhedra show structural distortions that are trivial compared to their counterparts. Meanwhile, the Cu(1<sup>ii</sup>) S<sub>4</sub>, Cu(2<sup>ii</sup>) S<sub>3</sub> and Cu(2<sup>iv</sup>)S<sub>3</sub> polyhedra are subject to comparatively large distortion parameters. In particular, the huge distortions in S(2)Cu(2)<sub>6</sub> may influence the behaviour across each of these structural units. Each of these distortion parameters show some temperature dependence. Both octahedral distortion parameters show a weak temperature dependence.  $\sigma_{oct}^2$  becomes more distorted with decreasing temperature, whilst  $\Delta_{oct}$  shows the opposite behaviour.

Transformation to the low temperature tetragonal phase is accompanied by a sharp increase in angular and bond distance distortion parameters. At temperatures below the phase transition, the  $\sigma^2(T)$  and  $\Delta(T)$  plots reveals an anomaly between the 10 K and 40 K data (Figure 6-8(a-d)). A marked drop is observed in the tetrahedral bond length distortion parameter. An anomaly is also observed in the bond angle parameter for Cu(1<sup>i</sup>) and Cu(1<sup>iv</sup>). The temperature dependence of  $\sigma_{trig}^2$  and  $\Delta_{trig}$  for Cu(2)S<sub>3</sub> units also reveal a similar anomaly across the temperature range  $T = 10$  to 40 K. The origins of this change in

structural behaviour are not understood, diffraction experiments with finer temperature resolution across the temperature range  $T = 1.5$  to 60 K would be required to understand this behaviour.

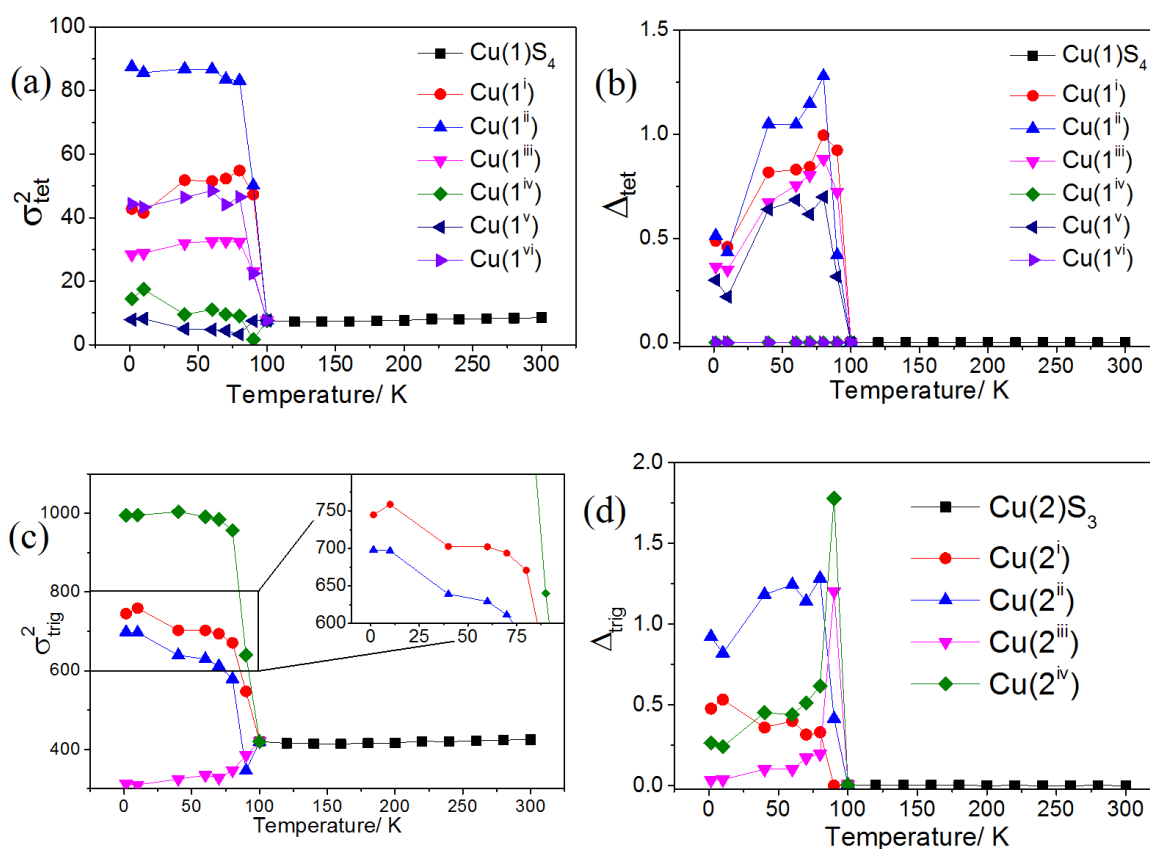


**Figure 6-8** – Temperature dependence of the distortion parameters for each of the copper centred polyhedra in tetrahedrite. (a) tetrahedral bond angle variance for  $\text{Cu}(1^n)$  cations; (b) tetrahedral bond length deviation for  $\text{Cu}(1^n)$  cations; (c) trigonal bond angle variance for  $\text{Cu}(2^n)$  cations; (d) trigonal bond length deviation for  $\text{Cu}(2^n)$  cations.

#### 6.4. Investigating Charge Ordering within Tetrahedrite

##### 6.4.1. Copper-Copper Interactions in the Low-Temperature Structure

The polyhedral distortion of the  $\text{SCu}_6$  octahedron in the tetragonal phase is accompanied by the formation of new Cu-Cu interactions. These metal-metal interactions are not observed in the high-temperature cubic phase, which has Cu(2)-Cu(2) distances of 3.18 Å. Three of the Cu-Cu distances increase across the structural phase transition whilst three contract to distances of Cu(2)-Cu(2) = 2.857(4), 2.956(3) and 2.673(3) Å at 1.5 K (Figure 6-9). These interatomic distances are approaching, or below, the van der Waals' radii for two copper cations, 2.8 Å and the Cu-Cu distance in copper metal, 2.56 Å.<sup>310</sup> The shortened metal-metal distances are indicative of the formation of Cu-Cu bonds. This suggests the

formation of a mixed valent, pentameric cluster of copper cations over the  $\text{Cu}(2^{\text{i}}, 2^{\text{ii}}, 2^{\text{iv}})$  sites in tetrahedrite (Figure 6-9).

Copper-copper bonding is known to occur for both oxidation states, Cu(I) and Cu(II). Formation of homoatomic metal clusters is known to occur in copper(I) and silver chalcogenides through  $d^{10}$ - $d^{10}$  interactions that significantly influence the structure and properties of the material. In these instances, bond distances are on the order of 2.35 to 2.8 Å.<sup>284</sup> Meanwhile, Cu-Cu distances in cuprous organic clusters are generally of the order of 2.6 to 2.8 Å.<sup>311-315</sup> Cu(II) dimers, such as copper (II) acetate,<sup>316</sup> are observed in cases where bridging ligands stabilise the  $d^9$ - $d^9$  interactions and may lead to magnetic interactions. Spin-singlet and spin-triplet states may occur resulting in antiferromagnetic or ferromagnetic interactions, which are influenced by the bridging ligands in the metal-organic clusters.

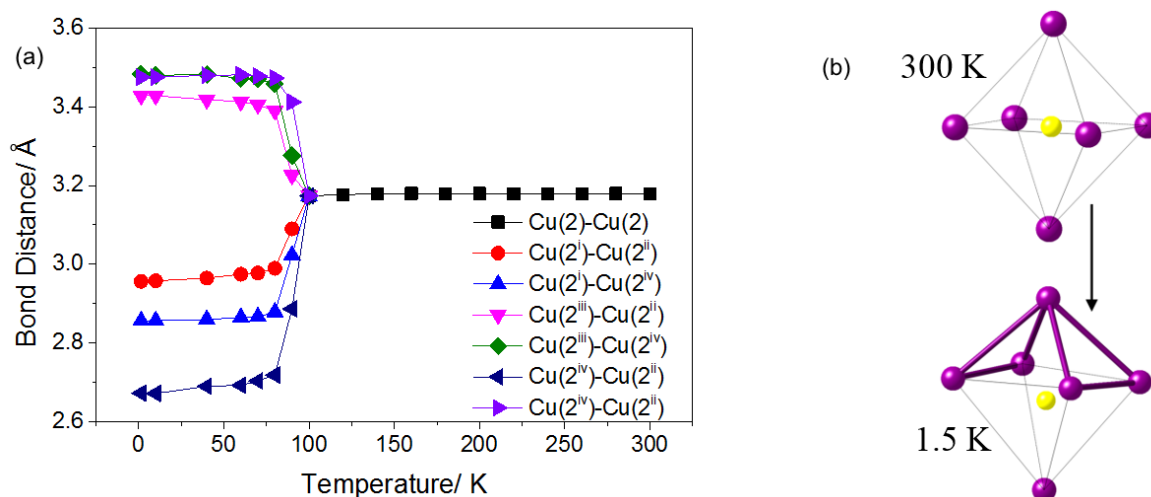


**Figure 6-9** – (a) - Temperature dependence of the Cu-Cu distances over the  $\text{SCu}_6$  octahedron and; (b) – view of the Cu-Cu interactions across the  $\text{SCu}_6$  octahedron highlighting the Cu-Cu bond distances shorter than 3 Å as bold purple lines. Purple spheres- copper atoms; Yellow spheres – sulphur atoms.

A molecular-orbital analysis of the  $(\text{Cu}(2)\text{S}(1)_2)_6\text{S}(2)$  structural cluster, in the high- and low-temperature phases, has allowed for identification and confirmation of structural location of the Cu(II) cations in the tetragonal phase of tetrahedrite. In the cubic phase, the copper atoms are known to be disordered over the tetrahedral sites and the octahedral cluster. Therefore, and in agreement with the average charge of a copper in tetrahedrite being +1.167, the octahedral cluster can be defined as  $\text{Cu}_6^{7+}$ . The low values of  $\Delta_{tet}$  at base temperature 1.5 K are characteristic of Cu(I) cations which are less inclined to show

structural distortion compared to  $d^9$ - Cu(II). This, along with the results from extended Hückel calculations (performed by Dr P. Vaqueiro) for the  $\text{Cu}_6^{7+}$  cluster -which reveals an electronic state susceptible to Jahn-Teller distortion, owing to the degenerate  $^2t_g$  HOMO occupied by 5 electrons- provides the basis to propose a  $\text{Cu}_5^{7+}$  metal cluster for the low-temperature phase (Figure 6-10(a)). The electron configuration of  $\text{Cu}_6^{7+}$  is in agreement with previous Hückel calculations on the octahedral molecular clusters.<sup>317</sup> The  $\text{Cu}_5^{7+}$  should consist of two  $\text{Cu}^{2+}$  and three  $\text{Cu}^+$ . The extended Hückel calculations for this cluster indicate that the HOMO is a singlet state,  $^1b_1$ . Hence there should not be any magnetic ordering within the structure, which is consistent with the absence of magnetic scattering in the neutron diffraction pattern for tetragonal tetrahedrite. Furthermore, the observations from  $^{63}\text{Cu}$  NMR reveal no internal magnetic field over the tetrahedral sites, supporting the idea of  $\text{Cu}^{2+}$  occurring in the trigonally coordinated sites in the low-temperature phase.

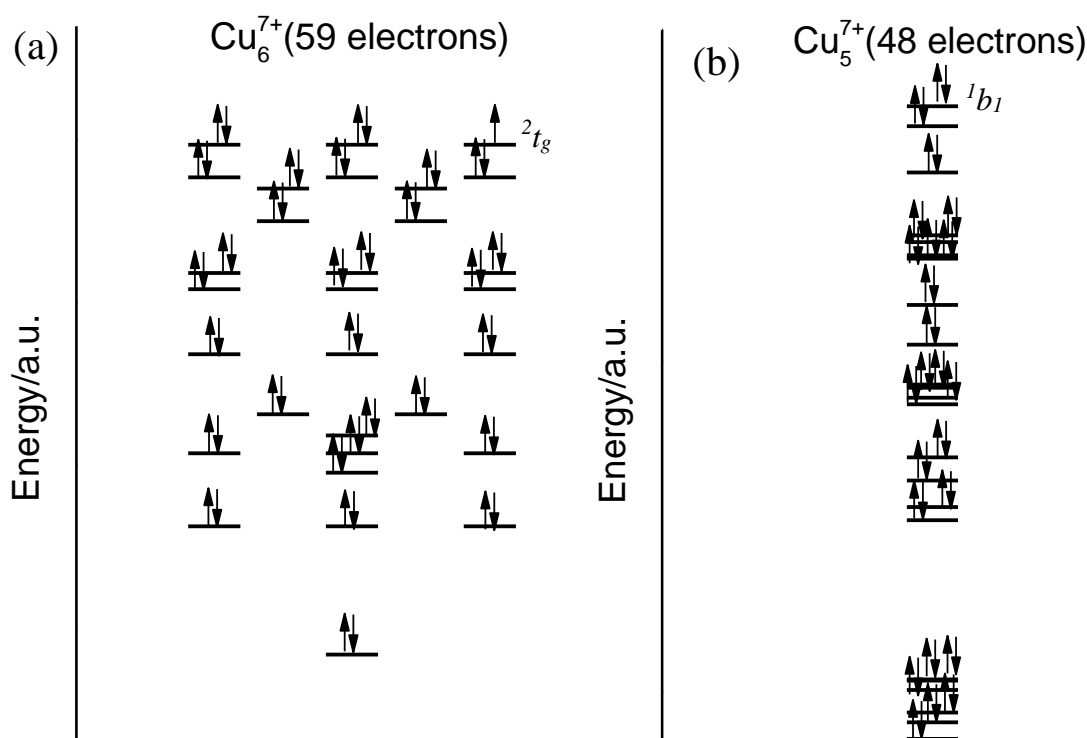


**Figure 6-10** – Molecular orbital diagrams as determined using the Hyperchem software package for: (a) – an octahedral  $\text{Cu}_6^{7+}$  cluster, point group  $O_h$ ; (b) – a distorted square pyramidal  $\text{Cu}_5^{7+}$  cluster, point group  $C_{2v}$ .

### 6.4.2. Temperature Dependence of the Atomic Displacement Parameters

The low thermal conductivity of cubic tetrahedrite has been linked to the thermal motion of the trigonally coordinated copper cations, Cu(2).<sup>318</sup> A weak bonding mode of the copper to the lone pairs located on axial antimony cations leads to an out-of-plane vibrational mode for Cu(2). This behaviour is modelled in the high-temperature phase with anisotropic atomic displacement parameters (ADP) for the Cu(2) cations. At low temperatures, a common value for isotropic ADPs was used to model the cations Cu(2<sup>i</sup>)- Cu(2<sup>iv</sup>). The ADPs of Cu(1<sup>i</sup>)-Cu(1<sup>vi</sup>), Sb<sup>(all)</sup> were constrained to a common value during refinement of both the cubic and tetragonal phases, as were S(1<sup>i</sup>)- S(1<sup>vi</sup>), S(2).

The ADPs of the Cu(1) and Sb cations decrease with decreasing temperature across the entire temperature range  $T = 1.5$  to 300 K. On the other hand, the thermal parameter of the Cu(2) cation shows a marked discontinuity at the phase transition. Here the  $U_{iso}$  value decreases by *ca.* 65 %. Furthermore, there is a divergence in the Cu-Sb bond distances across the phase transition. Half of these distances increase significantly, by *ca.* 15%, whilst some of the distances between the antimony cations and the pentameric cluster cations decrease (Figure 6-11). This behaviour, along with the suppression of the large ADP for the trigonal Cu(2) cation indicates that the rattling mode may be inhibited in the tetragonal phase. This is supported by observations from inelastic neutron scattering experiments on low temperature tetrahedrite.<sup>299</sup> These showed a disappearance of the low-energy vibrational mode corresponding to the rattling mode of the Cu(2) cation.

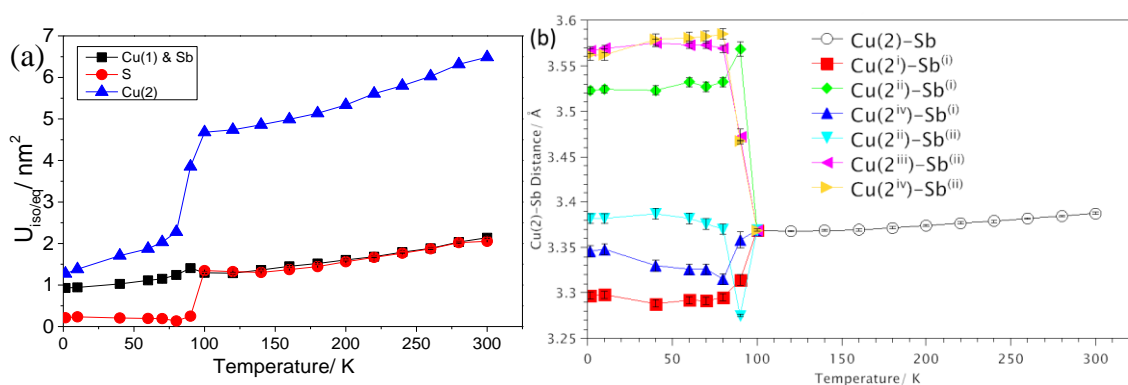


**Figure 6-11** – Temperature dependence of the: (a) anisotropic displacement parameters in tetrahedrite; (b) copper antimony distances in tetrahedrite.

### 6.5. Physical Properties

In the high-temperature cubic phase and across the temperature range  $T = 90$  to 300 K, Curie-Weiss behaviour is followed in the reciprocal magnetic susceptibility data (Figure 6-12(b)). The Weiss constant of  $\theta = -170$  K suggests there are antiferromagnetic

interactions of moderate strength. A similar behaviour in the temperature dependence is followed for the field cooled (FC) and zero field cooled (ZFC) magnetic susceptibility data. There is a marked drop in the magnetic susceptibility at the phase-transition temperature, *ca.* 85 K, followed by an exponential increase in  $\chi_{mol}$  with decreasing temperature (Figure 6-12(a)). This behaviour is consistent with previous reports on the temperature dependence of the magnetic susceptibility.<sup>300,303</sup> At  $T < 10$  K there is a divergence in the behaviour of the FC and ZFC data, here the ZFC continues to increase with decreasing temperature whilst the FC plateaus at *ca.*  $\chi_{mol} = 0.0075$  emu mol<sup>-1</sup>. The Curie constant was determined to be  $\Theta_C = 0.54$  cm<sup>3</sup> K<sup>-1</sup> mol<sup>-1</sup> and calculated from a linear interpolation of the ZFC  $\chi_{mol}^{-1}$  data over the temperature range  $T = 120$  to 175 K (Figure 6-12(b)). This would be consistent with the findings of Di Benedetto as this corresponds to an effective magnetic moment per Cu<sup>2+</sup> of  $\mu_{eff} = 1.5$ , which is close to the expected value for spin-only behaviour for the two copper ions.<sup>303</sup>

The magnetisation data, recorded at  $T = 1.5$  K, reveal a linear increase in magnetisation with increasing field strength (Figure 6-12(c)). The curve passes through the origin and shows no magnetic hysteresis, indicating that there is no spontaneous magnetisation. These observations, along with anomalous behaviour in the magnetic susceptibility, a negative Weiss constant and an absence of magnetic scattering indicates a non-magnetic ground state. This would be consistent with the singlet state pentameric Cu<sub>5</sub><sup>7+</sup> cluster suggested above that accounts for all of the Cu<sup>2+</sup> cations within (Cu<sup>2+</sup>)<sub>2</sub>(Cu<sup>+</sup>)<sub>10</sub>(Sb<sup>3+</sup>)<sub>4</sub>(S<sup>2-</sup>)<sub>13</sub>. The curve of  $\mu_{eff}(T)$  also reveals the phase transition at 90 K. At this temperature there is a marked drop in  $\mu_{eff}$  which then plateaus across the temperature range,  $T = 10$  to 80 K (Figure 6-12(d)). A second anomaly in the ZFC and FC magnetisation data is observed at 10 K, which is consistent with the temperature for the observed anomaly in  $\chi_{mol}(T)$  for the FC data.

The origins of the magnetic anomaly observed at lower temperatures remain unclear. The heat capacity data recorded here show a spike in intensity at 90 K corresponding to the first order structural phase transition, for which we have provided a new structural model for the low temperature phase (Figure 6-13(a)). There are no additional signatures in the temperature range of 10 K, which is in agreement with heat capacity data presented in the literature.<sup>298</sup> This anomaly cannot be accredited to the impurity phase with composition Cu<sub>3</sub>SbS<sub>4</sub>, because each of the copper cations for this material is a closed shell cation, Cu<sup>+</sup>, which is not magnetic in nature. The presence of weak anomalies at *ca.* 10 K in the

polyhedral distortion data support the possibility that; tetrahedrite is subject to a second order phase-transition at 10 K.

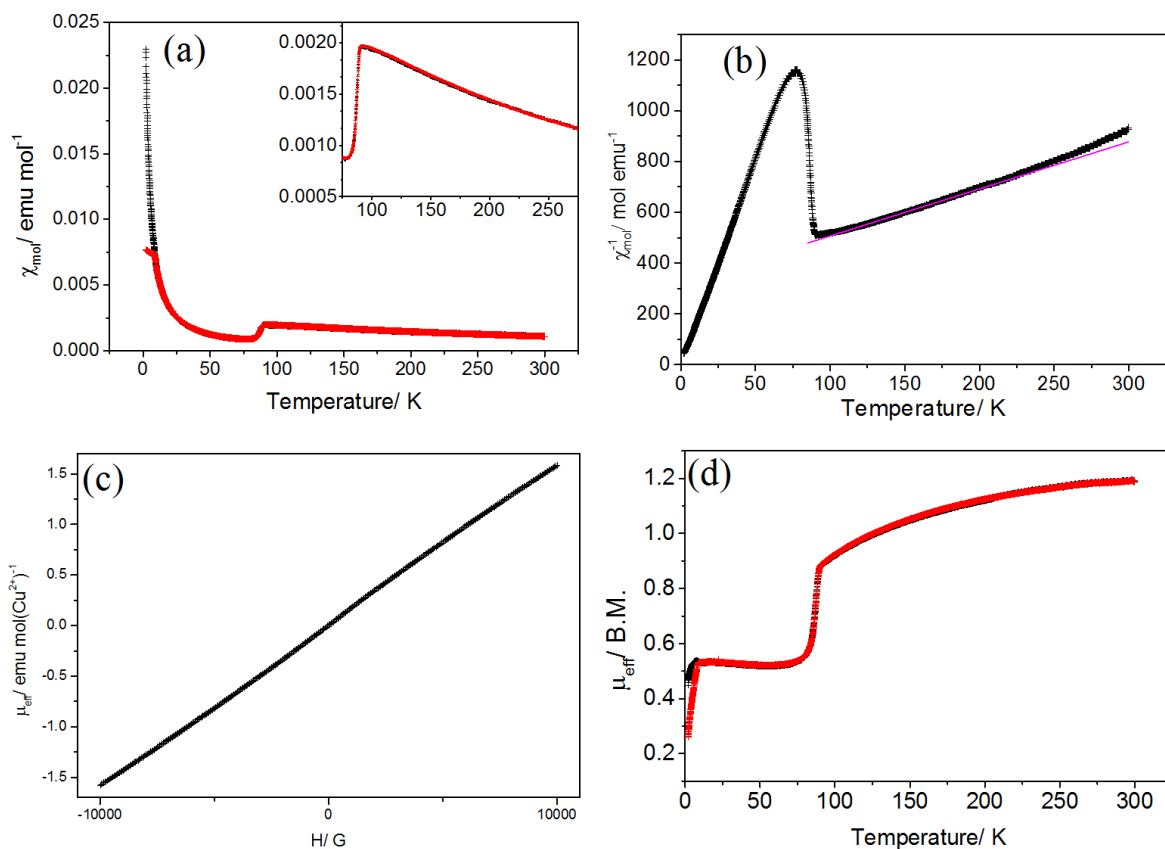


**Figure 6-12** – The temperature dependence of magnetic properties determined from field cooled – red; and zero field cooled – black measurements (a) – magnetic susceptibility; (b) inverse magnetic susceptibility; (d) effective magnetic moment. Field dependence of the magnetisation of tetrahedrite (c).

The electrical resistivity data collected on this sample show strikingly similar temperature dependence to previous low-temperature studies on tetrahedrite.<sup>161,300</sup> The influence of the structural phase transition is observed as an anomaly at the expected phase transition temperature (Figure 6-13(b)). Above 90 K,  $\rho(T)$  shows an anomaly in the region of  $T = 200$  to 250 K where the resistivity increases by almost a factor 5 from *ca.*  $\rho = 0.005$  m $\Omega$  m at 250 K to  $\rho = 0.025$  m $\Omega$  m at 175 K, then plateaus across the temperature range  $T = 90$  to 200 K. This anomaly which is observed across the temperature range for the cubic phase, exists in low temperature electrical resistivity data presented by Tanaka *et al.* and James *et al.*<sup>300,308</sup> The heat capacity data presented here and in previous studies do not provide evidence of a first-order phase transition across this temperature range. So far, the origins of this anomaly have not been elucidated. The structural investigations presented here do

not provide any evidence that this anomaly is structural in origin. The temperature dependence of the electric resistivity above and below the phase transition shows a decrease with increasing temperature for both the cubic and tetragonal phases. This indicates semiconductor or insulator type behaviour above and below the phase transition temperature. The band structure calculations for this phase are presented as part of a following publication and they provide further insight toward the electrical behaviour in the low temperature structure of tetrahedrite.<sup>297</sup> These calculations are possible as a result of the work carried out here because a new and complete magnetic and structural description of the low temperature phase of tetrahedrite has been provided.

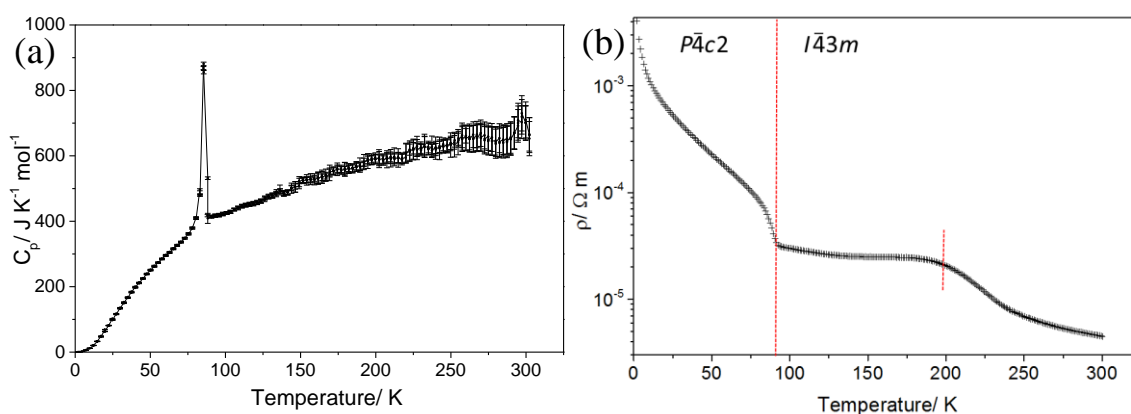


**Figure 6-13** – Temperature dependence of the: (a) heat capacity of tetrahedrite; (b) electrical resistivity of tetrahedrite. The full red dotted line signifies the phase transition temperature, the partial red line is used to highlight the anomaly in the electrical behaviour at ca. 200 K.

### 6.6. Conclusions

The neutron diffraction data collected here do not reveal any evidence of residual magnetic scattering as a result of the low-temperature structural phase transition. This observation indicates that the low-temperature magnetic transition seen in the magnetic susceptibility data does not lead to a magnetically ordered ground state. Structural characterisation of the low-temperature phase reveals the origins of this magnetic transition. A new description of this phase is presented which accounts for the ordering of all Cu(II) cations across a tetragonal unit cell with parameters  $\sqrt{2}a_c \times \sqrt{2}a_c \times a_c$  and space group  $P\bar{4}c2$ . The structural transformation is driven by a distortion of the  $S(2)Cu(2)_6$  octahedra that is accompanied by a suppression by 65% of the copper rattling mode of the trigonally coordinated cations within this cluster. The sulphur centred octahedron has a regular geometry in the high-temperature phase. The large polyhedral distortion parameters seen at low temperature are

synonymous with a Jahn-Teller distortion. Copper-copper interactions within the  $\text{Cu}_6\text{S}$  octahedron and the tendency of  $\text{Cu(II)}$  cations to induce Jahn-teller instability leads to the formation of a localised copper cluster. Short copper-copper interactions are observed between 3 of the crystallographically distinct sites that are now interconnected to form a distorted square pyramid pentameric cluster. The assignment of the  $\text{Cu(II)}$  into this pentameric cluster gives a  $\text{Cu}_5^{7+}$  cluster with point group  $\text{C}_{2v}$ . All of the electrons are paired giving a singlet ground state ( $^1b_1$ ) and this cluster accounts for all of the  $\text{Cu(II)}$  in  $(\text{Cu}^{2+})_2(\text{Cu}^+)_{10}(\text{Sb}^{3+})_4(\text{S}^{2-})_{13}$  with the holes becoming localised across the cluster.

## Chapter 7 Conclusions and Further Work

Copper-Sulphide based mineral type thermoelectric materials have attracted interest in recent years owing to their potential to offer low-cost low-toxicity alternatives to state-of-the-art thermoelectrics.<sup>131</sup> Recent research efforts into the performance of these mineral type phases or their selenide-base analogues has revealed numerous materials that exhibit  $ZT$ s close to unity. The material families in which this has been demonstrated include  $\alpha$ -chalcocite, tetrahedrite, argyrodite, kuramite, kesterite and colusite. For these materials the  $ZT_{max}$  is observed at high temperatures of 700 K or above.

### 7.1. Diffraction Resistance Seebeck Cell

Many of the Cu-S based thermoelectrics are known to show structural phase transitions with increasing temperature. These structural transitions are usually accompanied by electrical or thermal transitions that have a remarkable influence on the performance of the material and are often observed as anomalies in the electrical or thermal transport data.

A novel cell for the study of the structure-property relationships in thermoelectric materials was developed, built and tested. This *in-situ* cell provides a first-of-its kind sample environment, allowing for the simultaneous collection of neutron diffraction data along with electrical transport property data. Experiments utilising this cell on the POLARIS diffractometer will allow for the collection of excellent quality diffraction data over the same time scale as diffraction only experiments. Therefore, any variable temperature diffraction experiments on thermoelectric materials which show structural transitions can greatly benefit from using this equipment.

The experiments performed on this device and presented above have demonstrated that the advantages of neutron scattering can be exploited using this *in-situ* cell, thus allowing for the study of magnetic, mixed transition metal or nano-structured materials. Furthermore, the sensitivity of neutrons to the ADPs of atoms makes them ideal for studying the thermal behaviour of thermoelectric materials.

This device has allowed for the monitoring of changes in the structural and electrical behaviour of multiple thermoelectric materials. Currently the collection of the electrical data for characterisation of the Seebeck coefficient and electrical resistivity takes *ca.* 30 minutes for each temperature increment. The high-quality diffraction data takes at least 60 minutes to collect. Future work on this project should seek to further improve the electrical resistivity measurements. These experimental procedures may be optimised to allow for

the electrical resistivity to be determined from electrical impedance spectroscopy rather than DC methods.

### ***7.2. Chalcopyrite Related Samples of the Cu-Fe-S System***

All of the high-performance copper-sulphide and selenide-based thermoelectric materials discovered to date are p-type semiconductors. For low cost thermoelectric modules to be developed, it is crucial that high performance n-type materials are also developed. The chalcopyrite system has been studied extensively as it is one of few potential n-type copper-sulphide thermoelectrics. However, its performance is modest compared to its counterparts. The mooihoekite and talnakhite systems are structurally similar to the chalcopyrite phase and early studies by a solid-state chemistry group at the University of Reading have revealed the potential of talnakhite for thermoelectric applications.<sup>152</sup> The talnakhite-type samples exhibit a  $ZT_{max}=0.17$  at the relatively low temperature of 475 K. This performance is not outstanding, but future work on optimising the thermoelectric properties could achieve a more impressive performance. More importantly, the peak in performance is observed close to a structural phase transition.

The structural investigations here have revealed that the structural behaviour of talnakhite does not result in a direct transition from one phase to another. However, the phase transition leads to a solid-state mixture of two chalcopyrite-related phases at high temperature. In fact a secondary chalcopyrite-type phase begins to exsolve from the single phase sample with minimal heating. The experiment has provided diffraction data for the magnetic phase in the sample and this should allow for the magnetic characterisation of the material in the following analysis of these data.

A novel observation of an intermediate temperature, *ca.*  $T = 450$  K, magnetic transition has been observed in a copper-rich chalcopyrite sample. This behaviour has a marked influence on the electrical transport properties of the chalcopyrite-type phase resulting in a local maximum in the power factor. This type of behaviour has not previously been reported in the chalcopyrite mineral. This could offer new opportunities to optimise the lower temperature thermoelectric performance of chalcopyrite by exploiting this local maximum. The nature of the magnetic transition has not been determined, but future work in uncovering the magnetic behaviour might reveal the influence of additional copper cations on the magnetic structure.

For chalcopyrite-type phases presented in the literature, the behaviour of  $S(T)$  can differ between studies.  $S(T)$  has been shown to decrease with increasing temperature and to

increase with increasing temperature at  $T > 300$  K.<sup>96,97</sup> Often the phase of the material is determined by a rudimentary peak analysis of the X-ray diffraction pattern of the chalcopyrite-type phase at room temperature. However, at room temperature the overlap of reflections corresponding to talnakhite-type phases and chalcopyrite-type phases makes it impossible to determine whether the chalcopyrite is single phase. The sample synthesised here appeared to be single phase by peak analysis of the X-ray diffraction data. The observations from the *in-situ* analysis of the mixed phase ‘chalcopyrite’ sample revealed that the  $S(T)$  decreases as a result of an increasing weight fraction of the intermediate solid-state *iss* phase. Therefore, samples of chalcopyrite which show decreasing  $S(T)$  are suspected to exhibit the dynamic exsolution of an *iss* phase with increasing temperature. This set of experiments outlines and supports Cabri’s observations on the complexity involved in investigating this region of the Cu-Fe-S phase diagram.<sup>146</sup> A deeper understanding of this region of the phase diagram will be crucial in unlocking the potential offered by these n-type thermoelectric materials and this set of studies will certainly contribute towards this.

### ***7.3. Structural and Thermoelectric Behaviour of Bornite***

The structural analysis of bornite using neutron diffraction techniques has for the first time unequivocally determined that the iron cations are ordered within the AF sub-cells of the  $4a$  phase of bornite. Meanwhile, the RMC analysis has revealed that the iron cations are highly ordered in the  $4a$  phase and there are channels parallel to the  $z$ -axis and with dimensions *ca.*  $5.5 \times 5.5$  Å, that are iron-deficient. A partially ordered arrangement of the iron cations can be mapped onto the crystallographic sites of the *Pbca* unit cell, but the symmetry of the space group cannot model these iron deficient channels.

The observations from Rietveld and RMC analysis have revealed that iron cations will occupy both the AF and ZB\* sub-cells in the  $2a$  phase. The majority of the iron cations are situated within the AF sub-cells. However, there is a shift in the iron-iron correlations within the structure as the sample transforms from the  $4a \rightarrow 2a$ . In the  $4a$  phase there are many more face-diagonal correlations than face-edge and body-diagonal correlations. In the  $2a$  phase the number of face-diagonal and face-edge iron-iron correlations are comparable. Whilst the  $a$  phase shows a disordering of the cations in the structure as the AF-ZB sub-cell type ordering is lost, the iron ordering within the structure remains similar to the  $2a$  phase. Therefore, the two structural phase transitions in bornite can be attributed to, firstly an disordering of the iron cations within the structure, followed by a disordering

of the copper cations. These transitions are accompanied by an increase in the number of strong Cu-Cu interactions with increasing temperature. To uncover the influence of these iron-iron correlations and short copper-copper distances on the electronic structure the changes in electronic structure should be investigated by computational methods.

The investigations into the thermoelectric properties of bornite has allowed for high thermoelectric performance to be obtained in samples with a small degree of chemical substitution. This has been achieved by controlling the nominal Cu(II) concentration of the material. A number of copper-sulphide based materials have greater absolute figures of merit, however, for low- to mid- grade waste heat recovery purposes their peak performance is outside of the desired temperature range. It is demonstrated here that bornite is capable of far surpassing the  $ZT_{550K}$  of most Cu-S based thermoelectrics within this temperature range and achieving comparable  $ZT$  to substituted tetrahedrites (Figure 7-1). Thus far there have been relatively few studies on the thermoelectric performance of bornite and further improvements in the thermoelectric performance may yet be achieved by utilising techniques to further increase the Seebeck coefficient of bornite.

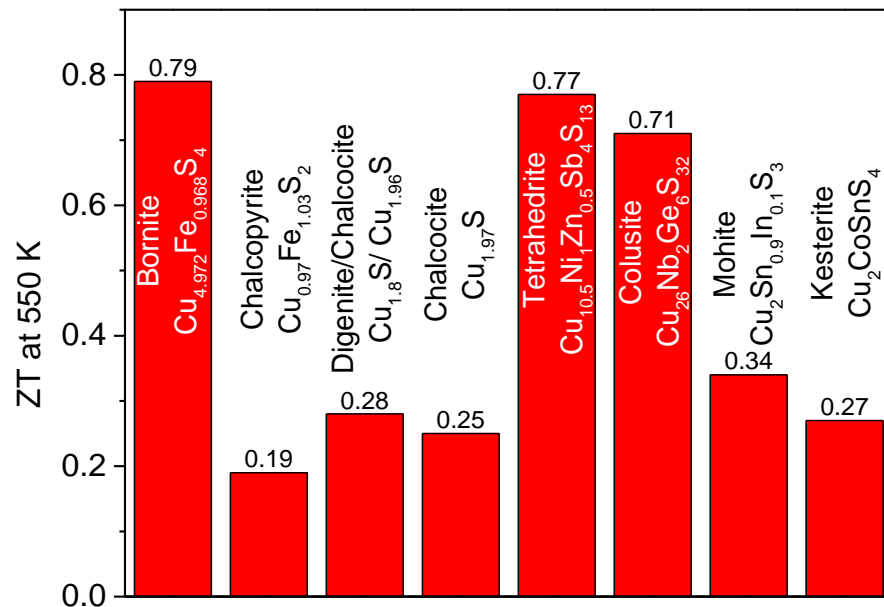


**Figure 7-1** – Highest reported  $ZT$  values at 550 K for mineral-type copper sulphide based thermoelectric materials. A table comparing the  $ZT$  max is available in the Table 5-4. 71,99,108,135,173,319,320

This local maximum in the  $ZT$  is observed across the  $2a \rightarrow a$  transition and can be attributed to a minimum in the lattice thermal conductivity observed at *ca.*  $T = 550$  K.

Variable temperature neutron diffraction experiments have been used to extract the Debye

temperature of each structural phase and a minimum in this value is observed for the intermediate phase. This may be linked to the minimum in the lattice thermal conductivity but inelastic neutron scattering experiments would be needed to confirm whether there is indeed a change in the vibrational behaviour of bornite.

#### ***7.4. Structural Observations in Tetrahedrite***

Tetrahedrite is a recently researched high-performance thermoelectric material which shows a low-temperature magnetic transition. The high-temperature structure of tetrahedrite has been studied extensively, but prior to this work the low-temperature structure had not been fully described. Previous variable temperature diffraction experiments had revealed evidence of a structural transition and the neutron diffraction experiments performed here intended to allow for low-temperature structure to be resolved. The experiment and the subsequent analysis of neutron diffraction data allowed for a successful characterisation of the low-temperature structure of tetrahedrite, as well as revealing that the low-temperature phase does not show any magnetic reflections. This, along with linear behaviour in the field-dependent magnetic susceptibility data suggested that tetrahedrite has a non-magnetically ordered ground state. Observations of copper-copper interactions in the low temperature structure allowed for the assignment of the Cu(II) in the structure to be disordered over a  $\text{Cu}_5^{7+}$  pentameric cluster. This pentameric cluster occupies the cage of the sodalite framework and Hückel calculations performed by Dr. Paz Vaqueiro revealed a singlet ground state for this pentameric cluster. Therefore, revealing the origin of the non-magnetically ordered ground state. Following this new characterisation of the low-temperature structure and non-magnetic state, DFT calculations have allowed for an accurate characterisation of the ground state electronic structure of tetrahedrite for the first time.<sup>297</sup>

#### ***7.5. Further Work***

The *in-situ* cell is now available as part of the user programme at the ISIS neutron facility, it can further contribute to the study of thermoelectric materials for any users who aim to perform diffraction experiments on the POLARIS and GEM diffractometers. No further development of the cell is required, as intended it provides an opportunity to study of the structure and electrical properties simultaneously in solid state materials. The work in this thesis has demonstrated that the goals envisioned for this project have been accomplished. A user manual and data-extraction python script are available in the e-appendix.

The diffraction experiments on the copper-rich chalcopyrite-type phase and the talnakhite type phase have provided novel magnetic structural data that might allow for characterisation of the magnetic phases within these materials. Given the time scale between collecting those data and presenting this thesis, a full description of the magnetic structure was not presented. Future work will strive to uncover the origins of the magnetic behaviour through the collection of magnetic susceptibility data. Along with this a complete analysis of the magnetic scattering data will allow for the magnetic structure to be revealed. Further optimisation of the synthetic techniques will also need to be pursued in order to stabilise the mooihoekite phase; spark plasma sintering techniques could provide an effective method to stabilising this phase. Furthermore, a low-temperature DSC study of these materials could provide crucial information on the phase and magnetic behaviour.

The resulting data from the PDF analysis of bornite revealed that with each structural phase transition, there is an increase in the number of short Cu-Cu interactions in the high-temperature phase. Complementary  $^{63}\text{Cu}$  NMR spectroscopy experiments would be useful in observing the evolution of these copper environments. Analysis of such data might provide confirmation to the existence of these intermetallic bonding states. It will be important to confirm these observations before performing any DFT calculations as the Cu-Cu interactions will have a marked impact on the calculated band structure of the material.

The neutron diffraction data collected on the chemically substituted samples of bornite,  $\text{Cu}_{4.96}\text{Fe}_{0.98}\text{S}_4$  and  $\text{Cu}_{5.08}\text{Fe}_{0.92}\text{S}_4$ , revealed a change in the Debye temperature across each of the structural phase transitions. The extracted values of the Debye temperatures for each structural phase provided some preliminary insight into the possible origins of the minimum in the lattice thermal conductivity. Accompanying low temperature  $C_p$  data will be needed to extract more reliable values of  $\theta_D$  and  $\theta_E$  for each of the samples and contribute to validating the observations made here.

The investigations into chemically substituted bornite samples led to improvements in the electrical transport properties. These are suspected to be driven by the formation of additional Cu(II) in the material. Near-edge absorption spectroscopy experiments would allow for confirmation of whether this species is forming. The deviation from ideal stoichiometry is also expected to change the concentration of charge carriers in bornite, Hall effect measurements would be useful in quantifying this change in charge carrier

concentration and provide further insight into the influence of the Cu:Fe:Va ratio in bornite. The thermal cycling shown here along with constant current stress tests in the literature demonstrate the electrical stability of bornite. Related  $\text{Cu}_2\text{S}$  phases show fast ion conduction and ion migration across the sample, it would be useful to use impedance spectroscopy techniques to probe the ionic conductivity of bornite to investigate the effect of iron cations in reducing the mobility of copper in the structure.

The electronic band structure calculations for the low temperature structure of tetrahedrite have now been presented in the literature resulting from the structural insights provided by the studies here. The neutron studies revealed a suppression of the rattling mode at low temperature. Collection of inelastic neutron scattering data at low- and high-temperature would allow us to probe the impact of this transition on the acoustic phonon branch.

## References

- 1 G. Boden, T. A.; Andres, R. J. Marland, *Global, Regional, and National Fossil-Fuel CO<sub>2</sub> Emissions (1751 - 2014) (V. 2017)*, 2017.
- 2 C. MacFarling Meure, D. Etheridge, C. Trudinger, P. Steele, R. Langenfelds, T. Van Ommen, A. Smith and J. Elkins, *Geophys. Res. Lett.*, 2006, **33**, 2000–2003.
- 3 C. P. Morice, J. J. Kennedy, N. A. Rayner and P. D. Jones, *J. Geophys. Res. Atmos.*, 2012, **117**, 1–22.
- 4 J. C. Comiso, *J. Clim.*, 2012, **25**, 1176–1193.
- 5 R. J. Nicholls and A. Cazenave, *Science*, 2010, **328**, 1517–1520.
- 6 M. Collins, R. Knutti, J. Arblaster, J.-L. Dufresne, T. Fichet, P. Friedlingstein, X. Gao, W. J. Gutowski, T. Johns, G. Krinner, M. Shongwe, C. Tebaldi, A. J. Weaver, M. F. Wehner, M. R. Allen, T. Andrews, U. Beyerle, C. M. Bitz, S. Bony and B. B. Booth, in *Climate Change 2013 - The Physical Science Basis*, ed. P. M. M. Thomas F. Stocker, Dahe Qin, Gian-Kasper Plattner, Melinda M.B. Tignor, Simon K. Allen, Judith Boschung, Alexander Nauels, Yu Xia, Vincent Bex, Cambridge University Press, New York NY USA, 2013, pp. 1029–1136.
- 7 *World Population Prospects 2019: Data Booklet*, U.N. department of Economic and Social Affairs, 2019.
- 8 V. Smil, *Energy Transitions*, ABC-Clio, Santa Barbara, 2nd edn., 2017.
- 9 IRENA, *REthinking Energy 2017: accelerating the global energy transformation*, Agency, International Renewable Energy, Abu Dhabi, 2017.
- 10 F. Lafond, A. G. Bailey, J. D. Bakker, D. Rebois, R. Zadourian, P. McSharry and J. D. Farmer, *Technol. Forecast. Soc. Change*, 2018, **128**, 104–117.
- 11 A. Jäger-Waldau and E. Commission, *Energies*, 2019, **12**, 769.
- 12 C. Forman, I. K. Muritala, R. Pardemann and B. Meyer, *Renew. Sustain. Energy Rev.*, 2016, **57**, 1568–1579.
- 13 C. Haddad, C. Perilhon, A. Danlos, M.-X. Francois and G. Descombes, *Energy Procedia*, 2014, **50**, 1056–1059.
- 14 C. T. Hsu, G. Y. Huang, H. S. Chu, B. Yu and D. J. Yao, *Appl. Energy*, 2011, **88**, 5173–5179.
- 15 X. Gou, H. Xiao and S. Yang, *Appl. Energy*, 2010, **87**, 3131–3136.
- 16 D. Champier, *Energy Convers. Manag.*, 2017, **140**, 167–181.
- 17 T. J. Seebeck, *Ann. Phys.*, 1826, **82**, 133–160.
- 18 L. E. Bell, *Science*, 2008, **321**, 1457–1461.
- 19 T. Hammel, R. Bennett, W. Otting and S. Fanale, in *7th International Energy Conversion Engineering Conference*, American Institute of Aeronautics and Astronautics, 2009.
- 20 A. Schock, *RTGs Using PbTe/TAGS Thermoelectric Elements for Mars Environmentatl Survey (MESUR) Mission*, 1992.
- 21 R. C. O'Brien, R. M. Ambrosi, N. P. Bannister, S. D. Howe and H. V. Atkinson, *J. Nucl. Mater.*, 2008, **377**, 506–521.
- 22 J. Yang and T. Caillat, *MRS Bull.*, 2006, **31**, 224–229.
- 23 X. Liu, Y. D. Deng, Z. Li and C. Q. Su, *Energy Convers. Manag.*, 2015, **90**, 121–127.
- 24 J. LaGrandeur, D. Crane, S. Hung, B. Mazar and A. Eder, in *International Conference on Thermoelectrics, ICT, Proceedings*, IEEE, 2006, pp. 343–348.
- 25 S. J. Kim, J. H. We and B. J. Cho, *Energy Environ. Sci.*, 2014, **7**, 1959–1965.
- 26 D. Kraemer, B. Poudel, H. P. Feng, J. C. Caylor, B. Yu, X. Yan, Y. Ma, X. Wang, D. Wang, A. Muto, K. McEnaney, M. Chiesa, Z. Ren and G. Chen, *Nat. Mater.*,

- 2011, **10**, 532–538.
- 27 R. Bjørk and K. K. Nielsen, *Sol. Energy*, 2015, **120**, 187–194.
- 28 H. J. Goldsmid and R. W. Douglas, *Br. J. Appl. Phys.*, 1954, **5**, 386–390.
- 29 S. B. Riffat and X. Ma, *Appl. Therm. Eng.*, 2003, **23**, 913–935.
- 30 R. P. Chasmar and R. Stratton, *J. Electron. Control*, 1959, **7**, 52–72.
- 31 D. M. Rowe, in *Thermoelectrics Handbook: Macro to Nano*, ed. D. M. Rowe, CRC Press, Boca Raton, 2005, pp. 1-1-1–14.
- 32 G. J. Snyder and E. S. Toberer, *Nat. Mater.*, 2008, **7**, 105–114.
- 33 X. Zhang and L. D. Zhao, *J. Mater.*, 2015, **1**, 92–105.
- 34 H. S. Kim, W. Liu, G. Chen, C.-W. Chu and Z. Ren, *Proc. Natl. Acad. Sci.*, 2015, **112**, 8205 LP-8210.
- 35 A. K. Cheetham, P. Day and A. Hamnett, *Solid State Chemistry Techniques*, Oxford University Press, Oxford, 1st edn., 1987.
- 36 M. Cutler, J. F. Levy and R. L. Fitzpatrick, *Am. Phys. Soc.*, 1964, **133**, A1143.
- 37 G. Tan, L. D. Zhao and M. G. Kanatzidis, *Chem. Rev.*, 2016, **116**, 12123–12149.
- 38 A. Despotuli and A. Andreeva, *Int. J. Nanosci.*, 2009, **8**, 389–402.
- 39 A. Hamnett, in *Solid State Chemistry Techniques*, eds. A. K. Cheetham and P. Day, Oxford University Press, Oxford, 1st edn., 1987, pp. 279–321.
- 40 L. E. Smart and E. A. Moore, in *Solid State Chemistry*, eds. L. E. Smart and E. A. Moore, CRC Press, Boca Raton, 4th edn., 2012, pp. 159–218.
- 41 M. J. Graf, S.-K. Yip, J. A. Sauls and D. Rainer, *Phys. Rev. B*, 1996, **53**, 15147–15161.
- 42 C. M. Bhandari, in *Handbook of Thermoelectrics*, ed. D. M. Rowe, CRC Press, Boca Raton, first., 1995, pp. 55–64.
- 43 S. Stackhouse and L. Stixrude, *Rev. Mineral. Geochemistry*, 2010, **71**, 253–269.
- 44 R. W. Keyes, *Phys. Rev.*, 1959, **115**, 564–567.
- 45 J. Yang, in *Thermal Conductivity*, ed. T. Tritt, Kluwer Academic/ Plenum, New York, 1st edn., 2006, pp. 1–20.
- 46 J. R. Sootsman, D. Y. Chung and M. G. Kanatzidis, *Angew. Chemie - Int. Ed.*, 2009, **48**, 8616–8639.
- 47 L. E. Smart and E. A. Moore, in *Solid state Chemistry an Introduction*, eds. L. E. Smart and E. A. Moore, CRC Press, Boca Raton, 4th edn., 2012, pp. 179–199.
- 48 P. A. Cox, in *Solid State Chemistry Compounds*, eds. A. K. Cheetham and P. Day, Oxford University Press, Oxford, 1st edn., 1992, pp. 1–30.
- 49 P. A. Cox, in *Electronic Structure and Chemistry of Solids*, Oxford University Press, Oxford, 1st edn., 1989, pp. 39–133.
- 50 P. Blanchard and E. Brüning, in *Progress in Mathematical Physics*, eds. K. Fukui and B. Pullman, Springer Netherlands, Dordrecht, 2015, vol. 69, pp. 563–573.
- 51 R. N. Hall, *Phys. Rev.*, 1952, **87**, 387.
- 52 C. M. Bhandari and D. M. Rowe, in *Handbook of Thermoelectrics*, ed. D. M. Rowe, CRC Press, Boca Raton, first., 1995, pp. 43–51.
- 53 H. J. Goldsmid and J. W. Sharp, *J. Electron. Mater.*, 1999, **28**, 869–872.
- 54 E. Rausch, B. Balke, T. Deschauer, S. Ouardi and C. Felser, *APL Mater.*, 2015, **3**, 041516.
- 55 E. Lkhagvasuren, S. Ouardi, G. H. Fecher, G. Auffermann, G. Kreiner, W. Schnelle and C. Felser, *AIP Adv.*, 2017, **7**, 045010.
- 56 J. Corps, P. Vaqueiro, A. Aziz, R. Grau-Crespo, W. Kockelmann, J. C. Jumas and A. V Powell, *Chem. Mater.*, 2015, **27**, 3946–3956.
- 57 Y. Takagiwa, Y. Pei, G. Pomrehn and G. J. Snyder, *Appl. Phys. Lett.*, 2012, **101**, 1–4.

- 58 Q. Zhang, B. Liao, Y. Lan, K. Lukas, W. Liu, K. Esfarjani, C. Opeil, D. Broido, G. Chen and Z. Ren, *Proc. Natl. Acad. Sci. U. S. A.*, 2013, **110**, 13261–13266.
- 59 M. Falmbigl, A. Grytsiv, P. Rogl, P. Heinrich, E. Royanian and E. Bauer, *J. Alloys Compd.*, 2013, **567**, 65–72.
- 60 J. Zhang, R. Liu, N. Cheng, Y. Zhang, J. Yang, C. Uher, X. Shi, L. Chen and W. Zhang, *Adv. Mater.*, 2014, **26**, 3848–3853.
- 61 Y. Pei, X. Shi, A. Lalonde, H. Wang, L. Chen and G. J. Snyder, *Nature*, 2011, **473**, 66–69.
- 62 H. S. Kim, N. A. Heinz, Z. M. Gibbs, Y. Tang, S. D. Kang and G. J. Snyder, *Mater. Today*, 2017, **20**, 452–459.
- 63 M. Jonson and G. D. Mahan, *Phys. Rev. B*, 1980, **21**, 4223–4229.
- 64 G. Springholz, M. Pinczolits, P. Mayer, V. Holy, G. Bauer, H. H. Kang and L. Salamanca-Riba, *Phys. Rev. Lett.*, 2000, **84**, 4669–4672.
- 65 J. P. Heremans, *Acta Phys. Pol. A*, 2005, **108**, 609–634.
- 66 L. D. Hicks, T. C. Harman, X. Sun and M. S. Dresselhaus, *Phys. Rev. B*, 1996, **53**, 493–496.
- 67 M. S. Dresselhaus, G. Chen, M. Y. Tang, R. Yang, H. Lee, D. Wang, Z. Ren, J. P. Fleurial and P. Gogna, *Adv. Mater.*, 2007, **19**, 1043–1053.
- 68 Fitriani, R. Ovik, B. D. Long, M. C. Barma, M. Riaz, M. F. M. Sabri, S. M. Said and R. Saidur, *Renew. Sustain. Energy Rev.*, 2016, **64**, 635–659.
- 69 A. J. Minnich, M. S. Dresselhaus, Z. F. Ren and G. Chen, *Energy Environ. Sci.*, 2009, **2**, 466–479.
- 70 M. G. Kanatzidis, *Chem. Mater.*, 2010, **22**, 648–659.
- 71 Y. He, T. Day, T. Zhang, H. Liu, X. Shi, L. Chen and G. J. Snyder, *Adv. Mater.*, 2014, **26**, 3974–3978.
- 72 M. Christensen, S. Johnsen and B. B. Iversen, *Dalt. Trans.*, 2010, **39**, 978–992.
- 73 B. Feng, J. Xie, G. Cao, T. Zhu and X. Zhao, *J. Mater. Chem. A*, 2013, **1**, 13111–13119.
- 74 L.-D. Zhao, B.-P. Zhang, J.-F. Li, M. Zhou, W.-S. Liu and J. Liu, *J. Alloys Compd.*, 2008, **455**, 259–264.
- 75 S. Il Kim, K. H. Lee, H. A. Mun, H. S. Kim, S. W. Hwang, J. W. Roh, D. J. Yang, W. H. Shin, X. S. Li, Y. H. Lee, G. J. Snyder and S. W. Kim, *Science*, 2015, **348**, 109–114.
- 76 J. D. Sugar and D. L. Medlin, *J. Alloys Compd.*, 2009, **478**, 75–82.
- 77 M. Rull-Bravo, A. Moure, J. F. Fernández and M. Martín-González, *RSC Adv.*, 2015, **5**, 41653–41667.
- 78 L. Yang, Z. G. Chen, M. S. Dargusch and J. Zou, *Adv. Energy Mater.*, 2018, **8**, 1–28.
- 79 X. Shi, L. Chen and C. Uher, *Int. Mater. Rev.*, 2016, **61**, 379–415.
- 80 E. Davies, *Chem. World*, 2011, **January**, 50–54.
- 81 U. S. D. of the Interior, *Mineral Commodity Summaries*, Reston, Virginia, 2019.
- 82 Jefferson\_Lab, It's Elemental - The Periodic Table of Elements, <http://education.jlab.org/itselemental/ele092.html>, (accessed 10 December 2018).
- 83 A. V Powell and P. Vaquero, in *Thermoelectric Materials and Devices*, eds. I. Nandhakumar, N. M. White and S. Beeby, The Royal Society of Chemistry, 2017, pp. 27–59.
- 84 G. Dennler, R. Chmielowski, S. Jacob, F. Capet, P. Roussel, S. Zastrow, K. Nielsch, I. Opahle and G. K. H. Madsen, *Adv. Energy Mater.*, 2014, **4**, 1301581.
- 85 H. Liu, X. Shi, F. Xu, L. Zhang, W. Zhang, L. Chen, Q. Li, C. Uher, T. Day and G. J. Snyder, *Nat. Mater.*, 2012, **11**, 422–425.

- 86 B. Yu, W. Liu, S. Chen, H. Wang, H. Wang, G. Chen and Z. Ren, *Nano Energy*, 2012, **1**, 472–478.
- 87 E. Hirahara, *J. Phys. Soc. Japan*, 1951, **6**, 422–427.
- 88 A. L. N. Stevels and F. Jellinek, *Recl. des Trav. Chim. des Pays-Bas*, 1971, **90**, 273–283.
- 89 E. Eikeland, A. B. Blichfeld, K. A. Borup, K. Zhao, J. Overgaard, X. Shi, L. Chen and B. B. Iversen, *IUCrJ*, 2017, **4**, 476–485.
- 90 D. R. Brown, T. Day, T. Caillat and G. J. Snyder, *J. Electron. Mater.*, 2013, **42**, 2014–2019.
- 91 K. Zhao, A. B. Blichfeld, E. Eikeland, P. Qiu, D. Ren, B. B. Iversen, X. Shi and L. Chen, *J. Mater. Chem. A*, 2017, **5**, 18148–18156.
- 92 D. J. Voneshen, H. C. Walker, K. Refson and J. P. Goff, *Phys. Rev. Lett.*, 2017, **118**, 1–5.
- 93 N. Tsujii and T. Mori, *Appl. Phys. Express*, 2013, **6**, 043001.
- 94 R. Lefèvre, D. Berthebaud, M. Y. Mychinko, O. I. Lebedev, T. Mori, F. Gascoin and A. Maignan, *RSC Adv.*, 2016, **6**, 55117–55124.
- 95 J. Li, Q. Tan and J. F. Li, *J. Alloys Compd.*, 2013, **551**, 143–149.
- 96 J. Navratil, J. Kašparová, T. Plecháček, L. Beneš, Z. Olmrová-Zmrhalová, V. Kucek and Č. Drašar, *J. Electron. Mater.*, 2019, **48**, 1795–1804.
- 97 W. D. Carr and D. T. Morelli, *J. Electron. Mater.*, 2016, **45**, 1346–1350.
- 98 L. Vaure, Y. Liu, D. Cadavid, F. Agnese, D. Aldakov, S. Pouget, A. Cabot, P. Reiss and P. Chenevier, *ChemNanoMat*, 2018, **4**, 982–991.
- 99 Y. Li, T. Zhang, Y. Qin, T. Day, G. Jeffrey Snyder, X. Shi and L. Chen, *J. Appl. Phys.*, 2014, **116**, 203705.
- 100 P. Wyzga, M. Bobnar, C. Hennig, A. Leithe-Jasper, T. Mori and R. Gumeniuk, *Zeitschrift fur Anorg. und Allg. Chemie*, 2017, **643**, 858–863.
- 101 H. Xie, X. Su, G. Zheng, T. Zhu, K. Yin, Y. Yan, C. Uher, M. G. Kanatzidis and X. Tang, *Adv. Energy Mater.*, 2017, **7**, 1–14.
- 102 D. Berthebaud, O. I. Lebedev and A. Maignan, *J. Mater.*, 2015, **1**, 68–74.
- 103 J. Park, Y. Xia and V. Ozoliņš, *J. Appl. Phys.*, 2019, **125**, 125102.
- 104 N. Tsujii, T. Mori and Y. Isoda, *J. Electron. Mater.*, 2014, **43**, 2371–2375.
- 105 S. R. Hall and J. M. Stewart, *Acta Crystallogr. Sect. B Struct. Crystallogr. Cryst. Chem.*, 1973, **29**, 579–585.
- 106 T. E. Engin, A. V. Powell and S. Hull, *J. Solid State Chem.*, 2011, **184**, 2272–2277.
- 107 E. Makovicky, *Rev. Mineral. Geochemistry*, 2006, **61**, 7–125.
- 108 Q. Tan, W. Sun, Z. Li and J. F. Li, *J. Alloys Compd.*, 2016, **672**, 558–563.
- 109 H. Zhao, X. Xu, C. Li, R. Tian, R. Zhang, R. Huang, Y. Lyu, D. Li, X. Hu, L. Pan and Y. Wang, *J. Mater. Chem. A*, 2017, **5**, 23267–23275.
- 110 X. Shi, L. Xi, J. Fan, W. Zhang and L. Chen, *Chem. Mater.*, 2010, **22**, 6029–6031.
- 111 E. J. Skoug, J. D. Cain and D. T. Morelli, *Appl. Phys. Lett.*, 2011, **98**, 15–18.
- 112 A. Suzumura, M. Watanabe, N. Nagasako and R. Asahi, *J. Electron. Mater.*, 2014, **43**, 2356–2361.
- 113 K. Chen, C. Di Paola, B. Du, R. Zhang, S. Laricchia, N. Bonini, C. Weber, I. Abrahams, H. Yan and M. Reece, *J. Mater. Chem. C*, 2018, **6**, 8546–8552.
- 114 S. Adachi, in *Earth-Abundant Materials for Solar Cells*, ed. Sadao Adachi, Wiley, Chichester, 1st edn., 2015, pp. 21–61.
- 115 A. Le Donne, V. Trifiletti and S. Binetti, *Front. Chem.*, 2019, **7**, 297.
- 116 S. Bag, O. Gunawan, T. Gokmen, Y. Zhu, T. K. Todorov and D. B. Mitzi, *Energy Environ. Sci.*, 2012, **5**, 7060–7065.
- 117 W. Wang, M. T. Winkler, O. Gunawan, T. Gokmen, T. K. Todorov, Y. Zhu and D.

- B. Mitzi, *Adv. Energy Mater.*, 2014, **4**, 1–5.
- 118 K. J. Yang, D. H. Son, S. J. Sung, J. H. Sim, Y. I. Kim, S. N. Park, D. H. Jeon, J. Kim, D. K. Hwang, C. W. Jeon, D. Nam, H. Cheong, J. K. Kang and D. H. Kim, *J. Mater. Chem. A*, 2016, **4**, 10151–10158.
- 119 S. Adachi, in *Earth-Abundant Materials for Solar Cells*, ed. S. Adachi, Wiley, Chichester, 1st edn., 2015, pp. 173–236.
- 120 X. Y. Shi, F. Q. Huang, M. L. Liu and L. D. Chen, *Appl. Phys. Lett.*, 2009, **94**, 122103.
- 121 R. Chetty, M. Falmbigl, P. Rogl, P. Heinrich, E. Royanian, E. Bauer, S. Suwas and R. C. Mallik, *Phys. Status Solidi Appl. Mater. Sci.*, 2013, **210**, 2471–2478.
- 122 F. S. Liu, B. Wang, W. Q. Ao, Y. Li and J. Q. Li, *Intermetallics*, 2014, **55**, 15–21.
- 123 M. L. Liu, I. W. Chen, F. Q. Huang and L. D. Chen, *Adv. Mater.*, 2009, **21**, 3808–3812.
- 124 C. Raju, M. Falmbigl, P. Rogl, X. Yan, E. Bauer, J. Horky, M. Zehetbauer and R. Chandra Mallik, *AIP Adv.*, 2013, **3**, 032106.
- 125 R. Chetty, J. Dadda, J. De Boor, E. Müller and R. C. Mallik, *Intermetallics*, 2015, **57**, 156–162.
- 126 M. Ibáñez, D. Cadavid, R. Zamani, N. García-Castelló, V. Izquierdo-Roca, W. Li, A. Fairbrother, J. D. Prades, A. Shavel, J. Arbiol, A. Pérez-Rodríguez, J. R. Morante and A. Cabot, *Chem. Mater.*, 2012, **24**, 562–570.
- 127 O. V. Parasyuk, L. D. Gulay, Y. E. Romanyuk and L. V. Piskach, *J. Alloys Compd.*, 2001, **329**, 202–207.
- 128 S. Schorr, *Sol. Energy Mater. Sol. Cells*, 2011, **95**, 1482–1488.
- 129 A. V. Chichagov, E. G. Osadchii and Z. V. Usyakovskaya, *Neues Jahrb. für Mineral. Abhandlungen*, 1986, **155**, 15–22.
- 130 O. V. Frank-Kamenetskaya, I. V. Rozhdestvenskaya and L. A. Yanulova, *J. Struct. Chem.*, 2002, **43**, 89–100.
- 131 K. Suekuni and T. Takabatake, *APL Mater.*, 2016, **4**, 104503.
- 132 K. Suekuni, F. S. Kim and T. Takabatake, *J. Appl. Phys.*, 2014, **116**, 63706.
- 133 K. Suekuni, F. S. Kim, H. Nishiate, M. Ohta, H. I. Tanaka and T. Takabatake, *Appl. Phys. Lett.*, 2014, **105**, 132107.
- 134 Y. Kikuchi, Y. Bouyrie, M. Ohta, K. Suekuni, M. Aihara and T. Takabatake, *J. Mater. Chem. A*, 2016, **4**, 15207–15214.
- 135 Y. Bouyrie, M. Ohta, K. Suekuni, Y. Kikuchi, P. Jood, A. Yamamoto and T. Takabatake, *J. Mater. Chem. C*, 2017, **5**, 4174–4184.
- 136 K. Suekuni, Y. Shimizu, E. Nishibori, H. Kasai, H. Saito, D. Yoshimoto, K. Hashikuni, Y. Bouyrie, R. Chetty, M. Ohta, E. Guilmeau, T. Takabatake, K. Watanabe and M. Ohtaki, *J. Mater. Chem. A*, 2019, **7**, 228–235.
- 137 V. Pavan Kumar, A. R. Supka, P. Lemoine, O. I. Lebedev, B. Raveau, K. Suekuni, V. Nassif, R. Al Rahal Al Orabi, M. Fornari and E. Guilmeau, *Adv. Energy Mater.*, 2019, **9**, 1–11.
- 138 Y. Bouyrie, V. Ohorodniichuk, S. Sassi, P. Masschelein, A. Dauscher, C. Candolfi and B. Lenoir, *J. Electron. Mater.*, 2017, **46**, 2684–2690.
- 139 C. Bourgès, Y. Bouyrie, A. R. Supka, R. Al Rahal Al Orabi, P. Lemoine, O. I. Lebedev, M. Ohta, K. Suekuni, V. Nassif, V. Hardy, R. Daou, Y. Miyazaki, M. Fornari and E. Guilmeau, *J. Am. Chem. Soc.*, 2018, **140**, 2186–2195.
- 140 C. Bourgès, M. Gilmas, P. Lemoine, N. E. Mordvinova, O. I. Lebedev, E. Hug, V. Nassif, B. Malaman, R. Daou and E. Guilmeau, *J. Mater. Chem. C*, 2016, **4**, 7455–7463.
- 141 F. S. Kim, K. Suekuni, H. Nishiate, M. Ohta, H. I. Tanaka and T. Takabatake, *J.*

- Appl. Phys.*, 2016, **119**, 175105.
- 142 V. Pavan Kumar, L. Paradis-Fortin, P. Lemoine, V. Caignaert, B. Raveau, B. Malaman, G. Le Caër, S. Cordier and E. Guilmeau, *Inorg. Chem.*, 2017, **56**, 13376–13381.
- 143 S. O. J. Long, A. V. Powell, P. Vaqueiro and S. Hull, *Chem. Mater.*, 2018, **30**, 456–464.
- 144 D. S. Prem Kumar, R. Chetty, P. Rogl, G. Rogl, E. Bauer, P. Malar and R. C. Mallik, *Intermetallics*, 2016, **78**, 21–29.
- 145 V. Raghavan, *J. Phase Equilibria Diffus.*, 2004, **25**, 450–454.
- 146 L. J. Cabri, *Econ. Geol.*, 1973, **68**, 443–454.
- 147 S. R. Hall and E. J. Gabe, *Am. Mineral.*, 1972, **57**, 368–380.
- 148 B. S. R. Hall and J. F. Rowland, *Acta Crystallogr. Sect. B*, 1973, **29**, 2365–2372.
- 149 J. E. Hiller and K. Probsthain, *Zeitschrift für Krist. - New Cryst. Struct.*, 1956, **108**, 108–129.
- 150 L. J. Cabri, *Econ. Geol.*, 1967, **62**, 910–925.
- 151 N. Tsujii and T. Mori, *MRS Proc.*, 2014, **1680**, 1–6.
- 152 S. Athar, University of Reading, MSc Thesis, 2018.
- 153 H. Xie, X. Su, X. Zhang, S. Hao, T. P. Bailey, C. C. Stoumpos, A. P. Douvalis, X. Hu, C. Wolverton, V. P. Dravid, C. Uher, X. Tang and M. G. Kanatzidis, *J. Am. Chem. Soc.*, 2019, **141**, 10905–10914.
- 154 R. H. Sillitoe, *Econ. Geol.*, 2010, **105**, 3–41.
- 155 K. Koto and N. Morimoto, *Acta Crystallogr. Sect. B Struct. Crystallogr. Cryst. Chem.*, 1975, **31**, 2268–2273.
- 156 P. Qiu, T. Zhang, Y. Qiu, X. Shi and L. Chen, *Energy Environ. Sci.*, 2014, **7**, 4000–4006.
- 157 G. Guélou, A. V. Powell and P. Vaqueiro, *J. Mater. Chem. C*, 2015, **3**, 10624–10629.
- 158 A. Ostovari Moghaddam, A. Shokuhfar, P. Guardia, Y. Zhang and A. Cabot, *J. Alloys Compd.*, 2019, **773**, 1064–1074.
- 159 V. Pavan Kumar, T. Barbier, P. Lemoine, B. Raveau, V. Nassif and E. Guilmeau, *Dalt. Trans.*, 2017, **46**, 2174–2183.
- 160 R. Chetty, A. Bali and R. C. Mallik, *J. Mater. Chem. C*, 2015, **3**, 12364–12378.
- 161 D. I. Nasonova, V. Y. Verchenko, A. A. Tsirlin and A. V. Shevelkov, *Chem. Mater.*, 2016, **28**, 6621–6627.
- 162 Y. Bouyrie, C. Candolfi, V. Ohorodniichuk, B. Malaman, A. Dauscher, J. Tobola and B. Lenoir, *J. Mater. Chem. C*, 2015, **3**, 10476–10487.
- 163 T. Barbier, P. Lemoine, S. Gascoin, O. I. Lebedev, A. Kaltzoglou, P. Vaqueiro, A. V. Powell, R. I. Smith and E. Guilmeau, *J. Alloys Compd.*, 2015, **634**, 253–262.
- 164 P. Vaqueiro, G. Guélou, A. Kaltzoglou, R. I. Smith, T. Barbier, E. Guilmeau and A. V. Powell, *Chem. Mater.*, 2017, **29**, 4080–4090.
- 165 R. Chetty, P. K. D S, G. Rogl, P. Rogl, E. Bauer, H. Michor, S. Suwas, S. Puchegger, G. Giester and R. C. Mallik, *Phys. Chem. Chem. Phys.*, 2015, **17**, 1716–27.
- 166 J. Wang, M. Gu, Y. Bao, X. Li and L. Chen, *J. Electron. Mater.*, 2016, **45**, 2274–2277.
- 167 T. Barbier, S. Rollin-Martinet, P. Lemoine, F. Gascoin, A. Kaltzoglou, P. Vaqueiro, A. V. Powell and E. Guilmeau, *J. Am. Ceram. Soc.*, 2016, **99**, 51–56.
- 168 Y. Bouyrie, C. Candolfi, S. Pailhès, M. M. Koza, B. Malaman, A. Dauscher, J. Tobola, O. Boisron, L. Saviot and B. Lenoir, *Phys. Chem. Chem. Phys.*, 2015, **17**, 19751–19758.

- 169 W. Lai, Y. Wang, D. T. Morelli and X. Lu, *Adv. Funct. Mater.*, 2015, **25**, 3648–3657.
- 170 K. Suekuni, C. H. Lee, H. I. Tanaka, E. Nishibori, A. Nakamura, H. Kasai, H. Mori, H. Usui, M. Ochi, T. Hasegawa, M. Nakamura, S. Ohira-Kawamura, T. Kikuchi, K. Kaneko, H. Nishiata, K. Hashikuni, Y. Kosaka, K. Kuroki and T. Takabatake, *Adv. Mater.*, 2018, **30**, 1706230.
- 171 X. Lu and D. T. Morelli, *Phys. Chem. Chem. Phys.*, 2013, **15**, 5762–5766.
- 172 X. Lu, D. T. Morelli, Y. Xia, F. Zhou, V. Ozolins, H. Chi, X. Zhou and C. Uher, *Adv. Energy Mater.*, 2013, **3**, 342–348.
- 173 X. Lu, D. T. Morelli, Y. Xia and V. Ozolins, *Chem. Mater.*, 2015, **27**, 408–413.
- 174 R. Chetty, A. Bali, M. H. Naik, G. Rogl, P. Rogl, M. Jain, S. Suwas and R. C. Mallik, *Acta Mater.*, 2015, **100**, 266–274.
- 175 W. F. Kuhs, R. Nitsche and K. Scheunemann, *Mater. Res. Bull.*, 1979, **14**, 241–248.
- 176 H.-J. Deiseroth, S.-T. Kong, H. Eckert, J. Vannahme, C. Reiner, T. Zaiß and M. Schlosser, *Angew. Chemie Int. Ed.*, 2008, **47**, 755–758.
- 177 S. Boulineau, M. Courty, J.-M. Tarascon and V. Viallet, *Solid State Ionics*, 2012, **221**, 1–5.
- 178 M. Chen and S. Adams, *J. Solid State Electrochem.*, 2015, **19**, 697–702.
- 179 R. B. Beeken, J. J. Garbe and N. R. Petersen, *J. Phys. Chem. Solids*, 2003, **64**, 1261–1264.
- 180 B. K. Heep, K. S. Weldert, Y. Krysiak, T. W. Day, W. G. Zeier, U. Kolb, G. J. Snyder and W. Tremel, *Chem. Mater.*, 2017, **29**, 4833–4839.
- 181 A. Charoenphakdee, K. Kurosaki, H. Muta, M. Uno and S. Yamanaka, *Jpn. J. Appl. Phys.*, 2009, **48**, 8–10.
- 182 B. Jiang, P. Qiu, E. Eikeland, H. Chen, Q. Song, D. Ren, T. Zhang, J. Yang, B. B. Iversen, X. Shi and L. Chen, *J. Mater. Chem. C*, 2017, **5**, 943–952.
- 183 L. Li, Y. Liu, J. Dai, A. Hong, M. Zeng, Z. Yan, J. Xu, D. Zhang, D. Shan, S. Liu, Z. Ren and J. M. Liu, *J. Mater. Chem. C*, 2016, **4**, 5806–5813.
- 184 B. Jiang, P. Qiu, H. Chen, Q. Zhang, K. Zhao, D. Ren, X. Shi and L. Chen, *Chem. Commun.*, 2017, **53**, 11658–11661.
- 185 A. A. Olvera, N. A. Moroz, P. Sahoo, P. Ren, T. P. Bailey, A. A. Page, C. Uher and P. F. P. Poudeu, *Energy Environ. Sci.*, 2017, **10**, 1668–1676.
- 186 S. Bhattacharya, R. Basu, R. Bhatt, S. Pitale, A. Singh, D. K. Aswal, S. K. Gupta, M. Navaneethan and Y. Hayakawa, *J. Mater. Chem. A*, 2013, **1**, 11289–11294.
- 187 A. J. Hong, L. Li, H. X. Zhu, X. H. Zhou, Q. Y. He, W. S. Liu, Z. B. Yan, J. M. Liu and Z. F. Ren, *Solid State Ionics*, 2014, **261**, 21–25.
- 188 C. P. Heinrich, T. W. Day, W. G. Zeier, G. J. Snyder and W. Tremel, *J. Am. Chem. Soc.*, 2014, **136**, 442–448.
- 189 V. Pavan Kumar, T. Barbier, V. Caignaert, B. Raveau, R. Daou, B. Malaman, G. Le Caër, P. Lemoine and E. Guilmeau, *J. Phys. Chem. C*, 2017, **121**, 16454–16461.
- 190 N. R. Keskar and J. R. Chelikowsky, *Phys. Rev. B*, 1992, **46**, 1–13.
- 191 R.-R. Xu and Q. Su, in *Modern Inorganic Synthetic Chemistry*, eds. R. Xu and Y. Xu, Elsevier, Amsterdam, 2nd edn., 2017, pp. 9–43.
- 192 C. L. De Castro and B. S. Mitchell, in *Synthesis, Functionalization and Surface Treatment of Nanoparticles*, ed. M. I. Baraton, American Science, Valencia, CA, USA, 2002, pp. 1–15.
- 193 Y. R. Miao and K. S. Suslick, in *Advances in Inorganic Chemistry*, Elsevier Inc., 1st edn., 2018, vol. 71, pp. 403–434.
- 194 Q. Zhang and F. Saito, *Adv. Powder Technol.*, 2012, **23**, 523–531.
- 195 P. Baláž, M. Baláž, M. Achimovičová, Z. Bujňáková and E. Dutková, *J. Mater. Sci.*,

- 2017, **52**, 11851–11890.
- 196 T. Tsuzuki and P. G. McCormick, *J. Mater. Sci.*, 2004, **39**, 5143–5146.
- 197 C. Suryanarayana, *Prog. Mater. Sci.*, 2001, **46**, 1–184.
- 198 G. Delaizir, G. Bernard-Granger, J. Monnier, R. Grodzki, O. Kim-Hak, P. D. Szkutnik, M. Soulier, S. Saunier, D. Goeriot, O. Rouleau, J. Simon, C. Godart and C. Navone, *Mater. Res. Bull.*, 2012, **47**, 1954–1960.
- 199 L. D. Zhao, S. H. Lo, Y. Zhang, H. Sun, G. Tan, C. Uher, C. Wolverton, V. P. Dravid and M. G. Kanatzidis, *Nature*, 2014, **508**, 373–377.
- 200 W. C. Röntgen, *Nature*, 1896, **53**, 274–277.
- 201 J. B. Kortright and A. C. Thompson, in *X-Ray Data Booklet*, eds. A. C. Thompson and D. Vaughan, Lawrence Berkeley National Laboratory, U.S. DOE., California, 2009, pp. 8–27.
- 202 W. H. Bragg and W. L. Bragg, *Proc. R. Soc. London. Ser. A*, 1913, **88**, 428–438.
- 203 B. A. GmbH, 2007.
- 204 P. W. Lisowski, C. D. Bowman, G. J. Russell and S. A. Wender, *Nucl. Sci. Eng.*, 1990, **106**, 208–218.
- 205 D. S. Sivia, in *Elementary Scattering Theory*, ed. D. S. Sivia, Oxford University Press, Oxford, 1st edn., 2011, pp. 61–91.
- 206 B. T. M. . Willis, *Zeitschrift für Krist. - Cryst. Mater.*, 1994, **209**, 385.
- 207 M. O. Jones, A. D. Taylor and S. F. Parker, *Appl. Petrochemical Res.*, 2012, **2**, 97–104.
- 208 STFC, How ISIS works - in depth, <https://www.isis.stfc.ac.uk/Pages/How-ISIS-works--in-depth.aspx>, (accessed 28 January 2019).
- 209 A. C. Larson and R. B. Von Dreele, *Los Alamos Natl. Lab. Rep. LAUR*, 1994, 86–784.
- 210 O. Arnold, *Nucl. Inst. Meth. Phys. Res. A*, 2014, **764**, 156–166.
- 211 R. I. Smith, S. Hull, M. G. Tucker, H. Y. Playford, D. J. McPhail, S. P. Waller and S. T. Norberg, *Rev. Sci. Instrum.*, 2019, **90**, 115101.
- 212 L. C. Chapon, P. Manuel, P. G. Radaelli, C. Benson, L. Perrott, S. Ansell, N. J. Rhodes, D. Raspino, D. Duxbury, E. Spill and J. Norris, *Neutron News*, 2011, **22**, 22–25.
- 213 D. Duxbury, D. Khalyavin, P. Manuel, D. Raspino, N. Rhodes, E. Schooneveld and E. Spill, *J. Instrum.*, 2014, **9**, C12008–C12008.
- 214 H. M. Rietveld, *J. Appl. Crystallogr.*, 1969, **2**, 65–71.
- 215 R. A. Young, *The Rietveld method*, Oxford University Press, Chester, England, 1st edn., 1993.
- 216 K. Robinson, G. V Gibbs and P. H. Ribbe, *Science*, 1971, **172**, 567–570.
- 217 R. D. Shannon, *Acta Crystallogr. Sect. A*, 1976, **32**, 751–767.
- 218 M. E. Fleet, *Mineral. Mag.*, 1976, **40**, 531–533.
- 219 A. Le Bail, *Powder Diffr.*, 2005, **20**, 316–326.
- 220 V. Petkov, S. J. L. Billinge, J. Heising and M. G. Kanatzidis, *J. Am. Chem. Soc.*, 2000, **122**, 11571–11576.
- 221 G. E. M. Jauncey, *Phys. Rev.*, 1931, **37**, 1193–1202.
- 222 K. Yamada, N. Niimura, A. Matsumoto, T. Fukunaga, N. Hayashi and N. Watanabe, *J. Phys. Soc. Japan*, 1986, **55**, 831–837.
- 223 A. C. Hannon, D. I. Grimley, R. A. Hulme, A. C. Wright and R. N. Sinclair, *J. Non. Cryst. Solids*, 1994, **177**, 299–316.
- 224 T. Egami, in *Local Structure from Diffraction*, eds. S. J. L. Billinge and M. F. Thorpe, Springer, Boston, MA, Billinge S., 2002, pp. 1–21.
- 225 M. Dove, M. Tucker and D. Keen, *Eur. J. Mineral.*, 2002, **14**, 331–348.

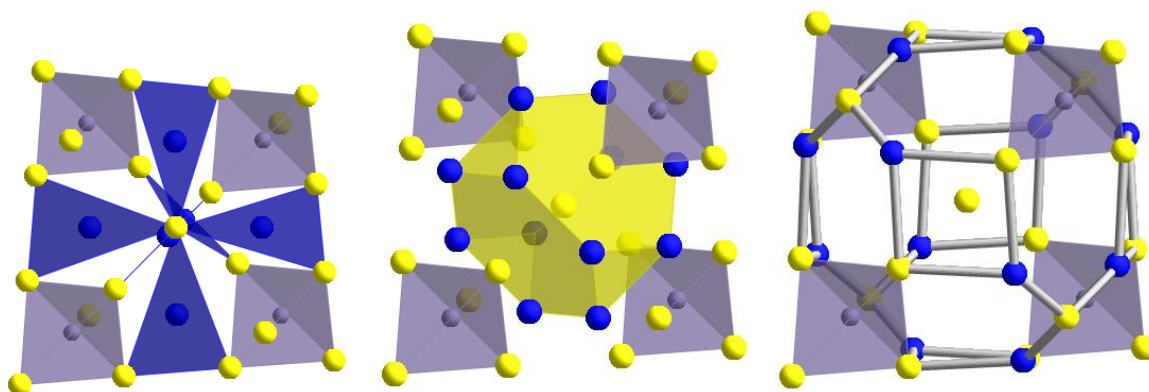
- 226 STFC, *Gudrun*, Didcot, Oxfordshire, 2017.
- 227 M. Tucker, M. Dove, A. Goodwin, A. Phillips, D. Keen, H. Playford, W. A. Slawinski, I. Levin, V. Krayzman, M. Eremenko and Y. Zhang, *RMCPProfile User Manual*, Didcot, 2018.
- 228 B. Zhang, T. Zheng, Q. Wang, Z. Guo, M. J. Kim, H. N. Alshareef and B. E. Gnade, *Scr. Mater.*, 2018, **152**, 36–39.
- 229 D. Kraemer, J. Sui, K. McEnaney, H. Zhao, Q. Jie, Z. F. Ren and G. Chen, *Energy Environ. Sci.*, 2015, **8**, 1299–1308.
- 230 M. Sophocleous, in *Electrical Resistivity and Conductivity*, ed. A. El-Shahat, Intech Open Ltd., Web Edn., 2017, p. 619.
- 231 K. A. Borup, J. De Boor, H. Wang, F. Drymiotis, F. Gascoin, X. Shi, L. Chen, M. I. Fedorov, E. Müller, B. B. Iversen and G. J. Snyder, *Energy Environ. Sci.*, 2015, **8**, 423–435.
- 232 L. J. Van der Pauw, *Philips Tech. Rev.*, 1958, **20**, 220–224.
- 233 Keithley instruments Ltd., *Techniques for Measuring Resistivity for Materials Characterization: 4200A-SCS Paramater Analyzer Applications Guide*, Tektronix, 2019.
- 234 S. Iwanaga, E. S. Toberer, A. LaLonde and G. J. Snyder, *Rev. Sci. Instrum.*, 2011, **82**, 063905.
- 235 J. Martin, T. Tritt and C. Uher, *J. Appl. Phys.*, 2010, **108**, 121101.
- 236 J. Martin, *Rev. Sci. Instrum.*, 2012, **83**, 065101.
- 237 W. J. Parker, R. J. Jenkins, C. P. Butler and G. L. Abbott, *J. Appl. Phys.*, 1961, **32**, 1679–1684.
- 238 R. D. Cowan, *J. Appl. Phys.*, 1963, **34**, 926–927.
- 239 L. M. Clark and R. E. Taylor, *J. Appl. Phys.*, 1975, **46**, 714–719.
- 240 A.-T. Petit and P. L. Dulong, *Ann. Chim. Phys.*, 1819, **10**, 395–413.
- 241 Linseis, LSR-3, <https://www.linseis.com/wp-content/uploads/2018/07/LINSEIS-LSR-v3.pdf>, (accessed 14 February 2019).
- 242 L. Adnane, N. Williams, H. Silva and A. Gokirmak, *Rev. Sci. Instrum.*, 2015, **86**, 105119.
- 243 Z. Zhou and C. Uher, *Rev. Sci. Instrum.*, 2005, **76**, 1–5.
- 244 M. Gunes, M. Parlak and M. Ozenbas, *Meas. Sci. Technol.*, 2014, **25**, 055901.
- 245 A. V Powell, T. Erinc Engin, P. Vaqueiro and S. Hull, *J. Phys. Chem. Solids*, 2007, **68**, 1052–1056.
- 246 T. E. Engin, A. V Powell, R. Haynes, M. A. H. Chowdhury, C. M. Goodway, R. Done, O. Kirichek and S. Hull, *Rev. Sci. Instrum.*, 2008, **79**, 095104.
- 247 J. Liu, S. Hull, I. Ahmed and S. J. J. Skinner, *Nucl. Instruments Methods Phys. Res. B*, 2011, **269**, 539–543.
- 248 B. Yuan, Q. Tao, X. Zhao, K. Cao, T. Cui, X. Wang and P. Zhu, *Rev. Sci. Instrum.*, 2014, **85**, 7–11.
- 249 A. T. Burkov, in *Thermoelectrics Handbook: Macro to Nano*, ed. D. M. Rowe, CRC Press, Boca Raton, 1st edn., 2006, pp. 22-1-22–12.
- 250 R. I. Smith, S. Hull and A. R. Armstrong, *Mater. Sci. Forum*, 1994, **166–169**, 251–256.
- 251 W. G. Williams, R. M. Ibberson, P. Day and J. E. Enderby, *Phys. B Condens. Matter*, 1997, **241–243**, 234–236.
- 252 D. D. Pollock, *Thermocouples: Theory and Properties*, CRC, Boca Raton, FL, 1991.
- 253 C. Elliott, V. Vijayakumar, W. Zink and R. Hansen, *JALA J. Assoc. Lab. Autom.*, 2007, **12**, 17–24.
- 254 J. E. Baucrlle, P. H. Sutter and R. W. Ure, in *Thermoelectricity: Science and*

- Engineering*, eds. R. R. Heikes and R. W. Ure, Interscience Publishers, New York, 1st edn., 1961, pp. 285–334.
- 255 Keithley Instruments Inc., *Model 2100 6 1/2-Digit Resolution Digital Multimeter – User’s Manual*, Cleveland, 2007.
- 256 Keithley instruments inc., *Model 2400 Series sourceMeter: User’s Manual*, Cleveland, 1998.
- 257 F. Akeroyd, *IBEX*, ISIS, STFC, Didcot, 2016.
- 258 Keithley instruments Ltd., *Low Level Measurements Handbook*, Tektronix, 7th edn., 2016.
- 259 A. Brandolini and A. Gandelli, in *The Measurement, Instrumentation and Sensors Handbook*, ed. J. G. Webster, CRC press, 1999.
- 260 B. Beltrán-Pitarch, J. Prado-Gonjal, A. V Powell and J. García-Cañadas, *J. Appl. Phys.*, 2019, **125**, 025111.
- 261 L. W. Chen, C. Wang, Y. C. Liao, C. L. Li, T. H. Chuang and C. H. Hsueh, *J. Alloys Compd.*, 2018, **762**, 631–636.
- 262 B. Song, S. Lee, S. Cho, M. J. Song, S. M. Choi, W. S. Seo, Y. Yoon and W. Lee, *J. Alloys Compd.*, 2014, **617**, 160–162.
- 263 C. C. Li, F. Drymiotis, L. L. Liao, M. J. Dai, C. K. Liu, C. L. Chen, Y. Y. Chen, C. R. Kao and G. J. Snyder, *Energy Convers. Manag.*, 2015, **98**, 134–137.
- 264 X. R. Ferreres and S. Aminorroaya Yamini, *J. Mater. Res. Technol.*, 2019, **8**, 8–13.
- 265 N. H. Pham, N. Farahi, H. Kamila, A. Sankhla, S. Ayachi, E. Müller and J. de Boor, *Mater. Today Energy*, 2019, **11**, 97–105.
- 266 Y. Singh, *Int. J. Mod. Phys. Conf. Ser.*, 2013, **22**, 745–756.
- 267 R. Gunder, J. A. Marquez-Prieto, G. Gurieva, T. Unold and S. Schorr, *CrystEngComm*, 2018, **20**, 1491–1498.
- 268 G. Gurieva, D. M. Többens, M. Y. Valakh and S. Schorr, *J. Phys. Chem. Solids*, 2016, **99**, 100–104.
- 269 P. Mangelis, University of Reading, PhD Thesis, 2017.
- 270 W. G. Zeier, C. P. Heinrich, T. Day, C. Panithipongwut, G. Kieslich, G. Brunklaus, G. Je and W. Tremel, *J. Mater. Chem. A*, 2014, **2**, 1790–1794.
- 271 W. G. Zeier, A. Lalonde, Z. M. Gibbs, C. P. Heinrich, M. Panthöfer, G. J. Snyder and W. Tremel, *J. Am. Chem. Soc.*, 2012, **134**, 7147–7154.
- 272 B. H. Toby, *J. Appl. Crystallogr.*, 2001, **34**, 210–213.
- 273 O. O. Kurakevych and V. L. Solozhenko, *Acta Crystallogr. Sect. C Cryst. Struct. Commun.*, 2007, **63**, 80–82.
- 274 T. E. Engin, Heriott-Watt University, PhD Thesis, 2008.
- 275 N. Morimoto, *Acta Crystallogr.*, 1964, **17**, 351–360.
- 276 Y. Kanazawa, K. Koto and N. Morimoto, *Can. Mineral.*, 1978, **16**, 397–404.
- 277 A. Martinelli, G. O. Lepore, F. Bernardini, A. Giaccherini and F. Di Benedetto, *Acta Crystallogr. Sect. B Struct. Sci. Cryst. Eng. Mater.*, 2018, **74**, 405–415.
- 278 Y. Ding, D. R. Veblen and C. T. Prewitt, *Am. Mineral.*, 2005, **90**, 1265–1269.
- 279 Y. Ding, *Am. Mineral.*, 2005, **90**, 1256–1264.
- 280 B. A. Grguric, A. Putnis and R. J. Harrison, *Am. Mineral.*, 1998, **83**, 1231–1239.
- 281 K. Zhao, P. Qiu, X. Shi and L. Chen, *Adv. Funct. Mater.*, 2019, **0**, 1903867.
- 282 G. Tunell and C. E. Adams, *Am. Mineral.*, 1949, **34**, 824–829.
- 283 M. Tucker, Y. Zhang, M. McDonnel, W. Slawinski, H. Playford, I. Levin, V. Krayzman, M. Dove, D. Keen and A. Goodwin, *RMCPprofile*, STFC, ISIS, Didcot, Oxfordshire, 2018.
- 284 M. Jansen, *Angew. Chemie Int. Ed. English*, 1987, **26**, 1098–1110.
- 285 O. Arnold, J. C. Bilheux, J. M. Borreguero, A. Buts, S. I. Campbell, L. Chapon, M.

- Doucet, N. Draper, R. Ferraz Leal, M. A. Gigg, V. E. Lynch, A. Markvardsen, D. J. Mikkelsen, R. L. Mikkelsen, R. Miller, K. Palmén, P. Parker, G. Passos, T. G. Perring, P. F. Peterson, S. Ren, M. A. Reuter, A. T. Savici, J. W. Taylor, R. J. Taylor, R. Tolchenov, W. Zhou and J. Zikovsky, *Nucl. Instruments Methods Phys. Res. A*, 2014, **764**, 156–166.
- 286 B. A. Grguric and A. Putnis, *Can. Mineral.*, 1998, **36**, 215–227.
- 287 A. Zhang, X. Shen, Z. Zhang, X. Lu, W. Yao, J. Dai, D. Xie, L. Guo, G. Wang and X. Zhou, *J. Mater. Chem. C*, 2017, **5**, 301–308.
- 288 M. G. Townsend, J. R. Gosselin, R. J. Tremblay, L. G. Ripley, D. W. Carson and W. B. Muir, *J. Phys. Chem. Solids*, 1977, **38**, 1153–1159.
- 289 Y. Li, T. Zhang, Y. Qin, T. Day, G. J. Snyder, X. Shi and L. Chen, *J. App. Phys.*, 2014, **116**, 203705.
- 290 Z.-H. Ge, B.-P. Zhang, Y.-X. Chen, Z.-X. Yu, Y. Liu and J.-F. Li, *Chem. Commun.*, 2011, **47**, 12697–12699.
- 291 J. Heo, G. Laurita, S. Muir, M. A. Subramanian and D. A. Keszler, *Chem. Mater.*, 2014, **26**, 2047–2051.
- 292 Y. Bouyrie, M. Ohta, K. Suekuni, Y. Kikuchi, P. Jood, A. Yamamotoa and T. Takabatake, *J. Mater. Chem. C*, 2017, **5**, 4174–4184.
- 293 B. C. Sales, D. G. Mandrus and B. C. Chakoumakos, in *Recent Trends in Thermoelectric Materials Research II*, ed. T. M. Tritt, Elsevier, 2001, vol. 70, pp. 1–36.
- 294 X. Lu, D. T. Morelli, Y. Wang, W. Lai, Y. Xia and V. Ozolins, *Chem. Mater.*, 2016, **28**, 1781–1786.
- 295 P. Qiu, X. Shi and L. Chen, *Energy Storage Mater.*, 2016, **3**, 85–97.
- 296 B. J. Wuensch, *Zeitschrift fur Krist.*, 1964, **119**, 437–453.
- 297 S. O. Long, A. V. Powell, S. Hull, F. Orlandi, C. C. Tang, A. R. Supka, M. Fornari and P. Vaqueiro, *Adv. Funct. Mater.*, 2020, 1909409.
- 298 E. Lara-Curzio, A. F. May, O. Delaire, M. A. McGuire, X. Lu, C. Y. Liu, E. D. Case and D. T. Morelli, *J. Appl. Phys.*, 2014, **115**, 193515.
- 299 A. F. May, O. Delaire, J. L. Niedziela, E. Lara-Curzio, M. A. Susner, D. L. Abernathy, M. Kirkham and M. A. McGuire, *Phys. Rev. B*, 2016, **93**, 1–8.
- 300 H. I. Tanaka, K. Suekuni, K. Umeo, T. Nagasaki, H. Sato, G. Kutluk, E. Nishibori, H. Kasai and T. Takabatake, *J. Phys. Soc. Japan*, 2016, **85**, 1–6.
- 301 V. R. Hathwar, A. Nakamura, H. Kasai, K. Suekuni, H. I. Tanaka, T. Takabatake, B. B. Iversen and E. Nishibori, *Cryst. Growth Des.*, 2019, **19**, 3979–3988.
- 302 K. Suekuni, K. Tsuruta, T. Ariga and M. Koyano, *Appl. Phys. Express*, 2012, **5**, 3–6.
- 303 F. Di Benedetto, G. P. Bernardini, C. Cipriani, C. Emiliani, D. Gatteschi and M. Romanelli, *Phys. Chem. Miner.*, 2005, **32**, 155–164.
- 304 S. Kitagawa, T. Sekiya, S. Araki, T. C. Kobayashi, K. Ishida, T. Kambe, T. Kimura, N. Nishimoto, K. Kudo and M. Nohara, *J. Phys. Soc. Japan*, 2015, **84**, 93701.
- 305 Y. Kosaka, K. Suekuni, K. Hashikuni, Y. Bouyrie, M. Ohta and T. Takabatake, *Phys. Chem. Chem. Phys.*, 2017, **19**, 8874–8879.
- 306 F. H. Sun, C. F. Wu, Z. Li, Y. Pan, Asfandiyar, J. Dong and J. F. Li, *RSC Adv.*, 2017, **7**, 18909–18916.
- 307 R. Chetty, A. Bali, M. H. Naik, G. Rogl, P. Rogl, M. Jain, S. Suwas and R. C. Mallik, *Acta Mater.*, 2015, **100**, 266–274.
- 308 D. J. James, X. Lu, D. T. Morelli and S. L. Brock, *ACS Appl. Mater. Interfaces*, 2015, **7**, 23623–23632.
- 309 B. J. Campbell, H. T. Stokes, D. E. Tanner and D. M. Hatch, *J. Appl. Crystallogr.*, 2006, **39**, 607–614.

- 310 E. A. Owen and E. L. Yates, *London, Edinburgh, Dublin Philos. Mag. J. Sci.*, 1933, **15**, 472–488.
- 311 J. Catterick and P. Thornton, *Adv. Inorg. Chem. Radiochem.*, 1977, **20**, 291–362.
- 312 M. L. Tonnet, S. Yamada and I. G. Ross, *Trans. Faraday Soc.*, 1964, **60**, 840–849.
- 313 J. E. Weder, T. W. Hambley, B. J. Kennedy, P. A. Lay, D. MacLachlan, R. Bramley, C. D. Delfs, K. S. Murray, B. Moubaraki, B. Warwick, J. R. Biffin and H. L. Regtop, *Inorg. Chem.*, 1999, **38**, 1736–1744.
- 314 B. Liu, C. Chen, Y. Zhang, X. Liu and W. Chen, *Organometallics*, 2013, **32**, 5451–5460.
- 315 D. M. Zink, M. Bächle, T. Baumann, M. Nieger, M. Kühn, C. Wang, W. Klopfer, U. Monkowius, T. Hofbeck, H. Yersin and S. Bräse, *Inorg. Chem.*, 2013, **52**, 2292–2305.
- 316 D. M. L. Goodgame, N. J. Hill, D. F. Marsham, A. C. Skapski, M. L. Smart and P. G. H. Troughton, *J. Chem. Soc. D*, 1969, 629–630.
- 317 R. G. Woolley, *Inorg. Chem.*, 1985, **24**, 3519–3525.
- 318 W. Lai, Y. Wang, D. T. Morelli and X. Lu, *Adv. Funct. Mater.*, 2015, **25**, 3648–3657.
- 319 Z. H. Ge, B. P. Zhang, Y. X. Chen, Z. X. Yu, Y. Liu and J. F. Li, *Chem. Commun.*, 2011, **47**, 12697–12699.
- 320 C. Xiao, K. Li, J. Zhang, W. Tong, Y. Liu, Z. Li, P. Huang, B. Pan, H. Su and Y. Xie, *Mater. Horizons*, 2014, **1**, 81–86.

## Appendix A.



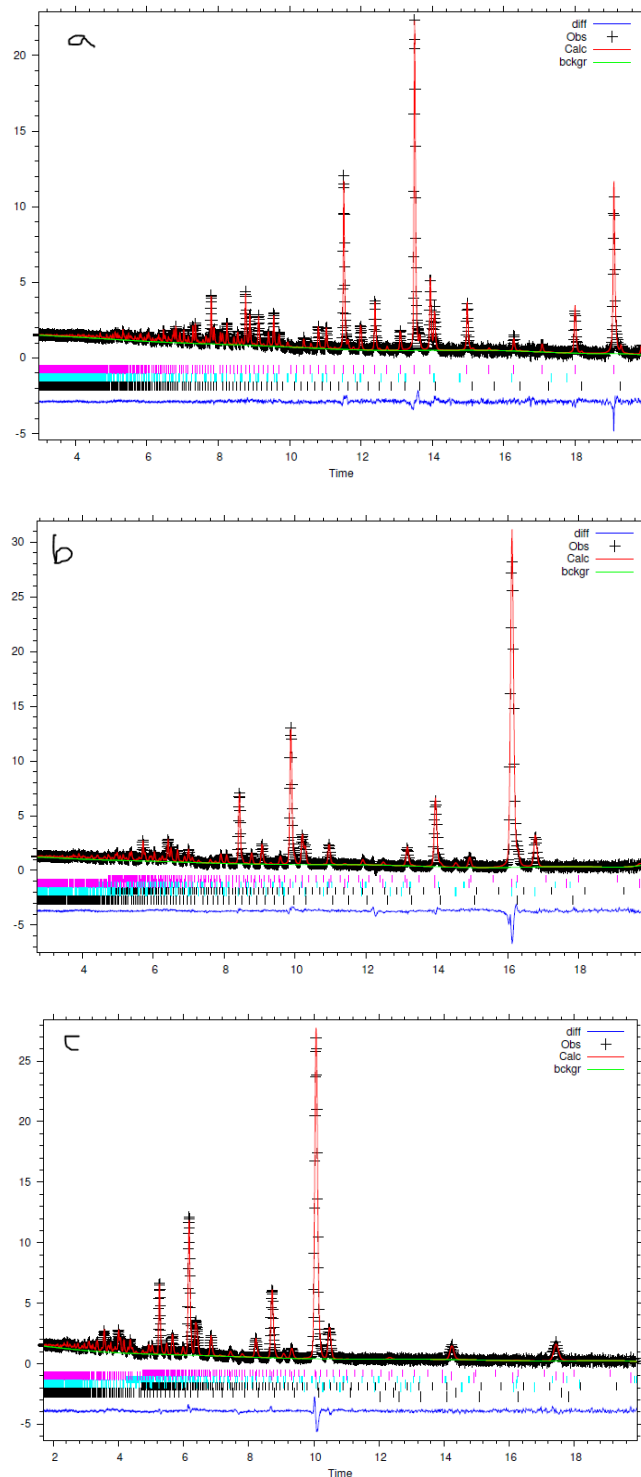
Perspective view of specific cation sites in argyrodite  $\text{Cu}_8\text{GeS}_6$  (a) - cation (1) that forms the spinner; (b) – cation (2) that forms the Laves polyhedra; (c) - cation (3) which caps the triangular faces of the cage. Grey – Germanium; Yellow – sulphur; blue – copper cations.

Crystallographic parameters determined from Rietveld analysis of neutron diffraction data collected at 400 K for a sample with composition  $\text{Cu}_8\text{GeS}_6$

Temperature	400 K					
Space group	$F-43m$					
$a/\text{\AA}$	=	9.94515(9)				
Name	sym	$x$	$y$	$z$	$U_{iso}/\text{\AA}^2$	$SOF$
Ge(1)	$4b$	0.5	0.5	0.5	0.78(5)	1
Cu(1)	$16e$	0.8897(8)	0.8897(8)	0.88968(80)	37(2)*	0.236(16)
Cu(2)	$24f$	0.25	0.25	0.02700(23)	13(2)*	0.685(13)
Cu(3)	$48h$	-0.1587(6)	-0.1587(6)	0.01288(203)	13(2)*	0.225(9)
S(1)	$4a$	0	0	0	0.78(5)	1
S(2)	$4c$	0.25	0.25	0.25	0.78(5)	1
S(3)	$16e$	0.6243(4)	0.6243(4)	0.6243(4)	0.78(5)	1

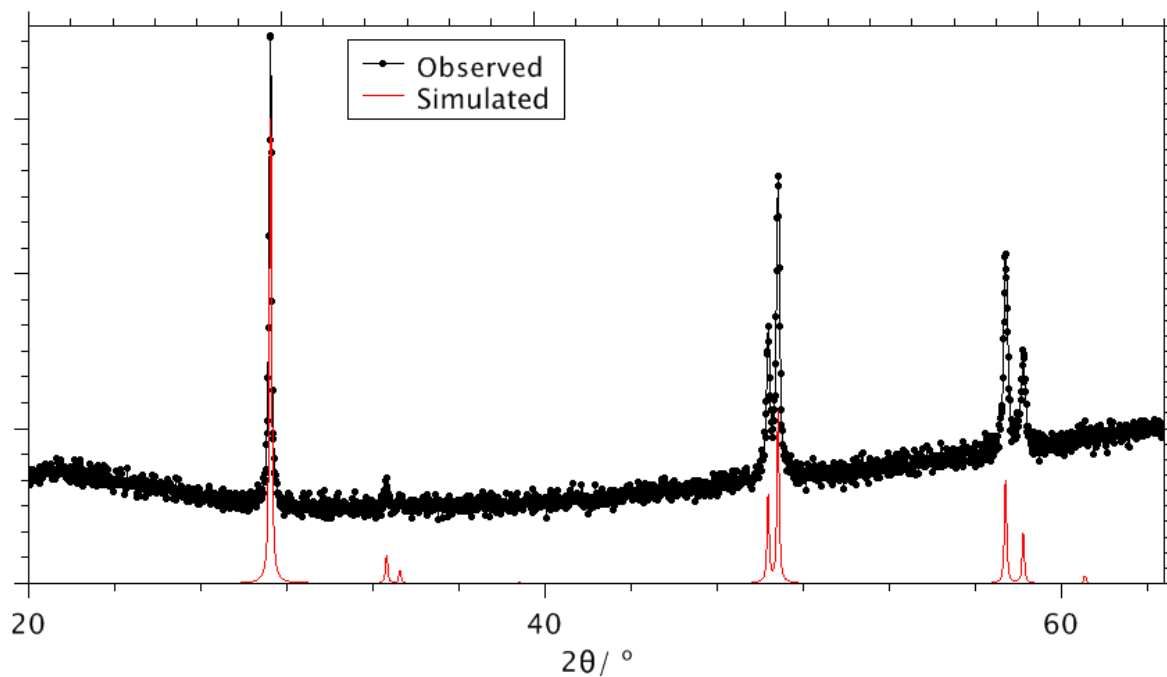
\* - isotropic equivalent of anisotropic displacement parameter

## Appendix B.



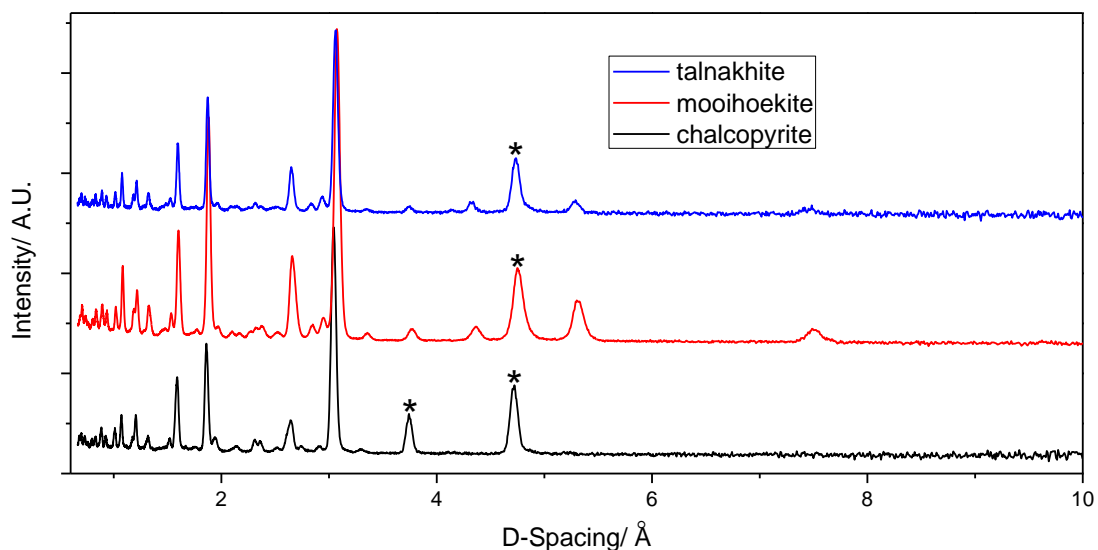
Full Rietveld refinement profiles from multi-bank refinements for the neutron diffraction data collected on  $\text{Cu}_{12}\text{Sb}_4\text{S}_{13}$  with the background subtracted; (a),(b) and (c) correspond to the diffraction data collected at 293 K for the  $150^\circ$ ,  $90^\circ$  and  $50^\circ$  degree banks respectively. Black points – observed, Red line – calculated, Blue line – difference profile. Pink markers -  $-I\bar{4}3m$  phase of tetrahedrite and blue markers -  $-I\bar{4}2m$  phase of kuramite-type phase.

## Appendix C.



Observed powder X-ray diffraction pattern for the sample with composition  $\text{CuFeS}_2$  and the simulated diffraction pattern of the chalcopyrite-type phase.

## Appendix D.



Room-temperature neutron diffraction data from the  $25^\circ$  bank of POLARIS for the samples with chalcopyrite, talnakhite and mooihoekite type phases. The asterisk signifies predominant magnetic reflections.

## Appendix E.

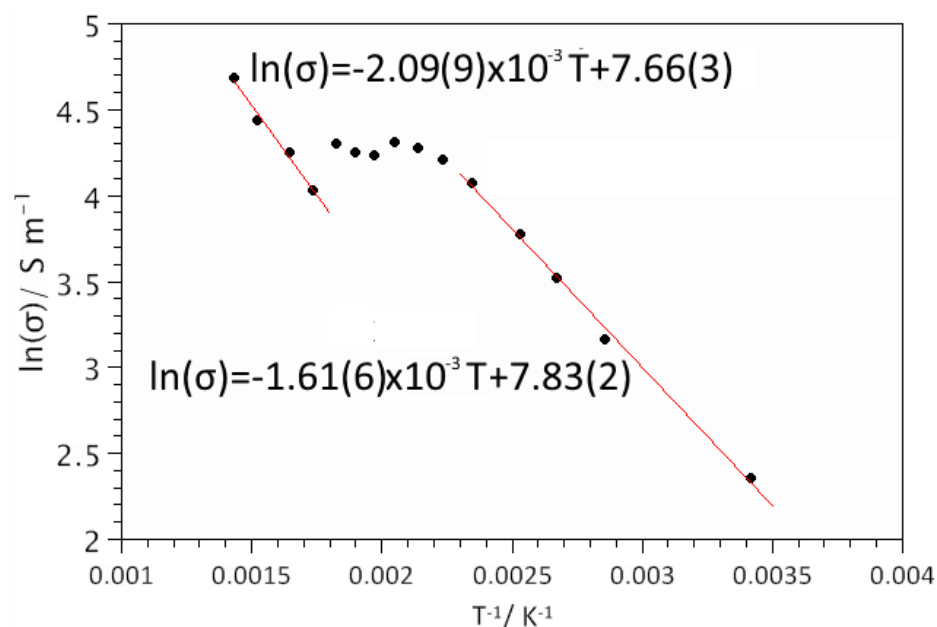
Crystallographic parameters for the mixed phase mooihoekite-chalcopyrite type sample with composition  $\text{Cu}_9\text{Fe}_9\text{S}_{16}$  as determined from the Rietveld analysis of neutron diffraction data at 298 K

Mooihoekite wt %	0.706(2)					
Space group	<i>P-42m</i>					
	<i>a</i> / Å	10.59115(18)	<i>c</i> / Å		5.37099(11)	
Name	Sym.	<i>x</i>	<i>y</i>	<i>z</i>	$U_{iso}$ / Å <sup>2</sup>	<i>SOF</i>
Cu(1)	<i>4n</i>	0.256189	0.256189	0.479934	0.0101(2)	1
Cu(2)	<i>4k</i>	0.237604	0.5	0	0.0101(2)	0.1576
Cu(3)	<i>4i</i>	0.251755	0	0	0.0101(2)	0.1576
Cu(5)	<i>1c</i>	0	0	0.5	0.0101(2)	1
Cu(6)	<i>1b</i>	0.5	0.5	0.5	0.0101(2)	0.8424
Cu(7)	<i>1d</i>	0	0	0	0.0101(2)	0.8424
S(1)	<i>8o</i>	0.113641	0.378684	0.244312	0.0028(1)	1
S(2)	<i>4n</i>	0.123488	0.123488	0.755317	0.0028(1)	1
S(3)	<i>4n</i>	0.375496	0.375496	0.773559	0.0028(1)	1
Fe(2)	<i>4k</i>	0.237604	0.5	0	0.0101(2)	0.8424
Fe(3)	<i>4i</i>	0.251755	0	0	0.0101(2)	0.8424
Fe(4)	<i>2f</i>	0.5	0	0.5	0.0101(2)	1
Fe(6)	<i>1b</i>	0.5	0.5	0.5	0.0101(2)	0.1576
Fe(7)	<i>1a</i>	0	0	0	0.0101(2)	0.1576
Fe(8)	<i>1d</i>	0.5	0.5	0	0.0101(2)	1
Talnakhite wt%	0.293(2)					
Space group	<i>I-43m</i>					
	<i>a</i> / Å	10.61883(24)				
Name	sym	<i>x</i>	<i>y</i>	<i>z</i>	$U_{iso}$ / Å <sup>2</sup>	<i>SOF</i>
Fe(1)	<i>2a</i>	0	0	0	1.54(4)	1
Cu(1)	<i>12e</i>	0.2571	0	0	1.54(4)	0.8355
Fe(2)	<i>12e</i>	0.2571	0	0	1.54(4)	0.1645
Cu(2)	<i>12e</i>	0.5	0.25	0	1.54(4)	0.1645
Fe(3)	<i>12e</i>	0.5	0.25	0	1.54(4)	0.8355
Cu(3)	<i>8c</i>	0.248682	0.248682	0.248682	1.54(4)	1
Cu(4)	<i>6b</i>	0.5	0	0	1.54(4)	0.2492
S(1)	<i>8c</i>	0.11787	0.11787	0.11787	0.281(14)	1
S(2)	<i>24g</i>	0.12533	0.36384	0.36384	0.281(14)	1
Overall	$R_{wp}/\%$	3.52	$R_p/\%$	4.78		
150 ° bank	$R_{wp}/\%$	3.33	$R_p/\%$	4.44		
90 ° bank	$R_{wp}/\%$	3.45	$R_p/\%$	4.35		
50 ° bank	$R_{wp}/\%$	3.94	$R_p/\%$	5.71		
	$\chi^2$	4.6				

## Appendix F.

Crystallographic parameters for the sample with composition  $\text{Cu}_9\text{Fe}_9\text{S}_{16}$  as determined from the Rietveld analysis of the neutron diffraction data collected at 298 K.

Temperature	298 K					
Space group	$I-43m$					
$a/\text{\AA}$	10.59829(9)					
Name	sym	$x$	$y$	$z$	$U_{iso}/\text{\AA}^2$	$SOF$
Fe(1)	$2a$	0	0	0	0.936(16)	1
Cu(1)	$12e$	0.26656	0	0	0.936(16)	0.627(11)
Fe(2)	$12e$	0.237819	0	0	0.936(16)	0.373(11)
Cu(2)	$12e$	0.5	0.25	0	0.936(16)	0.373(11)
Fe(3)	$12e$	0.5	0.25	0	0.936(16)	0.627(11)
Cu(3)	$8c$	0.2537(5)	0.2537(5)	0.2537(5)	0.936(16)	1
Cu(4)	$6b$	0.5	0	0	0.936(16)	0
S(1)	$8c$	0.1280(9)	0.1280(9)	0.1280(9)	0.54(6)	1
S(2)	$24g$	0.1147(8)	0.3758(5)	0.3758(5)	0.54(6)	1
Overall	$R_{wp}/\%$	3.35	$R_p/\%$	5.05		
150 ° bank	$R_{wp}/\%$	3.26	$R_p/\%$	4.99		
90 ° bank	$R_{wp}/\%$	3.04	$R_p/\%$	4.57		
50 ° bank	$R_{wp}/\%$	3.99	$R_p/\%$	5.60		
	$\chi^2$	1.753				

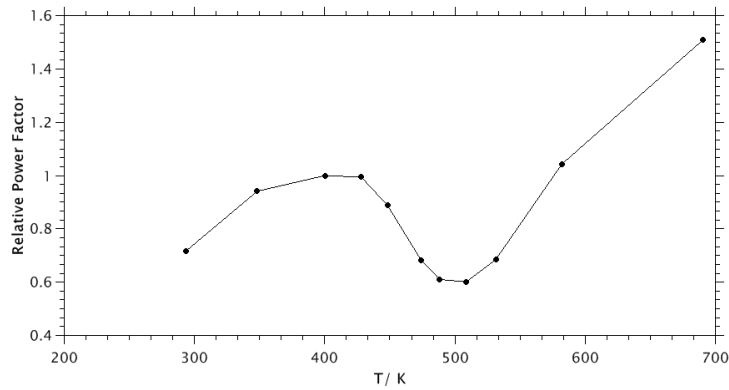


Arrhenius plot of the electrical resistivity data for the sample with composition  $\text{Cu}_9\text{Fe}_9\text{S}_{16}$

Crystallographic parameters for the sample with composition  $\text{Cu}_9\text{Fe}_9\text{S}_{16}$  as determined from the Rietveld analysis of the neutron diffraction data collected at 680 K.

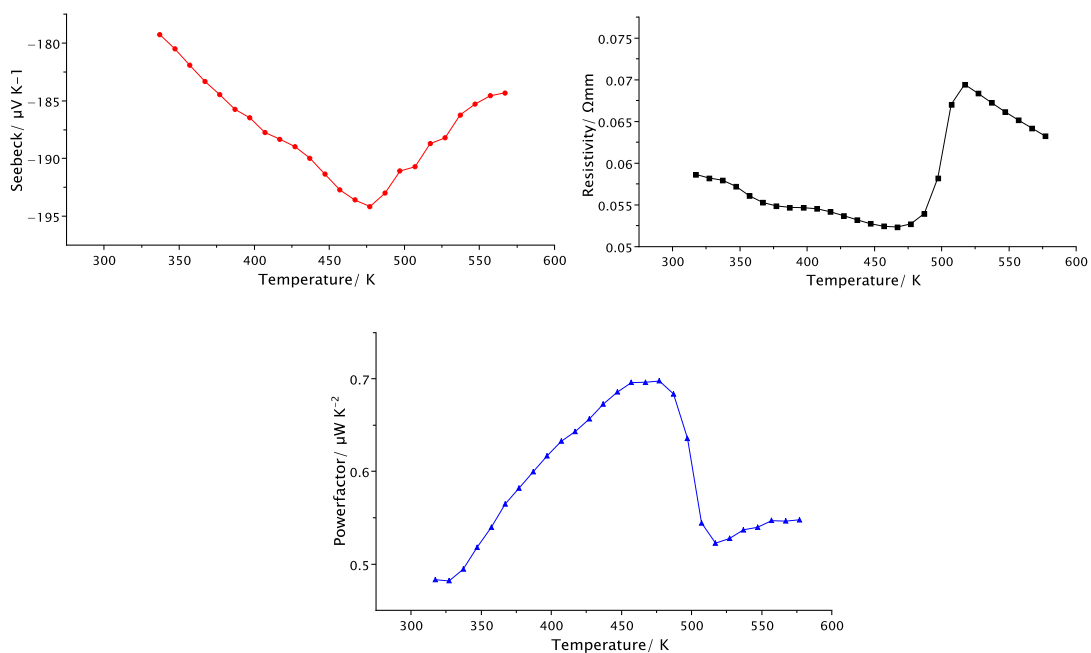
Chalcopyrite phase	680 K					
Space group	<i>I-42d</i>					
Fraction	21.23(39)					
	<i>a</i> / Å	5.3116(1)	<i>c</i> / Å	=	10.462(1)	
Name	Wycoff.	<i>x</i>	<i>y</i>	<i>z</i>	$U_{iso}$ / Å <sup>2</sup>	<i>SOF</i>
Fe	<i>4a</i>	0	0	0	0.0253(8)	1
Cu	<i>4b</i>	0	0	0.5	0.0253(8)	1
S	<i>8d</i>	0.247817	0.25	0.125	0.0271(28)	1
Intermediate cubic phase						
Space Group	<i>F-43m</i>					
Fraction	0.76026					
	<i>a</i> / Å	5.3410(2)				
Name	Wycoff.	<i>x</i>	<i>y</i>	<i>z</i>	$U_{iso}$ / Å <sup>2</sup>	<i>SOF</i>
Fe(1)	<i>4a</i>	0	0	0	0.0345(5)	0.4615
Cu(1)	<i>4a</i>	0	0	0.5	0.0345(5)	0.0389
Cu(2)	<i>4b</i>	0	0	0	0.0345(5)	0.4599
Fe(2)	<i>4b</i>	0	0	0.5	0.0345(5)	0.0395
S(1)	<i>4c</i>	0.25	0.25	0.25	0.0272(5)	1
Overall	$R_{wp}/\%$	3.81	$R_p/\%$	4.53		
150 ° bank	$R_{wp}/\%$	3.45	$R_p/\%$	4.17		
90 ° bank	$R_{wp}/\%$	3.26	$R_p/\%$	4.21		
50 ° bank	$R_{wp}/\%$	5.09	$R_p/\%$	5.24		
	$\chi^2$	6.996				

## Appendix G.



Relative power factor, determined by dividing all values of  $S^2\sigma(T)$  by  $S^2\sigma_{425K}$ , of the sample with chalcopyrite type structure and nominal composition  $\text{Cu}_9\text{Fe}_8\text{S}_{16}$ . Electrical data collected from the in-situ cell.

## Appendix H.



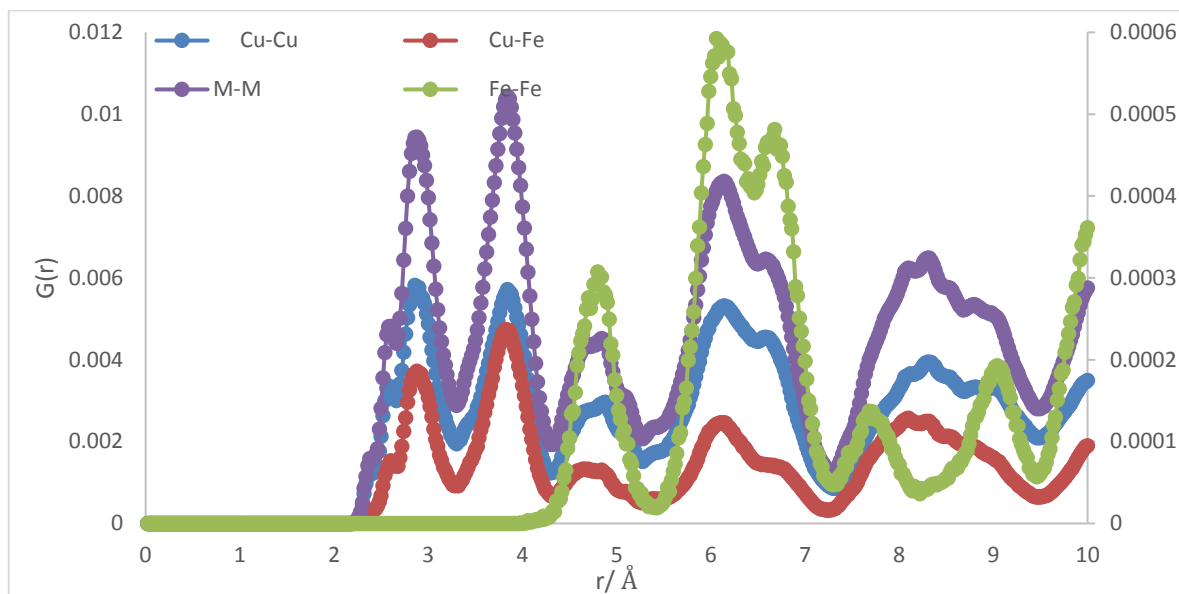
Top, middle and bottom: Seebeck coefficient; electrical resistivity and power factor. The temperature dependence of the electrical transport properties for the talnakhite-type sample with composition  $\text{Cu}_9\text{Fe}_9\text{S}_{16}$  as determined from measurements on the Linseis LSR-3.

## Appendix I

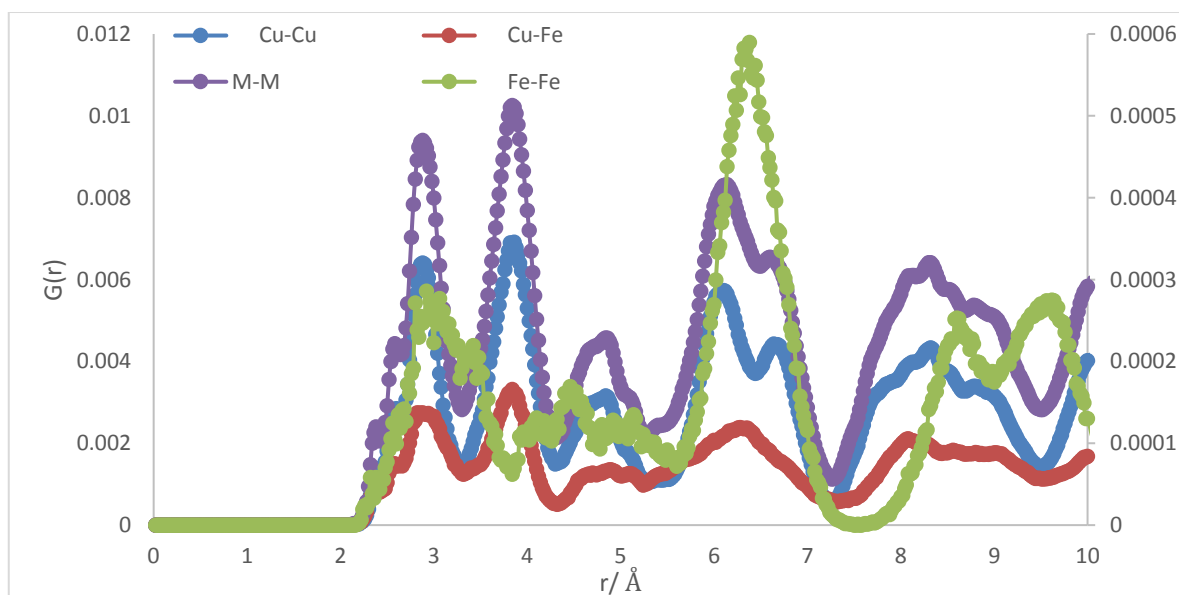
List of the mean bond distances and angles for each cation sites for the room temperature phase of bornite as determined from Rietveld analysis for three samples. The ‘trig.’ angles were determined using the 3 largest bond angles to show the sites were trigonal geometry is observed.

Atom Label	Cu <sub>5</sub> FeS <sub>4</sub>			Cu <sub>4.96</sub> Fe <sub>0.98</sub> S <sub>4</sub>			Cu <sub>5.08</sub> Fe <sub>0.92</sub> S <sub>4</sub>		
	Mean Distance/ Å	Mean angle/ °	Mean Trig. angle/ °	Mean Distance/ Å	Mean angle/ °	Mean Trig. angle/ °	Mean Distance/ Å	Mean angle/ °	Mean Trig. angle/ °
Cu(1)	2.35	109.4	112.2	2.37	109.2	114.0	2.35	109.3	113.2
Cu(2)	2.42	109.3	113.1	2.37	109.4	112.4	2.39	109.3	113.3
Cu(3)	2.50	109.4	112.4	2.35	109.4	114.1	2.38	109.2	113.4
Fe(4)	2.33	109.4	112.1	2.32	109.5	112.7	2.34	109.5	111.9
Fe(5)	2.38	109.5	111.5	2.38	109.5	112.2	2.35	109.5	113.0
Cu(6)	2.40	109.1	114.8	2.44	108.2	117.9	2.45	108.0	118.3
Cu(7)	2.39	109.2	114.0	2.40	109.4	113.3	2.36	109.3	113.4
Cu(8)	2.26	109.5	110.8	2.36	109.4	111.9	2.37	109.4	112.1
Cu(9)	2.44	108.6	116.9	2.40	108.2	117.8	2.42	108.4	117.6
Cu(10)	2.54	103.9	119.9	2.52	104.7	120.0	2.45	104.7	120.0
Cu(11)	2.47	108.4	117.2	2.50	108.8	116.1	2.52	108.3	117.7
Cu(12)	2.32	109.1	114.8	2.30	109.2	113.0	2.34	109.4	112.3
				2.66	N/A	111.0	2.37	109.2	114.2
				2.42	107.1	119.3	2.37	109.5	113.0
				2.51	105.3	120.0	2.56	103.3	119.7
				2.36	109.2	114.2	2.31	N/A	112.4

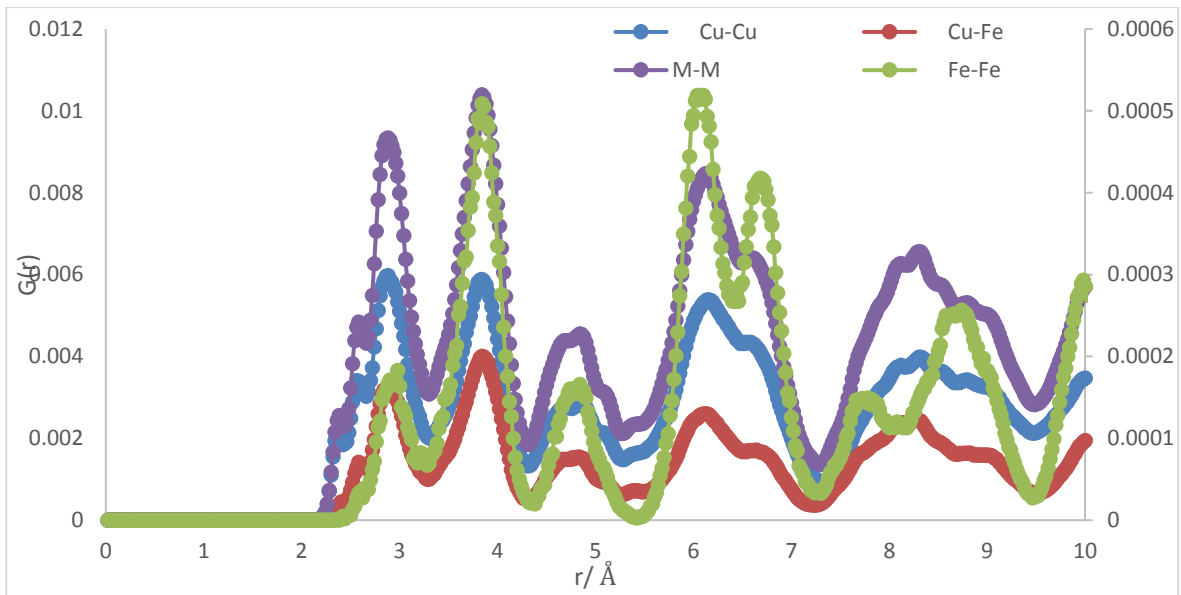
## Appendix Ja



PDF partials of the metal-metal distances in stoichiometric bornite at 300 K and averaged over all runs using calculation parameters *i-a*. Cu-Cu, M-M, Cu-Fe y-axis on the left; Fe-Fe y axis on the right.



PDF partials of the metal-metal distances in stoichiometric bornite at 300 K and averaged over all runs using calculation parameters *ii-a*. Cu-Cu, M-M, Cu-Fe y-axis on the left; Fe-Fe y axis on the right.



PDF partials of the metal-metal distances in stoichiometric bornite at 300 K and averaged over all runs using calculation parameters *ii-b*. Cu-Cu, M-M, Cu-Fe y-axis on the left; Fe-Fe y axis on the right.

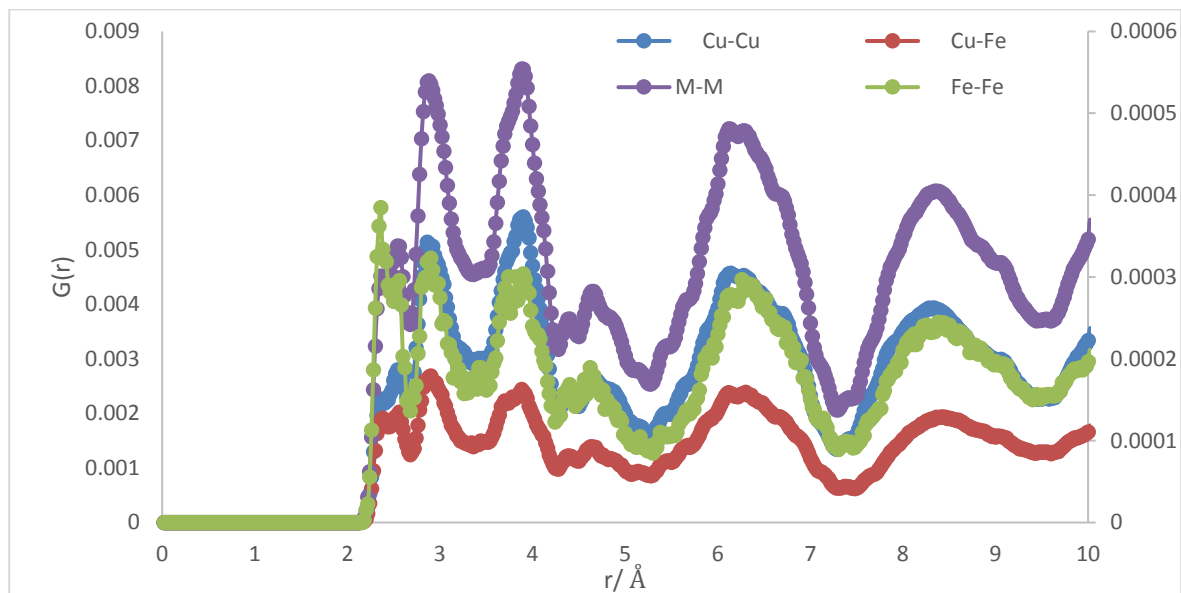
## Appendix Jb.

<i>i-b</i> $SOF_{Fe}$	M(4)	M(8)	M(5)	M(1)
layer n0 i	0.09	0.99	0.27	0.74
layer n0 ii	0.23	0.97	0.98	0.02
layer n1/4 i	0.34	0.87	0.27	0.74
layer n1/4 ii	0.07	1.00	0.44	0.18
layer n1/2 i	0.82	0.77	0.81	0.04
layer n1/2 ii	0.03	1.00	0.68	0.14
layer n3/4 i	0.04	0.97	0.43	0.23
layer n3/4 ii	0.28	0.85	0.83	0.02
average	0.24	0.93	0.59	0.26

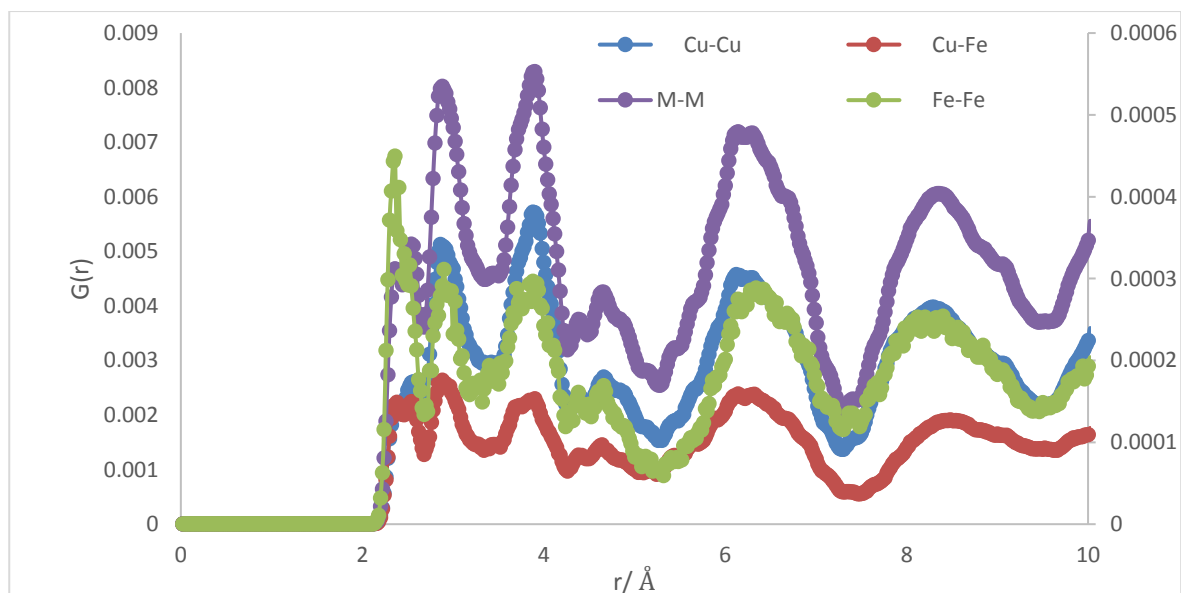
<i>ii-b</i> $SOF_{Fe}$	M(4)	M(8)	M(5)	M(1)
layer n0 i	0.11	0.96	0.15	0.53
layer n0 ii	0.25	0.84	0.93	0.04
layer n1/4 i	0.73	0.96	0.86	0.01
layer n1/4 ii	0.22	0.99	0.08	0.38
layer n1/2 i	0.70	0.55	0.66	0.06
layer n1/2 ii	0.02	0.98	0.46	0.17
layer n3/4 i	0.02	0.99	0.65	0.53
layer n3/4 ii	0.52	0.46	0.95	0.12
average	0.32	0.84	0.59	0.23

Site occupancy factors determined from RMCprofile analysis for the tetrahedral sites in the space group P1 and which are equivalent to the M(1,4,5 and8) cation positions in the Pbcu unit cell for: top – calculation parameters *i-b*; calculation parameters *ii-b*. The coloured boxes correspond to the low occupancy sites that appear in the ‘empty’ 1D channels.

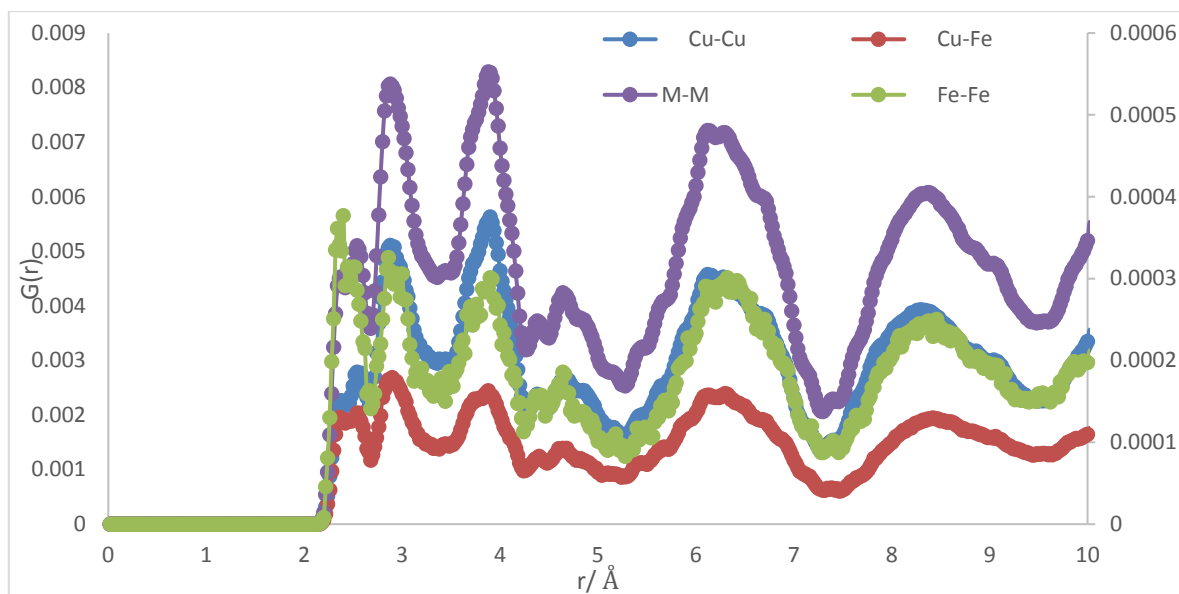
## Appendix K.



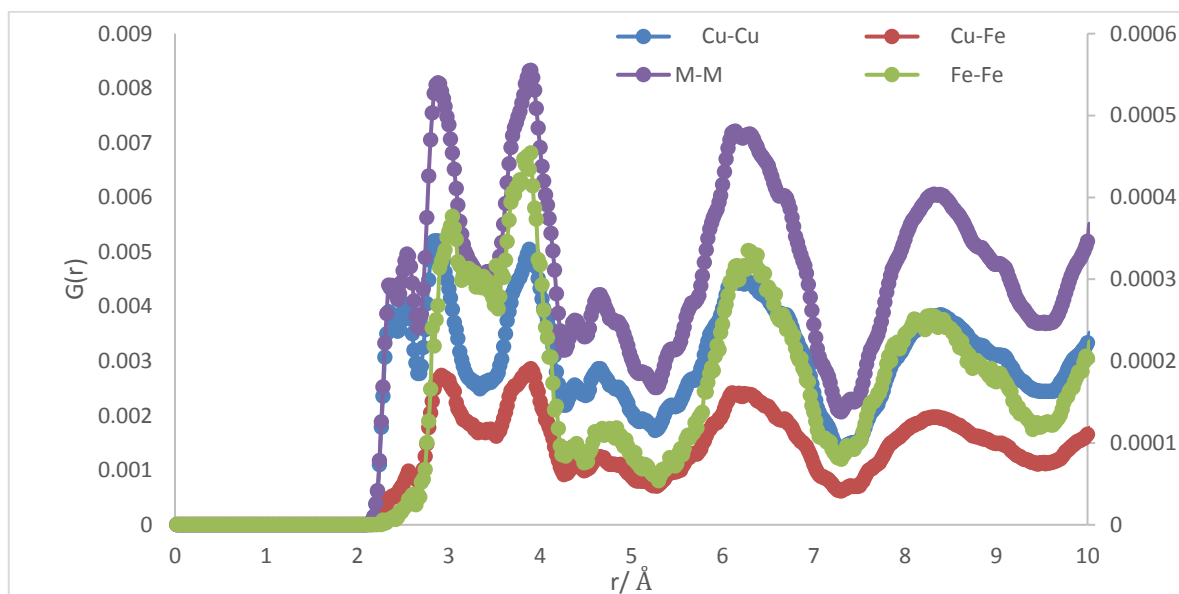
PDF partials of the metal-metal distances in stoichiometric bornite at 500 K and averaged over all runs from using calculation parameters (*i-a*). Cu-Cu, M-M, Cu-Fe y-axis on the left; Fe-Fe y axis on the right.



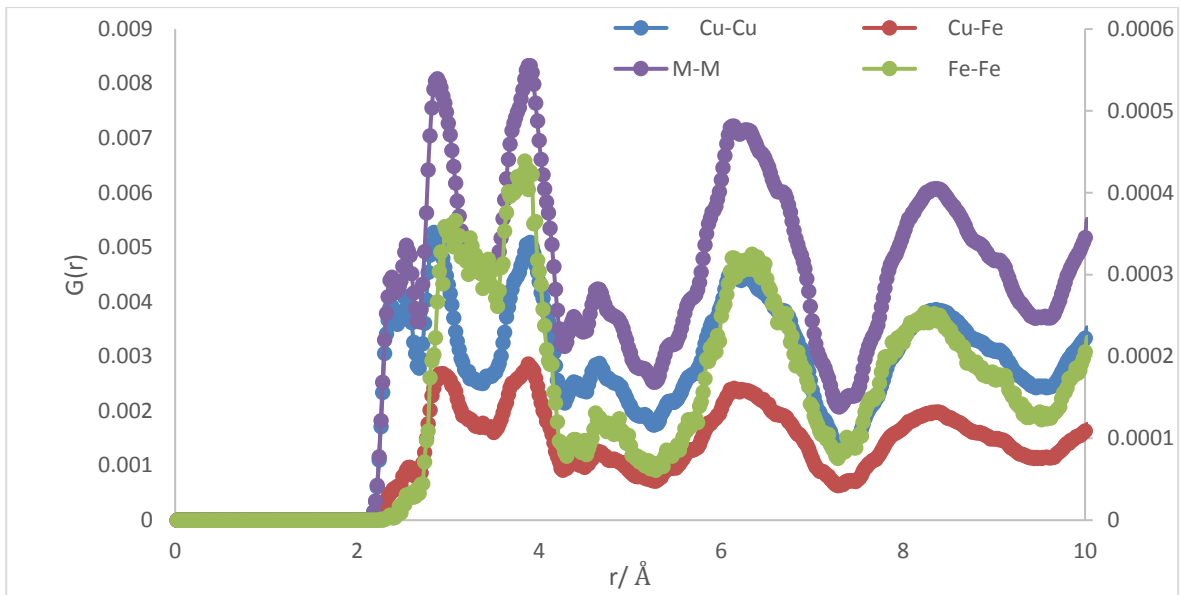
PDF partials of the metal-metal distances in stoichiometric bornite at 500 K and averaged over all runs from using calculation parameters (*ii-a*). Cu-Cu, M-M, Cu-Fe y-axis on the left; Fe-Fe y axis on the right.



PDF partials of the metal-metal distances in stoichiometric bornite at 500 K and averaged over all runs from using calculation parameters (*iii-a*). Cu-Cu, M-M, Cu-Fe y-axis on the left; Fe-Fe y axis on the right.

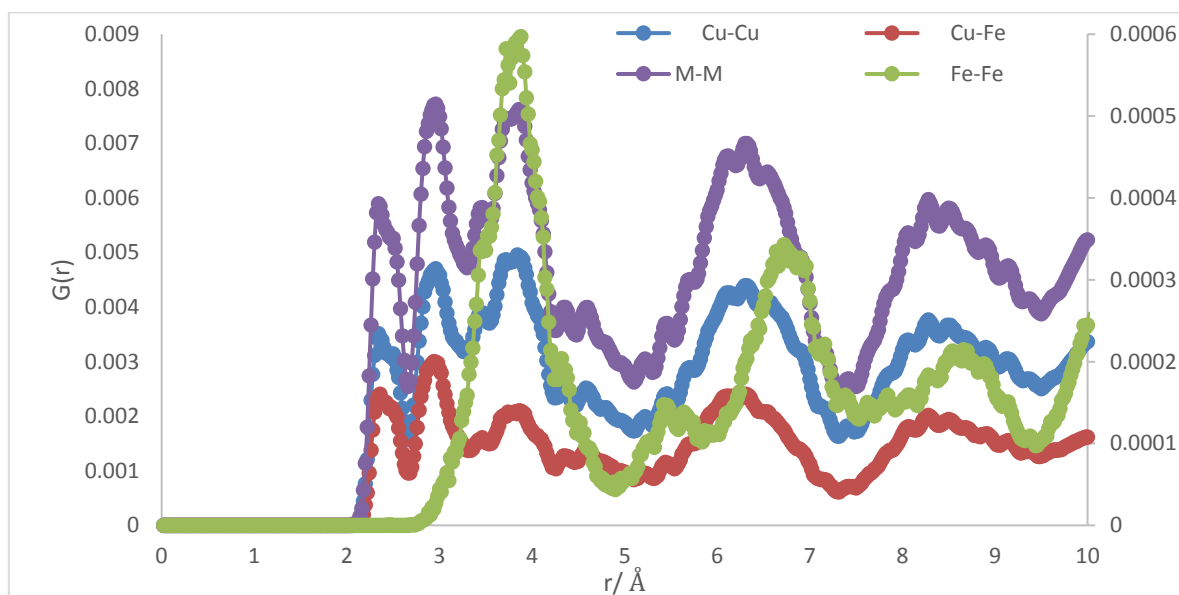


PDF partials of the metal-metal distances in stoichiometric bornite at 500 K and averaged over all runs from using calculation parameters (*ii-b*). Cu-Cu, M-M, Cu-Fe y-axis on the left; Fe-Fe y axis on the right.

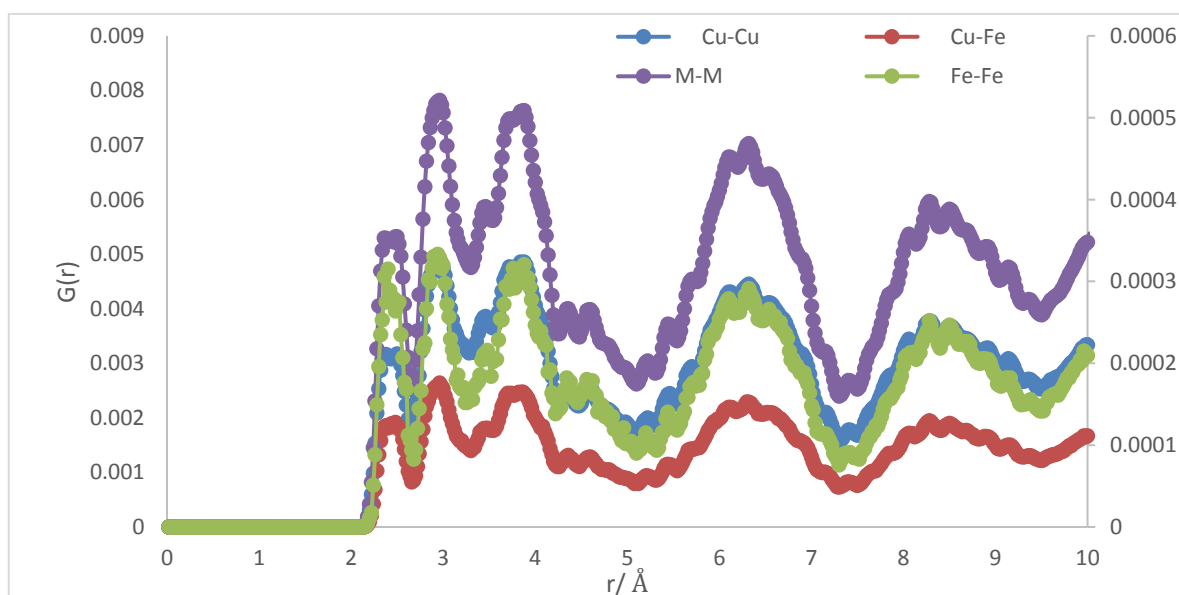


PDF partials of the metal-metal distances in stoichiometric bornite at 500 K and averaged over all runs from using calculation parameters using calculation parameters using calculation parameters using calculation parameters (*iii-b*). Cu-Cu, M-M, Cu-Fe y-axis on the left; Fe-Fe y axis on the right.

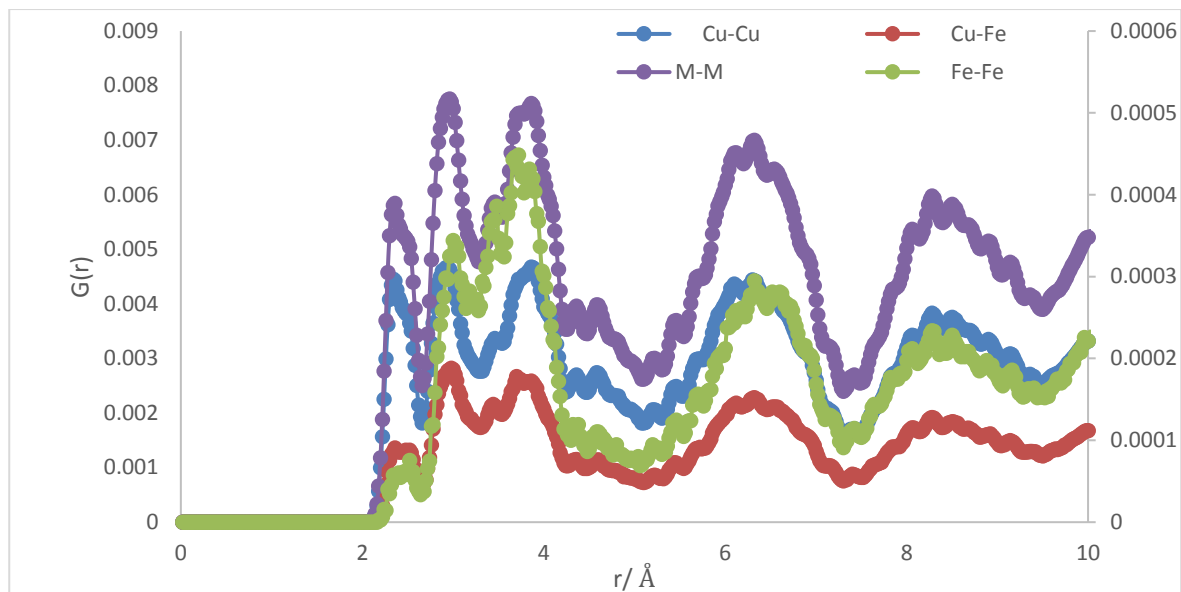
## Appendix L.



PDF partials of the metal-metal distances in stoichiometric bornite at 575 K and averaged over all runs from using calculation parameters (*i-a*). Cu-Cu, M-M, Cu-Fe y-axis on the left; Fe-Fe y axis on the right.

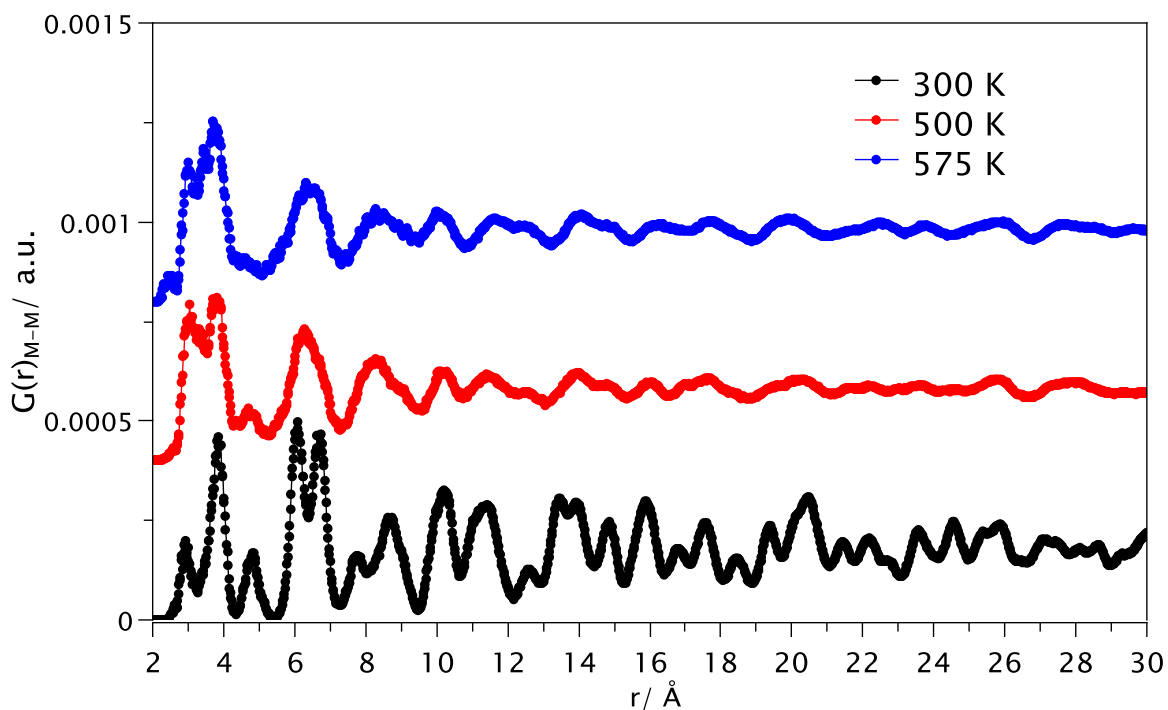


PDF partials of the metal-metal distances in stoichiometric bornite at 575 K and averaged over all runs from using calculation parameters (*ii-a*). Cu-Cu, M-M, Cu-Fe y-axis on the left; Fe-Fe y axis on the right.



PDF partials of the metal-metal distances in stoichiometric bornite at 575 K and averaged over all runs from using calculation parameters (*i-b*). Cu-Cu, M-M, Cu-Fe y-axis on the left; Fe-Fe y axis on the right.

## Appendix M.



PDF partials for the M-M distances over long  $r$ -range to show the disorder as a result of the  $4a$ - $2a$  transition.

## Appendix N.

Crystallographic parameters for the cation-poor bornite sample,  $\text{Cu}_{4.96}\text{Fe}_{0.98}\text{S}_4$ , at 300 K determined from Rietveld analysis.

Temperature/ K	300			
Space group	<i>Pbca</i>			
Lattice Parameters/ Å	<i>a</i> / Å	10.9417(8)		
	<i>b</i> / Å	21.9010(10)		
	<i>c</i> / Å	10.9390(7)		
S(all)	$U_{iso}$ / Å <sup>2</sup>	0.0001		
Cu,Fe(all)	$U_{iso}$ / Å <sup>2</sup>	0.01942(13)		
Cu,Fe(1-8),S(all)	SOF	1		
Wyckoff symbol – 8c all	<i>x</i>	<i>y</i>	<i>z</i>	<i>SOF</i>
S(1)	0.0034(17)	0.0009(13)	0.2472(23)	
S(2)	-0.0175(21)	0.2572(11)	0.2591(19)	
S(3)	0.2442(20)	0.1262(13)	0.2563(26)	
S(4)	0.2385(20)	0.0045(10)	0.4988(27)	
S(5)	-0.0099(21)	0.1310(10)	0.5024(27)	
S(6)	0.0042(18)	0.1139(9)	0.0039(24)	
S(7)	0.2531(20)	0.1222(12)	0.7427(27)	
S(8)	0.2532(22)	0.2499(12)	0.4902(29)	
Cu(1)	0.1319(13)	0.0569(7)	0.3660(12)	
Cu(2)	0.1111(10)	0.0651(4)	0.6315(9)	
Cu(3)	0.3839(14)	0.0620(6)	0.3664(11)	
Fe(4)	0.3728(11)	0.0596(6)	0.6252(12)	
Fe(5)	0.1229(10)	0.1900(5)	0.3737(12)	
Cu(6)	0.1407(11)	0.1974(5)	0.6476(11)	
Cu(7)	0.3739(13)	0.1914(6)	0.3623(14)	
Cu(8)	0.3801(12)	0.1884(5)	0.6255(13)	
Cu(9)	0.1469(13)	0.0724(6)	0.8969(14)	0.883(11)
Cu(10)	0.3312(12)	0.0854(6)	0.0826(14)	0.769(15)
Cu(11)	0.1469(15)	0.1793(7)	0.1040(18)	0.708(17)
Cu(12)	0.3738(13)	0.1861(7)	0.8879(14)	0.814(19)
Cu(13)	0.0492(62)	0.1002(27)	0.2046(65)	0.117(11)
Cu(14)	0.3409(56)	0.0765(25)	0.9015(55)	0.231(15)
Cu(15)	0.1711(31)	0.1654(15)	0.9147(34)	0.292(17)
Cu(16)	0.3729(56)	0.1820(23)	0.1206(58)	0.186(19)
Overall	$R_{wp}/\%$	3.49	$R_p/\%$	6.12
150 ° bank	$R_{wp}/\%$	3.51	$R_p/\%$	6.32
90 ° bank	$R_{wp}/\%$	3.45	$R_p/\%$	5.36
50 ° bank	$R_{wp}/\%$	3.55	$R_p/\%$	6.78
	$\chi^2$	2.43		

Crystallographic parameters for the 2a phase of cation-poor bornite sample,  $\text{Cu}_{4.96}\text{Fe}_{0.98}\text{S}_4$ , at 498 K determined from Rietveld analysis.

Space Group	<i>F</i> 23					
Temperature	498 K					
<i>a</i> / Å	=	10.98869(4)				
Name	sym	<i>x</i>	<i>y</i>	<i>z</i>	<i>U</i> <sub>iso</sub> / Å <sup>3</sup>	<i>SOF</i>
Cu(3t') M(3)	<i>16e</i>	0.117(1)	0.117(1)	0.383(1)	0.0491(3)	0
Cu(1) M(1)	<i>16e</i>	0.8760(4)	0.8760(4)	0.8760(4)	0.0491(3)	0.854(5)
Cu(2) M(2)	<i>16e</i>	0.8822(3)	0.8822(3)	0.618(3)	0.0491(3)	0.659(5)
S(1)	<i>4a</i>	0	0	0	0.0163(3)	1
S(2)	<i>4b</i>	0	0	0.5	0.0163(3)	1
S(3)	<i>24g</i>	0.25	0.25	-0.0028(3)	0.0163(3)	1
Cu(3t'')M(3)	<i>16e</i>	0.1662(5)	0.1662(5)	0.3338(5)	0.0491(3)	0.304(4)
Cu(4t') M(4)	<i>16e</i>	1.1314(4)	1.1314(4)	1.1314(4)	0.0491(3)	0.521(4)
Cu(4t'') M(4)	<i>16e</i>	1.1774(9)	1.1774(9)	1.1774(9)	0.0491(3)	0.175(8)
Fe(1) M(1)	<i>16e</i>	0.8760(4)	0.8760(4)	0.8760(4)	0.0491(3)	0.125
Fe(2) M(2)	<i>16e</i>	0.8822(3)	0.8822(3)	0.618(3)	0.0491(3)	0.125
Fe(3t') M(3)	<i>16e</i>	0.117(1)	0.117(1)	0.383(1)	0.0491(3)	0.125
Fe(4t') M(4)	<i>16e</i>	1.1314(4)	1.1314(4)	1.1314(4)	0.0491(3)	0.125
Overall	<i>R</i> <sub>wp</sub> /%	3.68	<i>R</i> <sub>p</sub> / %	5.63		
150 ° bank	<i>R</i> <sub>wp</sub> /%	3.57	<i>R</i> <sub>p</sub> / %	5.07		
90 ° bank	<i>R</i> <sub>wp</sub> /%	3.60	<i>R</i> <sub>p</sub> / %	4.53		
50 ° bank	<i>R</i> <sub>wp</sub> /%	3.98	<i>R</i> <sub>p</sub> / %	7.85		
	$\chi^2$	2.141				

Crystallographic parameters for the *a* phase of the cation-poor bornite sample,  
 $\text{Cu}_{4.96}\text{Fe}_{0.98}\text{S}_4$ , 565 K determined from Rietveld analysis.

Space group	<i>F23</i>					
Temperature	565 K					
Weight fraction	98.38(1)					
<i>a</i> / Å	=	5.50678(2)				
Name	sym	<i>x</i>	<i>y</i>	<i>z</i>	<i>U</i> <sub>iso</sub> / Å <sup>3</sup>	<i>SOF</i>
Cu(1t')	<i>4c</i>	0.25	0.25	0.25	0.0533(4)	0.473(5)
Cu(2t')	<i>4d</i>	0.25	0.25	0.75	0.0533(4)	0.354(8)
Fe(1t')	<i>4c</i>	0.25	0.25	0.25	0.0533(4)	0.018(7)
Fe(2t')	<i>4d</i>	0.25	0.25	0.75	0.0533(4)	0.231(7)
S	<i>4a</i>	0	0	0	0.0268(3)	1
Cu(1t'')	<i>16e</i>	0.328	0.633	0.633	0.0533(4)	0.080(2)
Cu(2t'')	<i>16e</i>	0.633	0.633	0.633	0.0533(4)	0.025(1)
Chalcopyrite phase						
spacegroup	<i>Fm-3m</i>					
<i>a</i> / Å	=	5.3030(8)				
Name	sym	<i>x</i>	<i>y</i>	<i>z</i>	<i>U</i> <sub>iso</sub> / Å <sup>3</sup>	<i>SOF</i>
Cu	<i>4a</i>	0	0	0	0.0327	1
Fe	<i>4b</i>	0	0	0.5	0.0327	1
S	<i>8d</i>	0.25	0.25	0.125	0.0327	1
Overall	<i>R</i> <sub>wp</sub> /%	3.16	<i>R</i> <sub>p</sub> / %	4.80		
150 ° bank	<i>R</i> <sub>wp</sub> /%	3.33	<i>R</i> <sub>p</sub> / %	4.63		
90 ° bank	<i>R</i> <sub>wp</sub> /%	3.10	<i>R</i> <sub>p</sub> / %	3.81		
50 ° bank	<i>R</i> <sub>wp</sub> /%	3.01	<i>R</i> <sub>p</sub> / %	6.33		
	$\chi^2$	1.566				

## Appendix O.

Crystallographic parameters for the copper-rich bornite sample,  $\text{Cu}_{5.08}\text{Fe}_{0.92}\text{S}_4$ , at 330 K determined from Rietveld analysis

Temperature/ K		330			
Space group	<i>Pbca</i>	<i>wt %</i>	96.4(2)		
<i>a/ Å</i>	10.9417(8)	<i>b/ Å</i>	21.9010(1)	<i>c/ Å</i>	10.9390(7)
Wy. Sym. – $\delta c$ all	<i>x</i>	<i>y</i>	<i>z</i>	<i>SOF</i>	$U_{iso} / \text{Å}^2$
S(1)	0.0066(16)	0.0012(13)	0.2510(24)	1	$6(1) \times 10^{-5}$
S(2)	-0.0089(20)	0.2555(10)	0.2537(19)	1	$6(1) \times 10^{-5}$
S(3)	0.2491(18)	0.1262(14)	0.2604(23)	1	$6(1) \times 10^{-5}$
S(4)	0.2328(22)	0.0007(11)	0.5068(25)	1	$6(1) \times 10^{-5}$
S(5)	-0.0111(20)	0.1322(10)	0.4871(22)	1	$6(1) \times 10^{-5}$
S(6)	0.0002(20)	0.1151(9)	0.0019(21)	1	$6(1) \times 10^{-5}$
S(7)	0.2505(18)	0.1209(11)	0.7478(21)	1	$6(1) \times 10^{-5}$
S(8)	0.2582(20)	0.2465(12)	0.4936(28)	1	$6(1) \times 10^{-5}$
Cu(1)	0.1291(10)	0.0591(6)	0.3685(12)	1	0.0210(1)
Cu(2)	0.1101(9)	0.0645(4)	0.6330(9)	1	0.0210(1)
Cu(3)	0.3900(11)	0.0637(5)	0.3634(11)	1	0.0210(1)
Fe(4)	0.3709(10)	0.0589(5)	0.6302(13)	1	0.0210(1)
Fe(5)	0.1251(9)	0.1892(5)	0.3719(10)	1	0.0210(1)
Cu(6)	0.1446(8)	0.1984(4)	0.6494(11)	1	0.0210(1)
Cu(7)	0.3782(12)	0.1891(6)	0.3630(12)	1	0.0210(1)
Cu(8)	0.3807(10)	0.1880(5)	0.6217(12)	1	0.0210(1)
Cu(9)	0.147636	0.072083	0.899562	0.864(13)	0.0210(1)
Cu(10)	0.334458	0.083282	0.08586	0.821(10)	0.0210(1)
Cu(11)	0.151069	0.177889	0.098497	0.753(14)	0.0210(1)
Cu(12)	0.373422	0.187015	0.890558	0.833(10)	0.0210(1)
Cu(13)	0.133197	0.068661	0.118809	0.223(13)	0.0210(1)
Cu(14)	0.380416	0.063189	0.878012	0.199(10)	0.0210(1)
Cu(15)	0.183684	0.161306	0.916054	0.200(14)	0.0210(1)
Cu(16)	0.302312	0.146219	0.066445	0.107(10)	0.0210(1)
Chalcocite -like phase	Space group	Fm-3m	<i>wt %</i>	3.6(2)	
<i>a/ Å</i>	5.5105(4)				
Label, Wy. Sym.	<i>x</i>	<i>y</i>	<i>z</i>	<i>SOF</i>	$U_{iso} / \text{Å}^2$
S(1), <i>4a</i>	0	0	0	1	0.0162(21)
Cu(1), <i>8c</i>	0.25	0.25	0.25	0.52	0.0162(21)
Cu(2), <i>32f</i>	0.339(3)	0.339(3)	0.339(3)	0.095	0.0162(21)
Overall	$R_{wp}/\%$	3.64	$R_p/\%$	6.15	
150 ° bank	$R_{wp}/\%$	3.74	$R_p/\%$	6.18	
90 ° bank	$R_{wp}/\%$	3.54	$R_p/\%$	5.53	
50 ° bank	$R_{wp}/\%$	3.67	$R_p/\%$	6.92	
	$\chi^2$	2.639			

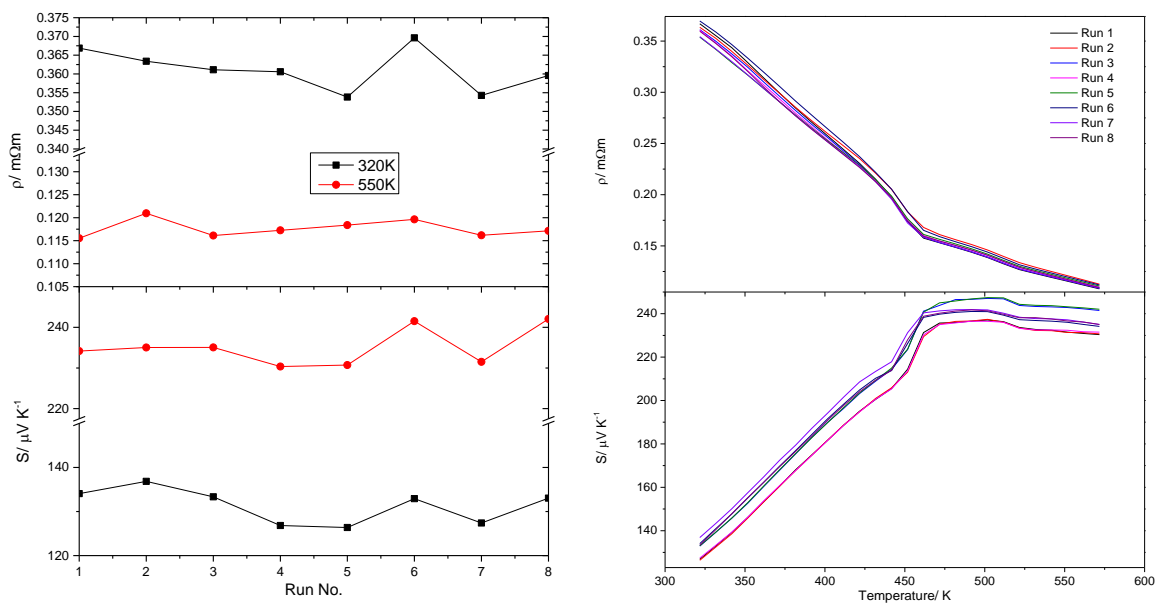
Crystallographic parameters for the 2a phase of copper rich bornite sample,  $\text{Cu}_{5.08}\text{Fe}_{0.92}\text{S}_4$ , at 475 K determined from Rietveld analysis.

Space Group	<i>F23</i>					
Temperature	475 K					
Wt. Frac.	0.8821					
<i>a</i> / Å	=	10.97974(5)				
Name	sym	<i>x</i>	<i>y</i>	<i>z</i>	<i>U</i> <sub>iso</sub> / Å <sup>3</sup>	<i>SOF</i>
Cu(3t') M(3)	16e	0.19529(119)	0.19529(119)	0.30471(119)	0.0435(3)	0.080(4)
Cu(1) M(1)	16e	0.88031(30)	0.88031(30)	0.88031(30)	0.0435(3)	0.722(4)
Cu(2) M(2)	16e	0.87752(32)	0.87752(32)	0.62248(32)	0.0435(3)	0.875
S(1)	4a	0	0	0	0.0185(3)	1
S(2)	4b	0	0	0.5	0.0185(3)	1
S(3)	24g	0.25	0.25	-0.00126(23)	0.0185(3)	1
Cu(3t'')M(3)	16e	0.15875(50)	0.15875(50)	0.34125(50)	0.0435(3)	0.381(4)
Cu(4t') M(4)	16e	1.12563(101)	1.12563(101)	1.12563(101)	0.0435(3)	0.168(9)
Cu(4t'') M(4)	16e	1.15148(104)	1.15148(104)	1.15148(104)	0.0435(3)	0.225(4)
Fe(1) M(1)	16e	0.88031(30)	0.88031(30)	0.88031(30)	0.0435(3)	0.125
Fe(2) M(2)	16e	0.87752(32)	0.87752(32)	0.62248(32)	0.0435(3)	0.125
Fe(3t') M(3)	16e	0.12133(166)	0.12133(166)	0.37867(166)	0.0435(3)	0.125
Fe(4t') M(4)	16e	1.12563(101)	1.12563(101)	1.12563(101)	0.0435(3)	0.125
chalcocite-like						
space group	<i>Fm-3m</i>					
weight fraction	11.08(3)					
<i>a</i> / Å	=	5.50976(25)				
Name	sym	<i>x</i>	<i>y</i>	<i>z</i>	<i>U</i> <sub>iso</sub> / Å <sup>3</sup>	<i>SOF</i>
S1	4a	0	0	0	0.0167(9)	1
Cu1	8c	0.25	0.25	0.25	0.0167(9)	0.407(9)
Cu2	32f	0.3377(10)	0.3377(10)	0.3377(10)	0.0167(9)	0.123(2)
Overall	<i>R</i> <sub>wp</sub> /%	3.44	<i>R</i> <sub>p</sub> / %	5.35		
150 ° bank	<i>R</i> <sub>wp</sub> /%	3.37	<i>R</i> <sub>p</sub> / %	4.85		
90 ° bank	<i>R</i> <sub>wp</sub> /%	3.41	<i>R</i> <sub>p</sub> / %	4.59		
50 ° bank	<i>R</i> <sub>wp</sub> /%	3.60	<i>R</i> <sub>p</sub> / %	7.08		
	$\chi^2$	2.219				

Crystallographic parameters for the *a* phase of the copper-rich bornite sample,  $\text{Cu}_{5.08}\text{Fe}_{0.92}\text{S}_4$ , 565 K determined from Rietveld analysis.

Space group	<i>F23</i>						
Temperature	565 K						
Weight fraction	0.9400(4)						
<i>a</i> / Å	=	5.51688 (2)					
Name	sym	<i>x</i>	<i>y</i>	<i>z</i>	<i>U</i> <sub>iso</sub> / Å <sup>3</sup>	<i>SOF</i>	
Cu(1t')	<i>4c</i>	0.25	0.25	0.25	0.0533(4)	0.369(8)	
Cu(2t')	<i>4d</i>	0.25	0.25	0.75	0.0533(4)	0.440(12)	
Fe(1t')	<i>4c</i>	0.25	0.25	0.25	0.0533(4)	0.093(9)	
Fe(2t')	<i>4d</i>	0.25	0.25	0.75	0.0533(4)	0.157(9)	
S	<i>4a</i>	0	0	0	0.0279(4)	1	
Cu(1t'')	<i>16e</i>	0.330	0.330	0.330	0.0533(4)	0.080(3)	
Cu(2t'')	<i>16e</i>	0.648	0.648	0.648	0.0533(4)	0.030(2)	
Chalcopyrite phase							
spacegroup	<i>Fm-3m</i>						
<i>a</i> / Å	=	5.3010(2)					
Name	sym	<i>x</i>	<i>y</i>	<i>z</i>	<i>U</i> <sub>iso</sub> / Å <sup>3</sup>	<i>SOF</i>	
Cu	<i>4a</i>	0	0	0	0.0327	1	
Fe	<i>4b</i>	0	0	0.5	0.0327	1	
S	<i>8d</i>	0.25	0.25	0.125	0.0327	1	
Overall	<i>R</i> <sub>wp</sub> /%	2.92	<i>R</i> <sub>p</sub> / %	2.84			
150 ° bank	<i>R</i> <sub>wp</sub> /%	2.96	<i>R</i> <sub>p</sub> / %	3.33			
90 ° bank	<i>R</i> <sub>wp</sub> /%	2.85	<i>R</i> <sub>p</sub> / %	2.30			
50 ° bank	<i>R</i> <sub>wp</sub> /%	2.99	<i>R</i> <sub>p</sub> / %	3.08			
	$\chi^2$	1.629					

## Appendix P.



Left: Electronic transport properties at a given temperature as a function of successive thermal cycling measurements for  $\text{Cu}_{4.972}\text{Fe}_{0.968}\text{S}_4$ . Right: Stacked plots of each individual measurement of  $\text{Cu}_{4.972}\text{Fe}_{0.968}\text{S}_4$  in the thermal cycling sequence. Both: Top panel, resistivity; bottom panel, Seebeck coefficient.